EFFECTS OF FUEL PARTICLE AND REACTOR CORE DESIGN ON MODULAR HTGR SOURCE TERMS

Vol. 1

by

Michael G. Izenson

B.S. Nuclear Engineering, Massachusetts Institute of Technology (1983)

M.S. Nuclear Engineering, Massachusetts Institute of Technology (1983)

SUBMITTED IN PARTIAL FULFILLMENT
OF THE REQUIREMENTS FOR THE DEGREE OF

DOCTOR OF PHILOSOPHY
IN NUCLEAR ENGINEERING

at the

MASSACHUSETTS INSTITUTE OF TECHNOLOGY

February, 1987

Signature of Author _____
Department of Nuclear Engineering
September 22, 1986

Certified by _____
David D. Lanning
Thesis Supervisor

Certified by _____
Lawrence M. Lidsky
Thesis Supervisor

Accepted by _____
Allan F. Henry
Chairman, Department Graduate Committee

EFFECTS OF FUEL PARTICLE AND REACTOR CORE DESIGN ON MODULAR HTGR SOURCE TERMS

by

Michael G. Izenson

Submitted to the Department of Nuclear Engineering on September 21, 1986, in partial fulfillment of the requirements of the Degree of Doctor of Philosophy in Nuclear Engineering

ABSTRACT

The modular high-temperature gas-cooled reactor (HTGR) is a passively safe nuclear power plant. In this work, the influence of important fuel quality and reactor design parameters on radionuclide release from modular HTGR cores is investigated. Attention is restricted to "well designed" reactors, which utilize high quality fuel and are able to passively dissipate all decay heat without exceeding fuel temperature limits. Under these circumstances, fission product release during operation and thermal transients is quite low, and arises due to a small number of simple mechanisms. This release is highly dependent on fuel quality.

A new mathematical technique for describing fuel processes in a randomly, continuously refueled pebble bed reactor is proposed. This "branch notation" provides a probabilistic description of the fuel state distribution in a stationary reactor. The branch variable β summarizes a fuel element's path through the core. For any fuel property which can be expressed as a function of β, the expected value and variance in any core location may be calculated. Techniques for estimating the probability that a group of reactive pebbles coalesces at random to form a stochastic "hot spot" are developed.

The nuclear reactions which determine heavy metal and fission product concentrations are described by linear differential equations. In a stationary reactor, an analytic solution takes the form of position dependent transition matrices. These matrices allow fuel isotopic composition to be expressed as a function of the branch variable β. The expected value and variance of isotopic number densities, burnup, and local power density are calculated by the FUPAR code. FUPAR used in conjunction with the already existing VSOP code calculates a complete set of operating parameters. Results of FUPAR/VSOP analysis are in good overall agreement with published design data.

The severity of random hot spots is shown to vary directly with local mean power density. It is shown that the probabilities of severe hot spots are very low during operation, and much lower during core heatup accidents.

Three reactor design variants are analyzed with FUPAR/VSOP. The cores differ in the inclusion of gadolinia burnable poisons (to mitigate water ingress reactivity effects), or in coolant temperatures (for direct cycle application). The three cores are compared in terms of their operating parameters, the probability of random hot spots, and temperatures achieved following a hypothetical depressurization accident.

A release model for metallic fission products is formulated. Fission product concentration profiles within fuel particles are expressed as functions of the branch variable, and the core-wide distribution of profiles and release rates may be calculated. This distribution provides the initial conditions for a transient analysis. The PDIF computer code performs these calculations.

The PDIF code has analyzed fission product release from fuel particles in the three cores treated above. Steady state activity is dominated by release due to heavy metal contamination and recoil from kernels with damaged coatings. Accident induced releases are dominated by release from kernels with damaged coatings as well, except for the most severe transients in which diffusion through intact coatings becomes significant. Analysis of nominal and hypothetical very high quality fuel indicates significant further reductions in release are possible.

Thesis Supervisor: Dr. David D. Lanning
Title: Professor of Nuclear Engineering
Thesis Supervisor: Dr. Lawrence M. Lidsky
Title: Professor of Nuclear Engineering

ACKNOWLEDGMENTS

I would like to express my appreciation to Doctors David D. Lanning and Lawrence M. Lidsky for their guidance in the course of this work. Not only have they assisted with specific research issues, they have also set examples of professionalism and engineering insight which I shall always try to emulate. I am fortunate to have had the chance to work with these men.

Thanks are due as well to my office mates. Mr. Raymond Coxe (soon to be Dr. Coxe) gave me invaluable assistance with the computers upon which this document was written. Dr. Joy Maneke assisted in the production of several previous reports leading up to this thesis, and provided much information regarding fission product transport.

I owe many thanks to the people of Stone and Webster Engineering Corporation, without whose computational assistance my work could not have been completed. Mr. Paul Burger's patient help with the computer is much appreciated, as well as Mr. Charles Doherty's assistance with administrative issues. The help of Mr. William Sheridan and Mr. Alan Isherwood in arranging for the use of Stone and Webster's computational facilities was invaluable.

The financial assistance of the National Science Foundation is greatly appreciated. The aid of Gas Cooled Reactor Associates during the final stage of my research is gratefully acknowledged.

Researchers at the Kernforschungsanlage, Jülich provided much of the information upon which this report is based. Dr. H.J. Rütten, in

particular, provided the VSOP and THERMIX computer programs, as well as numerous documents dealing with all aspects of gas cooled reactors and fuel. Dr. Heinz Nabielek was very helpful, as were as Drs. Moorman, Verfondern, and Teuchert.

Thanks also to Paul Kasten, Mike Kania, Bob Wichner, Dave Vondy, David Moses, and John Cleveland at Oak Ridge National Laboratory for many helpful discussions.

The help of Walt Simon and Fred Silady of GA Technologies is gratefully acknowledged.

The assistance of Ray Coxe and Melissa Rathmell during the final stages of preparation of this document is deeply appreciated.

Finally, my wife, Nancy, deserves all my gratitude for her love and support. Thanks also to my son Benjamin, for compelling me to complete my research and for sleeping often enough to let me do so.

TABLE OF CONTENTS

LIST OF FIGURES

LIST OF TABLES

CHAPTER 1: INTRODUCTION

1.1 SCOPE AND OBJECTIVES OF THIS WORK

The Modular High Temperature Gas-cooled Reactor (MHTGR) promises to offer a more attractive option to US electric utilities than the current generation of water-cooled nuclear plants. Fundamental characteristics of this reactor design reduce the risk to the public by reducing both the frequency and consequences of fission product release. These reductions could enable entirely new forms of construction, regulation, and operation. The characteristics of such a power system may be better suited to the financial and regulatory environment currently faced by utilities. This work examines the effects of reactor and fuel design on the amount of fission products released from an MHTGR core due to an important class of accidents.

In this study we restrict ourselves to what shall be defined as the class of "well designed" MHTGR reactors, which have the following characteristics:

- High quality fuel: Due to the importance of minimizing fission product release, the fuel used in the reactor will be manufactured to as high a quality as economically achievable.

- Passively safe core: The reactor's thermal characteristics enable passive dissipation of all decay heat without exceeding the fuel's critical failure temperature.

Advances in fuel fabrication technology and core design have now been combined to make such a reactor a realistic concept [R2, H2]. Work

is presently under way in the US with the goal of demonstrating the operation of such a reactor, and several such reactors have been proposed by companies in the Federal Republic of Germany (FRG) [R2].

The goal of this work is to examine the effects of important fuel and reactor core design parameters on the fission product release from the fuel. We particularly wish to identify the features which are most important in achieving passive safety in light of recent advances in fuel fabrication technology. Development of methods for probabilistic analysis of continuously refueled pebble bed reactors is also necessary. This dissertation is undertaken as part of a group project studying many aspects of possible commercial reactors based on the MHTGR. Accordingly, the following specific objectives are to be met:

(1) Prediction of reactor operating parameters: Given a few general design parameters, we wish to calculate detailed neutron flux and materials concentration distributions in the steady state reactor. Such information is the starting point for fission product release calculations.

(2) Development of terminology, mathematics, and procedures for analyzing fuel behavior in a continuously fueled pebble bed reactor: The goal is to incorporate and investigate a new method to study the effects of the stochastic refueling process on fuel performance.

(3) Quantification of the uncertainty associated with the continuous fueling process: The aim is to calculate the probability that "random hot spots," of arbitrary size and severity, will form inside the pebble bed.

(4) Examination of the effects of Gadolinium burnable poisons on fuel performance, particularly regarding water ingress effects, power peaking, and pebble recycle rates: Due to the energy-dependence of gadolinium's neutron absorption cross section, it is possible that inclusion of small amounts of gadolinium in fresh fuel as a burnable poison can reduce the reactivity effects of water ingress into the pebble bed.

(5) Examination of the effects of increased core temperatures: The direct cycle gas turbine is a promising future application of modular HTGR technology. The goal is to investigate the effects of this mode of operation of fission product retention.

(6) Prediction of the steady-state release of fission products during reactor stationary operation: The rate of fission product release from fuel determines the circulating and plated-out activity in the primary system. These fission products contribute significant fractions to potential source terms.

(7) Prediction of the release of fission products during thermal transients: Diffusive release of fission products from fuel particles during high-temperature transients may also contribute significant amounts to the reactor source term.

(8) Investigation of the effects of fuel design parameters on fission product release: Recent advances in fuel fabrication technology indicate the possibility of higher levels of fuel quality than currently specified in reactor designs. It is desired to investigate the effects of such ultra-high quality fuel on fission product release.

1.2 PASSIVELY SAFE REACTORS

In recent years, a number of proposals have been made for the design and testing of passively safe nuclear reactors. The goal is to design a nuclear power plant which is more attractive to the US electric utility industry than the current generation of light water reactors. Specific objectives to be met vary from design to design, and may include:

- reduction of uncertainty regarding the length of the licensing and construction period;
- reduction of the risk of events which could result in the full or partial loss of investment in the plant;
- placing the bulk of regulatory accountability (i.e., quality control and assurance) in the hands of vendor companies;
- reduction of emergency planning requirements associated with nuclear plants; and finally
- reducing the costs and requirements placed on balance of plant systems by decoupling them from the primary nuclear system.

These goals are attained through two design criteria:

- *Increased level of safety:* Under all conditions, no credible event (frequencies greater than approximately 5×10^{-7} per year) can cause a significant release of fission products from the reactor core.
- *Use of passive safety features:* the reliance on engineered safety systems to achieve the desired level of safety is minimized or eliminated. Retention of fission products is to be accomplished to as great an extent possible by inherent properties of the core and fuel alone.

Of course, different passively safe reactors may meet the above criteria to varying extents, depending on the details of their designs. Three reactor designs in particular have been seriously investigated. One is ASEA-ATOM's PIUS reactor, which achieves passive safety by submerging the reactor core in a large pool of cool borated water. Enough water is provided to absorb decay heat from the reactor for one week without operator intervention [L1]. A second design involves a liquid metal-cooled reactor (LMR), which takes advantage of the heat transfer properties of liquid sodium to passively remove decay heat from the reactor core and transport it to the reactor vessel walls, from whence it is removed by natural air circulation [L1]. This work concerns the third type of passively safe reactor, the modular high-temperature gas-cooled reactor (MHTGR). This reactor employs an all-ceramic core with unique coated particle fuel which can endure extremely high temperatures without losing retention of fission products. Combined with proper core design, such a reactor can lose all coolant yet still successfully conduct and radiate away all decay heat without releasing significant amounts of fission products.

1.3 THE PEBBLE BED MHTGR

The pebble bed modular high-temperature gas-cooled reactor is graphite-moderated and helium-cooled. Its passive safety features arise from two fundamental design characteristics:

(1) High quality coated particle fuel construction ensures almost complete fission product retention up to some relatively high critical temperature; and

(2) The reactor core's thermal characteristics (high heat capacity and large surface/volume ratio) enable dissipation of decay heat following a loss of coolant through passive conduction and radiation without exceeding the fuel's critical temperature.

Thus, retention of radionuclides does not depend on maintaining a supply of coolant to the reactor core. Risk dominance is thereby shifted to an entirely different (and much lower frequency) class of accidents [L3]. The result is a nuclear power plant which satisfies the passive safety requirements.

The coated nuclear fuel particle is the basis of the MHTGR's safety characteristics. Figure 1.1 presents a cross sectional view of one of these particles, whose total diameter is about one millimeter. The central spherical core is the fuel kernel, which contains the reactor's fissile material. The kernel is surrounded by several pyrolytic coating layers, which serve as a pressure vessel to retain gaseous fission products and a barrier to the diffusive release of volatile metallic fission products. A detailed description of the coating layers and

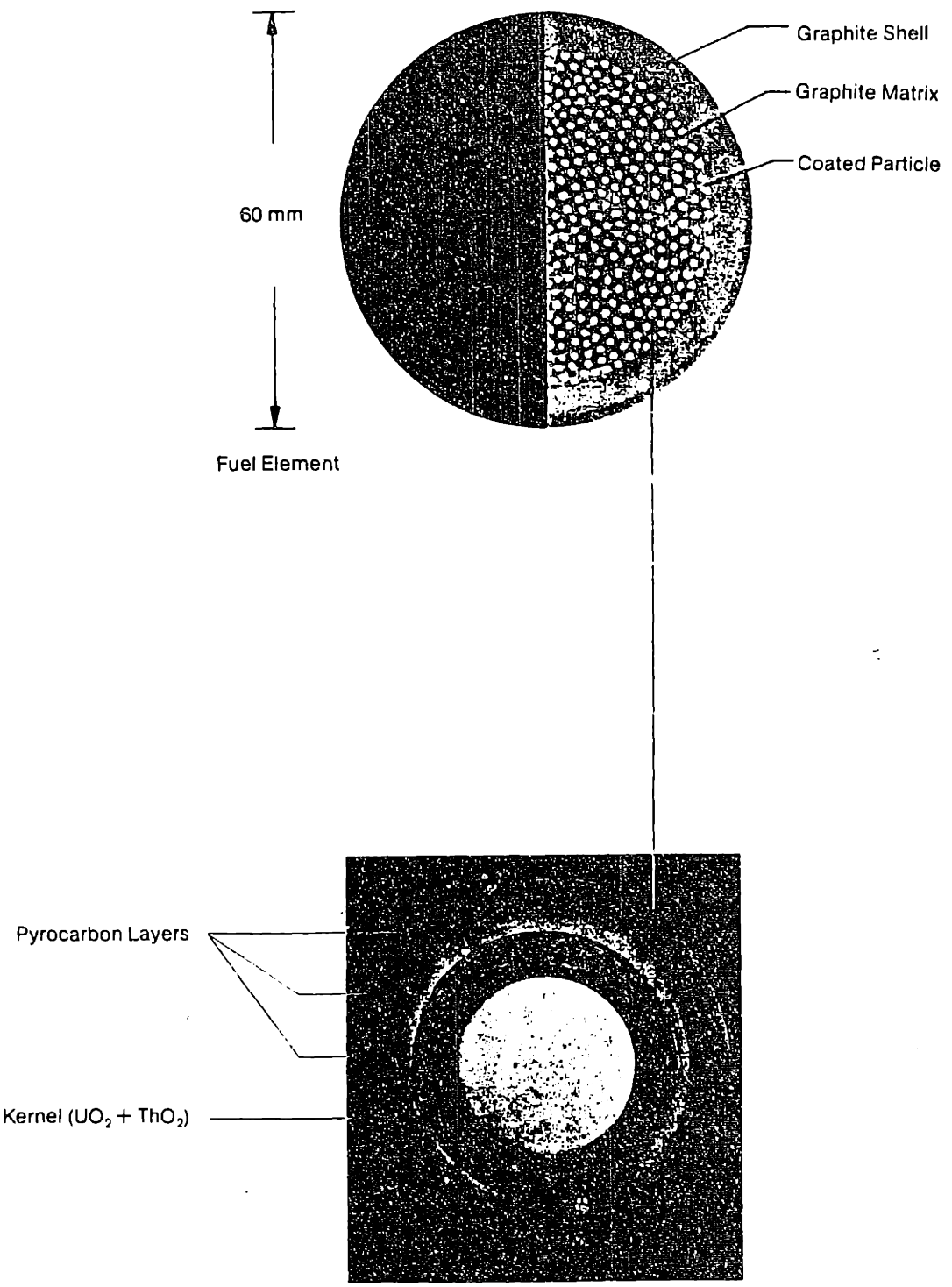

FIG. 1.1: An HTGR coated fuel particle and fuel element.

their functions is given in Chapter 2.

Roughly 10,000 coated particles are loaded into a single pebble fuel element, also shown in Figure 1.1. The coated particles are embedded in a graphite matrix, and a 0.5 cm-thick layer of unfueled graphite surrounds the entire construction. A typical MHTGR core contains approximately 360,000 such fuel elements.

Figure 1.2 illustrates one proposed pebble bed MHTGR, the 200 MWth HTR-MODUL designed by KWU/Interatom. The reactor core is enclosed in a steel pressure vessel, located alongside and above the steam generator vessel. Helium coolant flows downward through the pebble bed, through the inside of the annular duct to the steam generator, and then through the steam generator tubes. The helium circulator (located atop the steam generator) then forces the helium back through the connecting duct to the reactor. The entire nuclear steam supply system is located below grade in a concrete silo. The reactor's passive safety features are independent of containment building design or containment failure. Design parameters for the reactor are presented in Table 1.1.

The MHTGR's salient design features are a direct consequence of the passive safety goal. The core's relatively small diameter (3.0 m) arises from the need to shut the reactor down without inserting control rods into the pebble bed. Control rods in a passively safe pebble bed HTGR enter only the reflector (in contrast to other HTGR designs such as the THTR, in which control rods are inserted directly into the pebble bed). In addition to the control rods, a backup shutdown system of small absorber balls (or KLAK system) is provided.

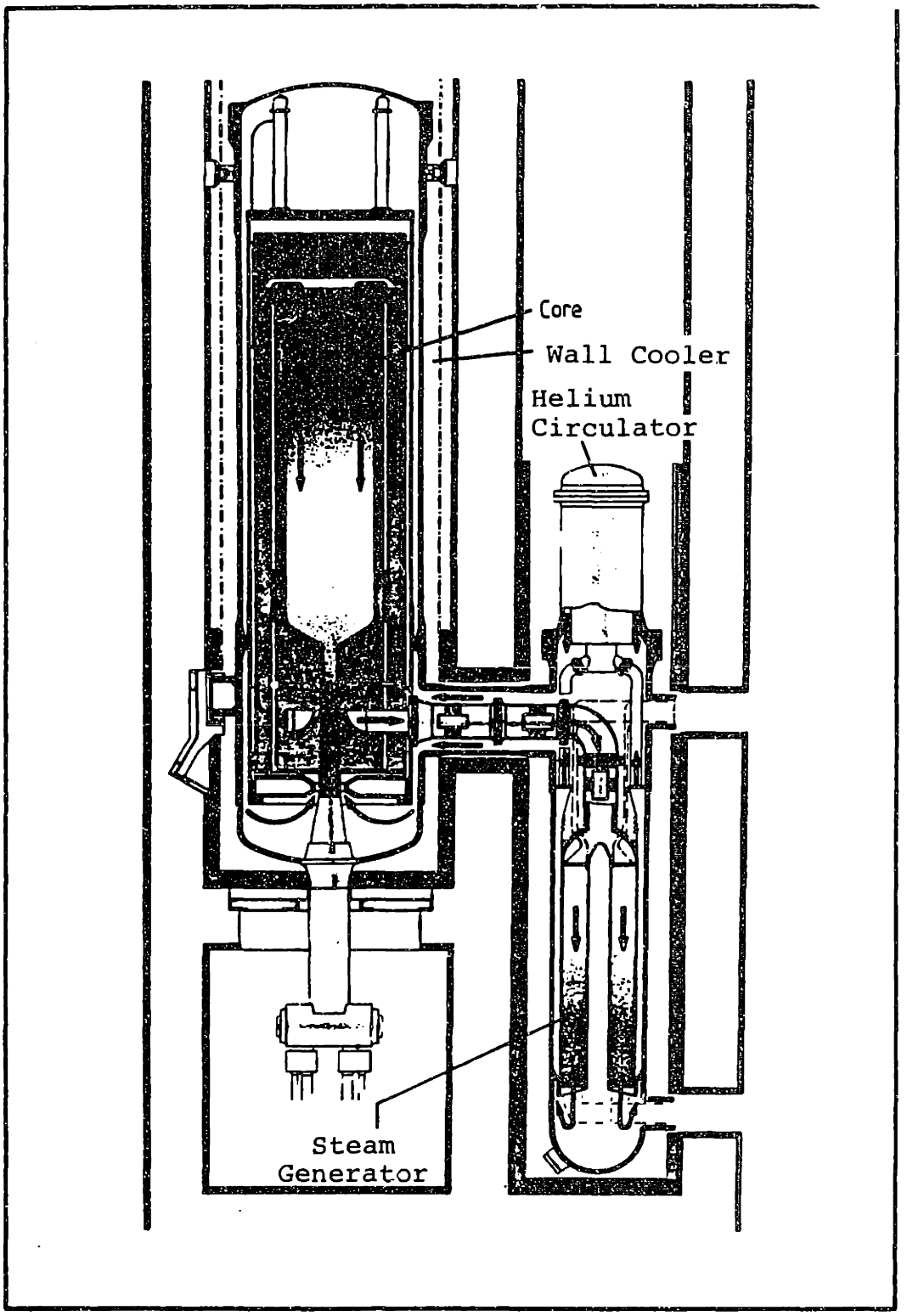

FIG. 1.2: The 200 MWth KWU/Interatom HTR-Modul.

TABLE 1.1: DESIGN PARAMETERS FOR THE KWU/INTERATOM 200 MWTH HTR-MODUL

Thermal power	200 MW
Core diameter	3.0 m
Core height	9.0 m
Mean power density	3.0 MW/m^3
Helium temperatures	250/700 C
System pressure	60 bar
Number of control rods	6
Number of absorber ball systems	18
Diameter of pressure vessel	5.8 m
Height of pressure vessel	23.8 m
Fuel cycle	uranium/plutonium
Loading scheme	multi-pass
Fuel element heavy metal loading	7 g/pebble
Discharge burnup	80,000 MWD/MTHM
Fuel in-core residence time	1,020 days
Feed fuel enrichment	7.8%
Fissile material in core	94 kg
Helium mass flow	76 kg/sec
Primary circuit pressure drop	1.2 bar

(SOURCE: Ref. R2)

The fission product retention requirement limits maximum core temperatures following depressurization to 1600C, and thus places a limit on average power density of about 3 MW/m^3. In order to maximize power output under these constraints, the core is made as tall as possible. The upper limit of about 10m in height is due to pressure drop and xenon stability considerations [L3].

Wall coolers are located outside the reactor vessel to remove decay heat radiated from the vessel walls; no decay heat removal systems are necessary inside the reactor vessel. This is a direct consequence of the reactor's ability to passively dissipate decay heat through conduction and radiation. These wall coolers limit investment risk, but are not required to meet the safety goals. The steam generator and the reactor core are physically separated in order to protect the steam generator and helium circulator from overheating in the event that core cooling is interrupted.

A reactor with the above design features has effectively eliminated the loss of coolant accident as a dominant source of risk. As a result, the major contributor to the residual risk from an MHTGR is the class of water ingress accidents [L3]. Limitation of the heavy metal loading in fresh fuel is a passive design feature which reduces the severity of water ingress. A maximum value of 7 grams of heavy metal per pebble limits the reactivity increase due to water ingress to levels which do not result in dangerous power surges [L3].

The reactor core design considered here differs significantly from that chosen by participants in the U.S. modular HTGR program. The U.S. reactor core is made of prismatic fuel elements, arranged in an annulus with inner and outer graphite reflectors. This arrangement permits higher overall reactor powers.

A pebble bed core requires a continuously operating refueling system. A schematic diagram of the refueling system at the THTR reactor (whose basic operation is similar to that of an MHTGR) is shown in Figure 1.3. Fuel is withdrawn from the bottom of the reactor core, and is first passed through a "singularizer," which passes only a single pebble at a time to the following stages. A damaged sphere separator next removes fuel elements which are broken or cracked, and then the pebbles are passed through a burnup measurement device. In the case of THTR, this is a small subcritical reactor whose neutronic response to the passage of a fuel element is an indicator of the burnup. Fuel elements which exceed a specified discharge limit are sent to a discharge facility, while the rest are recycled to the top of the pebble bed.

Pebble refueling systems are able to operate at rather high frequencies, which is fortunate for the modular HTGR. In order to achieve as uniform an axial power shape as possible (to limit peak power densities and thus post-depressurization temperatures), it is necessary to recycle the fuel as quickly as possible. The HTR-MODUL recycles a fuel element an average of 15 times prior to discharge. At an 80%

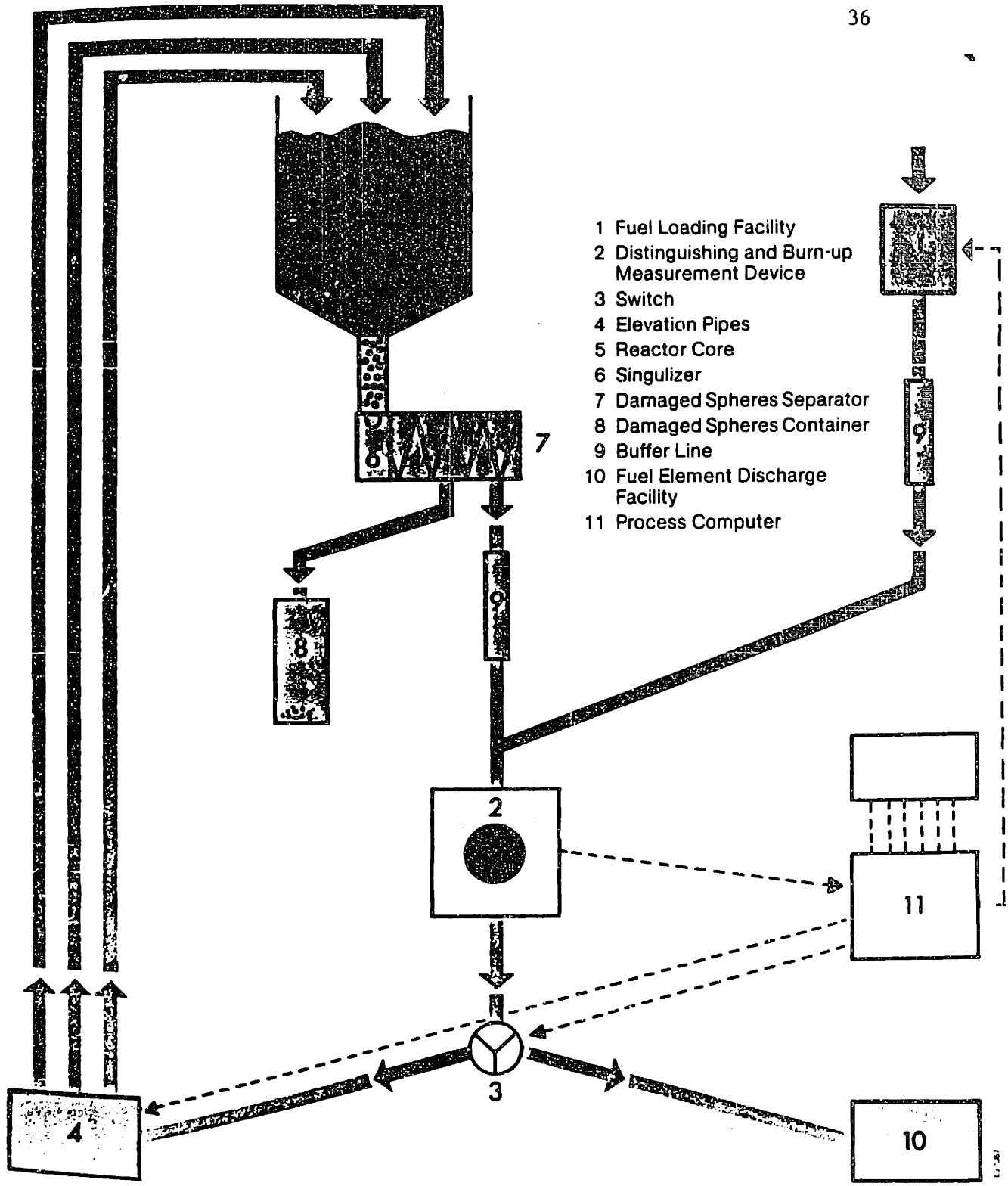

FIG. 1.3: A pebble-bed reactor refueling system.

capacity factor, this corresponds to over 3000 pebbles per day.

1.4: OVERVIEW OF RESEARCH

The remainder of this report is organized as follows. Chapter 2 covers HTGR fuel, treating in detail the mechanisms by which fission products may be released. Recent experimental results on state-of-the-art high-quality fuel indicate that modes of particle failure which have historically been significant have effectively been eliminated through advanced manufacture. The result is a fuel particle with extreme resilience, able to survive operation and modular-HTGR transients without losing its retentive ability. It is shown that the only release mechanisms which need be considered are those due to manufacturing defects (heavy metal contamination and defective coating layers) and high temperature diffusion through intact coatings. Based on this proposition, a simple model for fuel particle behavior during reactor operation and high-temperature transients is proposed.

Chapter 3 develops a new mathematical technique for describing processes in a continuously and randomly refueled pebble bed reactor. This is accomplished by dividing the reactor core into a finite number of radial "drop zones." Each drop zone is characterized by a drop probability, which is the probability of a pebble traveling through that drop zone on any pass through the core. The branch variable β is introduced as a means of summarizing a fuel element's irradiation

history in terms of the drop zones through which it has traveled. It is shown that if the drop probabilities and pebble flow rates are known, the number of pebbles in the stationary core with any particular irradiation history may be calculated. For any fuel property which may be expressed as function of β, the spatial distribution may be calculated the same way. Probability density functions, or "branch probabilities," are derived which characterize the likelihood of finding any particular sort of pebble in any core zone. Expectation operators are defined which enable the computation of expected values of fuel parameters as a function of their pass number. Methods are derived for the conversion of "Lagrangian" quantities, which apply to particular fuel elements, to "Eulerian" quantities, which apply to a particular region of the core. The quasi-two dimensional approximation is introduced as a practical means of computing late-pass fuel parameters when a variable number of passes through the core is possible prior to discharge. Finally, the basic concepts of random hot spot analysis are introduced. Methods are derived for estimating the probability of random groupings of fuel elements with higher than expected values of important parameters. Should pebble bed HTGRs be licensed for operation in the US, it is expected that this information will be required. Heretofore, it has simply been assumed that these probabilities are very small; this work develops a method to quantify them.

Chapter 4 addresses calculation of operating parameters of a steady state equilibrium (stationary) pebble bed reactor. Based on the nuclear reactions which control the generation and decay of heavy metal and

fission product isotopes, matrix differential equations are developed which summarize the changes in vectors of heavy metal and fission product concentrations subject to a neutron flux. Since the reactor core is stationary (i.e., the probability functions associated with reactor operating parameters are constant in time), these equations are linear and time invariant if applied within a region that is small compared to the entire reactor. In this case, analytic solutions for vectors of heavy metal and fission product concentrations at the exit of such a region are derived in terms of the region's properties. These solutions are expressed in the form of transition matrices, a set of which may be calculated for each discrete core zone. By grouping transition matrices in the proper order, fuel isotopic composition may be expressed as a function of the branch variable. Use of branch expectation operations enables the calculation of expected materials densities as a function of position in the stationary core, if an input neutron flux distribution is known. The FUPAR computer code has been developed to perform these calculations. When used iteratively with the already-existing VSOP code (from KFA Jülich), FUPAR can compute detailed reactor operating parameters. This is an entirely new method for calculating reactor parameters, whereas previous methods rely on simulation of core operation through the entire "running in" period prior to achieving steady state.

Chapter 5 summarizes results of FUPAR/VSOP analyses of several MHTGR design variants of interest. A base case 200 MWth core, which is quite similar to the HTR-MODUL design by KWU/Interatom, is discussed

first. As this reactor has been discussed extensively in the literature, FUPAR/VSOP's results may be compared with those found in the literature. Stationary power and temperature distributions are presented, as well as the results of random hot spot analyses. It is found that the probability of random groupings of pebbles with off-normal characteristics significant from a safety standpoint are extremely small. The THERMIX code [V3] is used to analyze the response of this reactor to a depressurized core heatup accident. A second core is similar to the base core, except for the inclusion of a small quantity of gadolinium burnable poison in the feed fuel elements. The same analyses are presented as for the previous case, as well as a brief analysis of the effects of water ingress on the core's reactivity. Use of burnable poisons to offset these effects has not been examined previously. The final core to be analyzed is also similar to the base case, but operates with higher coolant temperatures to drive a direct-cycle gas turbine system. The analyses emphasize the importance of a uniform power density distribution, both in reducing the severity of random hot spots and in maintaining accident temperatures beneath 1600C.

Chapter 6 develops techniques for the analysis of fission product diffusion and release within fuel particles, during both reactor operation and high-temperature thermal transients. A fuel particle is idealized as a one-dimensional spherical system, in which effective diffusivities for the transport of metallic fission products are known input quantities. The particle is discretized into a set of concentric

spherical shells. Difference equations are derived for the concentrations of the fission product of interest in each spherical shell in the particle model as a function of time. Once again, since the reactor is stationary, the difference equations may be written in linear, time-invariant, vector/matrix form within a small zone of the reactor. The vector of interest actually represents the fission product concentration profile within the fuel particle. An analytic solution is derived and expressed as position dependent transition matrices. Using branch notation, expected values of fission product release and concentration profiles can be calculated in each zone of the operating stationary reactor. Application of probabilistic methods to calculate expected values of particle concentration profiles is another original technique. The transition matrix solutions also apply to small time intervals within a thermal transient. Based on the steady-state expected profiles, the diffusive release during a high temperature excursion can be calculated. The PDIF computer code performs these calculations. It is anticipated that the linear nature of the analytic model will lead to consistent underprediction of release (the severity of this effect is to be determined in the next chapter). In addition, the chapter contains a brief analysis of the effects of pebble matrix graphite on fission product retention. Chapter 6 concludes with comparisons of PDIF results to analytic predictions from simple systems.

Chapter 7 details the results of PDIF analyses applied to the cores analyzed in Chapter 5. The steady state and transient reactor analyses from Chapter 5 are the basis for the release estimates. Assumptions are

necessary regarding the disposition of fission products generated by heavy metal contaminants and the rate of particle failure during irradiation. A simple analytic model is proposed with which to place an upper limit on the release from bare kernels during the depressurization transient. This release is often the dominant contribution, and it is found that PDIF's underestimation of kernel release is not more than a factor of two. All cores analyzed have very small release rates. Comparison between the reactors indicates that the base core has the lowest overall releases, while both the poisoned core and the direct-cycle core have higher transient release.

The last chapter presents a final summary of results and indicates avenues for further research.

CHAPTER 2: HTGR FUEL PERFORMANCE

HTGR fuel has two distinct advantages. First, the small size of the fundamental units, or fuel particles, enables large numbers of them to be studied simultaneously. Second, they remain stable under almost all conceivable reactor conditions. Experiments to study fuel performance under accident conditions are thus relatively easy to perform. For this reason, a large base of knowledge has been accumulated regarding fuel performance under both operating and accident conditions.

This chapter reviews the current status of HTGR coated particle fuel. Following a brief description and discussion of particle component functions, the techniques of fuel fabrication are discussed. Fuel manufacture is important because important performance parameters are determined at this stage. State of the art fabrication techniques can produce fuel with extremely low defect rates.

The identities of important fission products which the fuel particles must retain are reviewed, followed by a discussion of their irradiation behavior. There are a variety of phenomena which can damage fission product retention, but proper design and manufacture can minimize (or often eliminate) their occurence. Fuel performance under accident conditions is influenced by the much higher temperatures. These temperatures increases fission product mobility and may induce additional particle failures.

Finally, the possible release of fission products due to the most

significant hypothetical accidents is reviewed. The two most risk-dominant scenarios, core heatup and steam/water ingress, both may lead to fission product release. The source terms are comprised not only of fission products released from fuel which is damaged directly from the accident, but significant fractions may be due to activity released during reactor operation and accumulated within the primary circuit. In cores which are properly designed, the magnitude of release is highly dependent on fuel quality.

Finally, based upon recent advances in fuel fabrication technology and the design objectives of the modular HTGR, a performance model is proposed. This model is the basis for source term estimation in later chapters, and is intended to provide a simple but realistic picture of fuel performance in modular high temperature gas cooled reactors.

2.1: COATED PARTICLE FUEL: A GENERAL DESCRIPTION

The fuel is a key passive safety feature in modular high temperature gas-cooled reactors. Its unique, coated particle design essentially provides every milligram of fissile material with its own, miniature cladding. Furthermore, this cladding is all-ceramic, capable of withstanding extremely high temperatures (up to 1600C) without rupturing, melting, or becoming unacceptably permeable to fission products.

An idealized sketch (not to scale) of a fuel particle is presented in Fig. 2.1. Figure 2.2 is a ceramographic cross section of actual fuel particles. Design details given here reflect fuel particles

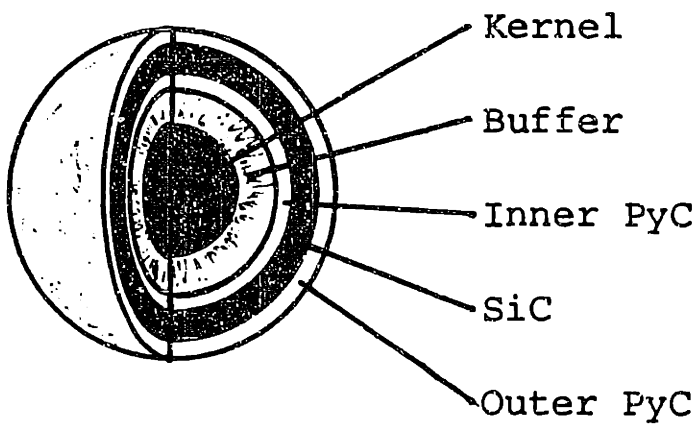

FIG. 2.1: The TRISO fuel particle design.

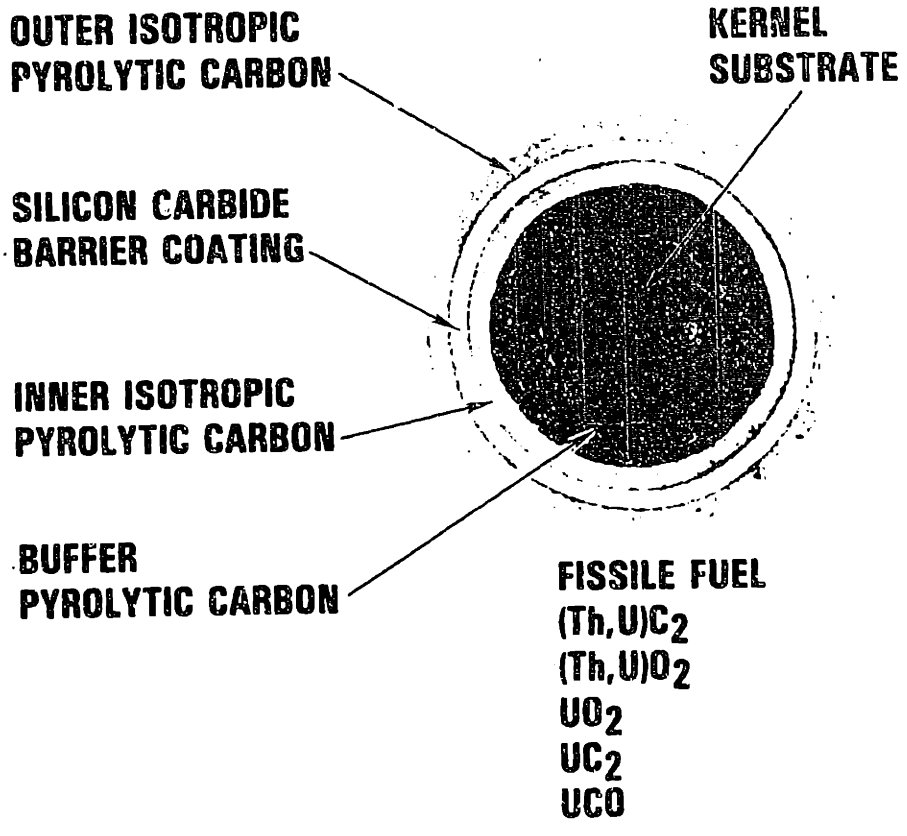

FIG. 2.2: Ceramographic cross section of HTGR coated fuel particles [K5].

manufactured in the FRG by Hochtemperatur Brennelement Gebau (HOBEG) GmbH. HOBEG is a subsidiary of Nuclear-Chemie und Metallurgie (NUKEM), and has fabricated fuel particles and pebbles for both the AVR research reactor and the 300 MWe THTR. The overall diameter of the entire particle is 800 microns (μ) or 0.8 millimeters. Actual fissile or fertile material is contained in the central *kernel*, which is approximately 500 μ in diameter. In general, the kernel may be composed of one of a variety of materials: UO_2, UC, UC_2, UCO, UO_2-ThO_2, UC-ThC, UC_2-ThC_2, PuO_2-ThO_2, PuO_2-UO_2, and PuO_xC_y are all possible materials [ref. T2]. The kernel is surrounded by a low-density pyrolytic carbon *buffer* layer, which is approximately 90 μ thick. Surrounding the buffer are three high-density pyrolytic layers. First is the inner pyrolytic carbon layer (IPyC), followed by the silicon carbide layer (SiC), and then the outer pyrolytic carbon (OPyC) layer. These layers are of roughly equal thicknesses. Design parameters for the reference fuel particle employed in German MHTGR designs are presented in Table 2.1.

The particle design shown in Fig. 2.1 is called "TRISO," because of the three high density layers. A simpler particle design, with only a single PyC layer surrounding the buffer, is called "BISO" for "buffered isotropic." As TRISO particles are the universal selection for passively safe reactors, issues concerning the BISO variety will not be discussed in this work. All particles referred to are to be assumed of the TRISO design.

Each of the particle components plays an important role in fission product retention. The kernel itself is an important diffusive barrier,

TABLE 2.1: TRISO FUEL PARTICLE DESIGN PARAMETERS

LAYER	MATERIAL	OUTER RADIUS	DENSITY
Kernel	UO_2	250 μ	10.8 g/cm^3
Buffer	Pyrolytic Carbon	340 μ	0.94 g/cm^3
Inner PyC	LTI[1] Carbon	380 μ	1.93 g/cm^3
SiC	Silicon Carbide	405 μ	3.19 g/cm^3
Outer PyC	LTI Carbon	445 μ	1.91 g/cm^3

(parameters are for standard LEU particles, HBK Project [H2])

(1) "LTI" stands for "Low Temperature Isotropic," referring to coating bed conditions.

delaying the release of gaseous fission products (FPs) into the buffer layer. The chemical properties of the kernel are also important. For example, carbide kernels have been found to release lanthanide fission products, which can eventually react with and damage the SiC layer. Oxide kernels, on the other hand, have ample free oxygen (due to fissions) to react with the lanthanides, forming very stable refractory oxide compounds which cannot migrate from the kernel.

Kernel composition also affects the rate at which internal fission product gas pressure increases. Oxygen released due to fissions in oxide kernels will react with free carbon to from CO gas, which may contribute significantly to particle internal pressure. Pure carbide kernels, on the other hand, cannot from CO. Kernel enrichment affects the relative generation of fission products. Low-enriched fuel, for example, will experience a greater number of Pu fissions than will high-enriched fuel. The fission yield of Ag-110m, a radiologically important fission product, is significantly higher for plutonium than uranium, resulting in increased production of this fission product in low-enriched fuel.

The buffer layer performs three primary tasks. First, it attenuates fission product recoils, protecting the outer structural layers from direct damage. Second, it provides a void volume into which fission product gases (escaping from the kernel) may expand. Third, the buffer accomodates dimensional changes due to kernel swelling or coating contraction.

The IPyC layer is one of the particle's primary structural layers,

acting to maintain particle integrity as internal pressure increases due to FP gas release. In addition, the IPyC layer protects the SiC layer from chemical attack by diffusing lanthanide or palladium fission products, which may escape the kernel but cannot penetrate high density PyC. Finally, the IPyC layer protects the buffer and kernel from chlorine intrusion during the SiC coating phase (see section 2.2).

The silicon carbide layer is the particle's most effective diffusion barrier to the release of volatile metallic fission products. Furthermore, it is the primary pressure bearing layer, on whose integrity that of the entire particle depends.

Finally, the outer pyrolytic carbon layer performs two major functions. First, it provides for better bonding between the particle and the graphite fuel matrix in which the particle resides. Second, the OPyC tends to shrink under irradiation (as does the IPyC), and thus acts to reduce the level of tensile stress in the SiC layer.

Table 2.2 presents a summary of all particle layer functions which affect fission product release.

TABLE 2.2: PARTICLE COATING LAYER FUNCTIONS

LAYER	FUNCTIONS
Kernel	• contains fissile and fertile material • diffusion barrier to metallic FP release • chemical holdup of metallic FPs • C/O ratio controls carbon monoxide generation • enrichment affects fission product yields
Buffer	• attenuate and absorb recoil FPs • accommodate kernel swelling and PyC shrinkage • provide void volume for gaseous FPs • sacrificial layer for amoeba migration
Inner PyC	• protect SiC layer from FP corrosion • reduce tensile stresses in SiC layer • protect buffer and kernel from chlorine intrusion during particle coating process
SiC	• primary diffusion barrier for metallic FPs • primary pressure-retaining layer
Outer PyC	• reduce tensile stresses in the SiC layer • provides better bonding with matrix • gaseous FP barrier should SiC fail

2.2: MANUFACTURE OF PEBBLE BED FUEL

Since a single fuel element may contain 10,000 or more individual fuel particles, and a modular core contains 360,000 fuel elements, the particles must obviously be produced in very large quantities. Since the fuel plays an important role in the MHTGR's passive safety behavior, it is important to understand the processes used to create the particles and fuel elements. In particular, since the fission product release from a nominal particle in a modular HTGR is extremely small, significant fractions of predicted source terms are due to particles which are defective in some way. In this section, the origins and effects of various defects will be discussed, and levels of fuel quality attained in production and in the laboratory will be reviewed.

2.2.1 Pebble Bed Fuel Fabrication

The processes described in this section are those employed by the German firm Hochtemperatur Brennelement Gebau (HOBEG) in manufacturing state-of-the-art pebble fuel elements [N1]. Many techniques are similar to those employed in the U.S. for prismatic fuel elements, but the reader is referred to Ref. G5 for a more detailed description of these (the US) processes.

Fuel kernels are produced by "gel precipitation," a wet chemical process which is capable of producing kernels of varying chemical compositions and ranging in diameter from 200 to 600 μ [K1]. Fig. 2.3 presents a simplified flow diagram of the gel precipitation process.

To create $(Th,U)O_2$ fuel kernels, for example, solutions of uranyl nitrate and thorium nitrate are mixed with water and polyvinyl alcohol

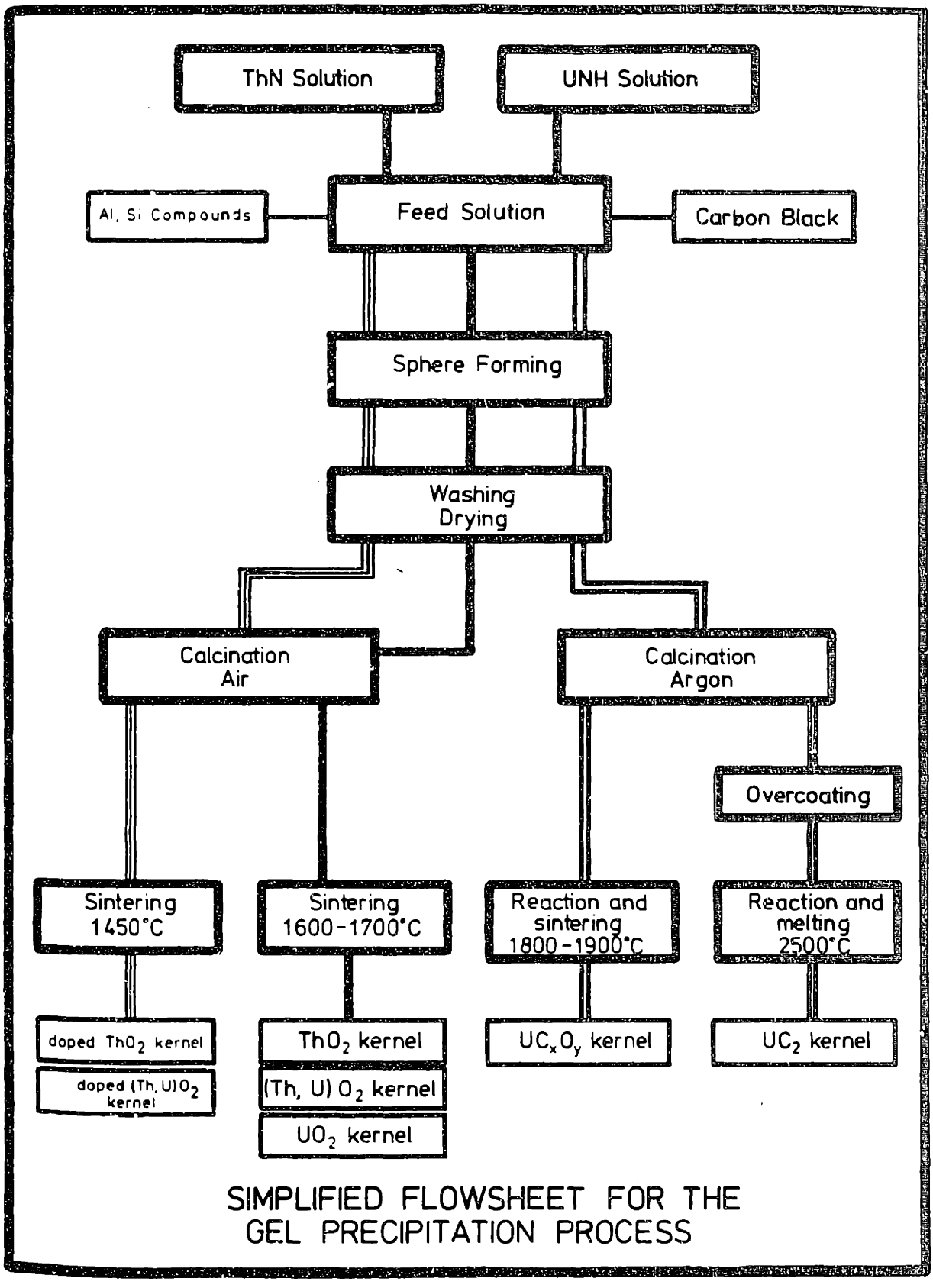

FIG. 2.3: The gel precipitation method for fuel kernel manufacture [K1].

solution. This feed solution is passed through nozzles generating jets of liquid in air. The nozzles are acted on by an electromagnetic vibration system which induces uniform sphericity. The droplets are then solidified through reaction with NH_3, and are subjected to several additional steps to remove process impurities. Sintering in a hydrogen atmosphere completes the process, yielding spherical kernels of 97%-99% theoretical density.

The coating layers are applied in a high temperature fluidized bed chemical reactor. Figure 2.4 presents a schematic diagram of such a device. The central feature is a cylindrical, graphite-lined chamber, heated from the outside, into which the fuel kernels are loaded. A modern particle coating furnace may be loaded with a charge of 10^6 to 10^8 fuel kernels. The bed of kernels is fluidized by a flow of gas pumped into the bottom of the furnace, which flows up through the bed and out the top. The fluidizing gas consists of two components: an inert diluent which enables fluidization, and a coating gas which decomposes in the furnace. This coating gas is either a hydrocarbon (yielding PyC layers) or methyl-trichlorosilane (CH_3SiCl_3, which produces SiC layers). The thermal decomposition of the coating gases is termed "pyrolysis," hence the coating layers are "pyrolytic."

A number of common hydrocarbons are suitable for particle coating. Four which have been seriously investigated are acetyline or ethine (C_2H_2), propylene or propene (C_3H_6), butane (C_4H_{10}), or methane (CH_4). In general, any hydrocarbon may be represented by the chemical formula C_xH_y. The ratio x/y has been found to control a number of important

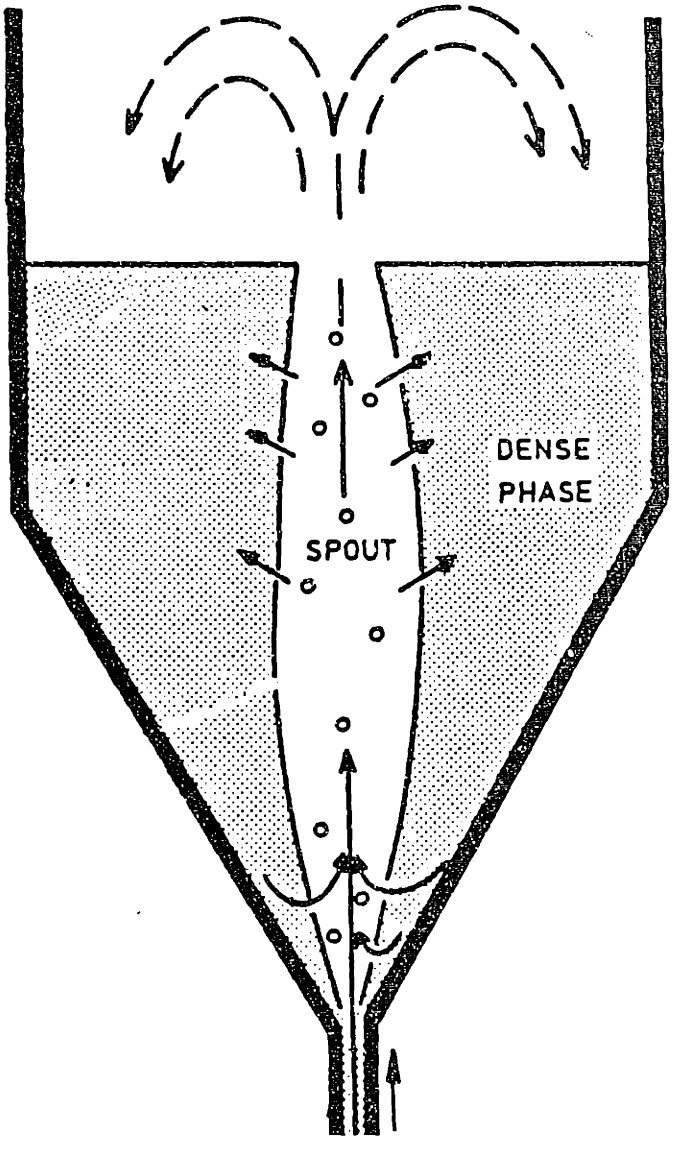

FIG. 2.4: Schematic diagram of a fuel particle coating furnace.

coating process parameters which ultimately affect particle performance during irradiation. In modern fuel particles, the buffer layer is deposited at a rapid rate from decomposing ethine. LTI-PyC layers are derived from propene or mixed propene/ethine gases at temperatures from 1200 - 1450 C [K1].

In order to minimize coating damage in the cold pressing process which follows, the coated particles are placed in a drum and a 200 μ "overcoating" of matrix graphite is deposited. This procedure is only possible when there are relatively low packing densities of particles within the fuel element [N1].

The overcoated particles are next mixed with graphite powder and pressed into a 5.0 cm diameter sphere. All pressing is done at ambient temperature in rubber molds. Next the outer unfueled layer is applied at 50,000 psi, and the pebbles are then machined to final sphericity. Finally, the pebbles are heat treated at 1950C to crack any organic products which may be present.

2.2.2. Manufacturing Defects and Heavy Metal Contamination

Though the technology of particle coating has advanced to a point where high levels of quality are attainable, the large numbers of particles which must be manufactured imply that some small number of them will receive deficient coatings. Coatings are deficient to the extent that some fraction of heavy metal atoms will inevitably not be completely surrounded by the complete coating layer structure. There are two fundamental mechanisms by which this may occur. The heavy metal atoms themselves may be deposited outside the enclosed kernels, due to

heavy metal contamination. On the other hand, one or several of the coatings may be damaged or missing, or the kernel itself may be excessively irregular, due to various possible manufacturing defects.

Heavy metal contamination occurs during the particle coating process. When the kernels are loaded into the coating furnace, small granules of fissile or fertile material are deposited on the walls of the furnace, from which they are later picked up by partially- or fully-coated particles. The result is that a small fraction of the active fuel material is not fully enclosed by all the coating layers. These contamination granules can be dispersed over surfaces of particles and in the fuel element matrix. In high quality fuel, in which other mechanisms of particle failure occur only rarely, heavy metal contaminiation (HMC) can account for significant fractions of circulating activity and the radionuclide release during accidents.

The level of heavy metal contamination is expressed as the following fraction:

$$\Phi_{HMC} = \frac{\text{exposed HM atoms}}{\text{total HM atoms}}$$

The magnitude of Φ_{HMC} can, to a large extent, be controlled by simple processing techniques. For example, smaller coating batch sizes and more frequent cleanings of the coating furnace walls can lead to significant reductions. In this manner, fuel particles have been produced experimentally in the FRG with values of Φ_{HMC} as low as 10^{-6} [K2]. In the U.S., GA Technologies uses somewhat larger coating batches, and produces fuel with $\Phi_{HMC} \approx 2\times10^{-5}$ [S1].

Any flaw in a fuel kernel or particle coating layer which causes a

loss in fission product retention ability and arises in the fabrication process is termed a "manufacturing defect." There are six categories of defects:

- missing or defective buffer layers;
- missing or defective PyC layers;
- missing or defective SiC layers;
- fuel dispersion into the buffer layer;
- highly irregular kernels;
- coatings broken during the pressing of fuel elements.

The fraction of defective particles can, to some extent, be controlled simply through more elaborate quality control techniques [S2]. The eventual fraction allowed in a design represents a trade-off between practical manufacturing capability and core design requirements.

As the buffer layer provides no direct structural support during irradiation, the only way it can be defective is by being absent or unacceptably thin. If this is the case, particle failure will be accelerated as internal pressure increases beyond design levels due to insufficient void volume for FP gas expansion. Additionally, it is also possible for fission product recoils to directly damage the IPyC layer in the case of extremely thin buffers. Defective OPyC layers result in premature particle failure for reasons similar to the case of the defective buffer. Without the "prestressing" provided by this layer, the SiC will exceed its ultimate tensile strength too rapidly, resulting in premature particle rupture. Since defective buffers and OPyC layers cause complete coating layer failure, both result in the release of gaseous and metallic fission procucts. Defects in the inner PyC layer,

and heavy metal dispersion into the buffer, can lead to accelerated SiC corrosion by fission products (see below).

There are three categories of SiC defects: partially or completely missing layers, microcracks or fissures, and microstructural flaws. Mercury intrusion tests have revealed higher SiC defect rates for particles after fuel element fabrication than for particles which were never used to create entire fuel elements. Thus, SiC defects may arise both in the coating and the fuel element pressing stage [K3].

Partially or completely missing SiC layers have two effects: increased metallic FP diffusion and premature pressure vessel rupture. Microcracks or fissures have been found to reduce silicon carbide's load bearing capacity. Increased pressure vessel failure due to this effect has been verified by in-pile tests [K3]. Microstructural flaws, such as excess silicon or grain boundary disorders, increase the diffusivity of metallic FPs in the SiC layer. By themselves, SiC defects result primarily in the increased release of metallic fission products. Only if the PyC layers fail will gaseous FPs be released as well [S2].

2.2.3 Modern Fuel Quality: Achievements and Implications

The technology of coated particle fuel fabrication has advanced to the point where very high quality fuel may be produced. "High quality" implies two characteristics:

- low levels of heavy metal contamination;
- low rates of manufacturing-induced particle defects.

In both the US and the FRG, design specifications for standard fuel have been selected at levels which are judged to be achievable

economically and to yield satisfactory performance. These levels are displayed in Table 2.3. As the Table indicates, both countries have adopted similar quality standards.

These levels represent an historic high in fuel quality. Even so, recent advances in the FRG imply that even stricter levels may yet be achieved. Their experience [H1] has been that:

(1) SiC defects during operation are controlled by proper particle design and narrow variances of particle propoerties (expecially layer thicknesses). Recent tests on LEU fuel elements detected no SiC layer failures during operation in irradiation batches consisting of 10^5 particles. Therefore, extremely high fuel quality appears to be achievable.

(2) SiC defects during manufacture are controlled by the matrix-pressing step. Procedures have been developed to avoid these failures, which include overcoating the particles with a layer of matrix material prior to pressing, and elimination of odd shaped particles by vibration tabling. Defect rates as low as 1.5×10^{-6} have been achieved when all such precautions are taken.

These experimental failure rates appear alongside the specifications in Table 2.3. They are well within both the US and FRG limits, the margin giving assurance that quality levels can be met under full scale manufacturing conditions. They also indicate the potential of significant increases in quality standards, should such measures be necessary in the future.

TABLE 2.3: DESIGN SPECIFICATIONS AND ACHIEVEMENTS IN FUEL QUALITY

	FRG DESIGN SPECIFICATION [ref. H1]	US DESIGN SPECIFICATION [ref. S1]	LEVEL ACHIEVED [ref. H1]
SiC defects due to manufacture	$< 60 \times 10^{-6}$	$< 40 \times 10^{-6}$	1.5×10^{-6}
SiC defects due to operation	$< 200 \times 10^{-6}$	$< 50 \times 10^{-6}$	0
heavy metal contami-nation	$< 60 \times 10^{-6}$	$< 20 \times 10^{-6}$	1×10^{-6}

2.3 SAFETY-RELATED FISSION PRODUCTS

A large variety of fission products is generated within the fuel. Fortunately, only a small subset need be examined in depth for source term evaluation. For a particular isotope to warrant detailed calculations it must be generated in significant amounts, escape from the fuel in significant quantity, and pose significant health hazards once released. Although there are no fixed criteria for selecting such isotopes, a review of the relevent literature reveals that the following list contains those which have historically been considered the most important.

Cesium: Cesium has a high fission yield, but is well retained by PyC. Deposition in the primary circuit can affect plant maintainability [N2], and plateout in the steam generators contributes to the source term in the event of water ingress [M1].

Silver: Ag-110m, radiologically the most important of silver's isotopes, is produced by neutron activation of its relatively low-yield parent, Ag-109. Its overall behavior is qualitatively simlar to cesium's [N11], and its relatively high diffusivity in both PyC and SiC can compensate for its lower inventories. Ag-110m is usually considered significant only in LEU fuels, in which the production rate of Ag-109 is increased due to plutonium fissions.

Strontium: Sr-90 has a high fission yield, but is retained very well in oxide fuel kernel material during operation. In certain accident scenarios, strontium release can cause significant health effects [N11].

Stable Noble Gases: Long-lived inert gases, such as xenon or krypton, contribute to particle internal pressure once released from the fuel kernel, and thus may contribute to particle failure.

Short-lived Noble Gases: Unstable isotopes of krypton and xenon are released from failed fuel particles or from heavy metal contamination, contributing to the activity level of the primary coolant [N11]. Circulating activity can be a major fraction of the total release due to depressurization accidents.

Iodine: Isotopes of iodine have relatively high fission yields and severe biological consequences if released to the environment. They are often conservatively assumed to behave as noble gas atoms.

Tellurium: Tellurium would have significant health effects if ever released from the reactor. Little is presently known about its release characteristics [K4], so it is sometimes included in the list of important isotopes.

2.4: FUEL PERFORMANCE

The mechanisms by which fission products may escape from fuel particles may be classified into a multi-dimensional regime space. The regime in which a given particle/fission product must be analyzed is specified by the following three conditions:

- coating layers may be intact or failed;
- particle temperatures may correspond to reactor operating conditions or a thermal transient;
- the fission product may be gaseous or metallic.

In this section, the behavior of fuel particles and fission products in such situations are discussed, and approaches to modelling these phenomena reviewed.

2.4.1 Fuel Particle Failure

An intact set of coating layers has the following effect: It is essentially impermeable to noble gas fission products, and volatile metallic FPs have very low diffusivities through them (though during temperature transients, the diffusivities may become significant). Once failed, all FPs are released directly from the kernel to the pebble matrix graphite (an exception is the case of failure by SiC corrosion, explained below). The following four mechanisms are the most significant for HTGR fuel particles, listed not necessarily in order of importance:

- pressure vessel failure of standard particles;
- SiC/fission product chemical interaction;
- kernel migration (the "amoeba effect"); and
- SiC thermal decomposition.

These failure modes are reviewed to assess their causes and the modes of operation in which they are significant. It will be seen that well designed fuel in a modular HTGR suffers these events only with extreme rarity.

Pressure Vessel Failure

Pressure vessel failure refers to the mechanical rupture of a particle's coating layers due to overpressurization. Many defective particles will eventually fail for this reason, however we are concerned here only with the potential for standard particles to fail this way.

Particle internal pressure is caused by gas which escapes from the fuel kernel into the void volume within the buffer. This gas may be fission product atoms (krypton or xenon) or arise from the chemical interaction of free oxygen (from fissioned UO_2) with carbon to form carbon monoxide (CO). Since noble gas atoms diffuse slowly through UO_2, only the stable gaseous fission products will contribute significantly to internal pressure. Over time, the number of these atoms which reach the buffer increases, and the tensile stress induced in the SiC may eventually exceed its ultimate tensile stress (UTS). Should this happen, the SiC will rupture, releasing enough mechanical energy to destroy the PyC layers as well. The result is essentially a bare kernel with no additional release barriers before the pebble matrix.

The buildup of particle internal pressure over time is straightforward to calculate given the particle's dimensions. The total number of stable noble gas atoms created is a function of burnup and the cumulative fission yield; correlations exist to predict the fraction of

these atoms which escape from UO_2 fuel grains (e.g. R/B equations based on an equivalent sphere model [N2]). The amount of free oxygen generated is also a function of burnup; correlations have been developed [K3] for "O/F," the number of free oxygen atoms per fission which react with carbon to form CO. Buffer void volume is calculated based on its actual and theoretical densities, and the volume occupied in the fuel particle. Using a known particle temperature and an equation of state for the gases (ref. K7 suggests the Redlich-Kwong equation), particle internal pressure may be calculated as a function of burnup.

Transmission of internal pressure to the SiC layer is complicated by creep of the pyrolytic carbon. Both PyC layers undergo dimensional changes which are a complex function of fast neutron fluence. The layers shrink under irradiation, which tends to reduce the tensile stress in the SiC layer. Bongartz [B4] has detailed how particle internal pressure is modified by PyC creep before inducing a radial force on the SiC layer. This radial force has a tangential component in the SiC, and it is this tensile force which may eventually exceed the ultimate tensile strength.

To complicate matters further, almost all of the relevent phenomena are functions of stochastic variables. Particle dimensions, which have random variation due to manufacturing methods, play a significant role [G1]. Table 2.4 lists values of the standard deviations of coating layer thicknesses and densities in current HOBEG fuel. The silicon carbide UTS is random as well, and has been found to be distributed approximately as a Weibull random variable [B4].

TABLE 2.4: STANDARD DEVIATIONS FOR LAYER THICKNESSES AND DENSITIES IN HBK TRISO FUEL PARTICLES

LAYER PROPERTY	MEAN VALUE	STANDARD DEVIATION
KERNEL		
radius	250 μ	3 μ
density	10.8 g/cm^3	0.05 g/cm^3
BUFFER		
thickness	90 μ	14.9 μ
density	0.94 g/cm^3	0.05 g/cm^3
INNER PYC		
thickness	40 μ	5.4 μ
density	1.93 g/cm^3	0.012 g/cm^3
SIC		
thickness	35 μ	1.5 μ
density	3.19 g/cm^3	0.005 g/cm^3
OUTER PYC		
thickness	40 μ	4.4 μ
density	1.91 g/cm^3	0.010 g/cm^3

(parameters are for standard LEU particles, HBK Project [H2])

Several approaches have been used to address these uncertainties. A "direct method" was developed by Gulden [G1] which assumes that kernel diameter and buffer thickness are the primary variables. He assumes that both parameters are normally distributed, implying a known distribution of internal pressures after a specified burnup. This technique is illustrated in Figure 2.5, which presents a plot of kernel diameter/buffer thickness space. The points in the figure represent dimensions of particles which have been measured. The ellipses are lines of equal probability in the dimension space; additionally curves are drawn indicating SiC tensile stress as a function of these parameters at various particle burnups. The fraction of particles at any burnup which are found to have SiC stresses greater than the UTS (i.e., "below" the stress curve which corresponds to the UTS) are assumed to fail. This method was later extended at KFA to include a third normally distributed random variable, and an SiC ultimate tensile strength with a Weibull distribution.

Monte Carlo methods have also been developed [K5], in which a large number of imaginary test particles are constructed by randomly selecting values of the stochastic parameters. The resulting population of particles is analyzed for irradiation behavior, and their failure fractions indicate what might be expected from real particles with parameters distributed the same way. Any number of random parameters with arbitrary distributions may be modelled in this way. The drawback is the number of calculations which must be performed. To accurately determine failure fractions on the order of 10^{-4}, for example, many more

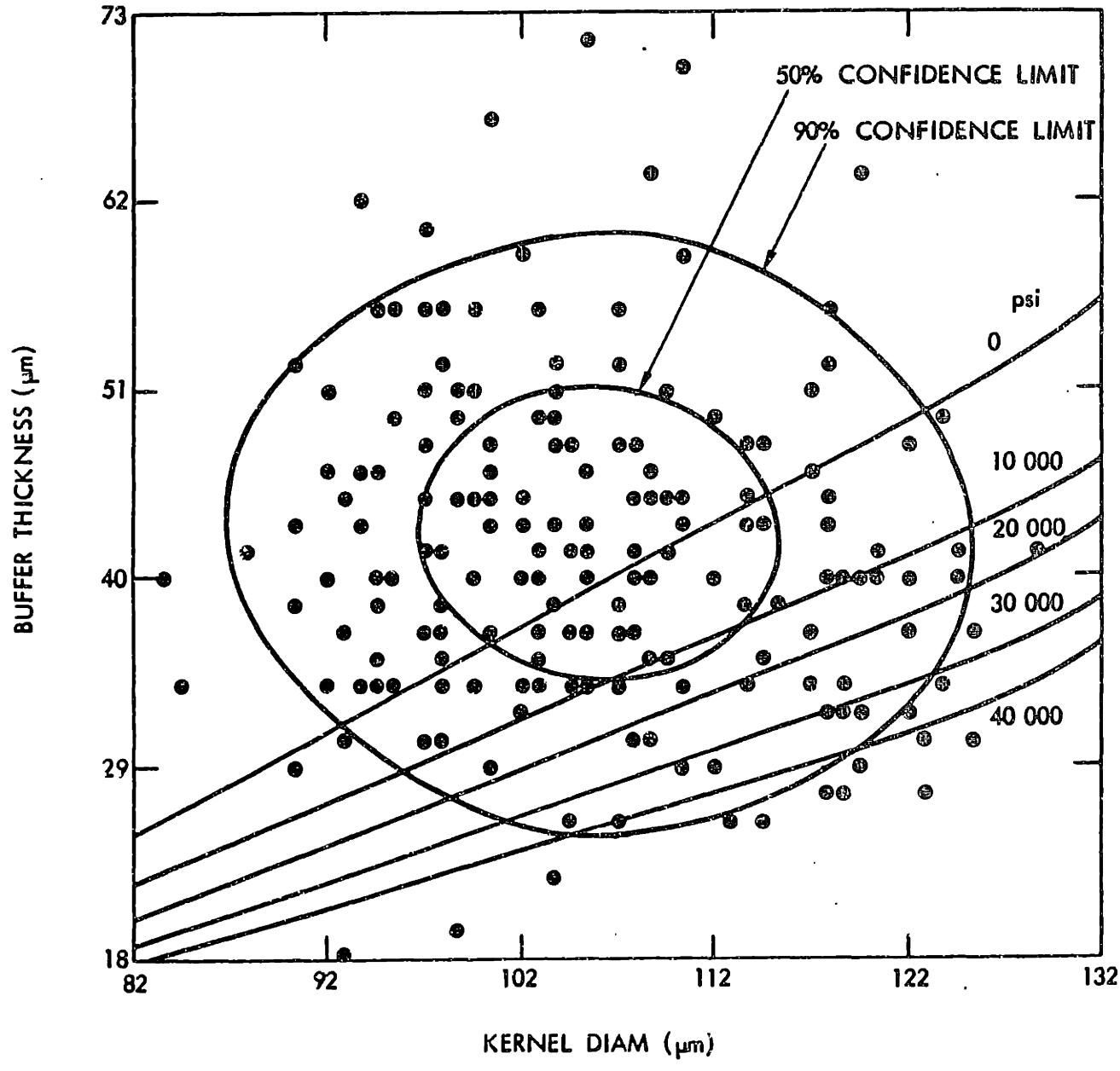

FIG. 2.5: Gulden's "direct method" for estimating pressure vessel failure fractions [G1].

than 10^4 particles must be analyzed.

A third technique is known as the "law of error propagation" method. All random variables (except for the UTS of SiC) are assumed to be normally distributed. The dependence of SiC tensile stress on all parameters can be shown to be linear [B4], except for the case of the buffer thickness. If the dependence on buffer thickness is linearized over small intervals in the region of interest, the SiC stress distribution may be determined analytically by combining the variances of the various random variables. Convolution of this distribution with the Weibull distribution representing SiC ultimate tensile strength yields the particle failure fraction.

The most recent attempt to predict particle performance with a pressure vessel model is the PANAMA code, developed by Verfondern and Nabielek at KFA Jülich. PANAMA calculates failure fractions for TRISO particles under accident conditions. The code calculates the particle internal pressure and accounts for a decrease in coating strength due to irradiation and chemical interaction with fission products. At very high temperatures, failures are dominated by SiC thermal decomposition. The code has been found to predict failure rates well when temperatures reach the 1600-2500C range.

The applicability of these analytic methods to particles of arbitrary design under *all* conditions is not clear. Recent experimental results from KFA Jülich [H2] indicate gross overprediction of failure rates for particles of recent manufacture during post-irradiation anneals at 1600C. Figure 2.6, reproduced from Ref. H2, compares

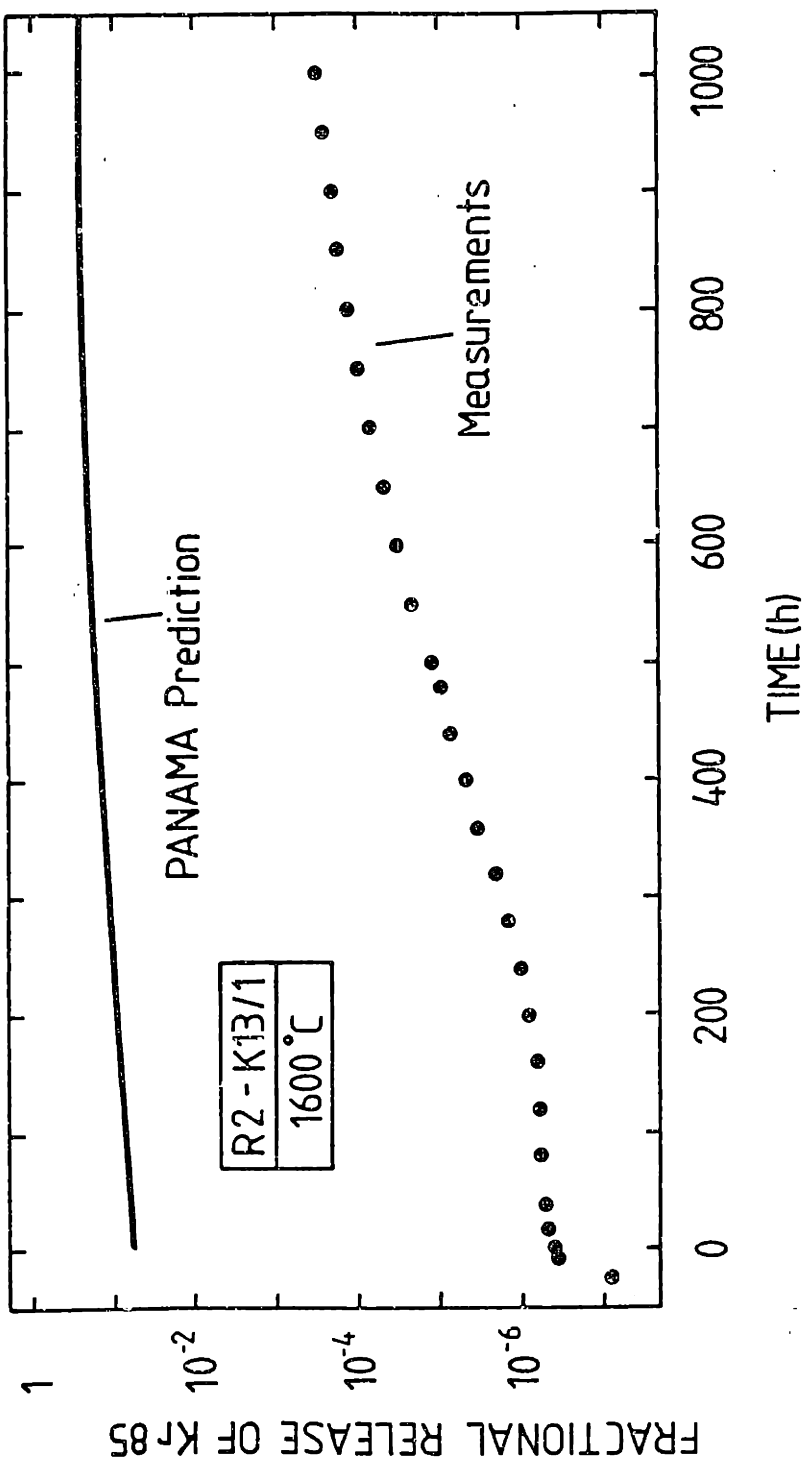

FIG. 2.6: Measured and predicted fractional release of Kr-85 during post-irradiation annealing at 1600 C [H2].

prediction of the PANAMA code with measured fractional releases of Kr-85. Even after 1000 hours, measured releases indicated failures only of about 10^{-3}, whereas the code predicts well over 10^{-1}. Furthermore, the discrepency is much worse at early times. Some modular reactor designs, such as KWU's HTR-MODUL, will not even achieve 1600C, and will remain above 1500C for only about 100 hours even when depressurized [J1]. Thus, not only has particle behavior during MHTGR-type transients defied analytic prediction, the experimental evidence indicates practically no pressure vessel failures for temperatures less than or equal to 1600C.

Fission Product/Silicon Carbide Interaction

Fission product palladium (Pd) does not form stable oxide compounds, and is thus free to diffuse in oxide fuel kernels once it is generated. The particle's temperature gradient can act as a driving force and the Pd may diffuse through the IPyC layer. If the palladium reaches the silicon carbide layer, chemical reactions will occur which can degrade the layer's microstructure. Should these reactions proceed far enough, the result can be increased diffusivity of metallic fission products through the SiC. These reactions can be the limiting thermal failure mechanism at temperatures less than 2000C [G2].

Extensive core heatup simulation tests have been performed to acquire data regarding this phenomenon. The onset of metallic fission product release was found to occur at approximately 2000C, while gaseous release was not detected until approximately 2200C [S3]. Evidently, the SiC layer may become permeable due to fission product interactions

without affecting PyC's ability to retain gases. Palladium was found to concentrate in nodules at the IPyC/SiC interface, and the chemical reaction occurs only at these locations [T3]. Figure 2.7 presents an electron microprobe analysis of a SiC layer undergoing chemical attack by palladium.

Investigators at Oak Ridge National Laboratory [T3] concluded that the major rate-determining variable for this reaction is particle temperature. The fission product inventory has only a secondary effect on the penetration rate, as the reaction occurs only at the Pd nodules. Inventory only affects the number of nodules.

Observations of fission product attacks on the SiC layer have been compiled by GA [S4]. A sample of such data obtained at ORNL is reproduced in Figure 2.8. The data correlates well with temperature [T3], and can be described by the following equation:

$$\dot{X} = 2.613 \times 10^5 \exp\left[\frac{-2.522 \times 10^5}{8.314\ T}\right]$$

where $\dot{X}$ = the rate of advance of the visible reaction front (μ/hr);

T = temperature (K).

Fuel designers have modeled SiC failure by this mechanism as follows: retentiveness is unaffected by chemical reactions until the visible reaction front (as calculated by an equation such as that above) penetrates 50% of the way through the SiC layer. At this point, the layer is assumed to become permeable to metallic fission products. Gaseous FPs are not released unless the PyC layers fail as well.

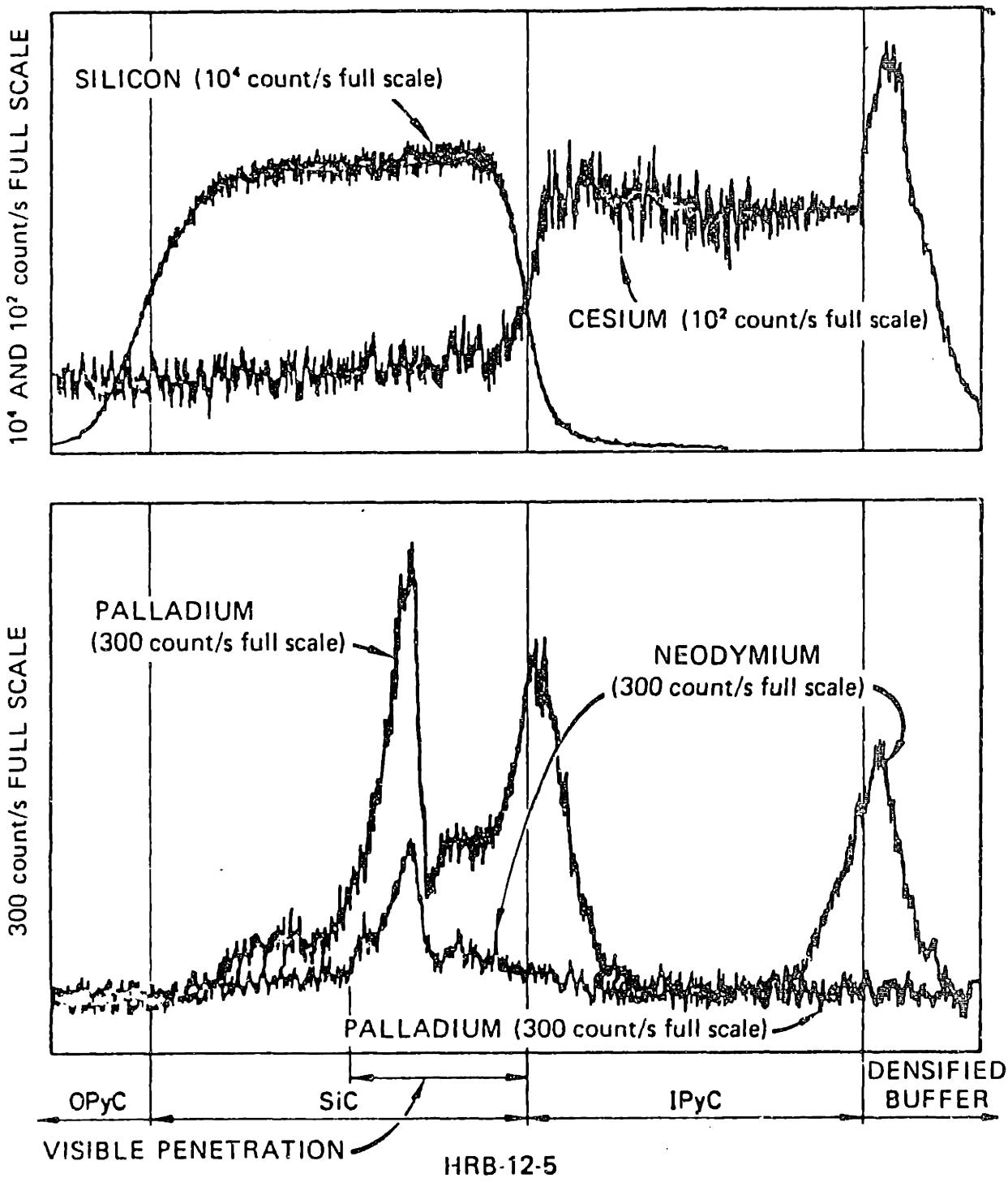

FIG. 2.7: Electron microprobe analysis of a SiC coating layer under corrosion attack by fission product palladium [T3].

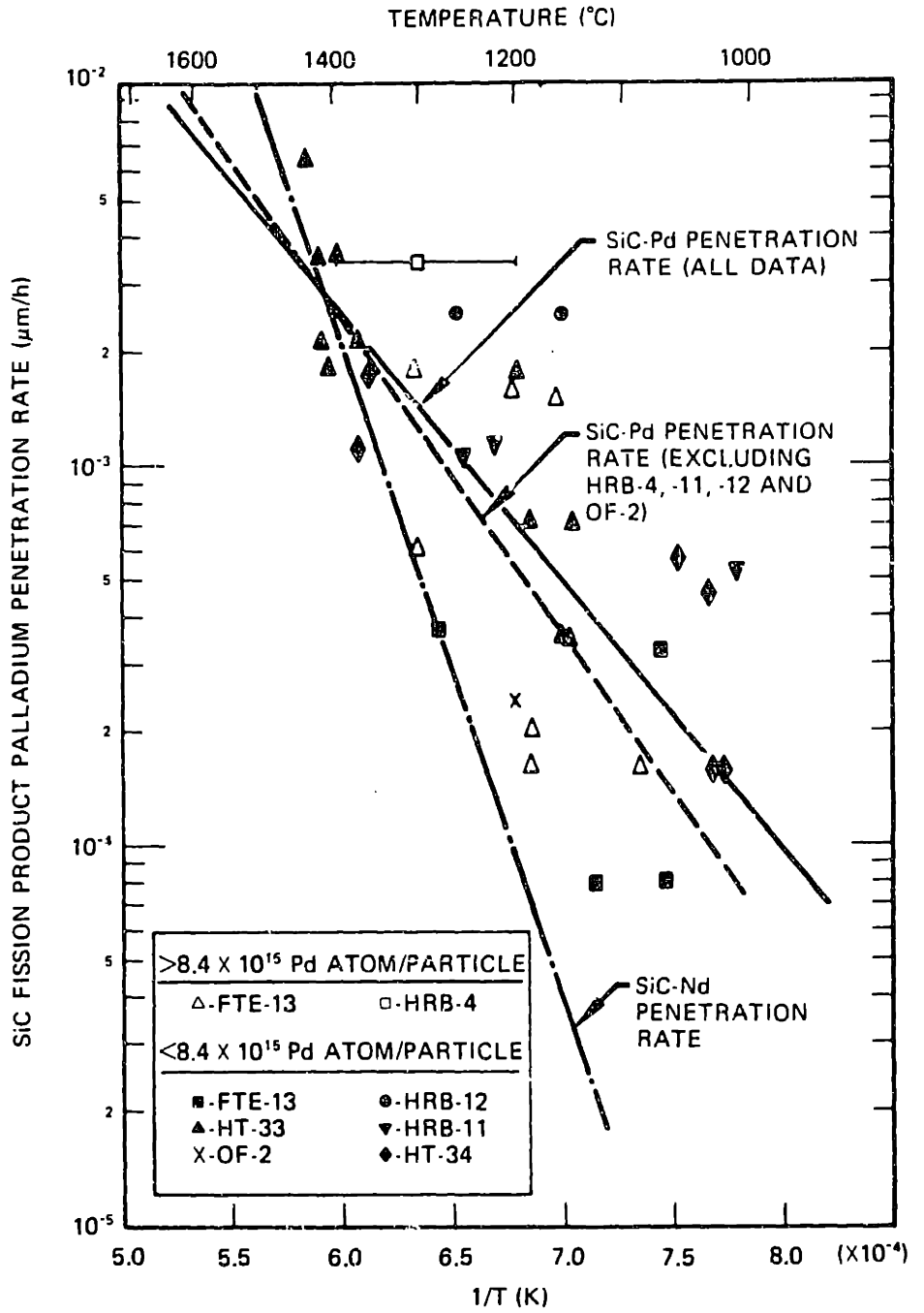

FIG. 2.8: Experimental corrosion rates indicating temperature dependence [T3].

Kernel Migration

Kernel migration, sometimes called the "amoeba effect," can occur if a fuel particle is subjected to a steady temperature gradient for long periods of time. The fuel kernel will tend to migrate up the temperature gradient towards the particle's hot side. Should the kernel reach the inner PyC layer, coating failure will result.

The mechanism for kernel migration, though well understood in the case of carbide fuel kernels [S2], is not as well understood for oxide kernels. Two mechanisms have been proposed: the rate may be controlled by CO/CO_2 gas-phase interdiffusion and decomposition or solid phase oxygen diffusion, or carbon may be transported along the UO_2 grain boundaries [S2]. Empirical correlations have been used for particle design. Relations for oxide fuel which correlate migration velocity with particle temperature and temperature gradient (the same form as for carbide kernels) have been developed. Measurements were made of kernel migration under various imposed temperatures and temperature gradients. Migration velocity is related to annealing parameters by a "kernel migration coefficient" (KMC), defined as:

$$KMC \equiv \frac{dx}{dt} T^2 \frac{\Delta T}{\Delta x} \qquad (2.1)$$

where dx/dt = observed rate of migration {m/sec};

T = average kernel temperature {K}; and

$\Delta T/\Delta x$ = average temperature gradient across the fuel particle {K/m}.

Typically, values of the kernel migration coefficient are displayed on an Arrhenius-type diagram, in which the logarithm of the KMC varies

linearly with inverse temperature [S2]. Values of the KMCs used for particle design at GA are displayed in Figure 2.9. Once the KMC is known, fuel designers can provide adequate buffer thicknesses to ensure that, for given core conditions, the kernel cannot migrate to the IPyC layer.

Silicon Carbide Thermal Decomposition

For completeness's sake, the failure mechanism of SiC decomposition will be briefly reviewed. However, the temperatures required to initiate this process are much higher (>2000C) than can be expected to occur in modular HTGRs. Thermal decomposition is of primary concern in analysis of particle behavior in large HTGRs during temperature excursions.

At very high temperatures, silicon carbide will decompose by the following chemical reaction:

$$SiC \leftrightarrow Si(g) + C$$

After gaseous Si has departed, a disordered carbon structure remains in place of the SiC layer. At temperatures above 2000C, this reaction becomes the dominant failure mechanism [N9]. Models predict exponential increases in failure fraction as a function of time under these reaction conditions. Once a particle has failed in this manner, the SiC layer has vanished for purposes of fission product retention [N4].

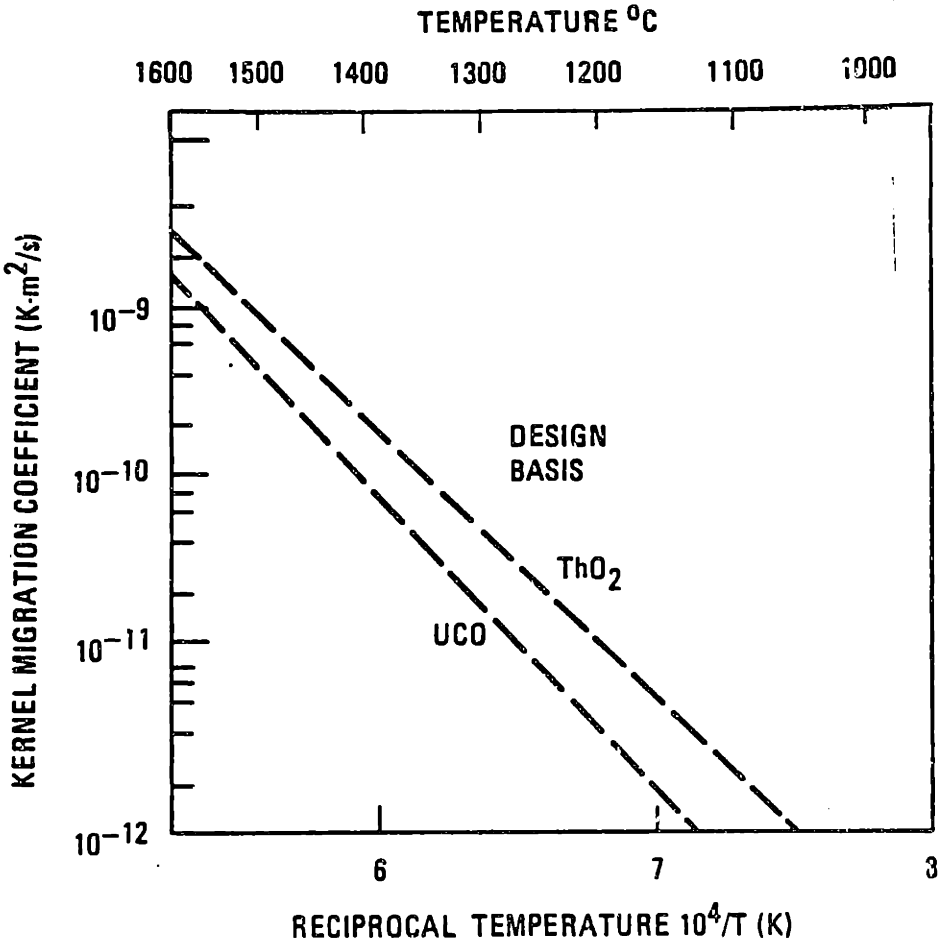

FIG. 2.9: Kernel migration coefficients for design calculations [S2].

2.4.2: Fuel Behavior in an Operating Reactor

The rate of fission product release during operation determines the activity level within the primary system. Besides the obvious impact on plant maintenance and inspection, these fission products may contribute a significant (sometimes dominant) fraction to releases due to postulated accidents. Operating conditions are characterized by two primary features:

(1) Relatively low maximum fuel temperatures: Typically less than 1100C, fuel temperatures during operation imply extremely low diffusivities for fission products in the kernel and coating layers.

(2) On-going irradiation: Due to the fissioning of heavy metal atoms, there is a source of new fission product atoms within the fuel.

Here we examine the mechanisms by which fission products can escape from fuel particles under such conditions. When the fuel is of high quality, only a very small fraction of the total inventory will be released.

Since the goal of fuel particle design are particle parameters which minimize operational failure, it is not surprising that defective particles release the majority of fission products under these circumstances. Heavy metal contamination is a very important defect source. Since contamination granules are not fully coated, fission products which are generated within them have a much shorter escape path than from inside an intact particle. Furthermore, contamination granules are much smaller than the UO_2 grains found within fuel kernels,

so there is relatively little decay time before release. A conservative design assumprion is that any gaseous fission product generated in a contamination granule is released immediately (see Krohn, for example [K4]); others (such as GA) have developed special "R/B" correlations for gaseous FPs produced in contamination granules [S2]. "R/B" stands for "release to birth ratio," and is defined as:

$$R/B \equiv R(t)/B(t) = \frac{\int_o^t \dot{R}(\tau)\, \exp[-\lambda(t-\tau)]\, d\tau}{\int_o^t \dot{Q}_f(\tau)\, \exp[-\lambda(t-\tau)]\, d\tau} \qquad (2.2)$$

where $\dot{R}(t)$ = release rate of fission product atoms from the particle or element surface {atoms/sec};

$\dot{Q}_f(t)$ = source rate of the isotope in question due to fissions {atoms/sec};

$R(t)$ = release; the total number of released fission product atoms up to time t, integrated over the entire irradiation interval {atoms};

$B(t)$ = birth; the total available number of fissios product atoms (both within and outside the fuel) at time t due to fission {atoms}; and

λ = decay constant of the isotope in question {sec^{-1}}.

In reality, of course, the integration for R/B need only be carried out over the past five or so half lives of the fission product. Thus, for short-lived isotopes, a quasi-steady approximation is reasonable and the above equation may be simplified:

$$R/B \cong \dot{R}/\dot{Q}_f \quad \text{(quasi-steady)} \qquad (2.3)$$

R/B ratios are useful because fission product birth rates can be calculated from reactor physics information (neutron flux, cross

sections, etc.) Given a birth rate, the R/B ratio immediately reveals the release rate for a short-lived isotope. The simple conservative assumption for contamination is that R/B from the granules is 1.0:

$$(R/B)_{HMC} = 1.0 \qquad (2.4)$$

whereas GA has developed temperature and half-life dependent correlations, displayed in Figure 2.10 [S2]:

$$(R/B)_{HMC} = (\text{constant}) + (½) \ln T_{½} \qquad (2.5)$$

For some fuel/reactor design combinations, heavy metal contamination can be responsible for 60% of the circulating activity.

Volatile metallic fission products are also generated in the contamination granules. The typical design assumption is that all such fission products immediately enter the fuel element matrix upon birth.

The fuel kernel itself is not as effective a diffusion barrier as the pyrolytic coating layers. Therefore fission products generated in the kernels of defective particles can escape at significant rates.

Failures due to manufacturing defects do not necessarily occur immediately upon irradiation. Some mechanisms (e.g. premature pressure vessel failure due to inadequate buffer thickness) require time for failure to occur. Stansfield, et. al. [S2] have compiled all the burnup-dependent design models for particle failure used at GA as of 1983. A relatively short delay (up to 25% maximum burnup) is assumed for missing/defective buffer layers; longer delays (up to 100% maximum burnup) are assumed for failure due to missing/defective IPyC or OPyC. Defective SiC implies immediate failure with regard to metallic fission product diffusion. Releases due to heavy metal contamination and

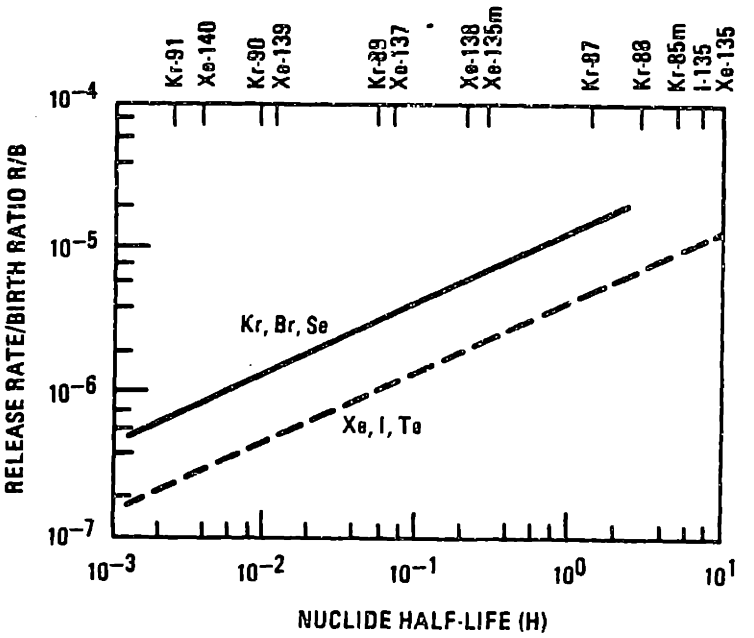

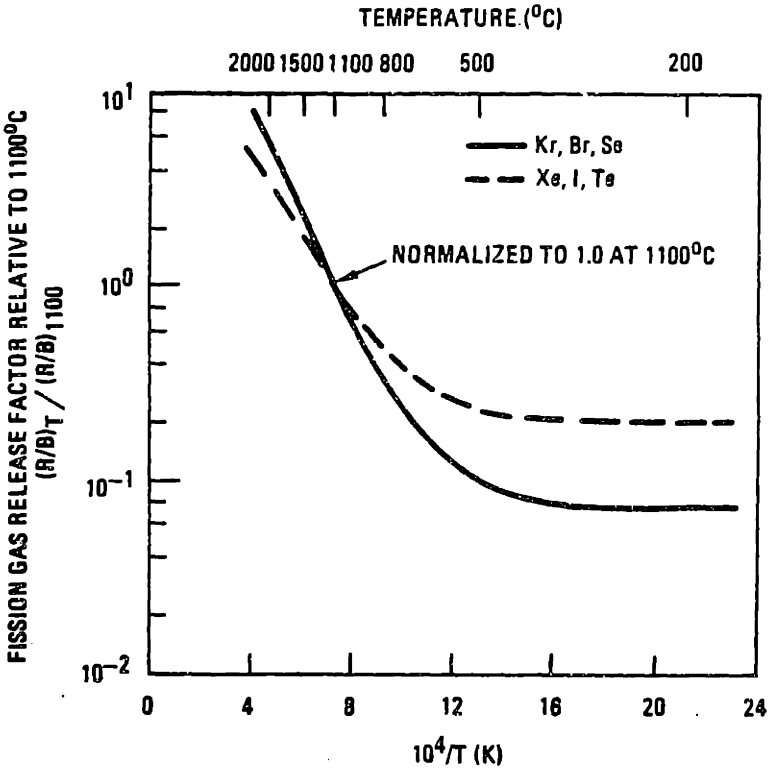

FIG. 2.10: R/B correlation for gaseous fission products generated in contamination granules [S2].

coatings damaged by matrix pressing occur immediately. Given manufacturing data for the rates of the various defect types, these models enable calculation of particle failure fractions as a function of irradiation history.

It is possible to measure release to birth rate ratios during irradiation by placing fuel elements or particles in special assemblies within an operating reactor. A sweep gas flows over the test fuel, transporting released fission products to ex-core detectors. Birth rates are calculated based on known reactor conditions. Figure 2.11 is a sample of some R/B measurements performed on intact and deliberately failed TRISO particles by researchers at KFA [H2]. Note that for failed particles, R/B is greater than the value of Φ_{HMC} (which is in the range 10^{-4} to 10^{-5}), while R/B is less than Φ_{HMC} for intact particles.

Theoretically, fission products can diffuse (albeit slowly) even through intact coating layers (Chapter 6 and Appendix E contain more thorough discussions of fission product diffusion). However, the diffusivities of gaseous fission products through both SiC anc PyC are so small that they can safely be assumed impermeable [N2]. Some metallic fission products, however, may be able to penetrate particle coating layers during operation. Silver atoms, for example, can diffuse at a slow but significant rate through SiC at operational temperatures. Though the amount of fission products released in this manner may be negligible during normal operation, the resulting concentration profiles in the particle can influence the release at high temperatures.

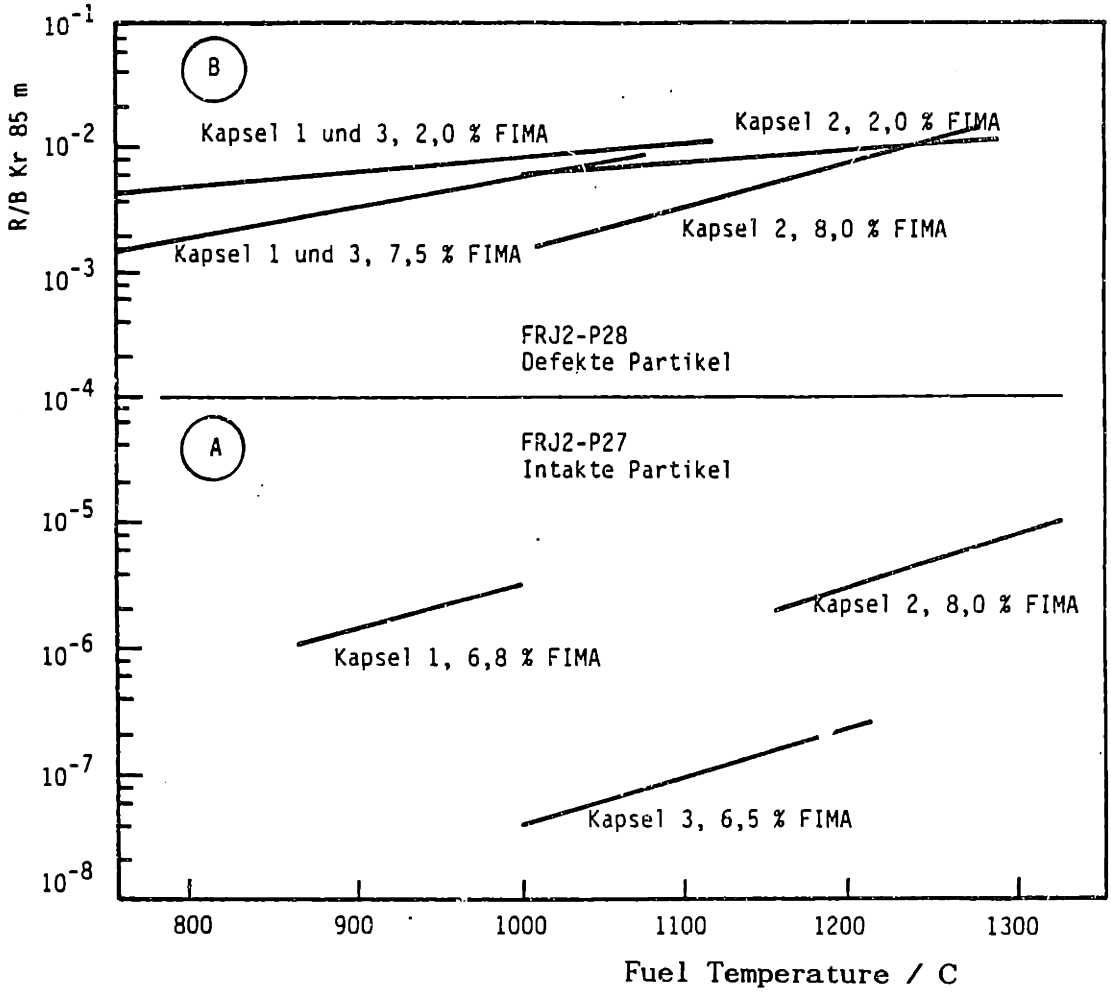

FIG. 2.11: In-core R/B measurements for failed and intact fuel particles [H2].

2.4.3: Fuel Behavior During Temperature Transients

Fuel particle and fission product behavior can change dramatically at high temperatures which may arise due to loss of reactor cooling. The important differences from operating conditions are

(1) The reactor is shut down, thus there is no fission induced source of fission products; and

(2) Temperatures in the core are significantly higher. Particle failures may become more frequent, and fission products will diffuse more readily due to the exponential dependence of diffusivities on temperature.

The temperatures encountered by fuel are dependent upon the design of the reactor. Larger HTGRs, such KWU's HTR-500, may reach temperatures in excess of 2500C [A1]. Modular HTGRs, on the other hand, are designed to limit accident temperatures to levels at which particle failure does not reach high levels.

The dependence of particle failure rate on the temperatures achieved in a transient is clearly illustrated by the results of core heatup simulation tests, in which irradiated fuel is subjected to a pre-defined temperature transient and release of fission products is measured as a function of applied temperature. Figure 2.12 presents the results of one such set of experiments conducted by GA [G5]. Since intact coating layers are impermeable to gaseous FPs even at transient temperatures, PyC failure fractions may be inferred directly from gas release measurements. As this technique fails to detect SiC failure by corrosion, more recent heatup simulations have measured release of

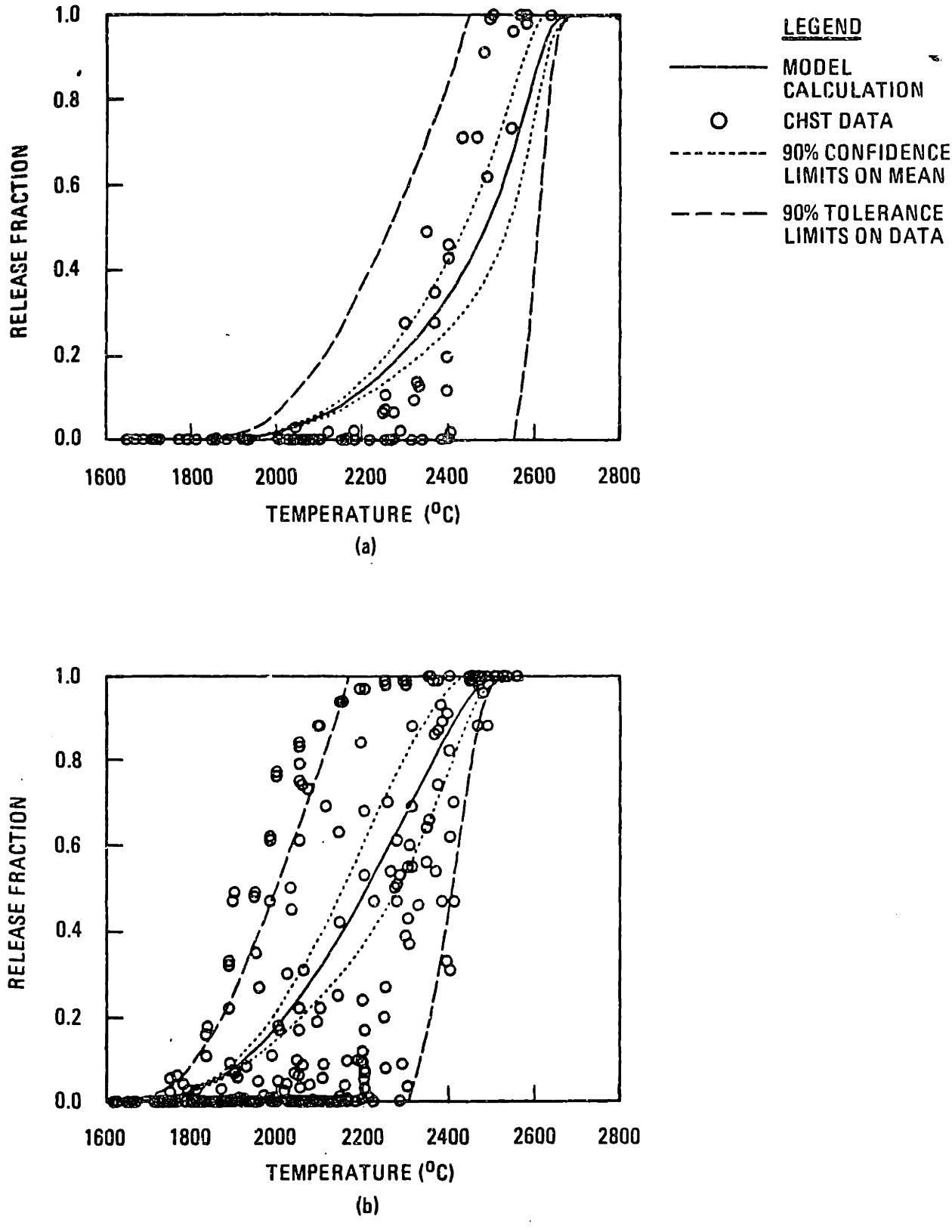

FIG. 2.12: Fuel particle failure rates measured in core heatup simulation tests [G5]

metallic fission products, such as cesium. The salient feature of Figure 2.12 is its non-linearity. Below a certain temperature (in the range 1600-1800C) coating failures occur at negligible rates. However, particle failure occurs extremely rapidly once this temperature is exceeded.

Mechanisms responsible for particle failure during transients have already been discussed in general. If temperatures do not exceed 2000C, the limiting failure mechanism is SiC corrosion by fission products [G2]. Once temperatures cross the 2000C boundary, SiC thermal decomposition rates increase rapidly, becoming the primary failure mechanism [N9]. Pressure vessel failures induced by increased internal pressure do not appear to play a significant role.

Diffusive transport of fission products is enhanced at higher temperatures due to increased diffusivity. Though most volatile metallic FPs are still retained, a handful of important nuclides (Cs, Ag, and Sr, for example) diffuse much more readily through the kernel and coatings as temperatures approach the 1600C level. This leads to two important effects. First, the fraction of metallic FPs released from failed particles can be quite high due to relatively high diffusivity in UO_2. Second, intact particles may release significant amounts of metallic fission products through diffusion alone [B5]. Since diffusion through intact coating layers is unavoidable, this mechanism becomes more significant (though total releases become smaller) as fuel quality is increased.

Release of gaseous fission products from fuel with failed coatings

during temperature transients exhibits complex diffusion/trapping behavior [M3]. In post-irradiation anneal tests, for example, fission products are initially released at greater rates than predicted by simple diffusion theory. At later times more moderate rates consistent with diffusive transport are observed. Noble gases do not react chemically with the fuel matrix. Once released from the fuel kernel, they migrate almost immediately to the reactor coolant.

Metallic fission products, on the other hand, can have quite strong chemical affinity for fuel element graphite. Not only does the pebble provide a significant diffusion barrier to metallic FP release, surface adsorption effects can hinder release to the coolant as well. Cool graphite surfaces can act as traps for metallic FPs, possibly acting to reduce radionuclide release in the event of core heatup accidents. Krohn [K4] has shown that in large HTGRs, relativley cool graphite surfaces (such as the reflector and cool fuel elements) can act to retain significant quantities of fission products.

2.5: RADIONUCLIDE RELEASE IN POSTULATED ACCIDENTS

To evaluate how well the modular HTGR meets its passive safety goals, reactor and fuel performance must be estimated under hypothetical accident conditions. The accidents analyzed should be those which present the dominant risk to public safety and/or the investment of the plant owners. The response of a passively safe reactor will ideally require no assumptions regarding the function of active mechanical systems. Often, the design approach is to select the "worst possible" combination of events and to insure negligible activity release even in these cases.

In this chapter, the risk-dominant accident scenarios for the modular HTGR are briefly reviewed. Special attention is paid to the mechanisms of activity release which contribute to the source terms. Releases due to accidents are classified as "steady state-" or "accident-dominated," depending on whether the fission product release mechanisms are initiated under operating or accident conditions. Fuel quality is demonstrated to have significant effects on steady state dominated releases. Finally, a simple model for fuel performance is proposed which assumes that a passively safe MHTGR must, *a priori*, have high quality fuel. This is the model which will be developed and used in later chapters.

2.5.1: Accident Scenarios Under Consideration

A detailed probabilistic risk assessment is necessary to determine which accident presents the most risk. Such an exercise requires a detailed system design, which is not yet available for the MHTGR.

Preliminary PRA studies have, however, narrowed down the number of accidents [M2]. Three general categories of accidents have been identified as the most important for MHTGRs. The categories are:

- core heatup;
- steam/water ingress; and
- air ingress.

Maneke [M2] has thoroughly reviewed analyses of all these scenarios conducted in both the US and the FRG. All three categories are briefly reviewed here.

Core Heatup

Once heated beyond a certain point, HTGR fuel loses the ability to retain fission products. For this reason, accidents involving loss of core cooling and elevated fuel temperatures play a central role in MHTGR design. In fact, many of the MHTGR's salient features are motivated by this scenario alone [L3].

Under the general category of core heatup accidents, several variations are possible depending on the status of important reactor systems and parameters. Among these are reactor pressure, control rod position, and availability of the cavity cooling system. Since the cavity cooling system is an investment protection device only, and has minimal effect on activity release from the core, its function is not significant to this study. Within these specific accident sequences, reactor design parameters such as power density have large effects on the ultimate severity of the accident.

There are two fundamentally different ways in which core cooling

can be lost. The first is a system failure, in which the helium circulators or steam generators malfunction resulting in a loss of forced cooling. The second involves an actual loss of the reactor's primary coolant. Helium pressure in the reactor vessel will remain at operating levels in the first case, but eventually drop to atmospheric pressure in the second.

Reactor pressure is a critical parameter for two reasons. First, the presence of pressurized helium, even after loss of forced circulation, improves the heat transfer from the fuel to the ultimate heat sink considerably. For example, a recent analysis of the 200 MWth HTR MODUL [J1] compared core response to loss of forced convection incidents with the reactor under pressure ("Reaktor unter Druck" = RuD) and following depressurization ("Druckentlastung" = DES). In the pressurized case (He pressure = 50 bar), maximum core temperatures remained below 1200C, while the maximum temperature climbed well above 1500C for the depressurized case (He pressure = 1 bar). These two transients can be compared in Figures 2.13a and 2.13b. Temperatures achieved in the pressurized transient are so far below those necessary for fuel particle damage or significant diffusion that the amount of release due to damage can safely assumed to be zero. More fundamentally, perhaps, unless reactor coolant has a pathway out of the pressure vessel, no fission products will escape in any case. Thus, from a fission product release standpoint, only depressurized core heatup accidents are of significance.

It is conceivable that the control rods could fail to insert during

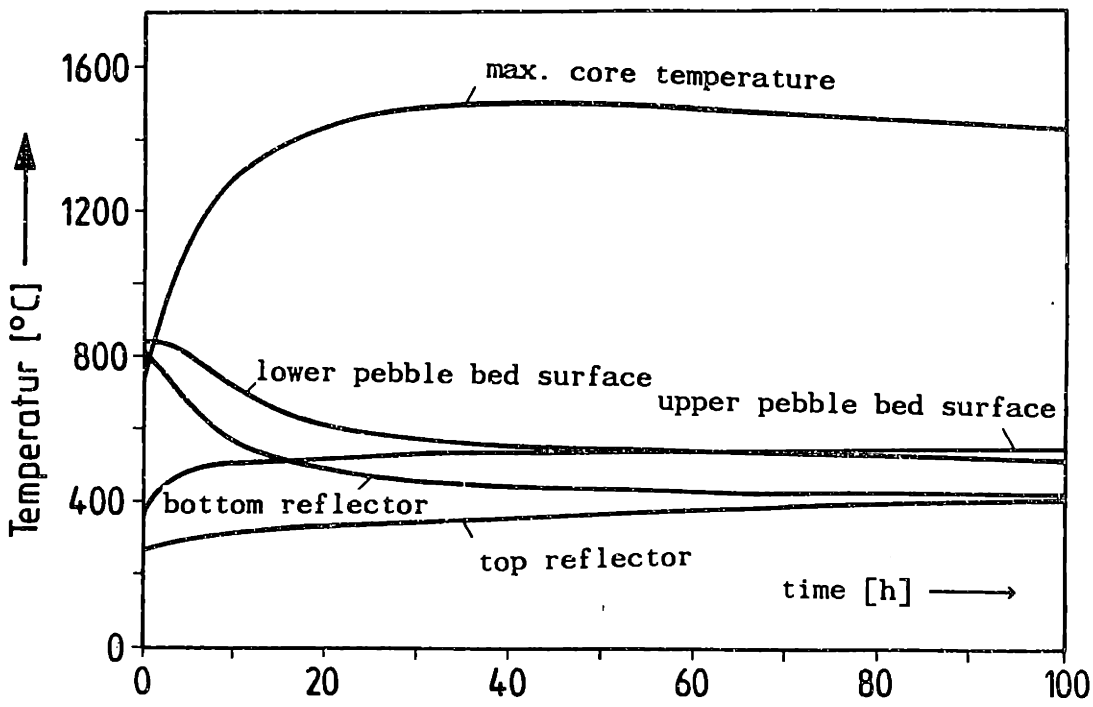

FIG. 2.13a: Temperature transient for loss of forced circulation, reactor under pressure (RuD) [J1].

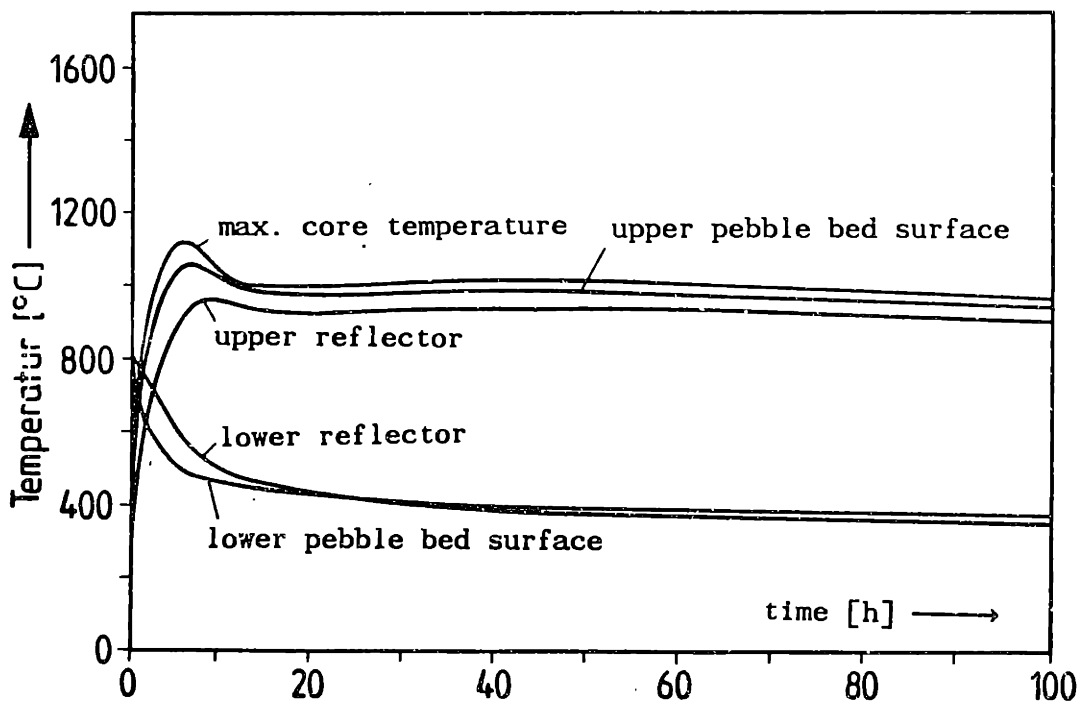

FIG. 2.13b: Temperature transient for loss of forced circulation, reactor depressurized (DES) [J1].

a core heatup event. Such an event is of little consequence to the reactor core, since the negative reactivity temperature coefficient quickly terminates fission in any case. An analysis performed by GHT (Gesellschaft für Hochtemperatur-Technik, GmbH) in 1981 for a 170 MWth module indicated only an 80C difference in maximum core temperatures between depressurized core heatups with and without control rod insertion [G3]. Even then, the maximum temperature in this case was below 1600C. The long term behavior of the un-scrammed reactor may be of greater significance, since once xenon has decayed and temperatures have fallen to lower levels, the reactor may become critical again. However, there are many hours available before this happens in which operators may attempt to reactivate the control rods or to activate reserve shutdown systems (e.g., KLAK absorbers). Furthermore, power levels after such a recriticality would be quite low, and the effects on fission product release would not be great.

Reactor design parameters can have large effects on core heatup transients. Core power density is one of the most important. Calculations were carried out at KFA [J1] to see the effects of increased power densities on peak core temperatures following depressurization. All other reactor parameters were held constant and equal to those of the 200 MWth HTR-MODUL. The results are displayed in Figure 2.14. Though a power increase to 225 MWth does not cause the core to exceed 1600C, 250 MWth results in excessive fuel temperatures. Given the extreme non-linearity of particle failure fractions once 1600C is exceeded, it appears that average power densities greater than 3.3

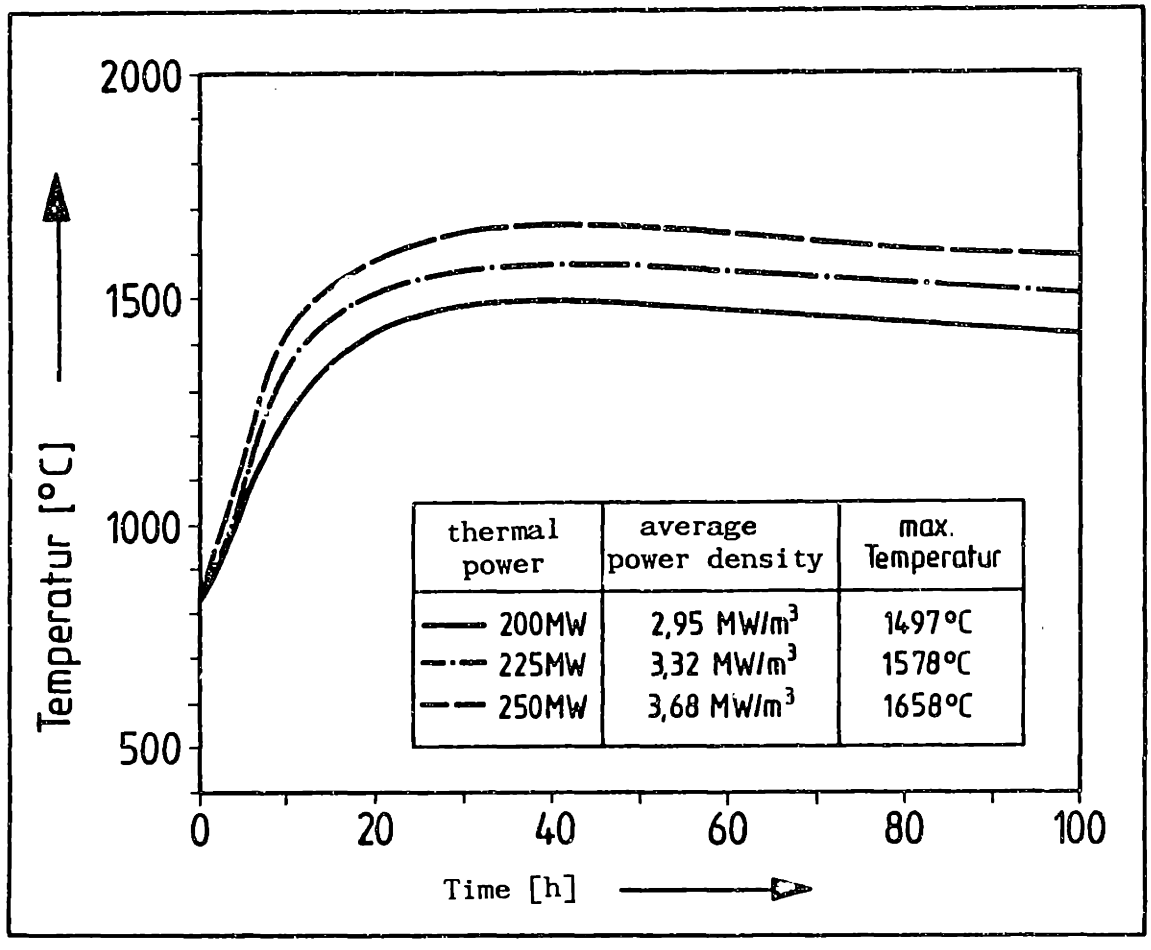

FIG. 2.14: Effects of reactor power density on maximum temperatures achived in core heatup accidents [J1].

W/cm^3 are not advisable.

Once a core has been designed to maintain fuel temperatures below 1600C (at least in core heatup scenarios), the fission product release will, of course, be very small. For this reason, several recent studies have concluded that core heatup accidents may not be the dominant risks to public safety [M1,L3]. Attention has been shifted now to the next general class of accidents, ingress of water into the core.

Steam/Water Ingress Accidents

For MHTGRs which interact with steam based secondary systems, the potential exists for ingress of steam or water. The rupture of a steam generator tube may inject water into the primary system and then into the core, as secondary systems are typically at higher pressures than the primary. Such an occurence has four potentially undesirable outcomes:

(1) the steam or water may cause a reactivity excursion;

(2) water reaching the core, heating up, and then turning into steam may cause a severe pressure transient;

(3) chemical reactions can occur between the water/steam and graphite, such as the fuel elements; and

(4) water entering the steam generator can remobilize fission products which have plated out there. Combined with the potential for a pressure transient which may open the reactor's relief valves, this becomes a mechanism for transporting fission products out of the primary system.

There are two reactivity effects when water is present in an MHTGR

core. Small amounts of water enhances neutron thermalization, increasing the overall resonance escape probability. This acts to increase the reactor's reactivity. However, water also absorbs neutrons, and if the concentration is too high the absorption effect outweighs moderation. Thus, a plot of a reactor's k_{eff} versus amount of water in the core will pass through a maximum. The extent to which the dry core is under- or over- moderated will obviously affect the location of this maximum. An upper limit of 7 grams of heavy metal per pebble minimizes the reactivity effects of water ingress [L3]. A greater mass of heavy metal is excessively under-moderated, resulting in severe reactivity effects upon water ingress.

General Electric has studied the reactivity effects of water ingress on the 200 MWth HTR-MODUL with 7 g heavy metal/pebble [G4]. A maximum reactivity increase of ~ 6% $\Delta k/k$ was found to occur when ~ 1400 kg of steam are present.

The other reactivity effect comes about because a neutron's mean free path is decreased by water in the core. Since modular HTGRs rely on reflector control rods only, this has the effect of reducing control rod worth. For a reactor in the cold shut-down state, in which the reactivity margin is slim to begin with, a reduction in rod worth may result in core criticality.

Graphite and water vapor react to form carbon monoxide and hydrogen gas. However, the reaction is endothermic and occurs at significant rates only at temperatures above 700C [L3]. During a water ingress event, fuel elements will be cooled by this reaction to the point where

it can no longer continue. No significant damage is expected [L3].

The steam generators are the coolest part of the primary system. Furthermore, they possess a large surface area to enhance heat transfer. Metallic fission products released from the fuel during operation will thus tend to plate out on the primary side of the steam generator tubes. It has recently been recognized that in the event of a water ingress, significant amounts of these plated out isotopes could be entrained with the water flowing into the core.

Calculations of the primary system pressure response to liquid water ingress scenarios have been performed [L3, W1]. If several auxiliary systems and the reactor's primary pressure relief valve are assumed to fail, the reactor's secondary pressure relief valve will open. The resulting flow of steam from the core is too large to be filtered [L3]. Since the steam would contain fission products remobilized from the steam generator, relatively large releases may result. Combined with this release would be any additional fission products which escape the fuel due to subsequent depressurization. Lohnert [L3] postulates that such events may be the primary contributors to the overall risk from an MHTGR.

Due to the small consequences of core heatup events, water ingress has been thrust into a major role. Though reactivity and corrosional effects are not limiting from a fission product release standpoint, a sequence of rapid ingress followed by rapid pressure relief could result in significant fission product release. Reference M2 contains a thorough review of recent work in this area.

Air Ingress

Chemical reactions between air and graphite may cause remobilization of fission products from graphite surfaces. Furthermore, these reactions are exothermic, and conceivably act to raise fuel temperatures to higher levels than achieved in simple core heatup accidents. However, recent analyses suggest that the safety implications of these reactions are probably not dominant.

A small amount of air will enter the core following any depressurization accident. After helium flow from the primary system has subsided, the reactor will slowly cool and the remaining gas will decrease in volume. The result is a small flow of air into the core at long times following the initial accident. However, the amounts are so small that essentially no damage is done to the core graphite. Over the first 500 hours of the accident, the average corrosion rate has been estimated at ~ 10 g/hr [W1]. This is to be compared with the total mass of graphite in the core, which is close to 500 tons.

Significant consequences result only in the case of some extremely unlikely events. Continued corrosion requires a continuous supply of air, plus the capability of sustained natural circulation. Such a situation is very improbable, as the reactor vessel's location in an underground silo limits possible air ingress. Three large breaks in the primary system are required: two in the pressure vessel, and one in the graphite bridge over the core [W1]. Under these circumstance calculations with the REACT/THERMIX code show that corrosion-induced fission product release would occur after 19 hours. It should be noted

that this is a significant period of time for counter measures to be taken. In any case, it is not surprising that once severe and improbable enough circumstances are imagined, the consequences will be high. The low frequency of such an event will probably place it in the "residual risk" category.

2.5.2: Classification of Source Terms

The radioisotopes released in any postulated MHTGR accident must arise from a particular *release mechanism*. We have seen that a properly functioning fuel particle, under normal conditions, will retain all fission products generated within it. A release mechanism is the fundamental event which leads to release from the fuel particle. Release mechanisms may be manufacturing defects (heavy metal contamination, for example), particle failure mechanisms (such as pressure vessel failure), or simply high temperature (which enable metallic fission products to diffuse out). The accident itself does not necessarily initiate the release mechanisms responsible for its source term. Some important release mechanisms are functional during reactor operation, and are responsible for the reactor's circulating and plated-out activity. The accident serves simply to let this activity out of the primary system. Since modular HTGRs are designed to minimize fuel damage under adverse circumstances, this is common in MHTGR accident analysis.

The source term from some postulated accident may thus be classified according to the release mechanisms responsible for the released fission products. If the majority of fission products arise due to steady state release mechanisms, the accident release will be said to be *steady state dominated*. On the other hand, if most of the fission products come from release mechanisms initiated by the accident itself, the release will be called *accident dominated*. Table 2.5 lists the release mechanisms which are important for modular HTGRs, and classifies them as steady state- or accident-initiated. The Table also states whether each release mechanism contributes to the source term in either of the two postulated accidents of primary concern: core heatup or water ingress.

Heavy metal contamination and defective coating layers are obviously steady state release mechanisms. Both are present from the start of irradiation, and both cause fission products to be generated in non-retentive areas. Pressure vessel ("PV") failure of standard particles is also a steady state mechanism. In some reactor designs, constraints on heavy metal loading can force particle designs to minimize buffer layer thickness. In this case, those particles in which thin buffer layers are randomly paired with large kernels may fail during irradiation. In the modular HTGR, however, in which water ingress considerations place a *maximum* limit on heavy metal loading, this is unlikely to occur.

PV failure is also listed as an accident initiated release mechanism. High accident temperatures cause particle internal pressure

TABLE 2.5: CLASSIFICATION OF RELEASE MECHANISMS AND SOURCE TERMS

RELEASE MECHANISM	STEADY STATE OR ACCIDENT INITIATION ?	CONTRIBUTES TO SOURCE TERM IN:	
		CORE HEATUP?	WATER INGRESS?
Heavy Metal Contamination	STEADY STATE	YES	YES
Defective Coating Layers	STEADY STATE	YES	YES
PV Failure of Standard Particles	STEADY STATE	NO	NO
PV Failure	ACCIDENT	NO	NO
High Temperature Diffusion	ACCIDENT	YES	YES
SiC Thermal Decomposition	ACCIDENT	NO	NO

(this table refers to Modular HTGRs with high quality fuel only)

to increase, and may also weaken SiC's tensile strength due to accelerated fission product corrosion [V2]. However, under the conditions anticipated for modular HTGR transients, this occurs with very low frequency [V2]. SiC thermal decomposition is also accident initiated, but is beyond even the accident temperature range in modular HTGRs. High temperature diffusion is, by definition, accident initiated.

The table also indicates that the source terms due to both core heatup and water ingress accidents have components which are steady state and accident initiated. In a reactor designed so that significant fractions of the core exceed 1600C, high temperature diffusion may contribute the majority of fission products to those released, thus the source term is accident dominated. On the other hand, reactors can be designed in which no fuel ever reaches 1600C; in this case the source term is primarily circulating and plated-out activity, thus is steady state dominated. Water ingress source terms may go either way as well. Since significant release from such an occurence only results from rapid ingress with quick depressurization [L3], the same reactors which have accident dominated depressurization source terms may well have accident dominated water-ingress source terms.

2.5.3 Effects of Fuel Quality

It was noted in Section 2.2.3 that high quality fuel is characterized by low levels of heavy metal contamination and manufacturing-induced particle defects. Thus, these two important release mechanisms are highly dependent on the quality of the reactor

fuel. Furthermore, they are the only two steady state release mechanisms of significance in modular HTGRs. *Thus, the source term from any steady state dominated accident sequence will be highly dependent on fuel quality.*

This has important implications for modular HTGRs. The two risk dominant accident sequences, core heatup and water ingress, both have source term components which are steady state dominated. In fact, proper core design (such as the 200 MWth HTR-MODUL, in which maximum depressurized fuel temperatures are always less than 1600C) can insure that this is the case. Therefore, it is conceivable that, in some cases, the magnitude of the risk-dominant source terms from a modular HTGR will vary directly with fuel quality.

Based on fuel quality and core design parameters, it is possible to estimate roughly whether the release will be steady state or accident dominated. Assume that we are concerned with a relatively short-lived, metallic fission product, such as Ag-110m. The total core inventory of this isotope (in units of activity) is given by:

$$I = (P/\epsilon)\, y \qquad (2.\ )$$

where P is the reactor thermal power (Watts); ϵ is the energy released per fission (also in watts); and y is the cumulative yield of the fission product. Assuming that a negligible quantity of fission products escape from intact particles during steady operation, the steady state circulating activity is equal to the fraction of this activity generated outside the intact coating layers. This fraction is simply Φ_{HMC}, the heavy metal contamination fraction, plus $\Phi_B\Phi_R$, where Φ_B

is the fraction of broken particles and Φ_R is the recoil fraction from a bare kernel. (In reality, there is as well a component due to diffusion from bare kernels, but this is generally much smaller than the recoil fraction). Thus, the steady state activity in the primary system, A_{ss}, is equal to:

$$A_{ss} = I (\Phi_{HMC} + \Phi_B\Phi_R) \qquad (2. \ )$$

Suppose that during a severe core heatup accident, a fraction Φ_{CORE} of the reactor exceeds some critical fuel temperature (1500 or 1600 C, for example--we shall see that the exact value is not very important). Furthermore, make the conservative assumption that any *exposed* kernel subject to this temperature will release its entire fission product inventory; and furthermore, that in a well designed core an intact particle will lose a negligible fraction of its inventory. Thus, the activity release due to the accident itself is given by:

$$A_a = I \Phi_B\Phi_{CORE} \qquad (2. \ )$$

If we assume that *all* steady state activity, including fission products which are plated out on metal or graphite surfaces, is released at the start of an accident, the condition which must be fulfilled for a source term to be accident dominated is:

$$\begin{bmatrix}\text{accident} \\ \text{dominated}\end{bmatrix} \quad \Longleftarrow \quad A_a >> A_{ss}$$

Substitute Eqs. (2.) and (2.) into the above condition:

$$I \Phi_B\Phi_{CORE} >> I (\Phi_{HMC} + \Phi_B\Phi_R) \qquad (2. \ )$$

Rearrange Eq. (2.) to obtain the following relation:

$$\Phi_{CORE} >> (\Phi_{HMC}/\Phi_B) + \Phi_R \qquad (2. \ )$$

Note that the recoil fraction Φ_R is typically on the order of 10^{-5},

and is actually redundant. Thus, the final form for the accident domination condition is:

$$\Phi_{CORE} \gg (\Phi_{HMC}/\Phi_B) \qquad (2.\ )$$

In order for an isotope's release from a well-designed MHTGR core to be accident dominated, the fraction of the core which exceeds the critical fuel temperature must surpass the ratio of the contamination fraction divided by the fraction of ruptured particles. Since Φ_{CORE} can certainly be no larger than 1.0, this is equivalent to the condition $\Phi_B \gg \Phi_{HMC}$ (as promised, the precise definition of Φ_{CORE} is unimportant). Typical "nominal" fuel quality parameters (see Table 2.3) are $\Phi_B \approx 10^{-4}$ and $\Phi_{HMC} \approx 0.2\times10^{-4}$ and their ratio (Φ_{HMC}/Φ_B) is thus 0.2. MHTGR cores with these design parameters will receive contributions to fission product release which are of the same order from both circulating activity and release due to accident temperatures. For fuel with very high quality (i.e., the highest achieved to date in laboratory batches), Φ_B and Φ_{HMC} are both approximately 10^{-6}. Again, this implies significant source term contributions from both steady state and accident-induced actvity.

2.5.4 Proposed Model for Fuel Performance

As previously stated, the goal of this work is prediction of radionuclide release due to important hypothetical accidents in modular HTGRs. The aim is to define an envelope of significant design parameters within which the reactor can be considered "passively safe." Thus, to focus on parameters which will truly have the greatest effects, we must make the following assumptions:

(1) Any modular HTGR has a primary design goal of minimizing fission product release. Since these releases have components which are steady state dominated, this goal is equivalent to minimizing steady state fission product releases, which have been shown to be highly dependent on fuel quality. Thus, the MHTGRs examined in this work are assumed to possess fuel with very low levels of heavy metal contamination and manufacturing defects.

(2) Due to the first assumption, the number of fuel particle failure mechanisms which must be modeled are greatly reduced. In fact, explicit accounting for particular mechanisms is unnecessary.

The claim is that modular HTGR fuel may be adequately and realistically modeled with only a small number of fission product release mechanisms. Under both operating and transient conditions below 1600C, the following are considered to be the only significant release mechanisms:

(1) heavy metal contamination;

(2) manufacturing-induced particle defects; and

(3) diffusion of metallic fission products through coating layers.

None of the other release mechanisms discussed earlier are considered. Furthermore, as long as tempertures do not exceed 1600 C by a significant margin, no particles will be assumed to fail during a core heatup. The details of release calculations under operating and transient conditions will be presented in Chapter 6.

CHAPTER 3: THE STATIONARY PEBBLE BED REACTOR: FUNDAMENTAL CONCEPTS

This chapter introduces basic concepts for describing processes in continuously fueled pebble bed reactors. Throughout, it is assumed that the reactor is in a stationary state--i.e., that the probability distribution functions associated with parameters at any location do not change over time. Some general assumptions regarding fuel flow through the reactor are also necessary. These are that the refueling process be independent of burnup, and that the fuel flow in the core is laminar and one dimensional. The last two assumptions have been extensively studied in scale model experiments, and have been found to hold well for pebble beds of modular geometries.

Central to the material which follows is the concept of a drop probability, characterizing the likelihood of a fuel element to flow through a radial section of the reactor core. These parameters may be estimated on the basis of core geometry and pebble velocity distributions measured in scale model experiments. The branch notation introduced below is a shorthand method of characterizing a fuel element's irradiation experience. Several operators can be defined using branch notation which simplify the mathematical descriptions of pebble bed processes.

Fuel elements may be considered in two ways--as entities flowing *through* the core, or as units belonging to a population in some *region* of the core. Borrowing terminology from fluid mechanics, the former

description is called *Lagrangian*, the latter *Eulerian*. In general, these descriptions are complementary and equivalent, and there are methods to transform between one and the other. Statistical properties of the fuel may be defined in either sense.

Fuel flow and drop probabilities do not, by themselves, provide sufficient information to calculate the populations a given type of fuel elements in a given region of the core. Fuel elements may be discharged after a variable number of passes though the core, and this naturally effects the populations of pebbles with higher numbers of passes. If the burnup behavior of fuel can be completely characterized, the populations of fuel at all states may be calculated. As this characterization may be extremely difficult to carry out, a "quasi two-dimensional" approximation may be used to simplify calculations.

Fuel flowing and accumulating burnup represents an energy flux; thus an energy balance performed on a control volume within the reactor core yields a relation between fuel velocity, power density, and the gradient of burnup. In particular, if the control volume to be analyzed is the entire reactor core, a simple relation between fuel discharge burnup, pebble heavy metal content, and fresh fuel injection rate may be derived. The injection rate of fresh fuel directly sets the level of all fuel flow rates and populations.

Results from this chapter will be drawn upon in the following chapters which develop methods for predicting various fuel state parameters in a stationary pebble bed reactor.

3.1: FUEL FLOW AND DROP PROBABILITIES

3.1.1 Experimental Investigations of Pebble Bed Flow Behavior

Two aspects of pebble bed flow behavior are best studied experimentally. The first is the dependence of void fraction on radial position and of the core-average void fraction on the ratio of core to pebble diameter. The second is the flow behavior of fuel through the core. Theoretical prediction of void fraction is difficult due to the random nature of packing in the pebble bed. Theoretical prediction of pebble flow behavior is also complex, because A) pebble bed friction is difficult to incorporate into the Navier-Stokes equations, B) pressure in a pebble bed is a complicated function of space and core geometry, and C) the flow is very sensitive to certain parameters (e.g., the core exit cone transition design) which a fluid model cannot incorporate [B1].

The void fraction in a pebble bed, denoted α, is defined as follows:

$$\alpha \equiv \frac{\text{free volume}}{\text{total volume}} \qquad (3.1)$$

The radial behavior of the local void fraction has been studied in scale model tests [E1]. Intuitively, the void fraction will attain a maximum value of 1.0 at the core wall, and decrease to a minimum at a distance of 1/2 of a pebble-diameter from the wall. This is borne out by the measured curves presented in Figure (3.1) [E1]. The figure presents the void fractions measured for two test beds, with two different values of the core diameter (D) to pebble diameter (d) ratio. The initial maximum and minimum behavior is clearly visible. Further inside the core, void fraction oscillates and settles to a constant

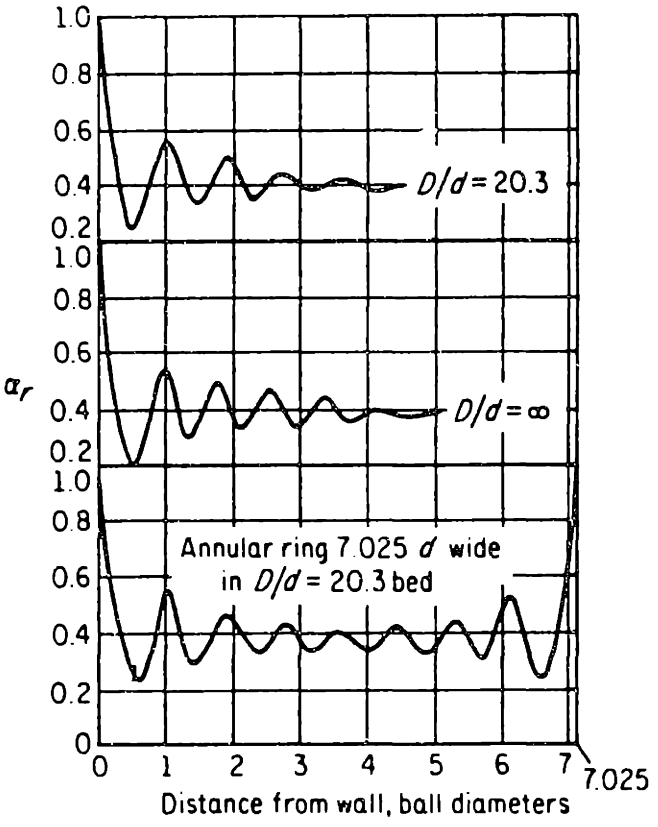

FIG. 3.1: Void fractions measured in scale model pebble beds [E1].

value of 0.39 once the distance from the wall is greater than about three pebble diameters. For the case of a modular HTGR, the value of D/d is 50, so that D/d = ∞ is a reasonable approximation.

The behavior of the core average void fraction is also of interest. Figure (3.2) presents the results of measurements of the core average void fraction for multiple scale models with varying values of D/d. Note that once the diameter ratio exceeds 5, the core average α has attained its assymptotic value of 0.39. No reactor design under serious consideration has diameter ratios which even approach this low value, and in this work it is assumed that the core average void fraction is always 0.39.

Two techniques are relevent for fuel flow investigation. The first is used to study the shapes of streamlines within a pebble bed; the second to determine the velocity distribution.

Streamlines are investigated using a transparent model core in which the motion of opaque test elements may be photographed and measured over time. Transparency is achieved by first filling the model core with transparent pebbles and then with a clear fluid with an index of refraction identical to the clear pebbles [V1]. allowing light to pass unobstructed through the core. As the clear pebbles are circulated, opaque test pebbles are inserted on the bed surface at fixed locations. Streamlines are indicated by the successive positions of opaque pebbles inserted at the same surface position at successive times. Fig (3.3) presents several photographs taken during such an experiment. These studies yielded the important qualitative result that

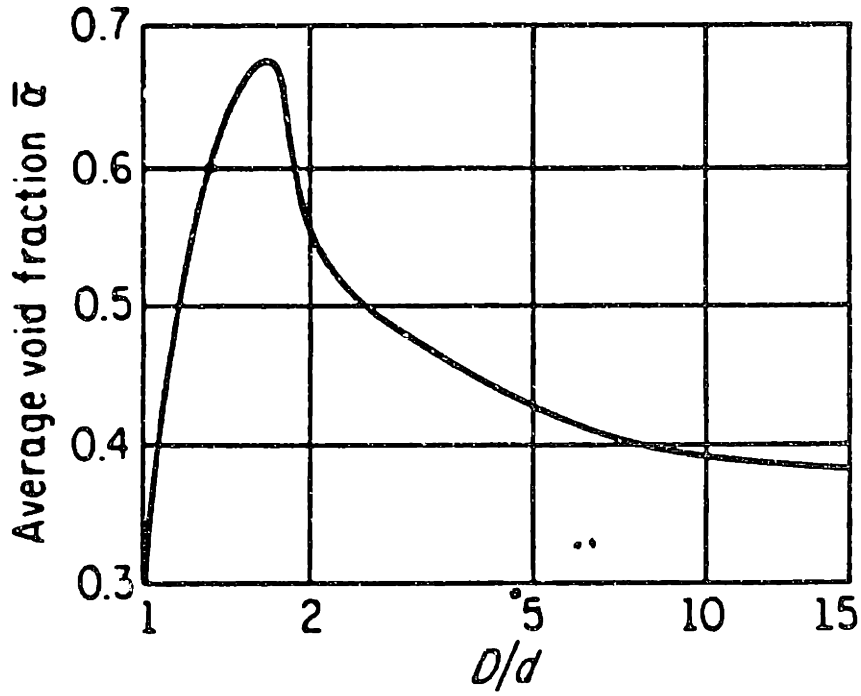

FIG. 3.2: Experimental measurements of core-average void fraction [E1].

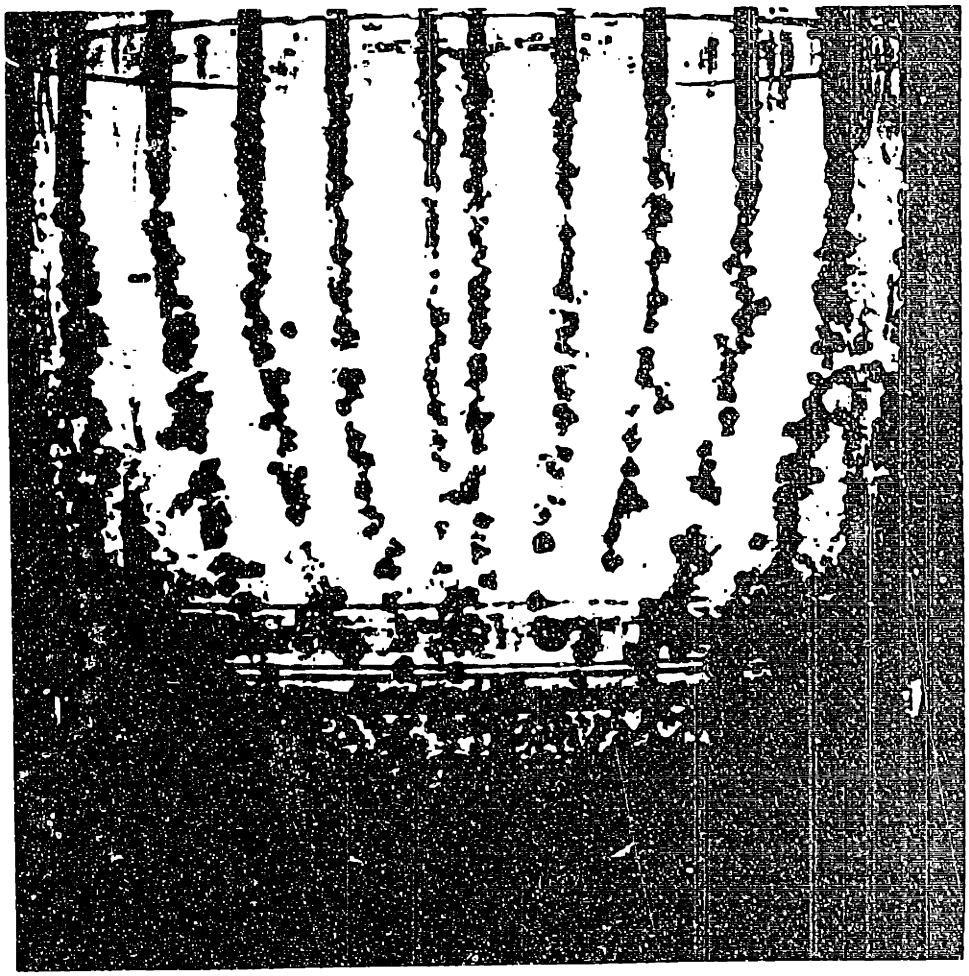

FIG. 3.3: Pebble streamlines photographed in model pebble beds [V1].

flow through a pebble bed can be considered "laminar," i.e., that streamlines of pebbles can be assumed not to cross over one another. The disadvantage of these tests are that parameter variations are difficult to study systematically.

The alternative technique does not require a transparent core. Rather, a single layer of test pebbles (tagged either with radioisotopes or of a slightly different diameter than the rest) is placed on the bed surface. The pebbles are set to circulating, and appearance of test pebbles at the core outlet is recorded as a function of time (actually as a function of the number of pebbles recirculated). The results are displayed as a "residence spectrum," giving the distribution of time required for top-layer pebles to traverse the pebble bed. Since streamlines do not cross one another, the initial radial position of each test pebble is known: the later the pebble is drawn from the core, the larger its initial radius must have been. Residence spectra may be measured for test cores with varying values of some parameter--e.g., the angle of the core exit cone. The time necessary for various percentages of the test layer to leave the core is sensitive to the varying parameter. This concept is illustrated in Figure (3.4), which shows how the residence spectra for cores with parameter variations may be combined into a single plot displaying residence times as a function of the parameter.

Figure (3.4a) represents the residence spectrum measured in a test core with the parameter of interest (e.g., reactor height/diameter) equal to "P1." The horizontal axis, V_{uc}, represents the fraction of

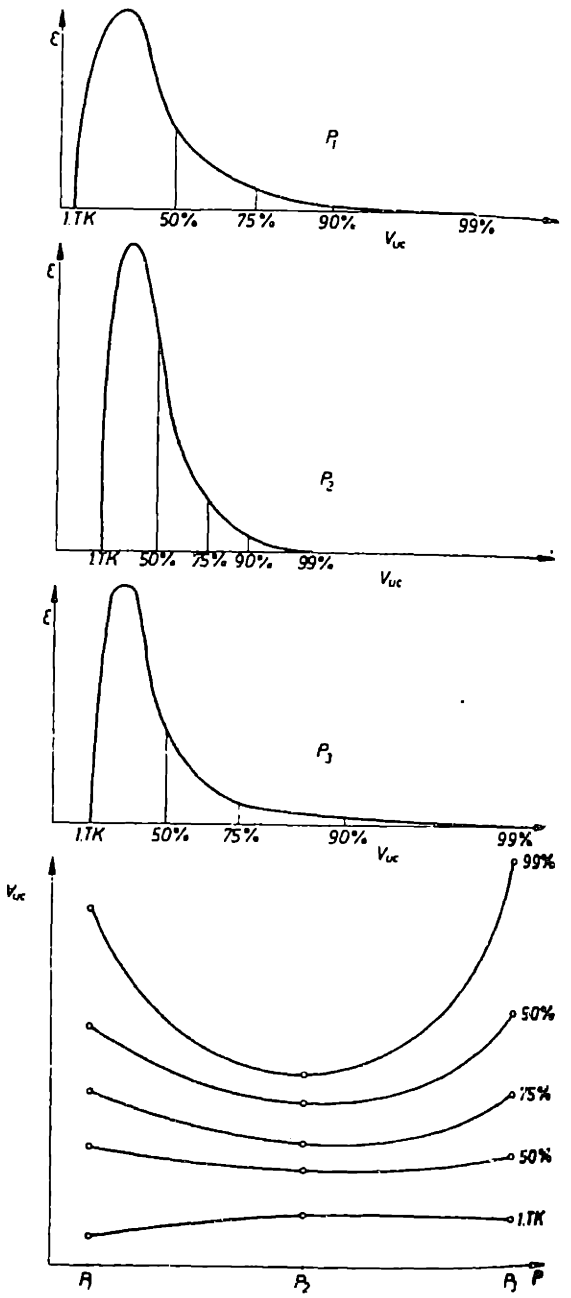

Schematic drawing of residence spectra and %TK representation.

FIG. 3.4: Residence spectra used to illustrate the effects of parameter variation [B1].

circulated core volumes, and is a measure of time normalized to account for variable rates of pebble circulation. For example, when $V_{uc} = 1.0$ the number of pebbles which have been circulated is equal to the number of pebbles in the core. The vertical axis (ϵ) is the magnitude of the residence spectrum. It is defined by [B1]:

$$\epsilon(V_{uc}) \equiv \frac{1}{\Sigma(TK)} \lim_{\Delta V_{uc} \to 0} \frac{\Delta TK(V_{uc})}{\Delta V_{uc}}$$

where $\Sigma(TK)$ = the total number of test (top layer) pebbles (a normalizing factor);

$\Delta TK(V_{uc})$ = the number of test pebbles observed at the core exit within "time" ΔV_{uc} of V_{uc}.

ΔV_{uc} = an incremental number of pebbles cycled.

Thus, ϵ is proportional to the instantaneous rate of test pebble removal, normalized so that the integral of ϵ over all "time" is 1.0. In Figure 3.4, positions along the V_{uc} axis are indicated by values of:

$$\int_0^{V_{uc}} \epsilon \, d(V_{uc})$$

Thus, the point on the V_{uc} axis in Figure (3.4a) marked 50% indicates the number of core volumes which must be circulated before one half of the top-layer pebbles appear at the core outlet.

The shape of the residence spectrum indicates how uniformly the top layer of pebbles flows through the core. If a core had perfect slug flow, $\epsilon(V_{uc})$ would be a delta function at $V_{uc} = 1.0$. The extent to which ϵ is spread out indicates the amount of non-uniformity in the pebble velocity distribution.

Figures (3.4b) and (3.4c) represent residence spectra obtained from

two cores with two other values of the interesting parameter (P2 and P3). Core P2 resulted in more uniform flow, while core P3's residence spectrum is more spread out. Figure (3.4d) shows how the three residence spectra may be combined to more clearly illustrate the effects of the parameter. The horizontal axis now represents values of the parameter of interest; the vertical axis is now the V_{uc} necessary to circulate various percentages of the top-layer pebbles. Points on the curves are read from the "$\int\epsilon$" points on the three previous figures.

Bedenig, et. al. [B1] performed numerous parameter studies using the residence spectrum method. The important results for the purposes of this work are presented in Figure (3.5), which shows the influence of the reactor height/diameter ratio on residence times for test cores with varied pebble/core diameter ratios. Note that once H/D is greater than approximately 1.0, the first and last test pebbles were found to leave the core at virtually the same time. This indicates a practically uniform flow of pebbles from the surface to the core exit. The same was found to be true in other parameter studies (e.g., specific sphere weight and core frictional properties). Since the typical modular HTGR core has an H/D value of approximatly 3.0, it is clear that a uniform flow assumption is justified for these cores on the basis of Bedenig's measurements. In this work, we treat the more general case in which radial variation of pebble axial velocity is possible.

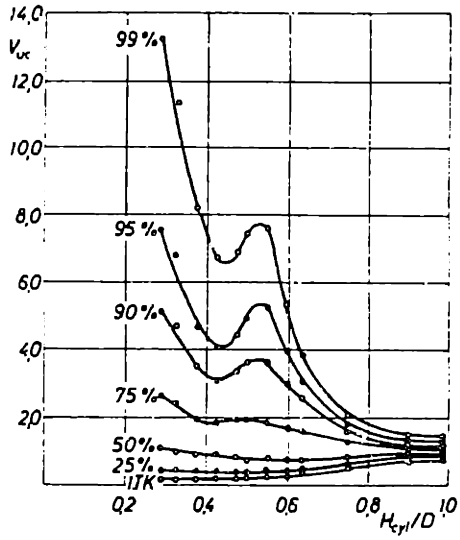

Fig. 7a

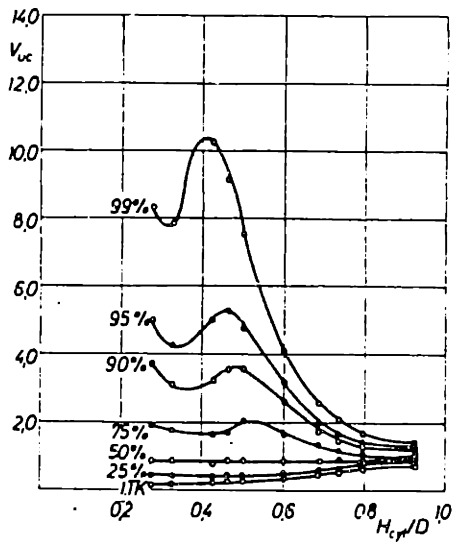

Fig. 7b

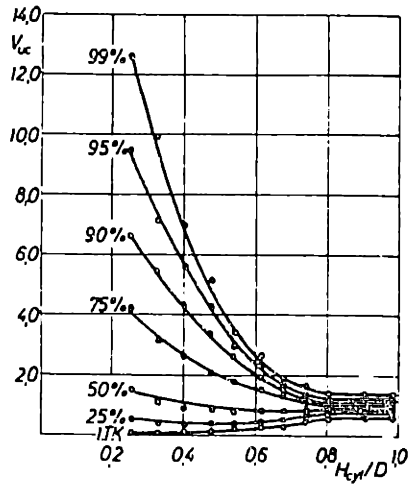

Fig. 7c

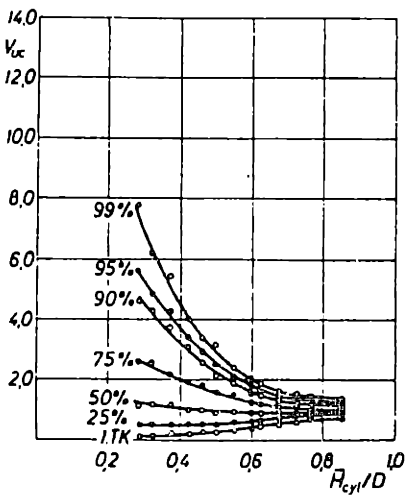

Fig. 7d

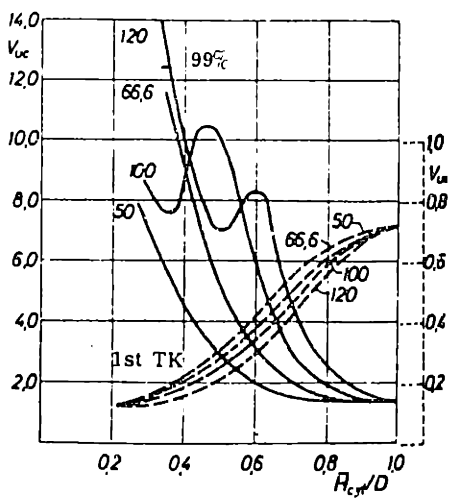

Influence of relative sphere diameter; steel balls.
a) D/d = 120 c) D/d = 66.6
b) D/d = 100 d) D/d = 50
e) Comparison of different sphere diameter results.

FIG. 3.5: Influence of reactor height/diameter (H/D) and pebble/core diameter (d/D) on test bed residence spectra [V1].

3.1.2: Mathematical Formulation

A pebble bed reactor is probabilistic in nature due to the random manner in which fuel is loaded onto the top of the core. It is possible to characterize this process with parameters called *drop probabilities*, which quantify the likelihood of a fuel element flowing through a radial subregion of the core. To derive a mathematical definition for the drop probability, consider the idealized pebble bed reactor shown in Fig. 3.6. In this reactor, fuel velocity is one-dimensional, varying in the r-direction and possessing only an axial component. The core itself is sectioned into several annular "drop zones." Now, except for entrance and exit effects, which may be ignored during the majority of the pebble's in-core career, a fuel element will flow through only one of these drop zones on each pass through the core. The drop probability is defined as the probability that a pebble will flow through a particular drop zone on any pass (once entrance/exit effects have subsided).

It is possible to calculate the drop probabilities from more fundamental parameters. Let $\dot{K}$ be the total flow rate of fuel elements through the pebble bed (pebbles/sec). The drop zones are indexed 1, 2, ... N, and $\dot{k}_i$ denotes the flow of pebbles through drop zone "i." The number of pebbles per second entering drop zone i is simply the total pebble flow rate times the drop probability. Thus, a mathematical definition of the drop probability is:

$$p_i \equiv \dot{k}_i / \dot{K} \quad . \tag{3.2}$$

The rate of injection of pebbles into a drop zone may be calculated

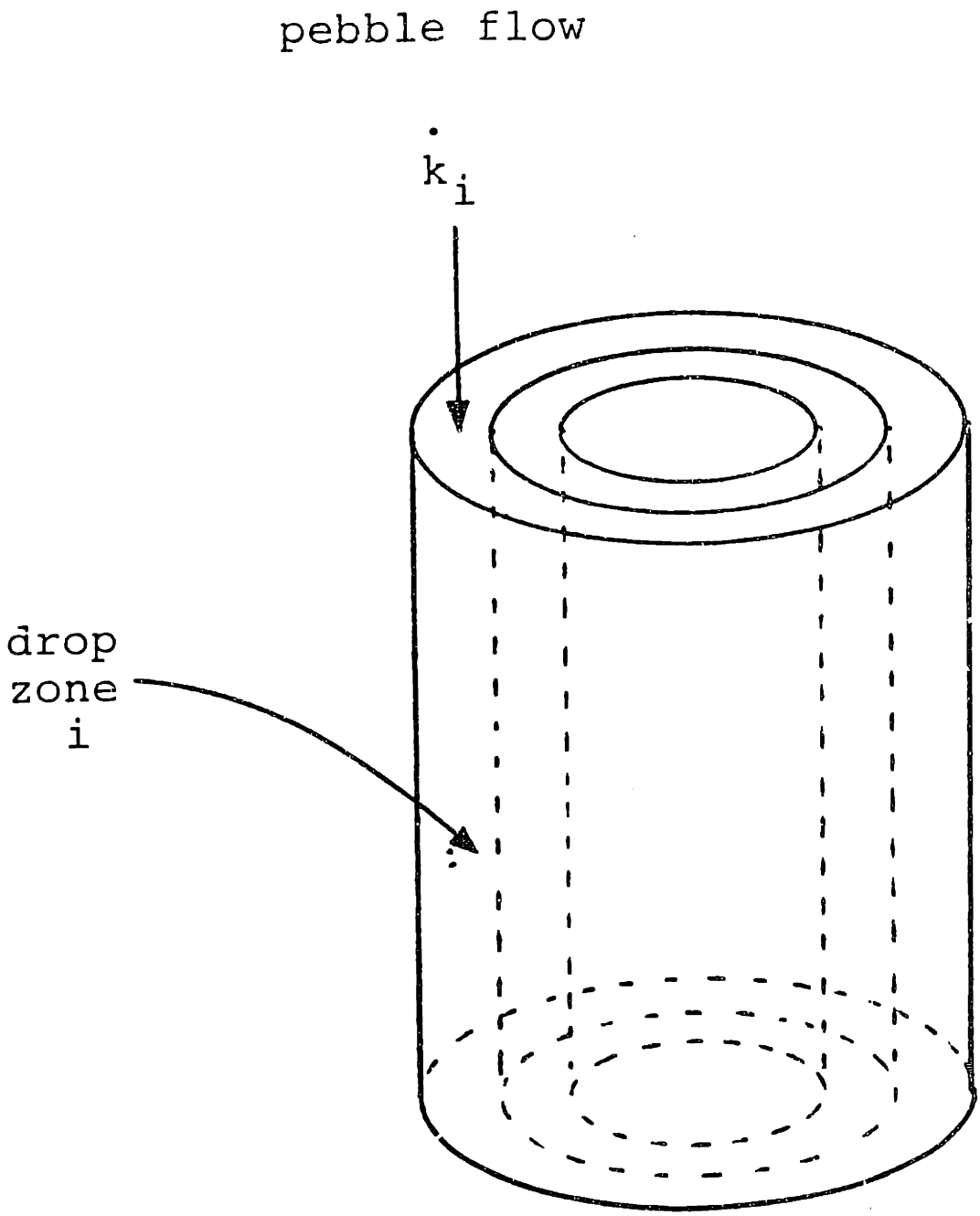

FIG. 3.6: Idealized pebble bed reactor with radial "drop zones."

based on a known pebble velocity distribution (measured in scale model experiments), pebble and zone geometry, and the void fraction within the drop zone. Let $\dot{Q}_i$ represent the volumetric flow through drop zone i (m^3 of pebbles + associated core volume/sec). Clearly, $\dot{Q}_i$ is equal to the pebble flow rate multiplied by the core volume occupied by a pebble:

$$\dot{Q}_i = \dot{k}_i \, v_p / (1-\alpha_i) \qquad (3.3)$$

where v_p = the volume of a single pebble (m^3), and

α_i = the void fraction in drop zone i.

The volumetric fuel flow through zone i may alternately be expressed in terms of the zone's cross sectional area and the fuel velocity:

$$\dot{Q}_i = A_i \, u_i \qquad (3.4)$$

where A_i = the cross sectional area of drop zone i (m^2), and

u_i = axial pebble velocity within drop zone i (m/sec).

Combine equations (3.3) and (3.4) for an expression for the pebble flow rate through zone i:

$$\dot{k}_i = \frac{A_i \, u_i \, (1-\alpha_i)}{v_p} \qquad (3.5)$$

The individual drop zone flow rates must add up to the total pebble flow rate:

$$\dot{K} = \sum_i \dot{k}_i \qquad (3.6)$$

Thus, combining Eqs. (3.2), (3.4), and (3.6), the drop probability becomes:

$$p_i = \frac{A_i\, u_i\, (1-\alpha_i)}{\sum_j A_j\, u_j\, (1-\alpha_j)} \qquad (3.7)$$

(where v_p has been eliminated since it is identical in all drop zones).

Equation (3.7) simplifies considerably if various assumptions can be made regarding pebble flow and core geometry. For example, if the core void fraction is assumed constant and pebble velocity uniform across the core, Eq. (3.6) becomes:

$$p_i = A_i \,/\, A_{tot} \qquad (3.8)$$

where A_{tot} is the core's total cross sectional area. However, such assumptions, though often justified, are not necessary in the work which follows.

By using drop probabilities, it is possible to calculate the rate at which fuel elements flow through any predetermined sequence of drop zones. This is possible because the fuel injection process in a simple pebble bed core is independent of the state of the pebbles which are refueled. For example, let $\dot{K}_f$ represent the rate at which fresh fuel elements are injected into the core. If there are N drop zones in the core, with associated drop probabilities p_1, p_2, ... p_N, then the flow rates of fresh fuel through each of these zones follows directly from the Definition (3.2):

the flow rate of fresh fuel into:

drop zone 1 = $p_1 \dot{K}_f$

drop zone 2 = $p_2 \dot{K}_f$

$\vdots$

drop zone N = $p_N \dot{K}_f$

Following the first pass, each of these sub-flows is once again redropped. If (i,j) represents any possible sequence of two drop zones, the rate at which fuel flows through (i,j) is simply:

$$\text{rate of fuel flow through sequence } (i,j) \equiv \dot{k}_{(i,j)} = p_i\, p_j\, \dot{K}_f$$

Of course, this reasoning may be extended to any drop zone sequence of arbitrary length. Thus:

$$\text{rate of fuel flow through sequence } (i,j,\ldots n) \equiv \dot{k}_{(i,j,\ldots n)} = p_i\, p_j \cdots p_n\, \dot{K}_f$$

3.2: Branch Notation

In the work which follows, it will be useful to have a short-hand method of referring to the sequences of drop zones discussed in the previous section. Such *branch notation* will prove to be a powerful tool for describing pebble bed processes.

> DEFINITION: A *branch variable* β is an ordered list of positive integers $(i,j,k \cdots l,m,n)$. The number of elements in the sequence is defined as the *order* w *of* β. Every element of β must be less than or equal to some maximum value N_{max}.

For our purposes, a branch actually represents an event in the probabilistic sense, namely: the sequence of drop zones which a fuel element has passed through is $\beta = (i,j,k \cdots l,m.n)$. The limiting value

for an element of β, N_{max}, is the number of radial drop zones into which the core is partitioned. In the core of an operating pebble bed reactor, fuel elements posses a range of possible β values, with orders ranging from 1 (only fresh fuel before it enters the core has a branch variable of order 0) to various terminal orders. All branches present in a core are said to comprise the *comprehensive sample space* B for that reactor. The comprehensive sample space may be subdivided into some finite number of mutually exclusive *sample spaces of order* w, denoted by B_w, where w may range from 0 to the maximum number of passes a fuel element can remain in the core. Each of these sub-sample spaces is composed of branches of identical order w. Thus, the statement

$$\beta \in B_w$$

is equivalent to the statement that a pebble with associated branch variable β is currently on its w'th pass through the core.

For the purposes of this work, the sequential order of the elements of β are significant. Thus, when it is necessary to include this information, the branch variable will be written as:

$$\beta = (i_1, i_2, \cdots i_{w-1}, i_w)$$

A useful function may be defined which expresses the sequentiality of two branches::

DEFINITION: The parent branch β' of branch β is defined as follows:

IF $\beta = (i_1, i_2 \cdots i_{w-1}, i_w)$ THEN $\beta' = (i_1, i_2 \cdots i_{w-1})$

where $\beta \in B_w$ and $\beta' \in B_{w-1}$.

Equivalently, we may also write $\beta \equiv (\beta', i_w)$. Three useful operators may be defined using branch notation: branch probability, branch summation, and branch expectation.

BRANCH PROBABILITY OPERATOR

The branch probability operator will be denoted by p_β. It is defined as:

$$p_\beta \equiv p_{(i_1, i_2 \cdots i_w)} \equiv p_{i_1} p_{i_2} \cdots p_{i_w}, \quad \beta \in B_w \tag{3.9}$$

where the quantities p_{i_j} are the drop probabilities associated with the j'th radial drop zone indicated by β. This operator is useful for expressing the rate of fuel flow through a branch β:

$$\dot{k}_\beta = p_{i_1} p_{i_2} \cdots p_{i_w} \dot{K}_f = p_\beta \dot{K}_f \tag{3.10}$$

Note also that the branch probability operator may be expressed in terms of parent branches:

$$p_\beta = (p_{i_1} p_{i_2} \cdots p_{i_{w-1}}) p_{i_w} = p_{\beta'} p_{i_w} \tag{3.11}$$

BRANCH SUMMATION OPERATOR

The branch summation operator is defined to enumerate all possible values of the w'th order branch variable. The definition is:

$$\sum_\beta \equiv \sum_{i_w=1}^{N_{max}} \sum_{i_{w-1}=1}^{N_{max}} \cdots \sum_{i_2=1}^{N_{max}} \sum_{i_1=1}^{N_{max}} \quad \text{for } \beta \in B_w \tag{3.12}$$

Note that whatever appears following the branch summation operator will be subjected to each value of the w'th order branch variable once

and only once. Also, note that the branch summation operator may be written in terms of parent branches as well:

$$\sum_{\beta} \equiv \sum_{i_w} \left\{ \sum_{i_{w-1}} \cdots \sum_{i_2} \sum_{i_1} \right\} = \sum_{i_w} \sum_{\beta'} \qquad (3.13)$$

where the limits on the summation signs have been ommited for brevity.

Using the two operators defined so far, it is possible to prove the following identity:

$$\sum_{\beta} p_{\beta} = 1 \qquad (3.14)$$

This is easily demonstrated by expanding both the summation and the probability with their definitions:

$$\begin{aligned} \sum_{\beta} p_{\beta} &= \left\{ \sum_{i_w} \sum_{i_{w-1}} \cdots \sum_{i_2} \sum_{i_1} \right\} \left\{ p_{i_w} p_{i_{w-1}} \cdots p_{i_2} p_{i_1} \right\} \\ &= \left\{ \sum_{i_w} p_{i_w} \right\} \left\{ \sum_{i_{w-1}} p_{i_{w-1}} \right\} \cdots \left\{ \sum_{i_2} p_{i_2} \right\} \left\{ \sum_{i_1} p_{i_1} \right\} \\ &= \left\{ 1 \right\} \left\{ 1 \right\} \cdots \left\{ 1 \right\} \left\{ 1 \right\} = 1 \end{aligned}$$

The middle step in the above demonstration is possible because the indices associated with each individual drop probability are independent.

BRANCH EXPECTATION OPERATOR

The branch- or L- expectation operator on some function $Z(\beta)$ is defined as follows:

$$E[\, Z(\beta) \,] \equiv \sum_{\beta} p_{\beta} Z(\beta) \equiv \overline{Z(\beta)} \qquad (3.15)$$

Note that the branch summation operation insures that the function

$Z(\beta)$ is completely enumerated over the w'th order event space. Furthermore, the branch probability operator weights each value $Z(\beta)$ by the pebble flow rate through that branch. The branch expectation operation may also be expressed in terms of parent branches:

$$E[\ Z(\beta)\ ] = \sum_{\beta} p_{\beta}\ Z(\beta) = \sum_{i_w} \sum_{\beta'} p_{i_w}\ p_{\beta'}\ Z(\beta) \qquad (3.16)$$

Note that the index "i_w" is independent of all indices contained within β'. Thus, the quantity p_{i_w} may be taken outside the β' summation:

$$E[\ Z(\beta)\ ] = \sum_{i_w} p_{i_w} \sum_{\beta'} p_{\beta'}\ Z(\beta) \qquad (3.17)$$

Equation (3.17) will prove useful when deriving recursive relations for changes in fuel states from one pass to the next.

The branch expectation operation has important physical significance. Suppose at the exit of a pebble bed core, data is recorded for every pebble exiting its w'th pass. The data recorded is the value of some fuel state property denoted $Z(\beta)$. For a particular value of β (denoted β_o) the frequency at which the property $Z(\beta_o)$ is observed is $\dot{k}_{\beta_o}$. If data is collected for some time Δt, the number of pebbles observed with state $Z(\beta_o)$ is:

$$\#\ \text{of pebbles with}\ Z(\beta_o) = \dot{k}_{\beta_o}\ \Delta t \qquad (3.18)$$

Since the branch summation operation will enumerate every w'th order branch fuel flow, the total number of pebbles observed during this time period is:

$$\text{total \# pebbles observed} = \Delta t \sum_{\beta} \dot{k}_{\beta} \tag{3.19}$$

Thus, the fraction of all the observed pebbles with $Z(\beta_o)$, which is simply the frequency- or flow-weighted probability of observing the value $Z(\beta_o)$, is:

$$P_o = \frac{\dot{k}_{\beta_o} \Delta t}{\sum_{\beta} \dot{k}_{\beta} \Delta t} = \frac{p_{\beta_o} \dot{K}_f}{\sum_{\beta} p_{\beta} \dot{K}_f} = p_{\beta_o} \tag{3.20}$$

Thus, the probability that one of the pebble observations results in $Z(\beta_o)$ is simply the branch probability p_{β_o}. The frequency- or flow-weighted expectation value of Z (observed at the core exit following pass w) is the sum of all possible observations multiplied by their frequency-weighted probabilities. Thus:

$$\overline{Z(\beta)} = \sum_{\beta} p_{\beta} Z(\beta) = E[\, Z(\beta) \,] \tag{3.21}$$

Finally, note that $E[\, Z(\beta) \,]$ has "integrated out" the branch variable β. However, $\overline{Z(\beta)}$ is still dependent on the order w of β. Thus, the symbol $\bar{Z}_w$ will be used as a convenient shorthand for $E[\, Z(\beta) \,]$, $\beta \in B_w$

3.3 FUEL POPULATIONS

It has been demonstrated that the rate of fuel flow through any branch, or sequence of radial drop zones, may be calculated using drop probabilities and a known injection rate of fresh fuel. It is also possible to calculate the *population* of a branch in a steady state core. Knowledge of these populations is the first step in discussing the volumetric or Eulerian properties of the reactor.

If the velocity of fuel is known in every drop zone, then elementary kinematics yields the residence time Δt_i for drop zone i:

$$\Delta t_i = H / u_i \qquad (3.22)$$

where H = the height of the core {m}, and

u_i = fuel velocity through drop zone i {m/sec}.

Consider a branch β in the stationary core. Its population may undergo random fluctuation, but its mean value over time is fixed (i.e., there can be no *systematic* fluctuations). Furthermore, it is clear upon reflection that if $\dot{k}_\beta$ pebbles per second enter the branch, and each remains in the branch for a period of time $\Delta t_{i_w} = H / u_{i_w}$, then the population of the branch must be:

$$\begin{matrix}\text{population} \\ \text{of branch } \beta\end{matrix} \equiv k_\beta = \dot{k}_\beta \, \Delta t_{i_w} \qquad [\, \beta = (i_1, i_2 \ldots i_w) \,] \qquad (3.23)$$

Every branch β is associated with a particular radial zone of the core--namely, the last element in the branch variable (i_w), which corresponds to the radial drop zone a fuel element currently resides in. The total number of pebbles within any zone is the sum of the populations of all branches with that zone as a terminal member. This

quantity will be denoted k_n, where n is the value of a radial drop zone index.

An Eulerian probability Π_β may be defined for a branch within its current drop zone:

$$\Pi_\beta \equiv \frac{k_\beta}{k_n} = \frac{\dot{k}_\beta \, \Delta t_n}{k_n} = p_\beta \frac{\dot{K}_f \, H}{k_n \, u_n} \qquad (3.24)$$

Π_β is the probability associated with a different probabilistic event than the fuel drop. If a pebble were drawn at random from drop zone n, the probability that β is its associated branch variable is Π_β. Thus, the Eulerian probabilities are associated with a particular region of the core, and not a particular fuel element. The drop probabilities p_β, on the other hand, are Lagrangian quantities associated with a particular fuel element. Section 3.4 will make more clear the distinction and applications of these two descriptive techniques.

It is sometimes useful to speak of the entire core as a single unit, or "point core." An average residence time, $\overline{\Delta t}$, may be defined by inverting a generalized version of Eq. (3.23) above. Suppose some flow of fuel $\dot{k}$ enters the core. If the core has N radial drop zones, the flow splits into N subflows whose magnitudes are determined by the appropriate drop probabilities. The average residence time is determined by the steady state population of these pebbles within the core:

$$\overline{\Delta t} \equiv \frac{k}{\dot{k}} = \frac{\sum_{i=1}^{N} p_i \, \Delta t_i \, \dot{k}}{\dot{k}} = \sum_i p_i \, \Delta t_i \qquad (3.25)$$

where p_i and Δt_i are the drop probability and residence time associated with radial drop zone i, respectively.

The concepts of branch flows and populations introduced so far are best illustrated by working through two simple examples. Both represent idealized systems which are simple enough so that core and branch flows and populations may be completely enumerated. The first example is a particularly simple case, in which all fuel elements are assumed to remain in the core for an identical number of passes. In the second case, the more general problem is addressed in which fuel elements may be discharged after a variable number of passes.

EXAMPLE 1

Consider a very simple pebble bed reactor core which is divided into three radial drop zones. For this example, no axial subdivision of the core is considered. Furthermore, suppose that the properties of this core are such that all pebbles are discharged following their third pass. This core shall be referred to as "core A." The possible fuel states in core A are displayed in Figure (3.7). Core A is assumed to be stationary--that is, all fuel flows and populations have achieved their steady state values.

The figure is divided into nine major compartments, arranged in a square array. Compartments in the same horizontal row represent pebbles traversing the core for the same pass; compartments in the same vertical

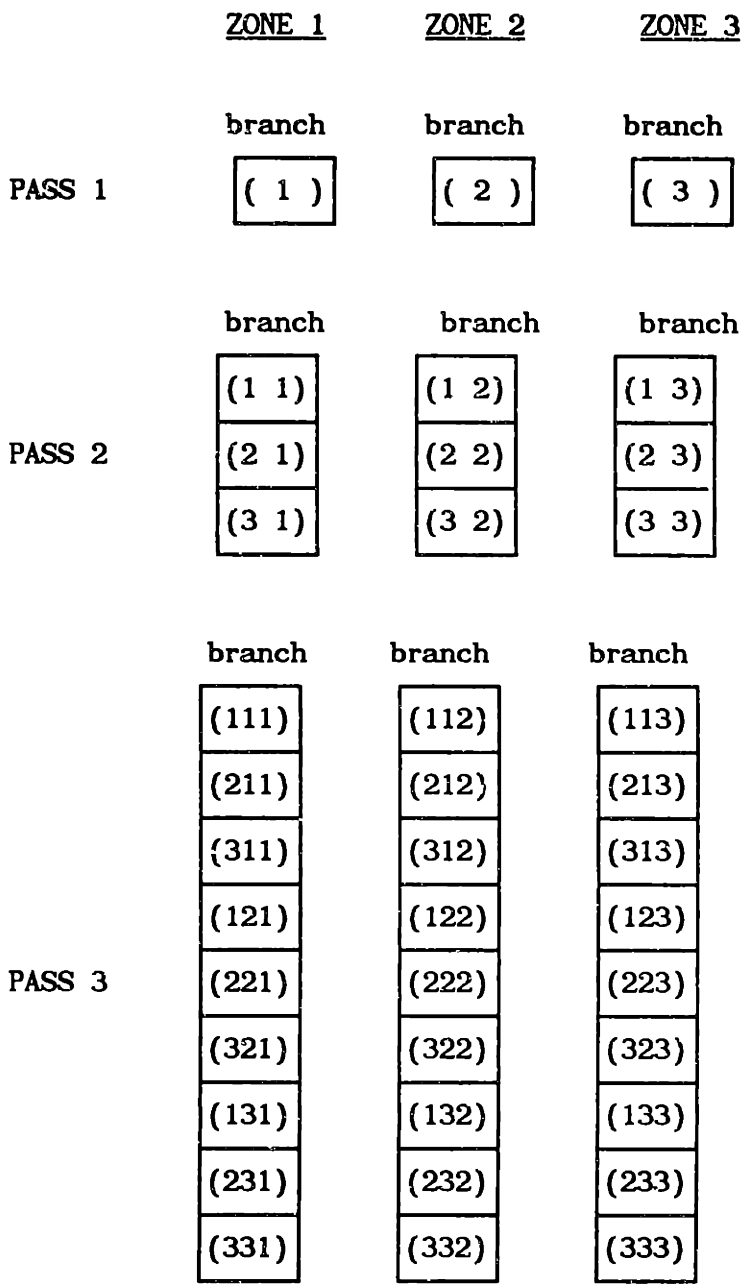

FIG. 3.7: The Comprehensive Sample Space for "Core A."

column represent pebbles in identical radial core zones. Each of the nine larger compartments is further subdivided: each row across is associated with a particular branch variable, whose value appears in the leftmost box. To the right of the branch name are two more boxes, one for the branch flow rate and the other for the branch population. Every possible fuel state appears somewhere in the figure.

The following steady-state parameters are postulated for core A:

fresh fuel injection rate: $\dot{K}_f$ = 216 pebbles/month;

drop probabilities: $p_1 = 3/6$, $p_2 = 2/6$, $p_3 = 1/6$;

residence times: Δt_1 = 3 mo., Δt_2 = 5 mo., Δt_3 = 6 mo.

Note that $\dot{K}_f$ is the *fresh* fuel injection rate, and not the total recirculation rate. Since all fuel goes through three passes prior to discharge, the total recirculation rate of fresh and burned fuel is 3×216 = 648 pebbles per month.

First consider the manner in which fuel flows distribute among the various branches. In Figure (3.8), arrows are included signifying the flow of fuel from some branches into others. For example, consider branch (1), which receives fresh fuel at a rate equal to $\dot{k}_{(1)} = p_1\dot{K}_f$ = 108 pebbles/month. Fuel leaving branch (1) flows into three second-order branches: (1,1), (1,2), and (1,3). The flow rate of fuel entering branch (1,2), for example, is simply $\dot{k}_{(1,2)} = p_2\dot{k}_{(1)} = p_2p_1\dot{K}_f$ = 36 pebbles/month. Every branch receives only one flow, which originates from its parent branch, and three flows (one per zone) leave every non-terminal branch. All flows which leave the core permamently are

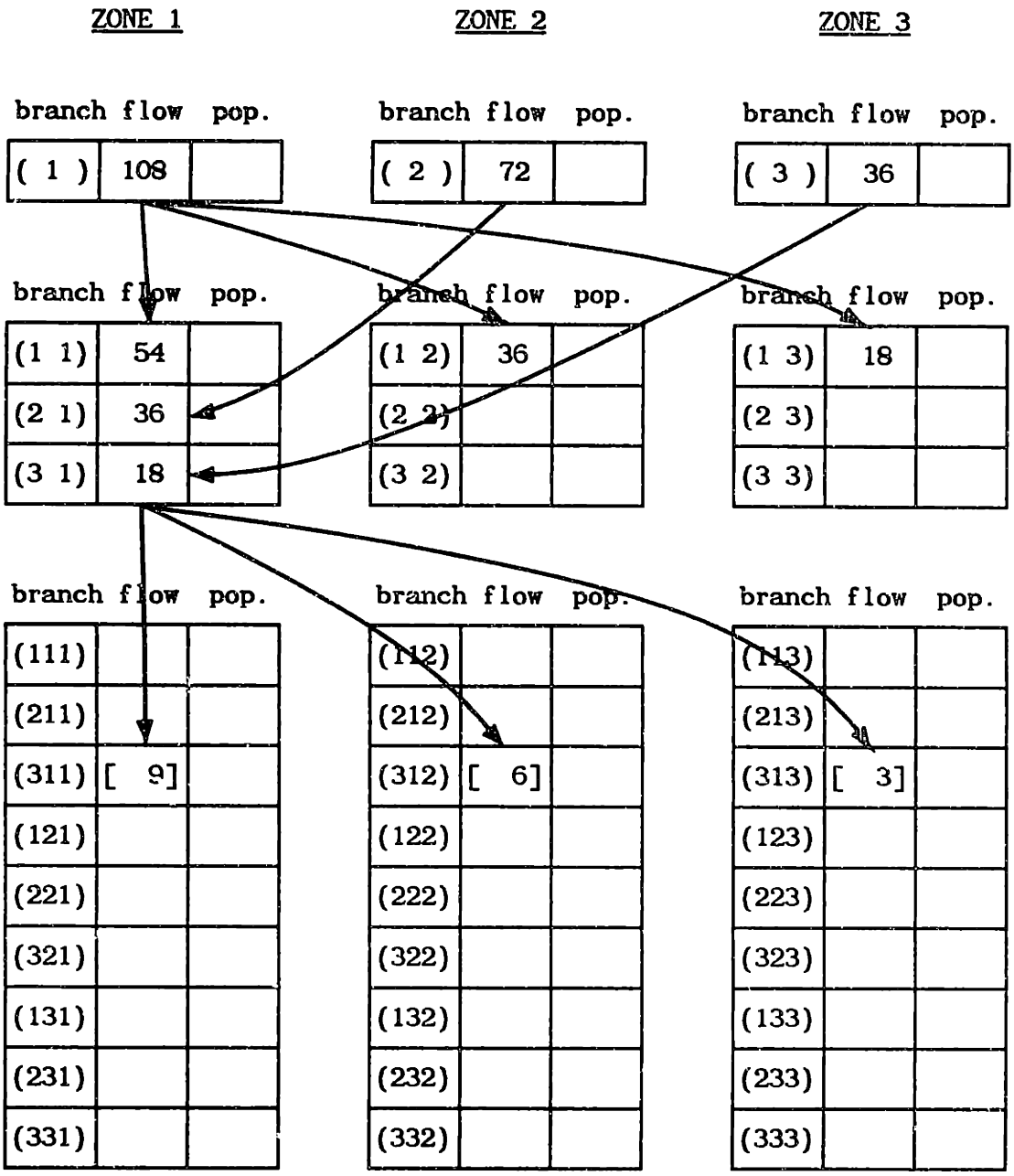

FIG. 3.8: Branch Flows and Populations in "Core A."

TABLE 3.1: EULERIAN PROBABILITIES FOR CORE A

RADIAL ZONE #	PASS NUMBER 1	2	3	
1	0.120	0.120	0.120	Σ = 0.360
2	0.133	0.133	0.133	Σ = 0.300
3	0.080	0.080	0.080	Σ = 0.240
	Σ = 0.330	Σ = 0.330	Σ = 0.330	

indicated by square brackets "[ ]" in the figure.

Note that the zone residence times have no direct influence on determining the magnitudes of these fuel flows (except for their influence on the drop probabilites themselves).

The next Figure (3.9) has completed the compartments for all branches. All flows were multiplied by the appropriate residence times (as per Eq. 3.23) to obtain branch populations, which also appear in the table. Examination of the figure reveals:

1. The total core population is 2700 pebbles.
2. The pebbles are evenly distributed among all three passes; each pass has a population of 900 pebbles.
3. The average residence time per pass is $\Sigma\, p_i \Delta t_i$ = 4.167 months.
4. Eulerian probabilities for each pass in a radial zone may be calculated from the population in Figure (3.9). These probabilities are presented in Table (3.1). The summations going *across* the table indicate the fractions of pebbles in the radial drop zones; the *vertical* summations yield the

ZONE 1

branch	flow	pop.
(1)	108	324

branch	flow	pop.
(1 1)	54	162
(2 1)	36	108
(3 1)	18	54

branch	flow	pop.
(111)	[27]	81
(211)	[18]	54
(311)	[9]	27
(121)	[18]	54
(221)	[12]	36
(321)	[6]	18
(131)	[9]	27
(231)	[6]	18
(331)	[3]	9

ZONE 2

branch	flow	pop.
(2)	72	360

branch	flow	pop.
(1 2)	36	180
(2 2)	24	120
(3 2)	12	60

branch	flow	pop.
(112)	[18]	90
(212)	[12]	60
(312)	[6]	30
(122)	[12]	60
(222)	[8]	40
(322)	[4]	20
(132)	[6]	30
(232)	[4]	20
(332)	[2]	10

ZONE 3

branch	flow	pop.
(3)	36	216

branch	flow	pop.
(1 3)	18	108
(2 3)	12	72
(3 3)	6	36

branch	flow	pop.
(113)	[9]	54
(213)	[6]	36
(313)	[3]	18
(123)	[6]	36
(223)	[4]	24
(323)	[2]	12
(133)	[3]	18
(233)	[2]	12
(333)	[1]	6

FIG. 3.9: Complete Branch Flows and Populations in "Core A."

fractions of pebbles at various pass numbers.

EXAMPLE 2:

The cutoff burnup is the value of burnup beyond which a fuel element will be discharged from the core. To illustrate the effects of a cutoff burnup on the populations of fuel in a steady state pebble bed reactor, another simple core designated "core B" is defined. In core B, shown in Figure (3.10), it is assumed that the rate of burnup accumulation in zones 1 and 2 are higher than in zone 3, so that fuel leaving branches (1,1), (1,2), and (2,1) is immediately discarded. All other fuel is discharged following its third pass. Figure (3.11) displays all calculted pebble flows and branch populations, with empty branches denoted by asterisks. The following points are important:

1. Total core population is now only 2,175 pebbles.
1. A constant flow of 126 pebbles/month leaves the core from the second-order branches. This flow originates from one-third of the second pass branches.
2. One-third of the possible third-order branches are unoccupied, corresponding to the one-third second-pass branches whose flows exited the core.
3. The flows and populations in all occupied branches are identical to the corresponding core-A branches.
4. However, the pass flows and populations are significantly different in cores A and B.
5. The total pebble populations for each pass/zone combination are presented in Table (3.2), along with the core-wide E-probabilities calculated from them.

The Eulerian probabilities calculated in the above example were based on the detailed populations calculated in Fig. (3.11). However, a

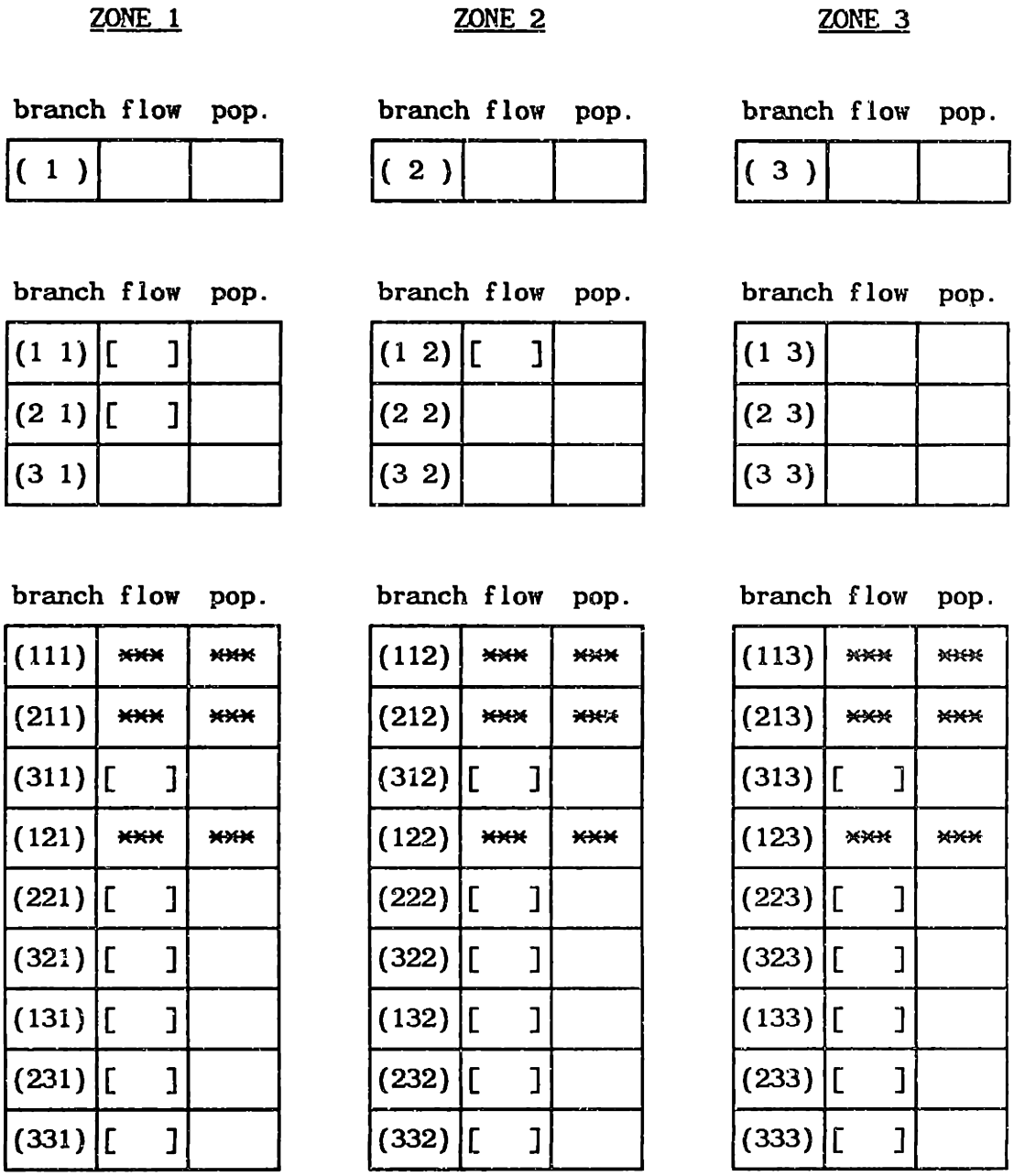

FIG. 3.10: Fuel Flow Pattern in "Core B."

ZONE 1

branch	flow	pop.
(1)	108	324

branch	flow	pop.
(1 1)	[54]	162
(2 1)	[36]	108
(3 1)	18	54

branch	flow	pop.
(111)	***	***
(211)	***	***
(311)	[9]	27
(121)	***	***
(221)	[12]	36
(321)	[6]	18
(131)	[9]	27
(231)	[6]	18
(331)	[3]	9

ZONE 2

branch	flow	pop.
(2)	72	360

branch	flow	pop.
(1 2)	[36]	180
(2 2)	24	120
(3 2)	12	60

branch	flow	pop.
(112)	***	***
(212)	***	***
(312)	[6]	30
(122)	***	***
(222)	[8]	40
(322)	[4]	20
(132)	[6]	30
(232)	[4]	20
(332)	[2]	10

ZONE 3

branch	flow	pop.
(3)	36	216

branch	flow	pop.
(1 3)	18	108
(2 3)	12	72
(3 3)	6	36

branch	flow	pop.
(113)	***	***
(213)	***	***
(313)	[3]	18
(123)	***	***
(223)	[4]	24
(323)	[2]	12
(133)	[3]	18
(233)	[2]	12
(333)	[1]	6

FIG. 3.11: Complete Branch Flows and Populations in "Core B."

TABLE 3.2: EULERIAN PROBABILITIES FOR CORE B

		PASS NUMBER 1	2	3	
RADIAL ZONE #	1	0.149	0.149	0.062	Σ = 0.360
	2	0.166	0.166	0.069	Σ = 0.401
	3	0.099	0.099	0.041	Σ = 0.239
		Σ = 0.414	Σ = 0.414	Σ = 0.172	

more general method may be formulated.

Let the symbol α_w denote the following ratio:

$$\alpha_w = \dot{k}_w / \dot{K}_f \tag{3.26}$$

where $\dot{k}_w$ represents the rate of fuel flowing through all w'th order branches. Furthermore, define the *discharge indicator function* $\phi_d(\beta)$:

$$\phi_d(\beta) \equiv \begin{cases} 0 \text{ if the pebble is discharged immediately following branch } \beta \text{ or if } \phi_d(\beta') = 0; \\ 1 \text{ if the pebble is recycled following branch } \beta. \end{cases} \tag{3.27}$$

The value of the indicator function is a complex function of the neutronic processes which a pebble experiences during its traversal of the core. Chapter 4 will address means by which the value of $\phi_d(\beta)$ may be calculated for any value of β. Evaluation of $\phi_d(\beta)$ for complex multi-pass cores is quite a difficult problem due to the potentially large number of branches to be evaluated. However, much can be accomplished using only the expectation of $\phi_d(\beta)$. For the present, assume that the indicator function is known.

The discharge indicator function may be used to express the rate of fuel flow through all w'th order branches:

$$\dot{k}_w = \sum_{\beta} \phi_d(\beta') \, p_\beta \, \dot{K}_f = \dot{K}_f \sum_{n} p_n \sum_{\beta'} p_{\beta'} \, \phi_d(\beta')$$

$$= \dot{K}_f \, E[\, \phi_d(\beta') \,] \qquad (3.28)$$

Substitute Eq. (3.28) into Eq. (3.26):

$$\alpha_w = \dot{k}_w \, / \, \dot{K}_f = E[\, \phi_d(\beta') \,] \qquad (3.29)$$

Thus, the α parameter is identical to the expectation value of the discharge indicator function at the exit of the previous order branch. For any pass less than the first pass after which fuel is discarded from the core, α_w is equal to 1, as all fuel is recycled. However, beginning at some finite order, some fuel elements leaving the core have burnup exceeding the discharge value, and the value of α_w drops to less than one. Since $(1-\alpha_w)$ is the flow rate of w'th order pebbles which permanently leave the core divided by $\dot{K}_f$, it is clear that:

$$(1-\alpha_w) = \mathbb{P}\left[\begin{array}{l}\text{a pebble is discharged} \\ \text{following pass w}\end{array}\right] \qquad (3.30)$$

The quantity $(1-\alpha_w)$ is the un-conditional probabilty that a pebble is discharged immediately following pass w (un-conditioned in the sense that α_w applies to a fresh fuel element, not one that has already survived w-1 passes).

Figure (3.12) represents a point-core version of a core with fuel discharged at various passes, with flows and α's labelled. Note that since the definition of $\overline{\Delta t}$ is independent of the magnitude of an incoming flow, the core average residence time may be used to calculate

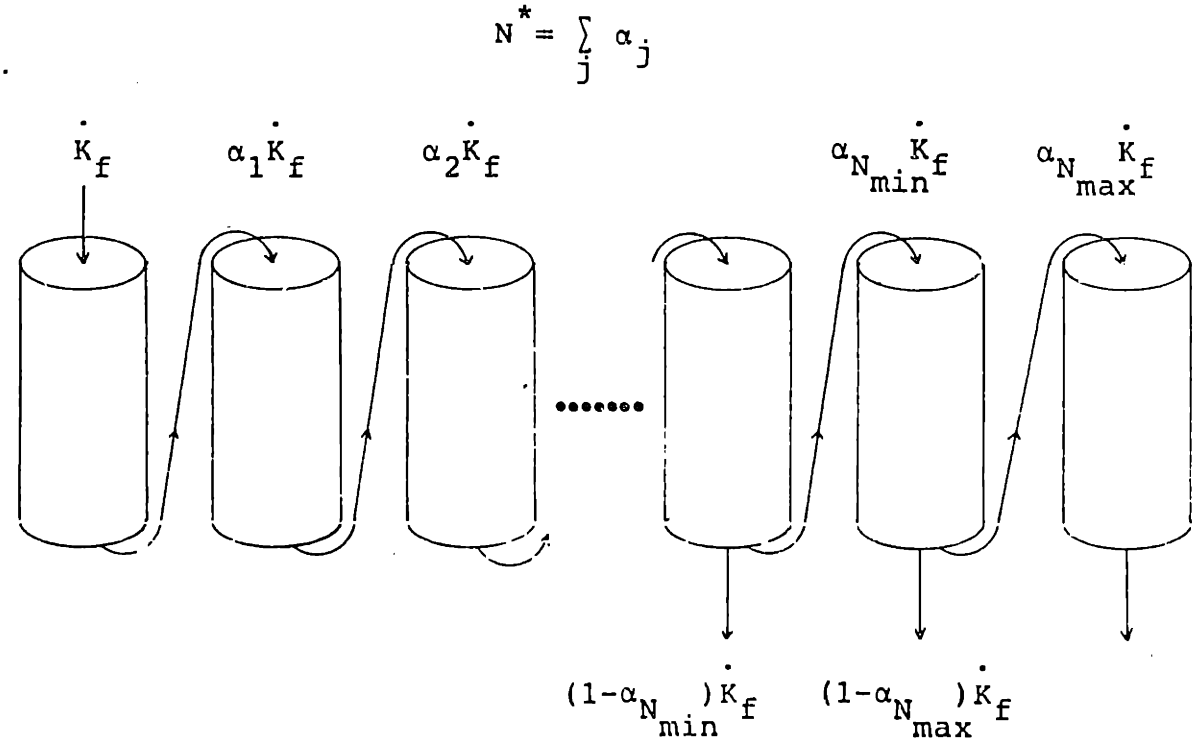

FIG. 3.12: Fuel flow through a multi-pass point core.

pass populations:

$$K_w \equiv \begin{bmatrix}\text{population}\\ \text{of pass } w\end{bmatrix} = \alpha_w \dot{K}_f \overline{\Delta t} \qquad (3.31)$$

If the maximum number of passes which a fuel element may remain in the core is denoted M, then the total core population must be:

$$K_{core} \equiv \begin{bmatrix}\text{total core}\\ \text{population}\end{bmatrix} = \sum_{i=1}^{M} \alpha_i \dot{K}_f \overline{\Delta t} \qquad (3.32)$$

Let N^* be the effective average number of passes prior to discharge;

$$N^* \equiv \sum_{i=1}^{M} \alpha_i \quad , \qquad (3.33)$$

then the total core population is determined by the simple expression:

$$K_{core} = \left\{ \sum_{i=1}^{M} \alpha_i \right\} \dot{K}_f \overline{\Delta t} = N^* \dot{K}_f \overline{\Delta t} \qquad (3.34)$$

Furthermore, note that the E-probability for the set of w'th order branches is:

$$\Pi_w \equiv \frac{K_w}{K_{core}} = \frac{\alpha_w \dot{K}_f \overline{\Delta t}}{N^* \dot{K}_f \overline{\Delta t}} = \alpha_w / N^* \qquad (3.35)$$

Π_w is the probability that a pebble drawn at random from anywhere in the core is on its w'th pass.

In summary, this section demonstrated the following relationships:

(1) The reactor core has a characteristic average residence time per pass which is independent of pebble properties:

$$\overline{\Delta t} = \sum_j p_j \Delta t_j \qquad (3.36)$$

(2) Every pass w may be characterized by a recycle probability α_w, such that:

$$\dot{k}_w = \alpha_w \dot{K}_f = E[\, \vartheta_d(\beta') \,] \dot{K}_f \qquad (3.37)$$

(3) The effective number of passes prior to discharge is N^*:

$$N^* \equiv \sum_i \alpha_i \qquad (3.38)$$

(4) The total core population is:

$$K_{core} = N^* \dot{K}_f \overline{\Delta t} \qquad (3.39)$$

(5) Core-wide Eulerian probabilities for order-w branches are:

$$\Pi_w = \alpha_w / N^* \qquad (3.40)$$

3.4: LAGRANGIAN AND EULERIAN PARAMETERS AND DISTRIBUTIONS

The previous section introduced the branch variable β as a shorthand means for denoting a fuel element's previous irradiation history. The functional notation $Z(\beta)$ was introduced to denote any fuel state parameter which is defined by the sequence of drop zones previously traversed by the fuel element. In a stationary core, of course, any fuel state parameter may be defined in this way. Each value of $Z(\beta)$ for $\beta \in B_w$ is associated with a branch probability p_β. These frequency- or flow-weighted probabilities are called the *Lagrangian* probabilities associated with pass w fuel. The set of p_β for $\beta \in B_w$ defines a Lagrangian probability density function for any parameter $Z(\beta_w)$. These terms are called Lagrangian because they must be measured at a particular *point* in the core as fuel flows by. The Lagrangian pdf determines the result of a fuel sampling experiment which intercepts a *flow* of fuel and thus weights paramter values by the frequency at which they are observed.

However, another type of experiment is possible. Suppose instead of sampling fuel as it flows by some point in the reactor, fuel is sampled from some finite *region* within the pebble bed at one instant in time. In this case, it is not the flowrate which determines the frequency of parameter observation, but rather the population associated with $Z(\beta)$ within the region under study. The probabilites which define the pdf for these region parameters will be called the *Eulerian* probabilities π_β. Using Eqs. (3.23) and (3.29), it is possible to derive a fundamental expression for the π_β's.

First consider the case where we include only the population of w'th order pebbles within radial drop zone "n." All of these pebbles must have a branch variable of the form (β',n), where $\beta' \in B_{w-1}$. The probability of selecting a pebble from a particular branch $\beta = (\beta_o,n)$, given that $\beta \in B_w$, is denoted π_β, and is easily calculated:

$$\pi_\beta \equiv \pi_{(\beta',n)}(\beta_o',n) \equiv \mathbb{P}[\ (\beta',n) = (\beta_o',n) \mid (\beta_o',n) \in B_w\ ]$$

$$= \left\{ \frac{\text{\# pebbles in branch } (\beta_o',n)}{\text{\# of } w\text{'th order pebbles in zone } n} \right\}$$

$$= \left\{ \frac{p_{(\beta_o',n)}\ \phi_d(\beta_o')\ \dot{K}_f\ \Delta t_n}{\alpha_w\ p_n\ \dot{K}_f\ \Delta t_n} \right\}$$

$$= \frac{1}{\alpha_w}\ p_{\beta_o'}\ \phi_d(\beta_o') \qquad (3.41)$$

since $p_n\ p_{\beta_o'} = p_{(\beta_o',n)}$. To verify that π_β does indeed represent a true probability density function, it is possible to show that the sum of all values of π_β is 1.0. To do so, first note that $\sum_{(\beta',n)} = \sum_{\beta'}$, since the last zone n is fixed and adds nothing to the enumeration. Thus, summing the π_β operator over all values of β:

$$\sum_{(\beta',n)} \pi_{(\beta',n)} = \sum_{\beta'} \frac{p_{\beta'}\ \phi_d(\beta')}{\alpha_w} = \frac{E[\ \phi_d(\beta')\ ]}{\alpha_w} = 1$$

An Eulerian expectation operator, E_e, may also be defined:

$$E_e[\ Y(\beta',n)\ ] \equiv \sum_{(\beta',n)} \pi_{(\beta',n)}\ Y(\beta',n)$$

$$= \frac{1}{\alpha_w} \sum_{\beta'} p_{\beta'} \, \phi_d(\beta') \, Y(\beta',n) \qquad (3.42)$$

Thus, the $\pi_{(\beta',n)}$'s define the pdf for the population-weighted experiment. Note that π_β is identical to the Lagrangian probability operator p_β except for the presence of the discharge indicator function to account for discarded branches. Thus, it is π_β which has true physical significance; the Lagrangian probabilities may include "phantom flows" of fuel which may not be present in the operating reactor.

It is also useful to consider the more general volumetric sampling problem, in which selection of pebble is not limited to those of a single order. If Π_β denotes the pdf for selecting a pebble with branch variable (β',n) from radial drop zone n, we have:

$$\Pi_\beta \equiv \Pi_{(\beta',n)}(\beta'_o,n) \equiv \left\{ \frac{\text{\# pebbles in branch } (\beta'_o,n)}{\text{\# pebbles in zone } n} \right\}$$

$$= \left\{ \frac{p_{(\beta'_o,n)} \, \phi_d(\beta') \, \dot{K}_f \, \Delta t_n}{\sum_{w=1}^{M} \alpha_w \, p_n \, \dot{K}_f \, \Delta t_n} \right\}$$

$$= \frac{1}{N^*} \, p_{\beta'_o} \, \phi_d(\beta') \qquad (3.43)$$

(since $N^* \equiv \sum_w \alpha_w$). To enumerate the Π_β's, we must sum over all order passes, as well as all branches within each order:

$$\sum_{w=1}^{M} \sum_{(\beta',n)} \Pi_{(\beta',n)} = \sum_{w=1}^{M} \left\{ \sum_{\beta'_{w-1}} \frac{p_{\beta'_{w-1}} \, \phi_d(\beta'_{w-1})}{N^*} \right\}$$

$$= \frac{1}{N^*} \sum_{w=1}^{M} \alpha_w = 1$$

The E-expectation operator under consideration of the total zone n population becomes:

$$E_{\mathcal{E}}[\ Y(\beta',n)\ ] = \sum_{w=1}^{M} \sum_{\beta'_{w-1}} \Pi_{(\beta',n)}\ Y(\beta',n)$$

$$= \frac{1}{N^*} \sum_{w} \sum_{\beta'} p_{\beta'}\ \vartheta_d(\beta')\ Y(\beta',n) \qquad (3.44)$$

For the Eulerian expectation to be meaningful, the function $Y(\beta',n)$ should be some *volume* related property of the pebbles in zone n. This is in contrast to some other quantity $Z(\beta)$ which might be operated on by the Lagrangian expectation operator, because in this case $Z(\beta)$ is properly a *point* value of Z at the location of the measurement.

Now, any function $Y(\beta',n)$ which is to be E-averaged in some radial drop zone should clearly represent some volumetric property of the pebbles within branch (β',n). In later chapters, it will be shown, however, that the most straightforward means of calculating fuel states yield parameters which are functions of *time*, not position, within a given branch. The problem at hand, therefore, is the transformation of such Lagrangian information into information useful for volumetric analysis.

The problem may be stated more generally as follows: Suppose that within a given branch, the behavior of a fuel parameter ξ with respect to time is known. The functional relation between the parameter and time is denoted $\xi = f_t(t)$, (where f_t is the *name* of the time function).

Furthermore, suppose that another one-to-one relation between time t and position z within the branch is known: $z = g(t)$. It is desired to determine the properties of the yet unknown function $f_z(z)$, which relates the fuel parameter ξ to position with the branch: $\xi = f_z(z)$.

The problem of mapping from one coordinate system to another is illustrated in Figure (3.13). Two general rules apply for this transformation:

(1) Functional *values* are equal at times and positions which satisfy the relation $z = g(t)$;

(2) The *differentials* dz and dt are related by the Jacobian:

$$dt = \left|\frac{dt}{dz}\right| dz = \left|\frac{d\, g^{-1}(z)}{dz}\right| dz$$

Thus, the transformation to ξ values in terms of the z coordinate is straightforward:

$$\xi = f_z(z) = f_t(\, g^{-1}(z)\,) \qquad (3.45)$$

For the case at hand, where $t = (z/u)$, this equation may be written:

$$\xi = f_z(z) = f_t(\, z/u\,) \qquad (3.46)$$

Also of interest, however, is the *spatially* averaged value of ξ in branch β. If we denote this parameter by $\langle\xi\rangle$, we wish to evaluate:

$$\langle\xi\rangle \equiv \frac{1}{\Delta z} \int_0^{\Delta z} f_z(z)\, dz \qquad (3.47)$$

where Δz denotes the spatial length of the branch in question ($\Delta z = u\, \Delta t$). Substituting for f_z, dz, and Δz:

$$\langle\xi\rangle = \frac{1}{u\, \Delta t} \int_0^{\Delta t=\Delta z/u} f_t(t) \left|\frac{dz}{dt}\right| dt =$$

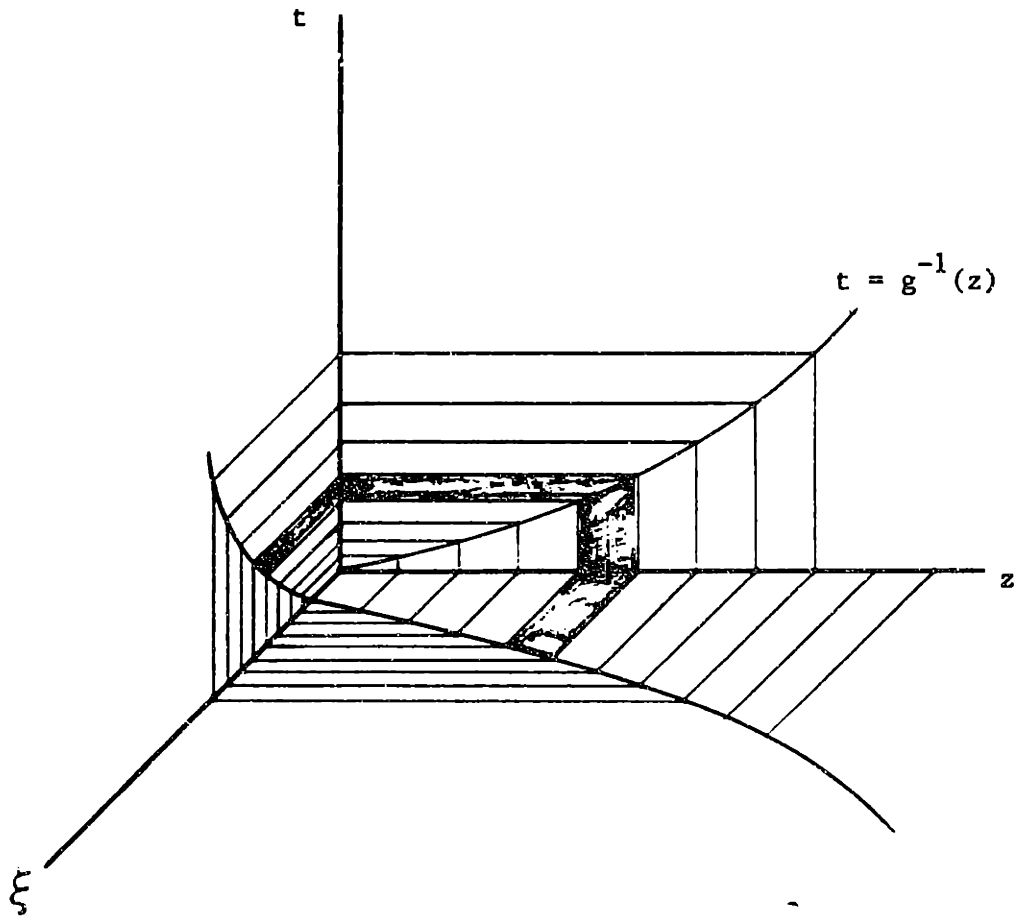

FIG. 3.13: Transforming from position to time coordinates.

$$\frac{1}{\Delta t} \int_0^{\Delta t} f_t(t)\, dt \tag{3.48}$$

Thus, the spatial average of ξ is identical to the time average of ξ while the pebble traverses the branch of interest. The parameter $\langle \xi \rangle$ should be used in the Eulerian expectation operations, since it is the volume averaged value of parameter ξ, and thus it makes logical sense to speak of its population-based expectation.

3.5: TRANSFORMATIONS BETWEEN L- AND E-EXPECTATIONS, AND THE QUASI-TWO DIMENSIONAL APPROXIMATION

It will often be necessary to perform the following sort of calculation: given the L-expectation for some fuel parameter ξ at the entrance to a branch β, what is the E-expectation of ξ within β? This question arises because the methods to be developed in the following chapters lead naturally to Lagrangian or time-dependent descriptions of fuel state evolution. Two transformations are necessary in this case. First, the time behavior of ξ must be transformed to a volume average $\langle\xi\rangle$ (i.e., integrated over the branch time interval); second, the transformed $\langle\xi\rangle$ must be summed over all branches and weighted by the appropriate probabilities.

First consider only pebbles of a single order w within drop zone n. Suppose further that we have performed calculations and know the value of $\bar{\xi}_{w-1}$, the L-expectation of ξ at the entrance to branch (β',n), $\beta \in B_w$. Now, since the transformation from ξ to $\langle\xi\rangle$ is linear, as is the L-expectation, we may write:

$$E[\, \langle \xi_{w-1} \rangle \,] = \langle E[\, \xi_{w-1} \,] \rangle \qquad (3.49)$$

Thus, the flow expectation of the volume parameter $\langle\xi\rangle$ is simply the "$\langle\ \rangle$" transformation applied to $E[\ \xi_{w-1}]$. The next step is to transform the flow average of Eq. (3.49) to a population-weighted expectation, $E_e(\xi)$. We have seen that the E_e operator, though similar to the Lagrangian expectation, has an important difference. While the simple Lagrangian expectation defined in section 3.2 takes no account of pebble discharge, and therefore may contain "phantom flows" of pebbles

which are not actually present, the Eulerian expectation, based on populations, must account for the absence of certain branches from the drop zone of interest. So, while $E_e[\ \xi(\beta',n)\ ]$ is exactly equal to $\bar{\xi}_{w-1}$ for values of $w-1$ less than the minimum for pebble discharge, such is no longer the case once the pass index exceeds the critical value. Without explicit knowledge of the discharge indicator function $\phi_d(\beta)$, exact evalution of $E_e[\ \xi(\beta',n)\ ]$ is not possible. The difficulty is that evaluation of $\phi_d(\beta)$ requires the calculation of fuel state transformations for every branch $\beta \in B_w$. For a reasonable number of drop zones (N_{rad}) in a multi-pass core, this task entails a tremendous amount of calculation and bookkeeping, as the number of w'th order branches is $(N_{rad})^w$.

An approximate method which requires a minimum of bookkeeping may be formulated, however. The method will be referred to as "quasi-two dimensional," and assumes that the burnup behavior of fuel leaving a branch may be inferred from the *expectations* of fuel properties at the branch inlet. First, suppose that a linear relation is known which gives the value of $\xi(\beta)$ for any known value of $\xi(\beta')$ (determination of such transformations is the subject of later chapters). This transformation depends on the value of n, the final drop zone indicated in β:

$$\xi(\beta) \;=\; \xi(\beta',n) \;=\; A_n\ \xi(\beta') \;+\; B_n \qquad (3.50)$$

Thanks to the linear nature of the above transformation and all of the expectation operators introduced so far, it is possible to calculate the dependence of $E[\ \xi(\beta)\ ]$ on $E[\ \xi(\beta')\ ]$:

$$E[\,\xi(\beta)\,] = E[\,A_n\,\xi(\beta')\;+\;B_n\,]$$

$$= \left\{\sum_n p_n \sum_{\beta'} p_{\beta'}\,A_n\,\xi(\beta')\right\} + \left\{\sum_n p_n \sum_{\beta'} p_{\beta'}\,B_n\right\}$$

$$= \left\{\sum_n p_n\,A_n\right\}\left\{\sum_{\beta'} p_{\beta'}\,\xi(\beta')\right\} + \left\{\sum_n p_n\,B_n\right\}$$

$$\equiv \quad \bar{A}\;E[\,\xi(\beta')\,] \quad + \quad \bar{B} \qquad (3.51)$$

Thus, for expectation operators with no indicator function, the means propagate from pass to pass in a deterministic fashion, subject to the expected value of the transformation for one pass. This reasoning may be extended to the case where the indicator function begins to take on zero values. Suppose that for some pass $w-1$, all values of $\phi_d(\beta')$ ($\beta' \in B_{w-1}$) are 1, but starting with larger pass numbers some fuel elements are discharged. Up to this point, it is a simple matter to calculate $E[\,\xi(\beta')\,]$ according to Eq. (3.51). Let pebble discharge be indicated by some function $F(\xi)$--i.e., a pebble is discharged if $F(\xi) > F_{dis}$, the critical value for discharge. Define the following approximate indicator function, ϕ'_d:

$$\phi'_d(w,n) \equiv \begin{cases} 0 \text{ if } F[\,A_n\,\bar{\xi}_{w-1} + B_n\,] > F_{dis} & (\beta \in B_w) \\ 1 \text{ otherwise} \end{cases} \qquad (3.52)$$

$\phi'_d(w,n)$ depends only on the expectation value of ξ from the previous pass. It is calculated without keeping track of the pebble transformations associated with every possible branch β' for passes previous to the one of interest.

Additionally, note that if we wish a Lagrangian expectation which

takes account of pebble discharge, yet another expectation operator must be defined:

$$E_\ell[\ \xi(\beta)\ ] \equiv (1/\alpha_w)\ E[\ \mathcal{P}_d(\beta)\ \xi(\beta)\ ] \tag{3.53}$$

E_ℓ is identical to E_e, the Eulerian expectation operator, but will be used for Lagrangian quantities (i.e., pebble state parameters at branch inlets or exits). Furthermore, E_ℓ is identical to E for all passes prior to the minimum for pebble discharge.

Next, define the following conditional discharge probability for pass w:

$$\delta_w \equiv \mathbb{P}\left[\begin{array}{c}\text{a pebble is discharged}\\ \text{following pass } w\end{array}\ \middle|\ \begin{array}{c}\text{it was not discharged}\\ \text{following pass } w-1\end{array}\right] \tag{3.54}$$

Assuming that pebble discharge is adequately indicated by the approximate indicator function $\mathcal{P}'_d(w,n)$, we may write:

$$\delta_w \cong \sum_n p_n\ \mathcal{P}'_d(w,n) \tag{3.55}$$

The quasi 2-D approximation assumes that the two new functions δ_w and $\mathcal{P}'_d(w,n)$ may be used in an approximate expression for $E_\ell[\ \xi\ ]$

$$E_\ell[\ \xi(\beta)\ ] \simeq (1/\delta_w) \sum_n p_n\ \mathcal{P}'_d(w,n) \left\{ A_n\ E_\ell[\ \xi(\beta')\ ] + B_n \right\} \tag{3.56}$$

Physically, Eq. (3.56) implies that either all or none of the fuel elements leaving zone n following pass w are discharged, depending on whether the "burnup" accrued by the expected inlet value exceeds the discharge value. The term "quasi two-dimensional" is used because we essentially assume a one-dimensional flow of fuel *into* each set of order branches, but determine burnup by looking at two dimensions (i.e., accounting for radial variation) within each order event space. Eq. (3.56) provides a reasonable approximation for pebble discharge without

requiring detailed enumeration of $\mathcal{P}_d(\beta)$.

The overall values of α_w for each pass may be estimated under the above approximations. Since $\delta_w = \sum_n p_n \mathcal{P}'_d(w,n)$ is approximately the probability of a fuel element surviving pass w, we may write:

$$\begin{aligned}
\alpha_w = \dot{k}_w / \dot{K}_f &\simeq \left\{ \sum_n p_n \mathcal{P}'_d(w,n) \right\} \dot{k}_{w-1} / \dot{K}_f \\
&\simeq \left\{ \sum_n p_n \mathcal{P}'_d(w,n) \right\} \left\{ \sum_n p_n \mathcal{P}'_d(w-1,n) \right\} \dot{k}_{w-2} / \dot{K}_f \\
&\vdots \\
&\simeq \left\{ \prod_{i=1}^{w} \delta_i \right\} \dot{K}_f / \dot{K}_f = \left\{ \prod_{i=1}^{w} \delta_i \right\} \qquad (3.57)
\end{aligned}$$

The quasi two dimensional approximation, though perhaps crude, has value due to its simplicity. In any fuel state calculation, the values of the $\mathcal{P}'_d(w,n)$ parameters will be evident as byproducts of the on-going calculations. The approximation (3.57) thus finds use in both the FUPAR and the PDIF computer codes. It will be shown (see section 4.10 and Chapter 5) that its use is justified in the case of modular pebble bed cores.

Return now to the original problem of calculating $\bar{E}$-expectations for fuel parameters in the later passes. Under the quasi-two dimensional approximation, the L expectation of ξ following pass $w-1$ is assumed to be:

$$\bar{\xi}_{w-1} = (1/\delta_{w-1}) \sum_n p_n \mathcal{P}'_d(w-1,n) \left\{ A_n E_\ell[\, \xi(\beta'') \,] + B_n \right\}$$

Denote the volume averaged property $\langle \xi \rangle$ for pass w fuel in drop

zone n by $\langle \xi \rangle_n$, where the "$\langle \rangle_n$" operator implies time integration over branch (β',n). Since the population-weighted expectation operation E_e is formally equal to the discharge-accounting E_ℓ, we may write:

$$E_e[\langle \xi(\beta',n) \rangle_n] = E_\ell[\langle \xi(\beta',n) \rangle_n] = \langle E_\ell[\xi(\beta',n)] \rangle_n$$
$$= \langle (1/\delta_{w-1}) \sum_j p_j \varphi_d^*(w-1,j) \left\{ A_j E_\ell[\xi(\beta'')] + B_j \right\} \rangle_n$$
$$= (1/\delta_{w-1}) \sum_j p_j \varphi_d^*(w-1,j) \langle \left\{ A_j E_\ell[\xi(\beta'')] + B_j \right\} \rangle_n \quad (3.58)$$

Note that the right-hand side of Eq. (3.58) contains only the expected values of ξ from previous passes. Eq. (3.58) will find wide application in later chapters.

3.6: THE FRESH FUEL INJECTION RATE

The rate of injection of fresh fuel into the core ($\dot{K}_f$) plays a significant role in the analysis of branch flows and populations which preceded this section. It is directly under the control of reactor operators, and thus is a key parameter by which core properties may be influenced.

$\dot{K}_f$ may be inferred directly from simple integral core parameters, starting with a partial differential equation which relates the core's burnup distribution, pebble flow field, and power density. Consider a finite control volume within the core, illustrated in Fig. (3.14). Pebbles flow in and out of the various surfaces of the volume, with velocity defined by the vector $\mathbf{u}(\mathbf{r})$. Consider the physical parameters implied in a flow of fuel elements from a surface of the control volume:

$$\left\{ \rho_{HM} \right\} \left\{ u \right\} \left\{ B \right\} = \{\text{energy flux}\} \qquad (3.59)$$

$$\left\{ \frac{\text{MTHM}}{\text{m}^3} \right\} \left\{ \frac{\text{m}}{\text{sec}} \right\} \left\{ \frac{\text{MWD}}{\text{MTHM}} \right\} = \left\{ \frac{\text{MWD}}{\text{m}^2\ \text{sec}} \right\}$$

where ρ_{HM} = homogenized heavy metal density;

u = fuel velocity; and

B = burnup of fuel in the flow.

Thus, the combination of parameters $\rho_{HM}\mathbf{u}B$ represents an energy flux within the pebble bed. If the energy produced within the control volume is balanced with the net energy flux into the volume plus the rate of burnup increase within the volume, the following equation is the result:

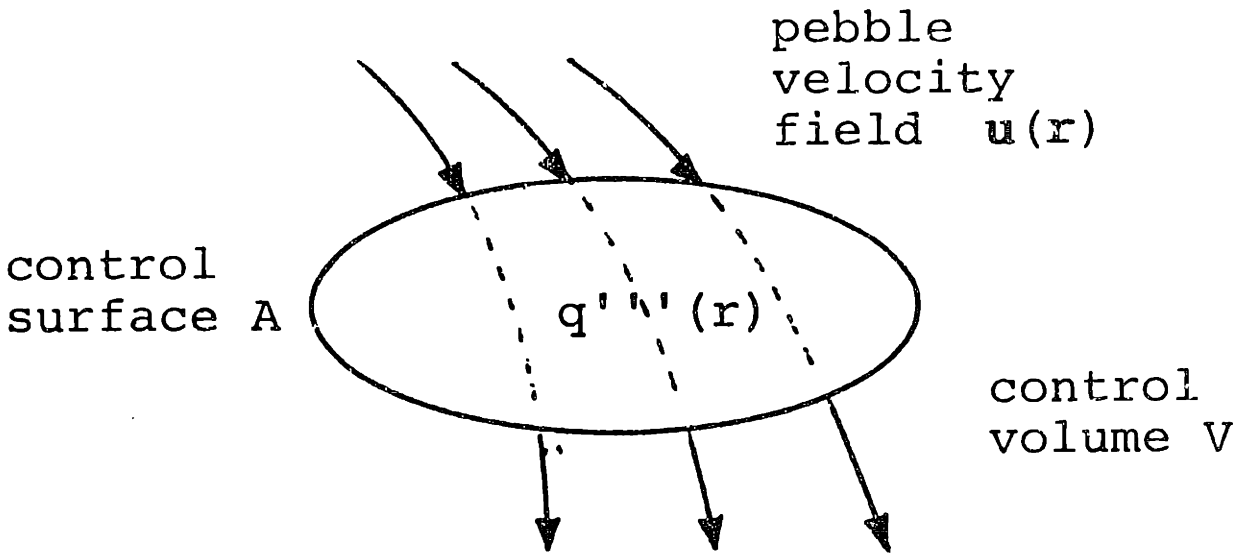

FIG. 3.14: Control volume for energy balance within the reactor.

$$\int_V q''' \, dV = \int_V \rho_{HM} \frac{\partial B}{\partial t} \, dV + \oint_A \rho_{HM} \, \mathbf{u} \, B \cdot d\sigma \qquad (3.60)$$

where q''' = reactor power density {MW/m^3};

σ = outward normal surface area vector {m^2};

V = volume of control volume {m^3}; and

A = control volume surface area {m^2}.

Application of Green's theorem to the surface integral yields:

$$\int_V q''' \, dV = \int_V \left\{ \rho_{HM} \frac{\partial B}{\partial t} + \nabla \cdot [\rho_{HM} \, \mathbf{u} \, B] \right\} dV \qquad (3.61)$$

The above relation is identically satisfied only if the integrands are always equal, or:

$$\frac{q'''}{\rho_{HM}} = \frac{\partial B}{\partial t} + \nabla \cdot [\, \mathbf{u} \, B \,] \qquad (3.62)$$

Since the pebble flow is incompressible, the divergence of the pebble velocity field is zero:

$$\nabla \cdot \mathbf{u} = 0 \qquad (3.63)$$

Thus, if the vector identity:

$$\nabla \cdot (\mathbf{u}B) = B \, \nabla \cdot \mathbf{u} + \mathbf{u} \cdot \nabla B$$

is substituted into Eq. (3.62), the result is:

$$\frac{\partial B}{\partial t} + \mathbf{u} \cdot \nabla B = \frac{q'''}{\rho_{HM}} \qquad (3.64)$$

Finally, recall the definition of the substantial derivative:

$$\frac{D}{Dt} \equiv \frac{\partial}{\partial t} + \mathbf{u} \cdot \nabla$$

Thus, the final relation between burnup, pebble flow and power density is:

$$\frac{DB}{Dt} = \frac{q'''}{\rho_{HM}} \qquad (3.65)$$

In the steady state case, in which $\partial/\partial t = 0$, Eq. (3.65) reduces to:

$$\mathbf{u} \cdot \nabla B = \frac{q'''}{\rho_{HM}} \tag{3.66}$$

A useful relation may be derived from the control volume analysis of Eq. (3.60). If the control volume selected is the entire steady state reactor core, we have:

$$\int_V q''' \, dV = P = \oint_A \rho_{HM} \, \mathbf{u} \, B \cdot d\sigma \tag{3.67}$$

where P represents the total reactor thermal power {MW}. Figure (3.15) illustrates a control volume surrounding the entire reactor core and refueling system. The only fuel which crosses the control boundary is fresh fuel entering the reactor for the first time and spent fuel which is permanently discharged from the system. If the fuel flowing across surface A has uniform burnup B, the surface integral in Eq. (3.67) may be simplified:

$$\oint_A \rho_{HM} \, \mathbf{u} \, B \cdot d\sigma = \dot{k} \, m_p \, B \tag{3.68}$$

where m_p represents the heavy metal mass per pebble. Since the two streams of fuel in Fig. (3.15) satisfy this condition, Eq. (3.68) may be simplified:

$$\dot{K}_f \, m_p \, B_d - \dot{K}_f \, m_p \, B_{in} = P \tag{3.69}$$

where B_d is the reactor discharge burnup and B_{in} is the burnup of fresh fuel. Since $B_{in} = 0$, the final expression for the fresh fuel injection rate is:

$$\dot{K}_f = \frac{P}{B_d \, m_p} \tag{3.70}$$

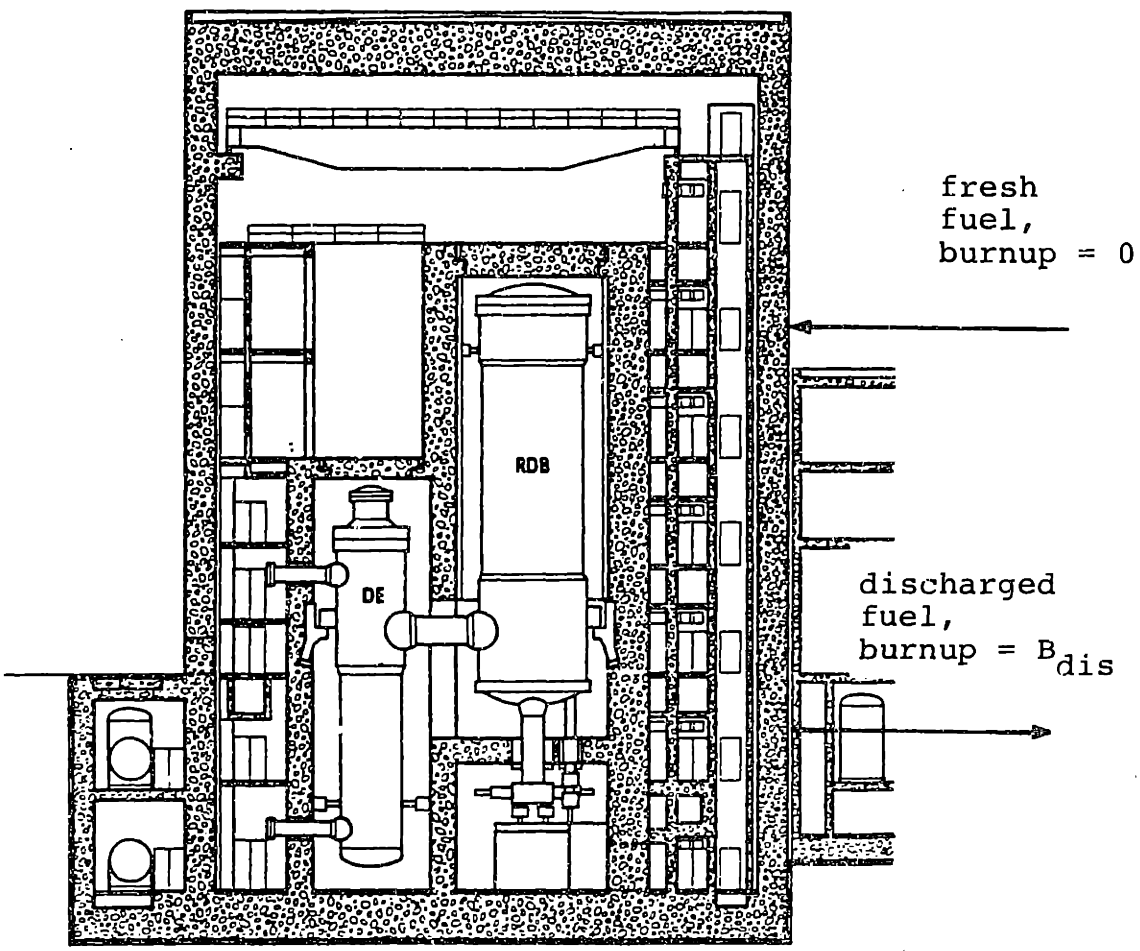

FIG. 3.15: Energy balance over the entire reactor.

Thus, the total core power, pebble discharge burnup, and the pebble heavy metal loading fix what the fresh fuel injection rate must be. An interesting additional result is obtained if we substitute Eq. (3.39) for $\dot{K}_f$ into the above expression:

$$\dot{K}_f = \frac{P}{B_d\, m_p} = \frac{K_{core}}{N^* \overline{\Delta t}} \tag{3.71}$$

Rearranging:

$$N^* = \frac{B_d\, m_p\, K_{core}}{P\, \overline{\Delta t}} \tag{3.72}$$

Thus, if the discharge burnup and the energy extraction per pebble ($B_d m_p$) is known, the core population determines the effective average number of passes prior to discharge. Of course, exact knowledge of the true average discharge burnup B_d is not really available before a detailed analysis is performed. If this is the case, it may be more useful to evaluate the ratio:

$$\frac{B_d\, m_p}{N^*} = \frac{P\, \overline{\Delta t}}{K_{core}} \tag{3.73}$$

3.7: RANDOM HOT SPOT ANALYSIS

The last topic to be addressed concerns application of Eulerian probability distributions to the problem of random "hot spot" analysis. There is the possiblity that in a large pebble bed core, a random group of pebbles with particularly "bad" qualities may group together on a random basis. If an unexpectedly large clump of fresh fuel elements were to arise, for example, power densities higher than those expected from zone average properties may result. It is desirable to quantify the probability associated with such an event.

Suppose that we are concerned with some pebble property ξ (burnup, e.g.) which safety related core properties (power density or temperature, for example) are dependent upon. Using methods discussed previously and those to be developed in the following chapters, the Eulerian probability distribution $\pi_{(\beta',n)}$ may been calculated for parameter $x(\beta',n)$. Let the event X_m = {m pebbles have attribute X}. Based on the probabilities $\pi_{(\beta',n)}$, the probability $\mathbb{P}[\ X_m\ ]$ may be calculated for any group of m pebbles, regardless of their location in the core. For example, if x = burnup, and X_m = the average burnup of m pebbles, then $\mathbb{P}[\ X_m\ ]$ may be calculated from each pebble's anticipated burnup and variance using the central limit theorem for numbers of pebbles which are significant. Let the probability $\mathbb{P}[\ X_m\ ]$ be denoted by "p(m)."

Suppose now that the region of the core under investigation consists of N pebbles in total. In this case, there are approximately (N/m) independent groups with volume m pebbles. The probabiltiy that

one of these groups does *not* have attribute X_m is simply:

$$\mathbb{P}[\ m \text{ pebbles do not have } X_m\ ] = 1 - p(m) \tag{3.74}$$

The probability that none of these (N/m) groups of pebbles have attribute X_m is therefore:

$$\mathbb{P}_m \equiv \mathbb{P}\left[\begin{array}{c}\text{no groups of } m \text{ pebbles} \\ \text{have attribute X}\end{array}\right] = \left[\ 1 - p(m)\ \right]^{(N/m)} \tag{3.75}$$

Finally, since p(m) is small and (N/m) large for cases of interest, we may approximate:

$$\mathbb{P}_m \cong \exp\left[-\frac{N\ p(m)}{m}\right] \tag{3.76}$$

A simple example has been worked through to illustrate these concepts. Consider an entire pebble bed reactor core of N = 360,000 pebbles (a standard number). Let burnup be the safety related parameter, and suppose that all pebbles possess a uniform E-distribution for burnup between the limits 0 and 80,000 MWD/MTHM. The "hot spot" attribute will be defined as: X_m = {*m* pebbles have average burnup less than some value B^*}. The probabilities p(*m*) were calculated for groups of pebbles of size $m > 20$, assuming a Gaussian distribution for the sample mean. The probabilities of *no* hot spots ($\mathbb{P}_m$) were calculated according to Eq. (3.76). Results are displayed in Fig. 3.16.

The figure shows that, for a given value of sample average burnup ($\bar{B}$), the probability of finding *no* such groupings of pebbles approaches 1.0 as the number of pebbles increases. Furthermore, as the sub-volume under consideration grows larger, sample burnups ever closer to the overall mean (40,000 MWD/MTHM) must be examined for $\mathbb{P}_m$ to be significantly less than one. Finally, note that for sample burnups

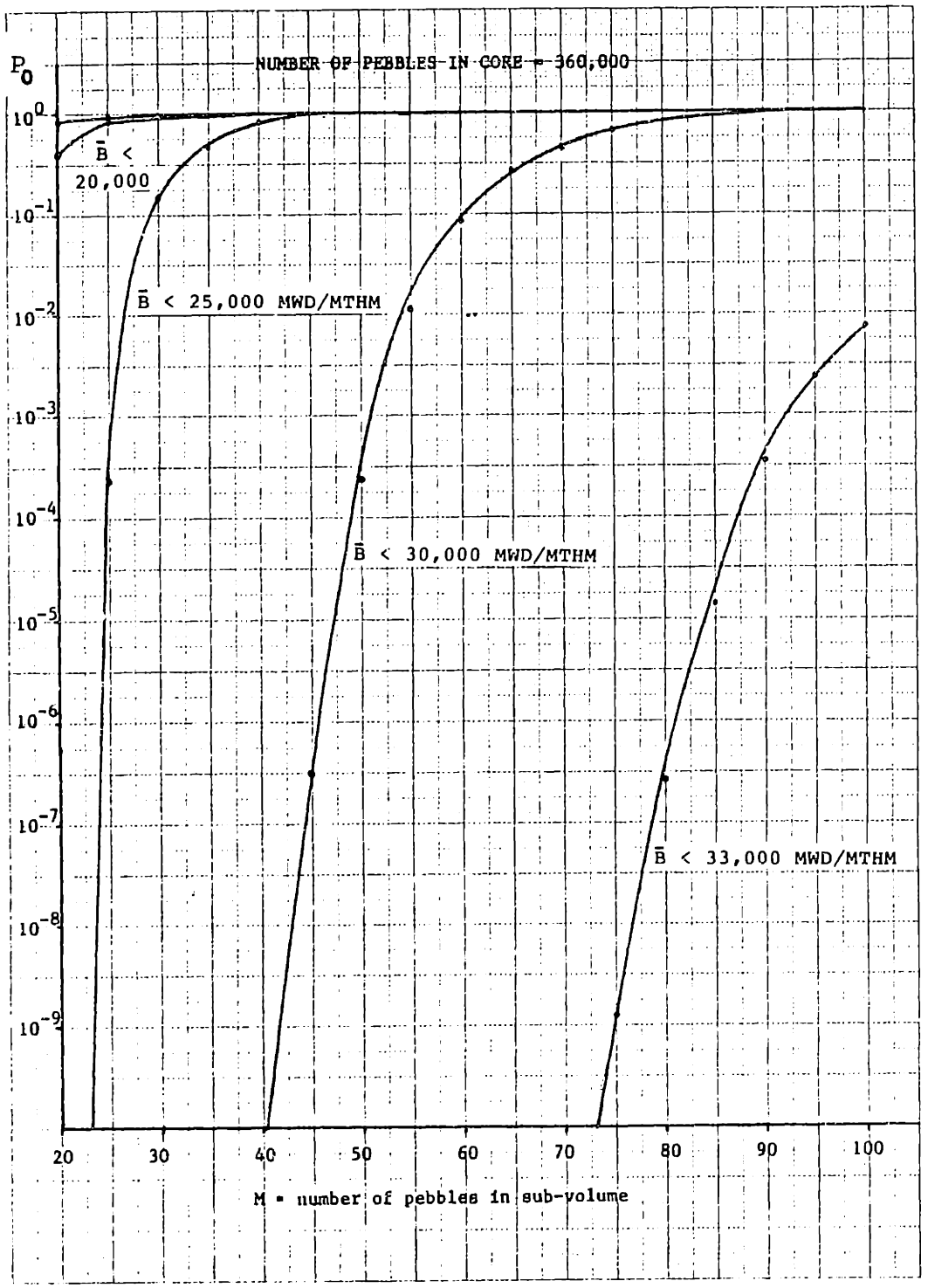

FIG. 3.16: Probability of no low-burnup groups as a function of sub-volume size.

significantly less than the overall mean, the behavior of $\mathbb{P}_m$ is approximatlely a step function. Groupings of 50 or more pebbles are necessary before the sub-volume dimensions approach that of the neutron mean-free path in the pebble bed. The Figure indicates that it is highly unlikely that groups of 50 or more pebbles will coalesce with average burnup $\bar{B} < 25{,}000$ MWD/MTHM. On the other hand, it is quite likely that groups with $\bar{B} < 30{,}000$ MWD/MTHM will exist.

CHAPTER 4: ESTIMATING THE CHARACTISTICS OF A STATIONARY PEBBLE BED REACTOR

This chapter addresses the most fundamental question regarding a pebble bed reactor: What is the distribution of heavy metals and fission products within the steady state reactor? The answer will be derived from fundamental principles, based on some general assumptions regarding the state of the reactor core.

Under these assumptions, the linear differential equations which govern the buildup and decay of all relevent materials are derived. The equations are written in matrix form, and the unknowns of interest (heavy metal and fission product number densities) are grouped into one dimensional vectors. Within regions of the core which are small enough to assume that core parameters (such as neutron flux) are approximately constant, these equations become time-invariant as well. Under these circumstances, the equations may be solved analytically for each discrete core zone, yielding input/output relations for the density vectors which are simple linear transformations. A single such transformation, or transition matrix, exists for the heavy metal densities in each zone, while three are required for fission products (one representing dependence on the input fission product concentrations, the other two for each input heavy metal concentration vector). A third type of transition matrix is derived which describes the burnup accumulation of a fuel element. It is shown that all of the matrices associated with consecutive axial zones in the core may be

"collapsed" into a single composite matrix, with the same input/output properties as the original chain of zones.

The collapsed transition matrices lead naturally to a description of fuel state evolution using the branch notation introduced in the previous chapter. The Eulerian and Lagrangian expectation operations yield analytic expressions for the expected values of materials densities and burnup in fuel flows or within specific core regions. The equations which result lead to the conclusion that the entire pebble bed core may be collapsed (both axially and radially) into a single set of transition matrices which determine the pass-to-pass evolution of expectation properties.

Further extension of these concepts leads to expressions for the second moments of fuel properties: covariance matrices for the heavy metal concentration vectors, and the variance of burnup as a function of pass number.

A computer program called FUPAR has been written to perform the calculations detailed in this chapter. FUPAR calculates the transition matrices for the entire reactor, then uses them to calculate materials densities and burnup as a function of position within the reactor. FUPAR may be run iteratively in conjunction with the VSOP reactor physics code system to converge on an equilibrium core distribution. This system has been tested and shown to be consistent with other current methods of pebble bed core design evaluation.

4.1: ASSUMPTIONS

The development which follows in this chapter depends upon the following general assumptions regarding the state of the pebble bed core:

(1) The core is in the stationary state--that is, the probability density functions associated with random in-core parameters do not change over time. Prerequisite for this is that controllable reactor parameters (e.g. power level) are held at steady state. The stationarity assumption is reasonable because of the eventual use to which results of this analysis is to be put: source term estimation. At the steady state, the reactor has built up its maximum fission product inventory, thus implying the maximum possible source term.

(2) The core is axisymmetric.

(3) Pebble flow is laminar and one-dimensional. Entrance and exit effects on fuel flow may be neglected.

(4) The core is discretized into enough radial drop zones and axial sections that all spatial parameters may be assumed constant within each zone.

In addition to the above assumptions, the following parameters are assumed to be known prior to beginning the calculations outlined in this chapter:

- one-group neutron flux as a function of (r,z);
- heavy metal and fission product cross sections as a function of (r,z);

- heavy metal and fission product transmutation chain structure;
- reactor thermal power;
- fuel cutoff burnup for discharge;
- fuel flow velocities as a function of radial position;
- core dimensions.

4.2 THE HEAVY METAL ISOTOPICS EQUATIONS

The most fundamental quantities to be analyzed to determine fuel state are the number densities of heavy metal isotopes in the fuel. Both the burnup and fission product densities depend directly on the heavy metal densities.

In the most general case, HTGR fuel will contain isotopes from two chains. The first begins with U-238, and the second with Th-232. Three nuclear processes control the transmutation of isotopes along these paths. They are nuclear fission, beta decay, and gamma decay. Fig. (4.1) contains two diagrams illustrating the processes occuring in both chains. Note that the U-238 and Th-232 chain are very similar. Even in a reactor which does not utilize thorium, the Th-232 chain must be accounted for because it contains U-235.

The general equation for the rate of chain of an isotope's concentration is:

$$\frac{d}{dt}(n_i) = -(\lambda_i + \sigma_a^i \phi) n_i + \sum_j \lambda_j a_j^i n_j + \phi \sum_k \sigma_a^k b_k^i n_k \quad (4.1)$$

where n_i = number density of isotope i {#/b-cm};

λ_i = decay constant for isotope i {sec^{-1}};

Thorium-232 Chain

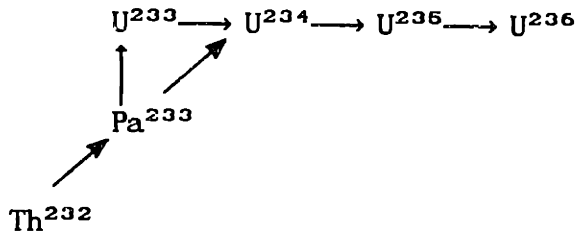

Uranium-238 Chain

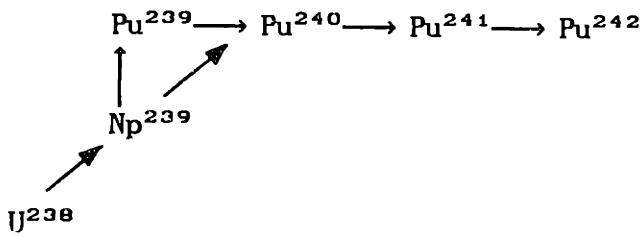

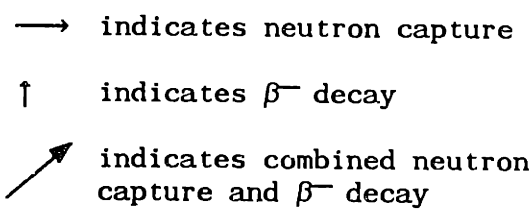

FIG. 4.1: Heavy metal isotopic chains.

σ_a^i = one-group neutron absorption cross section for isotope i {barns};

ϕ = one-group neutron flux {neutrons/barn-sec};

j = subscript for isotope i's precursors by beta decay;

k = subscript for isotope i's precursors by neutron absorption;

a_j^i = fraction of isotope j decays which yield isotope i;

b_k^i = fraction of isotope k which yields isotope i upon neutron absorption.

The complete set of isotopic equations for the U-238 heavy metal chain is presented below [T1]. The equations for the Th-232 chain are almost identical, with only the superscripts on the heavy metal density variables changed.

$$
\begin{aligned}
\dot{n}^{28} &= -\sigma_a^{28}\,\phi\,n^{28} \\
\dot{n}^{39} &= (\sigma_a^{28} - \sigma_f^{28})\,\phi\,n^{28} - (\lambda^{39} + \sigma_a^{39}\,\phi)\,n^{39} \\
\dot{n}^{49} &= \lambda^{39}\,n^{39} - \lambda^{49}\,n^{49} \\
\dot{n}^{40} &= (\sigma_a^{39} - \sigma_f^{39})\,\phi\,n^{39} - (\sigma_a^{49} - \sigma_f^{49})\,\phi\,n^{49} - \sigma^{40}\,\phi\,n^{40} \\
\dot{n}^{41} &= (\sigma_a^{40} - \sigma_f^{40})\,\phi\,n^{40} - (\lambda^{41} + \sigma_a^{41}\,\phi)\,n^{41} \\
\dot{n}^{42} &= (\sigma_a^{41} - \sigma_f^{41})\,\phi\,n^{41} - \sigma_a^{42}\,\phi\,n^{42}
\end{aligned}
\qquad (4.2)
$$

4.3 THE HEAVY METAL STATE TRANSITION MATRIX

The set of differential equations (4.2) may be much more conveniently written in matrix form:

$$\dot{\mathbf{n}}^{28} = \mathbf{H}^{28}(\phi)\ \mathbf{n}^{28} \qquad (4.3a)$$

$$\dot{\mathbf{n}}^{02} = \mathbf{H}^{02}(\phi)\ \mathbf{n}^{02} \qquad (4.3b)$$

where $\mathbf{n}^{28}$ and $\mathbf{n}^{02}$ = vectors of heavy metal densities in the U-238 and Th-232 chains, respectively {atoms/b-cm};

$\mathbf{H}^{28}(\phi)$ and $\mathbf{H}^{02}(\phi)$ = coefficient matrices for the U-238 and Th-232 equations, respectively.

Note that since no isotope's concentration can depend on that of an isotope which follows it in the chain, $\mathbf{H}$ is a lower triangular matrix. The notation $\mathbf{H}(\phi)$ emphasizes the dependence of the equation coefficients on the neutron flux. Let us now examine some region of the core in which ϕ is approximately constant. In this case, the set of Eqs. (4.2) becomes linear and time-invariant, and the solution is well known (see Appendix A.1). If the vector of concentrations of heavy metals in the U-238 chain is known at time t=0; then the concentration at time $t = \Delta t$ is:

$$\begin{aligned} \mathbf{n}^{28}(\Delta t) &= \mathbf{n}^{28}(0) + \int_0^{\Delta t} \dot{\mathbf{n}}^{28}(\tau)\, d\tau \\ &= \exp[\ \mathbf{H}^{28}(\phi)\ \Delta t\ ]\ \mathbf{n}^{28}(0) \end{aligned} \qquad (4.4)$$

where $\exp[\ \mathbf{H}^{28}(\phi)\ \Delta t\ ]$ represents a *matrix* exponential, and the same equation could have been written for the Th-232 chain. From this point onward, the superscripts on the HM concentration vectors will be omitted unless necessary, and all results are to be understood as

applying to both the U-238 and Th-232 isotope chains. For a brief discussion of the matrix exponential and its properties, see Appendix A.1.

It is important to remember that Eq. (4.4) applies only within some region where the neutron flux may be treated as constant. If this zone of the core is designated by the subscript "i," and the symbol $\mathbf{n}_i$ is understood to represent the HM concentration vector at the *exit* of zone i, and if we define the *heavy metal state transition matrix* $\mathbf{T}_i$:

$$\mathbf{T}_i \equiv \exp[\, \mathbf{H}(\phi_i)\, \Delta t_i \,] \qquad (4.5)$$

then the solution of Eq. (4.3) for a fuel element traversing zone i is:

$$\mathbf{n}_i = \mathbf{T}_i\, \mathbf{n}_{i-1} \qquad (4.6)$$

$\mathbf{T}_i$ is the input/output transformation for the heavy metal densities associated with zone i (see Figure 4.2). Its most useful property is its independence from any particular fuel state. Eq. (4.6) is valid regardless of the actual values contained in $\mathbf{n}_i$.

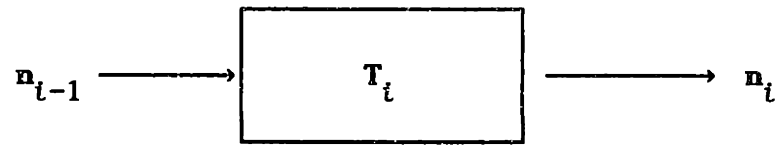

FIG. 4.2: Input/output relation for heavy metal concentration vectors

4.4: ZONE COLLAPSING AND BRANCH NOTATION

The utility of the heavy metal state transition matrices arises from their independence of fuel state. A transition matrix is the input/output transformation between inlet and outlet HM concentrations regardless of what those concentrations are. Therefore, they may be manipulated without reference to any particular fuel state. A particularly useful operation is that of zone collapsing.

Recall that the HM state transition matrix is defined for a region of the core in which it is reasonable to assume the neutron flux is spatially constant. In practical terms, this implies a region that is small compared to the entire reactor. In Figure (4.3), one possible method of dividing a cylindrical reactor core into such regions is illustrated. Regions are formed by first dividing the core into N_r radial drop zones, and then further dividing each of these into N_z axial regions. Thus, the core is sectioned into $N_r N_z$ annular regions, each of which may be assumed to contain an approximately constant flux. Thus, each zone of index (i,j) has associated with it a HM state transition matrix $\mathbf{T}_{(i,j)}$:

$$\mathbf{T}_{(i,j)} \equiv \exp[\, \mathbf{H}(\, \bar{\Phi}(i,j)) \, \Delta t(i,j) \,] \qquad (4.7)$$

where $\bar{\Phi}(i,j)$ is the average flux in zone (i,j) and $\Delta t(i,j)$ is the time required for a fuel element to traverse zone (i,j).

Let us now examine a single radial drop zone, divided into N axial zones indexed by subscript $i = 1, 2, \ldots N$. Let $\mathbf{n}_i$ represent the HMCV of a fuel element leaving zone i. This situation is illustrated in Figure

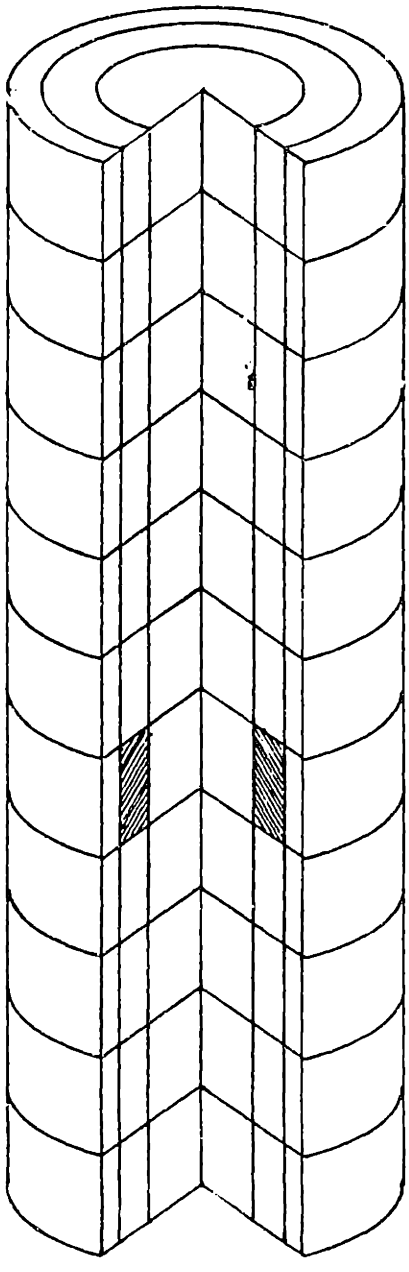

FIG. 4.3: An idealized pebble bed core divided into axial and radial regions.

(4.4). From Eq. (4.6):

$$\mathbf{n}_i = \mathbf{T}_i \, \mathbf{n}_{i-1} \tag{4.8}$$

A relation is desired relating the drop zone exit HMCV $\mathbf{n}_N$ to the drop zone inlet HMCV $\mathbf{n}_0$. After traversing the first zone, the HMCV is:

$$\mathbf{n}_1 = \mathbf{T}_1 \, \mathbf{n}_0 \tag{4.9}$$

After the second zone, we have:

$$\mathbf{n}_2 = \mathbf{T}_2 \, \mathbf{n}_1 = \mathbf{T}_2 \, \mathbf{T}_1 \, \mathbf{n}_0 \tag{4.10}$$

After the third zone:

$$\mathbf{n}_3 = \mathbf{T}_3 \, \mathbf{n}_2 = \mathbf{T}_3 \, \mathbf{T}_2 \, \mathbf{T}_1 \, \mathbf{n}_0 \tag{4.11}$$

...and so on. If we define $\boldsymbol{\theta}$, the collapsed heavy metal transition matrix:

$$\boldsymbol{\theta} \equiv \mathbf{T}_N \, \mathbf{T}_{N-1} \cdots \mathbf{T}_2 \, \mathbf{T}_1 = \prod_{i=1}^{N} \mathbf{T}_i \tag{4.12}$$

The the relation between $\mathbf{n}_N$ and $\mathbf{n}_0$ is simply:

$$\mathbf{n}_N = \boldsymbol{\theta} \, \mathbf{n}_0 \tag{4.13}$$

Note that the order of multiplication of the individual zone transition matrices is important. Thus, the definition (4.12) must be understood to imply multiplication in the proper sequence.

The collapsed state transition matrix $\boldsymbol{\theta}$ is associated with a particular radial drop zone. Thus, we can in general use the notation $\boldsymbol{\theta}_i$ to represent the collapsed HM state transition matrix associated with the i'th radial drop zone in the core. Such notation is useful because it allows us to express the fuel's HMCV as a function of the branch variable associated with a fuel element. If

$$\beta = (i_1, i_2, \cdots i_{w-1}, i_w)$$

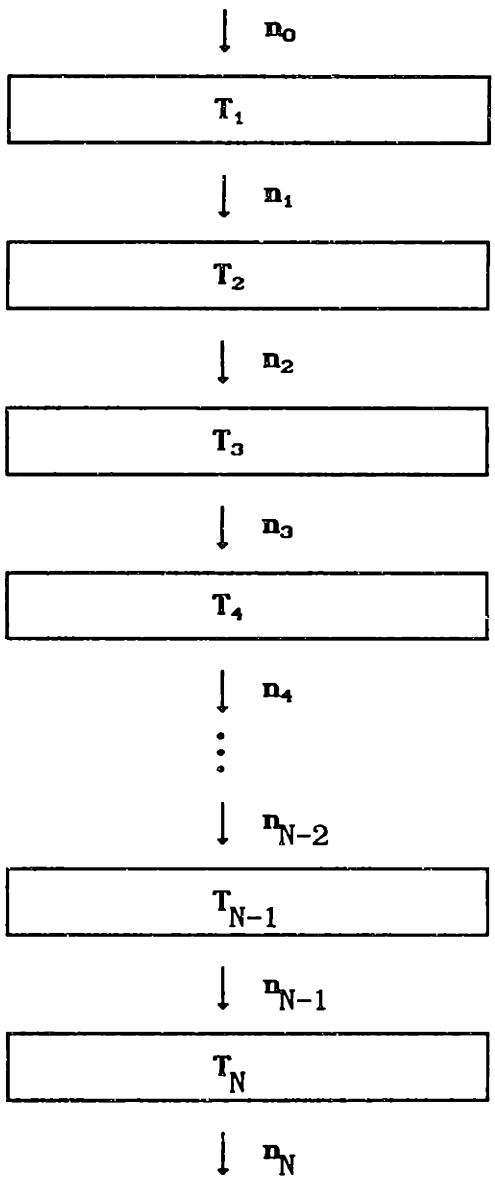

FIG. 4.4: Collapsing a single radial drop zone.

is the branch variable associated with the fuel elemtent under investigation, then the sequence of drop zones which the element has traversed is $(i_1, i_2, \cdots i_{w-1}, i_w)$. Let $\mathbf{n}(\beta)$ represent the HMCV of the fuel at the *exit* of the last drop zone i_w. Using the same arguments as above, it is straightforward to show that the following relations apply for $\mathbf{n}(\beta)$:

$$\begin{aligned} \mathbf{n}(\beta) &= \mathbf{n}(i_1, i_2, \cdots i_{w-1}, i_w) \\ &= \boldsymbol{\theta}_{i_w}\, \mathbf{n}(i_1, i_2, \cdots i_{w-1}) \\ &\vdots \\ &= \boldsymbol{\theta}_{i_w}\, \boldsymbol{\theta}_{i_{w-1}} \cdots \boldsymbol{\theta}_{i_2}\, \boldsymbol{\theta}_{i_1}\, \mathbf{n}_0 \end{aligned} \qquad (4.14)$$

It is also useful to express this relation *recursively*:

$$\mathbf{n}(\beta) = \mathbf{n}(\beta', i_w) = \boldsymbol{\theta}_{i_w}\, \mathbf{n}(\beta') \qquad (4.15)$$

4.5 BURNUP TRANSITION MATRICES

The fission rate for heavy metals can be expressed as a linear function of the heavy metal concentration vector (assuming a constant flux and known HM fission cross sections). In the case of a stationary pebble bed reactor, in which the flux is constant in time, this expression may be integrated over the residence time of the fuel in any core region, and the total incremental fission density, which is proportional to burnup, may be calculated. This procedure yields transition matrices for calculation of fuel burnup.

Let $\boldsymbol{\sigma}_f$ represent an N-element vector of fission cross sections which correspond to the isotopes in the HMCV $\mathbf{n}$. Again, let ϕ represent the neutron flux in the region of interest. For this derivation, we will treat only a single heavy metal chain. Extension to two chains is straightforward, and will be illustrated below. Under these conditions, the fission rate for a fuel element in this zone may be written as:

$$\begin{bmatrix}\text{fission}\\ \text{rate}\end{bmatrix} = \left\{\frac{\text{fissions}}{\text{b-cm-s}}\right\} \equiv \dot{F}(t) = \phi\, \boldsymbol{\sigma}_f^{+}\, \mathbf{n}(t) \qquad (4.16)$$

where the "+" superscript denotes the transposition operation. The total increase in fission density {fission/b-cm} accumulated during the interval Δt within a particular zone is given by the integral of the fission rate:

$$\begin{bmatrix}\text{accumulated}\\ \text{fissions per}\\ \text{barn-cm}\end{bmatrix} \equiv \Delta F(\Delta t) = \int_0^{\Delta t} \dot{F}(\tau)\, d\tau = \int_0^{\Delta t} \phi\, \boldsymbol{\sigma}_f^{+}\, \mathbf{n}(\tau)\, d\tau \qquad (4.17)$$

Now, ϕ and $\boldsymbol{\sigma}_f$ are independent of time within the zone of interest, and thus may be taken outside the integral. Substituting the known time-dependence of $\mathbf{n}$, we have:

$$\Delta F(\Delta t) = \phi \sigma_f^+ \left\{ \int_0^{\Delta t} \exp[\, \mathbf{H}\tau \,]\, \mathbf{n}_0 \, d\tau \right\}$$

$$= \phi \sigma_f^+ \left\{ \int_0^{\Delta t} \exp[\, \mathbf{H}\tau \,]\, d\tau \right\} \mathbf{n}_0$$

since $\mathbf{n}_0$ is constant as well. It is easily verified directly from the definition of the matrix exponential that the solution to the above integral is:

$$\int_0^{\Delta t} \exp[\, \mathbf{H}\tau \,]\, d\tau = \mathbf{H}^{-1} \left\{ \exp[\, \mathbf{H}\, \Delta t \,] - \mathbf{I} \right\} \qquad (4.18)$$

where $\mathbf{I}$ represents the N×N identity matrix. Substitute this result into the equation for the fission density increment:

$$\Delta F(\Delta t) = \phi \sigma_f^+ \mathbf{H}^{-1} \left\{ \exp[\, \mathbf{H}\, \Delta t \,] - \mathbf{I} \right\} \mathbf{n}_0 \qquad (4.19)$$

Finally, define a new transition matrix $\mathbf{D}_i$, the "fission decrement matrix" for zone i:

$$\mathbf{D}_i \equiv \mathbf{H}_i^{-1} \left\{ \exp[\, \mathbf{H}_i\, \Delta t \,] - \mathbf{I} \right\} = \mathbf{H}_i^{-1} \left\{ \mathbf{T}_i - \mathbf{I} \right\} \qquad (4.20)$$

Then the final expression for the fission density accumulated by a fuel element while traversing zone i is:

$$\Delta F_i = \phi_i \, \sigma_{f,i}^+ \, \mathbf{D}_i \, \mathbf{n}_{i-1} \qquad (4.21)$$

The cross section vector $\sigma_{f,i}$ has gained a positional subscript i because fission cross sections may vary with position in the reactor due to temperature effects. In actuality, of course, the total accumulated fission density is the sum of the fission densities attributable to fission in both the U-238 and the Th-232 isotope chains. Thus, the complete expression for ΔF_i is:

$$\Delta F_i = \Delta F_i^{02} + \Delta F_i^{28}$$
$$= \phi_i \, [\sigma_{f,i}^{02}]^+ \, D_i^{02} \, n_{i-1}^{02} + \phi_i [\sigma_{f,i}^{28}]^+ \, D_i^{28} \, n_{i-1}^{28} \qquad (4.22)$$

Fission decrement matrices may be collapsed in a manner analogous to the HM transition matrices. The resulting expression is complicated somewhat by the fact that burnup is a cumulative function. Once again, let us examine only a single radial drop zone, in which the axial zones are indexed $i = 1$ at the core top and $i = N$ at the core bottom. Also, assume only a single HM chain. Figure 4.5 is a block diagram illustrating this situation. The total fission density accumulated by a fuel element traversing this drop zone is:

$$\Delta F_{tot} = \sum_{i=1}^{N} \Delta F_i = \sum_{i=1}^{N} \phi_i \, \sigma_{f,i}^{+} \, D_i \, n_{i-1}$$
$$= \sum_{i=1}^{N} \phi_i \, \sigma_{f,i}^{+} \, D_i \, [\, T_{i-1} \, T_{i-2} \cdots T_2 \, T_1 \,] \, n_0 \qquad (4.23)$$

where n_0 represents the HMCV of the fuel element at the inlet to the drop zone under consideration. Thus, if we define the collapsed burnup increment transition matrix, A_i, where the "i" subscript indicates the i'th radial drop zone, as:

$$A_i \equiv \sum_{i=1}^{N} \phi_i \, \sigma_{f,i}^{+} \, D_i \, [\, T_{i-1} \, T_{i-2} \cdots T_2 \, T_1 \,] \qquad (4.24)$$

then the total burnup increment accumulated by a fuel element traversing radial drop zone i is simply:

$$\Delta F_i = A_i^+ \, n_0 \qquad (4.25)$$

Note that A_i^+ is an N×1 vector, so that the product $A_i^+ \, n_0$ results in a scalar quantity. If we choose to account for both heavy metal chains,

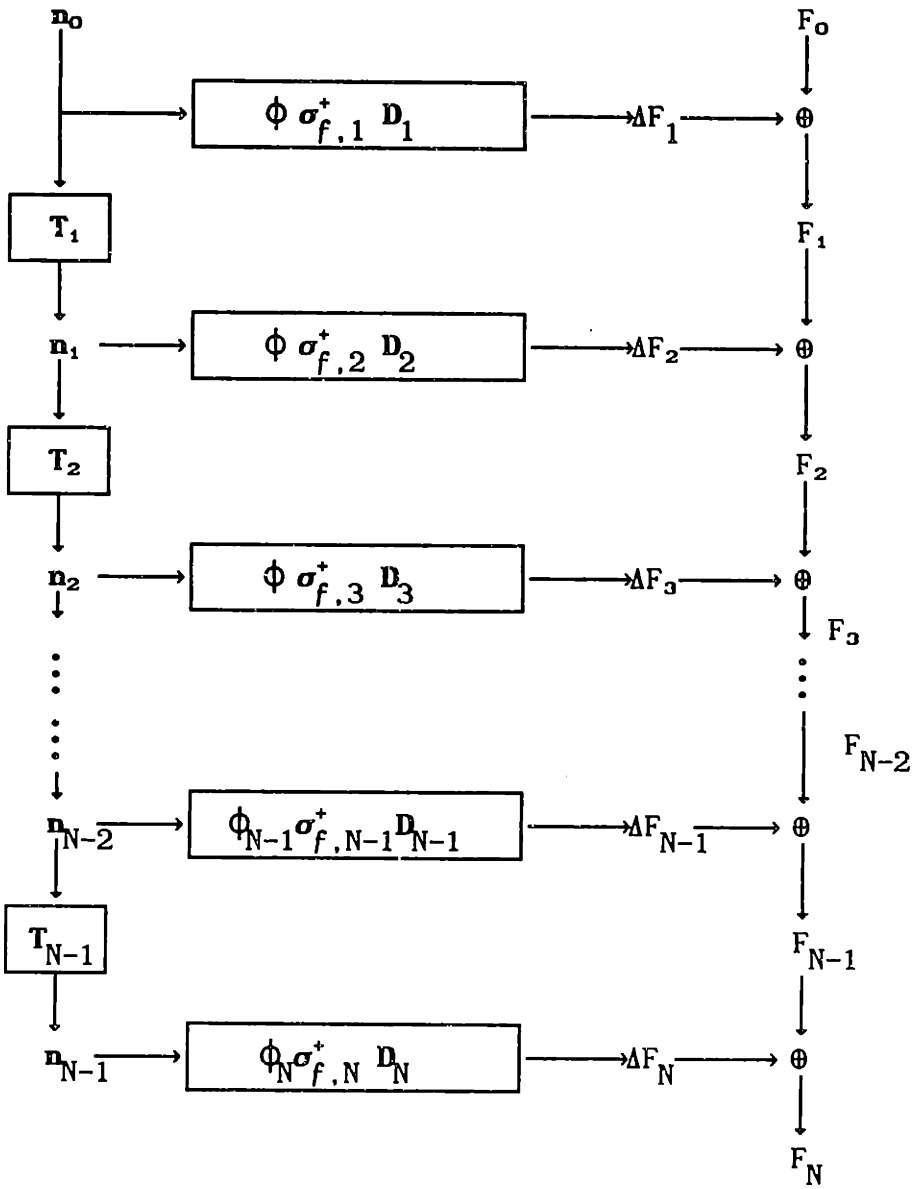

FIG. 4.5: Block diagram for collapsing the burnup transition matrices.

then we may write:

$$\Delta F_i = \Delta F_i^{28} + \Delta F_i^{02} = A_i^{28+} n_0^{28} + A_i^{02+} n_0^{02} \qquad (4.26)$$

The above equation may be used to express the pass-dependent burnup in branch notation. If $\Delta F(\beta)$ represents the incremental burnup accrued during the last pass indicated by β, then we may write:

$$\Delta F(\beta) = \Delta F(\beta', n) = A_n^{28} n^{28}(\beta') + A_n^{02+} n^{02}(\beta') \qquad (4.27)$$

Likewise, the total burnup accumulated by a fuel element as it exits branch β is:

$$F(\beta) = F(\beta') + \Delta F(\beta) = F(\beta') + A_n^{28+} n^{28}(\beta') + A_n^{02+} n^{02}(\beta') \qquad (4.28)$$

Finally, note that the quantity ΔF_i has the units of {fissions/ barn-cm}. To convert this quantity to conventional burnup units of "FIMA" (fissions per initial metal atom) one must simply divide by the initial heavy metal density (expressed in units of atoms/b-cm).

4.6 THE FISSION PRODUCT ISOTOPIC EQUATIONS

The equations describing the time dependent fission product behavior are similar to those for the heavy metal, with the added complication of a source term due to fissions of heavy metal atoms. The general equation for the rate of change of fission product i is:

$$\dot{f}_i = -(\lambda_i + \phi \sigma_a^i) f_i + \sum_j \phi \sigma_a^j a_j^i f_j + \sum_k \lambda_k b_k^i f_k + \sum_m \phi \sigma_f^m y_m^i n_m \qquad (4.29)$$

where f_i = number density of fission product "i" {atoms/b-cm};

λ_i = decay constant of fission product "i" {sec^{-1}};

ϕ = neutron flux {atoms/b-sec};

σ_a^i = neutron absorption cross section for isotope i {b};

j = index for fission product i's precursors by neutron absorption;

a_j^i = fraction of isotope j absorptions which yield isotope i;

k = index for isotope i's precursors by decay;

b_k^i = fraction of isotope k's decays which yield isotope i;

m = index for heavy metals;

σ_f^m = fission cross section for heavy metal m {b};

y_m^i = yield of isotope i per fission of heavy metal m;

n_m = number density of heavy metal m {atoms/b-cm}.

Upon reflection, it is clear that the entire set of equations such as Eq. (4.29) above, for all fission product isotopes of interest, may be abbreviated in the following matrix equation:

$$\dot{\mathbf{f}} = -\mathbf{A}\,\mathbf{f} + \mathbf{Y}^{02}\,\mathbf{n}^{02} + \mathbf{Y}^{28}\,\mathbf{n}^{28} \qquad (4.30)$$

where $\mathbf{f}$ ≡ an M element vector of fission product densities;

$\mathbf{n}^{02}$ ≡ the N element concentration vector for heavy metals in the Th-232 chain;

$\mathbf{n}^{28}$ ≡ the N element concentration vector for heavy metals in the U-238 chain;

$\mathbf{A}$ ≡ an MxM matrix such that:

$$-\{\Lambda_{ij}\} = \begin{cases} \text{source rate of isotope } i \text{ per atom of isotope } j \text{ (for } i \neq j\text{)} \\ \text{loss rate of isotope } i \text{ per atom of } i \end{cases}$$

[units of Λ_{ij} are $(\text{b-cm-sec})^{-1}$]

$\mathbf{Y}$ ≡ an MxN yield matrix, such that:

$$\{Y_{ij}\} = \text{source rate of fission product } i \text{ per atom of heavy metal } j$$

[units of Y_{ij} are $(\text{b-cm-sec})^{-1}$]

As was the case with the $\mathbf{H}$ matrices for the heavy metal chains, $\mathbf{A}$ must be lower triangular due to the sequential nature of the fission product isotopic chains.

4.7: THE FISSION PRODUCT STATE TRANSITION MATRIX

The matrix differential equation (4.30) for the time dependent behavor of the FPCV may also be solved analytically within a region where the neutron flux and cross sections are assumed constant in time. The solution is complicated by the presence of the source terms from the heavy metal concentration vectors.

First, write the equation for the FPCV in the following form:

$$\dot{\mathbf{f}} = -\mathbf{A}\,\mathbf{f} + \mathbf{Y}\,\mathbf{n} \qquad (4.31)$$

where, for brevity's sake, only one HM chain is considered. (Once the solution is derived, the actual case with two HM chains is an elementary extension). The first step in solving Eq. (4.31) is to define an integrating factor, the M×M matrix **K**:

$$\mathbf{K} \equiv \exp[\,\mathbf{A}\,t\,] \qquad (4.32)$$

such that the time derivitive of **K** is given by:

$$\dot{\mathbf{K}} = \mathbf{A}\exp[\,\mathbf{A}\,t\,] = \exp[\,\mathbf{A}\,t\,]\,\mathbf{A} = \mathbf{K}\,\mathbf{A} \qquad (4.33)$$

Premultiply both sides of Eq. (4.33) by **K**, and rearrange:

$$\mathbf{K}\,\dot{\mathbf{f}} + \mathbf{K}\,\mathbf{A}\,\mathbf{f} = \mathbf{K}\,\mathbf{Y}\,\mathbf{n}$$

or: $$\mathbf{K}\,\dot{\mathbf{f}} + \dot{\mathbf{K}}\,\mathbf{f} = \mathbf{K}\,\mathbf{Y}\,\mathbf{n}$$

or: $$\frac{d}{dt}\left\{\,\mathbf{K}\,\mathbf{f}\,\right\} = \mathbf{K}\,\mathbf{Y}\,\mathbf{n} \qquad (4.34)$$

Integrate Eq. (4.34) from time t_o to t:

$$\mathbf{K}(t)\,\mathbf{f}(t) - \mathbf{K}(t_o)\,\mathbf{f}(t_o) = \int_{t_o}^{t} \mathbf{K}(\tau)\,\mathbf{Y}\,\mathbf{n}(\tau)\,d\tau \qquad (4.35)$$

Or, rearranging:

$$\mathbf{f}(t) = \mathbf{K}^{-1}(t) \left\{ \mathbf{K}(t_o)\ \mathbf{f}(t_o) + \int_{t_o}^{t} \mathbf{K}(\tau)\ \mathbf{Y}\ \mathbf{n}(\tau)\ d\tau \right\} \qquad (4.36)$$

Using the definition of $\mathbf{K}$:

$$\mathbf{f}(t) = \exp[\ -\mathbf{A}\ (t-t_o)\ ]\ \mathbf{f}(t_o) + \int_{t_o}^{t} \exp[-\mathbf{A}\ (t-\tau)]\ \mathbf{Y}\ \mathbf{n}(\tau)\ d\tau \qquad (4.37)$$

Finally, insert the known time-dependent behavior of $\mathbf{n}$:

$$\mathbf{f}(t) = \exp[\ -\mathbf{A}\ (t-t_o)\ ]\ \mathbf{f}(t_o) + \left\{ \int_{t_o}^{t} \exp[-\mathbf{A}\ (t-\tau)]\ \mathbf{Y}\ \exp[\mathbf{H}\ (\tau-t_o)]\ d\tau \right\} \mathbf{n}(t_o) \qquad (4.38)$$

Eq. (4.38) may be expanded to account for both heavy metal chains:

$$\mathbf{f}(t) = \exp[\ -\mathbf{A}\ (t-t_o)\ ]\ \mathbf{f}(t_o) + \left\{ \int_{t_o}^{t} \exp[-\mathbf{A}\ (t-\tau)]\ \mathbf{Y}^{02}\exp[\mathbf{H}^{02}(\tau-t_o)]\ d\tau \right\} \mathbf{n}^{02}(t_o) + \left\{ \int_{t_o}^{t} \exp[-\mathbf{A}\ (t-\tau)]\ \mathbf{Y}^{28}\exp[\mathbf{H}^{28}(\tau-t_o)]\ d\tau \right\} \mathbf{n}^{28}(t_o) \qquad (4.39)$$

Define the following fission product state transition matrices:

$$\mathbf{L} \equiv \exp[\ -\mathbf{A}\ (t-t_o)\ ] \qquad (4.40)$$

$$\mathbf{J}^{02} \equiv \int_{t_o}^{t} \exp[-\mathbf{A}\ (t-\tau)]\ \mathbf{Y}^{02}\exp[\mathbf{H}^{02}(\tau-t_o)]\ d\tau \qquad (4.41a)$$

$$\mathbf{J}^{28} \equiv \int_{t_o}^{t} \exp[-\mathbf{A}\ (t-\tau)]\ \mathbf{Y}^{28}\exp[\mathbf{H}^{28}(\tau-t_o)]\ d\tau \qquad (4.41b)$$

Then the FPCV at time t is the following function of the FPCV and HMCVs at time t_o:

$$\mathbf{f}(t) = \mathbf{L}\ \mathbf{f}(t_o) + \mathbf{J}^{02}\ \mathbf{n}^{02}(t_o) + \mathbf{J}^{28}\ \mathbf{n}^{28}(t_o) \qquad (4.42)$$

where $\mathbf{L}$, $\mathbf{J}^{02}$, and $\mathbf{J}^{28}$ are all independent of the fission product or heavy metal concentration vectors.

The L(t) matrix by itelf represents the decay of the fission product chain when no fission source is present. J(t) may be physically interpreted as follows: the quantity Y $\mathbf{n}(\tau)\, d\tau$ is the density of atoms in f generated in time $d\tau$ around τ. From time τ until t, these fission products decay by a factor of $\exp[-A(t-\tau)]$. The J integral is thus the sum of all such contributions to f(t) for times τ ranging from t_o to t.

Finally, note that Eq. (4.42) may be represented in block diagram form, as in Figure (4.6).

Approximate Formula for the J Matrices

Equations (4.41a) and (4.41b) are the theoretically exact expressions for the integrated source contributions to changes in the fission product density vector. However, use of these equations has been found to lead to numerical difficulties, and to be quite time-consuming as well. For this reason, a simple and reasonable approximation is used to calculate the J matrices.

Recall that the J matrix arose from the following expression:

$$\begin{aligned} \mathbf{f}(t) &= L\, \mathbf{f}(t_o) \\ &\quad + \int_{t_o}^{t} \left\{ \exp[-A(t-\tau)]\; Y \exp[H(\tau-t_o)]\; d\tau \right\} \mathbf{n}(t_o) \\ &= L\, \mathbf{f}(t_o) + L \int_{t_o}^{t} \left\{ \exp[A\tau]\; Y\, \mathbf{n}(\tau)\; d\tau \right\} \end{aligned} \qquad (4.43)$$

For simplicity, and without loss of generality, let $t_o = 0$ for the development which follows. During the time interval 0 to t, during which core parameters are assumed constant, the heavy metal density vector n will not change by a large amount. Thus, it appears reasonable

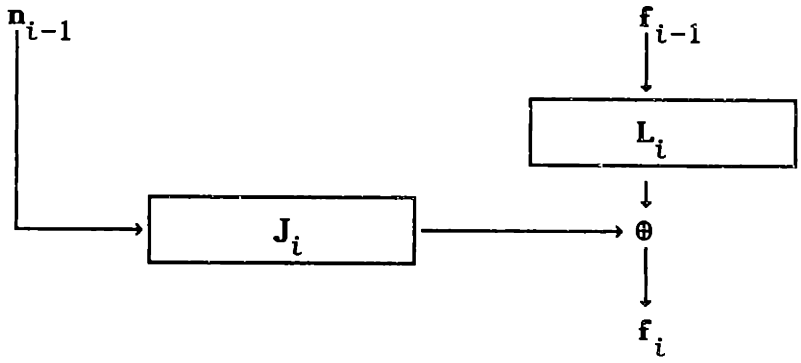

FIG. 4.6: Input/output diagram for fission product densities.

to approximate $\mathbf{n}$ by the constant time averaged value $\langle \mathbf{n} \rangle$ during the interval:

$$\mathbf{n}(\tau) \cong \langle \mathbf{n} \rangle = \frac{1}{t} \int_0^t \mathbf{n}(\tau)\, d\tau$$

$$= \left\{ \frac{1}{t} \right\} \mathbf{D}\, \mathbf{n}(0) \qquad (4.44)$$

where $\mathbf{D}$ is the fission decrement matrix defined in Section 4.5. Since $\mathbf{D}$ is independent of time, the integral for $\mathbf{f}(t)$ may be simplified as follows:

$$\mathbf{f}(t) = \mathbf{L}\, \mathbf{f}(0) + \mathbf{L} \left\{ \frac{1}{t} \right\} \int_0^t \exp[\mathbf{A}\tau]\, \mathbf{Y}\, \mathbf{D}\, \mathbf{n}(0)\, d\tau$$

$$= \mathbf{L}\, \mathbf{f}(0) + \mathbf{L} \left\{ \frac{1}{t} \right\} \left\{ \int_0^t \exp[\mathbf{A}\tau]\, d\tau \right\} \mathbf{Y}\, \mathbf{D}\, \mathbf{n}(0)$$

Evaluate the bracketed integral:

$$\mathbf{f}(t) = \mathbf{L}\, \mathbf{f}(0) + (1/t)\, \mathbf{L} \left\{ \mathbf{A}^{-1}[\, \exp(\mathbf{A}t) - \mathbf{I}\,] \right\} \mathbf{Y}\, \mathbf{D}\, \mathbf{n}(0)$$

But $\mathbf{L} \equiv \exp(-\mathbf{A}t)$, thus:

$$\mathbf{f}(t) = \mathbf{L}\, \mathbf{f}(0) + (1/t) \exp(-\mathbf{A}t) \left\{ \mathbf{A}^{-1}[\, \exp(\mathbf{A}t) - \mathbf{I}\,] \right\} \mathbf{Y}\, \mathbf{D}\, \mathbf{n}(0)$$

$$= \mathbf{L}\, \mathbf{f}(0) + (1/t)\, \mathbf{A}^{-1} \exp(-\mathbf{A}t) \left\{ \exp(\mathbf{A}t) - \mathbf{I} \right\} \mathbf{Y}\, \mathbf{D}\, \mathbf{n}(0)$$

$$= \mathbf{L}\, \mathbf{f}(0) + (1/t)\, \mathbf{A}^{-1} \left\{ \mathbf{I} - \exp(-\mathbf{A}t) \right\} \mathbf{Y}\, \mathbf{D}\, \mathbf{n}(0)$$

$$= \mathbf{L}\, \mathbf{f}(0) + (1/t)\, \mathbf{A}^{-1}\, (\, \mathbf{I} - \mathbf{L}\,)\, \mathbf{Y}\, \mathbf{D}\, \mathbf{n}(0)$$

Thus, if the following approximate definitions are utilized:

$$\mathbf{J}^{02} = (1/t)\, \mathbf{A}^{-1}\, (\, \mathbf{I} - \mathbf{L}\,)\, \mathbf{Y}^{02}\, \mathbf{D}^{02} \qquad (4.45a)$$

$$\mathbf{J}^{28} = (1/t)\, \mathbf{A}^{-1}\, (\, \mathbf{I} - \mathbf{L}\,)\, \mathbf{Y}^{28}\, \mathbf{D}^{28} \qquad (4.45b)$$

Then we may still write:

$$\mathbf{f}(t) = \mathbf{L}\, \mathbf{f}(0) + \mathbf{J}^{02}\mathbf{n}^{02}(0) + \mathbf{J}^{28}\mathbf{n}^{28}(0) \qquad (4.46)$$

and the calculations involved are simplified considerably.

Collapsing the Fission Product Transition Matrices:

The FP transition matrices possess the same useful property that the HM matrices do: they are independent of fuel state and thus may be manipulated independently of any particular fuel state or type. Once again, collapsed transition matrices may be defined for the fission products.

As before, let us examine a single radial drop zone divided into N axial segments, indexed 1 through N, each with associated FP transition matrices $\mathbf{L}_i$, $\mathbf{J}_i^{02}$ and $\mathbf{J}_i^{28}$. Let the symbol $\mathbf{f}_i$ represent the FP concentration vector of a fuel element as it leaves zone i. Thus, from Eq. (4.42), we know that:

$$\mathbf{f}_i = \mathbf{L}_i \mathbf{f}_{i-1} + \mathbf{J}_i \mathbf{n}_{i-1} \qquad (4.47)$$

where, once again, only one HM chain is considered for brevity. Figure (4.7) illustrates the system of equations for successive zones in block diagram form. Now, the FPCV following the first axial zone is therefore:

$$\mathbf{f}_1 = \mathbf{L}_1 \mathbf{f}_0 + \mathbf{J}_1 \mathbf{n}_0$$

Following the second:

$$\begin{aligned} \mathbf{f}_2 &= \mathbf{L}_2 \mathbf{f}_1 + \mathbf{J}_2 \mathbf{n}_1 \\ &= \mathbf{L}_2 \left[\mathbf{L}_1 \mathbf{f}_0 + \mathbf{J}_1 \mathbf{n}_0 \right] + \mathbf{J}_2 \left[\mathbf{T}_1 \mathbf{n}_0 \right] \\ &= \mathbf{L}_2 \mathbf{L}_1 \mathbf{f}_0 + \left[\mathbf{J}_1 + \mathbf{J}_2 \mathbf{T}_1 \right] \mathbf{n}_0 \end{aligned}$$

Following the third:

$$\begin{aligned} \mathbf{f}_3 &= \mathbf{L}_3 \mathbf{f}_2 + \mathbf{J}_3 \mathbf{n}_2 \\ &= \mathbf{L}_3 \left\{ \mathbf{L}_2 \mathbf{L}_1 \mathbf{f}_0 + \left[\mathbf{J}_1 + \mathbf{J}_2 \mathbf{T}_1 \right] \mathbf{n}_0 \right\} + \mathbf{J}_3 \left[\mathbf{T}_2 \mathbf{T}_1 \right] \mathbf{n}_0 \\ &= \mathbf{L}_3 \mathbf{L}_2 \mathbf{L}_1 \mathbf{f}_0 + \left[\mathbf{J}_1 + \mathbf{J}_2 \mathbf{T}_1 + \mathbf{J}_3 \mathbf{T}_2 \mathbf{T}_1 \right] \mathbf{n}_0 \end{aligned}$$

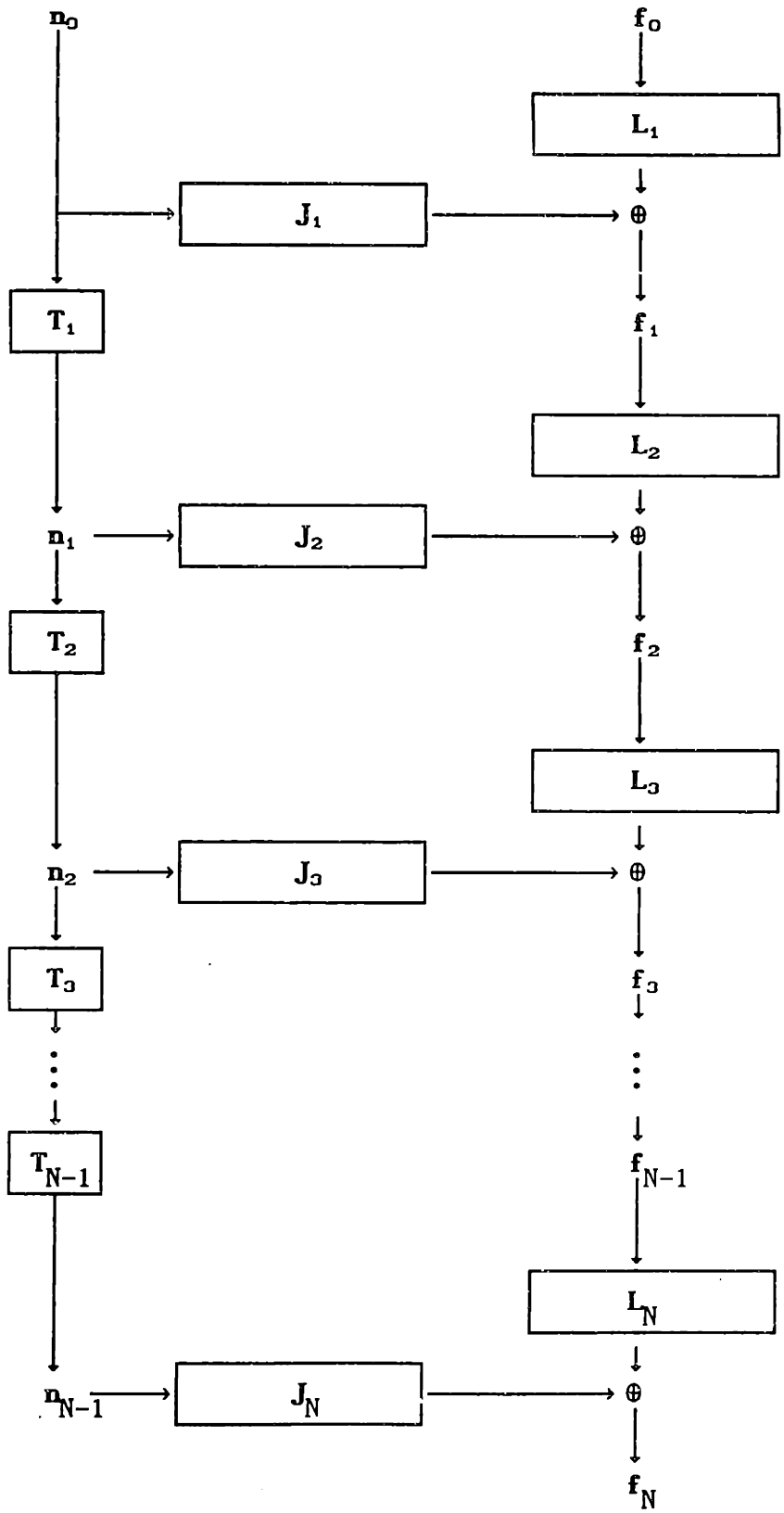

FIG. 4.7: Collapsing the fission product transition matrices.

...and so on. In general, the pattern is:

$$\mathbf{f}_n = \left[\mathbf{L}_n \mathbf{L}_{n-1} \cdots \mathbf{L}_2 \mathbf{L}_1 \right] \mathbf{f}_0 + \left[\mathbf{J}_1 + [\mathbf{J}_2 \mathbf{T}_1] + \cdots + [\mathbf{J}_n \mathbf{T}_{n-1} \cdots \mathbf{T}_2 \mathbf{T}_1] \right] \mathbf{n}_0$$

Thus, if we define the following collapsed fission product transition matrices:

$$\mathfrak{L} \equiv \prod_{i=1}^{N} \mathbf{L}_i \tag{4.48a}$$

$$\mathfrak{J} \equiv \sum_{i=1}^{N} \mathbf{J}_i \left\{ \prod_{j=0}^{i-1} \mathbf{T}_j \right\} \tag{4.48b}$$

where the $\mathbf{T}_0$ matrix is taken to be the identity matrix I. As before, the product must be assumed to be carried out in the proper order. The overall top-to-bottom transformation may then be written as:

$$\mathbf{f}_N = \mathfrak{L}\, \mathbf{f}_0 + \mathfrak{J}\, \mathbf{n}_0 \tag{4.49}$$

Now, the $\mathfrak{L}$ and $\mathfrak{J}$ matrices are associated with a particular radial drop zone, so it is reasonable to define the symbols $\mathfrak{L}_i$ and $\mathfrak{J}_i$ as the collapsed fission product transition matrices associated with the i'th radial drop zone. With this notation, the change in f for a single pass may be expressed using branch variables:

$$\mathbf{f}(\beta) = \mathbf{f}(\beta', n) = \mathfrak{L}_n\, \mathbf{f}(\beta') + \mathfrak{J}_n\, \mathbf{n}(\beta') \tag{4.50}$$

where n is the index of the last radial drop zone in β.

4.8: EULERIAN TRANSITION MATRICES

It is possible to derive expressions for the time-averaged values of the heavy metal, fission product, and burnup parameters during their passage through a core zone. Such analysis is required to calculate the spatial average of fuel parameters for use in further computations (e.g., neutron diffusion calculations). It has already been shown in Section 3.4 that the spatial average of some parameter ξ, denoted by $\langle \xi \rangle$, is computable from the known time-dependence of ξ within the zone of interest:

$$\langle \xi \rangle = (1/\Delta t) \int_0^{\Delta t} \xi_t(t)\, dt \qquad (4.51)$$

where ξ_t is the function relating the value of ξ to time.

For the remainder of this section, we will be investigating a single zone in the core. All transition matrices are those associated with the zone under investigation. Suppose that a fuel element enters this zone with initial HM concentration vector $\mathbf{n}_o$. Then the spatial average of $\mathbf{n}$ may be calculated using Eq. (4.51):

$$\langle \mathbf{n} \rangle = (1/\Delta t) \int_0^{\Delta t} \mathbf{n}(t)\, dt = (1/\Delta t) \left\{ \int_0^{\Delta t} \exp[\mathbf{H}t]\, dt \right\} \mathbf{n}_o$$

This integral was evaluated in Eq. (4.18), so:

$$\langle \mathbf{n} \rangle = (1/\Delta t)\, \mathbf{H}^{-1} \left[\exp(\mathbf{H}\, \Delta t) - \mathbf{I} \right] \mathbf{n}_o = (1/\Delta t)\, \mathbf{D}\, \mathbf{n}_o \qquad (4.52)$$

Thus, the spatial average of the HM concentration vector is a linear transformation of the initial vector. Furthermore, the transformation matrix (**D**) is already known from the burnup calculation. Suppose now we are interested in the zone-averaged burnup. Let F_o

represent the cumulative fission density of a fuel element as it enters the zone of interest (for the present derivation, consider only a single heavy metal chain). The spatial average of F is:

$$\langle F \rangle = (1/\Delta t) \int_0^{\Delta t} F(t)\, dt \tag{4.53}$$

The time-dependent behavior of F is given by:

$$F(t) = F_o + \phi\, \sigma_f^+\, H^{-1} \left[\exp(Ht) - I \right] n_o \tag{4.54}$$

Substitute into Eq. (4.53):

$$\langle F \rangle = (1/\Delta t) \int_0^{\Delta t} F_o\, dt + (1/\Delta t) \int_0^{\Delta t} \left\{ \phi\, \sigma_f^+\, H^{-1} \left[\exp(Ht) - I \right] n_o \right\} dt$$

$$= F_o + (1/\Delta t)\, \phi\, \sigma_f^+\, H^{-1} \left\{ \int_0^{\Delta t} \left[\exp(Ht) - I \right] dt \right\} n_o \tag{4.55}$$

Define the following new transition matrix:

$$G \equiv H^{-1} \int_0^{\Delta t} \left[\exp(Ht) - I \right] dt \tag{4.56}$$

G may be analytically evaluated, once again using the integral from Eq. (4.18):

$$G = H^{-1} \int_0^{\Delta t} \exp(Ht)\, dt - H^{-1} \int_0^{\Delta t} I\, dt = H^{-1} D - H^{-1} \Delta t$$

or

$$G = H^{-1} \left[D - I\Delta t \right] \tag{4.57}$$

Region average burnup is computed using both Eqs. (4.55) and (4.57):

$$\langle F \rangle = F_o + (1/\Delta t)\, \phi\, \sigma_f^+\, G\, n_o \tag{4.58}$$

In a similar manner, it is possible to derive an analytic expression for the region average fission product concentrations, $\langle f \rangle$.

However, the computations necessary to compute the exact transition matrices are prohibitively complex. Therefore, based on the assumption that fission product densities will not behave non-linearly during the transit of a single zone, the following simple approximation may be used:

$$\langle \mathbf{f} \rangle \equiv (1/\Delta t) \int_0^{\Delta t} \mathbf{f}\, dt \cong (\tfrac{1}{2}) [\, \mathbf{f}(\Delta t) + \mathbf{f}_o \,] \tag{4.59}$$

Or, since $\mathbf{f}(\Delta t) = \mathbf{L}\,\mathbf{f}_o + \mathbf{J}\,\mathbf{n}_o$,

$$\begin{aligned} \langle \mathbf{f} \rangle &= (\tfrac{1}{2}) [\, \mathbf{L}\,\mathbf{f}_o + \mathbf{f}_o + \mathbf{J}\,\mathbf{n}_o \,] \\ &= (\tfrac{1}{2}) [\, \mathbf{L} + \mathbf{I} \,]\, \mathbf{f}_o + (\tfrac{1}{2})\, \mathbf{J}\,\mathbf{n}_o \end{aligned} \tag{4.60}$$

Finally, for later applications, it is desirable to derive an expression for the volume-averaged rate of change of fission product densities. We know from Eq. (4.29) that:

$$\dot{\mathbf{f}} = \mathbf{A}\,\mathbf{f} + \mathbf{Y}\,\mathbf{n} \tag{4.61}$$

Apply the volume average operator:

$$\begin{aligned} \langle \dot{\mathbf{f}} \rangle &= \langle \mathbf{A}\,\mathbf{f} \rangle + \langle \mathbf{Y}\,\mathbf{n} \rangle \\ &= \mathbf{A} \langle \mathbf{f} \rangle + \mathbf{Y} \langle \mathbf{n} \rangle \\ &= (\tfrac{1}{2})\, \mathbf{A} [\, \mathbf{f}(\Delta t) + \mathbf{f}_o \,] + (1/\Delta t)\, \mathbf{Y}\,\mathbf{D}\,\mathbf{n}_o \end{aligned} \tag{4.62}$$

Once again, since $\mathbf{f}(\Delta t) = \mathbf{L}\,\mathbf{f}_o + \mathbf{J}\,\mathbf{n}_o$,

$$\begin{aligned} \langle \dot{\mathbf{f}} \rangle &= (\tfrac{1}{2})\, \mathbf{A} [\, \mathbf{L} + \mathbf{I} \,]\, \mathbf{f}_o \\ &\quad + \left[(\tfrac{1}{2})\, \mathbf{J} + (1/\Delta t)\, \mathbf{Y}\,\mathbf{D} \right] \mathbf{n}_o \end{aligned} \tag{4.63}$$

Eq. (4.63) will find application when it is necessary to calculate the source rate of a particular fission product as a function of position within the core.

4.9: EXPECTED VALUES OF FUEL PARAMETERS

This section treats the pass-to-pass propagation of fuel parameter distributions, in which the stochastic pebble-drop phenomenon must be taken into account. In this section we will deal only with collapsed core transition matrices.

Let the symbol $\mathbf{n}(\beta)$, $\beta \in B_w$, represent the heavy metal concentration vector at the exit of branch β. There are, in general, many possible discrete values for $\mathbf{n}(\beta)$, with a probability distribution determined by p_β. Let the symbol $\boldsymbol{\theta}_i$ represent the collapsed heavy metal transition matrix associated with drop zone i. Then the relation between $\mathbf{n}(\beta)$ and $\mathbf{n}(\beta')$ is:

$$\mathbf{n}(\beta) = \mathbf{n}(\beta',n) = \boldsymbol{\theta}_n \, \mathbf{n}(\beta') \tag{4.64}$$

where, as before, n is the index of the last radial drop zone in β. This relation enables us to calculate the L-expectation for $\mathbf{n}(\beta)$:

$$\overline{\mathbf{n}(\beta)} = E[\, \mathbf{n}(\beta) \,] = \sum_{\beta} p_\beta \, \mathbf{n}(\beta) = \sum_{n} \sum_{\beta'} p_n \, p_{\beta'} \, \boldsymbol{\theta}_n \, \mathbf{n}(\beta')$$

$$= \left\{ \sum_{n} p_n \, \boldsymbol{\theta}_n \right\} \left\{ \sum_{\beta'} p_{\beta'} \, \mathbf{n}(\beta') \right\} \tag{4.65}$$

since p_n and $\boldsymbol{\theta}_n$ are both independent of β'. The second term in brackets in Eq. (4.65) is simply $E[\, \mathbf{n}(\beta') \,]$, while the first term can be interpreted as the L-expectation of the HM transformation for a single pass. Thus, if we define a *core averaged heavy metal transition matrix*, $\overline{\boldsymbol{\theta}}$:

$$\overline{\boldsymbol{\theta}} \equiv \sum_{n} p_n \, \boldsymbol{\theta}_n \tag{4.66}$$

then the relation between L-expectation of $\mathbf{n}$ from one pass to the next is given by:

$$\overline{\mathbf{n}(\beta)} = \bar{\boldsymbol{\theta}}\,\overline{\mathbf{n}(\beta')} \tag{4.67}$$

Or, since the L-expectation reduces dependence on β to dependence on the pass number w:

$$\bar{\mathbf{n}}_w = \bar{\boldsymbol{\theta}}\,\bar{\mathbf{n}}_{w-1} \tag{4.68}$$

Thus, it is a rather remarkable fact that the entire stationary pebble bed core may be collapsed to a single transition matrix for calculation of the expected values of the heavy metal concentration vectors.

A similar relation may be derived for the fission product transition matrices. Let $\mathcal{L}_i$ and $\mathcal{F}_i$ represent the fission product transition matrices associated with radial drop zone i. The FP concentration vector exiting branch β, $\mathbf{f}(\beta)$, is related to the FP concentrations of its parent branch in this way:

$$\mathbf{f}(\beta) = \mathbf{f}(\beta',n) = \mathcal{L}_n\,\mathbf{f}(\beta') + \mathcal{F}_n\,\mathbf{n}(\beta') \tag{4.69}$$

(including only a single heavy metal chain for the present). The L-expectation of $\mathbf{f}(\beta)$ is thus:

$$\begin{aligned}
\overline{\mathbf{f}(\beta)} &= E[\,\mathbf{f}(\beta)\,] = \sum_{\beta} p_\beta\,\mathbf{f}(\beta) \\
&= \sum_{n}\sum_{\beta'} p_n\,p_{\beta'}\left\{\mathcal{L}_n\,\mathbf{f}(\beta') + \mathcal{F}_n\,\mathbf{n}(\beta')\right\} \\
&= \sum_{n}\sum_{\beta'} p_n\,p_{\beta'}\,\mathcal{L}_n\,\mathbf{f}(\beta') + \sum_{n}\sum_{\beta'} p_n\,p_{\beta'}\,\mathcal{F}_n\,\mathbf{n}(\beta') \\
&= \sum_{n} p_n\,\mathcal{L}_n \sum_{\beta'} p_{\beta'}\,\mathbf{f}(\beta') + \sum_{n} p_n\,\mathcal{F}_n \sum_{\beta'} p_{\beta'}\,\mathbf{n}(\beta')
\end{aligned} \tag{4.70}$$

In the same manner as for the heavy metal transition matrices, the above equation may be expressed in terms of L-averaged transition matrices and the L-expectations of the previous pass's concentration vectors. If we define the following core averaged fission product transition matrices:

$$\bar{\mathcal{L}} \equiv \sum_n p_n \mathcal{L}_n \qquad (4.71a)$$

$$\bar{\mathcal{F}} \equiv \sum_n p_n \mathcal{F}_n \qquad (4.71b)$$

$\bar{\mathcal{L}}$ and $\bar{\mathcal{F}}$ may be interpreted as the flow-weighted expected transormations for $\mathbf{f}$ over a single pass. Eq. (4.71) may be rewritten as:

$$\overline{\mathbf{f}(\beta)} = \bar{\mathcal{L}}\,\overline{\mathbf{f}(\beta')} + \bar{\mathcal{F}}\,\overline{\mathbf{n}(\beta')} \qquad (4\ 72a)$$

or:

$$\bar{\mathbf{f}}_w = \bar{\mathcal{L}}\,\bar{\mathbf{f}}_{w-1} + \bar{\mathcal{F}}\,\bar{\mathbf{n}}_{w-1} \qquad (4.72b)$$

Just as in the heavy metal case, the stationary pebble bed core can be reduced to a single pair of fission product transition matrices for calculation of expected fission product concentrations.

Yet a third similar relation may be derived, this time regarding burnup. Let $\Delta F(\beta)$ represent the incremental burnup accumulated by a fuel element during its residence in branch β. Then, for either HM chain:

$$\Delta F(\beta) = \Delta F(\beta', n) = \mathbf{A}_n^+ \mathbf{n}(\beta')$$

Thus, the expectation of the burnup increment is:

$$E[\ \Delta F(\beta)\ ] = \overline{\Delta F}_w = \sum_{\beta} p_{\beta}\ \Delta F(\beta) = \sum_{n}\sum_{\beta'} p_n\ p_{\beta'}\ \mathbf{A}_n^{+}\ \mathbf{n}(\beta')$$

$$= \sum_{n} p_n\ \mathbf{A}_n^{+} \sum_{\beta'} p_{\beta'}\ \mathbf{n}(\beta')$$

Define a third core average transition matrix:

$$\overline{\mathbf{A}} \equiv \sum_{n} p_n\ \mathbf{A}_n \tag{4.73}$$

Then the incremental burnup associated with pass w may be calculated by:

$$\overline{\Delta F}_w = \overline{\mathbf{A}}^{+}\ \overline{\mathbf{n}}_{w-1} \tag{4.74}$$

Finally, the expectation for the total burnup $F(\beta)$ may also be expressed in similar terms:

$$E[\ F(\beta)\ ] = E[\ F(\beta') + \Delta F(\beta)\ ] = E[\ F(\beta')\ ] + E[\ \Delta F(\beta)\ ]$$

Thus, using Eq. (4.74):

$$E[\ F(\beta)\ ] = \overline{F}_w = \overline{F}_{w-1} + \overline{\mathbf{A}}^{+}\ \overline{\mathbf{n}}_{w-1} \tag{4.75}$$

which yields the expected value of burnup as a function of the burnup and HM concentration vector expectations from the previous pass.

4.10: SECOND MOMENTS OF FUEL STATE DISTRIBUTIONS

The covariance matrix **V** provides a method for representing the "spread" of data abouts its expected value. Some general properties of covariance matrices are reviewed in Appendix A.2. For a single random vector **x**, let the covariance matrix **V** be defined as follows:

$$\mathbf{V}_x \equiv E[\ (\mathbf{x}-\bar{\mathbf{x}})\ (\mathbf{x}-\bar{\mathbf{x}})^+\ ] = E[\ \mathbf{x}\ \mathbf{x}^+\ ] - \bar{\mathbf{x}}\ \bar{\mathbf{x}}^+ \qquad (4.76)$$

For two random vectors **x** and **y** (with the same number of elements N), the cross-covariance in the "xy sense" is defined as follows:

$$\mathbf{X}_{xy} \equiv E[\ (\mathbf{x}-\bar{\mathbf{x}})\ (\mathbf{y}-\bar{\mathbf{y}})^+\ ] = E[\ \mathbf{x}\ \mathbf{y}^+\ ] - \bar{\mathbf{x}}\ \bar{\mathbf{y}}^+ \qquad (4.77)$$

4.10.1. Heavy Metal Covariance Matrices

Suppose we are interested in the pass-to-pass behavior of the covariance matrix associated with the vector **n** of heavy metal concentrations. Let the symbol $\mathbf{V}(w)$ represent this matrix:

$$\mathbf{V}(w) \equiv E[\ \mathbf{n}(\beta)\ \mathbf{n}(\beta)^+\ ] - \bar{\mathbf{n}}_w\ \bar{\mathbf{n}}_w^+ \qquad (4.78)$$

The above expression may be manipulated to yield an expression for $\mathbf{V}(w)$ in terms of the covariance matrix at the end of the previous pass, $\mathbf{V}(w-1)$, and the expected values of HM concentration vectors. Expand the first term on the right-hand side of Eq. (4.78):

$$\begin{aligned} E[\ \mathbf{n}(\beta)\ \mathbf{n}(\beta)^+\ ] &= E\left[\ \boldsymbol{\theta}_n\ \mathbf{n}(\beta')\ [\ \boldsymbol{\theta}_n\ \mathbf{n}(\beta')\ ]^+\ \right] \\ &= \sum_n \sum_{\beta'} p_n\ p_{\beta'}\ \left[\ \boldsymbol{\theta}_n\ \mathbf{n}(\beta')\ \mathbf{n}(\beta')^+\ \boldsymbol{\theta}_n^+\ \right] \end{aligned} \qquad (4.79)$$

where we have used the fact that:

$$[\ \mathbf{A}\ \mathbf{B}\ ]^+ = \mathbf{B}^+\ \mathbf{A}^+$$

The sum in Eq. (4.79) may be rearranged as follows:

$$E[\ \mathbf{n}(\beta)\ \mathbf{n}(\beta)^+\ ] = \sum_n p_n\ \boldsymbol{\theta}_n \left\{ \sum_{\beta'} p_{\beta'}\ \mathbf{n}(\beta')\ \mathbf{n}(\beta')^+ \right\} \boldsymbol{\theta}_n^+ \qquad (4.80)$$

The terms in the brackets in the above equation may be related to $\mathbf{V}$ from the previous pass using the Definition (4.76):

$$\sum_{\beta'} p_{\beta'}\ \mathbf{n}(\beta')\ \mathbf{n}(\beta')^+ = E[\ \mathbf{n}(\beta')\ \mathbf{n}(\beta')^+\ ]$$

$$= \mathbf{V}(w-1) + \bar{\mathbf{n}}_{w-1}\ \bar{\mathbf{n}}^+_{w-1} \qquad (4.81)$$

Substitute Eq. (4.81) into (4.80) to obtain:

$$E[\ \mathbf{n}(\beta)\ \mathbf{n}(\beta)^+\ ] = \sum_n p_n\ \boldsymbol{\theta}_n \left\{ \mathbf{V}(w-1) + \bar{\mathbf{n}}_{w-1}\ \bar{\mathbf{n}}^+_{w-1} \right\} \boldsymbol{\theta}_n^+ \qquad (4.82)$$

The second term on the right-hand side of Eq. (4.82) is simply a function of the expected values of $\mathbf{n}$ following pass β, which are easily calculated from Eq. (4.67). Thus, the recursive expression for the covariance matrix of the HM density vector is:

$$\mathbf{V}(w) = \sum_n p_n\ \boldsymbol{\theta}_n \left\{ \mathbf{V}(w-1) + \bar{\mathbf{n}}_{w-1}\ \bar{\mathbf{n}}^+_{w-1} \right\} \boldsymbol{\theta}_n^+ - \bar{\mathbf{n}}_w\ \bar{\mathbf{n}}^+_w \qquad (4.83)$$

Heavy Metal Cross Covariances

The pass-to-pass propagation of the heavy metal cross covariance vectors is calculated in a manner analogous to the simple covariance matrices. To simplify notation for this section, let the symbol "x" represent "28," when indicating that some parameter is associated with the U-238 heavy metal chain, and "y" stand for "02" in parameters associated with the Th-232 chain. In this case, the cross covariance matrix $\mathbf{X}_{xy}$, in the uranium/thorium sense, associated with the heavy metal concentration vectors at the exit of w-th order branches, is

defined as:

$$\mathbf{X}_{xy}(w) \equiv E[\, \mathbf{n}^x(\beta)\, \mathbf{n}^y(\beta)^+ \,] - \bar{\mathbf{n}}_w^x\, \bar{\mathbf{n}}_w^{y+} \qquad (4.84)$$

As before, the first term on the right-hand side of Eq. (4.84) may be related to the cross covariance matrix from the previous pass, $\mathbf{X}_{xy}(w-1)$. First expand it using Eqs. (4.15):

$$\begin{aligned} E[\, \mathbf{n}^x(\beta)\, \mathbf{n}^y(\beta)^+ \,] &= E\left[\, \boldsymbol{\theta}_n^x\, \mathbf{n}^x(\beta')\, [\, \boldsymbol{\theta}_n^y\, \mathbf{n}^y(\beta')\,]^+ \,\right] \\ &= \sum_n \sum_{\beta'} p_n\, p_{\beta'}\, \left[\, \boldsymbol{\theta}_n^x\, \mathbf{n}^x(\beta')\, \mathbf{n}^y(\beta')^+\, \boldsymbol{\theta}_n^{y+} \right] \\ &= \sum_n p_n\, \boldsymbol{\theta}_n^x \left\{ \sum_{\beta'} p_{\beta'}\, \mathbf{n}^x(\beta')\, \mathbf{n}^y(\beta')^+ \right\} \boldsymbol{\theta}_n^{y+} \end{aligned} \qquad (4.85)$$

The term in brackets is simply $E[\, \mathbf{n}^x(\beta')\, \mathbf{n}^y(\beta')^+ \,]$, which can be expressed in terms of the previous pass's parameters using the definition of the cross covariance matrix:

$$E[\, \mathbf{n}^x(\beta')\, \mathbf{n}^y(\beta')^+ \,] = \mathbf{X}_{xy}(w-1) + \bar{\mathbf{n}}_{w-1}^x \bar{\mathbf{n}}_{w-1}^{y\,+} \qquad (4.86)$$

Substituting this expression into Eq. (4.85):

$$E[\, \mathbf{n}^x(\beta)\, \mathbf{n}^y(\beta)^+ \,] = \sum_n p_n\, \boldsymbol{\theta}_n^x \left\{ \mathbf{X}_{xy}(w-1) + \bar{\mathbf{n}}_{w-1}^x \bar{\mathbf{n}}_{w-1}^{y\,+} \right\} \boldsymbol{\theta}_n^{y+} \qquad (4.87)$$

The final recursive expression for the pass-to-pass propagation of the cross covariance matrix is thus:

$$\mathbf{X}_{xy}(w) = \sum_n p_n\, \boldsymbol{\theta}_n^x \left\{ \mathbf{X}_{xy}(w-1) + \bar{\mathbf{n}}_{w-1}^x\, \bar{\mathbf{n}}_{w-1}^{y\,+} \right\} \boldsymbol{\theta}_n^{y+} - \bar{\mathbf{n}}_w^x\, \bar{\mathbf{n}}_w^y \qquad (4.88)$$

4.10.2. Propagation of Burnup Variance

Calculating the variance of a fuel element's burnup as a function of pass number can be divided into three separate tasks:

- calculation of the HM covariance and cross-covariance matrices;

- calculation of the variance of the *incremental* burnup for the pass of interest; and
- calculation of the variance of the *cumulative* burnup following the pass of interest.

Let us first adress the problem of calculating the variance of the incremental burnup for pass w. In general, the incremental burnup for a branch depends on previous branch parameters as follows:

$$\Delta F(\beta) = \Delta F(\beta',n) = \mathbf{A}_n^{\chi+}\mathbf{n}^{\chi}(\beta') + \mathbf{A}_n^{y+}\mathbf{n}^{y}(\beta') \qquad (4.89)$$

The covariance of ΔF will have cross terms depending on a product of both HM concentration vectors. The variance of the burnup increment (which is actually a scalar quantity) incurred on pass w is defined as:

$$V_{\Delta F}(w) \equiv E[\ \Delta F(\beta)^2\ ] - \overline{\Delta F}_w^{\,2} \qquad (4.90)$$

Since ΔF will depend on matrix quantities, it is useful to rewrite Eq. (4.90) in the following form:

$$V_{\Delta F}(w) = E[\ \Delta F(\beta)\ \Delta F(\beta)^+\ ] - \overline{\Delta F}_w\ \overline{\Delta F}_w^+ \qquad (4.91)$$

The terms $\overline{\Delta F}_w$ are straightforward to calculate with the expressions derived in the previous section. The term $E[\ \Delta F(\beta)\ \Delta F(\beta)^+\ ]$, on the other hand, introduces some new complications. To evaluate it, expand the internal product in terms of both heavy metal chains from the previous pass:

$$E[\ \Delta F(\beta)\ \Delta F(\beta)^+\ ]$$

$$= E\left[\ \left\{\mathbf{A}_n^{\chi+}\mathbf{n}^{\chi}(\beta') + \mathbf{A}_n^{y+}\mathbf{n}^{y}(\beta')\right\}\left\{\mathbf{A}_n^{\chi+}\mathbf{n}^{\chi}(\beta') + \mathbf{A}_n^{y+}\mathbf{n}^{y}(\beta')\right\}^+\ \right]$$

$$= E\left[\ \mathbf{A}_n^{\chi+}\mathbf{n}^{\chi}(\beta')\left\{\mathbf{A}_n^{\chi+}\mathbf{n}^{\chi}(\beta')\right\}^+ + \mathbf{A}_n^{\chi+}\mathbf{n}^{\chi}(\beta')\left\{\mathbf{A}_n^{y+}\mathbf{n}^{y}(\beta')\right\}^+ + \mathbf{A}_n^{y+}\mathbf{n}^{y}(\beta')\left\{\mathbf{A}_n^{\chi+}\mathbf{n}^{\chi}(\beta')\right\}^+ + \mathbf{A}_n^{y+}\mathbf{n}^{y}(\beta')\left\{\mathbf{A}_n^{y+}\mathbf{n}^{y}(\beta')\right\}^+\ \right]$$

$$= E\Big[\mathbf{A}_n^{x+} \mathbf{n}^x(\beta') \mathbf{n}^x(\beta')^+ \mathbf{A}_n^x \Big] + E\Big[\mathbf{A}_n^{x+} \mathbf{n}^x(\beta') \mathbf{n}^y(\beta')^+ \mathbf{A}_n^y \Big] + E\Big[\mathbf{A}_n^{y+} \mathbf{n}^y(\beta') \mathbf{n}^x(\beta')^+ \mathbf{A}_n^x \Big] + E\Big[\mathbf{A}_n^{y+} \mathbf{n}^y(\beta') \mathbf{n}^y(\beta')^+ \mathbf{A}_n^y \Big]$$

$$= \sum_n p_n \mathbf{A}_n^{x+} \left\{ \sum_{\beta'} p_{\beta'} \mathbf{n}^x(\beta') \mathbf{n}^x(\beta')^+ \right\} \mathbf{A}_n^x + \sum_n p_n \mathbf{A}_n^{x+} \left\{ \sum_{\beta'} p_{\beta'} \mathbf{n}^x(\beta') \mathbf{n}^y(\beta')^+ \right\} \mathbf{A}_n^y + \sum_n p_n \mathbf{A}_n^{y+} \left\{ \sum_{\beta'} p_{\beta'} \mathbf{n}^y(\beta') \mathbf{n}^x(\beta')^+ \right\} \mathbf{A}_n^x + \sum_n p_n \mathbf{A}_n^{y+} \left\{ \sum_{\beta'} p_{\beta'} \mathbf{n}^y(\beta') \mathbf{n}^y(\beta')^+ \right\} \mathbf{A}_n^y \qquad (4.92)$$

Using the definitions of the HM covariance and cross-covariance, we may substitute into Eq. (4.92):

$$E[\, \Delta F(\beta)\, \Delta F(\beta)^+ \,] = \sum_n p_n \mathbf{A}_n^{x+} \left\{ \mathbf{V}_x(w-1) + \bar{\mathbf{n}}^x_{w-1} \bar{\mathbf{n}}^{x\,+}_{w-1} \right\} \mathbf{A}_n^x + \sum_n p_n \mathbf{A}_n^{x+} \left\{ \mathbf{X}_{xy}(w-1) + \bar{\mathbf{n}}^x_{w-1} \bar{\mathbf{n}}^{y\,+}_{w-1} \right\} \mathbf{A}_n^y + \sum_n p_n \mathbf{A}_n^{y+} \left\{ \mathbf{X}_{yx}(w-1) + \bar{\mathbf{n}}^y_{w-1} \bar{\mathbf{n}}^{x\,+}_{w-1} \right\} \mathbf{A}_n^x + \sum_n p_n \mathbf{A}_n^{y+} \left\{ \mathbf{V}_y(w-1) + \bar{\mathbf{n}}^y_{w-1} \bar{\mathbf{n}}^{y\,+}_{w-1} \right\} \mathbf{A}_n^y \qquad (4.93)$$

where $\mathbf{X}_{yx} \equiv [\ \mathbf{X}_{xy}]^{+}$, the cross covariance in the thorium/uranium sense (see appendix A.2). Eq. (4.93) is the desired result, as it gives an expression for $E[\ \Delta F(\beta)\ \Delta F(\beta)^{+}\ ]$ in terms of known parameters from the previous pass.

The final step is calculation of the variance of the cumulative burnup, a procedure which introduces still further complications. The reason is that the variance of the cumulative burnup involves the expectation of the squared burnup, which forces consideration of an entirely new set of cross statistics. To see why, examine the definition of the cumulative burnup variance:

$$V_F(w) = E[\ (\ F(\beta) - \bar{F}_w)^2\ ] = E[\ F(\beta)^2\ ] - \bar{F}_w^2 \qquad (4.94)$$

The $\bar{F}_w$ term is straightforward. However, the $E[\ F(\beta)^2\ ]$ term introduces the complication:

$$E[\ F(\beta)^2\ ] = E\Big[\ [\ F(\beta') + \Delta F(\beta)\ ]^2\ \Big]$$

$$= E[\ F(\beta')^2\ ] + 2\,E[\ \Delta F(\beta)\ F(\beta')\ ] + E[\ \Delta F(\beta)^2\ ] \qquad (4.95)$$

Now, $E[\ F(\beta')^2\ ]$ is simply the recursive term, so we need go no further with it. $E[\ \Delta F(\beta)^2\ ] = E[\ \Delta F(\beta)\ \Delta F(\beta)^{+}\ ]$, which was calculated in Eq. (4.93). The only new term is:

$$E[\ \Delta F(\beta)\ F(\beta')\ ],$$

which indicates the dependence of the incremental burnup at branch β on the cumulative burnup after the previous branch. Begin by expanding the $\Delta F(\beta)$ term:

$$E[\ \Delta F(\beta)\ F(\beta')\ ] = E[\ \Delta F^{x}(\beta)\ F(\beta')\ ] + E[\ \Delta F^{y}(\beta)\ F(\beta')\ ] \qquad (4.96)$$

Use the **A** transition matrix to expand the first term on the right

hand side:

$$E[\ \Delta F^{\chi}(\beta)\ F(\beta')\ ] = \sum_{n} p_n \sum_{\beta'} p_{\beta'}\ A_n^{\chi+} n^{\chi}(\beta')\ F(\beta')$$

$$= \sum_{n} p_n\ A_n^{\chi+}\ E[\ n^{\chi}(\beta')\ F(\beta')\ ]$$

$$= \overline{A}^{\chi+}\ E[\ n^{\chi}(\beta')\ F(\beta')\ ] \qquad (4.97)$$

Of course, a similar expression could have been developed for the second term on the right hand side of Eq. (4.96) just as easily. To evaluate the expectation in Eq. (4.97), note that:

$$E[\ n^{\chi}(\beta')\ F(\beta')\ ] = E\left[\ n^{\chi}(\beta')\ \left\{\ F(\beta'') + \Delta F^{\chi}(\beta') + \Delta F^{y}(\beta')\ \right\}\ \right]$$

$$= E\left[\ n^{\chi}(\beta')\ F(\beta'')\ \right] + E\left[\ n^{\chi}(\beta')\ \Delta F^{\chi}(\beta')\ \right] + E\left[\ n^{\chi}(\beta')\ \Delta F^{y}(\beta')\ \right]$$

$$= \sum_{m} p_m \sum_{\beta''} p_{\beta''}\ \theta_m^{\chi}\ n^{\chi}(\beta'')\ F(\beta'') + E\left[\ n^{\chi}(\beta')\ \Delta F^{\chi}(\beta')\ \right] + E\left[\ n^{\chi}(\beta')\ \Delta F^{y}(\beta')\ \right]$$

$$= \overline{\theta}^{\chi}\ E[\ n^{\chi}(\beta'')\ F(\beta'')\ ] + E\left[n^{\chi}(\beta')\ \Delta F^{\chi}(\beta')\right] + E\left[n^{\chi}(\beta')\ \Delta F^{y}(\beta')\right] \qquad (4.98)$$

("term 1") ("term 2") ("term 3")

where $\beta' = (\beta'', m)$. "Term 1" in the above equation is recursive. Term 2 or term 3 on the right hand side of Eq. (4.98) may be evaluated in general as follows:

$$E\left[\ n^{\chi}(\beta')\ \Delta F^{y}(\beta')\ \right] = E\left[\ n^{\chi}(\beta')\ \Delta F^{y}(\beta')^{+}\right]$$

$$= \sum_{m} p_m \sum_{\beta''} p_{\beta''}\ \theta_m^{\chi}\ n^{\chi}(\beta'')\ [\ A_m^{y+} n^{y}(\beta'')\ ]^{+}$$

$$= \sum_{m} p_m\ \theta_m^{\chi} \left\{ \sum_{\beta'} p_{\beta''}\ n^{\chi}(\beta'')\ n^{y}(\beta'')^{+} \right\} A_m^{y}$$

$$= \sum_{m} p_m\ \theta_m^{\chi} \left\{ X_{\chi y}(w-2) + n_{w-2}^{\chi} n_{w-2}^{y\ +} \right\} A_m^{y} \qquad (4.99)$$

If $x = y$ in Eq. (4.99), simply substitute the appropriate simple covariance matrix for the cross covariance. With the above equations, the overall variance of the cumulative burnup may be calculated. Figure 4.8 illustrates the flow of calculations necessary to compute the cumulative burnup variance.

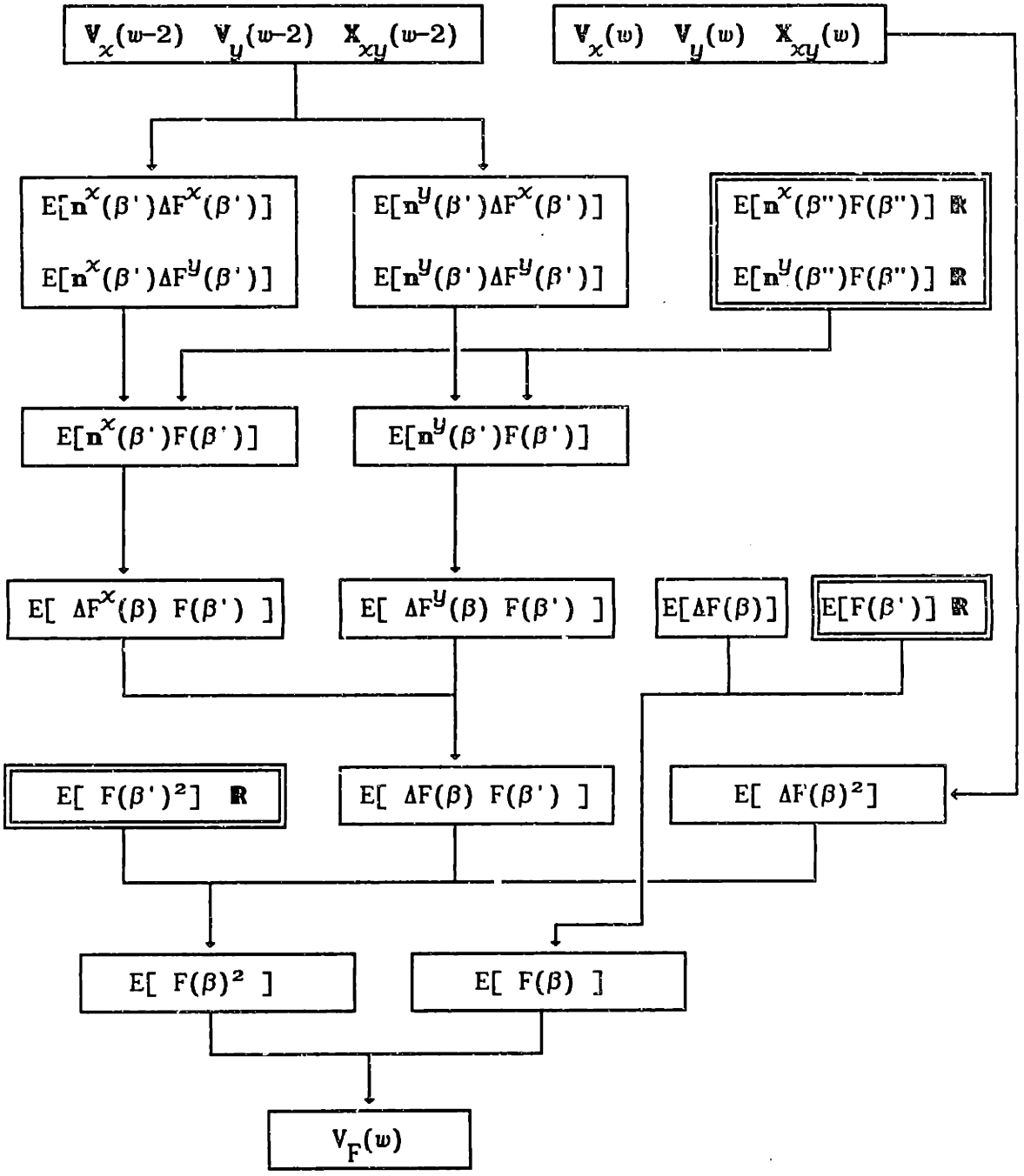

("R" indicates a recursive term)

FIG. 4.8: Sequence of calculations to determine cumulative burup variance.

4.10.3 Variance of the Power Density

The power density in a region may also be investigated for its second moments. In this section, relations between power density and heavy metal concentrations and transition matrices are developed. Equations for the variance of the power density as a function of pass number are derived, and finally it is shown how the expectations and variances of the power density for fuel in the same region but at different passes may be combined into a single set of parameters. Neutronic feedback effects are neglected in this analysis; we assume that the neutron flux level is not significantly affected by the presence of a hot spot. This assumption is reasonable due to the large mean free path of neutrons in graphite moderators.

Let the symbol ϵ designate the number of fissions per unit energy (usually taken to be 3.13×10^{10} fissions/Watt-second). The rate of power generation by a fuel element as it traverses zone i in the stationary core is:

$$\text{rate of power generation} = Q \{\text{Watts}\} = \eta \, \phi \, \sigma_f^+ \, \mathbf{n} \tag{4.100}$$

where the second heavy metal chain is neglected for the present, and η is a conversion factor:

$$\eta \equiv \frac{\{10^{24} \text{ b/cm}^2\}}{\{\epsilon \text{ fis/W-sec}\}} \tag{4.101}$$

η is necessary because the FUPAR/VSOP units of $\phi \, \sigma_f^+ \, \mathbf{n}$ are {neut/b-sec} x {b} x {#/b-cm} = {fissions/b-cm-sec}. Since the quantity of interest is actually the spatial average of Q over region i, we must apply the volume average operator to Eq. (4.100):

$$\langle Q \rangle_i = \langle \eta \phi \sigma_f^+ \mathbf{n} \rangle_i = \eta \phi_i \sigma_{f,i}^+ \langle \mathbf{n} \rangle_i$$
$$= \frac{\eta}{\Delta t_i} \phi_i \sigma_{f,i}^+ \mathbf{D}_i \mathbf{n}_{i-1} \qquad (4.102)$$

where Eq. (4.51) transforms the spatial average of a heavy metal concentration vector. $\mathbf{n}_{i-1}$ is the HM vector at the exit of the zone which precedes zone i. In reality, of course, Q is comprised of two components, due to the presence of two heavy metal chains. Thus,

$$\langle Q \rangle_i = \langle Q^{28} \rangle_i + \langle Q^{02} \rangle_i$$
$$= \frac{\eta}{\Delta t_i} \phi_i \sigma_{f,i}^{28+} \mathbf{D}_i^{28} \mathbf{n}_{i-1}^{28} + \frac{\eta}{\Delta t_i} \phi_i \sigma_{f,i}^{02+} \mathbf{D}_i^{02} \mathbf{n}_{i-1}^{02} \qquad (4.103)$$

Note that since $\Delta F_i = \phi_i \sigma_{f,i}^+ \mathbf{D}_i \mathbf{n}_{i-1}$, the region average power density is proportional to the burnup increment:

$$\langle Q \rangle_i = \langle Q^{28} \rangle_i + \langle Q^{02} \rangle_i = \frac{\eta}{\Delta t_i} \left[\Delta F^{02} + \Delta F^{28} \right] \qquad (4.104)$$

To simplify notation from this point on, let the symbol Q_i designate the volume averaged parameter $\langle Q \rangle_i$. Q_i is a function of two random vectors, $\mathbf{n}^{02}$ and $\mathbf{n}^{28}$. The expected value of Q_i is:

$$E[Q_i] = E\left[\frac{\eta}{\Delta t_i} \phi_i \sigma_{f,i}^{28+} \mathbf{D}_i^{28} \mathbf{n}_{i-1}^{28} + \frac{\eta}{\Delta t_i} \phi_i \sigma_{f,i}^{02+} \mathbf{D}_i^{02} \mathbf{n}_{i-1}^{02} \right]$$
$$= E\left[\frac{\eta}{\Delta t_i} \phi_i \sigma_{f,i}^{28+} \mathbf{D}_i^{28} \mathbf{n}_{i-1}^{28} \right] + E\left[\frac{\eta}{\Delta t_i} \phi_i \sigma_{f,i}^{02+} \mathbf{D}_i^{02} \mathbf{n}_{i-1}^{02} \right]$$
$$= \frac{\eta}{\Delta t_i} \phi_i \left[\sigma_{f,i}^{28+} \mathbf{D}_i^{28} \overline{\mathbf{n}}_{i-1}^{28} + \sigma_{f,i}^{02+} \mathbf{D}_i^{02} \overline{\mathbf{n}}_{i-1}^{02} \right] \qquad (4.105)$$

where $\overline{\mathbf{n}}_{i-1}^{28}$ and $\overline{\mathbf{n}}_{i-1}^{02}$ are the L-expectations of the uranium and thorium heavy metal concentration vectors at the exit of the previous zone.

Besides the expected value, another important quantity for random hot spot analysis is the variance of Q_i, denoted var(Q_i). Q_i is the sum of the two dependent random variables Q_i^{02} and Q_i^{28}, so the overall

variance may be decomposed:

$$\text{var}(\, Q_i) = \text{var}(\, Q_i^{28} + Q_i^{02}) = \text{var}(Q_i^{28}) + \text{var}(Q_i^{02}) + 2\,\text{cov}(Q_i^{28}, Q_i^{02}) \qquad (4.106)$$

where $\text{cov}(Q_i^{28}, Q_i^{02}) \equiv E[Q_i^{28} Q_i^{02}] - E[Q_i^{28}]E[Q_i^{02}]$ (see ref. D2). The simple variances also have terms such as $E[Q_i^{02} Q_i^{02}]$ and $E[Q_i^{28} Q_i^{28}]$. Thus, to evaluate power density variances, the expected values of squared power densities must be evaluated. Only the covariance case will be explicitly developed here. The two simple variance cases are elementary extensions, and only the results will be presented.

Note first that $E[Q_i^{28} Q_i^{02}] = E[Q_i^{28} Q_i^{02+}]$, since Q_i^{02} is a scalar and therefore symmetric. The first step is to expand the Q_i terms within the expectation:

$$E[Q_i^{28} Q_i^{02+}] = E\left\{ \left[\frac{\eta}{\Delta t_i} \phi_i \, \sigma_{f,i}^{28+} \, \mathbf{D}_i^{28} \, \mathbf{n}_{i-1}^{28} \right] \left[\frac{\eta}{\Delta t_i} \phi_i \, \sigma_{f,i}^{02+} \, \mathbf{D}_i^{02} \, \mathbf{n}_{i-1}^{02} \right]^+ \right\}$$

$$= \left\{ \frac{\eta \, \phi_i}{\Delta t_i} \right\}^2 E\left[\sigma_{f,i}^{28+} \, \mathbf{D}_i^{28} \, \mathbf{n}_{i-1}^{28} \, \mathbf{n}_{i-1}^{02+} \, \mathbf{D}_i^{02+} \sigma_{f,i}^{02} \right]$$

$$= \left\{ \frac{\eta \, \phi_i}{\Delta t_i} \right\}^2 \sigma_{f,i}^{28+} \, \mathbf{D}_i^{28} \, E[\mathbf{n}_{i-1}^{28} \, \mathbf{n}_{i-1}^{02+}] \, \mathbf{D}_i^{02+} \sigma_{f,i}^{02} \qquad (4.107)$$

Thus, if the expectation of $\mathbf{n}_{i-1}^{28} \, \mathbf{n}_{i-1}^{02+}$ is known, the expectation of $Q_i^{28} Q_i^{02+}$ is given by the transformation above. The second term in the covariance is $E[Q_i^{28}]E[Q_i^{02+}]$, which may also be expanded and expressed in terms of the heavy metal concentration vectors:

$$E[Q_i^{28}]E[Q_i^{02+}] = E\left[\frac{\eta}{\Delta t_i} \phi_i \, \sigma_{f,i}^{28+} \, \mathbf{D}_i^{28} \, \mathbf{n}_{i-1}^{28} \right] E\left[\frac{\eta}{\Delta t_i} \phi_i \, \sigma_{f,i}^{02+} \, \mathbf{D}_i^{02} \, \mathbf{n}_{i-1}^{02} \right]^+$$

$$= \left\{ \frac{\eta \, \phi_i}{\Delta t_i} \right\}^2 E\left[\sigma_{f,i}^{28+} \, \mathbf{D}_i^{28} \, \mathbf{n}_{i-1}^{28} \right] E\left[\mathbf{n}_{i-1}^{02+} \, \mathbf{D}_i^{02+} \sigma_{f,i}^{02} \right]$$

$$= \left\{ \frac{\eta \, \phi_i}{\Delta t_i} \right\}^2 \sigma_{f,i}^{28+} \, \mathbf{D}_i^{28} \, E[\mathbf{n}_{i-1}^{28}] \, E[\mathbf{n}_{i-1}^{02+}] \, \mathbf{D}_i^{02+} \sigma_{f,i}^{02} \qquad (4.108)$$

Combine Eqs. (4.107) and (4.108) to obtain:

$$\begin{aligned}\mathrm{cov}(\, Q_i^{28}, Q_i^{02+}) &= \left\{\frac{\eta\,\phi_i}{\Delta t_i}\right\}^2 \sigma_{f,i}^{28+}\, \mathbf{D}_i^{28}\, E[\mathbf{n}_{i-1}^{28}\, \mathbf{n}_{i-1}^{02+}]\, \mathbf{D}_i^{02+}\sigma_{f,i}^{02} \\ &\quad - \left\{\frac{\eta\,\phi_i}{\Delta t_i}\right\}^2 \sigma_{f,i}^{28+}\, \mathbf{D}_i^{28}\, E[\mathbf{n}_{i-1}^{28}]\, E[\mathbf{n}_{i-1}^{02+}]\, \mathbf{D}_i^{02+}\sigma_{f,i}^{02} \\ &= \left\{\frac{\eta\,\phi_i}{\Delta t_i}\right\}^2 \sigma_{f,i}^{28+}\, \mathbf{D}_i^{28}\left[\, E[\mathbf{n}_{i-1}^{28}\, \mathbf{n}_{i-1}^{02+}] - \overline{\mathbf{n}}_{i-1}^{28}\,\overline{\mathbf{n}}_{i-1}^{02+}\right] \mathbf{D}_i^{02+}\sigma_{f,i}^{02} \\ &= \left\{\frac{\eta\,\phi_i}{\Delta t_i}\right\}^2 \sigma_{f,i}^{28+}\, \mathbf{D}_i^{28}\, \mathbf{X}_{i-1}^{28,02}\, \mathbf{D}_i^{02+}\sigma_{f,i}^{02} \qquad (4.109)\end{aligned}$$

where $\mathbf{X}_{i-1}^{28,02}$ is the cross covariance matrix in the uranium/thorium sense at the exit of zone i-1. The derivations for the variances are entirely analogous:

$$\mathrm{var}(\, Q_i^{28}) = \left\{\frac{\eta\,\phi_i}{\Delta t_i}\right\}^2 \sigma_{f,i}^{28+}\, \mathbf{D}_i^{28}\, \mathbf{V}_{i-1}^{28}\, \mathbf{D}_i^{28+}\sigma_{f,i}^{28} \qquad (4.110)$$

$$\mathrm{var}(\, Q_i^{02}) = \left\{\frac{\eta\,\phi_i}{\Delta t_i}\right\}^2 \sigma_{f,i}^{02+}\, \mathbf{D}_i^{02}\, \mathbf{V}_{i-1}^{02}\, \mathbf{D}_i^{02+}\sigma_{f,i}^{02} \qquad (4.111)$$

Substitute Eqs. (4.109), (4.110), and (4.111) into Eq. (4.106) to obtain the final expression for power density variance:

$$\begin{aligned}\mathrm{var}(\, Q_i) = \left\{\frac{\eta\,\phi_i}{\Delta t_i}\right\}^2 \Big[\, &\sigma_{f,i}^{28+}\, \mathbf{D}_i^{28}\, \mathbf{V}_{i-1}^{28}\, \mathbf{D}_i^{28+}\sigma_{f,i}^{28} + 2\,\sigma_{f,i}^{28+}\, \mathbf{D}_i^{28}\, \mathbf{X}_{i-1}^{28,02}\, \mathbf{D}_i^{02+}\sigma_{f,i}^{02} \\ &+ \sigma_{f,i}^{02+}\, \mathbf{D}_i^{02}\, \mathbf{V}_{i-1}^{02}\, \mathbf{D}_i^{02+}\sigma_{f,i}^{02}\Big] \qquad (4.112)\end{aligned}$$

Note that the variance of Q_i has two multiplicative components. The first is a scalar factor proportional to the squared neutron flux in the zone of interest. This factor implies large variances in high power regions of the core and small variances in low power regions, regardless of the state of the heavy metal covariance matrices. The second factor depends on the covariance and cross-covariance matrices of the heavy metal concentration vectors, and incorporates the effects of the random

pebble drop process. First-pass pebble populations always have zero power density variance due to this factor.

Now, suppose that FUPAR has analyzed the variance of power density in some region of the stationary core. Expected values and variances of Q are calculated for fuel populations from each pass which is present. Let the total number of different pass populations which are present be denoted N, and let each pass i have the Eulerian probability $\Pi_i = \alpha_i / N^*$. The set of N expectations/variances may be combined into a single pair of parameters which applies to the region. Such a reduction is necessary for the random hot-spot analysis of Section 4.14.

The first step is to hypothesize, for each sub-population i (associated with pass i) within the region of interest a cumulative probability distribution function, $F_{Q,i}$, and a probability density function, $f_{Q,i}$. The pass-dependent cumulative distribution functions are defined such that:

$$F_{Q,i}(Q_o) \equiv \mathbb{P}\left[\begin{array}{c}\text{an } i\text{'th pass pebble in} \\ \text{the region of interest has} \\ \text{power density } Q \leq Q_o\end{array}\right] \tag{4.113}$$

The pass-dependent probability density functions are defined in terms of the distribution functions:

$$f_{Q,i}(Q_o) \equiv \frac{d}{dQ_o} F_{Q,i}(Q_o) \tag{4.114}$$

The exact form of the $F_{Q,i}$ and $f_{Q,i}$ are unknown, but the expectation of each pass is known to be μ_i and the standard deviation for each pass is known to be σ_i^2. Thus, we may write the following expressions for each pass-dependent density function:

$$\int_{-\infty}^{\infty} Q_o \, f_{Q,i}(Q_o) \, dQ_o = E_i[\, Q_o] = \mu_i \qquad (4.115a)$$

$$\int_{-\infty}^{\infty} Q_o^2 \, f_{Q,i}(Q_o) \, dQ_o = E_i[\, Q_o^2] = \sigma_i^2 + \mu_i^2 \qquad (4.115b)$$

Let the *overall* distribution and density functions be denoted $F_Q(Q_o)$ and $f_Q(Q_o)$, respectively. These functions quantify the uncertainty associated with the experiment of drawing pebbles at random from the zone of interest without regard to how many passes they have been in the core. The overall cumulative distribution function gives the probability that *any* pebble drawn at random has a power density less than the function value. There are clearly two probabilities involved: the first is the probability that a pebble drawn at random will be from some particular pass i, and the second is the probability that the pebble has burnup less than some value, given that it is on its i'th pass. This conditional probability has, in fact, already been defined as the $F_{Q,i}$:

$$\mathbb{P}\left[\begin{array}{l} \text{a pebble has power} \\ \text{density } Q \leq Q_o \end{array} \;\middle|\; \begin{array}{l} \text{the pebble is on} \\ \text{its } i\text{'th pass} \end{array} \right] = F_{Q,i}(Q_o) \qquad (4.116)$$

The first probability, that a randomly selected pebble comes from the i'th pass, is simply the E-probability for that pass (see section 3.3):

$$\mathbb{P}\left[\begin{array}{l} \text{a randomly selected} \\ \text{pebble is on pass } i \end{array} \right] = \Pi_i = \alpha_i / N^* \qquad (4.117)$$

Now, the event that a randomly selected pebble is on its i'th pass is clearly exclusive of any other such event (the pebble can only be on one pass at a time) Thus, the probability that a random pebble has power density less than some value Q_o is simply the sum of the

probabilities that i'th-pass pebbles have power density less than Q_o:

$$\mathbb{P}\left[\begin{array}{c}\text{a random pebble has}\\ \text{power density } Q \le Q_o\end{array}\right] = \sum_{i=1}^{N} \mathbb{P}\left[\begin{array}{c}\text{a pebble is}\\ \text{on pass } i\end{array}\right] \times \mathbb{P}\left[Q \le Q_o \,\middle|\, \begin{array}{c}\text{the pebble is}\\ \text{on pass } i\end{array}\right]$$

Eqs. (4.116) and (4.117) may be used to write this relation in terms of the overall and pass-dependent cumulative distribution functions:

$$F_Q(Q_o) = \sum_{i=1}^{N} \Pi_i \, F_{Q,i}(Q_o)$$

Differentiation with respect to Q_o yields the overall probability density function:

$$f_Q(Q_o) = \frac{d}{dQ_o} F_Q(Q_o) = \sum_{i=1}^{N} \Pi_i \frac{d}{dQ_o} F_{Q,i}(Q_o) = \sum_{i=1}^{N} \Pi_i \, f_{Q,i}(Q_o) \quad (4.118)$$

Thus, the overall distribution and density functions are simply the population-weighted sums of the pass-dependent functions. This makes intuitive sense, and is illustrated in Fig. (4.9).

Equations (4.115a) and (4.115b) may be used to derive expressions for the overall mean and variance of the power density. The overall mean is obtained by substituting Eq. (4.118) into the definition of the overall expectation:

$$\mu_Q \equiv \int_{-\infty}^{\infty} Q_o \, f_Q(Q_o) \, dQ_o = \int_{-\infty}^{\infty} Q_o \sum_{i=1}^{N} \Pi_i \, f_{Q,i}(Q_o) \, dQ_o$$

$$= \sum_{i=1}^{N} \Pi_i \int_{-\infty}^{\infty} Q_o \, f_{Q,i}(Q_o) \, dQ_o = \sum_{i=1}^{N} \Pi_i \, \mu_i \quad (4.119)$$

where Eq. (4.115) is used to eliminate the integral. As might have been expected, the overall mean is simply the population-weighted sum of

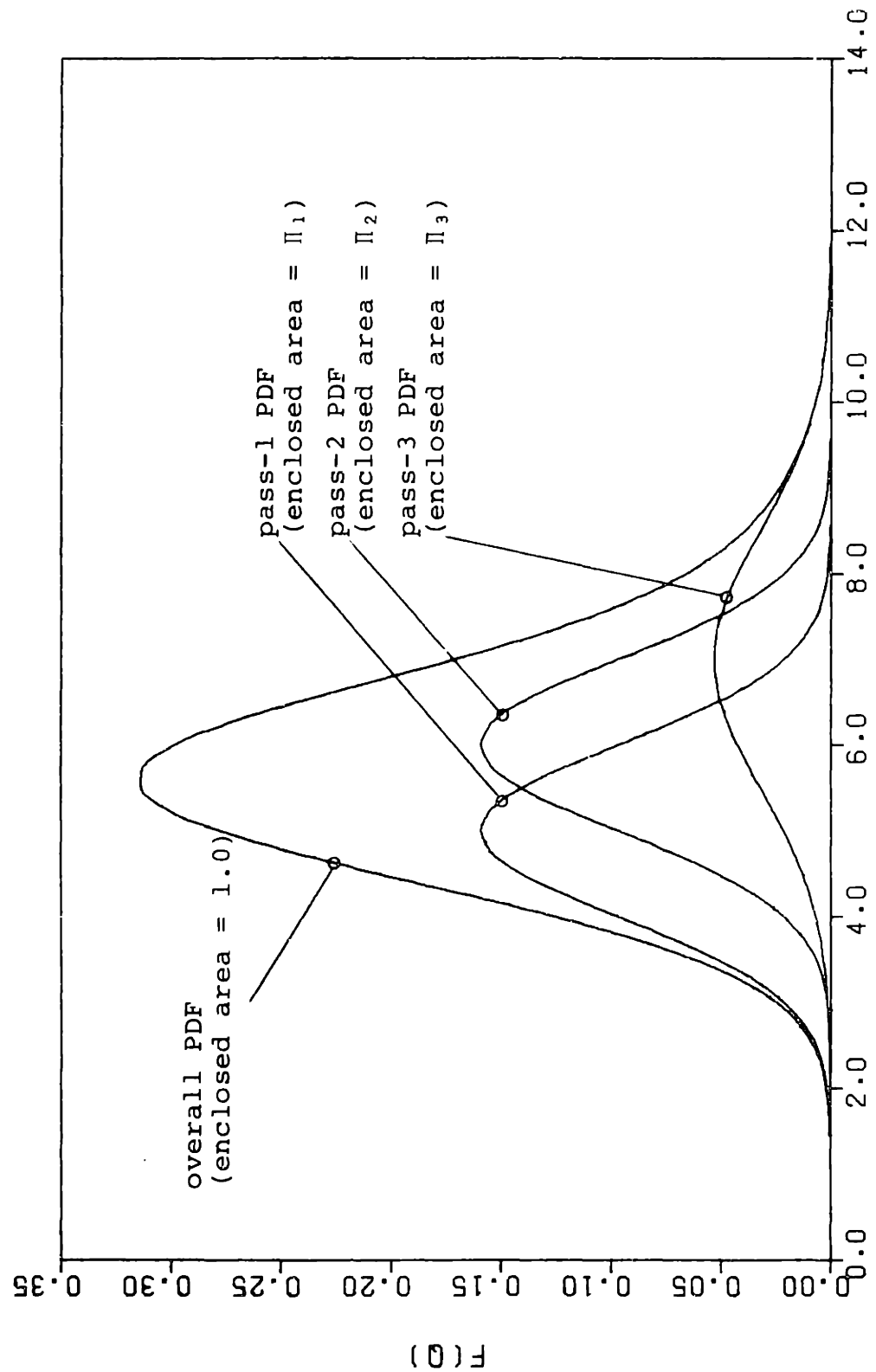

FIG. 4.9: Example of overall and pass-dependent probability density functions.

the pass-dependent means. To derive an expression for σ_Q^2, the overall variance, begin with the overall second moment, which is equal to $\sigma_Q^2 + \mu_Q^2$:

$$\sigma_Q^2 + \mu_Q^2 = \int_{-\infty}^{\infty} Q_o^2 \, f_Q(Q_o) \, dQ_o = \int_{-\infty}^{\infty} Q_o^2 \sum_{i=1}^{N} \Pi_i \, f_{Q,i}(Q_o) \, dQ_o$$

$$= \sum_{i=1}^{N} \Pi_i \int_{-\infty}^{\infty} Q_o^2 \, f_{Q,i}(Q_o) \, dQ_o = \sum_{i=1}^{N} \Pi_i \, (\sigma_i^2 + \mu_i^2) \qquad (4.120)$$

Rearrange Eq. (4.120) to obtain the final expression for the overall variance:

$$\sigma_Q^2 = \sum_{i=1}^{N} \Pi_i \, (\sigma_i^2 + \mu_i^2) - \mu_Q^2 \qquad (4.121)$$

Given the pass dependent Eulerian means and variances for the power density, Eqs. (4.120) and (4.121) allow computation of the zone's overall mean and variance. The development of the overall zone parameters σ_Q^2 and μ_Q depended in no way on the power density itself. The procedure is equally valid for any other quantity of interest.

Finally, note that Eq. (4.121) may be rearranged to "partition" the power density variance into two parts: one due to the change in mean power density with increasing pass number, and the other due to the actual spread of power density values around the pass means. The expression is:

$$\sigma_Q^2 = \underbrace{\left\{ \sum_{i=1}^{N} \Pi_i \, \mu_i^2 - \mu_Q^2 \right\}}_{\text{variance of the means}} + \underbrace{\sum_{i=1}^{N} \Pi_i \, \sigma_i^2}_{\text{mean variance}} \qquad (4.122)$$

The term in brackets ("variance of the means") is the contribution to the overall power density variance due to the variation in pass dependent mean power density μ_i. The second term is the contribution to overall variance due to the variance of pass dependent power density about the pass dependent means.

It is interesting that the ratio of the partitioned variances in the above equation:

$$R \equiv \frac{\sum_{i=1}^{N} \Pi_i \mu_i^2 - \mu_Q^2}{\sum_{i=1}^{N} \Pi_i \sigma_i^2} \qquad (4.123)$$

does not depend on the local neutron flux (it cancels in the numerator and the denominator). This ratio has important implications regarding the validity of the quasi-two dimensional approximation. If the ratio R is large, then the within-pass variance of the power density is much less than the pass-to-pass variance. In this case, we expect that the expected value for some parameter over all pass-i fuel is fairly representative of the values held by all pass-i fuel, and the quasi-2D approximation is a good one. If R is small, on the other hand, the within-pass variance outweighs the pass-to-pass variance, and the quasi-2D approximation is not reasonable.

An analysis of the 200 MWth KWU/Interatom HTR-MODUL (see sections 4.13 and 5.1) has yielded values for the between-pass and within-pass power density variances in the core's highest power density zone. Figure 4. 10 is a plot of the pass dependent expected power densities,

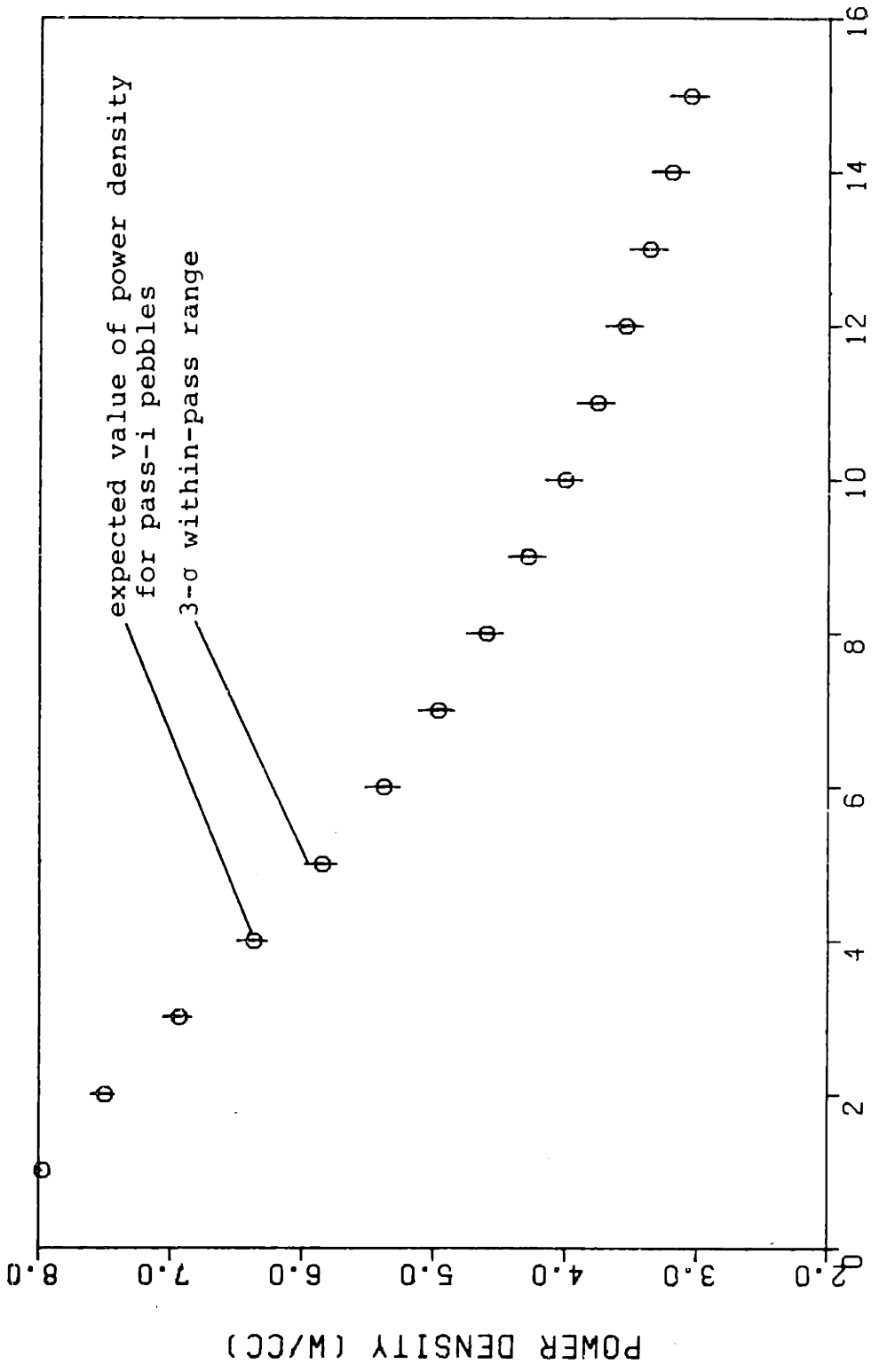

FIG. 4.10: Expected values and three-standard deviation ranges for power density as a function of pass number.

with the within-pass variances displayed as a three-standard deviation range about the pass mean. The values of partitioned variances and their ratio are:

$$\left.\begin{aligned} \sum_{i=1}^{N} \Pi_i \mu_i^2 - \mu_Q^2 &= 2.442\ (W/cm^3)^2 \\ \sum_{i=1}^{N} \Pi_i \sigma_i^2 &= 0.583\times10^{-2}\ (W/cm^3)^2 \end{aligned}\right\} \Longrightarrow R = 418.4$$

Thus, this analysis indicates that the quasi-two dimensional approximation is reasonable for the core under consideration.

4.11: THE FUPAR COMPUTER CODE

The FUPAR computer code (for FUel PARticle) performs the calculations described in the preceding sections. The code is written in Fortran 77 (actually IBM's VMS-FORTRAN) and runs on an IBM-3088 mainframe computer. Its primary purposes are:

A) to be used in conjunction with VSOP (see section 4.12) to compute fuel parameter distributions in stationary pebble bed reactors; and

B) to save data for further analysis, such as for use in the PDIF code (see chapter 6).

4.11.1 Data Requirements

The detailed input format for FUPAR is presented in Appendix C. Here we shall simply review the physical quantities which must be known to perform FUPAR's calculations. A summary list is presented in Table 4.1.

The first group of parameters (heavy metal per pebble, reactor thermal power) is used to normalize integral core parameters, such as the total number of pebbles in the core, or the fresh fuel injection rate. Table 4.2 lists the fission product and heavy metal isotopes currently in use in FUPAR (the current list corresponds to VSOP's maximum fission product chain). The maximum number of fission products which may be included is 43, and two chains of 6 heavy metal isotopes each are permitted. The core may be divided into a maximum of 18 axial and 5 radial zones. Arbitrary dimensions of these zones are input as well.

TABLE 4.1: FUPAR INPUT QUANTITIES

DESCRIPTION OF PARAMETERS	REQUIRED INPUT QUANTITIES
Integral core parameters	grams heavy metal per pebble reactor thermal power cutoff burnup for fuel discharge
Problem dimensions	number of heavy metals number of fission products
Core geometry	number of axial zones and zone spacing number of radial zones and zone spacing core collapsing parameters
Heavy metal nuclear data	1-group absorption cross sections (U & Th) 1-group fission cross sections (U & Th) (all are functions of r,z) decay constants initial densities in fresh fuel
Fission product nuclear data	1-group absorption cross sections decay constatns branching ratios chain structure any initial densities in fresh fuel non-depleting densities
Distributed core properties	1-group neutron flux (r,z) fast neutron flux & temperature (r,z) fuel flow velocities (r) core void fractions (r)

TABLE 4.2: FUPAR ISOTOPES

U-238 CHAIN	TH-232 CHAIN	FISSION PRODUCTS	
U-238	Th-232	Kr-83	Pr-143
Np-239	Pa-233	Zr-95	Nd-143
Pu-239	U-233	Mo-95	Nd-144
Pu-240	U-234	Mo-97	Nd-145
Pu-241	U-235	Tc-99	Nd-146
Pu-242	U-236	Ru-101	Pm-147
		Ru-103	Sm-147
		Rh-103	Pm-148m
		Rh-105	Sm-148
		Pd-105	Pm-148g
		Pd-108	Sm-149
		Ag-109	Sm-150
		Cd-113	Sm-151
		I-131	Sm-152
		Xe-131	Eu-153
		Xe-133	Eu-154
		Cs-133	Eu-155
		Cs-134	Gd-155
		Xe-136	Gd-156
		Pr-141	Gd-157

Decay constants and one-group fission and absorption cross sections for the U-238 and Th-232 heavy metal chains are required. Due to significant temperature effects, these parameters must be known as functions of position in the core (this data is supplied automatically if VSOP is used to provide nuclear data). Also, the initial heavy metal number densities in fresh fuel is required. All densities which are input, as well as those calculated in the code, are to be homogenized with an assumed void fraction $\alpha = 0.39$:

$$n_{homog.} = n_{peb.}\left\{ \frac{V_{peb.}}{V_{peb.} + V_{void}} \right\} = (1 - \alpha) n_{peb.} \qquad (4.122)$$

where $n_{peb.}$ = the local HM number density within the pebble;

$n_{homog.}$ = homogenized HM number density (to be input);

$V_{peb.}$ = volume of a pebble; and

V_{void} = void volume associated with a single pebble within the core.

The void fraction α must be input as a function of radial position, to be used in the drop probability calculation only. One group neutron fluxes as a function of r and z are also required (also automaticaly provided by VSOP). The code accepts fast neutron flux and fuel temperature inputs as well, though at the present time no calculations are performed which require these numbers.

Nuclear properties of all fission products are also required: decay constants, neutron absorption cross sections, fission yields, and branching ratios. If desired, some fission products may be given non-zero initial densities in fresh fuel (to simulate gadolinium

burnable poison, for example). Finally, the densities of several non-depleting nuclides is also required (e.g., carbon and oxygen) to be saved as input to VSOP.

4.11.2. Calculations

A flowchart detailing the sequence of calculations in FUPAR is presented in Figure 4.11. Once FUPAR has read in all necessary input data, the first task is to calculate the H heavy metal coefficient matrices according to Eq. (4.1). Since the temperature in an HTGR varies quite drastically from core top to bottom (coolant temperature increases 500C) it is important to include the effects of heavy metal cross section variation with position. Thus, for every core zone, the coefficient matrices differ not only in neutron flux level but also in basic nuclear parameters. This input is automatically provided by VSOP when the two codes are run in conjunction.

Next, FUPAR calculates transition matrices for each core zone: a T and a D matrix for each heavy metal chain. The calculations are iterative, based on the infinite series definition of the matrix exponential:

$$\exp(\mathbf{A}t) \equiv \sum_{k=0}^{\infty} (1/k!)\,(\mathbf{A}t)^k \qquad (4.1)$$

A finite number K of the terms in the above series is evaluated, at which point the maximum error in the approximate matrix is known to be less than some pre-defined error level. Details of this procedure are explained in Appendix A.

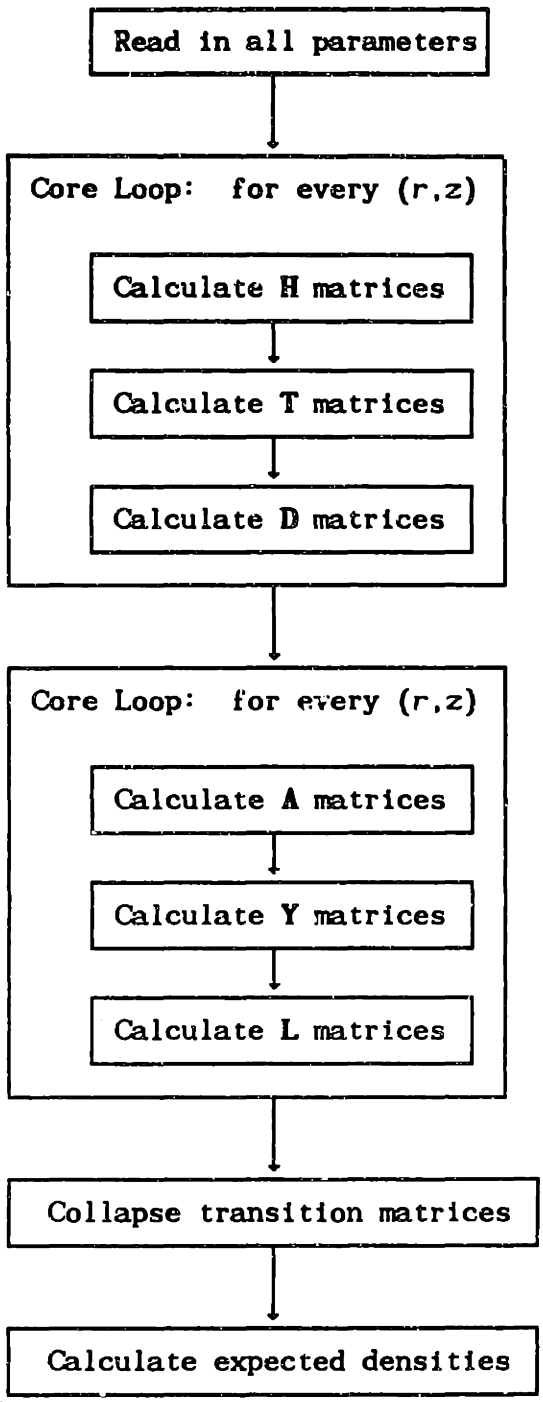

FIG. 4.11: Sequence of calculations in FUPAR.

Calculation of the **D** matrices according to Eq. (4.20) requires only the inversion of the 6x6 **H** matrices. This is a simple calculation due to the triangular arrangement of **H**.

Next, FUPAR calculates the **A** and **Y** coefficient matrices for the fission product equations in each core zone (see Eqs. (4.29) and (4.30)). **L** fission product transition matrices are then calculated. The same basic algorithm as for the **T** matrices is employed, but to reduce computational time and storage requirements, the chain of fission products is split into independent subchains, as illustrated in Figure 4.12. Since many of the sub-chains are of length 1 or 2, the associated matrix exponentials are calculated directly from:

$$\mathbf{A} = [a] \quad \Longrightarrow \quad \exp[\mathbf{A}t] = \exp[at] \tag{4.123}$$

$$\mathbf{A} = \begin{bmatrix} a & 0 \\ c & d \end{bmatrix} \quad \Longrightarrow \quad \exp[\mathbf{A}t] = \begin{bmatrix} e^{at} & 0 \\ \frac{c}{a-d}\left\{e^{at} - e^{dt}\right\} & e^{dt} \end{bmatrix} \tag{4.124}$$

For sub-chains of length 3 or more, the iterative procedure is used. In the standard VSOP fission product chain of total length 43, the largest sub-chain which must be evaluated has a length of 20 isotopes.

After the **L** matrix has been calculated for each zone, the **J** source matrix is calculated via the approximate formula (4.43). The only new calculation necessary for this step is the inversion of the 43x43 (max.) **A** matrix. As before, the triangular nature of **A** simplifies this step considerably. In addition, this calculation also takes advantage of the discrete sub-chain structure of **A**. For chains of length 1 or 2, the

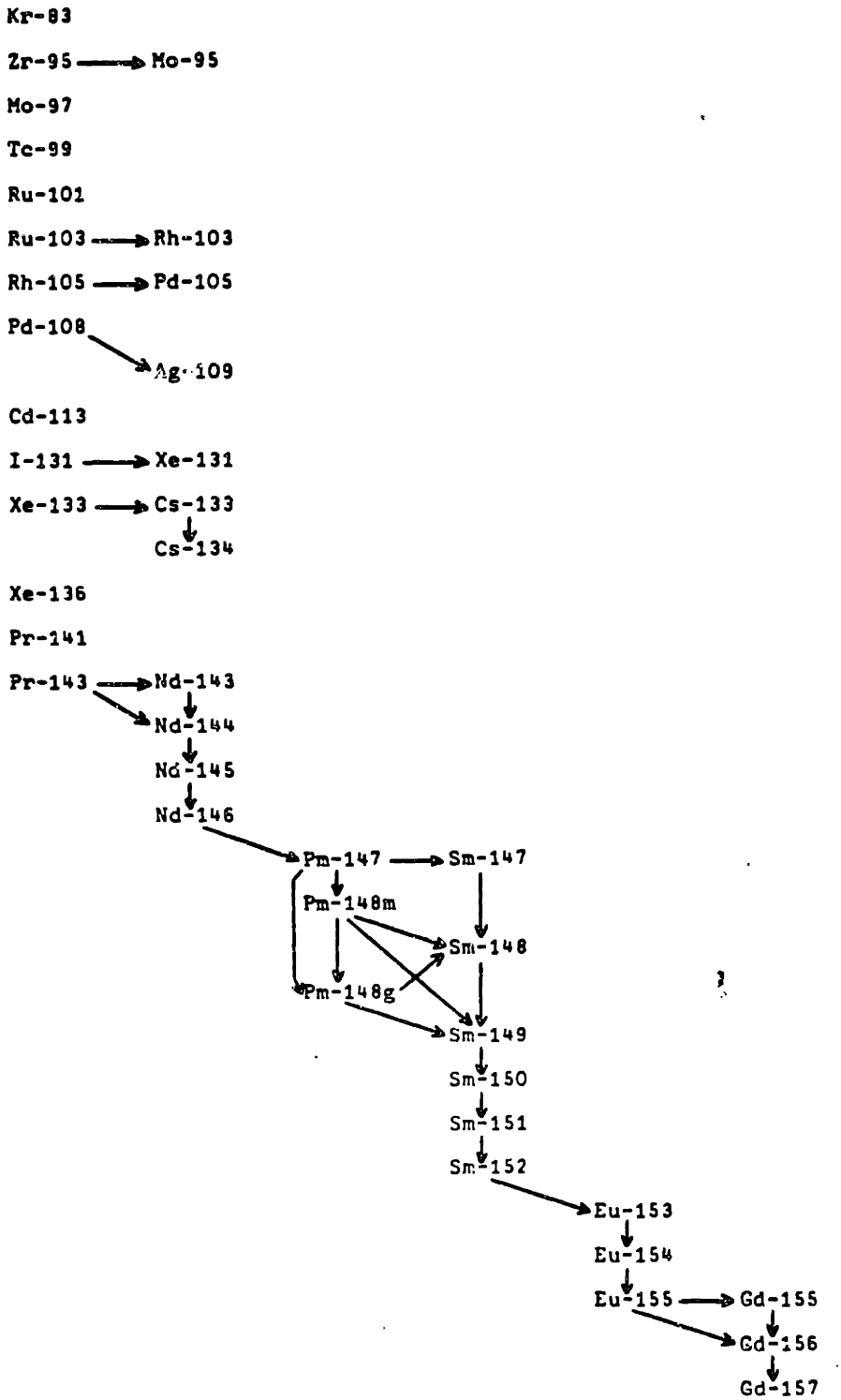

FIG. 4.12: Fission product chain structure in FUPAR.

code uses:

$$\mathbf{A} = [a] \quad \Longrightarrow \quad \mathbf{A}^{-1} = 1/a \tag{4.125}$$

$$\mathbf{A} = \begin{bmatrix} a & 0 \\ c & d \end{bmatrix} \quad \Longrightarrow \quad \mathbf{A}^{-1} = \begin{bmatrix} 1/a & 0 \\ -c/ad & 1/d \end{bmatrix} \tag{4.126}$$

Once the T, L, and D matrices have been calculated for all core regions, the code performs axial zone-collapsing operations. The user currently has the option of collapsing the core into an arbitrarily defined set of composite regions (see Appendix C). However, if the program is to be used to calculate the expected materials concentrations, it must be instructed to completely collapse the core (i.e., so that no axial sub-divisions remain). The equations used to collapse the various transition matrices are (4.13), (4.24), and (4.48).

Calculations of expected values of materials densities in each zone proceed using the quasi 2-dimensional (Q2D) approximation. This procedure is based on techniques outlined in section (3.5). Only the L-expectation values of the HM and FP density vectors are used at the beginning of each pass. These expectations take into account the discharge of fuel from the previous pass, in a manner to be explained. The burnup accumulated by this "quasi-fuel" in each of the N collapsed radial zones is determined as follows:

$$F_{w,i} = \bar{F}_{w-1} + \mathbf{A}_i^{+} \bar{\mathbf{n}}_{w-1} \tag{4.127}$$

where $F_{w,i}$ = the Q2D burnup for fuel leaving radial region i;

$\bar{F}_{w-1}$ = L-expectation burnup for all fuel entering pass w;

$\mathbf{A}_i^{+}$ = the collapsed burnup transition matrix for drop zone i;

$\bar{\mathbf{n}}_{w-1}$ = L-expectation HM density vector entering pass w.

FUPAR assumes that all fuel leaving zone i after pass w is discharged if $F_{w,i}$ is greater than the cutoff value for discharge, denoted F_{dis}. In this case, the Q2D indicator function becomes:

$$\mathcal{P}_d'(w,i) \equiv \begin{cases} 0 & \text{if } F_{w,i} > F_{dis}; \\ 1 & \text{otherwise.} \end{cases} \tag{4.128}$$

The Q2D δ_w probability is then:

$$\delta_w = \mathbb{P}\left[\begin{array}{c}\text{a fuel element is}\\ \text{discharged follow-}\\ \text{ing pass } w\end{array} \middle| \begin{array}{c}\text{it was not dis-}\\ \text{charged follow-}\\ \text{ing pass } w\text{-}1\end{array}\right] \simeq \sum_i p_i \; \mathcal{P}_d'(w,i) \tag{4.129}$$

The Q2D expected value is computed by:

$$\bar{F}_w = \frac{1}{\delta_w} \sum_i p_i \; \mathcal{P}_d'(w,i) \; F_{w,i} \tag{4.130}$$

Likewise, the Q2D expectation for *any* fuel property is:

$$\bar{\xi}_w = \frac{1}{\delta_w} \sum_i p_i \; \mathcal{P}_d'(w,i) \; \xi_{w,i} \tag{4.131}$$

where $\xi_{w,i} = \bar{\xi}_{w-} + \mathbb{M}_i(\xi) \; \bar{\mathbf{d}}_{w-1}$, ξ representing a general property of the fuel, $\mathbf{d}$ the materials density vector(s) which determine ξ, and $\mathbb{M}$ the transition matrix which yields ξ.

The value of α_w is approximated by:

$$\alpha_w \equiv k_w/K_f \simeq \prod_{i=1}^{w} \delta_i \tag{4.132}$$

FUPAR begins with fresh fuel, and calculates fuel states for each pass in succession. Since the α's for each pass w are known before the densities are calculated, the Eulerian expectations of the HM and FP density vectors are tallied as follows:

$$E_e[\,\mathbf{n}\,] = \sum_{w=1}^{N_{max}} \Pi_w \bar{\mathbf{n}}_w = (1/N^*) \sum_{w=1}^{N_{max}} \alpha_w \bar{\mathbf{n}}_w \qquad (4.133)$$

Once all fuel is discharged, FUPAR calculates the total core pebble population, mean discharge burnup, and fresh fuel injection rate.

4.11.3 FUPAR Results

The following parameters are output from FUPAR:

- E-expectation heavy metal densities;
- E-expectation fission product densities;
- burnup spectra for each core zone (i.e., the burnup value and associated E-probability for every pass pebble present in the zone); and
- total number of pebbles in the core, L-expected core residence time, and the L-expected number of passes per pebble.

All output may be stored in permanent data sets for retrieval and use at a later time.

4.12 ESTIMATING THE PARAMETERS OF A STATIONARY PEBBLE BED REACTOR

As implied in the previous section, the VSOP computer code system (see ref. T1) has been modified to produce output which is suitable to serve as FUPAR input. Appendix B contains a summary of VSOP's component programs and the calculations which they perform. The following parameters may be stored by VSOP for direct use in FUPAR:

- neutron flux (r,z);
- heavy metal cross sections (r,z); and
- fission product cross sections (r,z).

In addition, VSOP calculates the following parameters of interest:

- fuel temperatures (r,z) (using the TIK/LSD module); and
- k_{eff} for the reactor.

VSOP requires the reactor materials distribution (as well as fuel design parameters) as input. Thus an iterative scheme using both FUPAR and VSOP to provide the unknown parameters for each other seems reasonable. Such a system has been assembled, and is represented in flow-chart form in Figure 4.13. The procedure is:

1) Begin with an initial guess for the materials distribution within the steady state core. Such a distribution may come from a previous core analysis, or be synthesized by FUPAR using crude assumptions.

2) Run VSOP on the materials distribution to obtain an estimate of the neutron flux distribution, cross section distribution, reactor criticality, and perhaps the temperature distribution.

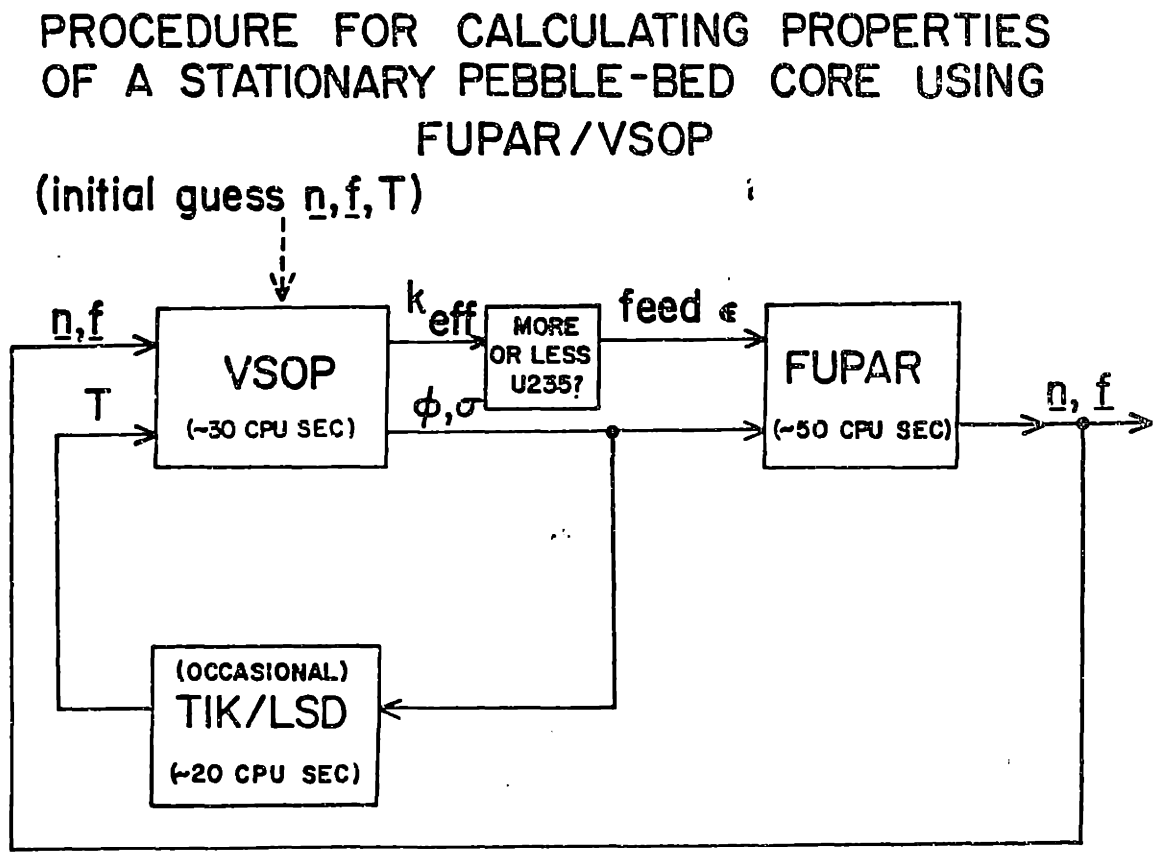

FIG. 4.13 : A simple iterative scheme for FUPAR/VSOP.

3) Based on the results of VSOP, alter the feed fuel enrichment and use FUPAR and the latest flux/cross section estimates to recalculate the reactor materials distribution. If all parameters are satisfactorily converged, then we are finished. Otherwise, return to step (2) to further refine our estimates.

The above procedure is conceptually simple, however in some cases (see the next section) a more complicated iterative scheme is necessary. The convergence of the procedure is, of course, dependent on how accurate the initial guess distributions are. For multi-pass cores, the flux and materials distributions have been found to converge rather rapidly, and a critical converged core may be obtained in less than ten iterations. Few-pass cores present special difficulties, and are addressed separately below. After some experience is gained, the number of iterations necessary for convergence should be quite reasonable (certainly less than 20, most probably approximately 10 per design). Chapter 5 reviews a number of case studies using FUPAR/VSOP to analyze MHTGR design variants.

Some Cautions

Future users should be aware of a potential instability in the FUPAR/VSOP iteration scheme. The problem arises when the core to be analyzed has only one or a few fuel passes before discharge. In these cases, fresh fuel may not traverse much of the length of the core before significant burnup and fission products have built up. The neutron flux shape will then be highly dependent on the axial rate of change of fresh

fuel reactivity.

The situation is illutrated in Figure 4.14. Burnup is used as a good single indicator of fuel reactivity (high burnup implies low reactivity). The Figure shows axial neutron flux and burnup distributions following FUPAR and VSOP in a proposed iterative calculation. Suppose that FUPAR is run on an initial-guess flux distribution, yielding some distribution of burnup with axial position (plot "A" in the Figure). However, this distribution is not exactly right, and for purposes of this example assume that the initial flux distribution was too heavily peaked toward the top of the core (z=0). If so, curve "A" rises too quickly (the fuel received too much exposure in the core top), causing the *bottom* of the core to have an unrealistically high burnup. Next, VSOP is run using the materials distribution indicated by curve A, producing the flux distribution shwon in curve B. Since burnup disribution A implied too little reactivity in the lower half of the core, curve B will be even more peaked towards the core top than even the initial guess. A FUPAR run on flux shape B will compound the problem even further, producing an even faster burnup rise in the core upper half, illustrated in curve C. This mechanism will eventually result in extremely unstable and unrealistic neutron flux distributions. In these cases, the simple interation scheme illustrated in Figure 4.13 is inadequate.

Four recommendations are made to alleviate this situation:

(1) Determination of a critical feed enrichment should be achived using only a single flux distribution, as k for the reactor is not very sensitive on the exact flux shape;

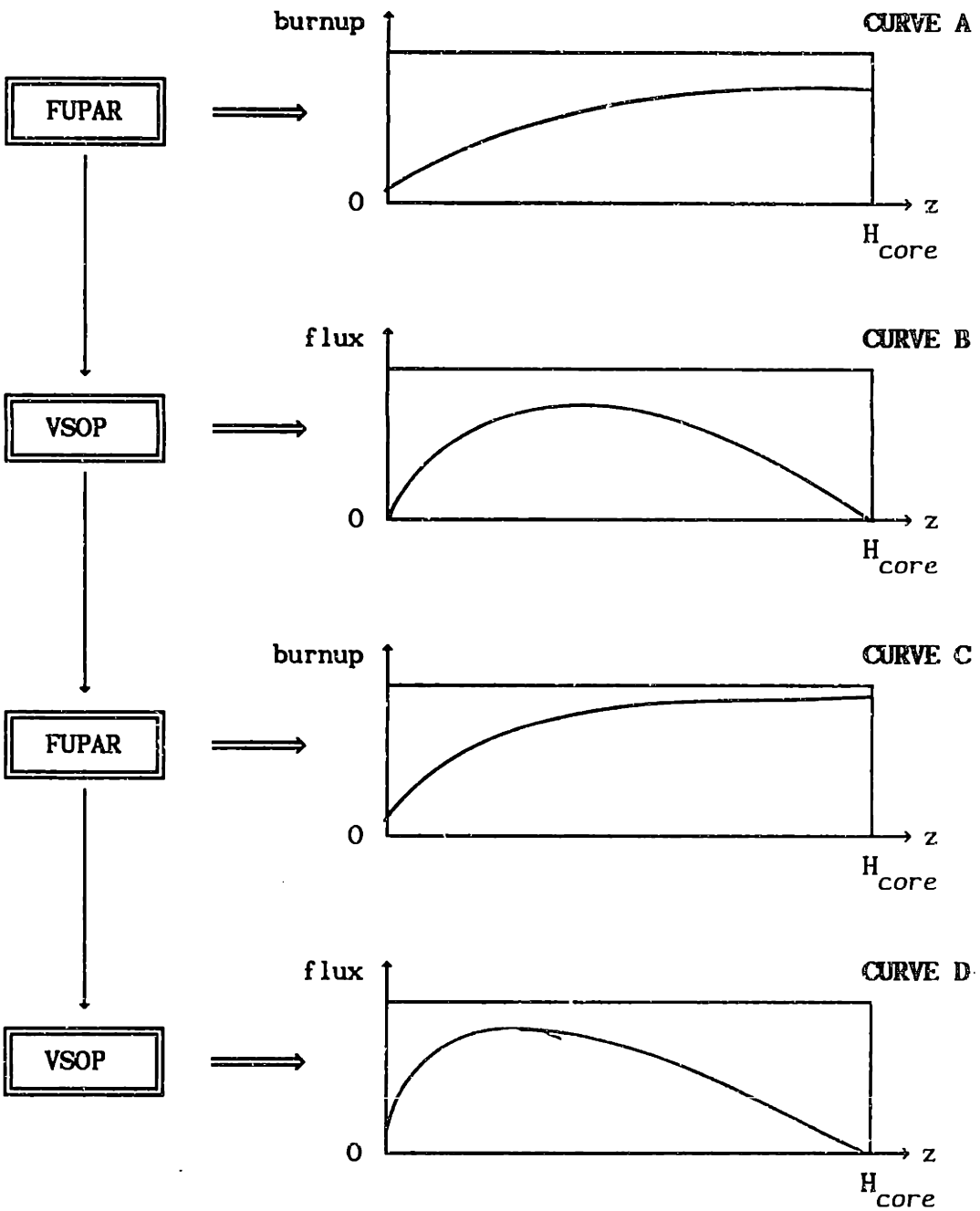

FIG. 4.14 : Potential instability using FUPAR/VSOP to analyze few-pass cores.

(2) The pebble cycling velocity can be used to dampen these oscillations once they are detected. For example, after VSOP has produced flux D in Figure (4.14), a proper user response would be to return to the second FUPAR step. This job should be re-run with an *increased* fuel velocity, which acts to more evenly distribute reactivity throughout the core.

(3) The user has the option of using a weighted average of two previously determined flux distributions. In this way, the flux can be forced into a more reasonable shape for the FUPAR calculation.

(4) The TIK/LSD module can be used to feedback temperature effects into the calculation. Since higher temperature fuel is less reactive, this will tend also to even out asymmetric reactivity distributions.

4.13: FUPAR VERIFICATION: ANALYSIS OF THE 200 MWth KWU HTR-MODUL

To verify that the FUPAR/VSOP method for pebble bed reactor analysis produces accurate results, a test case was performed for a well documented reactor design. The reactor selected is the same discussed in Section 1.3, Kraftwerk Union's 200MWth HTR-MODUL design. Table 4.3 presents some general design information.

FUPAR/VSOP was used to independently assess some of the major design features of the HTR-MODUL. The following parameters, identical to those for the KWU design, were used as inputs to the code system:

- reactor power = 200 MWth;
- fuel residence time = 1020 days;
- discharge burnup = 80,000 MWD/MTHM; and
- fuel loading = 7 g HM/pebble.

FUPAR/VSOP was used in a simple iterative mode, as was illustrated in Figure 4.13. When the calculations had converged, the following parameters were the result:

- number of fuel passes = 15;
- feed fuel enrichment = 7.8%;
- k_{eff} = 1.03; and
- number of pebbles in core = 360,000.

The above results match the design information presented in Table 4.3 quite closely. Thus, FUPAR/VSOP is comparable to those produced to the design methods currently in use by reactor designers in the Federal Republic of Germany.

TABLE 4.3: HTR-MODUL DESIGN PARAMETERS

Thermal power	200 MW
Core diameter	3.0 m
Mean core height	9.43 m
Average power density	3.0 MW/m^3
Average He temperature	250/700 C
Fuel cycle	U/Pu
Number of fuel elements	360,000
Number of passes	15
Enrichment	7.8
Heavy metal loading	7 g/pebble
Discharge burnup	80,000 MWD/MTHM

4.14 RANDOM HOT SPOTS AND TEMPERATURE PERTURBATIONS

It was shown in section 4.10 that calculations may be performed to determine statistical properties of the power density distribution in any region of a stationary pebble bed core. As in Section 3.7, the concern here is that a large enough group of reactive pebbles may randomly coalesce to cause a significant power density or temperature perturbation above the expected value in a region. In this section a procedure is developed to convert power density distribution parameters into temperature distribution parameters, which are more directly significant. First a method must be developed to estimate temperature differences based on power density perturbations, taking both convection and conduction heat transfer effects into account. Using the relation between power density and temperature, statements may be made regarding the probabilities of finding sub-volumes of pebbles at certain temperature levels. The effects of sub-volume size are explicitly included in these relations. Finally, results of this discussion are directly applicable to the "zero hot-spot" probabilities introduced in Section 3.7. It is concluded that the probability of a large region of the pebble bed operating at significantly higher powers or temperatures than expected is extremely small.

4.14.1 Relation Between Power Density and Temperature Perturbations

The first task is to relate a perturbation of power density above its expected value to a corresponding temperature perturbation. The physical system to be modeled is illustrated in Figure 4.15. The region of interest in the core has expected power density and temperature Q and

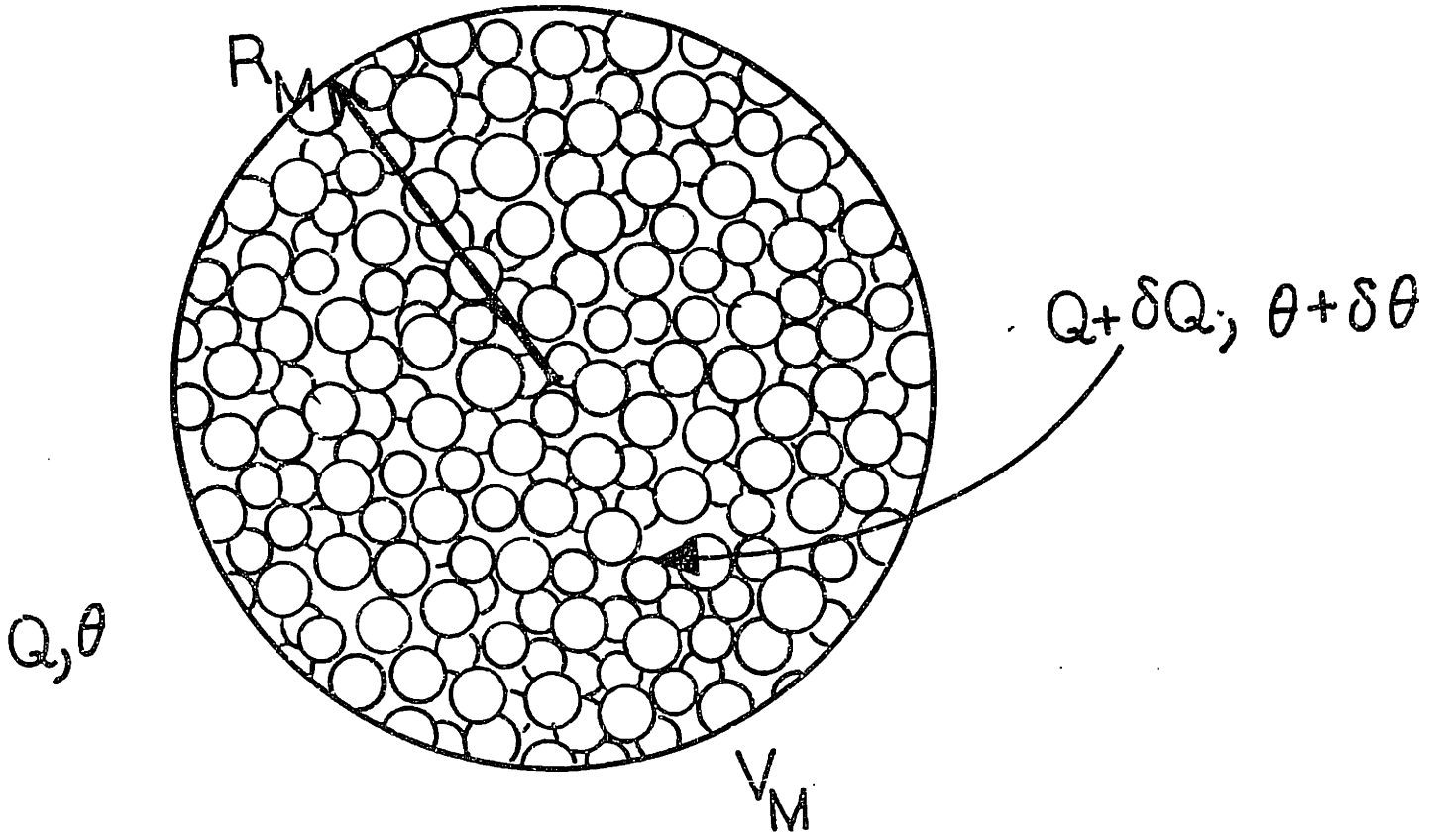

FIG. 4.15: A "hot spot" within a pebble bed reactor.

θ, respectively. The subvolume labelled V_m has power density $Q+\delta Q$ and temperature $\theta+\delta\theta$. Begin with the conservation of energy equation in the pebble bed, taking into account both conduction/radiation through the solid bed and convective heat transfer to the coolant:

$$k \nabla^2\theta - S U \theta = -Q \qquad (4.134)$$

where

k = effective thermal conductivity of the pebble bed, accounting for both conduction and radiation effects {W/cm K}. Correlations for k may be found in Ref. V.3;

$\theta = T - T_g$, where T = average fuel temperature in the pebble bed {K} and T_g = gas temperature in the zone of interest. T_g is assumed to be constant over the volumes of interest, so that $\nabla^2 T = \nabla^2\theta$;

S = heat transfer surface area per unit volume $\{cm^2/cm^3\}$;

U = overall heat transfer coefficient, relating the *average* pebble temperature to the gas temperature $\{W/cm^2K\}$;

Q = volumetric heat source $\{W/cm^3\}$, homogenized over pebble bed volume including voids.

The overall heat transfer coefficient U is used because the usual form of heat transfer coefficient relates heat flux to surface temperatures. Table 4.4 details the results of a simple heat transfer analysis of a fuel element, assuming uniform heat generation within the fueled region and temperature-independent thermal conductivity. The last line in the table is the analytic form of the overall heat transfer coefficient.

Note that Eq. (4.134) is additive in θ and Q. That is, $\delta\theta$ represents the increase in fuel temperature such that $(\theta+\delta\theta)$ is the

TABLE 4.4: TEMPERATURE DIFFERENCES WITHIN A FUEL ELEMENT

TEMPERATURE DIFFERENCE =	IN TERMS OF POWER DENSITY	IN TERMS OF TOTAL PEBBLE POWER
$\overline{T} - T(R_f)$	$\frac{Q R_f^2}{15 k (1-\alpha)}$	$\frac{(Q V_p)}{20\pi k R_f (1-\alpha)}$
$T(R_f) - T(R_u)$	$\frac{Q R_f^3}{3k(1-\alpha)}\left[\frac{1}{R_f} - \frac{1}{R_u}\right]$	$\frac{(QV_p)}{4\pi k(1-\alpha)}\left[\frac{1}{R_f} - \frac{1}{R_u}\right]$
$T(R_u) - T_g$	$\frac{Q R_f^3}{3 h R_u^2 (1-\alpha)}$	$\frac{(Q V_p)}{4\pi h R_u (1-\alpha)}$

OVERALL DIFFERENCE (AVERAGE - GAS TEMPERATURE):

$$\overline{T} - T_g = \frac{Q}{(1-\alpha)}\left\{\frac{R_f^2}{15 k} + \frac{R_f^3}{3 k}\left[\frac{1}{R_f} - \frac{1}{R_u}\right] + \frac{R_f^3}{3 h R_u^2}\right\}$$

OVERALL HEAT TRANSFER COEFFICIENT:

$$U = (1-\alpha)\left\{\frac{R_f^2}{15 k} + \frac{R_f^3}{3 k}\left[\frac{1}{R_f} - \frac{1}{R_u}\right] + \frac{R_f^3}{3 h R_u^2}\right\}^{-1}$$

(where h = the simple surface heat transfer coefficient;
k = thermal conductivity of pebble matrix graphite;
V_p = pebble volume;
R_f = radius of the inner fueled region of a pebble;
R_u = radius of the outer unfueled region of a pebble;
α = core void fraction;
Q = homogenized power density)

solution when the heat source is (Q+δQ):

$$k\,\nabla^2(\theta+\delta\theta) \;-\; S\,U\,(\theta+\delta\theta) \;=\; -\,(Q+\delta Q) \qquad (4.135)$$

The original solution, however, implies that $k\nabla^2\theta - SU\theta = -Q$. Thus, subtracting Eq. (4.134) from (4.135):

$$k\,\nabla^2\delta\theta \;-\; S\,U\,\delta\theta \;=\; -\delta Q \qquad (4.136)$$

Therfore, the incremental change in temperature distribution $\delta\theta$ may be calculated directly from δQ, independent of the original solution.

We are interested in the roughly spherical region in the pebble bed containing m pebbles, of radius r_m and volume V_m. The goal is to calculate the volume average temperature increase, $\overline{\delta\theta}$, due to an increase in the volume average power density $\overline{\delta Q}$. Since the exact heat source distribution is unknown, it would be pointless to attempt to calculate the temperature change in any more detail. The first step is to integrate Eq. (4.136) over the volume V_m to obtain:

$$\int_{V_m} k\nabla^2\delta\theta\; dV \;-\; \int_{V_m} SU\;\delta\theta\; dV \;=\; \int_{V_m} \delta Q\; dV \qquad (4.137)$$

Assume that the heat transfer parameters k and U are approximately constant over the (relatively) small volume V_m. In this case, Eq. (4.137) may be simplified:

$$k\int_{V_m} \nabla^2\delta\theta\; dV \;-\; S\,U\,V_m\,\overline{\delta\theta} \;=\; -V_m\overline{\delta Q} \qquad (4.138)$$

where $\overline{\delta\theta}$ represents the the parameter of interest--the volume average temperature increase due to δQ:

$$\overline{\delta\theta} \;\equiv\; \frac{1}{V_m}\int_{V_m} \delta\theta\; dV$$

and $\overline{\delta Q}$ is the volume-averaged power density perturbation:

$$\overline{\delta Q} \equiv \frac{1}{V_m} \int_{V_m} \delta Q \, dV$$

The remaining integral in Eq. (4.138) may be written in terms of $\overline{\delta\theta}$ using the divergence theorem:

$$\int_{V_m} \nabla^2 \delta\theta \, dV = \oint_{\sigma_m} \nabla(\delta\theta) \cdot d\sigma = A_m \nabla(\delta\theta)\Big|_{r_m} \tag{4.139}$$

where σ_m represents the surface surrounding the volume of interest, and $A_m = 4\pi r_m^2$. $\nabla(\delta\theta)\Big|_{r_m}$ is the gradient of the incremental distribution $\delta\theta$ evaluated at the outer radius r_m of our volume V_m. Approximate this gradient as follows:

$$\nabla(\delta\theta)\Big|_{r_m} \approx \frac{\delta\theta\Big|_{r_m} - \overline{\delta\theta}}{f \, r_m} \tag{4.140}$$

where

$\delta\theta\Big|_{r_m}$ = incremental temperature difference at $r = r_m$;

f = some constant, equal to 1.2 when there are no convection effects and δQ is uniformly distributed over V_m. Assume for now that $f \approx 1.0$ when convection is present.

Once again, the exact value of the "f" factor is not very important, as the exact heat source distribution is unknown. A more detailed analysis of the temperature distribution assuming a uniform incremental heat source (see the end of this section) and zero heat transfer to coolant yields the value f = 1.2. (The analysis does not assume $\delta T=0$ at the sub-volume boundary). As convective effects tend to flatten the distribution and thus steepen the gradient at the volume boundary, a somewhat smaller value should be assumed for f in this case.

Since the incremental heat source δQ is zero outside the volume V_m, and convection effects tend to dominate during operation, adopt the following approximate boundary condition:

$$\delta\theta\Big|_{r_m} = 0$$

Thus, the gradient approximation (4.140) simplifies to:

$$\nabla(\delta\theta)\Big|_{r_m} \approx - \frac{\overline{\delta\theta}}{f\, r_m} \tag{4.141}$$

which is exactly true for f=1.2 and U=0, and approximately true when convection effects dominate and f≈1.0. Substitute Eq. (4.141) into (4.139) and obtain:

$$-A_m k \frac{\overline{\delta\theta}}{f r_m} - S\, U\, V_m \overline{\delta\theta} = -V_m \overline{\delta Q} \tag{4.142}$$

Rearrange Eq. (4.142) to express $\overline{\delta Q}$ as a function of $\overline{\delta\theta}$:

$$\overline{\delta Q} = \left\{ \frac{A_m\, k}{f\, V_m\, r_m} + S\, U \right\} \overline{\delta\theta} \tag{4.143}$$

The final step is to introduce m, the number of pebbles in the sub-volume, into Eq. (4.143). Let α denote the void fraction in the pebble bed and r_p the radius of a single pebble. Note the following geometrical relations:

$$V_m = (4\pi/3)\, r_m^3 = \frac{m\, (4\pi/3)\, r_p^3}{(1-\alpha)};$$

$$\text{thus} \quad r_m = r_p (1-\alpha)^{1/3} m^{1/3} \tag{4.144a};$$

$$A_m/V_m = \frac{4\pi\, r_m^2}{(4\pi/3)\, r_m^3} = \frac{3}{r_p} (1-\alpha)^{1/3} m^{-1/3} \tag{4.144b};$$

$$S = \frac{4\pi\, r_p^2}{(4\pi/3)\, r_p^3 /(1-\alpha)} = \frac{3\,(1-\alpha)}{r_p} \tag{4.144c}.$$

Substitute these equations into Eq. (4.143) and obtain:

$$\overline{\delta Q} = \left\{ \left[\frac{3(1-\alpha)^{2/3}}{f\ r_p^2} \right] k\ m^{-2/3} + \left[\frac{3\ (1-\alpha)}{r_p} \right] U \right\} \overline{\delta\theta} \qquad (4.145)$$

Thus, the importance of the number of pebbles m in determining the magnitude of the temperature increase due to a power density abberation depends on the relative magnitude of the conductive and convective thermal resistances.

4.14.2 Effects on Hot Spot Probabilities

FUPAR yields information regarding the E-distributions of power densities. That is, if an experiment is performed which consists of selecting pebbles at random from the zone of interest, we are able to calculate the following properties of the population from which they are drawn:

A) the overall expected value of power density, μ_Q; and

B) the overall variance of power density, σ_Q^2.

Of interest is the possibility of m pebbles coalescing at random to form a sub-region with an overall power density greater than μ_Q. Since the pebbles in this zone have arrived at random, each has an independent E distribution. The average power density in the sub-zone will be:

$$\bar{Q} = \frac{1}{m} \sum_{i=1}^{m} Q_i \qquad (4.146)$$

where Q_i is the power density of the i'th pebble. Each Q_i is an independent random variable, with a probability density function and a mean and variance as calculated in section 4.10. (Note the change in notation from Section 4.10: the subscript i no longer indicates the

number of passes a pebble has been recirculated; it is simply a counting index). The variance of the observed mean power density is a function of the variance of the Q_i:

$$\text{var}(\,\bar{Q}\,) = \text{var}\left[\,\frac{1}{m}\sum_{i=1}^{m} Q_i\,\right] = \frac{1}{m^2}\sum_{i=1}^{m}\text{var}(\,Q_i) = \frac{1}{m^2}\, m\,\sigma_Q^2 = \frac{\sigma_Q^2}{m} \qquad (4.147)$$

According to the central limit theorem (see refs. C2 and D2) the probability distribution of a sum of independent random variables tends towards a normal distribution as the number of summed variables grows larger. In fact, this is quite a good approximation once the quantity of pebbles in the sub-volume reaches numbers of interest ($m > 20$, at least). Thus, to a good approximation, the quantity $\bar{Q}$ is distributed as a normal random variable with mean μ_Q and variance σ_Q^2/m:

$$\bar{Q} \sim N(\,\mu_Q,\, \sigma_Q^2/m) \qquad (4.148)$$

where the symbol "~" means "is distributed as," and "$N(\mu,\sigma^2)$" represents a normal random variable with mean μ and variance σ^2. Eq. (4.1) may be manipulated to form a standard normal random variable:

$$\frac{\bar{Q} - \mu_Q}{\sigma_Q/\sqrt{m}} \sim N(0,1) \qquad (4.149)$$

The numerator on the left-hand side of Eq. (4.149), $\bar{Q} - \mu_Q$, is identical to the $\overline{\delta Q}$ parameter from the previous discussion. That is, $\overline{\delta Q}$ is nothing more than the incremental surplus power density in V_m above the expected value. Therefore, based on Eq. (4.149), a standard normal variable may be expressed in terms of $\overline{\delta Q}$:

$$\frac{\overline{\delta Q}}{\sigma_Q/\sqrt{m}} \sim N(0,1) \qquad (4.150)$$

Given that the left-hand side of the above equation is distributed as a standard normal random variable, it is possible to find in tables a number Z_α, such that:

$$\mathbb{P}\left[\frac{\overline{\delta Q}}{\sigma_Q/\sqrt{m}} \geq Z_\alpha \right] = \alpha \qquad (4.151)$$

where $\mathbb{P}[x]$ represents the probability of event x. Z_α is simply the value above which a standard normal random variable has probability "α" of occuring. Figure 4.16 illustrates the location of Z_α in relation to a standard normal probability density function. Eq. (4.151) may be rearranged to directly express the probability that $\overline{\delta Q}$ exceeds some value:

$$\mathbb{P}\left[\overline{\delta Q} \geq \frac{\sigma_Q Z_\alpha}{\sqrt{m}} \right] = \alpha \qquad (4.152)$$

σ_Q, the power density standard deviation, is a fixed property of the reactor design. It serves to convert the standard normal value Z_α into a power density value. At a fixed probability level α, the parameter Z_α is fixed as well by the properties of the standard normal distribution. Thus, if the sub-volume size m is increased, the excess power level which can arise at the same probability level decreases as $1/\sqrt{m}$. For example, if 10 pebbles may arise with over-power $\overline{\delta Q}_1$ at probability α, 40 pebbles can only attain $\overline{\delta Q}_1/2$ at the same probability.

The hot spot "severity" for m pebbles at probability level α is defined as the right-hand term within the brackets in Eq. 4.152. It is the value of $\overline{\delta Q}$ which m randomly selected pebbles (selected without

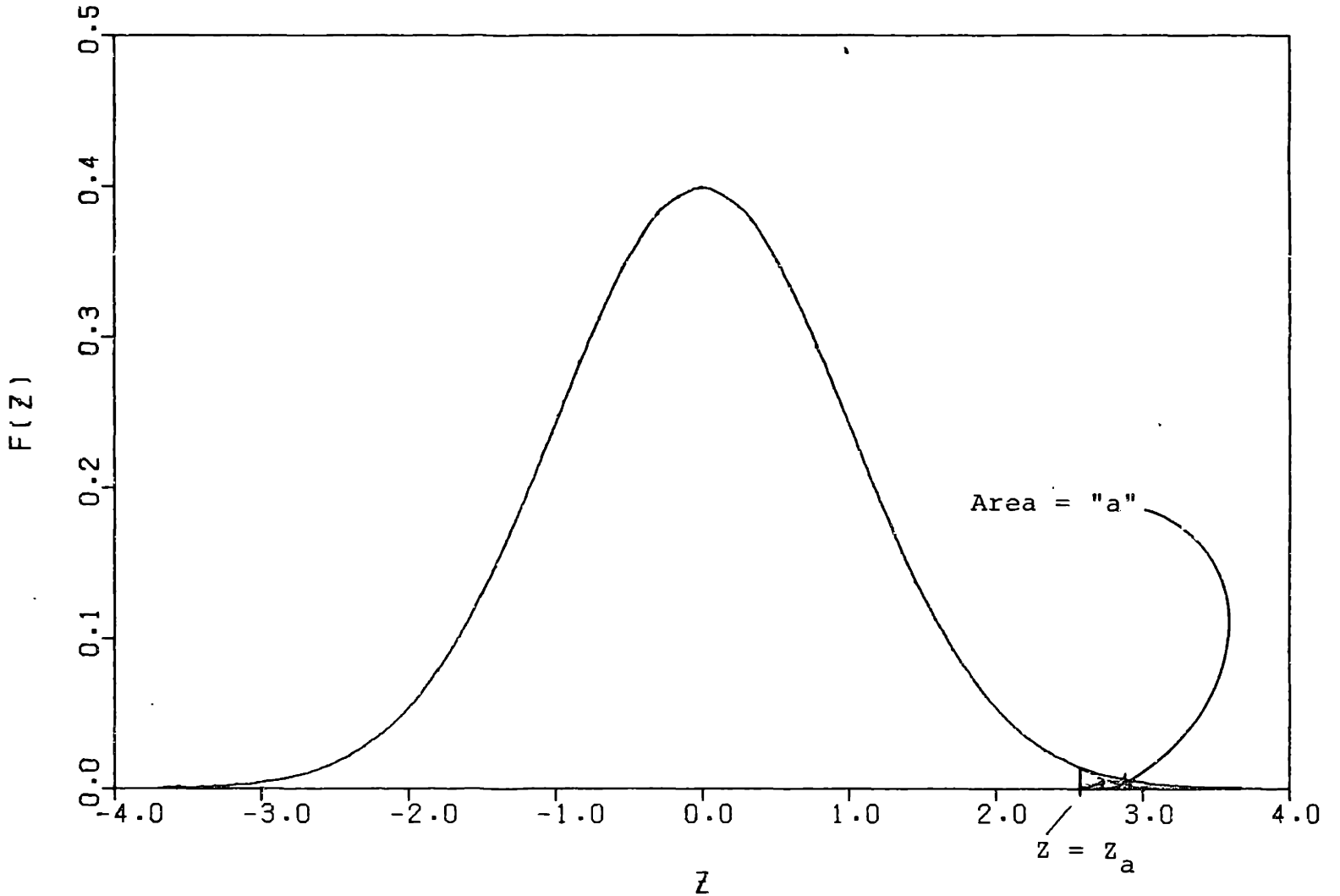

FIG. 4.16: The standard normal probability density function.

regard to their geometric relation to each other) have probability α of exceeding.

Eq. (4.152) may be converted to a relation for over-temperature $\overline{\delta\theta}$ by substituting from Eq. (4.145) for $\overline{\delta Q}$. Since:

$$\frac{\sqrt{m}\ \overline{\delta Q}}{\sigma_Q} \sim N(0,1),$$

it must also be true that:

$$\frac{\sqrt{m}}{\sigma_Q}\left\{\left[\frac{3(1-\alpha)^{2/3}}{f\ r_p^2}\right] k\ m^{-2/3} + \left[\frac{3\ (1-\alpha)}{r_p}\right] U\right\} \overline{\delta\theta} \sim N(0,1) \qquad (4.153)$$

Rearrange the above equation to obtain:

$$\left\{\left[\frac{3(1-\alpha)^{2/3}}{f\ r_p^2}\right] k\ m^{-1/6} + \left[\frac{3\ (1-\alpha)}{r_p}\right] U\ m^{1/2}\right\} \frac{\overline{\delta\theta}}{\sigma_Q} \sim N(0,1) \qquad (4.154)$$

In the same manner as for $\overline{\delta Q}$, we may use the Z_α parameter to express the probability that $\overline{\delta\theta}$ exceeds a given value:

$$\mathbb{P}\left[\overline{\delta\theta} \geq \frac{Z_\alpha\ \sigma_Q}{\left[\frac{3(1-\alpha)^{2/3}}{f\ r_p^2}\right] k\ m^{-1/6} + \left[\frac{3(1-\alpha)}{r_p}\right] U\ m^{1/2}}\right] = \alpha \qquad (4.155)$$

Thus, the dependence of the excess temperature probabilities on the number of pebbles is more complicated. There are two simple cases:

(1) <u>No conduction (k=0)</u>: In this case, $\overline{\delta\theta}$ is proportional to $\overline{\delta Q}$, and the m-dependence of the probabilities is the same is in the pure power density case. At a fixed probability level, as m increases, the temperature above expectation decreases with the square root of m.

(2) <u>No convection (U=0)</u>: In this case, $\overline{\delta\theta}$ is proportional to $m^{1/6}$. At a fixed probability level, an increase in the number of pebbles actually increases the temperature level

which can be attained. Physically, this arises because larger values of m correspond to an increased thermal resistance of the sub-volume. However, it is an inherently weak dependence--m must increase by a factor of 256 before $\overline{\delta\theta}$ will double.

When both conduction and convection effects are present, the net m-dependence of $\overline{\delta\theta}$ is determined by the relative importance of the two mechanisms in removing heat from the sub-volume. If both mechanisms are roughly equal in effect, the inverse ($m^{-\frac{1}{2}}$) effect will dominate due to the greater magnitude of the exponent.

For very small numbers of pebbles, the normal approximation breaks down due to the multi-peaked nature of an individual pebble's Eulerian PDF (see Figure 4.9) In fact, there is a maximum power density which no subvolume may exceed, which is simply the power density generated within the zone of interest by pebbles on their first pass through the core. This was illustrated in Figure 4.10, in which pass-1 pebbles generated the highest power density, and, since no shuffling had yet taken place, had zero within-pass variance. (Note that if the fresh fuel contains some burnable poison, the maximum power density may be generated by pebbles on later passes).

Let Π_1 represent the E-probability associated with pass-1 fuel, and let Q_1 represent the power density of pass-1 fuel within the core zone of interest. In this case, the maximum power density which can be generated within *any* sub-volume of m pebbles is $\overline{Q} = Q_1$, and the probability of randomly selecting m such pebbles (once again without regard to their locations) is simply:

$$\alpha = \Pi_1^m$$

The probabilty that $\overline{Q}$ exceeds Q_1 is zero:

$$\mathbb{P}[\overline{Q} > Q_1] = 0;$$

whereas the probability that $\overline{Q}$ is equal to Q_1 is "α":

$$\mathbb{P}[\overline{Q} = Q_1] = \Pi_1^m$$

Subtract the expected value μ_Q to obtain expressions in terms of $\overline{\delta Q}$:

$$\mathbb{P}[\overline{\delta Q} > Q_1 - \mu_Q] = 0 \quad \text{and} \quad \mathbb{P}[\overline{\delta Q} = Q_1 - \mu_Q] = \Pi_1^m$$

Thus, the maximum hot spot severity for power density is simply the power density of pass-1 pebbles within the zone of interest less the expected value. This severity applies at all probability levels equal to or less than Π_1^m. A similar pair of expressions may be written for the temperature severity:

$$\mathbb{P}\left[\overline{\delta\theta} > \frac{Q_1 - \mu_Q}{\left[\frac{3(1-\alpha)^{2/3}}{f\, r_p^2}\right] k\, m^{-2/3} + \left[\frac{3(1-\alpha)}{r_p}\right] U}\right] = 0$$

$$\mathbb{P}\left[\overline{\delta\theta} = \frac{Q_1 - \mu_Q}{\left[\frac{3(1-\alpha)^{2/3}}{f\, r_p^2}\right] k\, m^{-2/3} + \left[\frac{3(1-\alpha)}{r_p}\right] U}\right] = \Pi_1^m$$

Thus, for values of m large enough to justify the normal approximation, any probability level α is associated with a unique power or temperature excess. Furthermore, the smaller the probability level, the greater the hot spot severity. For very small numbers of pebbles, however, any probabilty level less than Π_1^m is associated with the maximum hot spot severities for the zone of interest, given by the

equations above.

Table 4.5 presents results from some rough calculations illustrating the severity of hot spots which might be expected at a fixed probability level. Values of parameters reflect operating conditions in the highest power-density zone of the 200 MWth KWU HTR-MODUL. A probability level $\alpha = 2.87 \times 10^{-7}$ (corresponding to $Z_\alpha = 5.0$ in the normal approximation) was selected, and the severity of hot spots (both in terms of power density and temperature) was calculated using the normal approximation for m>10, and the pass-1 power density for smaller numbers of pebbles.

For the case of power density severity, a constant severity equal to the difference between pass-1 power density and the mean power density applies out until m = 5. As the number of pebbles grows larger, the average power density behaves increasingly like a normal random variable, and the severity decreases as $m^{-1/2}$ (according to Eq. 4.152). The values calculated in Table 4.5 are plotted in Figure 4.17.

For the case of temperature, very small numbers of pebbles have decreased severity due to conduction effects. A maximum severity is reached at approximately m = 6 pebbles, at which point the denominator term in Eq. 4.155 (representing heat removal from the sub-volume) sums to a minimum. For larger values of m, the convection term dominates and steadily decreases the severity. Figure 4.18 is a plot of the severity values calculated in the Table.

During depressurized core heatup accidents only conduction heat removal is present. Since the denominator of Eq. (4.145) is much

TABLE 4.5: UN-GROUPED HOT-SPOT PROBABILITIES IN THE OPERATING REACTOR

HOT SPOT SEVERITY FOR 5σ UNGROUPED SELECTION PROBABILITY $p(m)= 2.87\times10^{-7}$

NUMBER OF PEBBLES	POWER DENSITY INCREASE	TEMPERATURE INCREASE (CONDUCTION AND CONVECTION)	TEMPERATURE INCREASE (CONVECTION ONLY)
1	2.99 W/cm^3	39.6 C	48.5 C
5	2.99 W/cm^3	45.1 C	48.5 C
10	2.64 W/cm^3	40.8 C	42.8 C
20	1.87 W/cm^3	29.4 C	30.3 C
30	1.52 W/cm^3	24.2 C	24.7 C
40	1.32 W/cm^3	21.0 C	21.4 C
50	1.18 W/cm^3	18.9 C	19.2 C
75	0.96 W/cm^3	15.4 C	15.6 C
100	0.84 W/cm^3	13.4 C	13.6 C
150	0.68 W/cm^3	11.0 C	11.1 C
200	0.59 W/cm^3	9.52 C	9.58 C
300	0.48 W/cm^3	7.79 C	7.82 C
400	0.41 W/cm^3	6.75 C	6.78 C

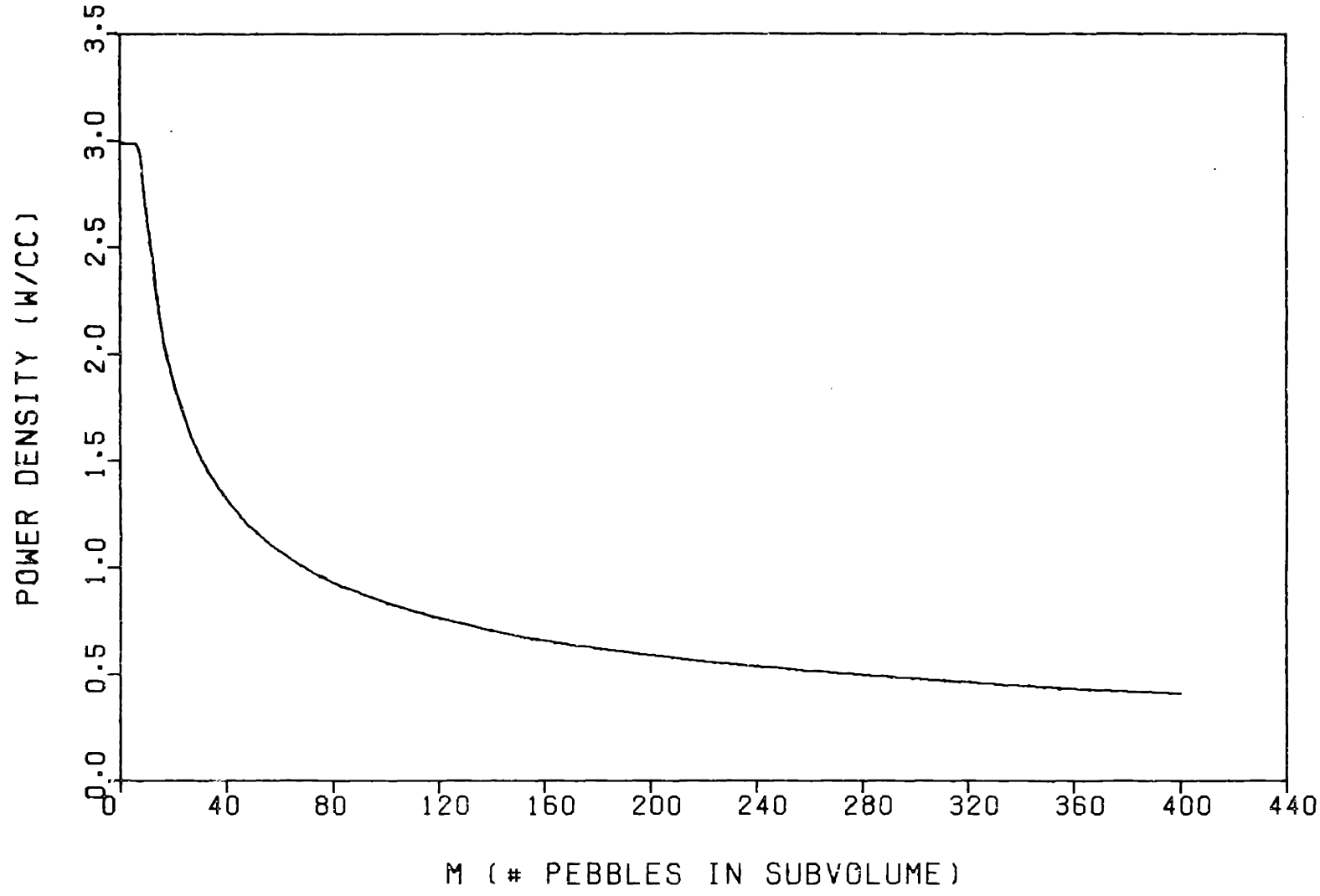

FIG. 4.17: Hot spot severity for power density during operation in the high power density zone of the 200 MWth HTR-MODUL.

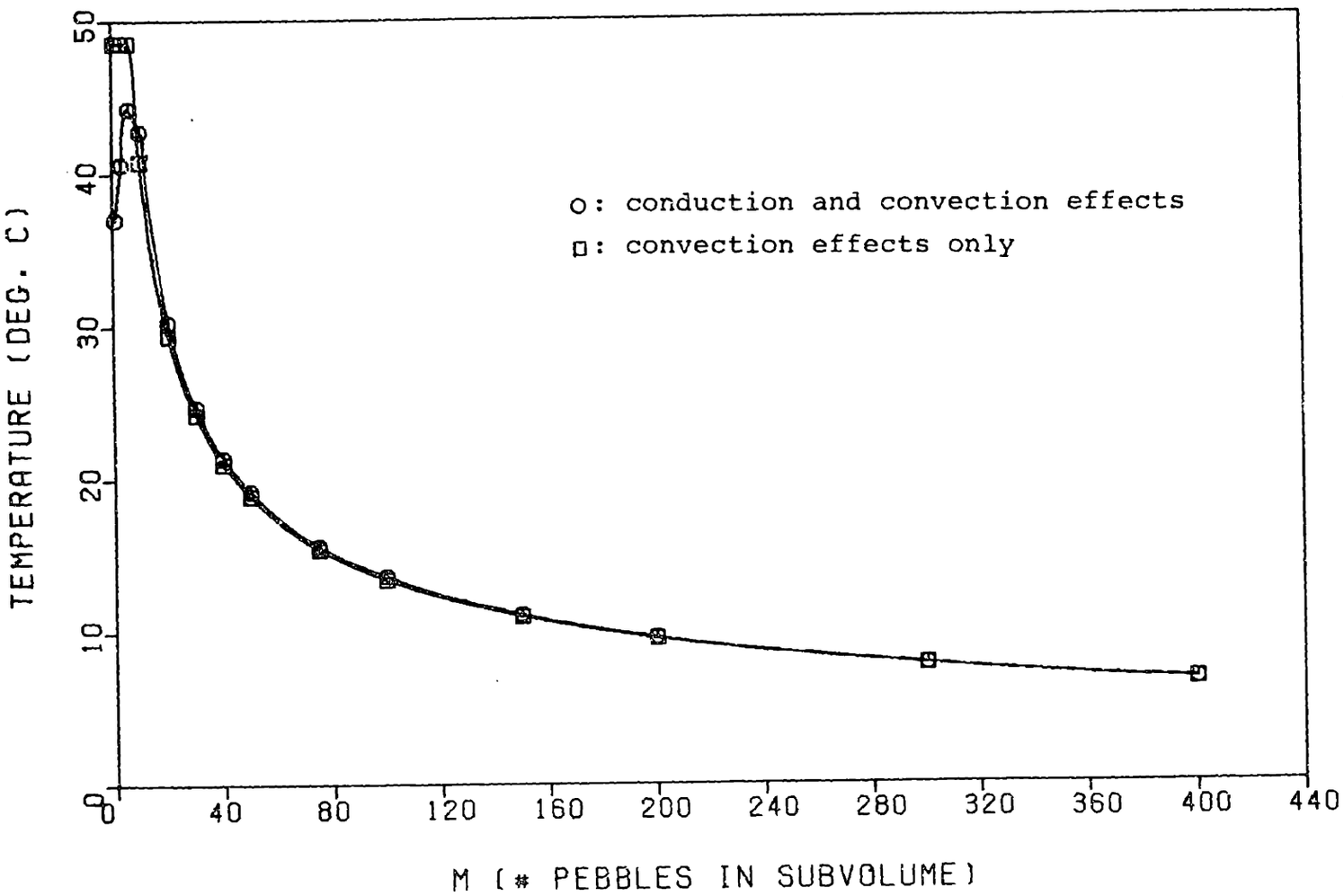

FIG. 4.18: Hot spot severity for temperature during operation in the high power density zone of the 200 MWth HTR-MODUL.

smaller without convection (see the values in Table 4.5), one would expect a higher value of temperature variance during transients. Offsetting this effect, however, is the lower level of power densities due to the decay of reactor power. If overall power density has decayed by some factor at the time maximum temperatures are reached, the standard deviation of the power density will have decreased by the same factor. Thus, the magnitude in the temperature perturbation above expectation is driven upwards by the absence of convection, but downwards by the decay of reactor power following shutdown. Table 4.6 details some additional calculations under depressurized, high temperature conditions. The table illustrates that the net effect of the accident, by the time the center of the core has achieved maximum temperature, is to decrease the magnitude of $\overline{\delta\theta}$ to very small values.

4.14.3 Calculation of Zero-Hot Spot Probabilities

The results of Section 3.7 may now be applied to the probability statements from the previous section. Recall the major result of Section 3.7:

$$P_o \equiv \mathbb{P}\left[\begin{array}{c}\text{no sub-region of m pebbles}\\ \text{out of a region of N}\\ \text{pebbles has severity} \geq S\end{array}\right] \simeq \exp\left[-\frac{N\, p(m,S)}{m}\right]$$

where p(m,S) denotes the probability of randomly selecting m pebbles with severity level S or greater. (In section 3.7, this parameter was denoted simply p(m)). p(m,S) will be referred to as the "un-grouped" selection probability, as it is does not depend upon the locations of the m pebbles.

The attributes of interest are average power density and

TABLE 4.6: UN-GROUPED HOT-SPOT PROBABILITIES DURING A HIGH TEMPERATURE TRANSIENT

HOT SPOT SEVERITY FOR UNGROUPED SELECTION PROBABILITY $p(m) = 2.87 \times 10^{-7}$

NUMBER OF PEBBLES	TEMPERATURE INCREASE (CONDUCTION ONLY)
1	0.27 C
5	0.80 C
10	1.13 C
20	1.27 C
30	1.35 C
40	1.42 C
50	1.47 C
75	1.58 C
100	1.65 C
150	1.77 C
200	1.86 C
300	1.99 C
400	2.08 C

temperature excesses above expected values. The un-grouped selection probability p(m,S) is simply the "α" parameter in Eqs. (4.152) and (4.155). For example, in the case of over-power $\overline{\delta Q}$:

$$p(m,\delta Q^{*}) = \mathbb{P}\left[\begin{array}{c}\text{average}\\ \text{power}\\ \text{density}\end{array} \geq \begin{array}{c}\text{some}\\ \text{critical}\\ \text{value}\end{array}\right] = \mathbb{P}[\,\overline{\delta Q} \geq \delta Q^{*}]$$

Since a hot spot is only of concern if it involves a significant number of pebbles, we shall treat only sub-volumes which are large enough so that the normal approximation is reasonable. Since the distribution of $\overline{\delta Q}$ is known in this case, the above expression may be further elaborated using standard normal parameters:

$$p(m,\delta Q^{*}) = \mathbb{P}\left[\,\overline{\delta Q} \geq \frac{Z_{\alpha}\,\sigma_{Q}}{\sqrt{m}}\right] = \alpha \qquad (4.156)$$

in which $\delta Q^{*} = Z_{\alpha}\sigma_{Q}/\sqrt{m}$. Z_{α} is a function of α, and may be looked up in standard normal tables or calculated with an appoximate formula such as [S5]:

$$\alpha \equiv \mathbb{P}[\,z \geq Z_{\alpha}] \simeq \frac{1}{2}\left\{1 - \left[1 - \exp\left(-\frac{2\,Z_{\alpha}^{2}}{\pi}\right)\right]^{1/2}\right\}; \quad [z \sim N(0,1)] \qquad (4.157)$$

These relations suggest the following method for graphically displaying the probability of zero hot spots as a function of volume size and hot spot severity. First, let us deal with power density as the variable of interest. Temperature is a straightforward extension:

(1) Power density variance σ_{Q} is a function of reactor design and is calculated using the equations developed in section 4.10.3. N is the number of pebbles in the core zone in which σ_{Q} is the overall power density variance;

(2) Region size m and excess power density δQ^* are parameters to be varied. Given values of these two parameters, the standard normal random variable Z_a is known :

$$Z_a = \frac{\sqrt{m}\ \delta Q^*}{\sigma_Q}$$

(3) The normal probability value $p(m,\delta Q^*)$, where severity $\delta Q^* \equiv Z_a \sigma_Q / \sqrt{m}$, is equal to "a," the value of the standard normal distribution curve at $z = Z_a$. These numbers are widely available in tables, or calculated from approximate forumlas such as Eq. (4.157). In this case, an approximate closed-form expression may be written for the un-grouped selection probability $p(m,\delta Q^*)$:

$$p(m,\delta Q^*) = \mathbb{P}\left[\ \delta Q \geq \frac{\sigma_Q\ Z_a}{\sqrt{m}}\right] \simeq \frac{1}{2}\left\{\ 1-\left[1-\exp\left(-\ \frac{2m\ \delta Q^{*2}}{\pi\ \sigma_Q^2}\right)\right]^{1/2}\right\}$$

(4) The zero hot-spot probability, P_o, is now calculated for the values of m and δQ^* which were selected:

$$P_o = \exp[-\ N\ p(m,\delta Q^*)/m\ ]$$

The procedure for hot spot temperatures is quite similar. The only difference is in step (2) above, in which the standard normal random variable is given by Eq. 4.155 instead of 4.152. The high temperature probabilities may be evaluated under operating or depressurized transient conditions through proper selection of base temperatures and heat transfer parameters and reduction of power density variance due to the decay of reactor power. Figures 4.19 and 4.20 illustrate the results of a random hot-spot analysis applied to the highest power-density zone in the FUPAR-analyzed 200 MWth KWU/Interatom HTR-Modul. Each curve represents a single hot-spot severity, plotted

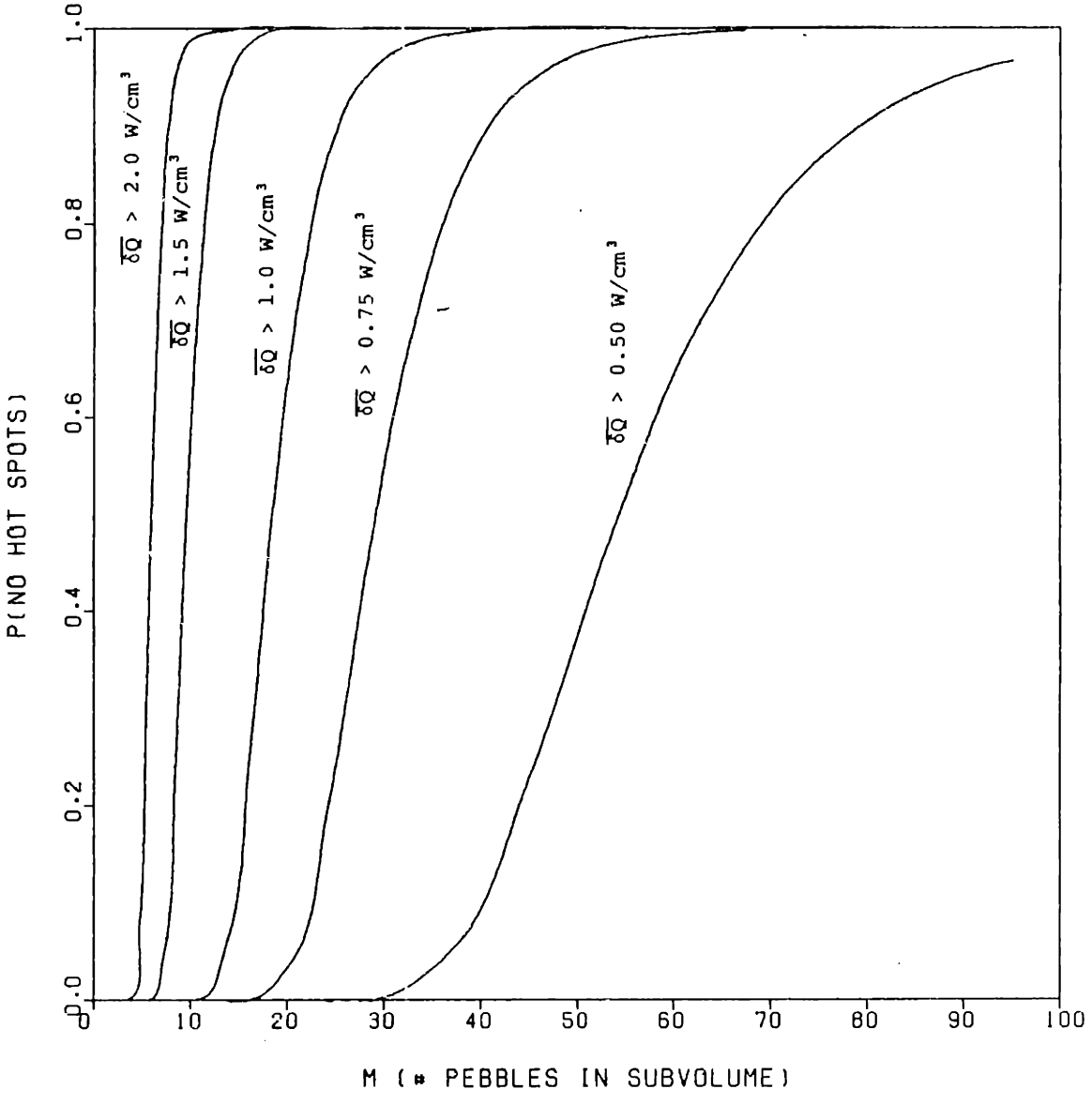

FIG. 4.19: Zero hot-spot probabilities for power density in the high power density zone of the 200 MWth HTR-Modul.

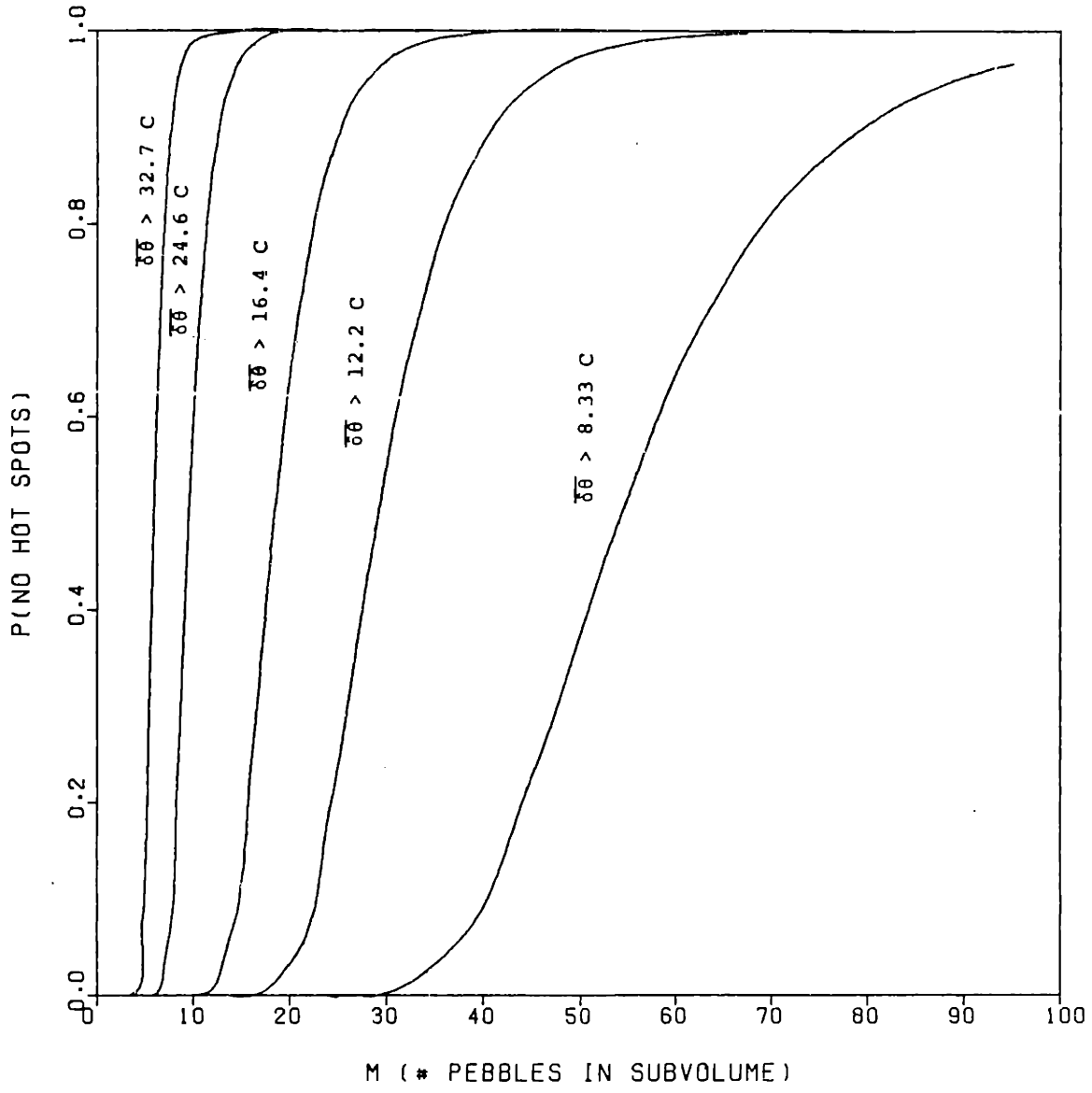

FIG. 4.20: Zero hot-spot probabilities for temperature in the high power density zone of the 200 MWth HTR-Modul.

versus the number of pebbles in a sub-volume (on the x-axis) and the probability of *no* such groupings existing in the zone of interest (the y-axis). The figure shows that once we examine sub-volumes of sufficient size to cause concern ($m > 50$, say), the magnitude of the hot spot severity which may be present is very small.

The procedure outlined above applies to a single zone of N pebbles with a single varying parameter. When examining a set of many core regions, each with its own expected values for power density and temperature, severity can no longer be characterized as a single power density *difference*. For example, suppose we are interested in the probability that no hot spots with average power density $\overline{Q} \geq \overline{Q}^*$ exist anywhere in the core . For such a hot spot to exist in any particular core zone, a local hot spot with a unique $\overline{\delta Q}$-severity must be present. That is, if zone i has expected power density $\mu_{Q,i}$, it must contain a hot spot of severity greater than or equal to $\delta Q_i \equiv \overline{Q}^* - \mu_{Q,i}$ to meet the core-wide hot-spot criterion. Let the un-grouped selection probability $p(m, \delta Q_i)$ characterize zone i (other zones, in general, have different ungrouped selection probabilities), and let the core contain z such zones. In this case, the *core wide* probability of no m-pebble hot spots, denoted $\mathbb{P}_o^*$, is given by:

$$\mathbb{P}_o^* \equiv \mathbb{P}\begin{bmatrix}\text{no m-pebble hot spots} \\ \text{in the entire core}\end{bmatrix}$$

$$= \mathbb{P}\begin{bmatrix}\text{no m-pebble hot} \\ \text{spots in zone 1}\end{bmatrix} \times \mathbb{P}\begin{bmatrix}\text{no m-pebble hot} \\ \text{spots in zone 2}\end{bmatrix} \times \ldots \times \mathbb{P}\begin{bmatrix}\text{no m-pebble hot} \\ \text{spots in zone z}\end{bmatrix}$$

$$= [1-p(m,\delta Q_1)]^{N_1/m} \times [1-p(m,\delta Q_2)]^{N_2/m} \times \ldots \times [1-p(m,\delta Q_z)]^{N_z/m}$$

Take the logarithm of both sides of the above equation, and note

that $\ell n(1-x) \simeq -x$ when $x \ll 1$:

$$\ell n \mathbb{P}_o^* = \frac{N_1}{m}\ell n[1-p(m,\delta Q_1)] + \frac{N_2}{m}\ell n[1-p(m,\delta Q_2)] + \ldots + \frac{N_z}{m}\ell n[1-p(m,\delta Q_z)]$$

$$\simeq -\frac{N_1}{m}p(m,\delta Q_1) - \frac{N_2}{m}p(m,\delta Q_2) - \ldots - \frac{N_z}{m}p(m,\delta Q_z)$$

$$= -\sum_{i=1}^{z}\frac{N_i}{m}p(m,\delta Q_i)$$

Take the exponential of both sides of the above equation to obtain:

$$\mathbb{P}_o^* \simeq \exp\left[-\frac{1}{m}\sum_{i=1}^{z} N_i p(m,\delta Q_i)\right] \qquad (4.158)$$

Equation 4.158 is an elegent expression for the core-wide zero hot spot probability, but in fact it is not really necessary to perform such calculations. Since the probability of no hot spots will equal 1.0 only if it is 1.0 in *every* core zone, and since the high power-density zone has zero-hot spot probabilities less than 1.0 for higher numbers of pebbles than any other, it is clear that the core-wide probabilities are contolled by zero-hot spot probabilities in the highest power density zone alone. Put another way, examination of Figures 4.18 and 4.19 shows that hot spot probability curves for large perturbations are approximately unit step functions. The product of many such step functions is simply equal to the single step function which changes values at the highest input value. Thus, in terms of the number of pebbles for which the probability of no hot spots is equal to 1.0, Figures 4.18 and 4.19 apply approximately to the entire core as well as to the high power density zone.

4.14.4 Distributed Analysis of the No-Convection Case.

For the case of no convective heat removal (which occurs, for example, during depressurized core heatup accidents), the heat transport equation is simplified and a simple analytic solution relates the boundary temperature gradient to the average temperature increase. The physical situation to be modeled was illustrated in Figure (4.15), in which a spherical volume of radius r_m is nested in an infinite medium of heat producing pebbles with identical thermal conductivity. The heat conduction equation is:

$$k \nabla^2\theta = -\delta Q$$

where the symbols have the same meaning as in Eq. (4.134). Expanding the ∇^2 operator in spherical coordinates under radial symmetry:

$$k \frac{1}{r^2} \frac{d}{dr} \left[r^2 \frac{d\theta}{dr} \right] = -\delta Q \qquad (4.159)$$

The equation is to be solved both inside and outside the subvolume. The appropriate boundary conditions are:

(1) Heat balance on the sub-volume: The total rate of heat conduction out of the subvolume must equal the total rate of heat production inside the subvolume. Thus:

$$-k A_m \left.\frac{d\theta}{dr}\right|_{r_m} = V_m \delta Q$$

or:

$$\left.\frac{d\theta}{dr}\right|_{r_m} = -\frac{V_m \delta Q}{k A_m} = -\frac{\delta Q\, r_m}{3k} \qquad (4.160)$$

(2) Temperature far from the subvolume: Far from the region of interest, the temperature is equal to the un-perturbed "background" temperature, θ_∞:

$$\theta\Big|_{r \to \infty} = \theta_\infty \qquad (4.161)$$

First, we shall solve the conduction equation outside the sub-volume ($r > r_m$) where the incremental heat source is zero. This will allow the boundary temperature $\theta(r_m)$ to be expressed in terms of known parameters. Since $\delta Q = 0$ outside r_m, we have:

$$k \frac{1}{r^2} \frac{d}{dr} \left[r^2 \frac{d\theta}{dr} \right] = 0 \qquad (r > r_m)$$

or

$$r^2 \frac{d\theta}{dr} = (\text{constant}). \qquad (4.162)$$

The constant may be evaluated at any radius, in particular at $r = r_m$. Insert the first boundary condition into Eq. (4.162) to obtain:

$$\left[r^2 \frac{d\theta}{dr} \right]\Big|_{r_m} = r_m^2 \frac{d\theta}{dr}\Big|_{r_m} = - \frac{\delta Q \, r_m^3}{3 k} \qquad (4.163)$$

Thus, the constant in Eq. (4.162) is $-\delta Q \, r_m^3/3k$. Insert this value into Eq. (4.159) and integrate once again:

$$r^2 \frac{d\theta}{dr} = - \frac{Q \, r_m^3}{3 k}$$

$$\int_{\theta(r_m)}^{\theta(r)} d\theta = - \frac{Q \, r_m^3}{3 k} \int_{r_m}^{r} \frac{dr}{r^2}$$

$$\theta(r) - \theta(r_m) = - \frac{Q \, r_m^3}{3 k} \left[- \frac{1}{r} + \frac{1}{r_m} \right]$$

$$\theta(r_m) = \theta(r) + \frac{Q \, r_m^3}{3 k} \left[\frac{1}{r_m} - \frac{1}{r} \right] \qquad (4.164)$$

Use the second boundary condition and Eq. (4.164) to express the boundary temperature $\theta(r_m)$ in terms of the background temperature, θ_∞:

$$\theta(r_m) = \theta_\infty + \frac{Q\, r_m^2}{3\, k} \tag{4.165}$$

The next step is to solve for radii less than r_m, where $\delta Q \neq 0$. The goal is to express the average temperature increase in V_m in terms of known parameters: δQ, k, and r_m. Begin by rearranging and integrating Eq. (4.159):

$$\frac{d}{dr}\left[r^2 \frac{d\theta}{dr} \right] = - \frac{\delta Q\, r^2}{k}$$

$$\int_{r_m}^{r} d\left[r^2 \frac{d\theta}{dr} \right] = - \frac{\delta Q}{k} \int_{r_m}^{r} r^2\, dr$$

$$r^2 \frac{d\theta}{dr} - r_m^2 \left.\frac{d\theta}{dr}\right|_{r_m} = - \frac{\delta Q}{3k} \left[r^3 - r_m^3 \right]$$

$$r^2 \frac{d\theta}{dr} - r_m^2 \left[- \frac{\delta Q\, r_m}{3k} \right] = - \frac{\delta Q}{3k} \left[r^3 - r_m^3 \right]$$

or

$$\frac{d\theta}{dr} = - \frac{\delta Q\, r}{3k} \tag{4.166}$$

Integrate both sides of Eq. (4.166) from $r = r_m$ to r:

$$\int_{\theta(r_m)}^{\theta(r)} d\theta = - \frac{\delta Q}{3k} \int_{r_m}^{r} r\, dr$$

$$\theta(r) - \theta(r_m) = - \frac{\delta Q}{6k} \left[r^2 - r_m^2 \right]$$

or

$$\theta(r) = \theta(r_m) + \frac{\delta Q}{6k} \left[r_m^2 - r^2 \right]$$

$$= \theta_\infty + \frac{\delta Q\, r_m^2}{3k} + \frac{\delta Q\, r_m^2}{6k} - \frac{\delta Q}{6k} r^2$$

Perform some final rearrangements to yield $\delta\theta(r)$, the incremental temperature distribution:

$$\delta\theta(r) \equiv \theta(r) - \theta_\infty = \frac{\delta Q}{2k} \left[r_m^2 - \frac{r^2}{3} \right] \tag{4.167}$$

Equation (4.167) may be integrated over V_m to yield the volume average incremental temperature increase, $\overline{\delta\theta}$:

$$\overline{\delta\theta} \equiv \frac{1}{V_m}\int_0^{r_m} \delta\theta(r)\, 4\pi\, r^2\, dr$$

$$= \frac{4\pi}{V_m}\int_0^{r_m} \frac{\delta Q}{2k}\left[\, r_m^2 - \frac{r^2}{3}\,\right] r^2\, dr$$

$$= \frac{3}{r_m^3}\,\frac{\delta Q}{2k}\int_0^{r_m} \left[\, r_m^2 - \frac{r^2}{3}\,\right] r^2\, dr$$

$$= \frac{3\ \delta Q}{2k\ r_m^3}\left[\, r_m^2\,(r_m^3/3) - (r_m^5/15)\,\right]$$

$$= \frac{3\ \delta Q}{2k}\,(4r_m^2/15) \;=\; \frac{2\ \delta Q\ r_m^2}{5\ k} \qquad (4.168)$$

Using Eq. (4.168), we may express the gradient at the sub volume boundary in terms of the volume-averaged incremental temperature:

$$\left.\frac{d\theta}{dr}\right|_{r_m} = -\frac{\delta Q\ r_m}{3k} = \frac{2\ \delta Q\ r_m^2}{5\ k} \times \frac{1}{(6/5)\ r_m}$$

$$= -\frac{\overline{\delta\theta}}{(6/5)\ r_m} \qquad (4.169)$$

Comparison of Eq. (4.169) with Eq. (4.140) reveals that the analytic "f" factor for the no-convection case is (6/5) = 1.2. f is greater than 1.0 due to the increase in θ at the zone boundary r_m.

4.15: SUMMARY

The equations relating isotopic densities, burnup, and power density have been solved analytically in a single discrete zone of the reactor. The solutions take the form of position-dependent transition matrices, relating fuel properties leaving each zone to the properties when it entered. The transition matrices allow isotopic densities, power density, and burnup to be expressed as functions of the branch variable. The linear, time independent nature of these transition matrices simplifies this function considerably. Probabilistic analysis using the branch techniques introduced in Chapter 3 is possible.

Branch expectation operations yield the volume-averaged expected values of all materials densities in each zone of the core. The FUPAR computer code performs these calculations, requiring a known neutron flux distribution as input. An iterative scheme using FUPAR and VSOP has been developed to analyze stationary pebble bed reactor cores. Results for an analysis of a 200 MWth modular HTGR are in good agreement with data in the literature.

Solutions for the second moments of fuel parameters enables estimation of the variance of fuel properties. Random hot spot analysis for power density is based directly on FUPAR-generated heavy metal covariance matrices. The severity of power density hot spots is proportional to the local mean power density. Severity in terms of fuel temperatures is derived by a heat balance on the hot spot volume. For hot spots containing significant numbers of pebbles, the temperature

severity also is directly proportional to the local mean power density.

Preliminary hot spot analysis of the 200 MWth MHTGR indicates that severe hot spot during operation are unlikely. Furthermore, since local power density is quite small during a depressurization transient, the probability of peak accident temperatures significantly exceeding expectation is extremely small.

CHAPTER 5: ANALYSIS OF MHTGR DESIGN VARIANTS

This chapter presents the results of FUPAR/VSOP analyses of several modular HTGR design variants. Emphasis is on design variants of interest due to some special feature or application. Others [B5, B3, J1] have already evaluated the effects on fission product release of such basic design parameters as average power density and reactor geometry. After reviewing the results obtained for the base case 200 MWth MHTGR, two cores with special features are analyzed. The first is identical to the base case except for the inclusion of a small amount of gadolinia in fresh fuel elements as a burnable poison. It is postulated that the properties of gadolinium's thermal neutron cross section can reduce reactivity increases caused by water ingress into the pebble bed. Thermal effects caused by a shift in the reactor's power peak compensate for the reactivity effects of increased gadolinium concentration. Thus, no increased feed enrichment is necessary, and neutron thermalization due to water ingress leads to a smaller reactivity increase than in the un-poisoned case. However, the effect is small for the amount of gadolinia analyzed.

The second core is identical to the base case except for the core temperatures and fuel enrichment. Inlet and outlet gas temperatures are raised to 600C and 800C, respectively, in order to examine the operation of a MHTGR core under direct-cycle gas-turbine conditions. To compensate for reduced core reactivity due to higher temperatures, the fresh fuel enrichment must be increased.

The calculations necessary to arrive at a converged solution for each core are discussed. Details of the reactor design, such as power density and temperature distributions, are reviewed, and results of random hot-spot analyses are presented. The THERMIX computer code has been used to evaluate the post-depressurization temperature transients experienced by all design variants, and these results are displayed as well. Finally, the results of these analyses are compared for the three design variants.

5.1 RESULTS OF THE BASE DESIGN CALCULATION

The base design selected for this work is a 200 MWth, multi-pass pebble bed MHTGR which is quite similar to the KWU/Interatom HTR-Modul (see Chapter 1). Several results of the analysis of this core have already been presented in Section 4.13 to demonstrate general agreement of FUPAR/VSOP with independent calculations. Here, a more thorough description of the reactor is provided, as well as new analyses related to hot-spot probabilities and post-depressurization temperature transients. Throughout this work, the base case core will be referred to as simply the "base core."

5.1.1 Review of calculations

The base core produces 200 MWth and has a mean height of 943 cm and a radius of 150 cm. Fuel elements are of standard HOBEG design, employing TRISO fuel particles with UO_2 kernels. Fuel is recycled an average of 15 times prior to discharge, and the cutoff burnup for discharge is 80,000 MWD/MTHM. These parameters imply an average axial velocity of 16.00×10^{-4} cm/sec. Helium enters the top of the core at 200C and exits at 700C. Pebbles loaded with 7 grams of uranium, and no thorium is utilized.

Based on this general information, we wish to calculate the following parameters:

(1) reactor power density distribution;
(2) power density variance distribution;
(3) reactor temperature distribution;
(4) the total number of pebbles in the core;

(5) reactor effective multiplication factor;
(6) required fresh fuel enrichment;
(7) fresh fuel injection rate.

Figure 5.1 illustrates the core discretization for these calculations. The core is divided into 15 axial zones of equal thickness, and 5 radial zones, each with equal cross sectional area. As uniform radial pebble flow profile and void fraction are assumed, each radial drop zone has an equal drop probability. An initial-guess neutron flux distribution was available from previous calculations. Several FUPAR/VSOP calculations were performed to determine a critical fresh fuel enrichment. Once an approximate feed enrichment was known, FUPAR/VSOP iterations refined the power density distribution until a converged solution was obtained. The TIK [T2] program was run in conjunction with VSOP to update fuel temperatures after each iteration. Final reactivity adjustments were accomplished through slight alterations of the fuel velocity to change the fuel's discharge burnup. Figure 5.2 shows the axial power density shapes for the final four iterations in this sequence. The iteration-dependent power shapes show no tendency to diverge; differences from one to the next decrease with further iteration. Figure 5.3 also illustrates convergence using plot of Gd-155's number density as a function of axial core position for the final four iterations. The gadolinium concentration is very sensitive to the local neutron flux due to its high absorption cross section. The convergence of the number density profile for such a complex isotope illustrates well that the calculations converge to a single solution.

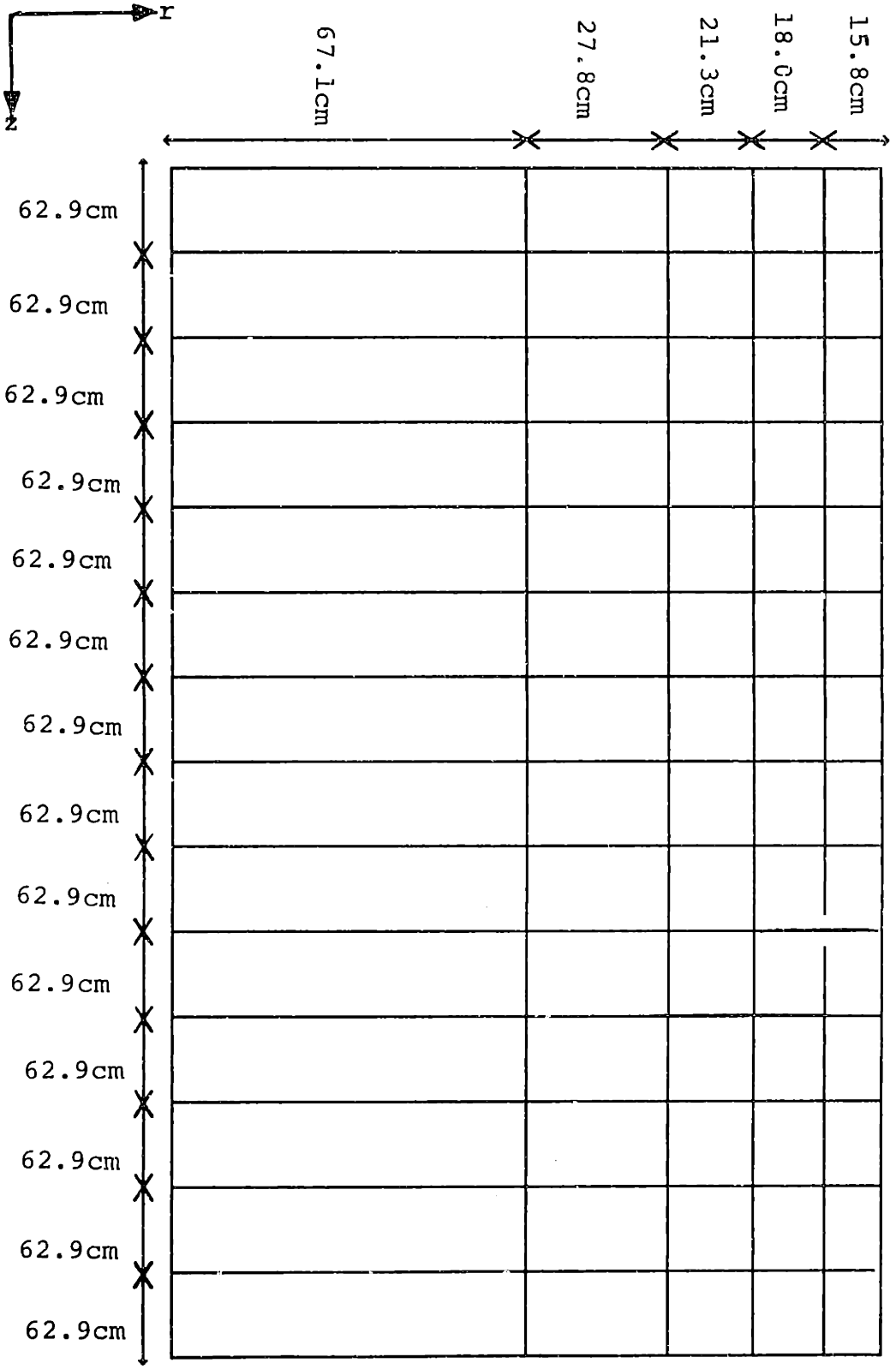

FIG. 5.1: Discretization used for reactor analysis.

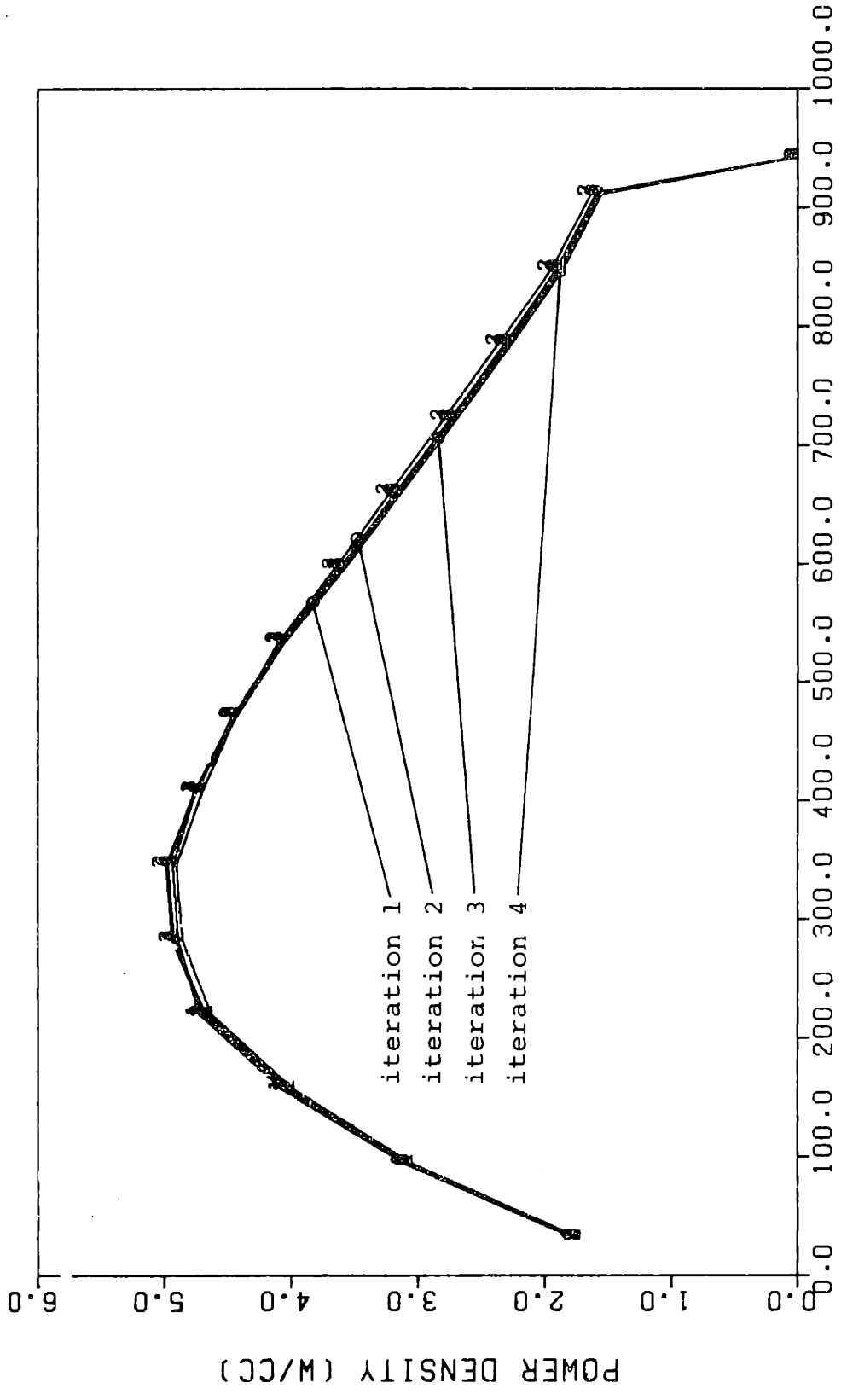

FIG. 5.2: Axial power density distribution in the base core as a function of iteration number.

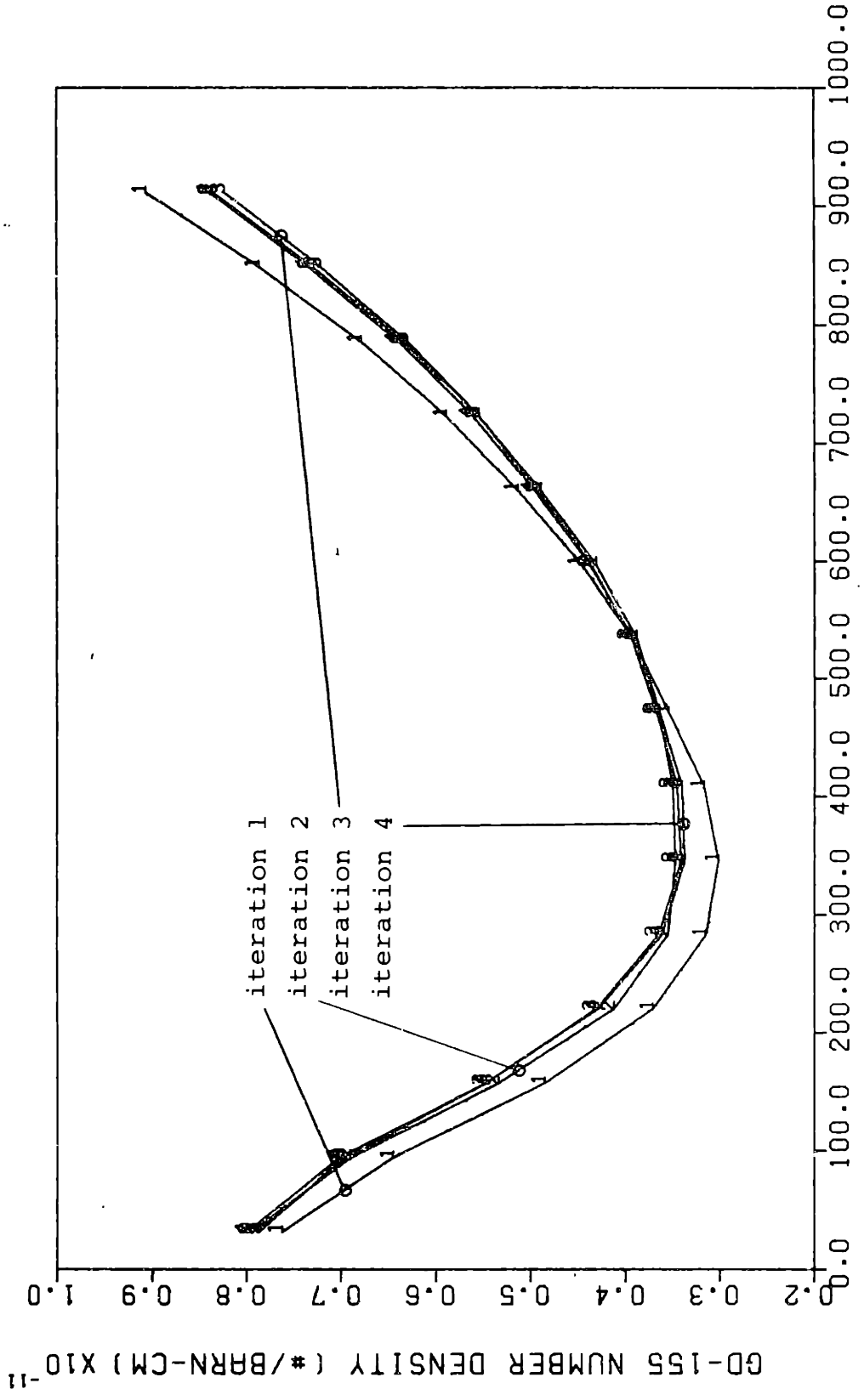

FIG. 5.3: Axial Gd-155 number density distribution in the base core as a function of iteration number.

5.1.2. Reactor operating parameters

Table 5.1 presents design information for the base core. Figure 5.4 illustrates the axial power density shape in the central drop zone. The spread of pebble powers about their expected value is indicated by the upper and lower curves, which extend over a range of plus-or-minus 1.5 standard deviations about the mean value. The figure illustrates the strong dependence of overall power density variance on the local power density. Figure 5.5 presents the local mean power density and power density standard deviation for every core zone. It is emphasized that this variation in power density does *not* apply to the core zone as a whole, which has an extremely small probability of differing significantly from its expected power density. Rather, the standard deviation in the Figure applies to individual pebbles within that zone. It is representative of the range in values obtained in an experiment consisting of selecting pebbles at random and recording their power density.

Figure 5.6 applies to the core's highest power zone, showing the dependence of power density and power density standard deviation on pebble pass number. The pass-dependent standard deviations are presented in the Figure as error bars of width 3σ. The Figure shows that the dominant contribution to the region's overall power density variance comes from the between-pass variance. The ratio of partitioned variances (the "R" parameter introduced in section 4.10) is 418 in this case, quantifying the small influence of the within-pass power density variance. The small dependence may seem unlikely, since the outer core

TABLE 5.1: PROPERTIES OF THE BASE CORE

THERMAL POWER	200 MW
CORE DIAMETER	300 cm
MEAN CORE HEIGHT	943 cm
AVERAGE POWER DENSITY	3.0 W/cm^3
HELIUM TEMPERATURE	200/700 ^oC
SYSTEM PRESSURE	40 bar
CORE PRESSURE DROP	0.99 bar
FUEL CYCLE	U-Pu
NUMBER OF FUEL ELEMENTS	360,000
NUMBER OF PASSES	15
FRESH FUEL INJECTION RATE	347 pebble/day
ENRICHMENT	7.3 %
HEAVY METAL LOADING PER FUEL ELEMENT	7 g
CORE K-EFFECTIVE (UNRODDED)	1.0090
AVERAGE DISCHARGE BURNUP	82,000 MWD/MT

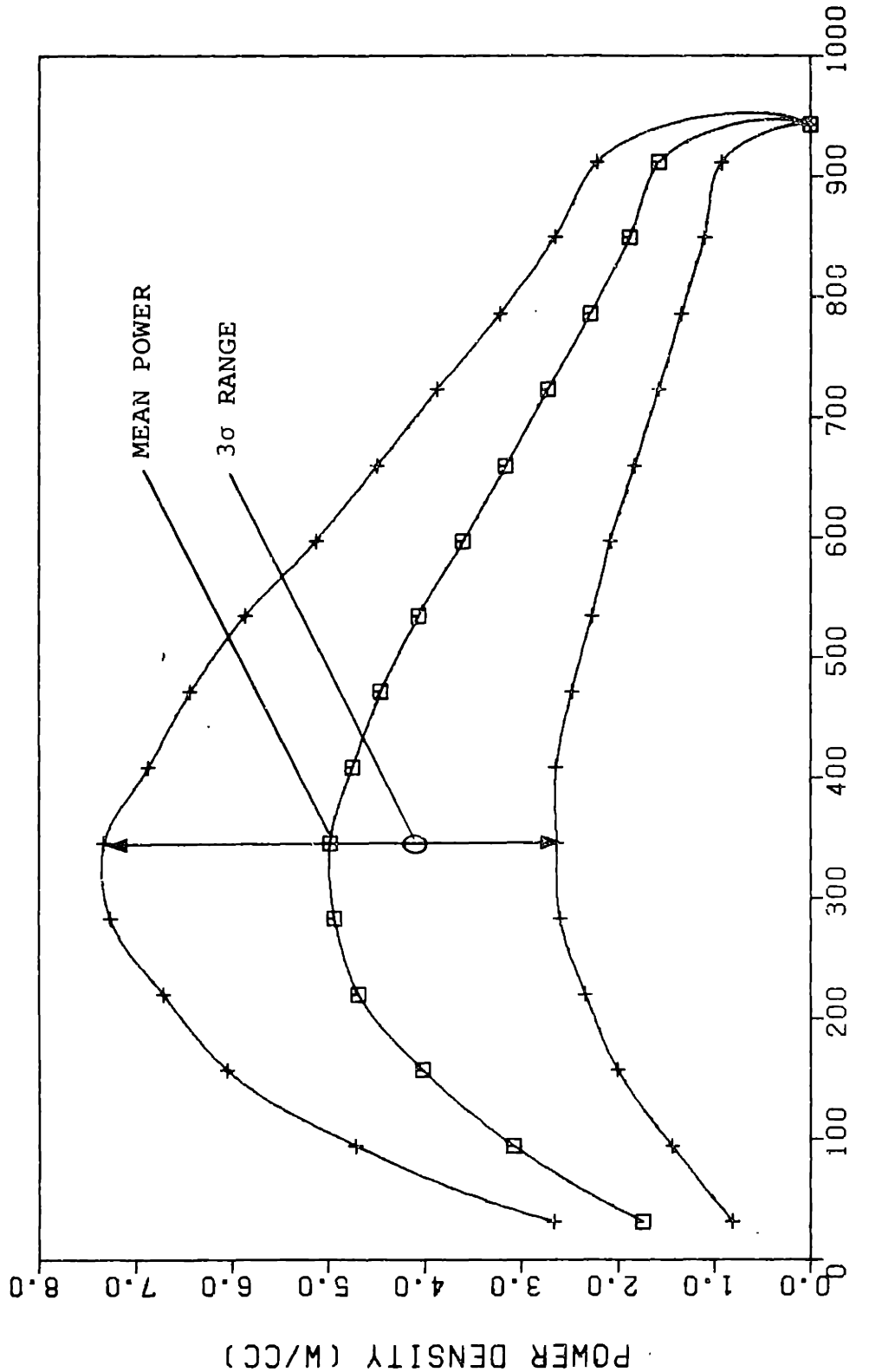

FIG. 4: Axial power density and power density standard deviation distribution in the base core.

z \ r	1	2	3	4	5
1	1.735 (0.617)	1.586 (0.564)	1.458 (0.518)	1.377 (0.489)	1.384 (0.49)
2	3.073 (1.091)	2.810 (0.998)	2.583 (0.917)	2.439 (0.865)	2.449 (0.87)
3	4.021 (1.347)	3.679 (1.233)	3.383 (1.134)	3.191 (1.070)	3.200 (1.072
4	4.679 (1.563)	4.283 (1.431)	3.938 (1.317)	3.713 (1.244)	3.713 (1.25)
5	4.924 (1.551)	4.509 (1.422)	4.144 (1.309)	3.901 (1.236)	3.890 (1.24)
6	4.973 (1.561)	4.555 (1.432)	4.186 (1.319)	3.936 (1.246)	3.914 (1.25)
7	4.747 (1.407)	4.348 (1.291)	3.994 (1.191)	3.748 (1.125)	3.713 (1.13)
8	4.451 (1.316)	4.078 (1.209)	3.745 (1.115)	3.510 (1.054)	3.467 (1.06)
9	4.072 (1.200)	3.732 (1.103)	3.426 (1.018)	3.207 (0.962)	3.159 (.964)
10	3.610 (1.018)	3.308 (0.936)	3.034 (0.864)	2.835 (0.817)	2.783 (.818)
11	3.173 (0.893)	2.908 (0.821)	2.667 (0.759)	2.489 (0.718)	2.439 (.718)
12	2.740 (0.769)	2.511 (0.708)	2.303 (0.654)	2.148 (0.619)	2.100 (.620)
13	2.306 (0.632)	2.114 (0.583)	1.937 (0.538)	1.805 (0.509)	1.761 (.510)
14	1.902 (0.521)	1.743 (0.480)	1.598 (0.444)	1.487 (0.420)	1.449 (.420)
15	1.593 (0.434)	1.460 (0.400)	1.338 (0.370)	1.246 (0.351)	1.214 (.352)

FIG. 5.5: Power density and power density (standard deviation) distribution in the base case core.

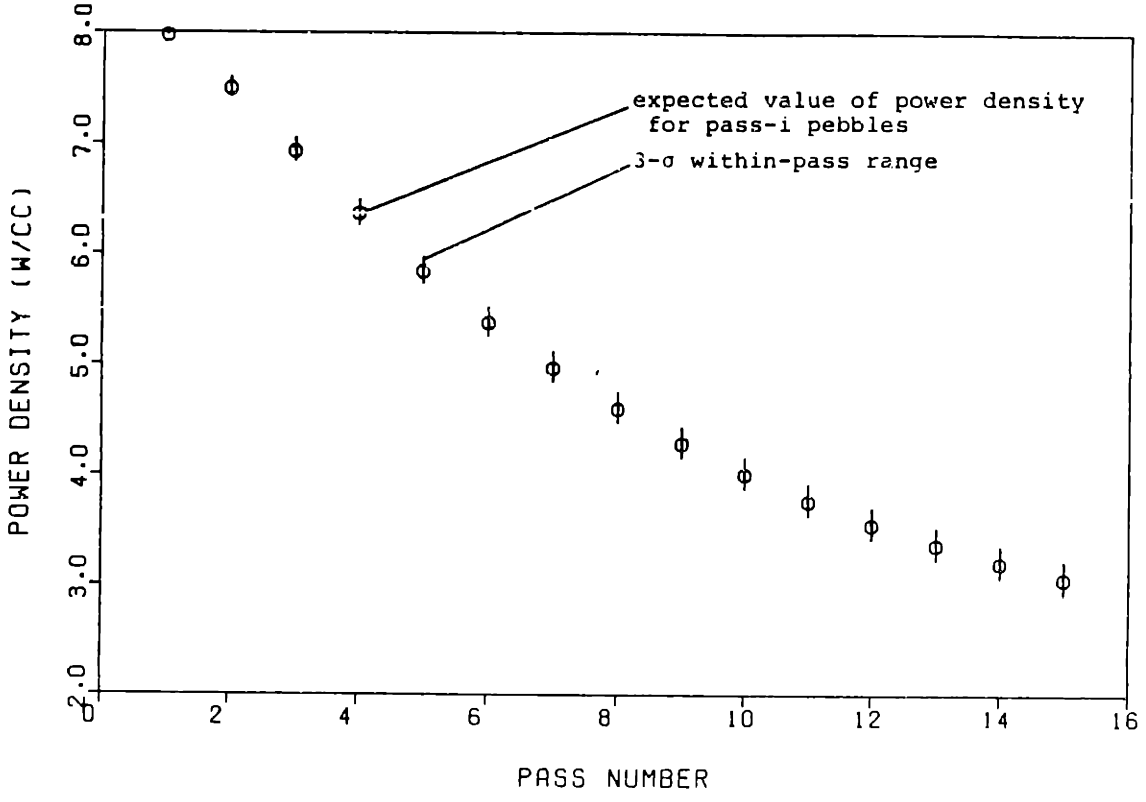

FIG. 5.6: Pass-dependent power densities and power density standard deviations in the high power zone of the base core.

zones have a significantly lower neutron flux than the inner zone. This feature is balanced by the self-correcting nature of pebble burnup. Any pebble which receives less than the expected burnup on a particular pass will be all the more reactive during the next pass. This effect compensates for exposure variance when power density is computed.

The core's steady-state temperature distribution was calculated using the TIK ("Temperatur In Kugelhaufen") component of VSOP, and the axial temperature profile (in the central radial drop zone) is presented in Figure 5.7. Figure 5.8 shows the expected temperature in each core zone.

A random hot-spot analysis was performed for the base core, and some results were already mentioned in Section 4.14. As the core wide zero-hot spot probability is driven very strongly by the zero-hot spot probability in the hottest core zone, we present here results for the the high power zone only. As illustrated in Figure 5.5, this is zone (6,1) in FUPAR/VSOP coordinates, with an expected power density μ_Q = 4.99 W/cm^3 and standard deviation σ_Q = 1.56 W/cm^3. Figure 5.9 presents essentially the same zero-hot spot curves which were presented earlier in Figure 4.19, with the exception that instead of referencing δQ^*, the severity relative to the expected value, the curves in this figure are indexed by the total power density Q^*:

$$Q^* \equiv \mu_Q + \delta Q^* \qquad (5.1)$$

For example, the figure indicates that at a hot spot severity of Q^* = 6.5 W/cm^3, sub-volumes of greater than size m≃15 pebbles are extremely unlikely.

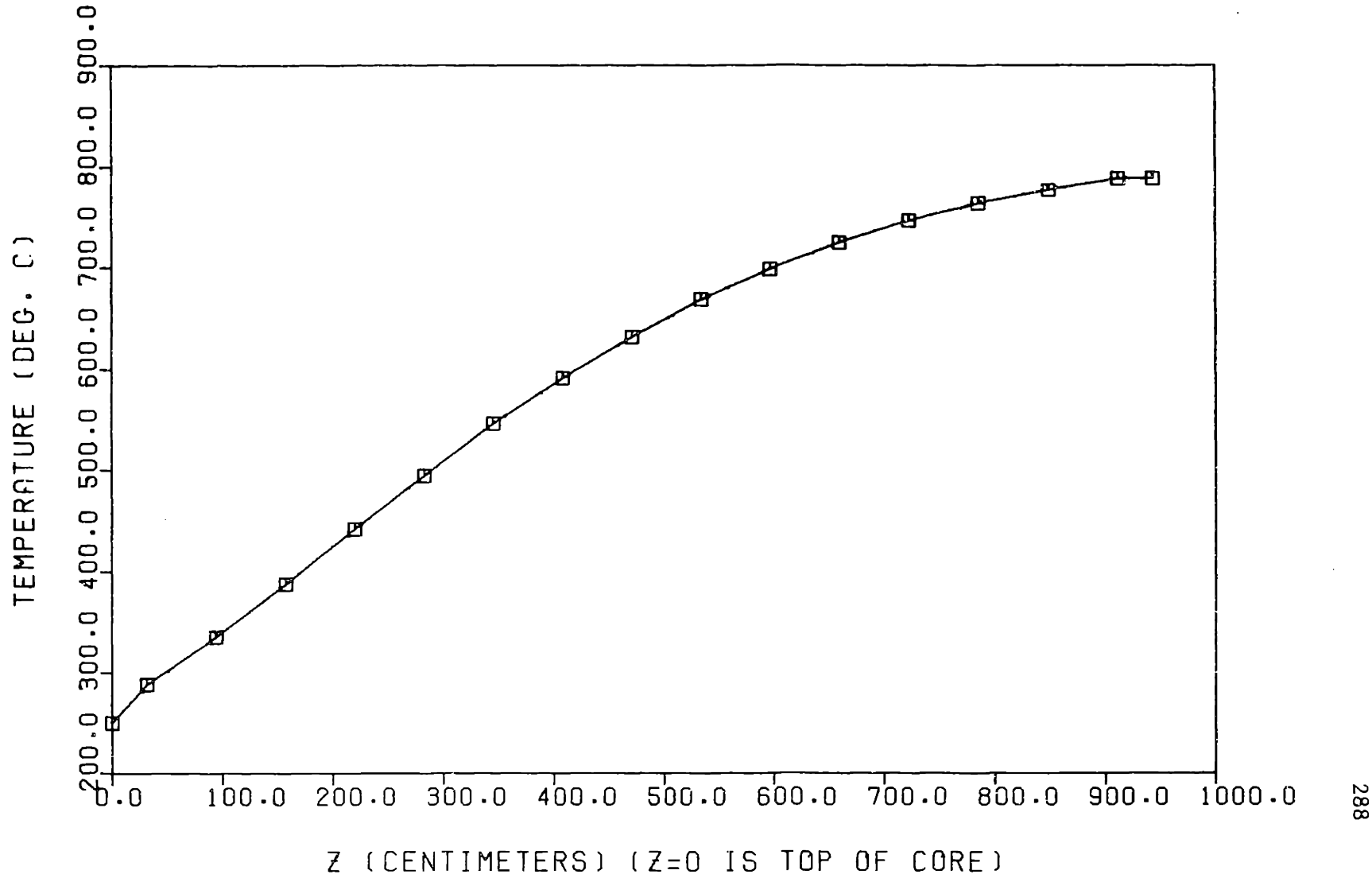

FIG. 5.7: Axial temperature profile in the base case core.

z \ r	1	2	3	4	5
1	288	285	282	280	281
2	335	328	321	317	318
3	387	375	365	359	359
4	442	425	411	402	402
5	495	474	456	445	443
6	546	520	498	484	482
7	591	561	536	520	517
8	632	599	570	553	549
9	669	632	601	582	577
0	699	659	627	607	601
11	725	683	649	628	621
12	747	703	667	646	639
13	764	719	682	661	653
14	777	731	694	672	664
15	788	741	704	683	674

FIG. 5.8: Core-wide temperature distribution (^{o}C) in the base core.

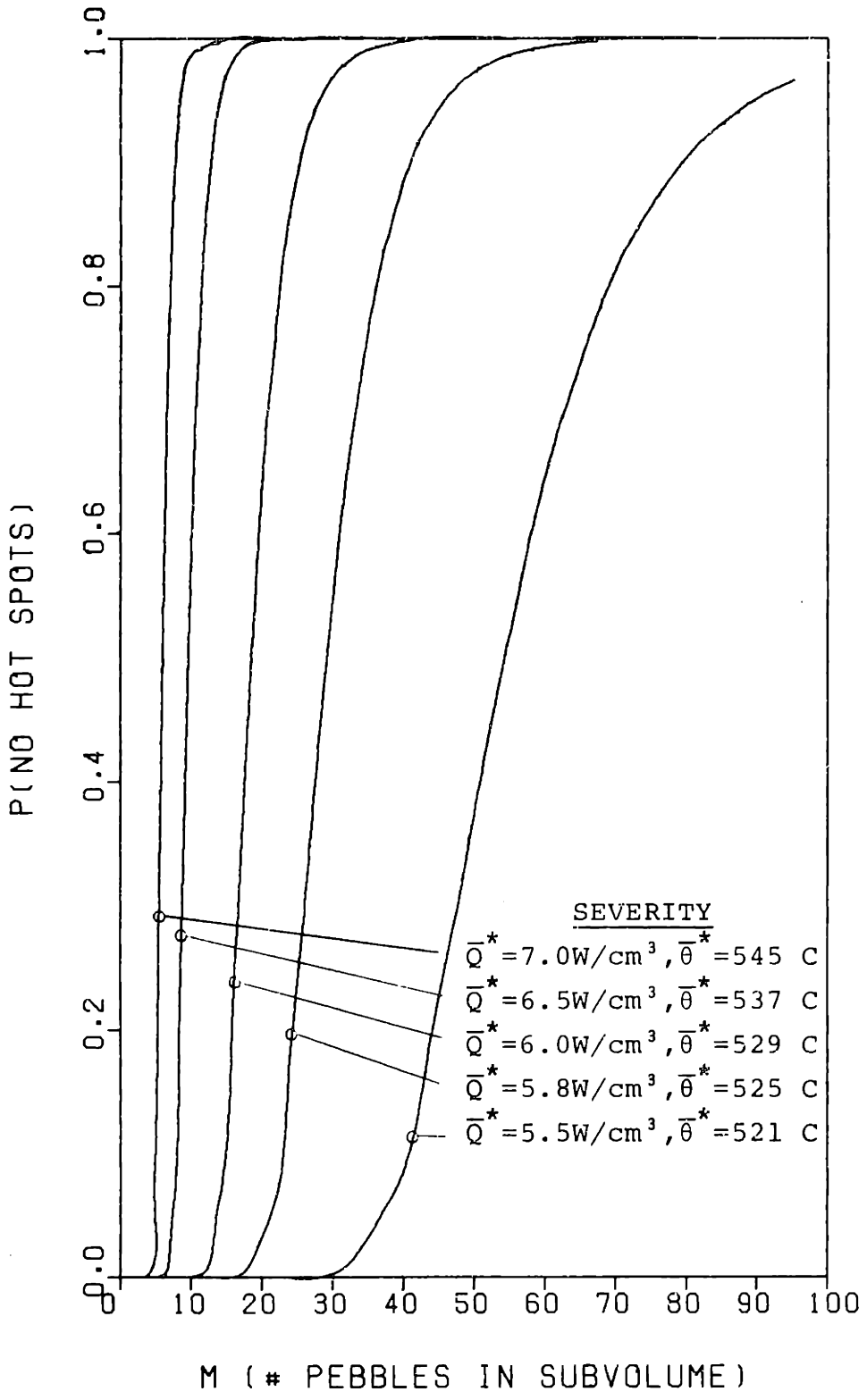

FIG. 5.9: **Zero hot spot probabilities in the base core's high power density zone.**

An alternate presentation of these results is useful, and its derivation is illustrated in Fig. 5.10. Suppose some fixed level of zero hot spot probability is selected, $\mathbb{P}_0$. Each value for subvolume size m has a corresponding *maximum* severity Q which is the index of the zero-hot spot probability curve at that level (higher severities only occur at probabilties higher than $\mathbb{P}_0$). A plot can thus be made of the maximum severity (at probability level $\mathbb{P}_0$) versus the number of pebbles, as shown in the Figure. Furthermore, the probability level can be expressed in a more physically meaningful form. Let $\mathbb{P}_{\geq 1}$ be the probability of one or more hot spots existing in the core at any time:

$$\mathbb{P}_{\geq 1} \equiv 1 - \mathbb{P}_0 \tag{5.2}$$

In general, $\mathbb{P}_{\geq 1}$ will be small for severe hot spots, which are unlikely occurences. These probabilities apply to a single *independent* sampling of pebbles from the zone of interest. Since the pebbles in the core zone are always changing, there will be many opportunities to make such an independent sampling experiment. For the core under consideration, in which a fuel element makes about 5 passes per year, and in which the zone under consideration is 1/15'th of the total reactor height, there will be approximately 5×15 = 75 independent samplings per year, each of which has the same probabilities $\mathbb{P}_0$ and $\mathbb{P}_{\geq 1}$. Thus, the expected *frequency* of one or more hot spots is given by:

$$F_{\geq 1} \equiv \mathbb{P}_{\geq 1} \times n \text{ (samples per year)} \tag{5.3}$$

where n is the number of independent pebble populations which occupy the zone of interest in one year. The fixed $\mathbb{P}_0$ level in Figure 5.10 is equivalent to a fixed probability per year of finding one or

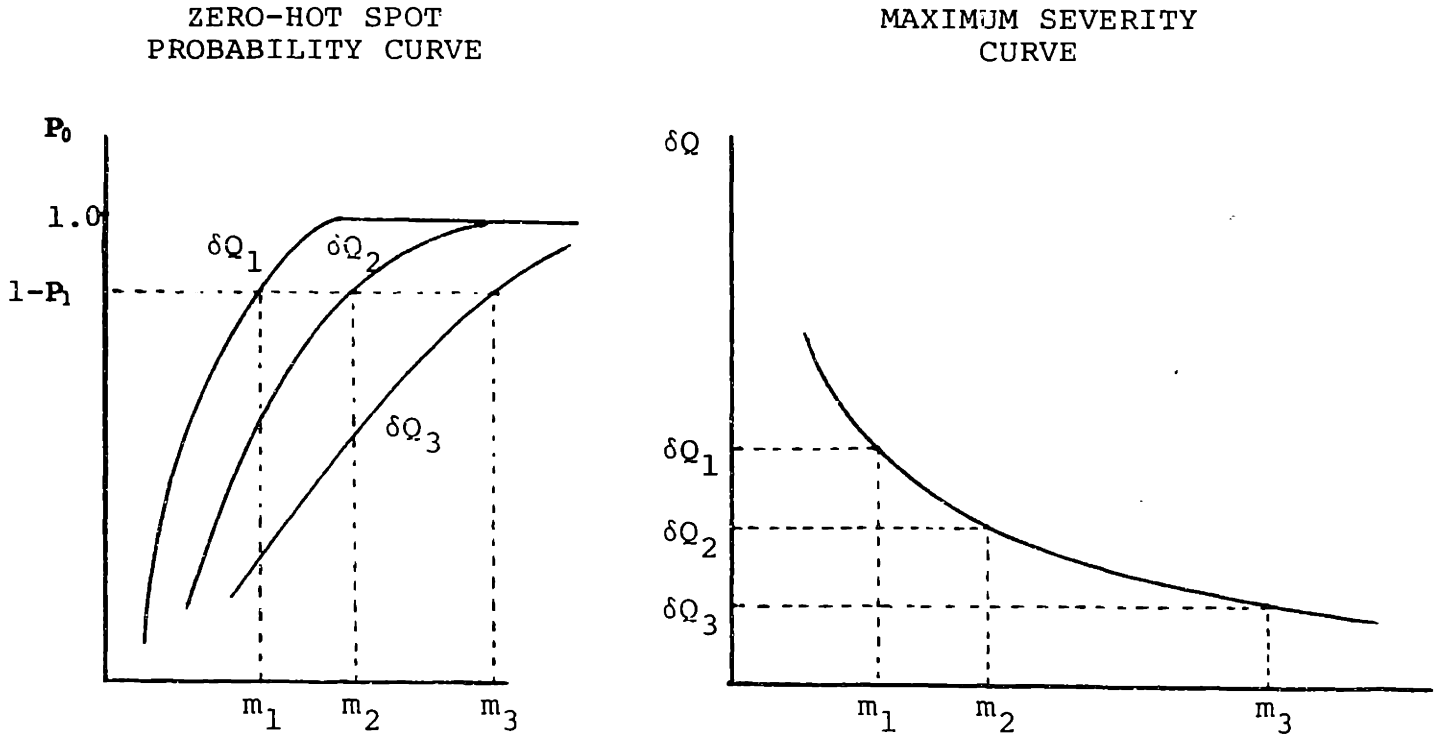

FIG. 5.10: Derivation of maximum severity curves.

more hot spots in the zone of interest. This analysis has been carried out for the base core, and results are presented in Figures 5.11 and 5.12. The difference between these plots and the severity plots presented in Chapter 4 is that geometric effects of pebble clumping are now accounted for. Three frequency level were selected (10^{-2}, 10^{-4}, and 10^{-6} per reactor year), and the maximum hot spot severity for power density Q^* (in Figure 5.11) or temperature θ^* (in Figure 5.12) at these frequencies is plotted as a function of hot spot size m. Higher severity levels than indicated in the figure are possible, but will occur at even lower frequencies. For small numbers of pebbles, the severity is limited by the maximum pebble power density within the zone. This applies for sub-volumes of five to ten pebbles. As expected, the severity at a fixed frequency decreases with increasing sub-volume size. For subvolumes of 50 pebbles, the hot spot severity at an annual frequency of 10^{-6} is about 1.4 W/cm^3 higher than the expected value, while for 120 pebbles the severity at this frequency is only about 0.7 W/cm^3 above expectation. The temperature severity plot (Figure 5.12) is quite similar. Note that for small numbers of pebbles, the temperature severity decrease due to conduction effects (see Figure 4.18) is not shown. If sub-volumes of greater size can exist at the same frequncy at higher severities, it is physically meaningless to say that small volumes cannot achieve the same severity. The "small" subvolume is present within the larger volume, even if it could not reach as high a temperature if surrounded by average pebbles.

An interesting feature of the maximum severity plots is the weak

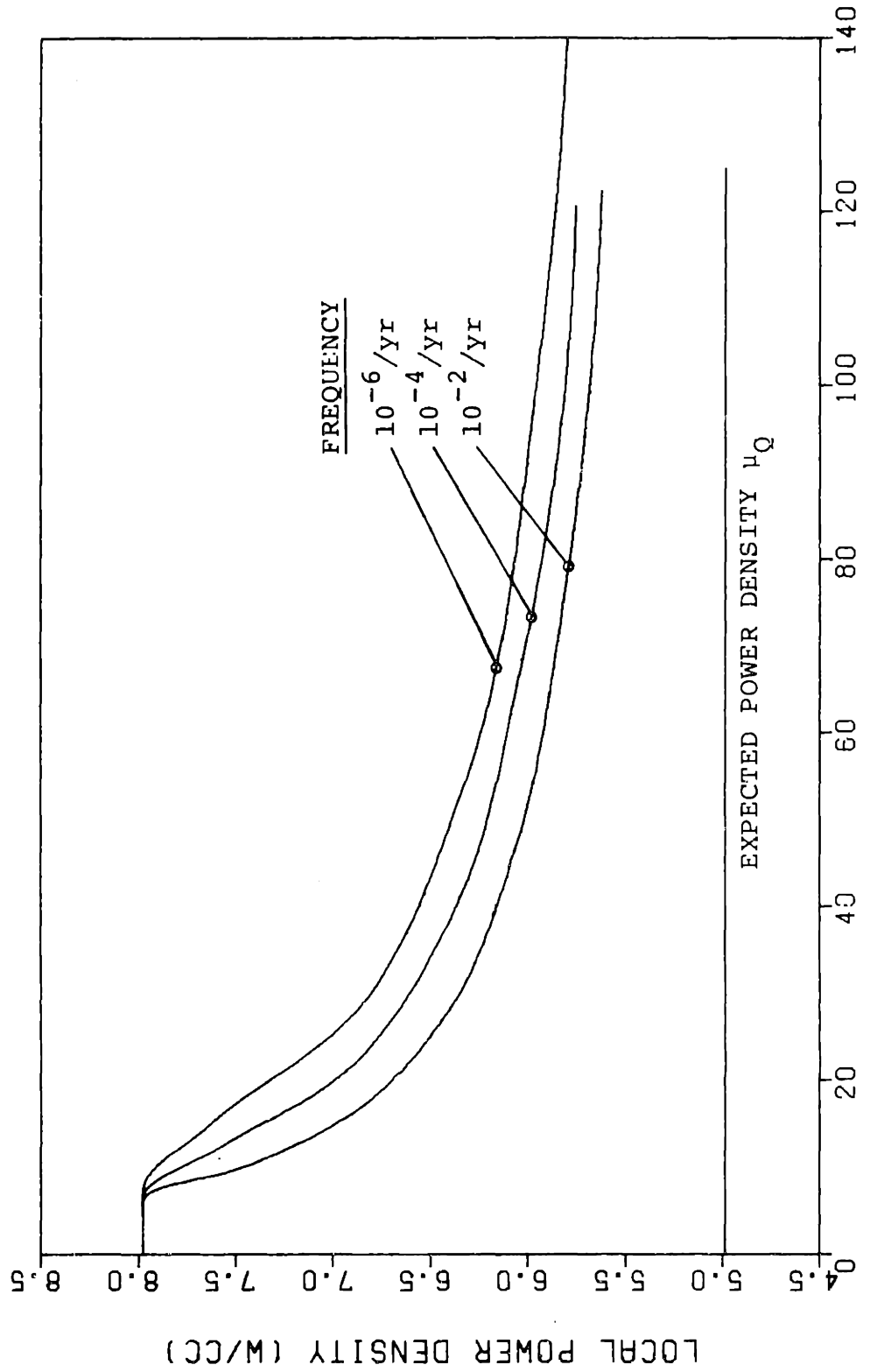

FIG. 5.11: Maximum hot spot severities in the base core's highest power density region.

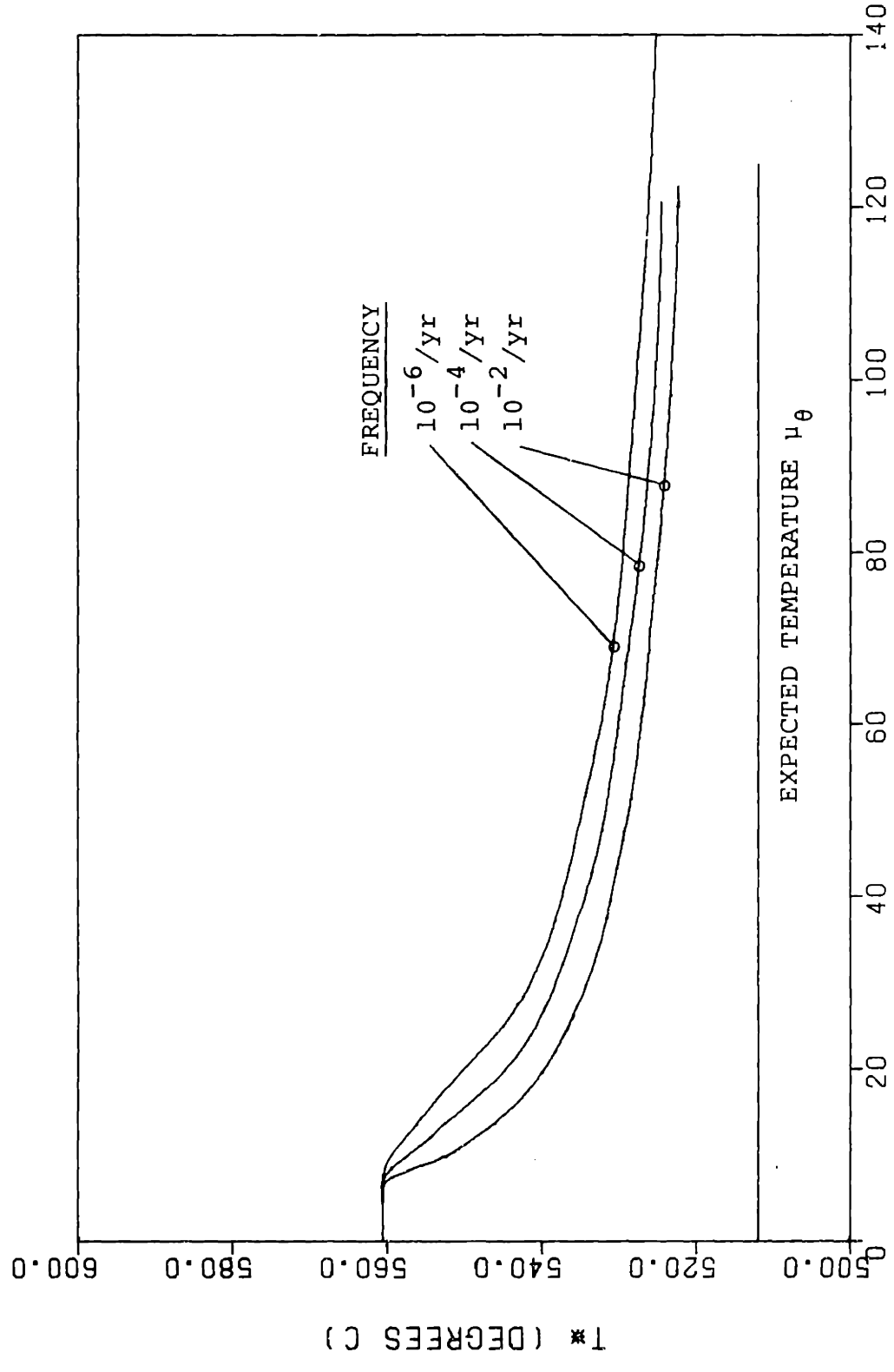

FIG. 5.12: Maximum hot spot severities in the base core's highest power density region

dependence on frequency. The curves span four orders of magnitude in frequency space, but the severity increase for large numbers of pebbles is only about 0.2 W/cm^3. The increase is more pronounced for smaller subvolumes, but always limited by the maximum pebble power density within the region. Extremely low frequencies are for large subvolumes to approach the maximum severity.

5.1.3. Analysis of a depressurized core heatup

The THERMIX/KONVEK computer code is a tool for thermal/hydraulic analysis of pebble bed reactor cores under a variety of conditions. It was developed at KFA Jülich, and has been extensively tested using model experiments. THERMIX itself solves unsteady heat conduction problems, but when used with the KONVEK program is able to model gas flow and heat transfer as well. Appendix D in this report and References B7 and V3 describe in more detail the operation of THERMIX/KONVEK. In this work, we accept results of the code as well proven and reliable.

The power density distribution calculated for the base core by FUPAR/VSOP was used as input to a THERMIX calculation of transient core temperatures following a postulated depressurization accident. The THERMIX simulation was run for approximately 100 hours, and fuel temperatures in each core zone were recorded as a function of time for use in fission product release calculations (see Chapters 6 and 7).

Figure 5.13 illustrates the temperatures of various parts of the core during the depressurization event. The maximum temperature in any FUPAR zone remains beneath 1500C at all times.

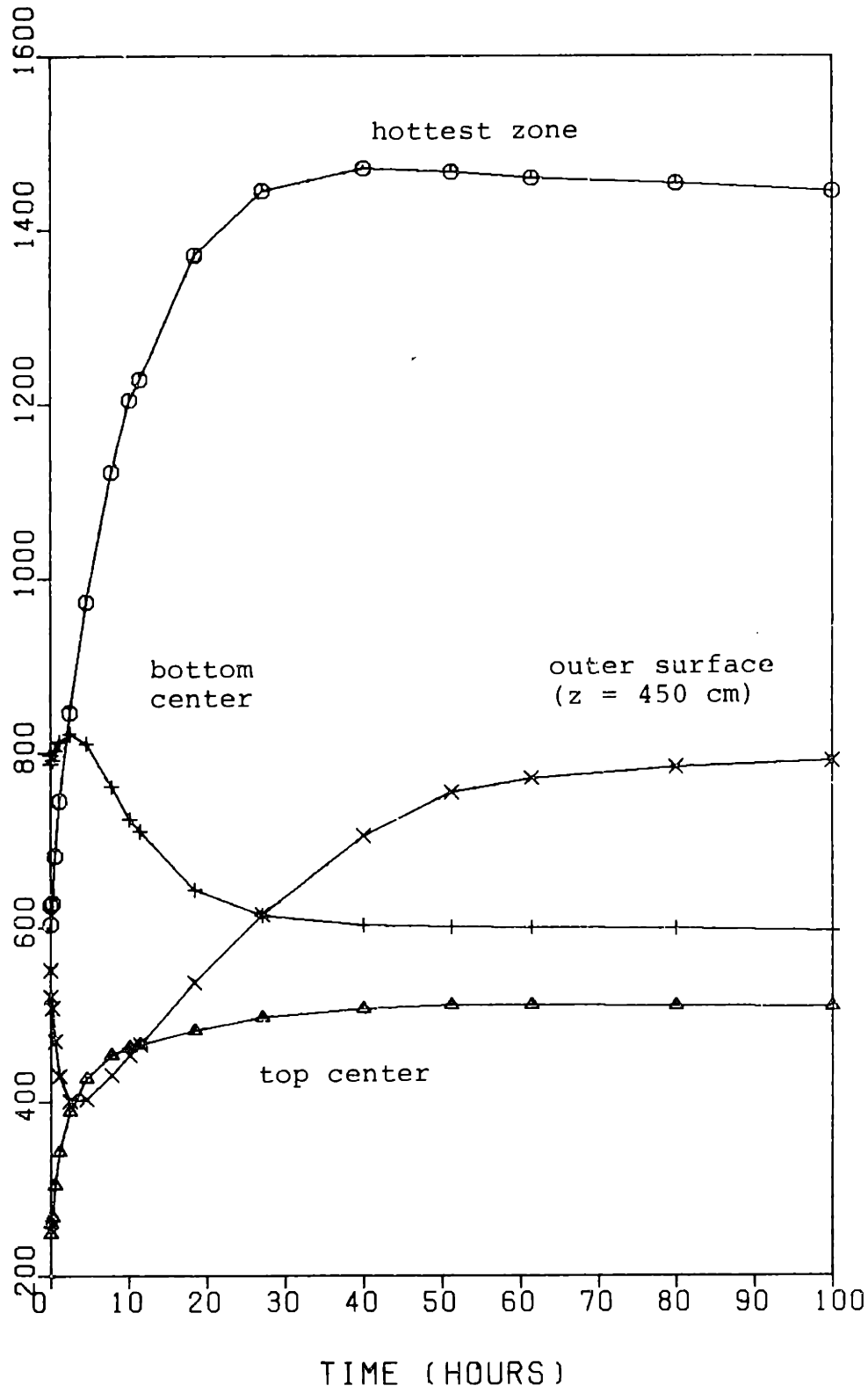

FIG. 5.13: Temperature behavior of the base core following a postulated depressurization accident.

5.2 A MODULAR HTGR CORE WITH GADOLIMIUM BURNABLE POISON

The first design variant addresses the problem of water ingress into the reactor core. These concerns are amplified for the pebble bed reactor, where exclusive use of reflector control rods limits the control margin. It is hoped that an additive might be found which, if included in fresh fuel elements, will change the core's neutronic properties to reduce the reactivity increase due to water. Therefore, the core analyzed here includes a small concentration of gadolinium oxide, or gadolinia, as a burnable poison. Hereafter, this design variant shall be referred to as the "poisoned core."

Figure 5.14 is a plot of the total neutron cross section for Gd-155 at thermal energies [B9]. Above approximately 0.04 eV , the energy dependence is steeper than 1/v. Since U-235 absorption is 1/v, and water ingress thermalizes the neutron energy spectrum, the addition of gadolinium could offset some of the positive reactivity due to water ingress.

Use of Gd_2O_3 has been investigated in the past as a means of increasing the discharge burnup of fuel from light water reactors [N5]. Fuel mixtures of uranium dioxide and gadolinia have been fabricated with up to 8 $^{w}/o$ Gd_2O_3. We assume that HTGR fuel with much lower concentrations of gadolinia (less than 0.1 $^{w}/o$) may be fabricated as well.

The poisoned core has input parameters identical to those of the base case reactor (see the previous section) with the exception of the

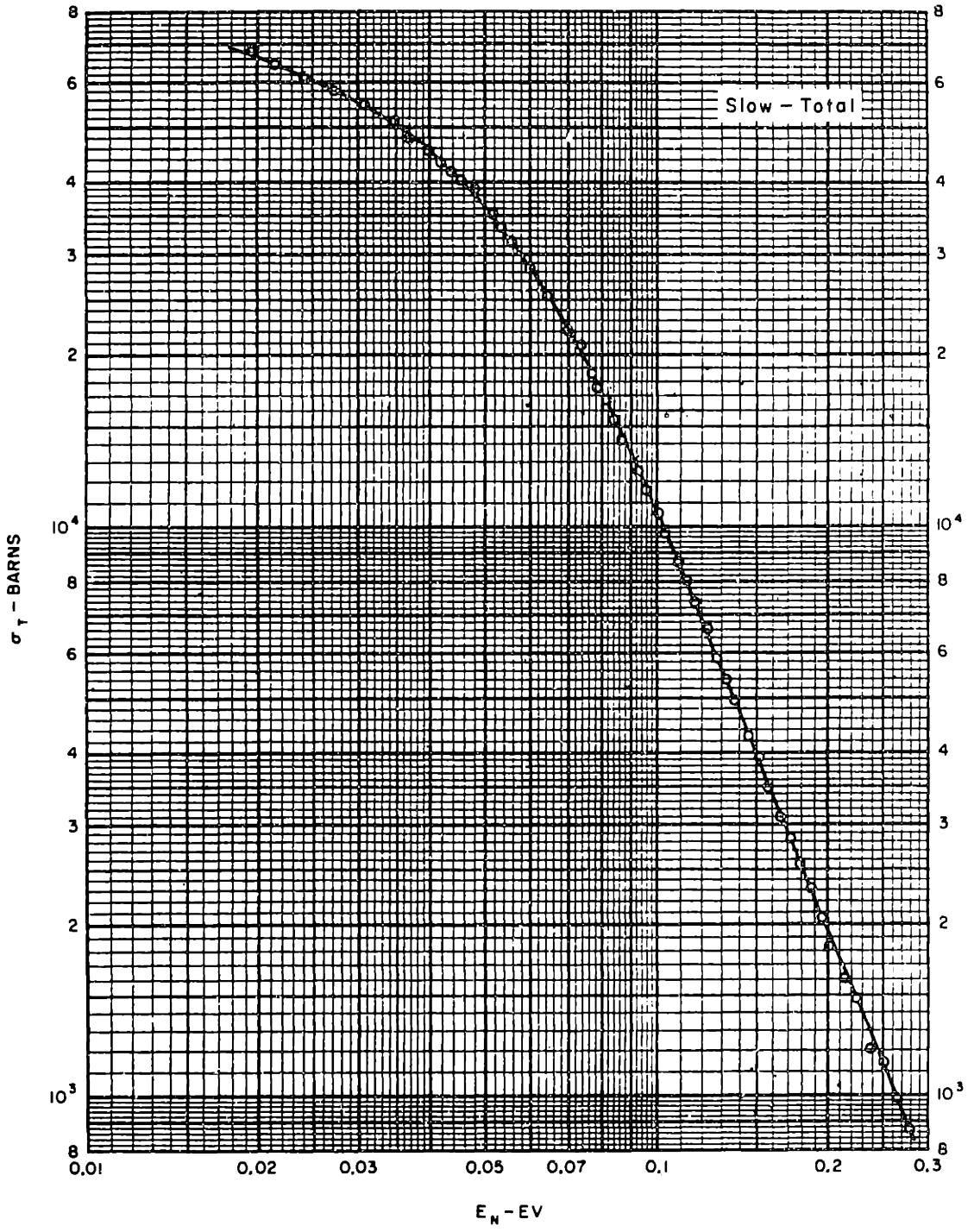

FIG. 5.14: Total neutron cross section for Gd-155 at thermal energies

burnable poison itself. The reactor analysis and a random hot-spot analysis are reviewed, and results from a thermal transient analysis are presented. The reactivity effects of water ingress in both the base core and the poisoned core are then compared.

5.2.1 Calculations

The same discretization as the base core was used for the poisoned reactor (see Figure 5.1). Convergence on a critical, equilibrium power and materials distribution proved more difficult with the poisoned core than the base core. Twenty five FUPAR/VSOP iterations were necessary, first to determine the critical feed enrichment, then to coverge on a stable power/materials distribution. FUPAR requires approximately (3.7×NPASS) CPU seconds to run (NPASS represents the maximum number of passes prior to fuel discharge), and VSOP/TIK requires about 45 seconds, so this analysis required $25\times[\ (3.7\times15) + 45\ ] \simeq 2500$ seconds or about 40 minutes of CPU time (on an IBM 3081 computer). This is still less than necessary to simulate the entire running-in period with VSOP alone, but points out the necessity of automating and optimizing FUPAR/VSOP iterations.

Figures 5.15 and 5.16 illustrate the axial power and Gd-155 number density distributions, respectively, during the final four iterations. These Figures illustrate the convergent properties of the iterations, even with a skewed power distribution.

5.2.2 Reactor operating parameters

Table 5.2 presents design parameters for the poisoned core. Figure 5.17 displays the axial distribution of power densities in the central

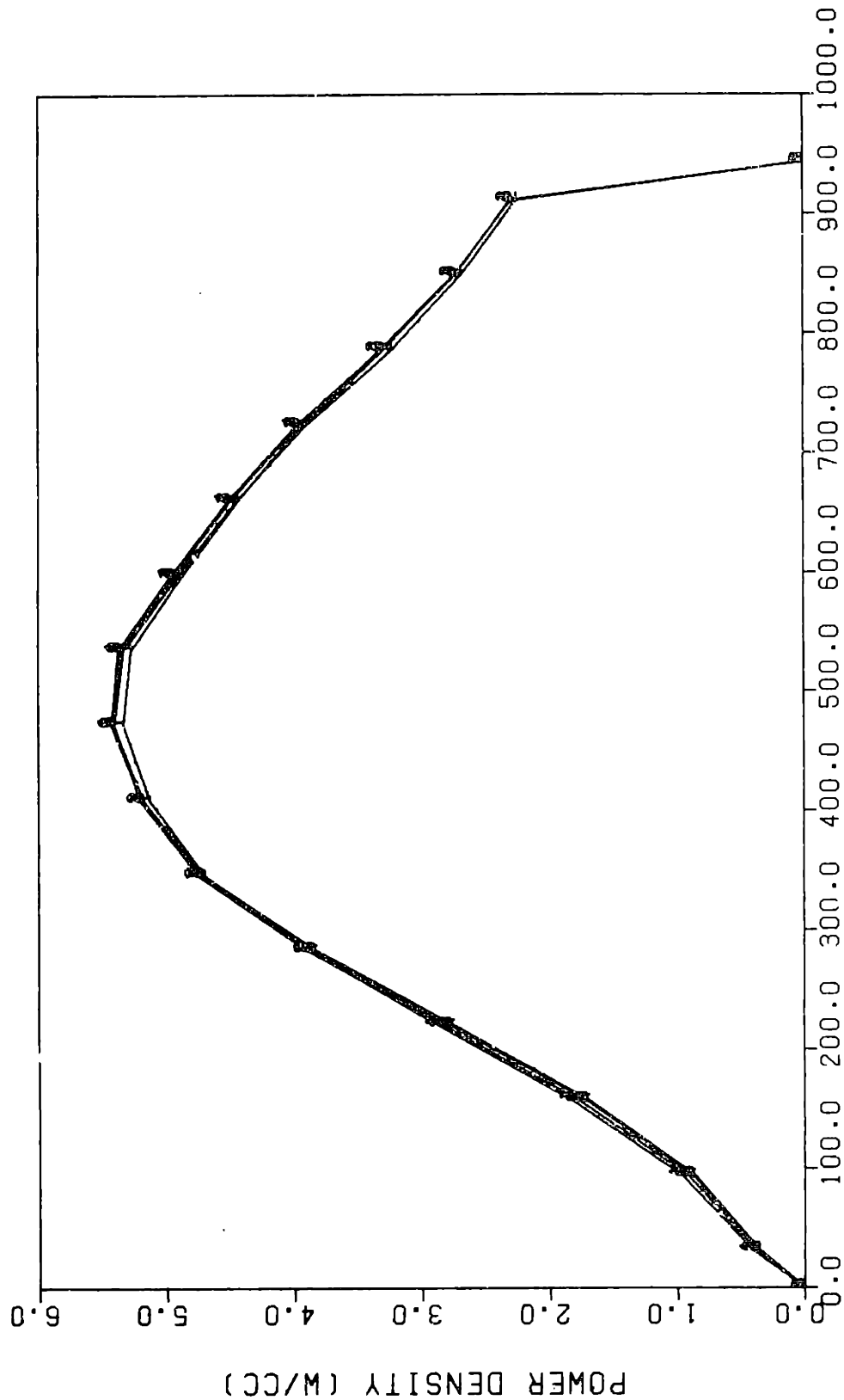

FIG. 5.15: Axial power density distribution in the poisonsed core as a function of iteration number.

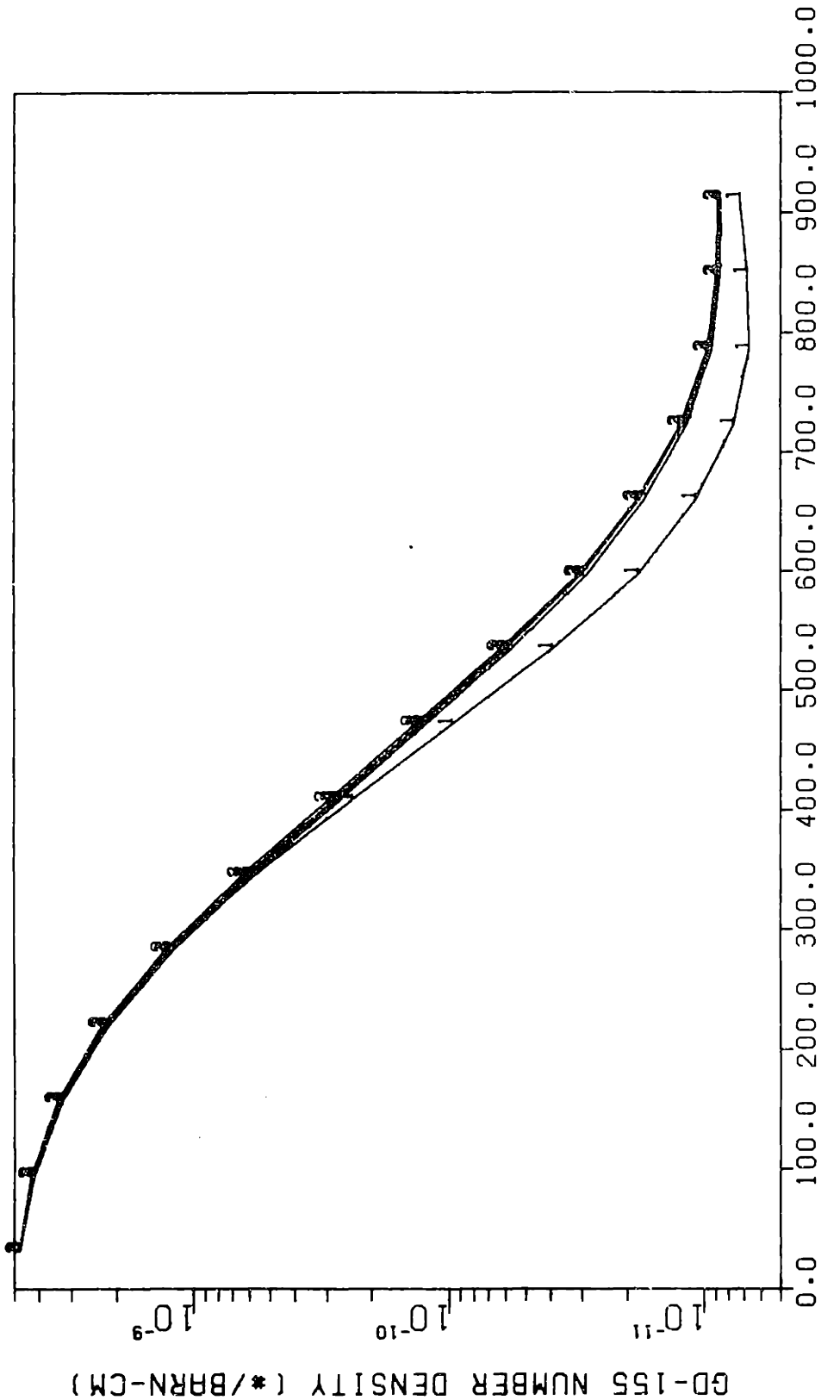

FIG. 5.16: Axial Gd-155 number density distribution in the poisoned core as a function of iteration number.

TABLE 5.2: PROPERTIES OF THE POISONED CORE

THERMAL POWER	200 MW
CORE DIAMETER	300 cm
MEAN CORE HEIGHT	943 cm
AVERAGE POWER DENSITY	3.0 W/cm^3
HELIUM TEMPERATURE	200/700 ^oC
SYSTEM PRESSURE	40 bar
CORE PRESSURE DROP	0.94 bar
FUEL CYCLE	U-Pu
NUMBER OF FUEL ELEMENTS	360,000
NUMBER OF PASSES	15
FRESH FUEL INJECTION RATE	346 pebble/day
ENRICHMENT	7.3 %
HEAVY METAL LOADING PER FUEL ELEMENT	7 g
CORE K-EFFECTIVE (UNRODDED)	1.0021
AVERAGE DISCHARGE BURNUP	82,700 MWD/MT

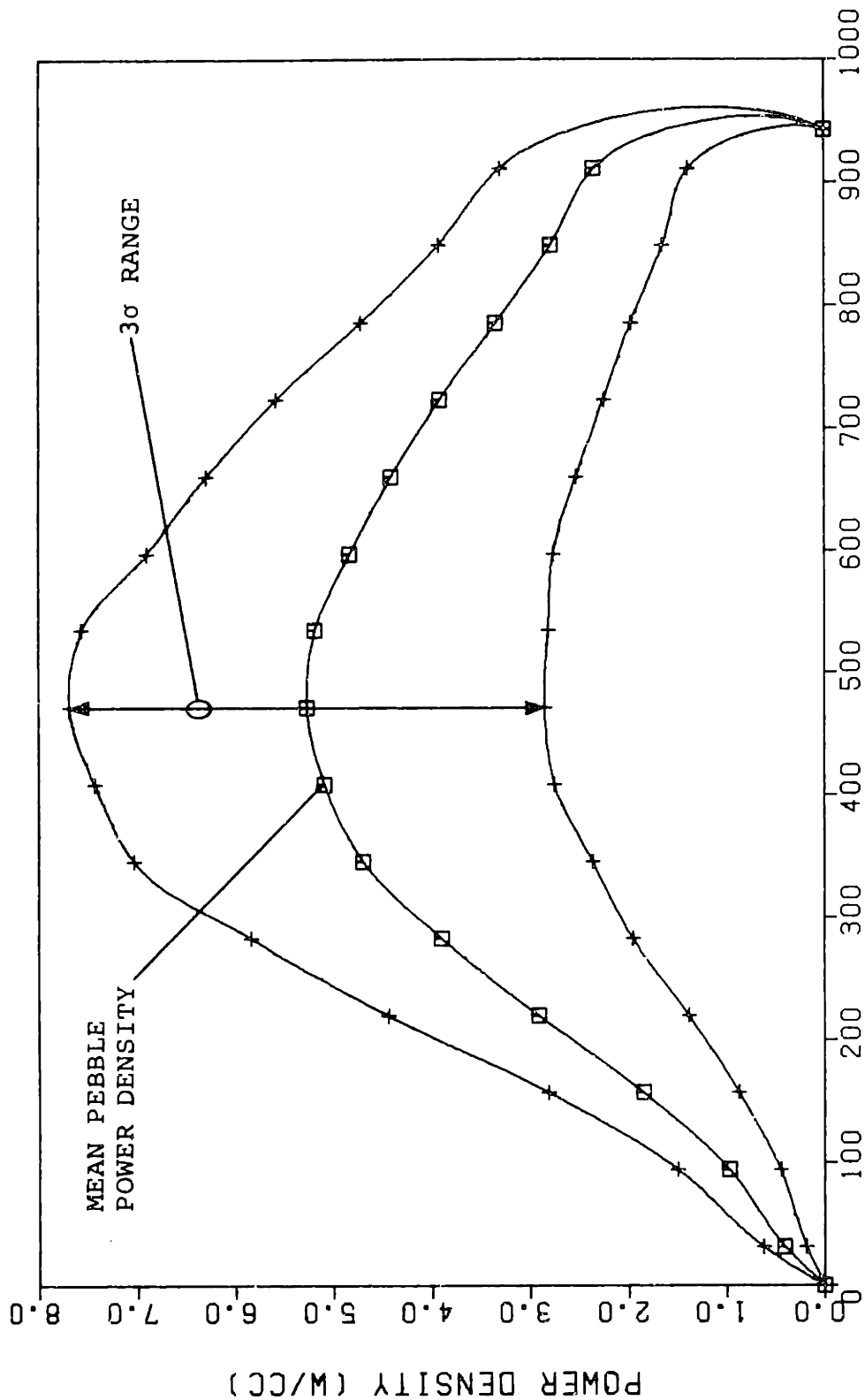

FIG. 5.17: Axial power density and power density standard deviation distribution in the poisoned core.

core zone, along with a 3σ range indicating the power density standard deviation. Figure 5.18 shows the core-wide distribution of power density means and standard deviations. The prominent feature is the location and magnitude of the peak power density region. It is shifted down two core regions from the base core to FUPAR zone (8,1), and has increased to 5.27 W/cm^3 (from 5.0 W/cm^3 in the base core). Both effects are due to power density depression in the upper core due to large gadolinium concentrations. Increased maximum power density is significant for both post depressurization temperatures and hot spot severity.

Figure 5.19 presents pass-dependent mean power densities in the hottest zone, along with the pass-dependent power density standard deviations represented by 3σ error bars about the mean values. The highest pebble power density is 8.34 W/cm^3 (homogenized), compared to 7.96 W/cm^3 in the base core. The ratio of partitioned variances (between pass/within pass) is R = 415. As in the previous base core, this justifies use of the Q2D approximation in the reactor analysis.

Figure 5.20 compares the axial temperature distributions in the poisoned and base cores, and Figure 5.21 shows the poisoned core's overall temperature distribution. The downward shift of the peak power region in the poisoned core results in a significant difference from the base core temperatures. Much of the poisoned core operates at lower temperatures than the base core. The result is a reactivity "bonus" due to decreased resonance absorption in U-238. The magnitude of the temperature reactivity increase is approximately equal to the penalty

z \ r	1	2	3	4	5
1	0.410 (0.247)	0.374 (0.134)	0.343 (0.123)	0.324 (0.116)	0.326 (0.116)
2	0.975 (0.348)	0.890 (0.318)	0.817 (0.292)	0.771 (0.275)	0.775 (0.276)
3	1.848 (0.647)	1.687 (0.591)	1.549 (0.543)	1.462 (0.512)	1.469 (0.514)
4	2.916 (1.020)	2.664 (0.932)	2.447 (0.856)	2.309 (0.808)	2.318 (0.811)
5	3.899 (1.294)	3.563 (1.184)	3.273 (1.088)	3.086 (1.026)	3.094 (1.030)
6	4.700 (1.556)	4.297 (1.424)	3.948 (1.310)	3.720 (1.237)	3.721 (1.241)
7	5.093 (1.562)	4.658 (1.430)	4.277 (1.316)	4.024 (1.242)	4.011 (1.246)
8	5.272 (1.613)	4.824 (1.478)	4.429 (1.361)	4.161 (1.286)	4.136 (1.290)
9	5.193 (1.583)	4.753 (1.453)	4.364 (1.339)	4.094 (1.265)	4.057 (1.269)
10	4.832 (1.378)	4.423 (1.264)	4.057 (1.166)	3.798 (1.101)	3.747 (1.104)
11	4.414 (1.256)	4.042 (1.154)	3.707 (1.064)	3.465 (1.006)	3.408 (1.008)
12	3.917 (1.111)	3.587 (1.021)	3.289 (0.943)	3.071 (0.892)	3.012 (0.894)
13	3.347 (0.916)	3.064 (0.843)	2.808 (0.778)	2.617 (0.736)	2.559 (0.737)
14	2.790 (0.762)	2.555 (0.701)	2.341 (0.648)	2.180 (0.613)	2.127 (0.614)
15	2.350 (0.639)	2.152 (0.588)	1.972 (0.544)	1.835 (0.515)	1.791 (0.517)

FIG. 5.18: Power density and power density (standard deviation) distribution in the poisoned core.

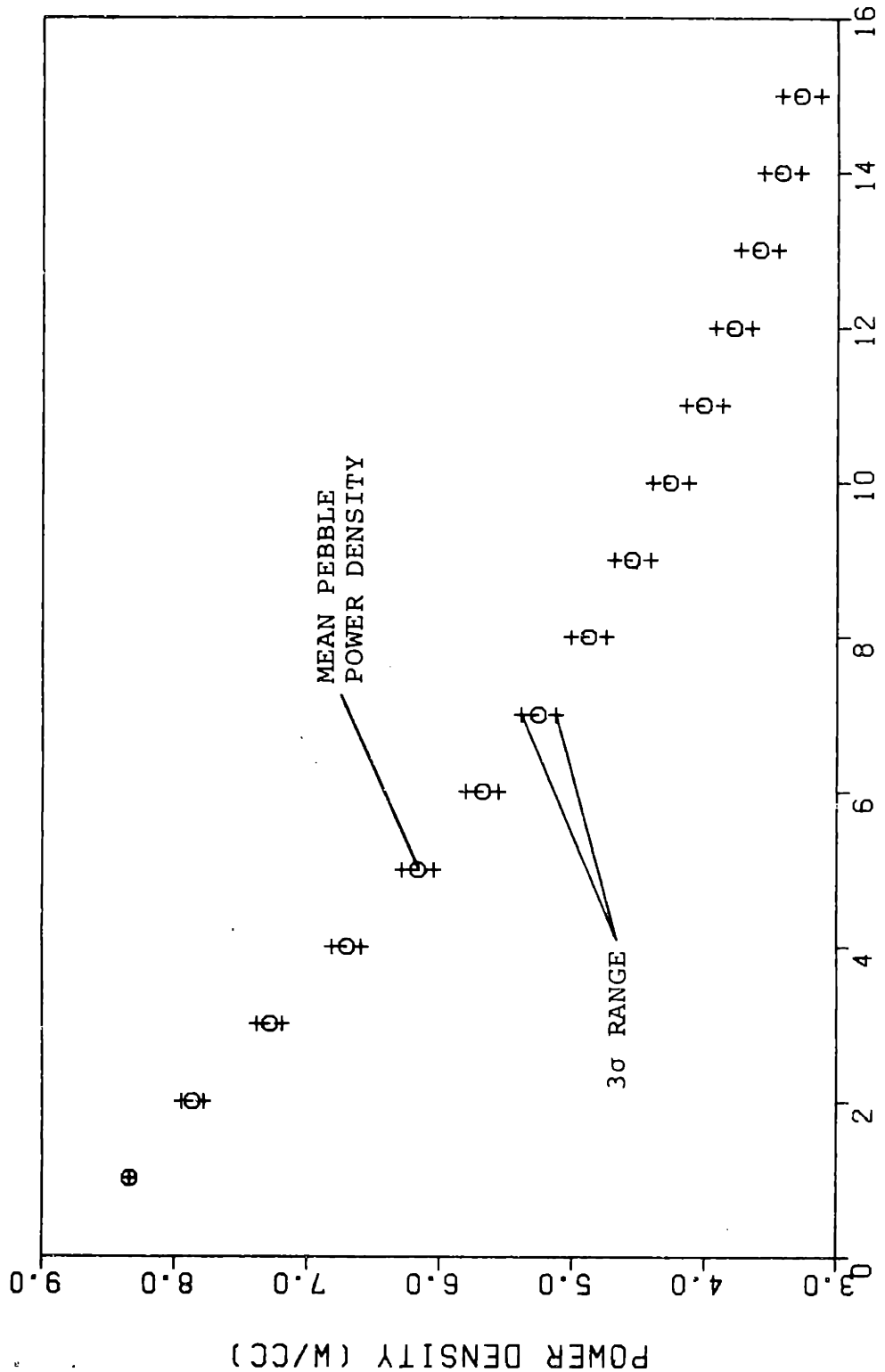

FIG. 5.19: Pass-dependent power density and power density standard deviation in the high power zone of the poisoned core.

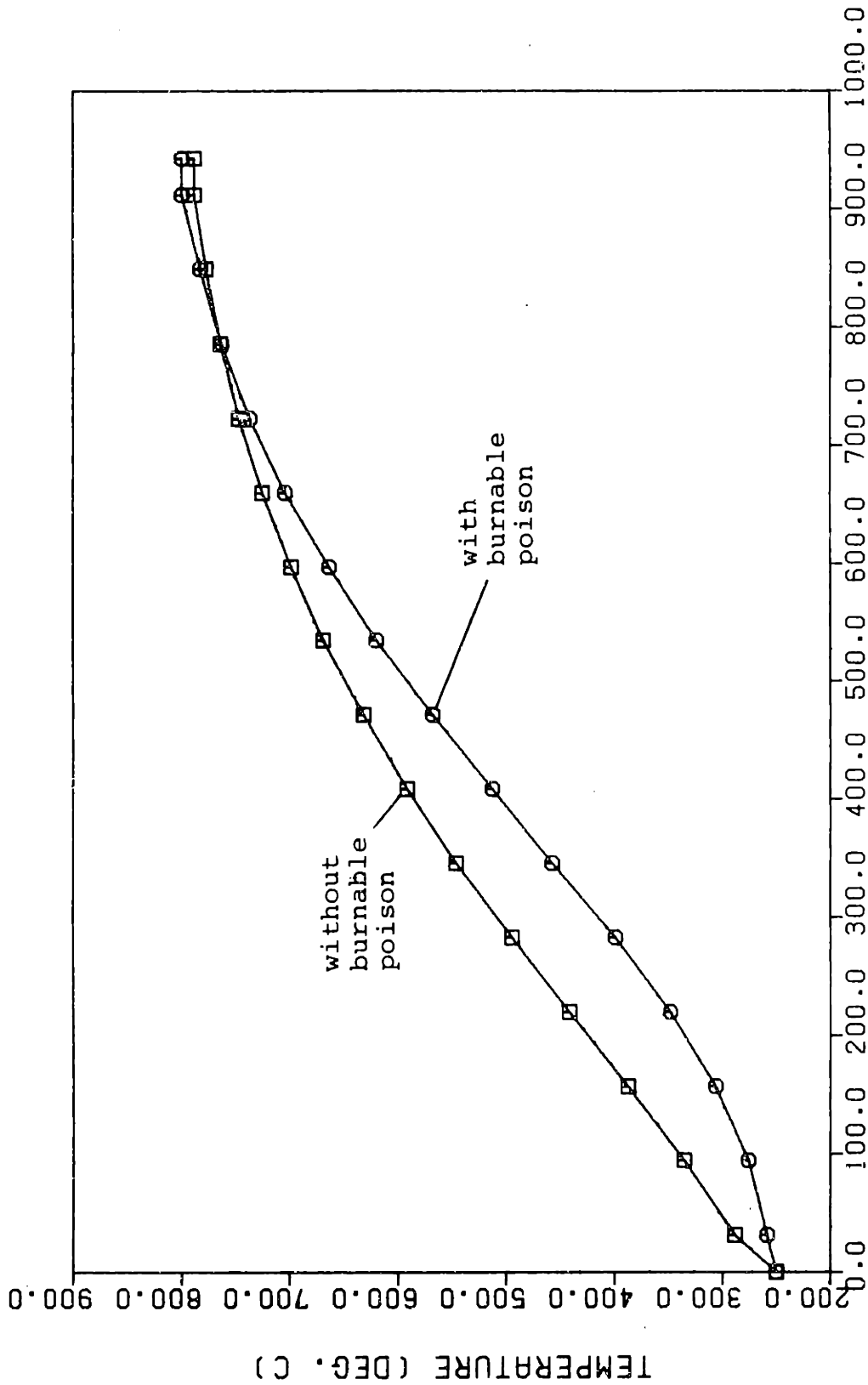

FIG. 5.20: Axial temperature profile in the poisoned core.

z \ r	1	2	3	4	5
1	259	259	258	258	258
2	276	274	272	271	271
3	306	301	297	294	294
4	348	340	332	328	328
5	399	386	375	369	368
6	457	439	423	414	413
7	513	490	470	458	457
8	568	540	516	502	499
9	620	587	559	543	539
0	664	627	596	578	573
11	704	663	629	609	603
12	737	693	657	635	628
13	763	716	679	656	649
14	783	735	697	674	665
15	800	751	712	688	680

FIG. 5.21: Core-wide temperature distribution (^{o}C) in the poisoned core.

for the gadolinia. The converged k_{eff} in the poisoned core was less than the base core, but still greater than 1.0. Thus, though the gadolinium decreases the core's reactivity, the critical feed enrichment for the poisoned core was not altered from the base core. The effects of gadolinium on the reactivity response to water ingress may thus be examined in isolation increased enrichment effects.

Random hot spot analysis on the poisoned core yields results similar to the base core's. Severities in the poisoned core are somewhat higher due to the increased maximum power density. Figure 5.22 shows the zero hot spot probabilities for the high power zone, and Figures 5.23 and 5.24 present the same information in a maximum severity plot. The general features of the curves have not changed: limiting severities are still determined by the maximum pebble power density in the region, and for large numbers of pebbles the maximum severity is a weak function of frequency.

5.2.3. Analysis of a depressurized core heatup

Results of a THERMIX analysis of a depressurized core heatup accident are displayed in Figure 5.25. Performance in this respect is noticeably worse than for the base core. The average temperature in the hottest core zone exceeds 1600C for roughly 50 hours of the transient. Temperatures in the other indicated locations behave in roughly the same way, however, indicating average core temperatures are similar.

Peak power density plays an important role in determining peak accident temperatures. Conduction is a relatively slow process in the pebble bed, and decay heat is deposited more quickly than it can be

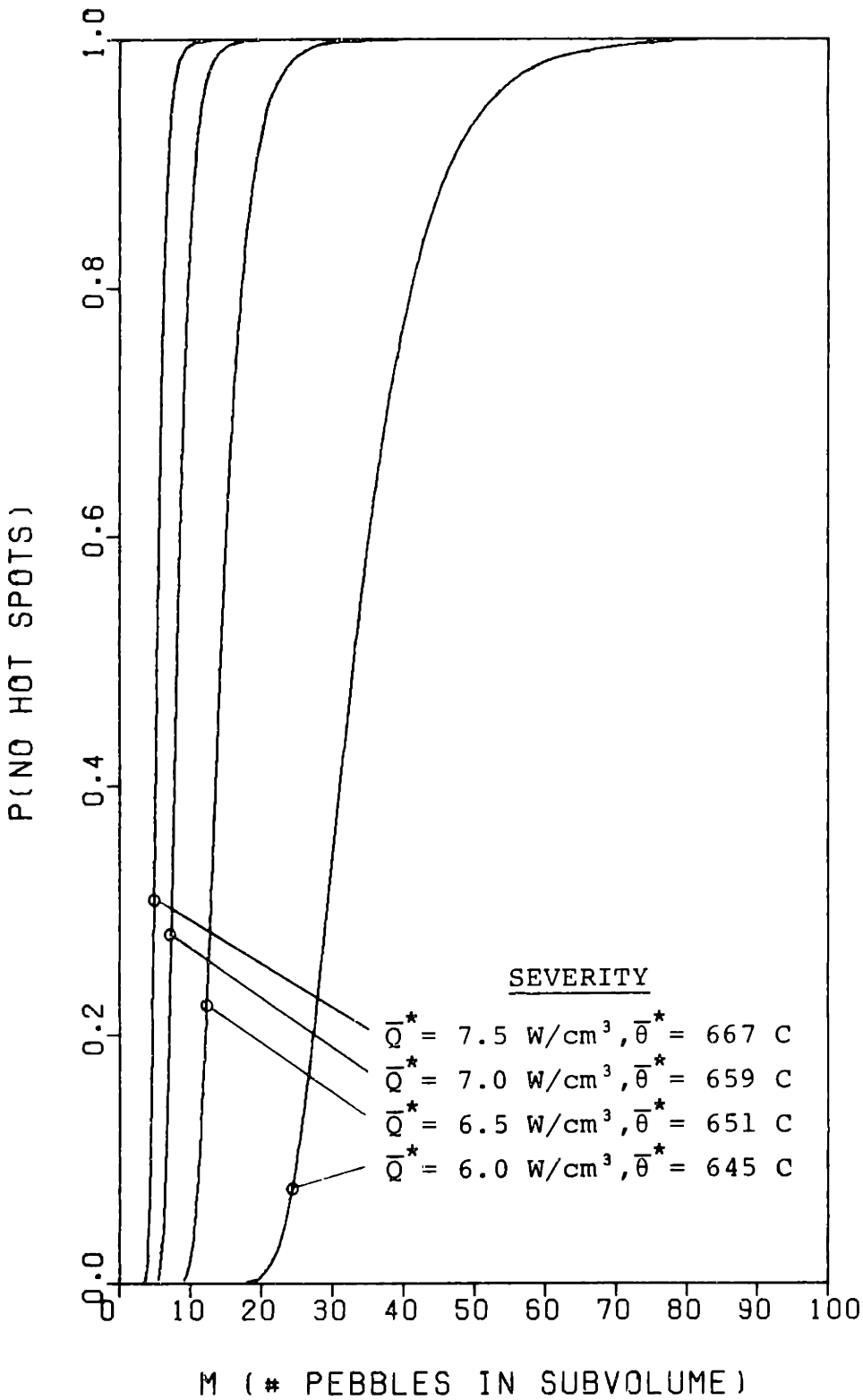

FIG. 5.22: **Zero hot spot probabilities in the poisoned core's high power density zone.**

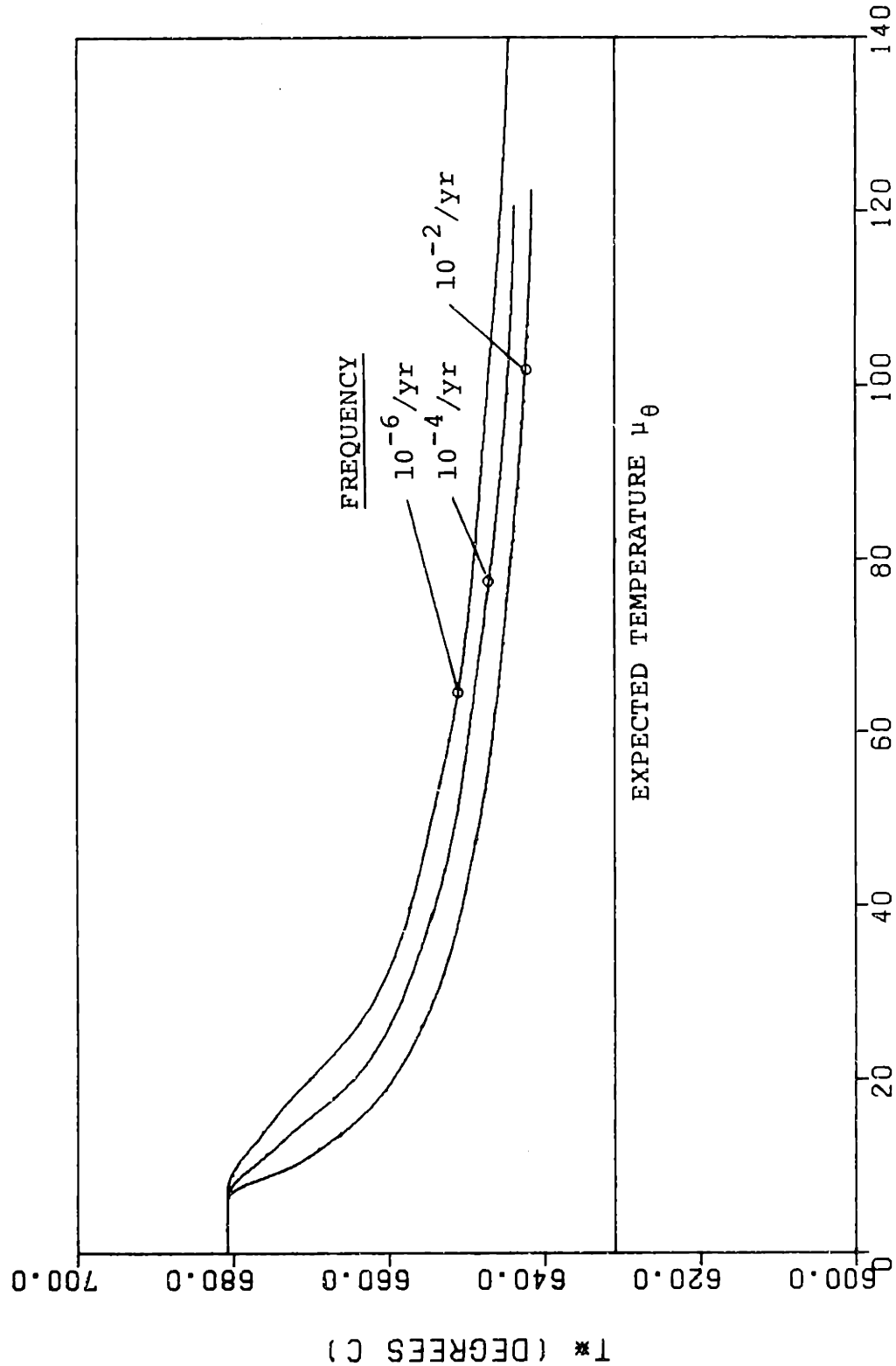

FIG. 5.23: Maximum hot spot severities in the poisoned core's high power zone.

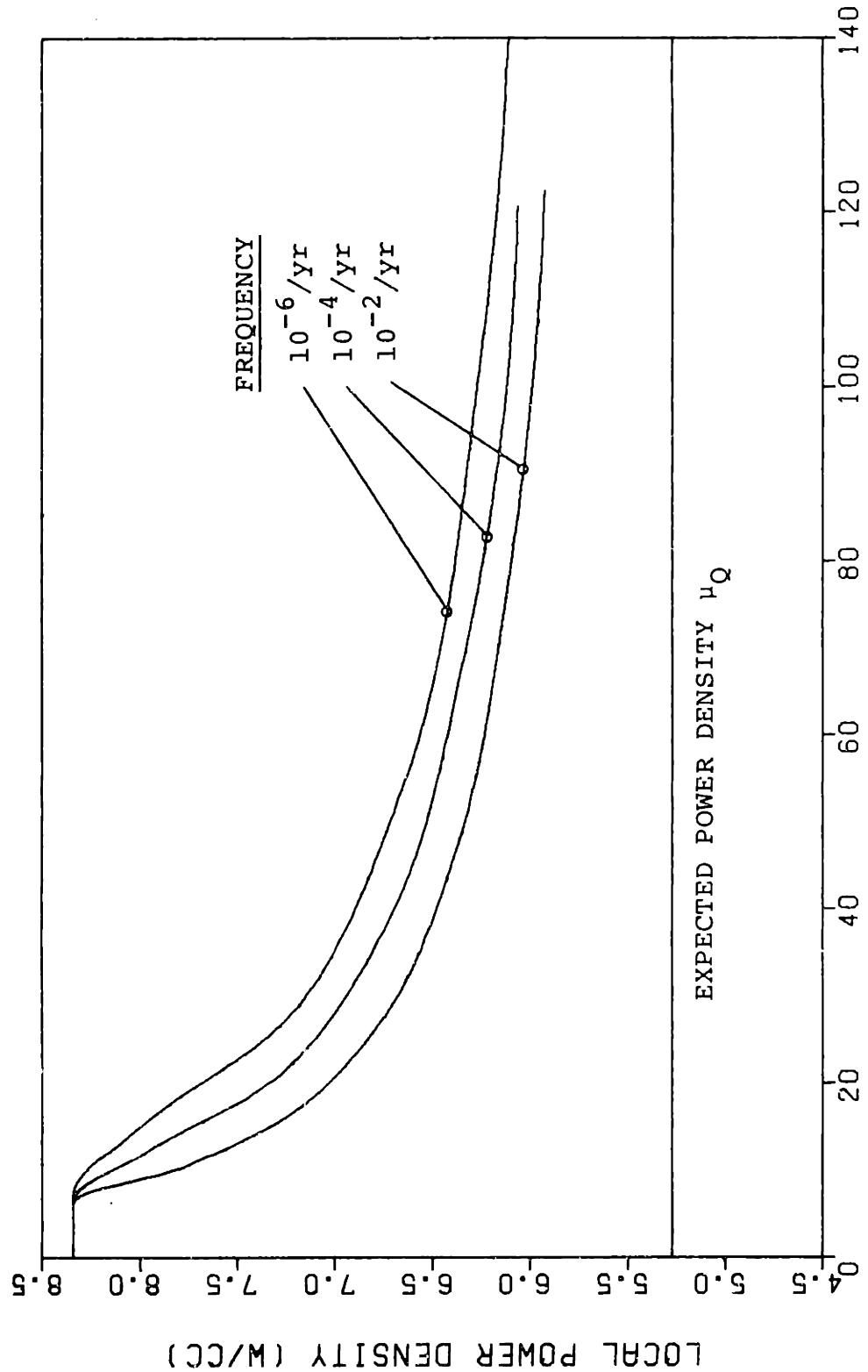

FIG. 5.24: Maximum hot spot severities in the poisoned core's high power zone.

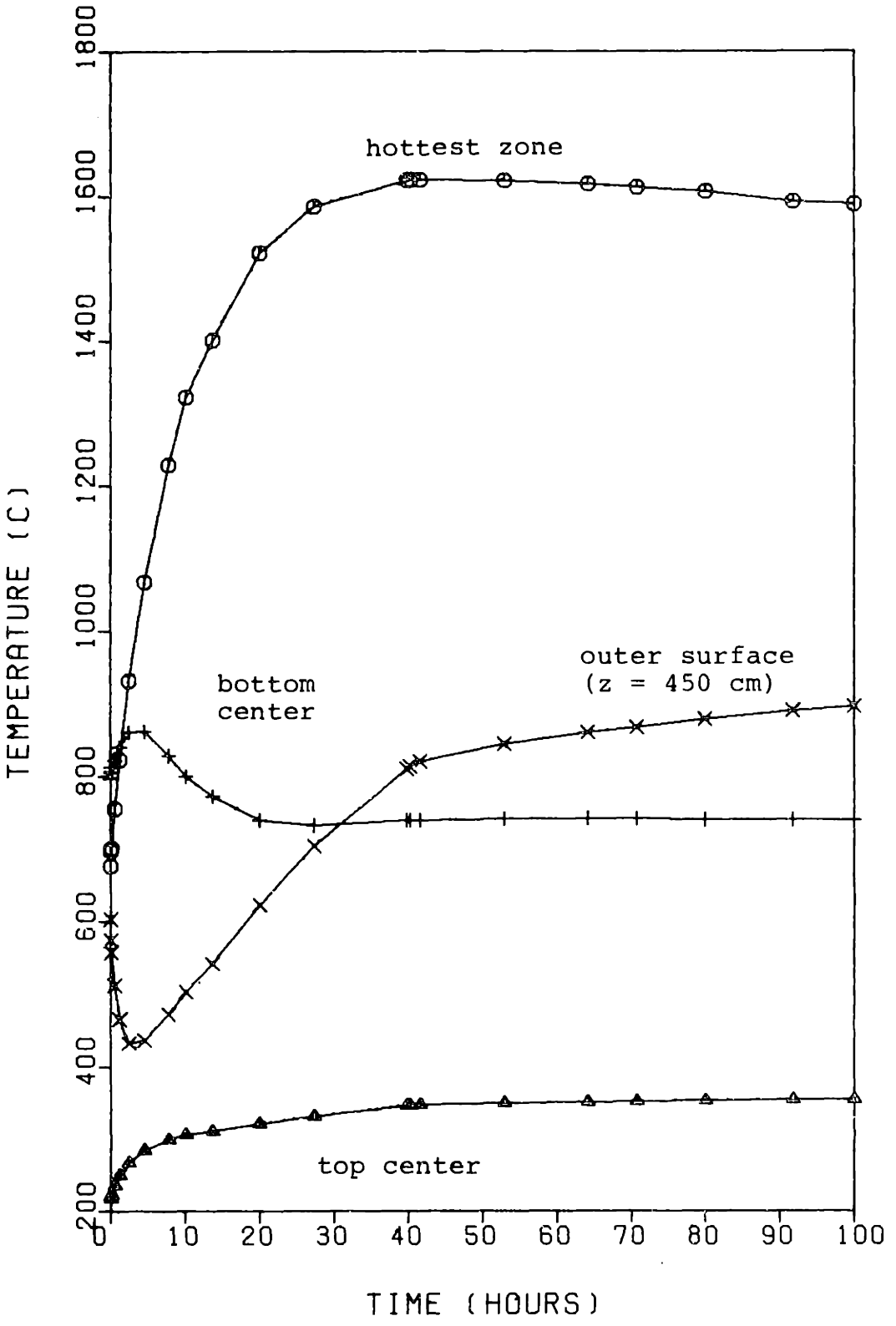

FIG. 5.25: Temperature behavior of the poisoned core following a postulated depressurization accident.

transported away from the high power regions. Though the initial temperatures of the poisoned core are less than or equal to those in the base core, peak accident temepratures are 150 C higher.

5.2.4 Effects of water ingress

The reactivity effects of water ingress on the base and poisoned cores are studied using the critical equilibrium materials distributions calculated by FUPAR/VSOP. Various concentrations of water are added uniformly over the volumes of both cores. VSOP analyzes the k_{eff} of the wet reactors, and the result is compared to the k_{eff} calculated for the dry equilibrium reactor. Figure 5.26 compares the change in k_{eff} for the base and poisoned cores over a range of water ingress.

The magnitude of the reactivity increase in both cores is relatively small compared to other published results due to the lower U-235 enrichment of the cores. Maximum reactivity increase in both cases is only about 2.4% Δk for about 700 kg of water entering the core. As expected, gadolinium decreases the reactivity rise in the poisoned core, but the difference is very small (only about 0.3% Δk for the maximum amount of water).

The disappointing magnitude of the gadolinium effect is due to two factors:

(1) The gadolinium is expended very quickly as the fuel is irradiated (see Figure 5.16). The overall increase in the reactor's average gadolinium concentration is not very great.

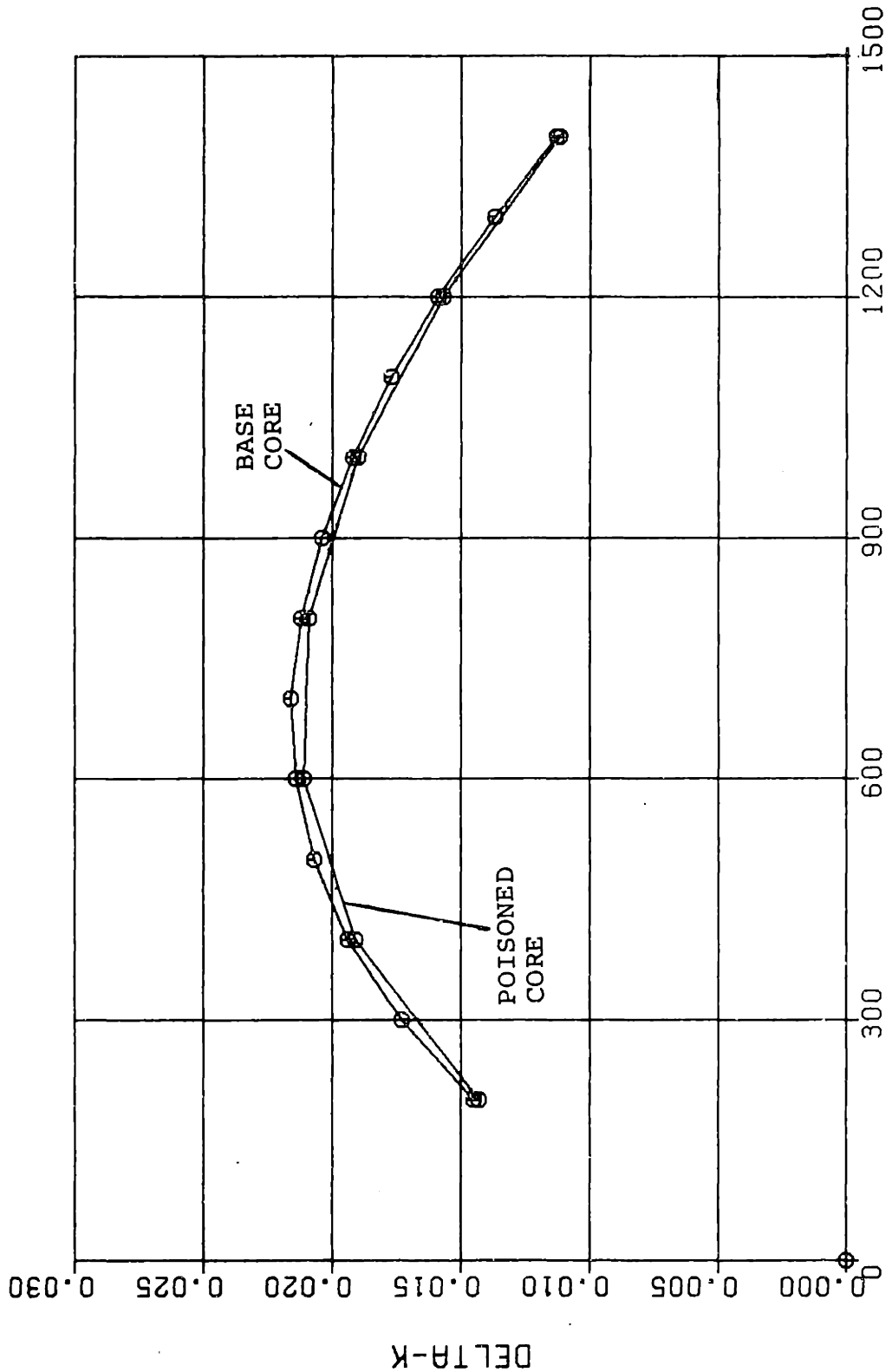

FIG. 5.26: Reactivity effects of water ingress on the base and poisoned cores.

(2) The parts of the reactor which do have high gadolinium concentrations are grouped together at the core entrance. Much of the contiguous reactor volume is not changed from the base core.

More work is necessary to judge the true worth of gadolinium as a burnable poison, and to investigate other poisons as well. In particular, proper modelling of lumped poison effects will change the rate at which the poison is predicted to burn out. The core average concentration and the distribution of the poison will be higher and more uniform in this case. Consideration must be given as well to the effects of the poison on the power density distribution, so that excess temperatures are not predicted for depressurization accidents.

5.3: A MODULAR HTGR CORE FOR DIRECT CYCLE GAS TURBINE APPLICATION

Application of an MHTGR as part of a direct cycle gas turbine system is a topic of current interest. Increased efficiency and modularity may improve the economic performance of the power system. A gas turbine requires higher reactor coolant temperatures and flow rates than the steam cycle, with gas inlet/exit temperatures of 600/850 C. The goal here is to evaluate the effects of high temperature operation on reactor performance. The direct cycle core shall be referred to as the "DCGT core" in the following sections.

5.3.1. Calculations

The DCGT core is much more closely related to the base core than is the poisoned core. Convergence on a critical, equilibrium power density and materials distribution required only five FUPAR/VSOP iterations, starting from the base core's equilibrium power shape. Thus, the computer time necessary to perform this analysis was only 5×[(3.5×15) + 45] = 500 seconds or about 8 CPU minutes.

5.3.2 Reactor operating parameters

Table 5.3 presents design parameters for the DCGT core. Note that enrichment is increased to 7.5% to compensate for increased resonance absorption at higher core temperatures. Another parameter of interest is the core pressure drop, which has increased by a factor of four to approximately 4 bars.

Figure 5.27 presents the axial power density and power density standard deviation distribution, and Figure 5.28 displays the core-wide

TABLE 5.3: PROPERTIES OF THE DOGT CORE

THERMAL POWER	200 MW
CORE DIAMETER	300 cm
MEAN CORE HEIGHT	943 cm
AVERAGE POWER DENSITY	3.0 W/cm^3
HELIUM TEMPERATURE	600/850 ^oC
SYSTEM PRESSURE	40 bar
CORE PRESSURE DROP	4.03 bar
FUEL CYCLE	U-Pu
NUMBER OF FUEL ELEMENTS	358,000
NUMBER OF PASSES	15
FRESH FUEL INJECTION RATE	346 pebble/day
ENRICHMENT	7.5 %
HEAVY METAL LOADING PER FUEL ELEMENT	7 g
CORE K-EFFECTIVE (UNRODDED)	1.0057
AVERAGE DISCHARGE BURNUP	82,500 MWD/MT

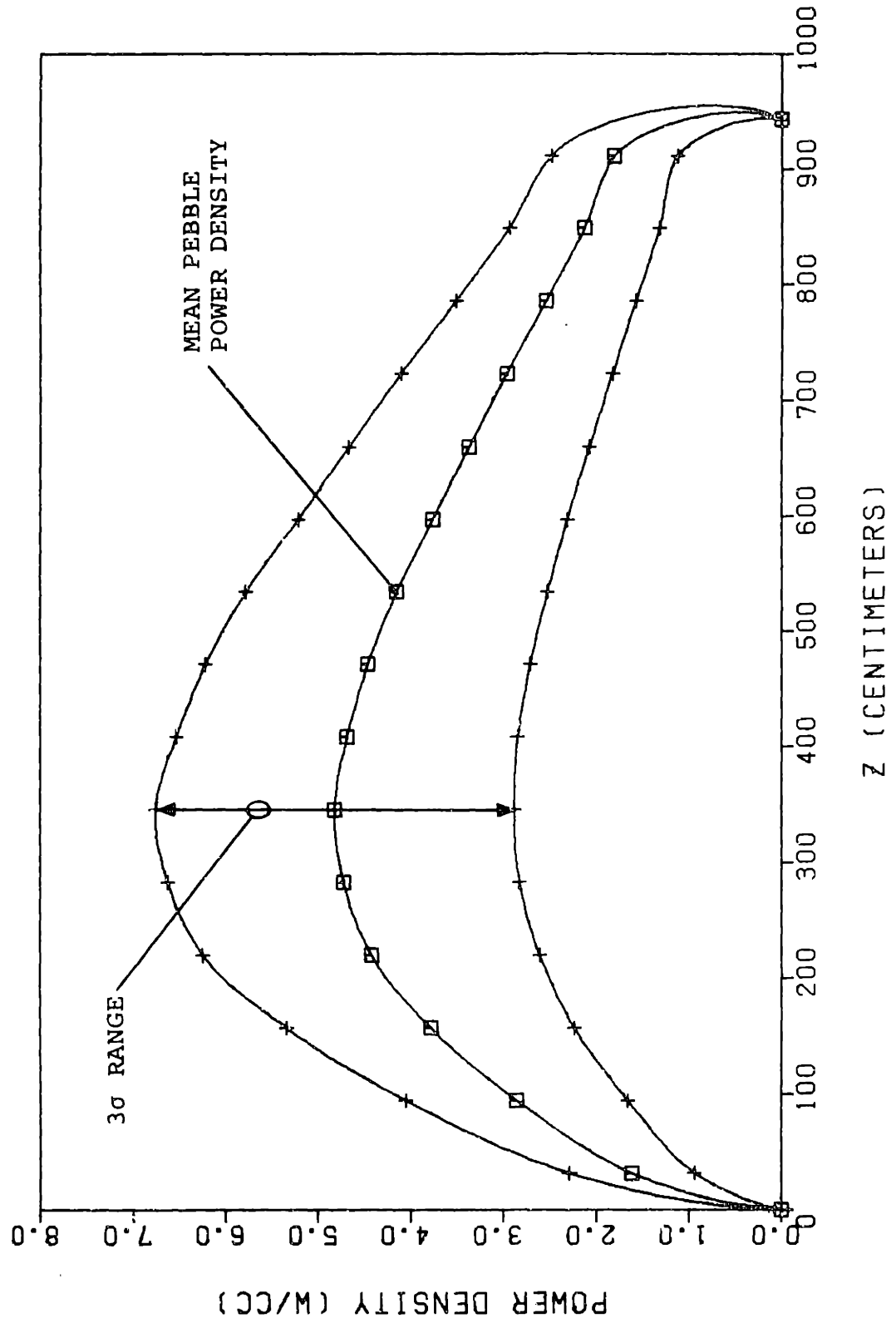

FIG. 5.27: Axial power density and power density standard deviation distributions in the DCGT core.

z \ r	1	2	3	4	5
1	1.613 (0.450)	1.476 (0.412)	1.359 (0.379)	1.285 (0.357)	1.292 (0 358)
2	2.858 (0.799)	2.616 (0.731)	2.408 (0.672)	2.276 (0.634)	2.285 (0.635)
3	3.790 (1.034)	3.471 (0.946)	3.195 (0.870)	3.017 (0.821)	3.023 (0.822)
4	4.431 (1.211)	4.060 (1.109)	3.736 (1.020)	3.524 (0.962)	3.523 (0.964)
5	4.731 (1.265)	4.335 (1.159)	3.987 (1.066)	3.756 (1.006)	3.743 (1.007)
6	4.826 (1.290)	4.423 (1.182)	4.067 (1.088)	3.825 (1.027)	3.800 (1.028)
7	4.692 (1.229)	4.300 (1.127)	3.951 (1.038)	3.709 (0.979)	3.672 (0.980)
8	4.468 (1.168)	4.095 (1.072)	3.762 (0.988)	3.526 (0.933)	3.480 (0.933)
9	4.158 (1.085)	3.811 (0.996)	3.499 (0.918)	3.275 (0.867)	3.223 (0.868)
10	3.769 (0.968)	3.455 (0.889)	3.171 (0.820)	2.963 (0.775)	2.907 (0.776)
11	3.376 (0.895)	3.094 (0.795)	2.839 (0.734)	2.650 (0.693)	2.594 (0.694)
12	2.969 (0.759)	2.722 (0.698)	2.496 (0.644)	2.328 (0.609)	2.274 (0.609)
13	2.548 (0.646)	2.336 (0.594)	2.141 (0.549)	1.995 (0.519)	1.945 (0.519)
14	2.133 (0.539)	1.955 (0.496)	1.792 (0.458)	1.668 (0.433)	1.624 (0.434)
15	1.808 (0.455)	1.658 (0.419)	1.520 (0.387)	1.415 (0.367)	1.377 (0.368)

FIG. 5.28: Power density and power density (standard deviation) distribution in the DCGT core.

distribution of these parameters. Due to the lower temperature drop across the core, the reactivity difference between top and bottom is relatively small, resulting in a power profile which is more uniform than in the base core (peak zone-average power density for the DCGT core is 4.83 W/cm^3, compared to 4.97 W/cm^3 in the base core). Both cores achieve maximum power density in FUPAR zone (6,1). The power density standard deviation in the hot zone has decreased, equal to 1.29 W/cm^3 in the DCGT versus 1.56 W/cm^3 in the base core. Figure 5.29 shows pass-dependent pebble power densities in high power zone of the DCGT. Pass-1 pebbles achieve the core-wide maximum power density of 7.08 W/cm^3 in the DCGT core, compared to 7.96 W/cm^3 in the base core, a significant reduction. The ratio of partitioned variances in the DCGT core is 254, somewhat less than in the other cores which have been analyzed. Thus, the between-pass power density variance contributes relatively less to the overall variance in the DCGT than in the other cores. Nevertheless, this value is sufficiently greater than 1.0 so that the Q2D approximation is still well justified.

Figure 5.30 compares the axial temperature profiles in the DCGT core and the base core, and Figure 5.31 displays the DCGT core's core-wide temperature distribution.

Random hot-spot analysis for the DCGT core also yields results similar to previous cases, with somewhat lower severities due to the more uniform power distribution. Figure 5.32 presents the zero-hot spot probabilities in the high power zone, and Figures 5.33 and 5.34 display the same results in maximum severity plots for power density and

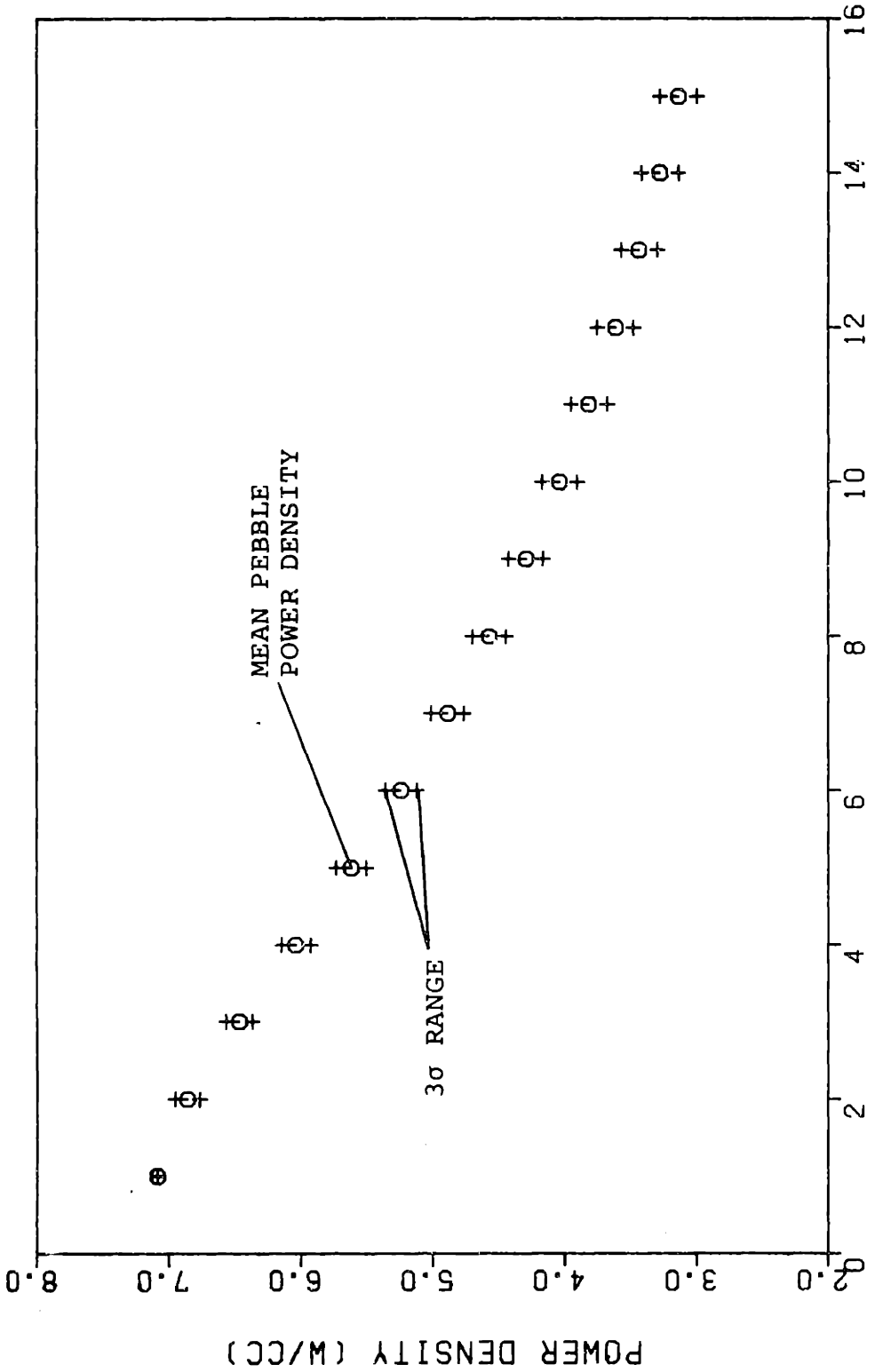

FIG. 5.29: Pass dependent power densities and power density standard deviations in the high power zone of the DCGT core.

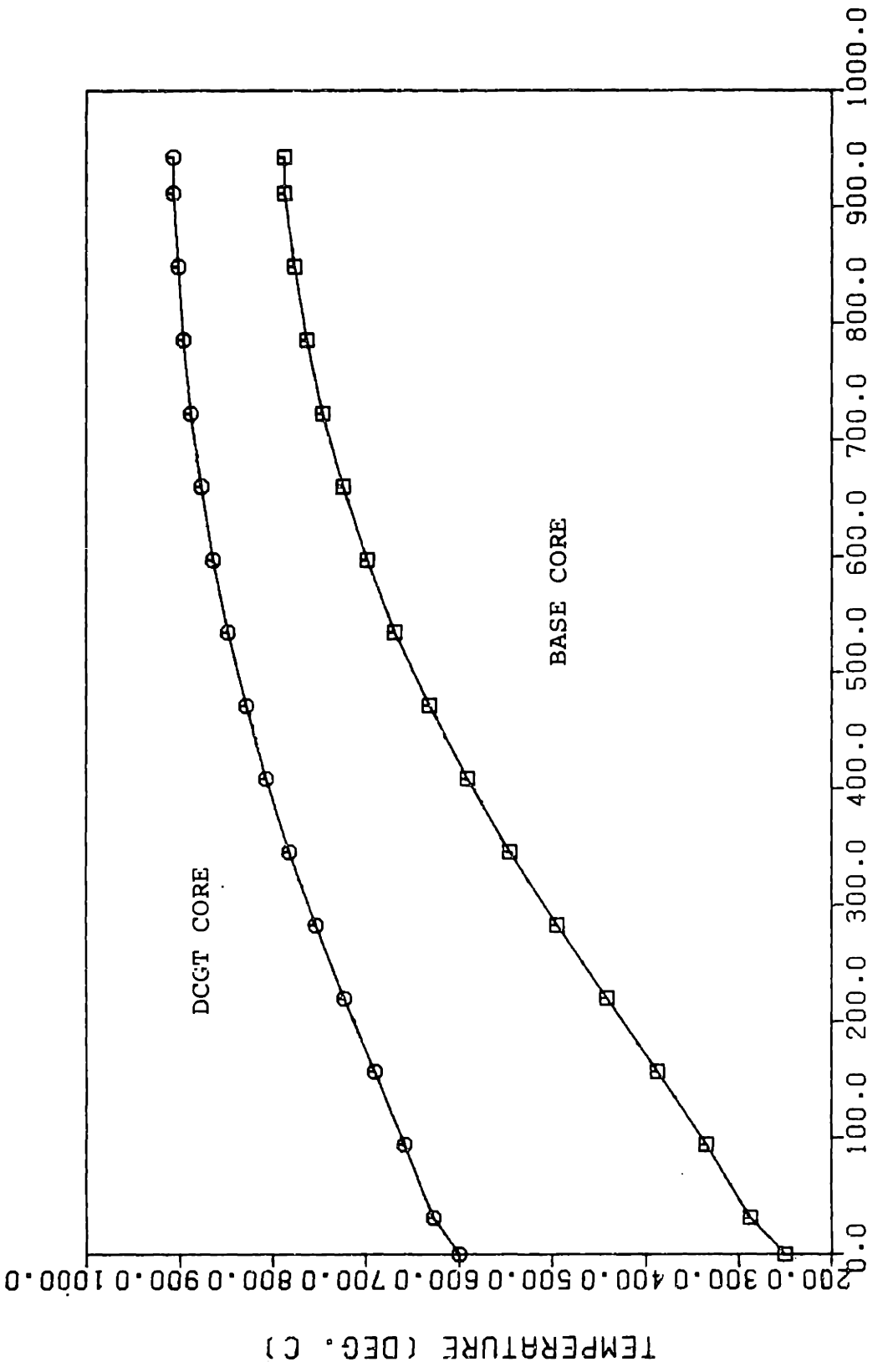

FIG. 5.30: Axial temperature profile in the DCGT core.

z \ r	1	2	3	4	5
1	628	626	624	623	623
2	659	654	650	647	647
3	691	684	677	673	673
4	724	713	704	699	699
5	754	741	730	723	722
6	782	767	754	746	744
7	807	789	775	765	763
8	829	809	793	783	781
9	848	827	810	799	796
0	864	842	823	812	808
11	877	854	835	823	819
12	888	864	845	832	828
13	896	872	852	840	835
14	902	877	858	846	841
15	907	882	863	851	846

FIG. 5.31: Core-wide temperature distribution (^{o}C) in the DCGT core.

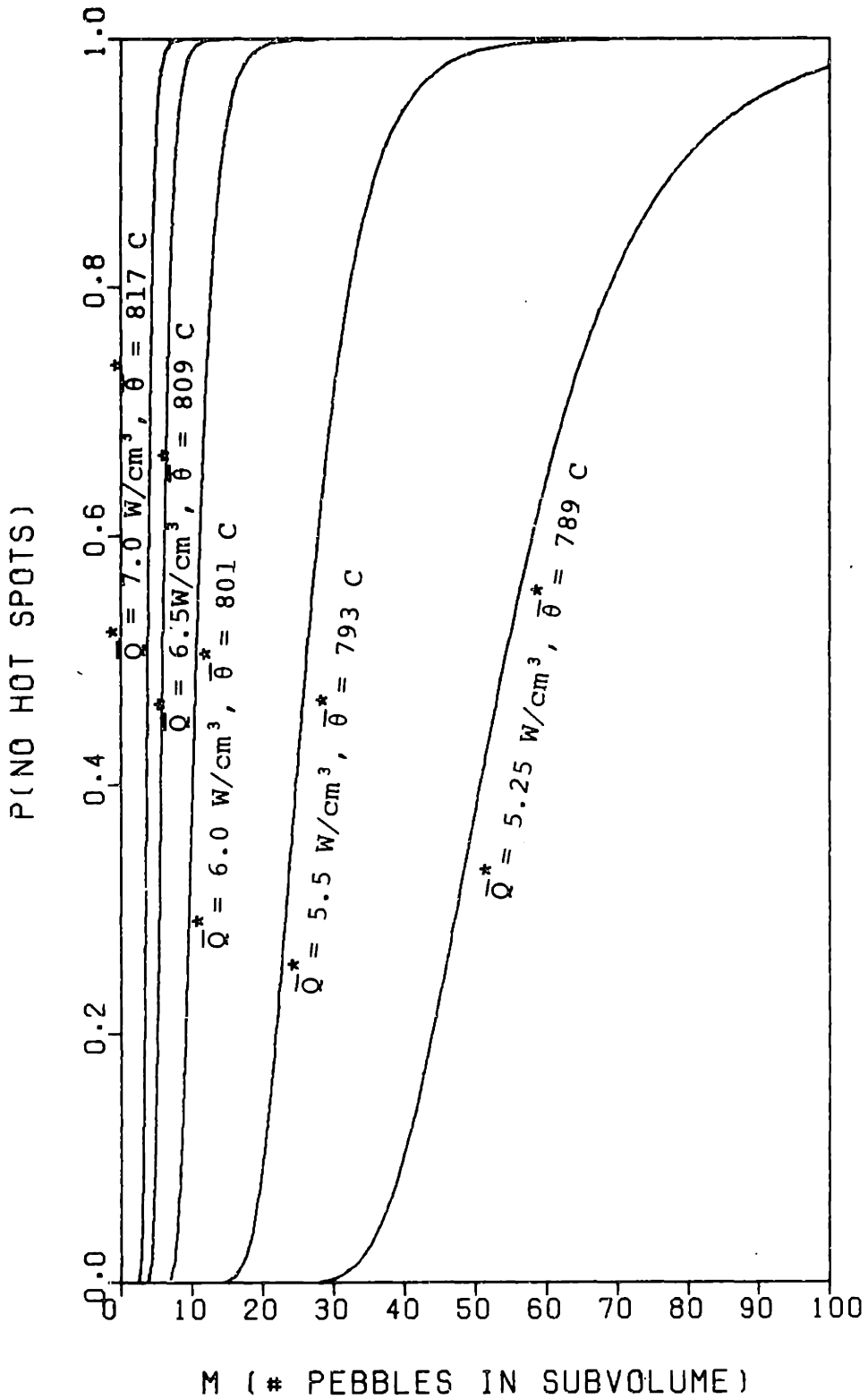

FIG. 5.32: **Zero hot spot probabilities in the DOGT core's high power density zone.**

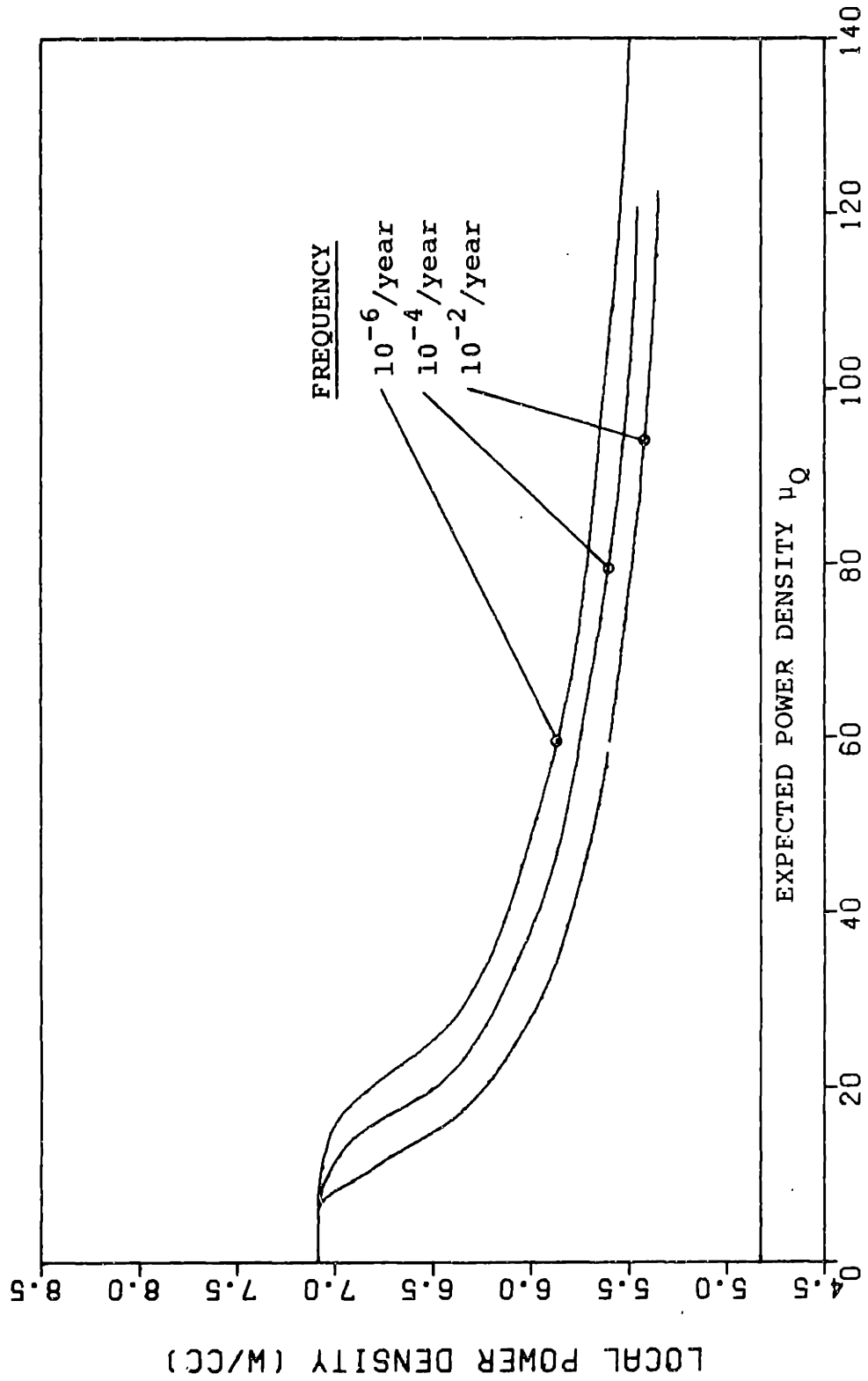

FIG. 5.33: Maximum hot spot severities in the DCGT core's high power zone.

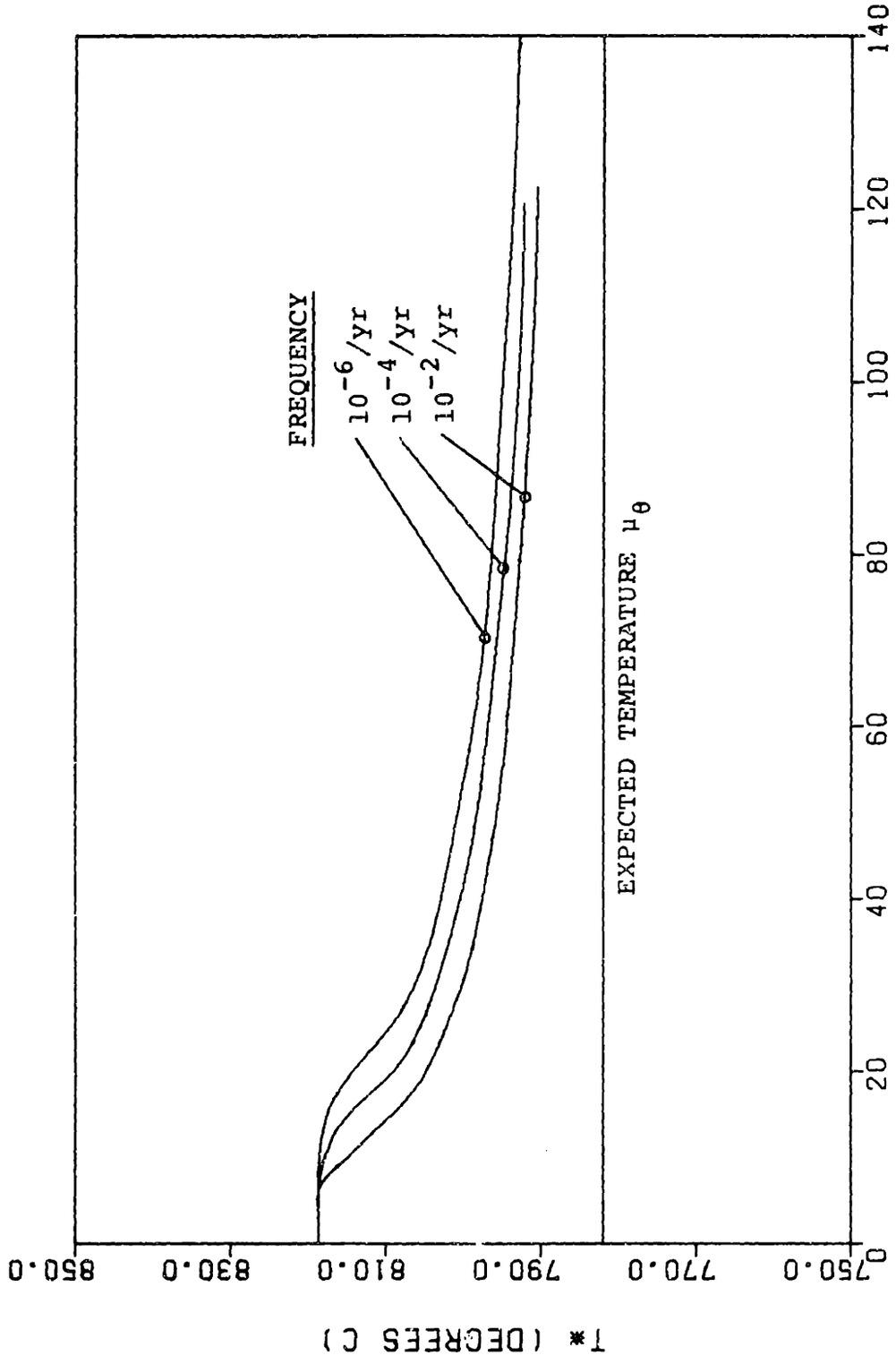

FIG. 5.34: Maximum hot spot severities in the DCGT core's high power zone.

temperature. The maximum power density severity for the DCGT core is significantly decreased from the base core, due to the combined effects of lower maximum pebble power density and lower overall variance. In addition, the weak dependence of maximum severity on frequency level for large numbers of pebbles remains in effect.

5.3.3. Depressurized transient analysis

Results of a THERMIX calculation of post-depressurization temperatures are displayed in Figure 5.35. Peak zone temperatures remain below 1600 C at all times, due to the low ratio of peak to average power during operation. This is somewhat unexpected when compared to the poisoned core analysis. The poisoned core began the transient at uniformly lower temperatures than the DCGT core, yet surpassed the DCGT core in transient temperature. The reason is the relatively slow nature of heat conduction in the pebble bed compared to the rate at which decay heat is deposited.

Comparison of the temperatures from three other locations displayed in the Figure indicate that the DCGT core as a whole experiences higher temperatures, which is expected. The core outer surface temperature, for example, is about 150 C higher after 100 hours than in the base case. The same general difference applies to the other locations as well.

5.3.4 Water ingress effects

The same method for water ingress analysis as applied to the base and poisoned cores was applied to the DCGT core. Results are displayed alongside those for the base core in Figure 5.36. Increased enrichment

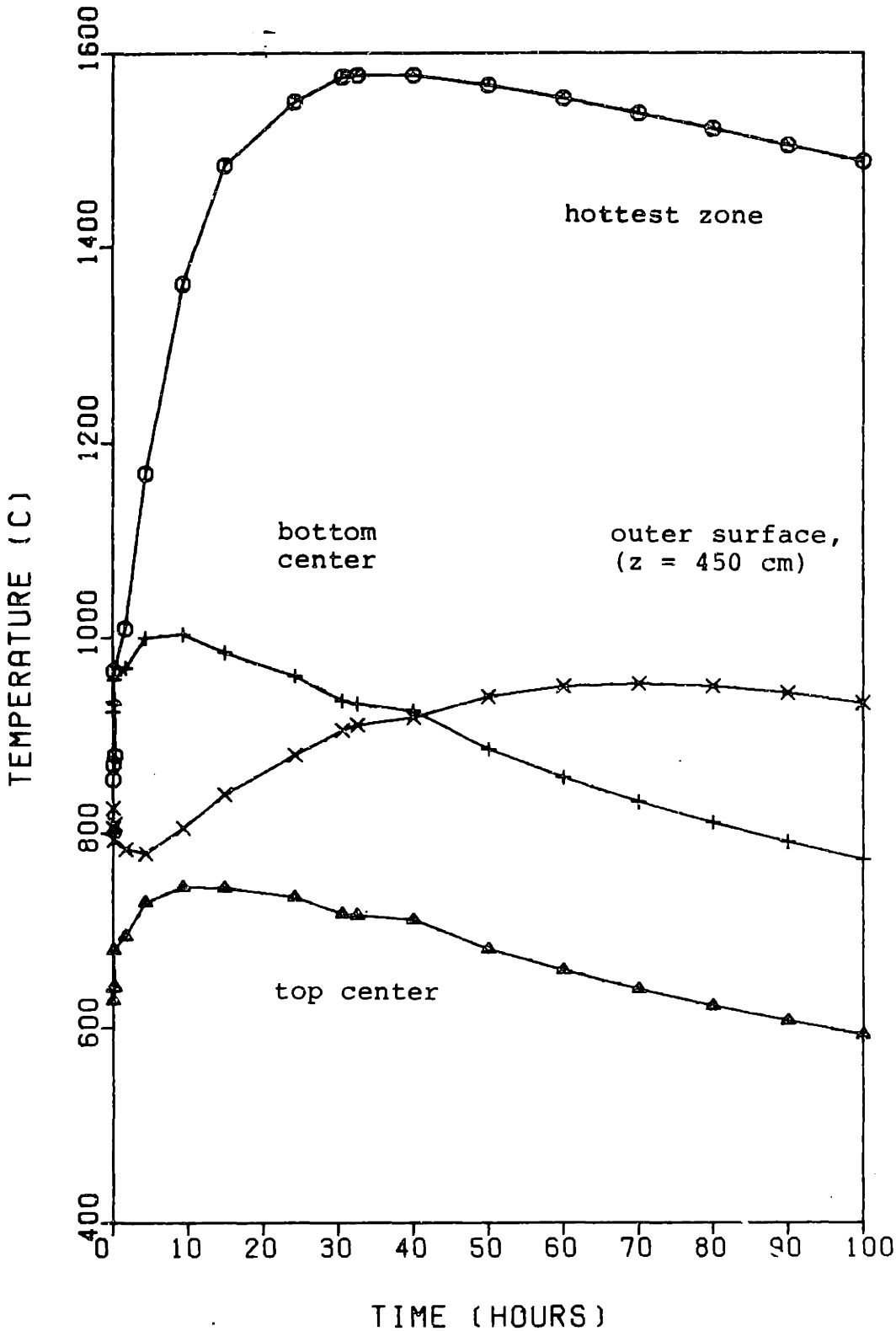

FIG. 5.35: Temperature behavior of the DCGT core following a postulated depressurization accident.

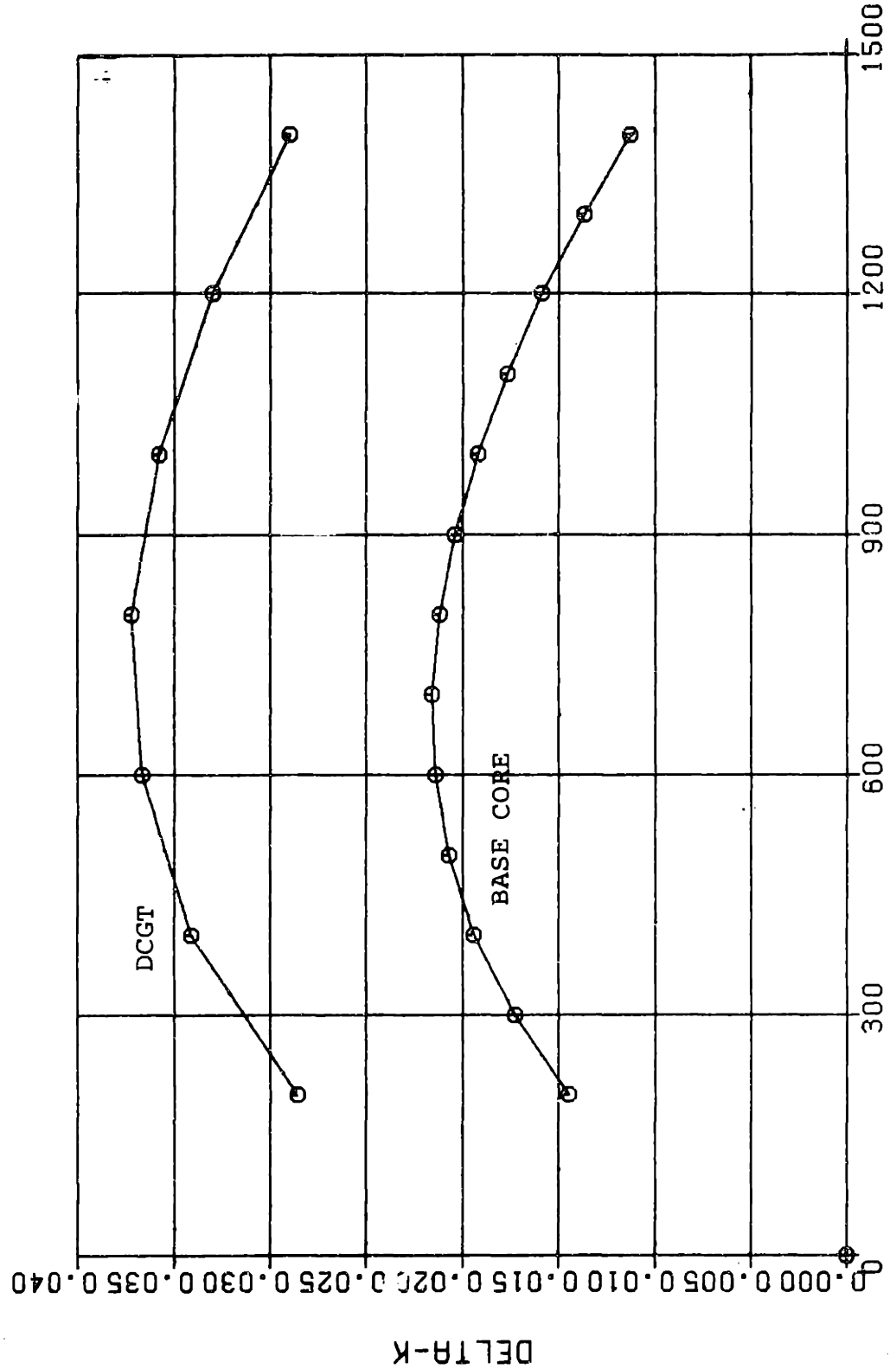

FIG. 5.36: Reactivy effects of water ingress on the base and DCGT cores

has enhanced the DOGT core's sensitivity to water ingress, with a peak reactivity increase of about 3.7% for 800 kg of water.

5.4: CONCLUSIONS

The following conclusions are drawn based on the reactor analyses:

(1) FUPAR/VSOP is an efficient method for calculating operating parameters of continuously refueled pebble bed reactors. FUPAR assumes *a-priori* that the reactor is in the stationary state, eliminating the need to simulate the running in period and significantly reducing computational time. FUPAR calculates power density variance as well as its expected value, thus enabling random hot spot analysis. Results from FUPAR/VSOP analyses agree well with published reactor design information.

(2) Random hot spots have been studied in all three design variants, and appear to be of minor significance. The dependence of pebble power density variance on the local power density ensures that the high *temperature* regions of the core have low hot spot severities. The highest severities occur in the center of the core, where temperatures are more moderate. For large hot spots, the dependence of severity on frequency level has been found to be very weak. Severe hot spots of large size can only be expected at frequencies much lower than 10^{-6} per reactor year.

(3) The ratio of peak/average power density is an important parameter in both hot spot analysis and in determining peak depressurization temperatures. The dependence of pebble power density variance on local mean power density implies that cores with high peak powers will suffer more severe hot spots. The deposition of decay heat in the pebble bed occurs more quickly than conduction and radiation can remove it. Therefore, cores with high peak powers will suffer more extreme maximum temperatures following depressurization.

(4) The effects of gadolinium burnable poisons on reactor operation have been studied. For the case analyzed, the effects on water ingress reactivity were very small, though in the proper direction. A high peak power results in undesirable transient temperatures.

(5) Operation of an MHTGR core under direct cycle gas turbine conditions has been studied. Increased coolant flow results in a relatively more uniform power density distribution, reducing hot spot severity and the maximum post-depressurization temperature. Enrichment is increased to compensate for higher temperatures, which increases the sensitivity of the core to water ingress events.

5.4: CONCLUSIONS

The following conclusions are drawn based on the reactor analyses:

(1) FUPAR/VSOP is an efficient method for calculating operating parameters of continuously refueled pebble bed reactors. FUPAR assumes *a-priori* that the is in the stationary state, eliminating the need to simulate the running in period and significantly reducing computational time. FUPAR calculates power density variance as well as its expected value, thus enabling random hot spot analysis. Results from FUPAR/VSOP analyses agree well with published reactor design information.

(2) Random hot spots have been studied in all three design variants, and appear to be of minor significance. The dependence of pebble power density variance on the local power density ensures that the high *temperature* regions of the core have low hot spot severities. The highest severities occur in the center of the core, where temperatures are more moderate. For large hot spots, the dependence of severity on frequency level has been found to be very weak. Thus, severe hot spots of large size can only be expected at frequencies much lower than 10^{-6} per reactor year.

(3) The ratio of peak/average power density is an important parameter in both hot spot analysis and in determining peak depressurization temperatures. The dependence of pebble power density variance on local mean power density implies that cores with high peak powers will suffer more severe hot spots. The deposition of decay heat in the pebble bed occurs more quickly than conduction and radiation can

remove it. Therefore, cores with high peak powers will suffer more extreme maximum temperautres following depressurization.

(4) The effects of gadolinium burnable poisons on reactor operation have been studied. For the case analyzed, the effects on water ingress reactivity were very small, though in the proper direction. A high peak power results in undesirable transient temperatures.

(5) Operation of an MHTGR core under direct cycle gas turbine conditions has been studied. Increased coolant flow results in a relatively more uniform power density distribution, reducing hot spot severity and the maximum post-depressurization temperature. Enrichment is increased to compensate for higher temperatures, which increases the sensitivity of the core to water ingress events.

CHAPTER 6: ANALYSIS OF FISSION PRODUCT TRANSPORT AND RELEASE

As mentioned in the introduction and implied by the title of this work, the ultimate goal is prediction of source terms due to hypothetical accidents in modular HTGRs. All development previous to this chapter has aimed at "setting up" this problem. The FUPAR/VSOP computation scheme produces core design information which is only the basis upon which to calculate source terms. In this chapter, methods are derived to estimate fission product release from the fuel of a modular HTGR under both operating and high temperature transient conditions.

First, the actual transport phenomena which govern fission product release are briefly reviewed for both gaseous and volatile metallic isotopes. The concept of effective diffusivities is introduced, and the experimental methods for determining these parameters are briefly discussed. One dimensional effective diffusion is selected to model transport of metallic fission products within coated fuel particles. Noble gas fission products are modeled with empirical release to birth rate expressions.

The one-dimensional diffusion equation is discretized to apply to a general spherical shell, and this general difference equation is then applied to the various situations which arise in TRISO coated particles. Boundary conditions at the particle center, materials interfaces, and the particle outer surface appear in the system of difference equations as altered coefficients.

Under circumstances of approximately constant conditions, the system of equations developed above may be written in linear time-independent form. These conditions exist either A) within a small discrete zone in the stationary operating reactor, or B) during a relatively short time interval during the course of a thermal transient. The vector of interest contains the volume averaged fission product concentrations in each of the discrete layers which comprises the particle model. In effect, this vector represents the fission product profile within the particle. The matrix equation for the evolution of the fission product profile may be solved in a manner analogous to that used for the fission product density vectors in Chapter 4. Release is a linear function of the profile vector, and transition matrices yielding release values are developed as well.

Release due to direct recoil is accounted for by modifying the fission product source vector. The transport of fission products through pebble matrix graphite is disussed, but no account is taken of this holdup mechanism in the computations which follow. However, a simple calculation based on equivalent sphere diffusion theory indicates that significant reductions in circulating activity may arise due to holdup in graphite.

A computer program has been written to execute the calculations derived in this chapter, and is known as PDIF (for Particle DIFfusion). The code analyzes both steady state and transient release, using FUPAR/VSOP generated core operating parameters THERMIX generated temperature transients. PDIF yields the steady state and transient

source of fission products from a modular HTGR core.

Finally, results of PDIF calculations are compared with various analytic diffusion calculations and source term predictions made by independent researchers. It is demonstrated that PDIF's results are indeed reasonable.

6.1 FISSION PRODUCT TRANSPORT AND EFFECTIVE DIFFUSIVITIES

The physical and chemical processes which occur on the microscopic scale during the irradiation of nuclear fuel are extremely complex. Elaborate models for fission product transport have been developed based upon the phenomenology of the various mechanisms which are believed to occur. However, these models are much too detailed and complex to apply to the analysis of entire reactor cores. Furthermore, they depend upon many empirical parameters which are difficult to estimate in general.

It has been observed, however, that fission product release increases with temperature and time. This is the behavior one expects when thermally activated diffusion is the rate determining transport mechanism. Thus, HTGR fuel irradiation and anneal data has been summarized in the form of *effective diffusivities*, which enable reproduction of experimental results via one-phase diffusion calculations. In somewhat different forms, this technique is applicable to both metallic and gaseous fission products.

In this section, we briefly review the actual phenomena which govern the transport of fission products through nuclear fuel during operation or transients. Techniques for determining the equivalent diffusivities of volatile metallic fission products are discussed, as well as an analogous but simpler procedure for gaseous fission products.

6.1.1 Metallic Fission Product Transport

Volatile metallic fission products are those such as cesium, strontium, or silver, which remain primarily in elemental form and are free to diffuse through the fuel matrix. A large number of other

metallic fission products will react with free oxygen released by fission reactions of UO_2, forming stable refractory compounds which are essentially immobile.

Metallic fission product transport has three basic phases [A2]: recoil from fission, volume diffusion through fuel grains, and surface diffusion over fuel grain surfaces. Immediately following the fission of a heavy metal atom, the fission products travel through the fuel matrix material, losing energy first through ionization and later through elastic collisions. The entire thermalization process occurs within approximately 10^{-13} seconds [A2]. Within 10^{-12} seconds, the effects of the collisions are felt in the fuel material as an extremely high temperature spike along the fission product's path. At this point, crystal defects produced by the fission product, plus chemical reactions enabled by the high local temperature, may trap some fission products.

The range of fission products in UO_2 fuel is on the order of several microns (7.7 microns for Cs-137 [N2]). Fission products born close to the outer surface of the fuel kernel may actually escape the kernel immediately through recoil. It can be deduced from geometrical considerations that the fraction of fisson products released from the kernel due to direct recoil is [N2]:

$$F_{rec} = \frac{3}{4}\left[\frac{R}{r}\right] - \frac{1}{16}\left[\frac{R}{r}\right]^3 \qquad (6.1)$$

where

R = the recoil range of the fission product; and
r = radius of the fuel kernel.

The recoil fraction becomes significant at lower temperatures where

diffusion effects are very small.

Once the fission product has reached thermal energies, further transport through the fuel crystal lattice occurs by volume diffusion. Random thermal motion causes the fission product atom to exchange positions with adjacent vacancies, resulting in a net mass flux from high to low fission product concentrations. This process continues until the fission product atom has diffused to the surface of the fuel grain in which it was initially deposited.

The diffusivity of fission products on the grain surfaces is much higher than in the grains themselves. Therefore, once released from the fuel grains, the fission products migrate relatively rapidly to the fuel kernel surface.

6.1.2 Effective Diffusivities for Metallic Fission Products

The phenomena believed to govern metallic fission product diffusion suggest that a two-phase mathematical model might be necessary to describe fission product transport. The disadvantage of such a technique, however, is that two diffusivities are necessary (one for volume and the other for surface diffusion), each of which requires two empirical constants (a frequency factor and an activation energy). Furthermore, the mathematics of a two-phase model are relatively complex.

In any event, even if the two-phase diffusion parameters were known, they are simply *statistics*, or functions of experimental data. Their usefulness (or not) depends on their ability to quantitatively predict the outcomes of future experiments. If another set of

statistics is known with adequate predictive capability and a sound physical basis, yet requiring fewer empirical parameters, common sense directs us to make use of the simpler model. Such is the case with the effective one-phase diffusivities for fission product transport in HTGR fuel. Effective one-phase diffusivities are statistics which enable adequate prediction of experimental results based on a one-phase mathematical diffusion model.

Effective diffusivities may be determined experimentally in two ways. The first is based upon measurements of fission product release in post-irradiation annealing experiments, and the second requires measurement of actual fission product profiles inside fuel particles. When used together, these techniques allow verification not only of the empirical parameters but also of the one-phase diffusion methodology itself.

In the release measurement technique, irradiated fuel particles are annealed at a known temperature outside the reactor. The release rate of the fission product under investigation is recorded as a function of time. An example of such a release curve is presented in Figure 6.1. The unknown parameters to be estimated are the effective diffusivities of the fission product in the various particle constituent materials. This is accomplished by comparing the measurements with the results of numerical release predictions based upon hypothesized diffusivity values. The values which minimize (in some sense particular the technique employed) the difference between prediction and measurement are the R-fit (for "Release" fit) diffusivities for that fission

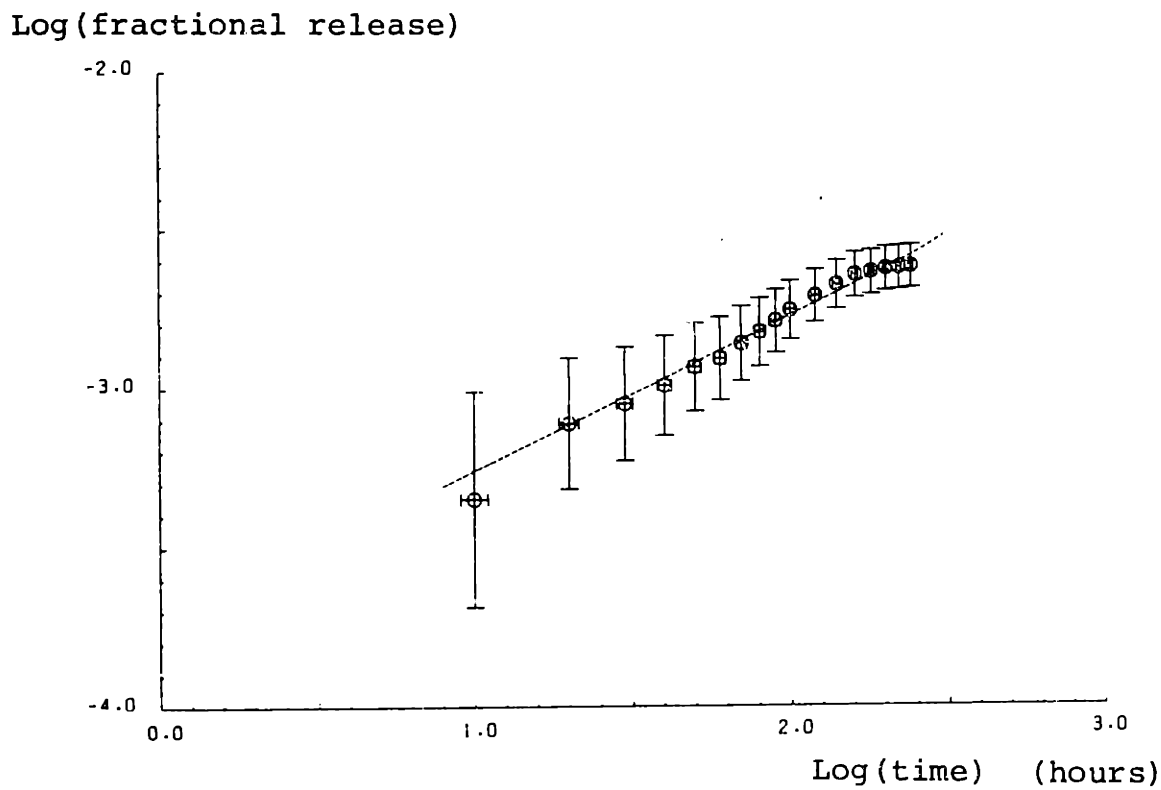

FIG. 6.1: Fission product release as a function of time during a post-irradiation annealing experiment [A3].

product. A complete discussion of the parameter estimation technique (a non-linear least-squares fit) used at KFA Jülich may be found in Ref. [A2]. Finally, the temperature dependence of the R-fit diffusivities may be estimated by comparing the results of different temperature anneals on particles with identical designs and irradiation histories. Figure 6.2 presents an Arrhenius diagram of effective cesium diffusivities in HTI pyrocarbon which were obtained by R-fits. The parameter estimation technique provided the error estimates in the Figure as well.

Diffusion coefficients determined using release measurements depend on the validity of the mathematical model used to calculate releases. The model may be verified by an independent technique, known as a "profile-" or "P-" fit. Besides calculating radioisotope release, the effective one phase diffusion model will just as easily predict the concentration profiles of fission products within the fuel particle. These profiles may be measured by laser drilling and gamma spectroscopy techniques (see [K1]) or by electron microprobe analysis. The profiles predicted by the one phase model can be compared with measured profiles. The unknown diffusivities may be varied in the model until predictions agree optimally with measurements. Thus, an additional check on the one phase model and the effective diffusivities is available.

When the irradiation and annealing experiments are both well defined, R-fit and P-fit diffusivities agree well and yield profile predictions which are very close to those measured. Figure 6.3 illustrates a case in which measured and predicted profiles of both

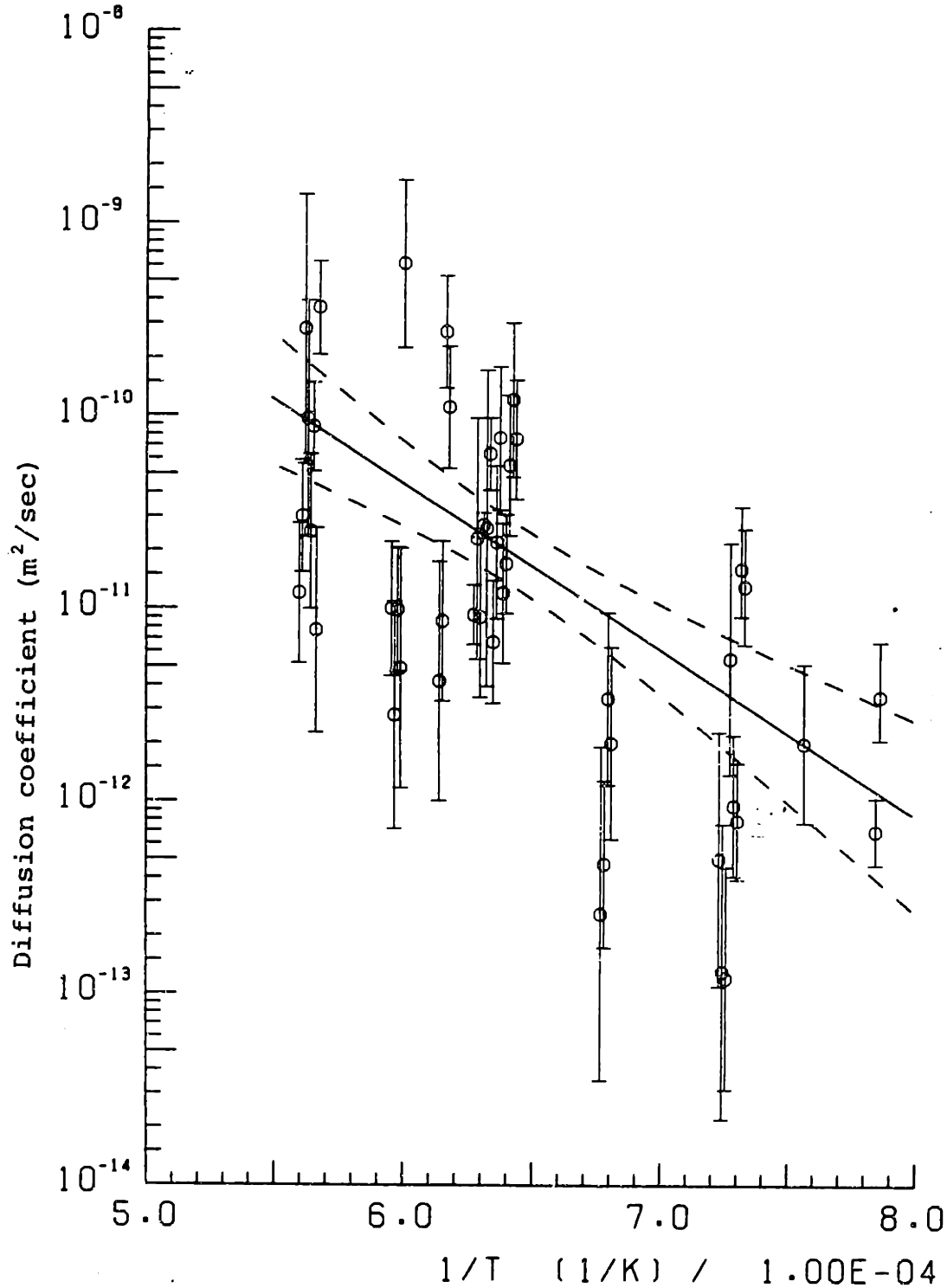

FIG. 6.2: Temperature dependence of R-fit diffusivities [A3].

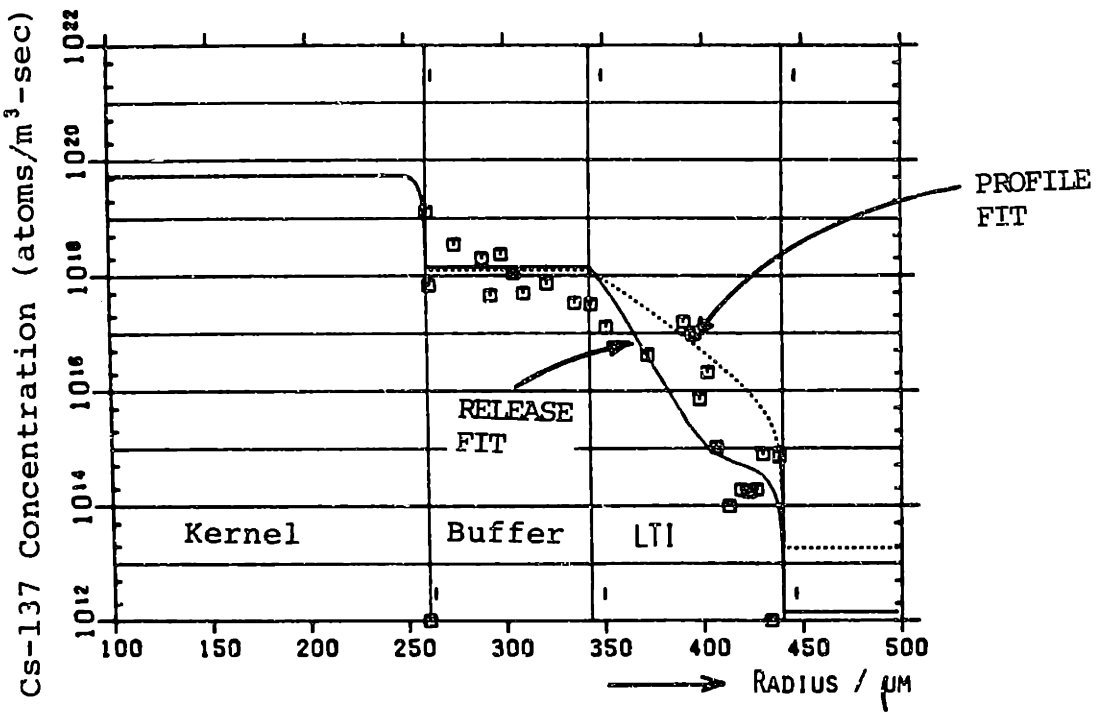

FIG. 6.3: Comparison of measured and predicted fission product profiles [A3].

sorts agree well. KFA Jülich maintains a data base of fission product diffusivities and publishes recommended values for use in fission product transport analysis. Figure 6.4 presents a recent set of diffusivities for three important fission product (Ag, Cs, and Sr) in fuel particle materials. In the work which follows, the KFA-recommended effective diffusivites will be used for all metallic fission product transport analysis.

6.1.3 Transport Processes for Gaseous Fission Products

The transport of gaseous fission products through fuel material differs somewhat from metallic fission products. Since fission product gases are inert, they have no chemical attraction for UO_2 grain surfaces. Therefore, they behave as free gas atoms immediately upon release from the fuel matrix of the original grain.

First we examine transport within the fuel material. At relatively low temperatures (less than ~1300K) the mobility of noble gas atoms within the fuel matrix is extremely low. There is essentially no movement to grain surfaces or to bubble sites. The primary release mechanisms at these temperatures are direct recoil and "knockout," which occurs when a fission product atom near the fuel surface is struck by an energetic fisssion product and is subsequently ejected from the fuel. As these processes occur only within a relatively short range of the fuel surface (about 10 microns), release rates at these temperatures are very low.

At intermediate temperatures (1300-1900K) the atomic motion of the gas atoms within the fuel matrix becomes significant. The gaseous

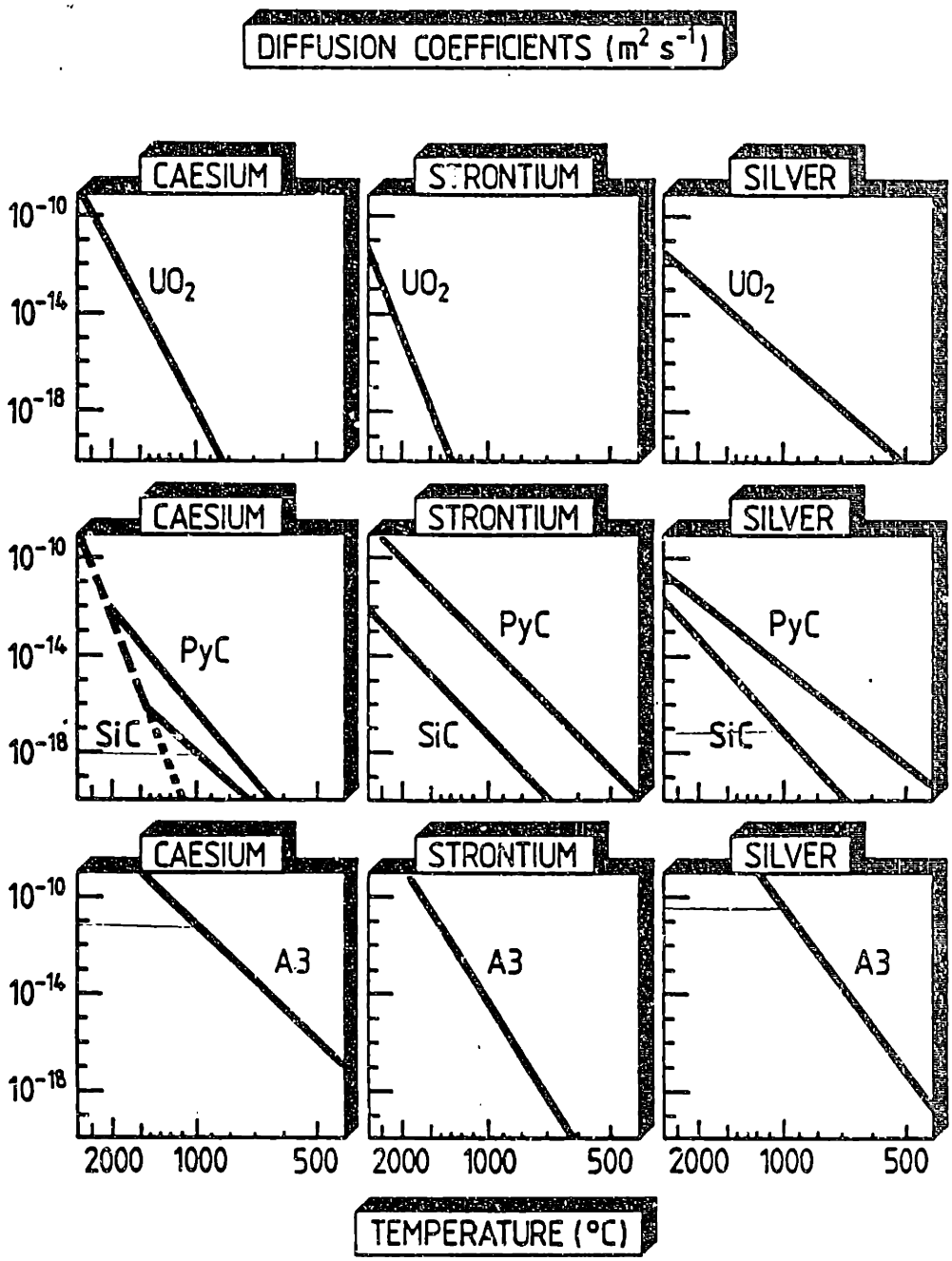

FIG. 6.4: Effective diffusivites for silver, cesium, and strontium in particle constituent materials [H2].

TABLE 6.1: EFFECTIVE ONE-PHASE DIFFUSIVITIES FOR METALLIC FISSION PRODUCTS IN FUEL PARTICLE CONSITUENT MATERIALS.

	Cs-137		Ag-110m		Sr-90	
	D_o	Q	D_o	Q	D_o	Q
UO_2	5.2×10^{-4}	362	1.1×10^{-4}	488	6.7×10^{-10}	165
HTI PyC	1.8×10^{-1}	493	2.3×10^{-6}	197	1.0×10^{-8}	164
SiC	1.8×10^{-11}	176	1.2×10^{-9}	205	3.6×10^{-9}	215
Matrix	2.0×10^{-4}	181	9.1×10^{-3}	301	1.6×10^{0}	258

frequency factor "D_o" is in units of m^2/sec;

activation energy "Q" is in units of kJ/mole;

diffusivity $D = D_o \exp[-Q/RT]$

[SOURCE: Ref. H2]

fission products can now migrate by diffusion to grain surfaces. Trapping effects may also occur, in which diffusing gas atoms are held up at natural or irradiation-caused defects in the UO_2 crystal lattice. Bubbles can form outside the grains at these temperatures, but cannot migrate. Gaseous fission product atoms which reach grain boundaries will escape if a pathway to the fuel surface exists. This is possible if the bubble density is high enough to cause interlinkage.

At very high temperatures (above 1900K) the intergranular gas bubbles themselves become very mobile, and can migrate to fuel surfaces in relatively short times (measured in days).

The permeability of pyrolytic carbon and silicon carbide to gaseous fission products is extremely low under almost all circumstances [N.2]. This has important consequences in modular HTGRs, since a well designed MHTGR core will have extremely few coating failures due to manufacture or accident conditions. Thus, regardless of the internal release of gaseous FPs from the fuel kernel, the large majority of particles with intact coatings have essentially zero release.

6.1.4 Effective Diffusivities for Gaseous Fission Products

Diffusion based models for the release of noble gas fission products are based upon the "equivalent sphere" model originally proposed by Booth (O.1). Diffusive release from UO_2 grains (which are assumed to be spheres with uniform radius "a") competes with radioactive decay to determine the overal release to birth ratio for each species. Kania (K.1) and Olander (O.1) give the following relation for the release to birth ratio:

$$(R/B)_i = 3\sqrt{D_i'/\lambda_i}\left[\coth\sqrt{\lambda_i/D_i'} - \sqrt{\lambda_i/D_i'}\right] \qquad (6.2)$$

where

$(R/B)_i$ = release to birth rate ratio for species i;

λ_i = decay constant of species i; and

D_i' = reduced diffusion coefficient for species i.

The *reduced* diffusion coefficient D_i' is equal to the diffusivity of the species in the fuel matrix divided by the squared grain radius, a^2:

$$D_i' \equiv D_i/a^2 \qquad (6.3)$$

Since the grain radius is an empirical parameter as well, gaseous FP release measurements are often summarized simply with the reduced diffusivity. The reduced diffusivity is assumed to display Arrhenius type temperature dependence:

$$D_i'(T) = D_{i_o}' \exp[-Q_i/RT] \qquad (6.4a)$$

or

$$\log_{10}(D_i') = \alpha - \frac{\beta}{T} \qquad (6.4b)$$

where the D_{i_o}' and Q_i parameters are characteristic of a particular fission product species in a particular fuel type. In general, these parameters may be dependent on burnup (perhaps representing a change in grain radius as a function of irradiation), but in practice this has been found to apply only for thorium-containing fuels (K.1).

Reduced diffusivities are determined experimentally. One technique is to measure the in-pile release of gaseous fission products from a batch of fuel particles with a known failure fraction. Table 6.2 presents the results of some of these experiments performed for UO_2 fuel.

TABLE 6.2: REDUCED DIFFUSIVITIES FOR NOBLE GAS FISSION PRODUCTS

$$\log D'_{Xe} = -5.05 - \frac{4516}{T}$$

$$\log D'_{Kr} = -4.43 - \frac{4516}{T}$$

$$\log D' = -2.60 - \frac{8220}{T} \quad (T < 900C)$$

$$= -7.97 - \frac{1920}{T} \quad (T > 900C)$$

(applicable to Xe, Kr, or I)

where:

D' = reduced diffusivity (sec^{-1})

T = temperature (K)

6.2 DISCRETE ANALYSIS OF UNSTEADY FISSION PRODUCT DIFFUSION AND RELEASE

Once effective diffusivities are determined which adequately model the behavior of volatile metallic fission products in fuel particles, analysis proceeds along the lines of classical one-phase diffusion. In this section, the diffusion equation is derived using Fick's Law and conservation of mass considerations. The various boundary conditions which are necessary for solution are reviewed. Integration of the partial-differential diffusion equation over a spherical shell within a fuel particle yields difference equations in terms of volume-average concentrations. Consecutive zones in a particle are coupled through proper treatment of the surface flux terms, which are approximated as functions of the differences in average concentrations between adjacent zones. A fuel particle has several distinct types of layer interfaces, some of which are unique. The mass flux approximations are reviewed for each combination which arises in practice.

6.2.1: The Diffusion Equation.

Derivation of the equation describing the time dependent behavior of the concentration of a diffusing species begins with two fundamental relations. The first is conservation of mass applied to a differential control volume. For a radioactive species undergoing diffusion and with the possible presence of sources, the conservation of mass equation is:

$$\frac{\partial C}{\partial t} = -\nabla \cdot J + Q - \lambda C \qquad (6.5)$$

where:

C = concentration of the diffusing species {atoms/cm^3};

t = time {sec};

J = mass flux of the species {atoms/cm^{2}sec};

Q = source of new diffusing atoms {atoms/cm^{3}sec}; and

λ = decay constant of the diffusing species {sec^{-1}}.

The divergence of J in Eq. (6.5) represents the net loss of diffusing atoms per unit volume due to diffusion. A second basic assumption is necessary to eliminate the unknown J term. This assumption is known as Fick's Law, and relates the directional mass flux J to the gradient of the concentration by a proportionality constant, D:

$$J = - D \nabla C \tag{6.6}$$

The proportionality constant D is known as the diffusivity or diffusion coefficient, and has units of {m^2/sec}. If Fick's Law is substituted into Eq. (6.5), the result is the well known *diffusion equation*:

$$\frac{\partial C}{\partial t} = D \nabla^2 C - \lambda C + Q \tag{6.7}$$

The diffusion equation presented above is entirely general. The discretization procedure which follows will remove the ∇^2 term without the need to first convert to a specific coordinate system.

6.2.2 Boundary Conditions

Solution of any equation such as (6.7) requires suitable boundary conditions. Three boundary conditions will be necessary for fuel particle analysis. The first type occurs at a boundary across which no net mass flux is permitted. This situation may arise due to the actual physical presence of an impermeable substance, or at an axis of symmetry at which there can be no net flux. By Fick's law, a mass flux of zero implies a concentration gradient of zero. Thus the first type of boundary condition (BC1) may be expressed mathematically as follows:

Boundary Condition 1:

$$\begin{bmatrix}\sigma \text{ is a surface across which} \\ \text{the net mass flux is zero}\end{bmatrix} \Rightarrow \nabla C\big|_{\sigma} = 0.$$

The second type of boundary condition is necessary at surfaces across which the substrate material changes. This situation is illustrated in Figure 6.5. Since the boundary itself is infinitesimally thin, no mass may accumulate there. Any mass flux into the boundary from the "left," for example, must be exactly matched by mass flux out of the boundary to the "right." Once again, Fick's law provides a means to relate the mass flux conditions to properties of the concentration distribution. Referring to the Figure, let the left-hand substance be denoted by the number "1," and the right-hand substance by the number "2." The diffusion coefficients in the two materials are D_1 and D_2, respectively. The flux "into" the boundary from material 1 is:

$$\text{flux from material 1} = J_1 = -D_1 \nabla C_1\big|_{\sigma},$$

where C_1 is the concentration profile in the first material. Likewise, the mass flux from the surface into material 2 may be written as:

$$\text{flux into material 2} = J_2 = -D_2 \nabla C_2\big|_{\sigma}.$$

Thus, conservation of mass applied to the boundary yields the second type of boundary condition:

Boundary Condition 2:

$$\begin{bmatrix}\sigma \text{ is a boundary between} \\ \text{substances 1 and 2}\end{bmatrix} \Rightarrow D_1 \nabla C_1\big|_{\sigma} = D_2 \nabla C_2\big|_{\sigma}$$

The final boundary condition (BC3) is simply that which applies at a surface at which the concentration of the diffusing substance is zero.

An initial condition is also necessary because the diffusion

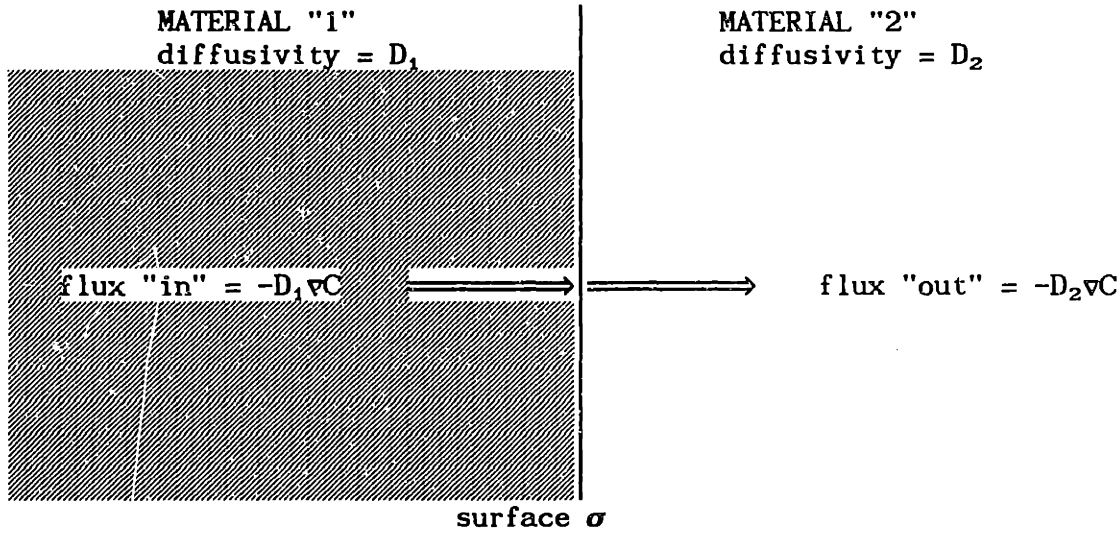

FIG. 6.5: Continuity of mass flux at a boundary between two different materials.

equation is time dependent. This is simply the concentration distribution at the initial time in the analysis.

6.2.3 Spatial Discretization of the Diffusion Equation.

Analytic solutions to the diffusion equation are available only for a limited number of situations. To increase the applicability, numerical solution techniques are required. The first step is to convert Eq. (6.7) to a discrete form which is suitable for manipulation by a digital computer. This will be accomplished by a volume averaging operation, application of Green's theorem, and use of finite differences to approximate mass fluxes.

First define the volume average operator:

$$\hat{C}_i \equiv \frac{1}{V_i} \int_{V_i} C \, dV \tag{6.8}$$

where V_i is some constant volume of interest. Apply the volume average operator to both sides of the diffusion equation:

$$\frac{1}{V_i} \int_{V_i} \frac{\partial C}{\partial t} dV = \frac{1}{V_i} \int_{V_i} D \, \nabla^2 C \, dV + \frac{1}{V_i} \int_{V_i} Q \, dV - \frac{1}{V_i} \int_{V_i} \lambda \, C \, dV \tag{6.9}$$

The second two terms convert easily to $\hat{Q}_i$ and $\lambda \hat{C}_i$. The term on the left hand side may be simplified because the integral limits are not time dependent, thus:

$$\frac{1}{V_i} \int_{V_i} \frac{\partial C}{\partial t} dV = \frac{\partial}{\partial t} \frac{1}{V_i} \int_{V_i} C \, dV = \frac{\partial \hat{C}}{\partial t} i \tag{6.10}$$

Finally, it is useful to manipulate the first term on the left hand side of Eq. (6.10). Recall the divergence theorem:

$$\int_V \nabla^2 C \, dV = \oint_{\sigma} \nabla C \cdot d\sigma \tag{6.11}$$

where σ is the surface which surrounds volume V. Apply the theorem

to the first term on the left hand side of Eq. (6.9):

$$\frac{1}{V_i}\int_{V_i} D\ \nabla^2 C\ dV \;=\; \frac{D_i}{V_i}\oint_{\sigma_i} \nabla C\cdot d\sigma \qquad (6.12)$$

Substitute Eqs. (6.10) and (6.12) into Eq. (6.9) to obtain:

$$\frac{\partial \hat{C}_i}{\partial t} \;=\; \frac{D_i}{V_i}\oint_{\sigma_i} \nabla C\cdot d\sigma \;+\; \hat{Q}_i \;-\; \lambda\,\hat{C}_i \qquad (6.13)$$

We shall now apply Eq. (6.13) to the situation of interest: a spherical shell within a radially symmetric fuel particle. Eq. (6.13) describes the time-dependent average concentration in each shell. Shells are coupled through the surface flux term, and concentration gradients at surfaces between shells are approximated using the differences between average shell concentrations.

Figure 6.6 presents a schematic diagram of a general spherical shell within a fuel particle. The layer of interest is denoted by subscript "i." Index i increases as the shell radius increases. Important geometrical parameters which refer exclusively to layer i are defined in the Figure:

δr_i = radial thickness of shell i;

r_i = *outer* radius of shell i;

A_i = *outer* surface area of shell $i = 4\pi r_i^2$;

V_i = volume of shell $i = (4\pi/3)(r_i^3 - r_{i-1}^3)$

Additionally, several parameters are defined which depend upon the surrounding layers as well

$A_{out} = A_i$ = outer surface area of shell i;

$A_{in} = A_{i-1}$ = inner surface area of shell i;

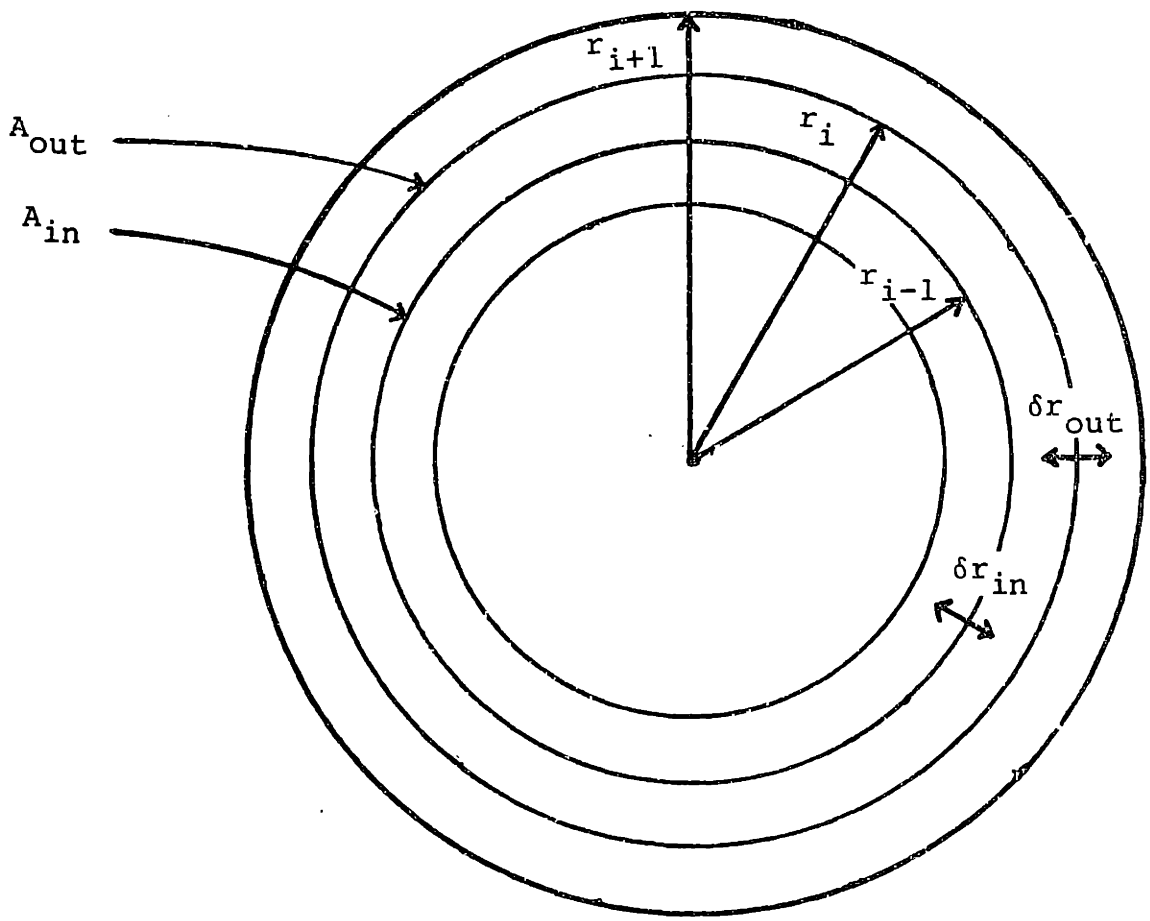

FIG. 6.6: A spherical shell within a fuel particle.

$\delta r_{in} = \frac{1}{2}(\delta r_{i-1} + \delta r_i)$; and

$\delta r_{out} = \frac{1}{2}(\delta r_{i+1} + \delta r_i)$.

For a given shell, assuming that the concentration gradient is spherically symmetric, the surface flux from Eq. (6.13) simplifies:

$$\oint_{\sigma_i} \nabla C \cdot d\sigma = -A_{in} \nabla C(r_{in}) + A_{out} \nabla C(r_{out}) \qquad (6.14)$$

The signs on the areas in the above equation result formally from the direction of the surface area vectors. However, the physical interpretaion is simple. A positive concentration gradient at the inner radius implies that the net mass flux is out of shell i into shell $i-1$. Thus, the term $\{A_{in} \nabla C(r_{in})\}$ must have a negative sign to have the proper effect on $\partial \hat{C}_i / \partial t$. Likewise, a positive concentration gradient at the outer shell radius implies a net mass flux *into* shell i, and a positive contribution to $\partial \hat{C}_i / \partial t$. If Eq. (6.14) is substituted into Eq. (6.13), the result is the general difference equation to applied to all spherical shells:

$$\boxed{\frac{d\hat{C}_i}{dt} = -A_{in} D_i \nabla C(r_{in}) + A_{out} D_i \nabla C(r_{out}) - \lambda \hat{C}_i + \hat{Q}_i \qquad (6.15)}$$

In general, the three spherical shells portrayed in Figure 6.6 may consist of three different materials with varying properties. The mass flux terms at the inner and outer radii of shell i must be approximated differently depending on the specific materials present. We shall next review all situations which arise in HTGR fuel particles, and develop the necessary approximations for the concentration gradients.

1. All materials identical.

This is the most common and straightforward case, which applies to all layers which are completely enclosed in a single particle coating layer or kernel. The situation is illustrated in Figure 6.7. The concentration gradients at r_{in} and r_{out} are approximated as follows:

$$\nabla C(r_{in}) \simeq \frac{\hat{C}_i - \hat{C}_{i-1}}{\delta r_{in}} \tag{6.16a}$$

$$\nabla C(r_{out}) \simeq \frac{\hat{C}_{i+1} - \hat{C}_i}{\delta r_{out}} \tag{6.16b}$$

Substitute Eqs. (6.16a) and (6.16b) into Eq. (6.15) to obtain:

$$\frac{d\hat{C}_i}{dt} = \frac{D_i}{V_i}\left\{-A_{in}\frac{\hat{C}_i - \hat{C}_{i-1}}{\delta r_{in}} + A_{out}\frac{\hat{C}_{i+1} - \hat{C}_i}{\delta r_{out}}\right\} - \lambda \hat{C}_i + \hat{Q}_i$$

$$= \hat{C}_{i-1}\left[\frac{D_i A_{in}}{V_i \delta r_{in}}\right] - \hat{C}_i\left[\frac{D_i A_{in}}{V_i \delta r_{in}} + \frac{D_i A_{out}}{V_i \delta r_{out}} + \lambda\right] + \hat{C}_{i+1}\left[\frac{D_i A_{out}}{V_i \delta r_{out}}\right] + \hat{Q}_i \tag{6.17}$$

2. Particle internal shell

It is not necessary that the innermost particle shell be at the very center of the particle. For cases in which the cumulative diffusion time remains very small, it is often wise to model only the particle's outermost volume. However, in either case, the same internal boundary condition may be applied. For the case in which the innermost shell is indeed at the particle center, the surface flux term only has a component due to the outer radius:

$$\oint_{A_i} \nabla C \cdot dA = A_{out} \nabla C(r_{out}) \quad \text{for the central zone}$$

since $A_{in} = 0$. In the alternate internal layer case the inner radius r_{in} is not equal to 0. However, the same expression for the

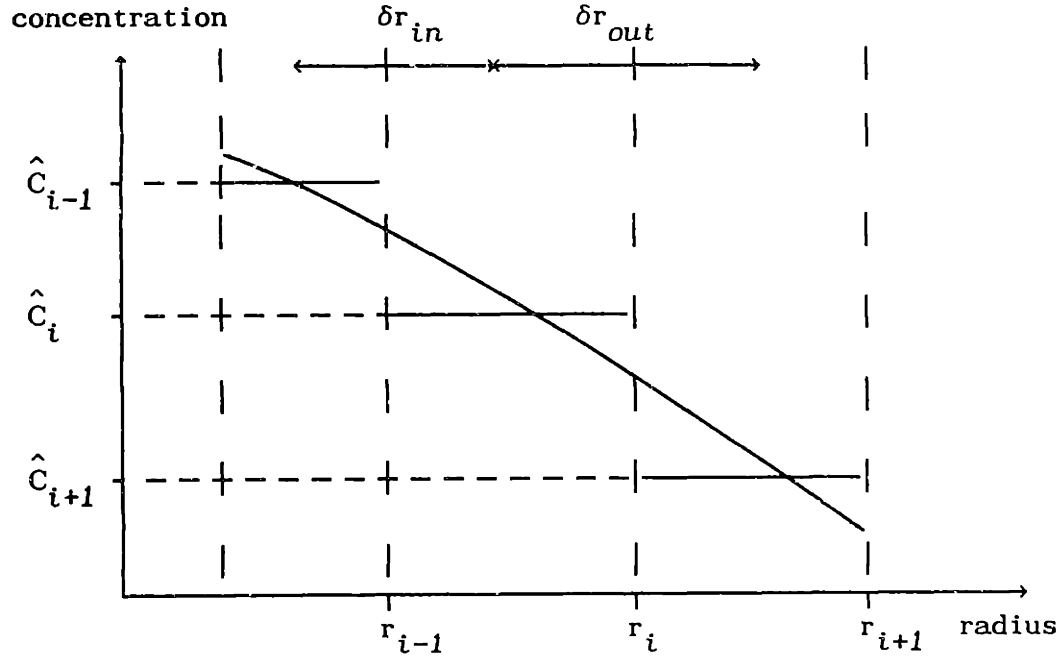

FIG. 6.7: Three adjacent spherical shells with identical materials.

surface integral applies because the concentration gradient at the inner surface is assumed to vanish (if not, more interior layers should be included):

$$\oint_{A_i} \nabla C \cdot dA = A_{out} \nabla C(r_{out}) \quad \text{for } \textit{any} \text{ internal zone;}$$

since $\nabla C(r_{in}) = 0$. Thus, the general difference equation for any inner most shell becomes:

$$\frac{d\hat{C}_i}{dt} = A_{out} \nabla C(r_{out}) - \lambda \hat{C}_i + \hat{Q}_i \qquad (6.18)$$

Figure 6.8 illustrates the innermost particle shells and the concentration profile within them. Approximate the concentration gradient at the outer surface as follows:

$$\nabla C(r_{out}) \simeq \frac{\hat{C}_{i+1} - \hat{C}_i}{\delta r_{out}}$$

Substitute this expression into Eq. (6.) and obtain:

$$\frac{d\hat{C}_i}{dt} = A_{out} \frac{\hat{C}_{i+1} - \hat{C}_i}{\delta r_{out}} - \lambda \hat{C}_i + \hat{Q}_i$$

$$= -\hat{C}_i \left[\frac{D_i A_{out}}{V_i \delta r_{out}} + \lambda \right] + C_{i+1} \left[\frac{D_i A_{out}}{V_i \delta r_{out}} \right] + \hat{Q}_i \qquad (6.19)$$

3. The buffer and surrounding layers.

Treatment of the buffer layer and adjacent shells requires special assumptions regarding mass transport in the buffer. The diffusivity of volatile metallic fission products in the buffer layer is so high compared with those in the kernel and high density coating layers that it is reasonable to approximate it as infinite. Such an assumption implies that no concentration gradients can exist in the buffer, which is borne out well by experimental profile measurements. Figure 6.9

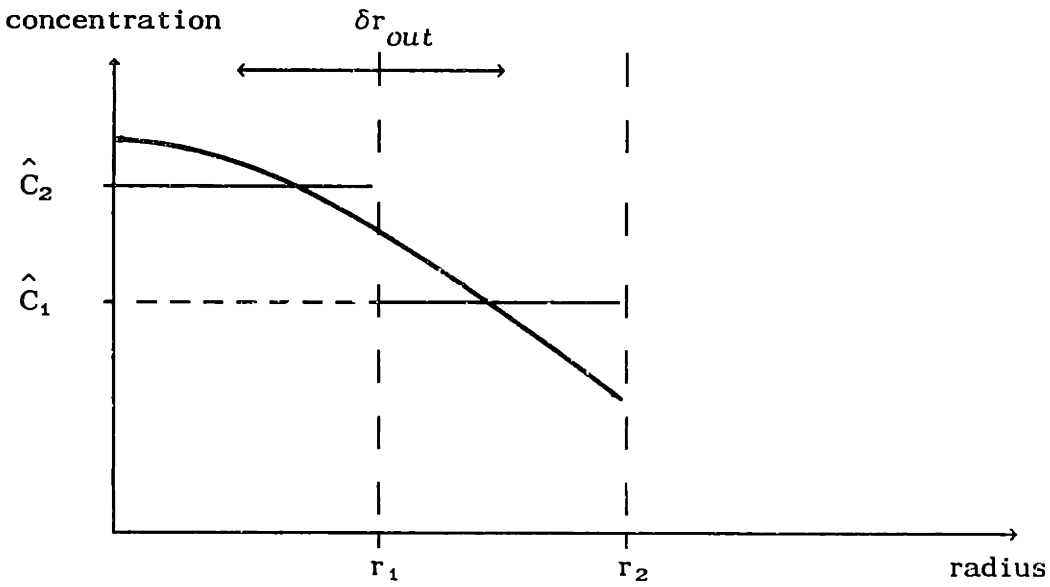

FIG. 6.8: Discrete and continuous fission product profiles in the innermost particle shells.

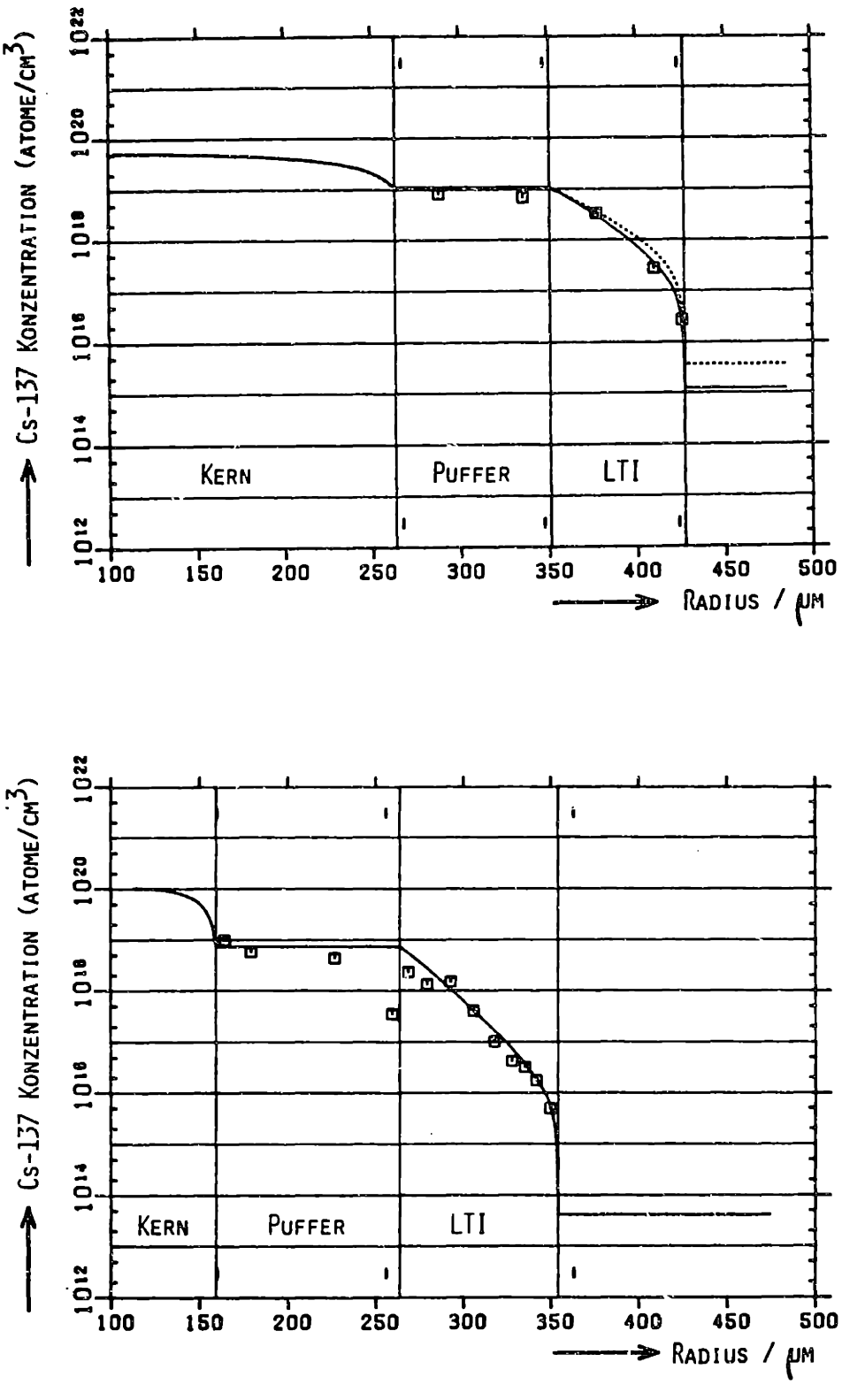

FIG. 6.9: Measured concentration profiles illustrating high buffer diffusivity [A3].

presents several fission product concentration profiles measured in irradiated fuel particles by a laser drilling technique [A2]. The concentration in the buffer is flat for all practical purposes. An infinite diffusivity implies that mass transfer can take place without a finite concentration gradient, which is clearly a good approximation for the particles which were measured.

In a buffer with infinite diffusivity, the concentrations at both the inner and outer buffer surfaces are exactly equal to the average buffer concentration. Since the buffer has only one concentration, it does not need to be subdivided into finer shells, and may be completely described with only one layer. First we shall develop the equations for the outermost kernel layer, then for the innermost IPyC layer, and finally that for the buffer layer itself.

First consider the outer kernel layer, whose outer surface is the inner buffer surface, illustrated in Figure 6.10. The concentration gradient at the inner surface is approximated in the same manner as for the homogeneous case:

$$\nabla C(r_{in}) \simeq \frac{\hat{C}_i - \hat{C}_{i-1}}{\delta r_{in}} \tag{6.20}$$

A somewhat different approximation is used for the outer surface, however, since the concentration there is known exactly in terms of the buffer concentration:

$$\nabla C(r_{out}) \simeq \frac{\hat{C}_{i+1} - \hat{C}_i}{\frac{1}{2}\,\delta r_i} \tag{6.21}$$

where $\hat{C}_{i+1}$ is the buffer concentration. Thus, the differential

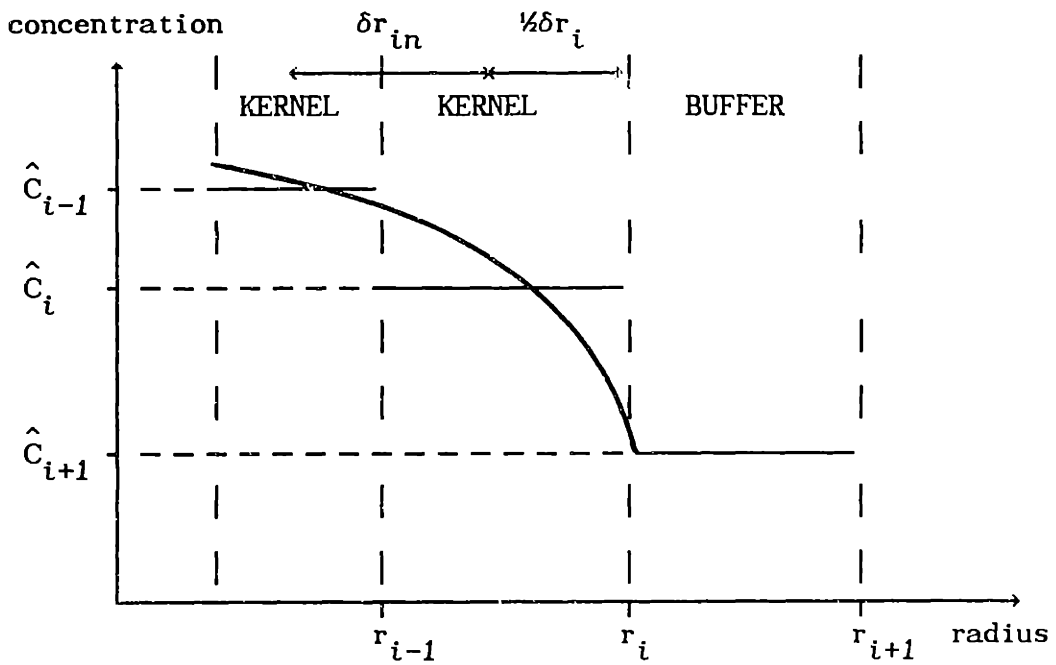

FIG. 6.10: Discrete and continuous fission product profiles near the inner buffer surface.

equation for the average fission product concentration when index i indicates the outer kernel layer is:

$$\frac{d\hat{C}_i}{dt} = \frac{D_i}{V_i}\left\{ -A_{in}\frac{\hat{C}_i - \hat{C}_{i-1}}{\delta r_{in}} + A_{out}\frac{\hat{C}_{i+1} - \hat{C}_i}{\tfrac{1}{2}\delta r_i} \right\} - \lambda \hat{C}_i + \hat{Q}_i$$

$$= \hat{C}_{i-1}\left[\frac{D_i A_{in}}{V_i \delta r_{in}}\right] - \hat{C}_i\left[\frac{D_i A_{in}}{V_i \delta r_{in}} + \frac{D_i A_{out}}{\tfrac{1}{2}V_i \delta r_i} + \lambda\right] + \hat{C}_{i+1}\left[\frac{D_i A_{out}}{\tfrac{1}{2}V_i \delta r_i}\right] + \hat{Q}_i \quad (6.22)$$

For the case of the inner IPyC layer, whose inner surface is the outer buffer surface, the following gradient approximations are used:

$$\nabla C(r_{in}) \simeq \frac{\hat{C}_i - \hat{C}_{i-1}}{\tfrac{1}{2}\delta r_i} \quad \text{and} \quad \nabla C(r_{out}) \simeq \frac{\hat{C}_{i+1} - \hat{C}_i}{\delta r_{out}} \quad (6.23)$$

The difference equation for index i designating the innermost IPyC layer is thus:

$$\frac{d\hat{C}_i}{dt} = \frac{D_i}{V_i}\left\{ -A_{in}\frac{\hat{C}_i - \hat{C}_{i-1}}{\tfrac{1}{2}\delta r_i} + A_{out}\frac{\hat{C}_{i+1} - \hat{C}_i}{\delta r_{out}} \right\} - \lambda \hat{C}_i + \hat{Q}_i$$

$$= \hat{C}_{i-1}\left[\frac{D_i A_{in}}{\tfrac{1}{2}V_i \delta r_i}\right] - \hat{C}_i\left[\frac{D_i A_{in}}{\tfrac{1}{2}V_i \delta r_i} + \frac{D_i A_{out}}{V_i \delta r_{out}} + \lambda\right] + \hat{C}_{i+1}\left[\frac{D_i A_{out}}{V_i \delta r_{out}}\right] + \hat{Q}_i \quad (6.24)$$

Finally, the buffer layer itself has a concentration which must be taken into consideration. The mass fluxes in and out of the buffer are calculated based on the diffusivities and approximate concentration gradients in the surrounding layers, as no gradient exists in the buffer. The situation is illustrated in Figure (6.11). If index i now represents the buffer, the following gradient approximations are used:

$$\nabla C(r_{in}) \simeq \frac{\hat{C}_i - \hat{C}_{i-1}}{\tfrac{1}{2}\delta r_{i-1}} \quad \text{and} \quad \nabla C(r_{out}) \simeq \frac{\hat{C}_{i+1} - \hat{C}_i}{\tfrac{1}{2}\delta r_{i+1}} \quad (6.25)$$

The difference equation for the buffer concentration is thus:

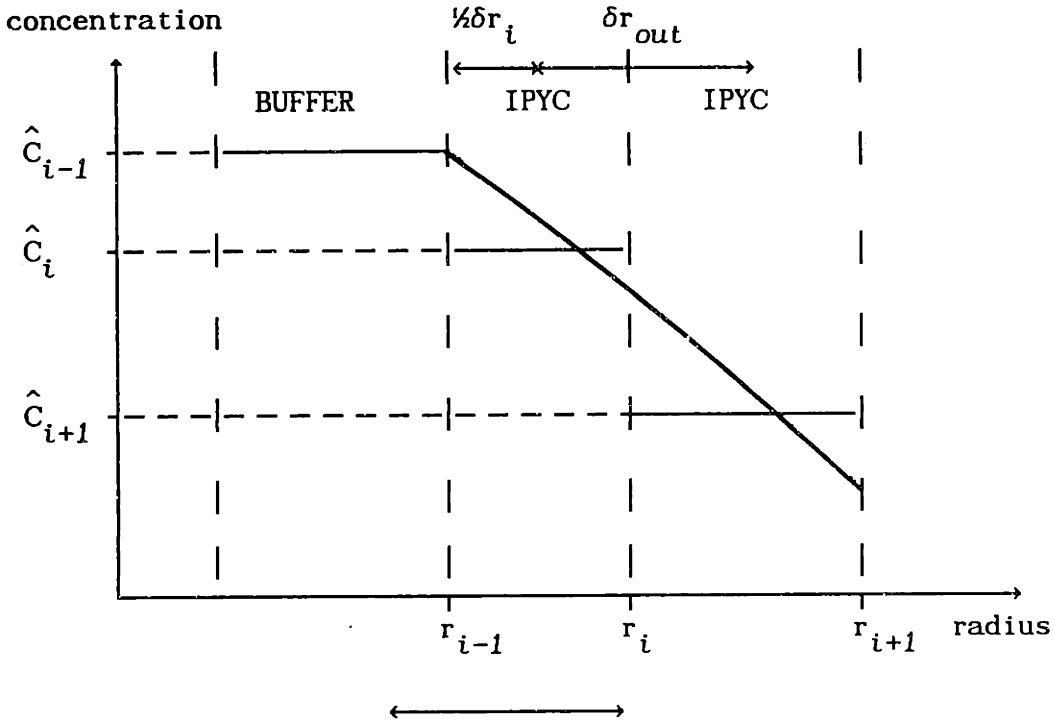

FIG. 6.11: Discrete and continuous fission product profiles in and adjacent to the buffer layer.

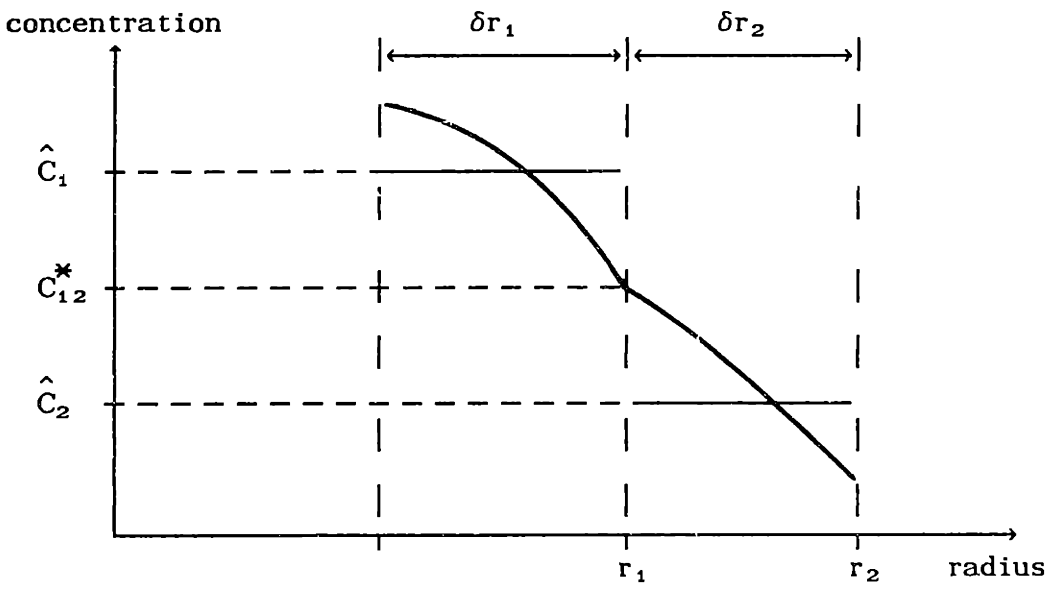

FIG. 6.12: Two adjacent spherical shells of differing materials.

$$\frac{d\hat{C}_i}{dt} = \frac{1}{V_i}\left\{-A_{in}D_{i-1}\frac{\hat{C}_i - \hat{C}_{i-1}}{\tfrac{1}{2}\,\delta r_{in}} + A_{out}D_{i+1}\frac{\hat{C}_{i+1} - \hat{C}_i}{\tfrac{1}{2}\,\delta r_{out}}\right\} - \lambda\,\hat{C}_i + \hat{Q}_i$$

$$= \hat{C}_{i-1}\left[\frac{D_{i-1}A_{in}}{\tfrac{1}{2}V_i\,\delta r_{in}}\right] - \hat{C}_i\left[\frac{D_{i-1}A_{in}}{\tfrac{1}{2}V_i\,\delta r_{in}} + \frac{D_{i+1}A_{out}}{\tfrac{1}{2}V_i\,\delta r_{out}} + \lambda\right] + \hat{C}_{i+1}\left[\frac{D_{i+1}A_{out}}{\tfrac{1}{2}V_i\,\delta r_{out}}\right] + \hat{Q}_i \quad (6.26)$$

Note the subscripts which appear on the diffusivities in the above equation. D_{i-1} is the kernel diffusivity and D_{i+1} is the IPyC diffusivity. The buffer diffusivity is not required for any of the coefficients.

4. Inner- and outer-most coating layer shells.

Slightly more complicated expressions arise when two materials of finite diffusivities are adjacent. In this case, boundary condition 2 is required to equate the mass fluxes. First let us examine a general case of two adjacent shells of differing materials, illustrated in Figure (6.12).

Let subscript "1" indicate the inner shell, and subscript "2" the outer. Let the concentration exactly *at* the boundary be designated C^*_{12}. Approximate the concentration gradients at the 1-2 boundary in the inner and outer materials as follows:

$$\nabla C_1\Big|_{r_{12}} \simeq \frac{C^*_{12} - \hat{C}_1}{\tfrac{1}{2}\,\delta r_1} \quad (6.27a)$$

$$\nabla C_2\Big|_{r_{12}} \simeq \frac{\hat{C}_2 - C^*_{12}}{\tfrac{1}{2}\,\delta r_2} \quad (6.27b)$$

Furthermore, application of boundary condition 2 implies that:

$$D_1\nabla C_1\Big|_{r_{12}} = D_2\nabla C_2\Big|_{r_{12}} \quad (6.28)$$

Eqs. (6.27) and (6.28) may be combined to eliminate the boundary concentration C^*_{12}:

$$D_1 \frac{C^*_{12} - \hat{C}_1}{\frac{1}{2}\delta r_1} = D_2 \frac{\hat{C}_2 - C^*_{12}}{\frac{1}{2}\delta r_2}$$

or $$C^*_{12}\left[\frac{D_1}{\delta r_1} + \frac{D_2}{\delta r_2}\right] = \hat{C}_1 \frac{D_1}{\delta r_1} + \hat{C}_2 \frac{D_2}{\delta r_2}$$

or $$C^*_{12} = \hat{C}_1 \frac{D_1/\delta r_1}{D_1/\delta r_1 + D_2/\delta r_2} + \hat{C}_1 \frac{D_2/\delta r_2}{D_1/\delta r_1 + D_2/\delta r_2} \qquad (6.29)$$

Define the following interface factor, Z_{12}:

$$Z_{12} \equiv \frac{D_1 \delta r_2}{D_1 \delta r_2 + D_2 \delta r_1}$$

Then Eq. (6.) may be written:

$$C^*_{12} = \hat{C}_1 Z_{12} + \hat{C}_2 (1 - Z_{12}) \qquad (6.30)$$

This equation lets us approximate the surface gradients without referencing the unknown interface concentration C^*_{12}, since Z_{12} is a function only of diffusivities and shell dimensions. Let subscript i indicate a shell whose outer boundary is adjacent to a different material, as illustrated in Figure 6.13. The following approximations for concentration gradients are used:

$$\nabla C(r_{in}) \simeq \frac{\hat{C}_i - \hat{C}_{i-1}}{\delta r_{in}} \qquad (6.31a)$$

and $$\nabla C(r_{out}) \simeq \frac{C^*_{i,i+1} - \hat{C}_i}{\frac{1}{2}\delta r_i}$$

$$= \frac{\hat{C}_i Z_{i,i+1} + \hat{C}_{i+1}(1-Z_{i,i+1}) - \hat{C}_i}{\frac{1}{2}\delta r_i}$$

$$= \frac{C_{i+1}(1-Z_{i,i+1}) - C_i(1-Z_{i,i+1})}{\frac{1}{2}\delta r_i} \qquad (6.31b)$$

Thus, the differential equation for layer i is thus:

$$\frac{d\hat{C}_i}{dt} = \frac{1}{V_i}\left\{-A_{in} D_i \frac{\hat{C}_i - \hat{C}_{i-1}}{\delta r_{in}} + A_{out} D_i \frac{\hat{C}_i(1-Z_{i,i+1}) + \hat{C}_{i+1}(1-Z_{i,i+1})}{\frac{1}{2}\delta r_i}\right\}$$

$$-\lambda \hat{C}_i + \hat{Q}_i$$

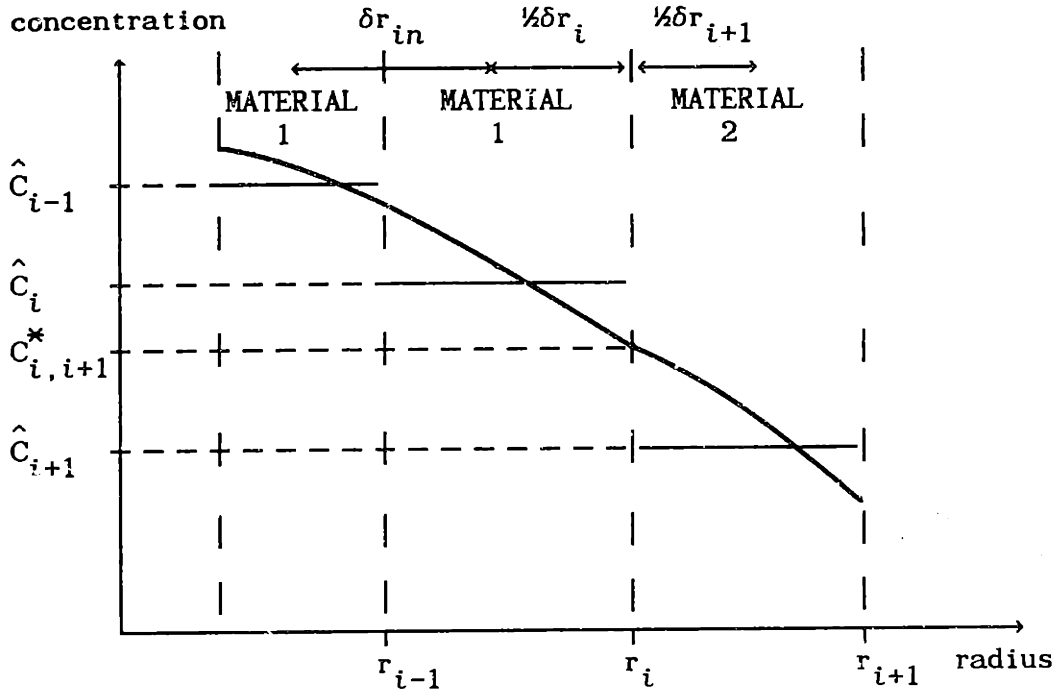

FIG. 6.13: Discrete and continuous fission product profiles near a shell with outer neighbor composed of a different material.

$$= \hat{C}_{i-1}\left[\frac{A_{in}D_i}{V_i \delta r_{in}}\right] - \hat{C}_i\left[\frac{A_{in}D_i}{V_i \delta r_{in}} + \frac{A_{out}D_i(1-Z_{i,i+1})}{\frac{1}{2} V_i \delta r_i} + \lambda\right] + C_{i+1}\left[\frac{A_{out}D_i(1-Z_{i,i+1})}{\frac{1}{2} V_i \delta r_i}\right] + Q_i \qquad (6.33)$$

The situation in which the index i designates a shell whose inner boundary borders on a different material is illustrated in Figure 6.14. The following gradient approximations are used:

$$\nabla C(r_{out}) \simeq \frac{\hat{C}_{i+1} - \hat{C}_i}{\delta r_{out}} \qquad (6.34)$$

$$\text{and} \quad \nabla C(r_{in}) \simeq \frac{\hat{C}_i - C^*_{i-1,i}}{\frac{1}{2} \delta r_i}$$

$$= \frac{\hat{C}_i - \hat{C}_{i-1}Z_{i-1,i} - \hat{C}_i(1-Z_{i-1,i})}{\frac{1}{2} \delta r_i}$$

$$= \frac{\hat{C}_i Z_{i-1,i} - \hat{C}_{i-1}Z_{i-1,i}}{\frac{1}{2} \delta r_i} \qquad (6.35)$$

Substitute Eqs. (6.34) and (6.35) into Eq. (6.15) to obtain the differential equation for the layer concentration:

$$\frac{d\hat{C}_i}{dt} = \frac{1}{V_i}\left\{-A_{in}D_i\frac{\hat{C}_i Z_{i-1,i} - \hat{C}_{i-1}Z_{i-1,i}}{\frac{1}{2} \delta r_i} + A_{out}D_i\frac{\hat{C}_{i+1} - \hat{C}_i}{\delta r_{out}}\right\} - \lambda \hat{C}_i + \hat{Q}_i$$

$$= \hat{C}_{i-1}\left[\frac{A_{in}D_i Z_{i-1,i}}{\frac{1}{2} V_i \delta r_i}\right] - \hat{C}_i\left[\frac{A_{in}D_i Z_{i-1,i}}{\frac{1}{2} V_i \delta r_i} + \frac{A_{out}D_i}{V_i \delta r_{out}} + \lambda\right] + \hat{C}_{i+1}\left[\frac{A_{out}D_i}{V_i \delta r_{out}}\right] + \hat{Q}_i \qquad (6.36)$$

Notice again the subscripts on the diffusivities in the above equations. The diffusivities for the other material do not explicitly appear in the expressions; their effect is felt only through the Z

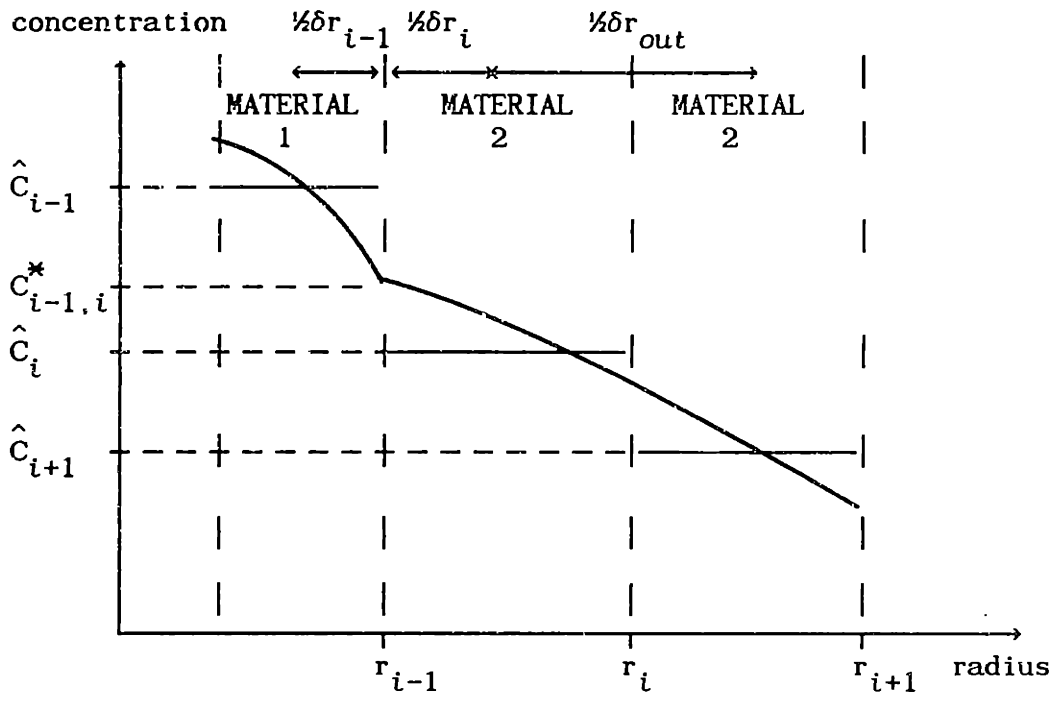

FIG. 6.14: Discrete and continuous fission product profiles near a shell with inner neighbor composed of a different material.

interface terms.

5. Outer particle shell.

The final situation which must be considered is that of the extreme outermost shell in the particle model. Here the third boundary condition (zero concentration) is used to define the concentration value at the shell outer boundary. The situation is illustrated in Figure 6.15. The following gradient approximations are used:

$$\nabla C(r_{in}) \simeq \frac{\hat{C}_i - \hat{C}_{i-1}}{\delta r_{in}} \tag{6.37a}$$

$$\text{and} \quad \nabla C(r_{out}) \simeq \frac{C(r_{out}) - \hat{C}_i}{\frac{1}{2}\delta r_i} = -\frac{\hat{C}_i}{\frac{1}{2}\delta r_i} \tag{6.37b}$$

Sutstituting Eqs. (6.37a) and (6.37b) into (6.15), we obtain the differential equation for shell i indicating the outermost layer in the particle model:

$$\frac{d\hat{C}i}{dt} = \frac{1}{V_i}\left\{-A_{in}D_i\frac{\hat{C}_i - \hat{C}_{i-1}}{\delta r_{in}} + A_{out}D_i\frac{-\hat{C}_i}{\frac{1}{2}\delta r_i}\right\} - \lambda\hat{C}_i + \hat{Q}_i$$

$$= \hat{C}_{i-1}\left[\frac{D_iA_{in}}{V_i\delta r_{in}}\right] - \hat{C}_i\left[\frac{D_iA_{in}}{V_i\delta r_{in}} + \frac{D_iA_{out}}{\frac{1}{2}V_i\delta r_i} + \lambda\right] + \hat{Q}_i \tag{6.38}$$

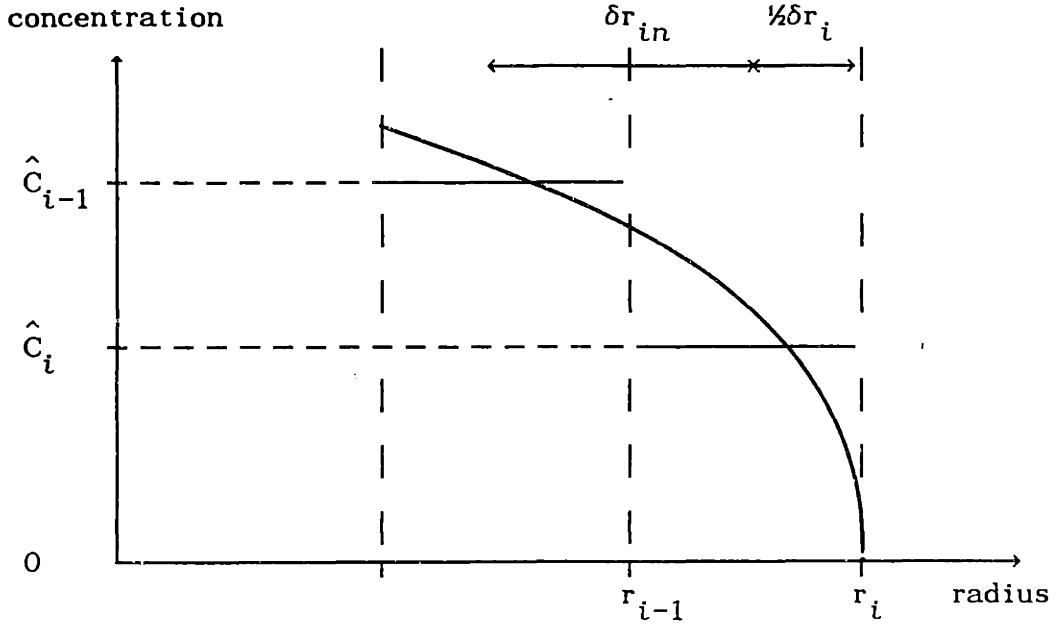

FIG. 6.15: Discrete and continuous fission product profiles near the outermost particle shell.

6.3 DIFFUSION TRANSITION MATRICES

In the previous section, equations were developed which relate the time dependent behavior of a discrete spherical shell's average fission product concentration to those of its neighbors. In this section, we consider the set of all such equations which apply for a fuel particle as a linear system. Under the proper circumstances, the system is time invariant and the analytic solution is easily obtained. Here we develop a general solution which applies either A) within a single region of a stationary MHTGR core, or B) during a relatively short time interval during a thermal transient. In addition, we shall also solve for the fission product release rate. Finally, some of the computational procedures utilized to compute these diffusion transition matrices are reviewed.

6.3.1 Solution of the Discrete Diffusion Equation.

Suppose that a fuel particle is divided into N discrete spherical shells, the innermost numbered 1, and the index increasing with each outward shell. Every shell is composed of only one material. The innermost shell need not have an inner radius of zero, but the concentration gradient at the inner radius must vanish. The buffer layer is considered a single shell, and all coating layers must have at least three sub-shells. In this case, the equations which were derived in the previous section may be written in vector/matrix form as follows:

$$\dot{\mathbf{c}} = -\mathbf{F}\,\mathbf{c} + \mathbf{q} \qquad (6.39)$$

where

$$\mathbf{c} = \begin{bmatrix} \hat{C}_1 \\ \hat{C}_2 \\ \hat{C}_3 \\ \vdots \\ \hat{C}_N \end{bmatrix} \quad ; \quad \mathbf{q} = \begin{bmatrix} \hat{Q}_1 \\ \hat{Q}_2 \\ \hat{Q}_3 \\ \vdots \\ \hat{Q}_N \end{bmatrix} \quad ; \text{ and}$$

F = an NxN coefficient matrix, with a single diagonal stripe of width three; the elements of **F** were derived in section 6.3, and are summarized in Table 6.3.

Note that the elements of **c** are all concentrations of the same fission product within a single fuel particle. Different elements of **c** are the concentrations at various radial positions. Hence, the vector **c** actually represents the fission product profile within a fuel particle.

The fission product source vector **q** is non-zero only for the stationary core analysis. Values of its elements are derived from fission rates calculated by FUPAR/VSOP, and from recoil considerations. Calculation of the elements of **q** is addressed in the next chapter.

The elements of the **F** matrix depend upon the diffusivities of the fission product in the fuel particle constituent materials, and thus upon the time-dependent temperature experienced by the fuel particle. Likewise, the fission product source vector **q** varies in time as well, since it is dependent on the local neutron flux. Suppose for the moment, however, that we focus either on A) a small enough region of the core so that fuel temperatures and neutron flux can be assumed reasonably constant, or B) a short enough time interval during a transient that fuel temperatures may be treated as approximately constant. Furthermore, let us assume that the particle enters the region or period of interest at time 0 with an initial concentration

TABLE 6.3: F MATRIX ELEMENTS

PARTICLE SHELL (row j of F)	IN (column j-1)	CENTER (column j)	OUT (column j+1)
central	**********	$-OUT - \lambda$	$\frac{A_{out}\ D_K}{V_j\ \delta r_{out}}$
mid kernel	$\frac{A_{in}\ D_K}{V_j\ \delta r_{in}}$	$-IN - OUT - \lambda$	$\frac{A_{out}\ D_K}{V_j\ \delta r_{out}}$
outermost kernel	$\frac{A_{in}\ D_K}{V_j\ \delta r_{in}}$	$-IN - OUT - \lambda$	$\frac{A_{out}\ D_K}{V_j\ (\delta r_j/2)}$
buffer	$\frac{A_{in}\ D_K}{V_j\ (\delta r_{j-1}/2)}$	$-IN - OUT - \lambda$	$\frac{A_{out}\ D'_I}{V_j\ (\delta r_{j+1}/2)}$
innermost IPyC	$\frac{A_{in}\ D_I}{V_j\ (\delta r_j/2)}$	$-IN - OUT - \lambda$	$\frac{A_{out}\ D_I}{V_j\ \delta r_{out}}$
mid IPyC	$\frac{A_{in}\ D_I}{V_j\ \delta r_{in}}$	$-IN - OUT - \lambda$	$\frac{A_{out}\ D_I}{V_j\ \delta r_{out}}$
outermost IPyC	$\frac{A_{in}\ D_I}{V_j\ \delta r_{in}}$	$-IN - OUT - \lambda$	$\frac{A_{out}\ D_I\ (1-Z_{IS})}{V_j\ (\delta r_j/2)}$

TABLE 6.3 (CONT'D): F MATRIX ELEMENTS

innermost SIC	$\frac{A_{in} D_S Z_{IS}}{V_j (\delta r_j/2)}$	-IN - OUT $-\lambda$	$\frac{A_{out} D_S}{V_j \delta r_{out}}$
mid SIC	$\frac{A_{in} D_S}{V_j \delta r_{in}}$	-IN - OUT $-\lambda$	$\frac{A_{out} D_S}{V_j \delta r_{out}}$
outermost SIC	$\frac{A_{in} D_S}{V_j \delta r_{in}}$	-IN - OUT $-\lambda$	$\frac{A_{out} D_S (1-Z_{SO})}{V_j (\delta r_j/2)}$
innermost OPyC	$\frac{A_{in} D_O Z_{SO}}{V_j (\delta r_j/2)}$	-IN - OUT $-\lambda$	$\frac{A_{out} D_O}{V_j \delta r_{out}}$
mid-OPyC	$\frac{A_{in} D_O}{V_j \delta r_{in}}$	-IN - OUT $-\lambda$	$\frac{A_{out} D_O}{V_j \delta r_{out}}$
outermost OPyC	$\frac{A_{in} D_O}{V_j \delta r_{in}}$	-IN $-\frac{A_{out} D_O}{V_j(\delta r_j/2)}$ $-\lambda$	********

"CENTER" refers to element (j,j) of **F**;
"IN" refers to element $(j,j-1)$ of **F**;
"OUT" refers to element $(j,j+1)$ of **F**.

subscripts: K ⇒ kernel;
I ⇒ IPyC layer;
S ⇒ SiC layer;
O ⇒ OPyC layer;

geometrical factors are defined in Fig. 6.6.

vector $\mathbf{c}_o$ and remains until time Δt. In this case, both $\mathbf{F}$ and $\mathbf{q}$ are constant during the interval $0 \rightarrow \Delta t$, and we may integrate equation (6.39) in much the same manner as the fission product isotopic equations in Chapter 4.

First, define the following integrating factor:

$$\mathbf{P} \equiv \exp[\,\mathbf{F}t\,] \tag{6.40}$$

$$\text{so that } \frac{d}{dt}\mathbf{P} = \mathbf{F}\exp[\,\mathbf{F}t\,] = \mathbf{F}\,\mathbf{P}$$

Multiply both sides of Eq. (6.39) by $\mathbf{P}$:

$$\mathbf{P}\,\dot{\mathbf{c}} = -\mathbf{P}\,\mathbf{F}\,\mathbf{c} + \mathbf{P}\,\mathbf{q}$$

Rearrange the above equation, and use the fact that $\mathbf{F}$ and $\mathbf{P}$ commute:

$$\mathbf{P}\,\dot{\mathbf{c}} + \mathbf{P}\,\mathbf{F}\,\mathbf{c} = \mathbf{P}\,\mathbf{q}$$

$$\mathbf{P}\,\dot{\mathbf{c}} + \dot{\mathbf{P}}\,\mathbf{c} = \mathbf{P}\,\mathbf{q}$$

$$\frac{d}{dt}[\,\mathbf{P}\,\mathbf{c}\,] = \mathbf{P}\,\mathbf{q}$$

Integrate the result from time 0 to time Δt:

$$\int_0^{\Delta t} \frac{d}{dt}[\,\mathbf{P}\,\mathbf{c}\,]\,dt = \int_0^{\Delta t} \mathbf{P}\,\mathbf{q}\,dt$$

$$\text{or } \mathbf{P}(\Delta t)\mathbf{c}(\Delta t) - \mathbf{P}(0)\mathbf{c}_o = \int_0^{\Delta t} \mathbf{P}\,\mathbf{q}\,dt \tag{6.41}$$

The integral on the right-hand side of Eq. (6.41) may be evaluated analytically:

$$\int_0^{\Delta t} \mathbf{P}\,\mathbf{q}\,dt = \int_0^{\Delta t} \exp[\mathbf{F}t]\,\mathbf{q}\,dt = \left\{\int_0^{\Delta t} \exp[\mathbf{F}t]\,dt\right\}\mathbf{q}$$

$$= \mathbf{F}^{-1}\left[\exp[\mathbf{F}t]\right]_0^{\Delta t}\mathbf{q} = \mathbf{F}^{-1}\left[\exp[\mathbf{F}\Delta t] - \mathbf{I}\right]\mathbf{q} \tag{6.42}$$

Substitute Eq. (6.42) into Eq. (6.41):

$$\exp[F\Delta t]\ \mathbf{c}(\Delta t) - \mathbf{c}_0 = F^{-1}\left[\exp[F\Delta t] - I\right]\mathbf{q}$$

since $P(0) = \exp[F\times 0] = I$. Add $\mathbf{c}_0$ to both sides of the above equation, then multiply by $\exp[-F\Delta t]$:

$$\mathbf{c}(\Delta t) = \exp[-F\Delta t]\ \mathbf{c}_0 + F^{-1}\left[I - \exp[-F\Delta t]\right]\mathbf{q}$$

This equation is the exact solution for $\mathbf{c}(\Delta t)$ under the assumptions of time independent diffusivities and fission product sources, as well as the finite difference approximations of the previous section. The equation may be abbreviated if we define the following diffusion transition matrices:

$$\mathbf{R}(\Delta t) \equiv \exp[-F\Delta t] \tag{6.43a}$$

$$\mathbf{S}(\Delta t) \equiv F^{-1}[I-\mathbf{R}(\Delta t)] \tag{6.43b}$$

so that:

$$\boxed{\mathbf{c}(\Delta t) = \mathbf{R}(\Delta t)\ \mathbf{c}_0 + \mathbf{S}(\Delta t)\ \mathbf{q}} \tag{6.44}$$

6.3.2. Fission Product Release.

It is also necessary to derive an expression for the time-averaged release rate of fission product atoms from the particle during the time interval $0 \rightarrow \Delta t$. Let the symbol $\dot{\rho}$ denote the rate of release of fission product atoms from the outer surface of the fuel particle. Fick's Law allows us to express this rate in terms of the concentration gradient at the particle surface:

$$\dot{\rho} = A_{surf}\ J_{surf} = -4\pi\ r_{out}^2 D_{surf} \nabla C(r_{out}) \tag{6.45}$$

where:

A_{surf}= particle outer surface area = $4\pi\ r_{out}^2$;

J_{surf}= fission product outward mass flux at outer surface;

D_{surf} = diffusivity at particle outer surface; and

$\nabla C(r_{out})$ = concentration gradient at particle outer surface.

The concentration gradient at the particle surface can be approximated in the same manner as in the finite difference development. Recall from Eq. (6.) in the previous section:

$$\nabla C(r_{out}) \simeq \frac{C(r_{out}) - \hat{C}_N}{\frac{1}{2}\,\delta r_N} = -\frac{\hat{C}_N}{\frac{1}{2}\delta r_N}$$

where:

$C(r_{out})$ = concentration at particle outer surface = 0;

$\hat{C}_N$ = average fission product concentration in outer shell;

δr_N = thickness of particle outer shell.

Substitute this equation into Eq. (6.45) to obtain:

$$\dot{\rho} = \frac{8\pi\, r_{out}^2 D_{out}}{\delta r_N} \hat{C}_N \qquad (6.46)$$

Thus, within our finite difference formulation, the fission product release rate is directly proportional to the average fission product concentration in the outer particle shell. If we define the N-element vector $\mathbf{u}_i$ as follows:

$$\mathbf{u}_i \equiv [\, 0,\ 0,\ 0,\ \ldots\ 0,\ \underset{i\text{'th element}}{\underset{\uparrow}{1}},\ 0,\ \ldots\ 0,\ 0\,]^+$$

Then the outer shell average concentration $\hat{C}_N$ may be written:

$$\hat{C}_N = \mathbf{u}_N^+ \mathbf{c}$$

and the release rate may be expressed as a linear function of the concentration profile vector $\mathbf{c}$:

$$\dot{\rho} = \frac{8\pi\, r_{out}^2 D_{out}}{\delta r_N} \mathbf{u}_N^+ \mathbf{c} \qquad (6.47)$$

We are interested in the release rate averaged over the time period from 0 to Δt, in which temperature and source rates are constant. Recall the linear time/volume average operator, $\langle\ \rangle_j$:

$$\langle\ \rangle_j \equiv \frac{1}{\Delta t_j} \int_0^{\Delta t_j} dt$$

The subscript "j" represents either A) zone "j" in the stationary reactor, or B) the j'th time step in a thermal transient. Apply the time average operator to both sides of Eq. (6.47):

$$\langle \dot{\rho} \rangle_j = \left\langle \frac{8\pi\, r_{out}^2 D_{out}}{\delta r_N} \mathbf{u}_N^+ \mathbf{c} \right\rangle_j$$

$$= \frac{8\pi\, r_{out}^2 D_{out}}{\delta r_N} \mathbf{u}_N^+ \langle \mathbf{c} \rangle_j \qquad (6.48)$$

The second operation is permissible because $\mathbf{c}$ is the only time-dependent variable on the right-hand side of the equation. The final step, therefore, is to determine an expression for the time-averaged fission product concentration profile vector, $\langle \mathbf{c} \rangle_j$. Begin by substituting the analytic expression for the time dependent behavior of $\mathbf{c}$ into the expression for $\langle \mathbf{c} \rangle_j$:

$$\langle \mathbf{c} \rangle_j \equiv \frac{1}{\Delta t_j} \int_0^{\Delta t_j} \mathbf{c}(t)\, dt$$

$$= \frac{1}{\Delta t_j} \int_0^{\Delta t_j} \left\{ \exp[-Ft]\, \mathbf{c}_0 + F^{-1} \left[I - \exp[-Ft] \right] \mathbf{q}_j \right\} dt$$

$$= \frac{1}{\Delta t_j} \left\{ \int_0^{\Delta t_j} \exp[-Ft] dt \right\} \mathbf{c}_0 + \frac{1}{\Delta t_j} \left\{ \int_0^{\Delta t_j} \mathbf{S}(t)\, dt \right\} \mathbf{q}_j$$

$$= \frac{1}{\Delta t_j}[-F^{-1}]\left[\exp[-Ft]\right]_0^{\Delta t} c_o + \frac{1}{\Delta t_j}\left\{\int_0^{\Delta t_j} S(t)\, dt\right\} q_j$$

$$= \frac{1}{\Delta t_j}F^{-1}\left[I-\exp[-F\Delta t]\right] c_o + \frac{1}{\Delta t_j}\left\{\int_0^{\Delta t_j} S(t)\, dt\right\} q_j$$

$$= \frac{1}{\Delta t_j} S(\Delta t_j)\, c_o + \frac{1}{\Delta t_j}\left\{\int_0^{\Delta t_j} S(t)\, dt\right\} q_j \qquad (6.49)$$

The second term on the right-hand side of this equation could be evaluated analytically in a manner similar to the first term. However, this results in further complication and is not felt to contribute considerably to the accuracy of the solution, since q_j (the fission product source within zone j) is only approximately constant in any case. Therefore, we will make a linear approximation within the above integral, based on the physical interpretation of the **S** matrix. Suppose **q** indicates a unit source of fission product in only one shell of the particle. Pre-multiplication by **S** yields a vector with values corresponding to the concentration increases after time Δt due to the single unit source. Thus, at times between 0 and Δt, it seems reasonable to approximate the contributions to fission product concentration due to source diffusion as a linear function of **S** which agrees completely at time Δt. The approximation is:

$$S(t) \approx (t/\Delta t_j)\, S(\Delta t_j)$$

Substitute this equation into Eq. (6.49):

$$\langle c \rangle_j = \frac{1}{\Delta t_j} S(\Delta t_j)\, c_o + \frac{1}{\Delta t_j}\left\{\int_0^{\Delta t_j} S(t)\, dt\right\} q_j$$

$$\approx \frac{1}{\Delta t_j} \mathbf{S}(\Delta t_j)\ \mathbf{c}_0 + \frac{1}{\Delta t_j}\left\{\int_0^{\Delta t_j} (t/\Delta t)\ \mathbf{S}(\Delta t)\ dt\right\} \mathbf{q}_j$$

$$\approx \frac{1}{\Delta t_j} \mathbf{S}(\Delta t_j)\ \mathbf{c}_0 + \frac{1}{\Delta t_j^2} \mathbf{S}(\Delta t_j)\left[\int_0^{\Delta t_j} t\ dt\right] \mathbf{q}_j$$

$$\approx \frac{1}{\Delta t_j} \mathbf{S}(\Delta t_j)\ \mathbf{c}_0 + \frac{1}{\Delta t_j^2} \mathbf{S}(\Delta t_j)\left[\Delta t_j^2/2\right] \mathbf{q}_j$$

or:
$$\langle \mathbf{c} \rangle_j \approx \frac{1}{\Delta t_j} \mathbf{S}(\Delta t_j)\ \mathbf{c}_0 + \tfrac{1}{2}\, \mathbf{S}(\Delta t_j)\ \mathbf{q}_j \qquad (6.50)$$

Eq. (6.50) may now be substituted into (6.48) for the zone-averaged release rate:

$$\langle \dot{\rho} \rangle_j = \frac{8\pi\ r_{out}^2 D_{out}}{\delta r_N} \mathbf{u}_N^+ \langle \mathbf{c} \rangle_j$$

$$= \frac{8\pi\ r_{out}^2 D_{out}}{\delta r_N} \mathbf{u}_N^+ \left[\frac{1}{\Delta t_j} \mathbf{S}(\Delta t_j)\ \mathbf{c}_0 + \tfrac{1}{2}\, \mathbf{S}(\Delta t_j)\ \mathbf{q}_j\right] \qquad (6.51)$$

6.3.3. Calculating the Diffusion Transition Matrices.

Recall that the **R** matrix is defined as a simple matrix exponential:

$$\mathbf{R}(\Delta t) \equiv \exp[-\mathbf{F}\Delta t\ ]$$

The procedure for calculating **R** is identical to that used to calculate the **T** and **L** transition matrices in FUPAR. Details of the method are presented in Appendix A.

The **S** source/diffusion matrix presents a more complicated problem, however. Recall the defintion of **S** from Eq. (6.43):

$$\mathbf{S} \equiv \int_0^{\Delta t} \mathbf{R}(\tau)\ d\tau = \mathbf{F}^{-1}\ [\ \mathbf{I} - \mathbf{R}(\Delta t)\ ] \qquad (4.52)$$

Problems arise in calculating both this matrix at extreme magnitudes of the norm of $\mathbf{F}\Delta t$. Different computational methods have been developed to use in different circumstances.

(1) Very small norms.

For values of $\|F\Delta t\|$ between 0 and 1.0, calculation of F^{-1} was found to lead to numerical difficulties. Specifically, elements of **S** calculated using inverse **F** matrices according to the second definition in Eq. (6.52) had negative magnitudes, which is clearly a physical impossibility. For this reason, an iterative approach is adopted to calculate **S**. The iterative technique is based on the integral definition of Eq. (6.52) applied to the series definition of $\mathbf{R}(\Delta t)$:

$$\begin{aligned}
\mathbf{S}(\Delta t) \equiv \int_0^{\Delta t} \mathbf{R}(\tau)\, d\tau &= \int_0^{\Delta t} \left[\sum_{k=0}^{\infty} \frac{(-F\tau)^k}{k!} \right] d\tau \\
&= \sum_{k=0}^{\infty} \frac{1}{k!} \int_0^{\Delta t} (-F\tau)^k d\tau = \sum_{k=0}^{\infty} \frac{-F^k}{k!} \frac{1}{k+1} (\Delta t)^{k+1} \\
&= \Delta t \sum_{k=1}^{\infty} \frac{(-F\Delta t)^k}{(k+1)!}
\end{aligned} \tag{6.53}$$

The summation in Eq. (6.53) is almost identical to that in the definition of the matrix exponential, except that the factorial term in the denominator is increased by one. Thus, for small norms of $\|F\Delta t\|$, the PDIF program uses a modified version of the same subroutine which calculates matrix exponentials, differing only in the denominator of the summation. A final multiplication by Δt yields the $\mathbf{S}(\Delta t)$ matrix. The same iterative technique and error criterion outlined in Appendix A.1 is used, as the change in the denominator serves only to decrease the residual errors.

(2) Intermediate norms.

For intermediate norms, in the range from $1 \leq \|F\Delta t\| \leq 20$, the

iterative summation procedure described above is no longer a feasible means of calculating **S**. The larger the norm, the more iterations which are necessary for a given level of convergence. When the number of iterations passes a certain limit, the precision required of the large power terms exceeds the computer's capacity. Negative elements of **S** may result in such cases, following several hundred iterations. Under these circumstances, it is necessary to use a different technique to calculate **S**.

The alternate method is based on the definition of **S** in terms of the **F** and **R**(Δt) matrices:

$$\mathbf{S}(\Delta t) \equiv \mathbf{F}^{-1} [\, \mathbf{I} - \mathbf{R}(\Delta t) \,]$$

Recall that the **F** matrix, though of large dimension (PDIF allows up to 40 layers per particle), represents a one dimensional diffusive system, and thus each diagonal element is coupled only to its immediate neighbors. Therefore, direct calculation of the inverse of **F** is possible, and becomes numerically feasible for norms in the intermediate range. The inversion is accomplished through Choleski factorization (see Appendix A.1), which factors **F** into two component matrices, $\mathbf{F}_L$ and $\mathbf{F}_U$. $\mathbf{F}_L$ is a lower-diagonal matrix, and $\mathbf{F}_U$ is an upper diagonal matrix:

$$\mathbf{F} = \mathbf{F}_L \mathbf{F}_U$$

The inverse of a triangular matrix is particularly easy to calculate by succesive elimination. Once the inverse matrices $\mathbf{F}_L^{-1}$ and $\mathbf{F}_U^{-1}$ are known, the inverse of F is found by their multiplication:

$$\mathbf{F}^{-1} = \mathbf{F}_U^{-1} \mathbf{F}_L^{-1}$$

The **S** matrix is then easily calculated:

$$\mathbf{S}(\Delta t) = \mathbf{F}_U^{-1}\,\mathbf{F}_L^{-1}\,[\,\mathbf{I} - \mathbf{R}(\Delta t)\,]$$

(3) Very large norms.

If the norm of $\mathbf{F}\Delta t$ is greater than 20, neither of the two techniques outlined above are reliable. The recourse in this case is to redefine the problem so that $\|\mathbf{F}\Delta t\|$ falls within the calculable range.

The definiton of the matrix norm used in this work is:

$$\|\mathbf{A}\| \equiv \max_i \left\{ \sum_j |a_{ij}| \right\}$$

where a_{ij} is the element of $\mathbf{A}$ in row i, column j. Refer to Table 6.3, which defines all elements of the $\mathbf{F}$ matrix. Note that every element of $\mathbf{F}$ in row j has the factors V_j (the volume of the j'th discrete shell) and δr_j (the thickness of shell j) in the denominator. Large norms correspond either to A) a particle discretization with excessively small layer volumes, or B) too large a time step Δt. Therefore, if a situation arises in which PDIF will not calculate $\mathbf{S}$ due to excess values of $\|\mathbf{F}\Delta t\|$, the user should either A) alter the input to create a coarser particle layer structure, or B) shorten the time step Δt. As the time step is fixed by the reactor design in the stationary core calculation, the second option is only available for the transient case.

The above discussion illustrates an interesting "perversity" inherent to the discrete diffusion analysis. Too coarse a mesh spacing results in underestimation of fission product release at small diffusion times. This is because at very small times, the fission product profile has a shape like that illustrated in Fig. 6.16, in which the diffusion

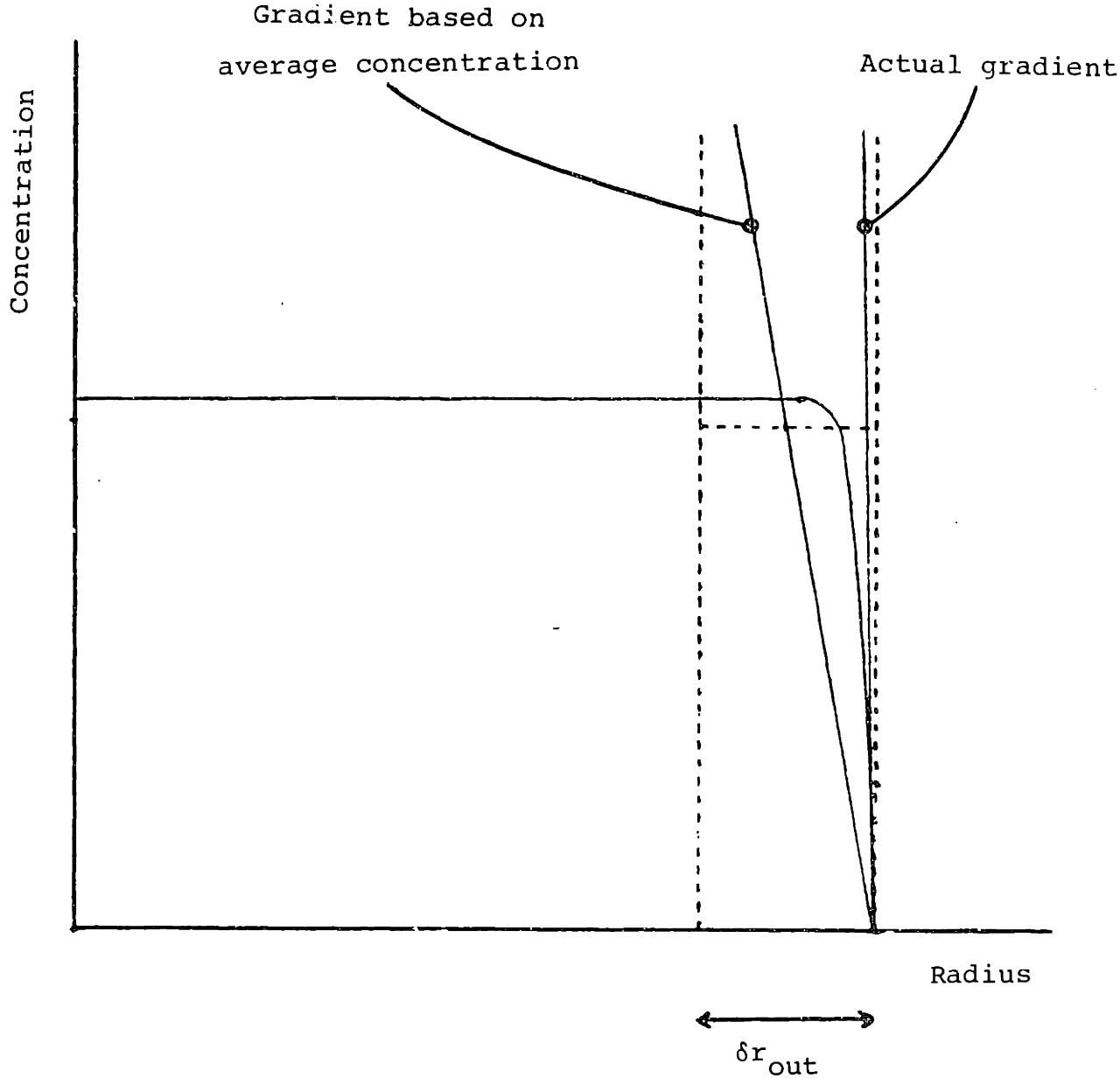

FIG. 6.16: Fission product concentration profile near the particle boundary at very short diffusion times.

front is highly non-linear and has not yet penetrated far into the outer shell. In this case, the actual concentration gradient at the particle surface is significantly greater than would be predicted on the basis of the outer shell's average concentration using Eq. (6.37). The discrete model will underpredict fission product release until the profile attains a more nearly linear shape.

In order to minimize this error, it is desirable to make the outer particle layers as thin as possible. If the thicknesses were adjustable to any degree, it would then be a simple matter to make the outer shells thin enough so that the profiles within them achieve an approximate linear shape within the first time step of analysis. However, a limit on minimimum shell volume is encountered due to the numerical prccedures for calculating **S** described above. It therefore falls upon the user to select, for a given size time step, the minimum possible mesh spacing which still allows reliable calculation of the **S** matrix.

Another problem then arises: If an adequate mesh spacing is selected for reactor operation, which is associated with certain values Δt_i and D_i of time steps and diffusivities, then it will in general *not* be a good discretization for the transient problem. A mesh spacing fine enough to predict releases in the steady state will in general cause $\|\mathbf{F}\Delta t\|$ to exceed 20 in the transient case, due to the increased diffusivities at higher temperatures. Thus, the PDIF program allows the user to redefine the particle layer structure following the operational calculations. In this way, underprediction of release can be minimized in both the operating and the transient calculations.

6.4 THE FISSION PRODUCT SOURCE VECTOR

The source of fission products within a fuel particle during operation is modeled by the **q** vector introduced in the previous section. The magnitude and distribution of the source vector elements are determined by the local fission rate or parent isotope concentration, and by the effects of fission product recoil near the boundaries of the kernel and outer coating layers. This section addresses the calculation of **q**, accounting for recoil and the effects of heavy metal contamination.

6.4.1 Release due to recoil

At low temperatures, the rate of diffusive fission product release becomes quite small, due to the strong inverse temperature dependence of the fission product diffusivities. Only the hottest sections of an operating MHTGR core will achieve significant rates of diffusive release. In the cooler portions of the reactor, the direct recoil mechanism contributes significantly to steady state release. In this section, a simple model is developed to incorporate direct recoil effects. The model determines a transformation on the fission product source vector **q** so that the net appearance of fission products reflects that which actually occurs. The contribution of recoil to the release rate is calculated as well.

The physical situation to be modeled is illustrated in Figure 6.17, in which a discrete spherical shell is located close to the outer surface of the fuel kernel or outer coating layer. Fissions are assumed to occur uniformly throughout the material, at volumetric rate F

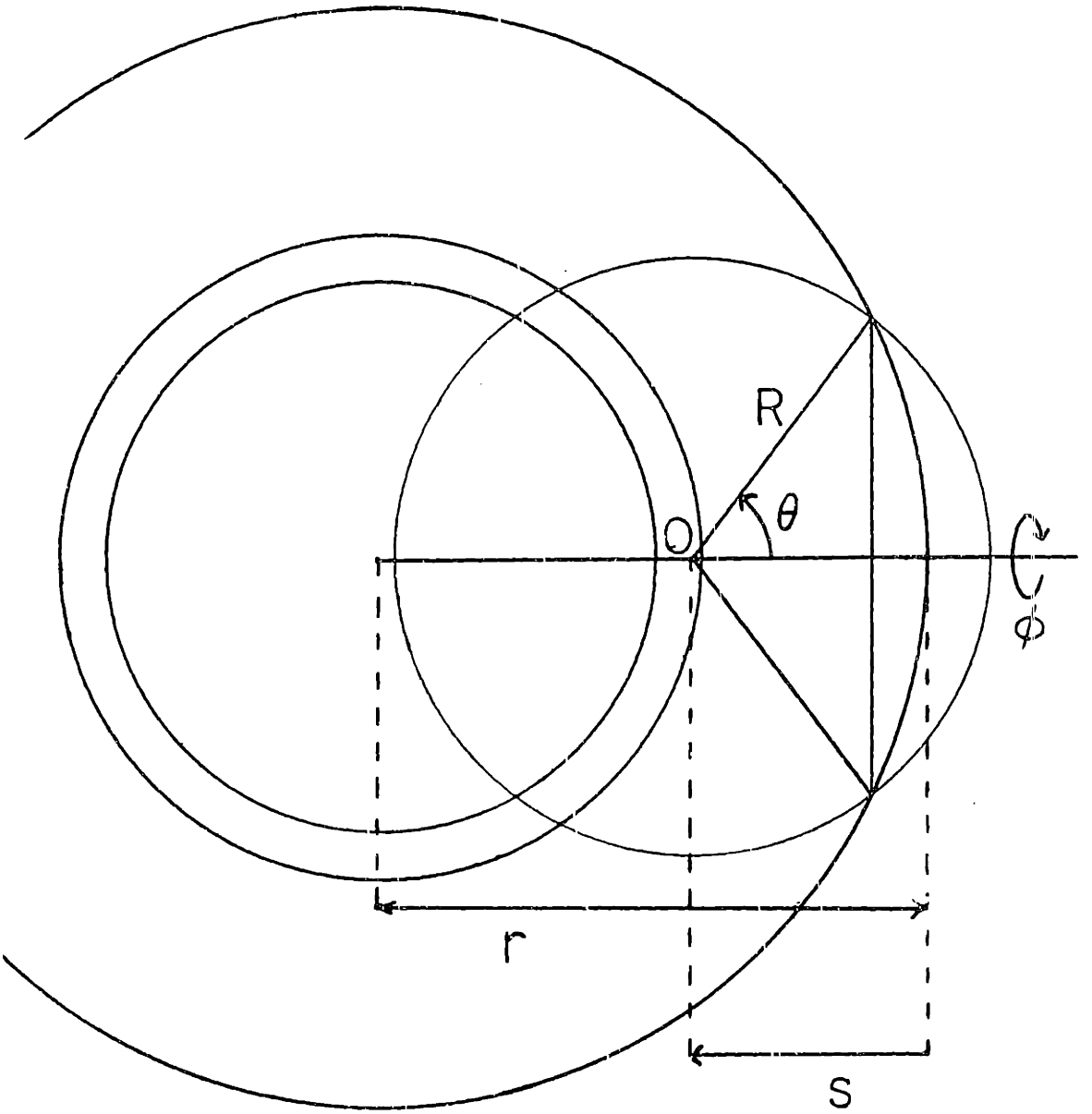

FIG. 6.17: Geometry for calculating fission product release due to direct recoil.

fissions/barn-cm-sec. The resulting fission products are assumed to have uniform range R, and are assumed to stop immediately after travelling this distance. Each fission produces y fission product atoms, thus deep within the sphere the volumetric birth rate is $B = yF$ FP's/barn-cm-sec. In a shell close to the sphere surface, however, some fraction of the fission products produced by a fission will escape the material and be released directly by recoil.

Consider a point O located some distance s less than R from the sphere's outer surface. The fraction of fission products released due to recoil is equal to the probability that a fission product will be emitted into a solid angle such that the distance to the material surface is less than the fission product range R. This solid angle is drawn as a cone in Figure 6.17. Assuming that fission products are emitted isotropically, this probability is simply the surface area of the sphere of radius R, centered at the point of fission, which lies outside the larger sphere, divided by the total surface area, $4\pi R^2$. If θ denotes the azimuthal angle between a diameter drawn through point O and a point on the sphere a distance R from O, this fraction is equal to:

$$f(s) = \frac{\int_0^{2\pi} d\phi \int_0^{\theta} d\xi \; R^2 \sin \xi}{4\pi R^2} \qquad (6.54)$$

where

ϕ = longitudinal spherical coordinate;

ξ = azimuthal spherical coordinate; and

$R^2 \sin\xi \, d\xi \, d\phi$ = differential unit of surface area on a sphere of radius R.

The integral in Eq. (6.54) is easily evaluated:

$$f(s) = \frac{2\pi R^2 \left[-\cos\xi\right]_0^\theta}{4\pi R^2} = \frac{1 - \cos\theta}{2} \qquad (6.55)$$

It is desired to integrate Eq. (6.55) over all s within the spherical shell of interest. To accomplish this, we assume that the fission product range is much less than the radius of the sphere, r; i.e., that $R \ll r$. In this case, we may approximate the sphere's outer surface in Figure 6.17 as a plane, and write the following approximate relationship:

$$s \simeq R\cos\theta$$

Substitute this relation into (6.55) to obtain:

$$f(s) \simeq \frac{1 - (s/R)}{2} \qquad (6.56)$$

The quantity f(s) represents the fraction of fission products created at distance s from the sphere's outer surface which escape due to direct recoil. If we carry this simple analysis further, approximating the spherical shell as a plane layer, we may evaluate the fraction of fission products born in the shell which escape due to recoil. Once again, let B represent the volumetric birth rate of fission products due to fission within the shell, and let the outer and inner distances of the shell to the sphere surface be S_1 and S_2, respectively. Then the total generation rate of fission products per unit surface area is:

$$\left[\begin{matrix}\text{generation rate of FP's} \\ \text{per unit surface area}\end{matrix}\right] = (S_2 - S_1)B$$

The fraction of FPs born within distance ds of some plane which is distance s from the surface which escape due to recoil is given by f(s). Thus, the rate of FP release due to recoil of FPs born within the shell is:

$$\left[\begin{matrix}\text{release rate of FPs}\\ \text{due to recoil}\end{matrix}\right] = \int_{S_1}^{S_2} f(s)\, B\, ds = B \int_{S_1}^{S_2} \frac{1-(s/R)}{2}\, ds$$

$$= \frac{B}{2}\left[s - \frac{s^2}{2R}\right]_{S_1}^{S_2} = B\left[\frac{S_2-S_1}{2} - \frac{S_2^2 - S_1^2}{4R}\right]$$

Divide Eq. (6.) by (6.) to obtain:

$$\left[\begin{matrix}\text{fraction of FPs born between } S_1\\ \text{and } S_2 \text{ which escape by recoil}\end{matrix}\right] = \frac{1}{2} - \frac{S_1 + S_2}{4R}$$

This equation may be specialized to yield the total release fraction due to recoil. Examine a spherical shell whose outer boundary is located at the sphere's outer surface (S_1=0) and whose inner surface is distance S_2=R from the outer surface. Clearly, all recoil release must originate in this shell. The fraction of FPs created in this shell which escape due to recoil is:

$$\left[\begin{matrix}\text{fraction of FPs generated between}\\ \text{s=0 and R which escape due to recoil}\end{matrix}\right] = \frac{1}{2} - \frac{0 + R}{4R} = \frac{1}{4}$$

Since the fraction of all fission products in the sphere which are generated in the outer shell is simply the volume fraction of the outer shell, the total release fraction due to recoil is thus:

$$f = (R/B)_{rec} = \left[\begin{matrix}\text{total release fraction}\\ \text{due to recoil}\end{matrix}\right] = \left[\frac{1}{4}\right]\cdot\left[\frac{r^3 - (r-R)^3}{r^3}\right]$$

$$= \frac{1}{4}\left[1 - [1-(R/r)^3]\right] = \frac{1}{4}\left[3(R/r) - 3(R/r)^2 + (R/r)^3\right]$$

$$= \frac{3R}{4r}\left[1 - (R/r) + \frac{1}{3}(R/r)^2\right]$$

$$\simeq \frac{3R}{4r}\left[1 - \frac{R}{r}\right] \qquad (6.57)$$

since we have already assumed R << r.

As it was derived, Eq. (6.57) gives the *release* fraction due to recoil, but says nothing about the diminution of the fission product source due to recoil losses. However, a kind of "reciprocity relation" must exist between the fissions and the fission product volumetric source rate. Consider a point O' deep within the sphere, so that no fission products born at O' can escape due to direct recoil. The fission product source at O' arises due to fissions which occur in the thin spherical shell a distance R from O', as illustrated in Figure 6.18. Now consider our original point O, located some distance $s < R$ from the sphere's outer surface. The sphere in which fissions may occur to produce fission products at point O is now truncated. In fact, the fraction of this sphere which is missing is exactly the fraction of fission products generated at point O which escape due to direct recoil. Thus, the expression for f(s) derived above applies not only to release fractions in the outer shells, but also to fission product source reductions.

6.4.2. Formulation of the fission product source vector.

Let q_h represent the "homogeneous" fission product source rate. In practice, this quantity is derived from fission density information or parent isotope concentrations generated by FUPAR/VSOP, and refers to the homogeneous core volume. The first task is to convert q_h into q_k, the true average fission product source rate within the fuel kernels. Let V_h represent the homogeneous core volume associated with a single pebble, and V_k the volume of a single fuel kernel. Let N_k represent the number of fuel kernels per fuel element. Since the homogeneous reaction

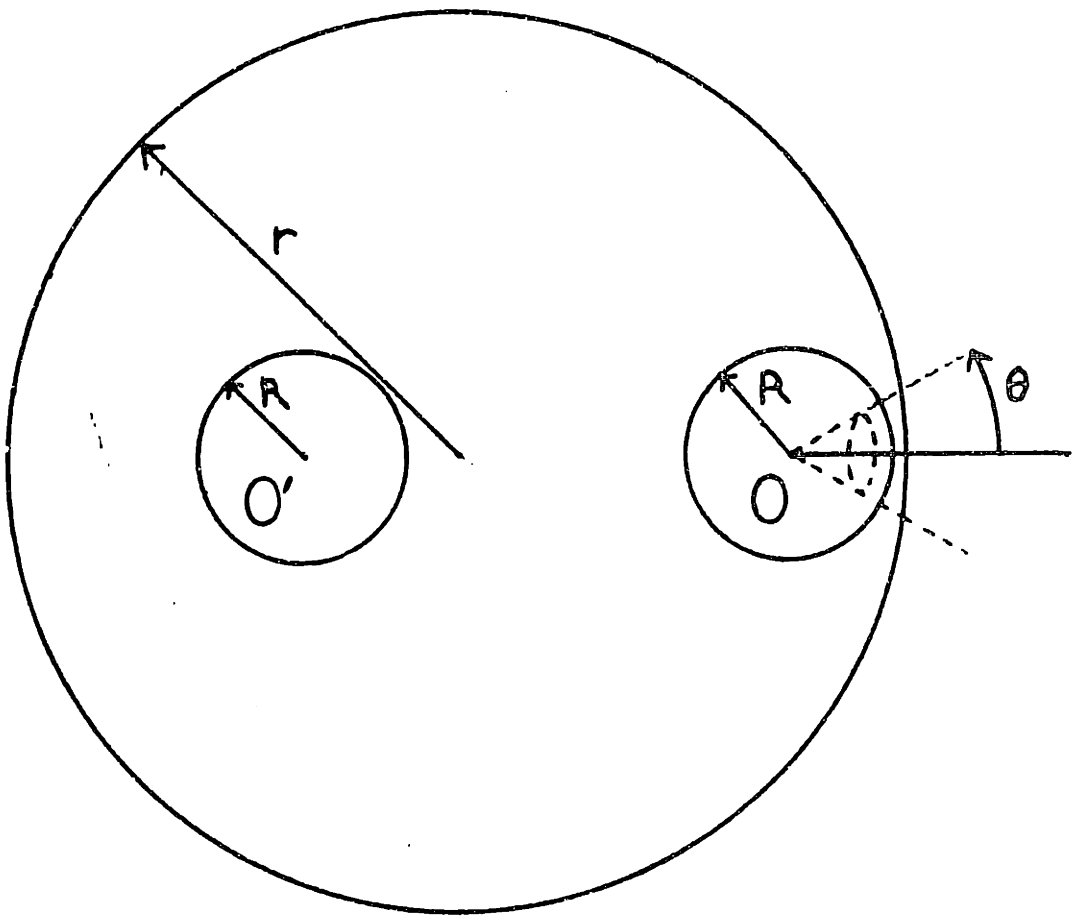

FIG. 6.18: Fission product source reduction due to recoil release.

rates must be consistent with those actually occuring, we may write:

$$q_h V_h = q_k N_k V_k$$

$$\text{or} \quad q_k = q_h V_h/(N_k V_k)$$

Finally, since $V_h = V_p/(1-\alpha)$, in which α is the void fraction, we have:

$$q_k = q_h \frac{V_h}{N_k V_k (1-\alpha)} \tag{6.58}$$

q_k represents the fission product volumetric source rate within the fuel kernels. However, due to heavy metal contamination, there is a source as well within the various coating layers. The overall rate of production of fission products in the coating layers is simply ϕ_{HMC} times the total production rate in the kernel. Thus, if V_c represents the volume of a single set of coating layers, we may write:

$$q_k V_k \phi_{HMC} = q_c V_c$$

where q_c is the source rate in the coating layers. Therefore, the coating layer source rate is the following fraction of that in the kernel:

$$q_c = q_k \frac{V_k \phi_{HMC}}{V_c} \tag{6.59}$$

Thus, suppose that the particle model being analyzed has NK layers within the kernel, and NTOT layers in all (including all coating shells). Without considering recoil effects, the **q** source vector may be written:

$$q = q_k \left[1,\ 1,\ \ldots\ 1,\ \phi_{HMC}(V_k/V_c),\ \ldots\ \phi_{HMC}(V_k/V_c) \right]^+$$

element #1 — element # NK+1 — element # NTOT

For a full particle model such as that above (i.e., one with a complete set of coating layers), recoil will have two effects

(1) Outer kernel layer sources will be decreased due to recoils into the buffer layer. The source within the buffer layer will be increased by a corresponding amount.

(2) Outer IPyC layer sources will be decreased, resulting in some direct release into the fuel element graphite.

Suppose that the kernel's outer m layers are all or partially within recoil range of the kernel surface. The reductions in their volumetric source rates may be calculated from the equations above. The factors of reduction will be labelled f_{NK-m}, f_{NK-m+1}, $\ldots$ f_{NK}. If V_i represents the volume of each spherical shell within range of the kernel outer surface, the overall birth rate in the buffer layer is then increased by:

$$\begin{bmatrix}\text{increase in buffer layer} \\ \text{total FP production rate}\end{bmatrix} = \sum_{i\ =\ NK-m}^{NK} q_k\ V_i\ f_i$$

Thus, the increase in the buffer's volumetric production rate is:

$$\begin{bmatrix}\text{increase in buffer layer volu-} \\ \text{metric FP production rate}\end{bmatrix} = \frac{q_k}{V_{NK+1}} \sum_{i\ =\ NK-m}^{NK} V_i\ f_i \equiv q_k\ \phi_B$$

where $\phi_B \equiv \frac{1}{V_{NK+1}} \sum_{i=\ NK-m}^{NK} V_i\ f_i$, and V_{NK+1} is the volume of the buffer layer. Note that since the f_i were derived from an infinite

radius approximation, the kernel radius does not appear in the expression for them. Thus, the f_i may be written without confusion regardless of the actual position in the particle; they depend only on the layer's distance from the outer surface of interest.

The outer shells in the OPyC layer lose fission products due to recoil. The total fraction of released FPs is not given simply by Eq. (6.57) because the volumetric source rate in the OPyC layer is much less than that in the kernel. Since ϕ_{HMC} is always much less than one, we can assume that the bulk of fission products are produced in the kernel. In this case, the direct recoil fractional release from the OPyC layer is:

$$f_{rec} = \frac{\text{loss rate from OPyC}}{\text{total FP production}} = \frac{(1/4)\left[r_p^3 - (r_p - R)^3\right](V_k/V_c)\,\phi_{HMC}\,q_k}{r_k^3\,q_k}$$

$$= \frac{\phi_{HMC}\,V_K}{4\,V_c}\left[\frac{3r_p^2R - 3r_pR^2 + R^3}{r_k^3}\right] \equiv \phi_{HMC}\,(V_K/V_C)\,\phi_O$$

$$\text{where } \phi_O \equiv \frac{3r_p^2R - 3r_pR^2 + R^3}{4\,r_k^3}.$$

In addition, if the n outer shells of the OPyC coating layer are within recoil range of the particle surface, each will suffer fractional reductions in the fission product source of f_{NTOT-n}, $f_{NTOT-n+1}$, $\cdots$ f_{NTOT}. Table 6.3 summarizes the recoil release rate and changes to the **q** source vector due to recoil for a full particle model.

When a defective particle is to be analyzed (i.e., one with no coating layers), the modifications to the recoil release and source vector are simple extensions. In this case, the previous release

fraction from the kernel to the buffer layer is now assumed to exit the particle directly. Thus for the kernel-only particle model, the direct recoil release is given by the expression already derived as Eq. (6.57):

$$f_{rec} \simeq \frac{3R}{4r}\left[1 - \frac{R}{r}\right]$$

Reductions in the fission product source within the outer kernel shells are identical to those in the full-particle case. The recoil release fraction and changes to the source vector for the kernel only model are summarized as well in Table 6.4.

TABLE 6.4: ELEMENTS OF THE FISSION PRODUCT SOURCE VECTOR

FULL PARTICLE MODEL

ELEMENT NUMBER	ELEMENT VALUE (DIVIDED BY q_k)
1	1
2	1
3	1
⋮	⋮
NK-m	f_{NK-m}
NK-m+1	f_{NK-m+1}
⋮	⋮
NK	f_{NK}
NK+1	$\phi_{HMC}(V_k/V_c) + \phi_B$
NK+2	$\phi_{HMC}(V_k/V_c)$
⋮	⋮
NTOT-n	$f_{NTOT-n}\phi_{HMC}(V_k/V_c)$
NTOT-n+1	$f_{NTOT-n+1}\phi_{HMC}(V_k/V_c)$
⋮	⋮
NTOT	$f_{NTOT}\phi_{HMC}(V_k/V_c)$

KERNEL-ONLY MODEL

ELEMENT NUMBER	ELEMENT VALUE / q_k
1	1
2	1
3	1
⋮	⋮
NK-m	f_{NK-m}
NK-m+1	f_{NK-m+1}
⋮	⋮
NK	f_{NK}

NK = number of kernel shells

NTOT = total number of shells in the particle model

m = number of kernel shells within recoil range of buffer

n = number of OPyC shells within recoil range of matrix

6.5: EULERIAN PARAMETERS OF FISSION PRODUCT DIFFUSION

The previous sections described how transition matrices may be calculated which transform the fission product profile vectors of a particle entering a given core region into the fission product release rate and the output profile vector from the region. In an operating pebble bed core, of course, the inputs to any region consist of a distribution of profile vectors. The release and profile transformations under these circumstances are functions of the input distributions. In this section, the procedure for using the diffusion transition matrices to calculate parameters for an operating multi-pass pebble bed core are derived.

The most logical question to be addressed first is: what is the release rate of a fission product from the fuel in a given core zone during operation? Summing these rates for all core zones yields the steady-state source of that fission product, which contributes to circulating and plated-out activity in the primary system. Depending on the accident scenario under analysis, these fission products may also contribute significantly to the source term.

Unlike the case for the multi-species concentration vectors described in Chapter 4, it has not been useful to develop collapsed transition matrices for the profile vectors (little useful information may be calculated with them). Thus, to describe the processes of fission product release in a core model that is discretized both axially *and* radially, we introduce the *augmented branch variable*, $(\beta|j)$:

$(\beta|j) \equiv (i_1, i_2, \ldots i_w| j)$

where $\beta \equiv (i_1, i_2, \ldots i_w)$ = the sequence of *radial* drop zones which the particle has traversed (the last being i_w); and j = the number of the last *axial* zone which the pebble has exited. Note that $(\beta|0) \equiv \beta'$.

The flow rates of pebbles through $(\beta|j)$ are the same as through the simple branch β. Thus, the L-probability distributions defined by the p_β apply equally well to the fuel flows through particular axial zones specified by $(\beta|j)$. Likewise, the L- and E-expectation operators are identical for simple and augmented branch variables. Only the transition matrices which describe specific processes are different in the collapsed and augmented cases.

Let any discrete zone in the core model under investigation be denoted (j,i), where j represents the discrete axial coordinate and i the discrete radial coordinate. The frequency-weighted distribution of w'th-pass concentration profiles entering a certain core zone (j,i_w) is described by the probability distribution p_β, where $\beta = (i_1, i_2, \ldots i_w)$. For any given profile $\mathbf{c}(\beta|j)$, the diffusive release in zone (j,i_w) is given by Eq. (6.47):

$$\dot{\rho}(j,i_w) = \left[\frac{8\pi\ r_{out}^2}{\delta r_{out}}\right] D_j\ \mathbf{u}_N^+\ \mathbf{c}(\beta|j) \qquad (6.60)$$

where:

r_{out} = particle outer radius;

δr_{out} = thickness of particle's outer shell;

D_j = outer shell diffusivity in zone (j,i_w); and

$\mathbf{c}(\beta|j)$ = time-dependent concentration profile in zone (j,i_w).

We are interested in the average of $\dot{\rho}$ during the particle's stay in zone j, thus:

$$\langle \dot{\rho}(j,i_w) \rangle_j = \left\langle \left[\frac{8\pi\, r_{out}^2}{\delta r_{out}} \right] D_j\, u_N^+\, \mathbf{c}(\beta|j) \right\rangle_j$$

$$= \left[\frac{8\pi\, r_{out}^2}{\delta r_{out}} \right] D_j\, u_N^+ \langle \mathbf{c}(\beta|j) \rangle_j \qquad (6.61)$$

The E-expectation of $\mathbf{c}(\beta|j)$ in zone j is known from Eq. (6.50) in terms of the L-expectation of $\mathbf{c}(\beta|j-1)$:

$$\langle \mathbf{c}(\beta|j) \rangle_j = \mathbf{S}_j \left[\frac{1}{\Delta t_j} \bar{\mathbf{c}}(\beta|j-1) + \frac{1}{2} \mathbf{q}(\beta|j) \right] \qquad (6.62)$$

Eqs. (6.61) and (6.62) allow the fission product diffusive release from particles in branch β, zone j, to be calculated from L parameters. Note that when j=1 in the above expression, the right-hand expression contains the term $\bar{\mathbf{c}}(\beta|0)$, which is simply $\bar{\mathbf{c}}(\beta')$. Also, note that the fission product source vector $\mathbf{q}(\beta|j)$ is branch dependent, since the source rate depends on the fuel state. In actual calculations, this is actually simplified to a pass-dependence, and the input source parameters $\mathbf{q}(w|j)$ are easily stored from FUPAR calculations.

Once pass-dependent parameters are calculated, the final task is to combine them to form overall Eulerian parameters as functions of core position. Suppose that W_{max} is the maximum number of passes which a fuel element can remain in the core. Let α_w represent the ratio of the fuel flow through pass w to the fresh fuel injection flow. Finally, let $\langle \mathbf{c}(\beta_w|j) \rangle$, in which $\beta_w \in B_w$ and $\beta_w = (\beta'_{w-1}, i)$, represent the volume-averaged fission product profile of pass-w fuel within core zone

(j,i). The overall volume average profile including contributions from all passes is then:

$$\langle \mathbf{c} \rangle_{i,j} \equiv E_{\mathcal{G}}[\mathbf{c}(\beta|j)] = \frac{1}{W_{max}} \sum_{w=1}^{W_{max}} \alpha_w \langle \mathbf{c}(\beta_{w-1}|j) \rangle \qquad (6.63)$$

where the expression "$E_{\mathcal{G}}[\mathbf{c}(\beta|j)]$" represents the overall Eulerian expectation of $\mathbf{c}$, considering pebbles from all passes (see Eq. 3.44). Note the term $\mathbf{c}(\beta_{w-1}|j)$ is necessary because the fuel represented by the augmented branch variable has not yet completed its w'th pass.

Likewise, the overall volume averaged release is given by:

$$\langle \dot{\rho} \rangle_{i,j} \equiv E_{\mathcal{G}}[\dot{\rho}(\beta|j)] = \frac{1}{W_{max}} \sum_{k=1}^{W_{max}} \alpha_w \langle \dot{\rho}(\beta_{w-1}|j) \rangle \qquad (6.64)$$

6.6: FISSION PRODUCT DIFFUSION IN PEBBLE MATRIX GRAPHITE

Fission products which are released from fuel particles or contamination granules are not necessarily released immediately to the reactor coolant. For some fission products, reactor structural graphite presents a significant additional barrier. Metallic fission products, for example, can react chemically with and adhere to graphite surfaces. Estimates of fission product release which do not account for the effects of structural graphite omit a potentially important reduction mechanism. In this section, the physical phenomena which govern fission product transport within graphite and on graphite surfaces are reviewed. Though it is concluded that fission product retention in pebble matrix graphite is not as certain a release barrier as the particle coating layers, a simple model to evaluate the effects of graphite surface adsorption is proposed.

6.6.1: Transport Processes

Noble gas fission products, of course, have little chemical attraction for graphite. The vast majority of them are able to diffuse very quickly (within several minutes [K4]) to the fuel element surface once released from the fuel grains. The exception is a very small fraction which are initially deposited within graphite grains and must first diffuse out of the grains.

Metallic fission products, on the other hand, have a strong adsorptive attraction for graphite surfaces. As a result, two retention mechanisms pertain to metallic FPs in graphite:

(1) Following release from a fuel particle, the fission product must first diffuse along graphite grain surfaces to reach the fuel element surface. Effective diffusivites for important metallic FPs within matrix graphite have been developed in the FRG [see Refs. K4 and B5].

(2) Fission products which reach the fuel element surface are chemically attracted to it. The fission product partial pressure in the boundary layer directly above the fuel element surface is described by an *adsorption isotherm*, which is a relation giving the boundary layer partial pressure as a function of temperature and surface concentration. Transport from the boundary layer into the coolant flow is determined by a mass transfer coefficient.

Figure 6.19 schematically illustrates the fuel element surface phenomena which limit fission product release to the coolant. c_g represents the fission product's concentration on the graphite surface, c_w is the boundary layer concentration, and c_∞ is the concentration in the bulk coolant. The adsorption isotherm gives c_w as a temperature dependent function of c_g. At high temperatures, c_w is a relatively large fraction of c_g, which generally exceeds the bulk coolant concentration. In this case fission product atoms are released. The higher the temperature, the higher the boundary layer concentration in relation to the surface concentration and the higher the release rate. At low temperatures, on the other hand, c_w is a much smaller fraction of c_g, and may actually drop below the bulk coolant concentration (see Figure (6.19b)). In this case, net mass transfer occurs from the coolant to the fuel element, and adsorption is said to occur. This

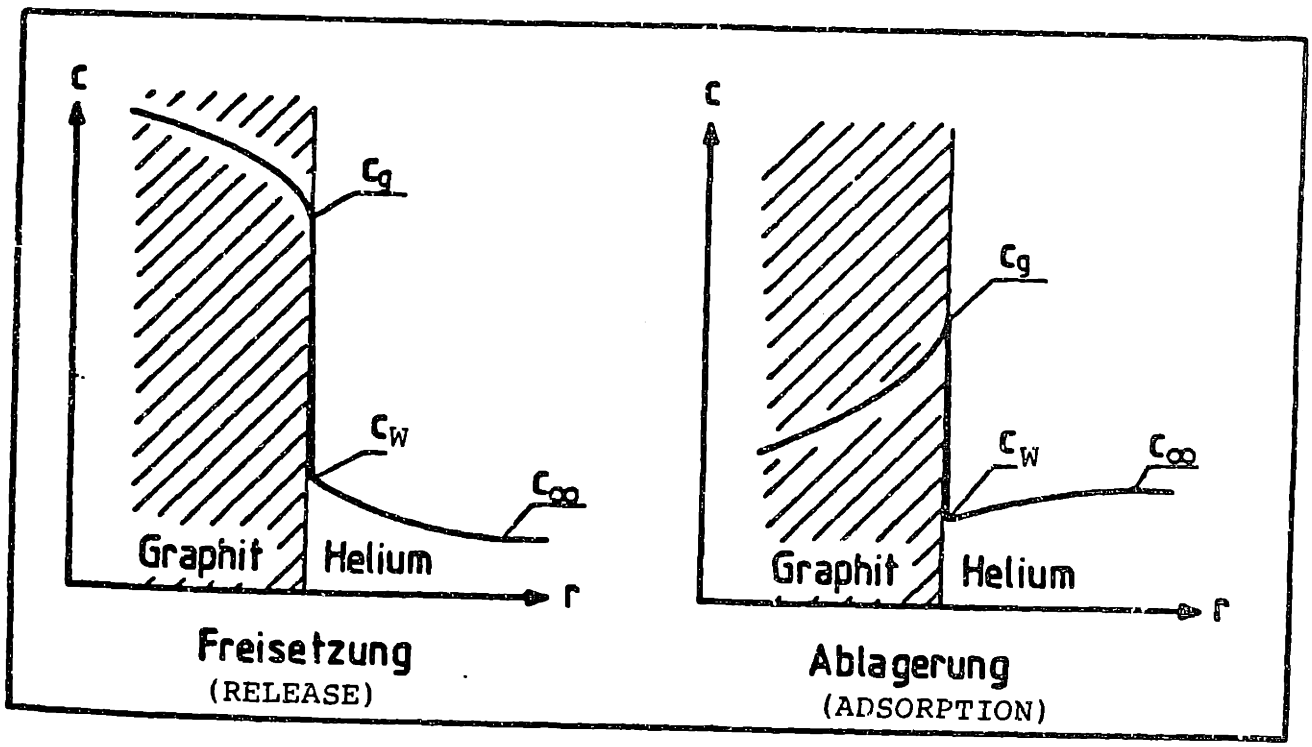

FIG. 6.19: Fission product release and adsorption on graphite surfaces.

effect has important implications for fission product release during thermal transients:

(1) A significant release barrier due to surface adsorption hinders the release of some metallic fission products into the coolant gas. This barrier is present even under the conservative assumption of zero fission product concentration in the coolant.

(2) Even during severe transients, most of the reactor core remains at relatively low temperatures. This low temperature graphite is an effective trap for fission products released from hotter portions of the reactor.

Detailed release calculations performed by Krohn [K4] for the PNP-500 (a 500 MWth process heat pebble bed reactor) indicate that structural graphite can greatly reduce the amount of cesium and strontium released from the reactor core. In the highest temperature core zones, surface adsorption reduced estimated release from the fuel by almost 20%. Mechanistic calculations of overall core release, in which cool graphite acts as a fission product trap, show source reductions of over three orders of magnitude (these reductions are with best-estimate adsorption isotherms). However, the fractional reduction is extremely sensitive to the coefficients in the adsorption isotherm, and applies only to the particular accident sequence which was analyzed.

In this work, the retentive effects of pebble structural graphite are conservatively ignored. One reason is that many workers have already calculated source terms; we are more interested in the relative effects of fuel quality and reactor design. The coated fuel particle,

which is the fundamental basis of the MHTGR's passive safety, is the most logical boundary beyond which to judge these effects. Another reason is that the particle coating layers are the only *assured* and *permanent* barrier to fission product release at temperatures below 1600C. Once fission products have escaped from the particles and entered the matrix graphite, their retention depends on the long term stability of the core. It is possible that events long after the initial transient could heat up pebbles with high matrix fission product concentrations, causing them to release isotopes which were previously retained. Therefore, this project has focused on fission product release from fuel *particles*, taking no credit for retention in matrix graphite.

6.6.2. Diffusive holdup in matrix graphite

Though it is felt that only the particle coating layers are a true *inherent* safety feature, graphite diffusion will indeed reduce metallic fission product circulating activity during the majority of a reactor's operation. Here a simple model is proposed to estimate the effects of surface adsorption on circulating activity.

Recall the "equivalent sphere" model for radioisotope diffusion through grains of UO_2 discussed in Section 6.1. A simple expression for the release/birth rate ratio was derived based on the following assumptions:

(1) The isotope of interest is generated uniformly within a sphere of radius "a," subject to constant irradiation conditions;

(2) The fission product concentration profile within the sphere has achieved a steady state.

The first condition may be approximated in the fueled zone of a pebble by using time-averaged fission product birth rates and temperatures. The second condition is also roughly true, as the diffusivities of fission products within matrix graphite are large enough so that the diffusion front has fully engulfed the fueled region prior to discharge. In any case, we are only interested in a rough estimate of the effects of graphite diffusion on the ultimate steady state release. If we make the two above assumptions, the release to birth rate ratio for the i'th metallic fission product is given by:

$$(R/B)_i = 3\sqrt{D_i'/\lambda_i}\left[\coth\sqrt{\lambda_i/D_i'} - \sqrt{D_i'/\lambda_i}\right]$$

where

D_i' = the reduced diffusivity of the isotope $\equiv D_i/a^2$, where a is the radius of the sphere; and

λ_i = the decay constant of the radioisotope.

Plots of metallic fission product diffusivities in matrix graphite were presented in Table 6.1. Table 6.5 presents values of the activation energies, frequency factors, and decay constants for the fission products Cs-137, Ag-110m, and Sr-90. Equivalent sphere release to birth rate ratios were calculated for these fission products within the fueled region of a pebble assuming steady state conditions have been achieved. Figure 6.20 is a plot of the equivalent sphere (R/B) as a function of fuel temperature.

TABLE 6.5: GRAPHITE DIFFUSION PARAMETERS FOR METALLIC FISSION PRODUCTS

	Cs-137	Ag-110m	Sr-90
Activation energy (kJ/mole)	181	258	301
Frequency factor (m^2/sec)	2.0×10^{-4}	1.6×10^{0}	9.1×10^{-3}
Decay constant (sec^{-1})	7.302×10^{-10}	3.18×10^{-8}	7.71×10^{-10}

As the figure implies, cesium is least effected by the matrix graphite. At core average conditions (about 500C) the steady state R/B is only about 0.05, though at peak core temperatures the ratio is quite close to 1.0. This is due primarily to Cs-137's relatively small decay constant (see Table 6.5). Ag-110m is retained more effectively by the matrix, especially at lower temperatures, and Sr-90 has very small R/B values even at 950C.

These values are not representative of the actual release behavior during the majority of the fuel's lifetime, as steady state conditions are only approached at the time of discharge. However, these simple calculations do indicate that diffusion through matrix graphite has the potential to cause significant reductions in ultimate fuel release. The effect certainly merits further investigation.

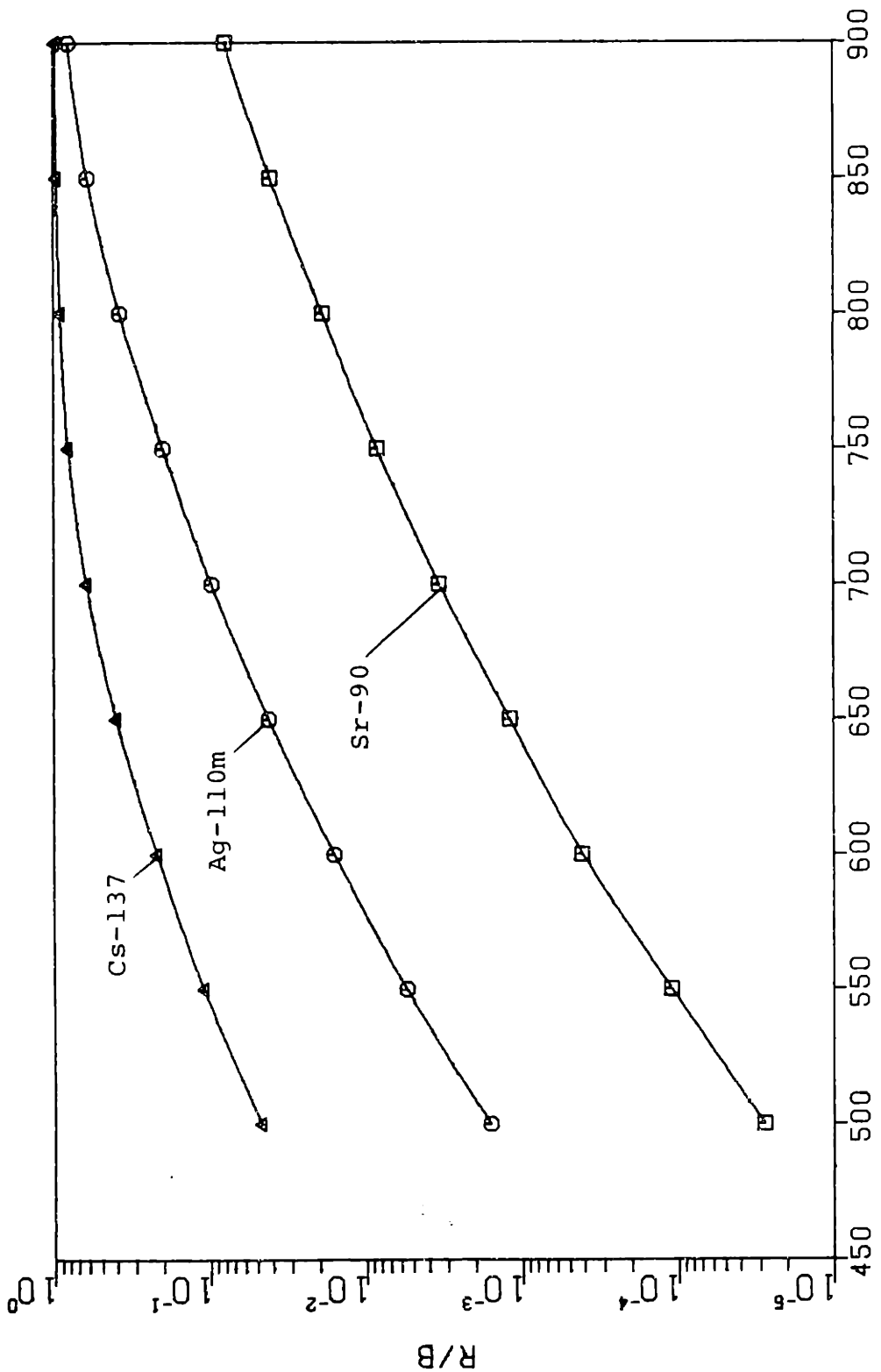

FIG. 6.20: Steady state R/B values for metallic fission products in the fueled region of a pebble.

6.7 ANALYSIS OF FISSION PRODUCT TRANSPORT WITH PDIF

The PDIF computer code performs the fission product diffusion calculations for pebble bed reactors outlined in the previous sections. PDIF calculates release rates both in the operating reactor and during high temperature transients. Input parameters are calculated by FUPAR (for the operating case) and by THERMIX (for the transient case). As in the previous sections, PDIF assumes a spherically symmetric fuel particle, in which fission product transport is described by effective one-phase diffusivities. The code can model particles with no coating layers (i.e. failed particles), BISO coating layers, or TRISO coating layers. PDIF contains no provision for time-dependent particle failure, so its use is limited to modular HTGR cores whose peak accident temperatures remain below 1600C. This section describes the specific computations performed by PDIF in both the steady state and transient modes of operation, and discusses the information necessary to run the code.

6.7.1 Transport in the operating reactor

Diffusion in the operating reactor is characterized by A) a non-zero source of fission products, and B) low temperatures which drastically reduce the diffusivity of the fission products. Small diffusivities imply strong non-linearity in the fission product concentration profiles, necessitating as fine a mesh spacing as possible near the outer particle surface.

The fission product volumetric source rate profiles within a fuel particle are derived from $\dot{q}_k$, as demonstrated in Section 6.4. $\dot{q}_k$, in turn, is a function of the homogenized fission product source rate, q_h, which is derived from information calculated by FUPAR (or another similar code). We shall define two different types of fission products, which differ in the manner in which their source rates are calculated. First, there are "cumulative yield" type fission products, whose birth rates are simply a fixed fraction of the local fission rate. Cesium-137 is an important fission product which may be modelled with a cumulative yield. There are also "activation" type fission products, whose birth rates are due to the nuclear transformation of some parent nuclide. For example, the important fission product Ag-110m arises from neutron activation of Ag-109. Yield-type fission products will be referred to as "type 1," and activation-type fission products will be referred to as "type 2."

The birth rates of type-1 fission products are calculated directly from burnup information calculated by FUPAR. Let $\dot{q}$ the represent the homogenized birth rate of some type-1 fission product. This birth rate is simply equal to the fission rate multiplied by y, the cumulative yield for the isotope:

$$\dot{q} = y \dot{F} = y \phi \sigma_f^* \mathbf{n}$$

where we have neglected the second heavy metal chain for the present. The parameter required for PDIF is $\langle \dot{q} \rangle_i$, the birth rate of the isotope of interest averaged over region i. Using the above equation, we find:

$$\langle \dot{q} \rangle_i = \langle y \phi \sigma_f^+ n \rangle_i = y \phi_i \sigma_{f,i}^+ \langle n \rangle_i$$
$$= y \phi_i \sigma_{f,i}^+ \frac{1}{\Delta t_i} D_i n_{i-1}$$
$$= y \left(\phi_i / \Delta t_i \right) \sigma_{f,i}^+ D_i n_{i-1}$$

where we have used Eq. (4.49) to express the volume average of a heavy metal concentration vector in terms of the previous zone's exit vector. Note that the quantity:

$$\phi_i \sigma_{f,i}^+ D_i n_{i-1}$$

is equal to ΔF_i, the total fission density accumulated in zone i. Thus, the volume averaged birth rate $\langle \dot{q} \rangle_i$ is proportional to the cumulative fission density in zone i:

$$\langle \dot{q} \rangle_i = \left(y/\Delta t_i \right) \Delta F_i \qquad (6.65)$$

Thus, the only information required by PDIF to calculate volume averaged birth rates are the burnup accumulation in each zone (as a function of pass number) and a cumulative yield for the fission product of interest. Note that in the actual FUPAR program, burnup is stored in units of FIMA; thus in the actual PDIF program Eq. (6.65) contains an additional factor (equal to the fuel's initial heavy metal concentration) to convert FIMA into fission density.

For the case of a type-2 fission product, calculation of volume-averaged source rates are even simpler, though they require FUPAR to store different information. Suppose that the parent isotope has homogenized number density f_p, an absorption cross section σ_a, and that a fraction γ of parent absorptions are converted to the daughter nuclide of interest. The homogenized volumetric source rate of the daughter nuclide at any time is simply:

$$\dot{q} = \nu \Phi \sigma_a f_p$$

where f_p is the homogenous number density of the parent isotope. Applying the volume average operator for a region i:

$$\langle \dot{q} \rangle_i = \langle \nu \Phi \sigma_a f_p \rangle_i = \nu \Phi \sigma_a \langle f_p \rangle_i \qquad (6.66)$$

Thus, the source rate of a type-2 nuclide averaged over some volume of the core is simply proportional to the parent's volume averaged number density in the same volume. In actuality, of course, the fission product source rates are branch dependent, and this must be taken account of in PDIF's calculations. Thus, the following more elaborate expressions are used in PDIF to accurately account for the source rate variation with fuel state. They refer to core zone (i,j) and to the augmented branch variable $(\beta_w|i)$, where $\beta_w \in B_w$ and $\beta_w = (\beta_{w-1}, j)$. Fuel remains in the core a maximum of W_{max} passes, and the expected number of passes prior to discharge is W^*. The E-probability associated with each pass w is $\Pi_w = \alpha_w / W^*$. The volume averaged source rates, dependent on complete branch, pass only, or simply position, are summarized below:

<u>TYPE 1 NUCLIDE</u>:

AVERAGE SOURCE RATE, ZONE (i,j), PASS w, BRANCH $(\beta_w|i)$:

$$\langle \dot{q}(\beta_w|i) \rangle_{i,j} = (y/\Delta t_i)\, \Delta F(\beta_w|i) \qquad (6.67a)$$

AVERAGE SOURCE RATE, ZONE (i,j), PASS w:

$$E\left[\langle \dot{q}(\beta_w|i) \rangle_{i,j}\right] = (y/\Delta t_i)\, \overline{\Delta F}(\beta_w|i) \qquad (6.67b)$$

AVERAGE SOURCE RATE, ZONE (i,j):

$$E_{\mathcal{E}}\left[\langle \dot{q}(\beta_w|i) \rangle_{i,j}\right] = (y/\Delta t_i) \sum_{w=1}^{W_{max}} \Pi_w \overline{\Delta F}(\beta_{w-1}|i) \qquad (6.67c)$$

TYPE 2 NUCLIDE:

AVERAGE SOURCE RATE, ZONE (i,j), PASS w, BRANCH $(\beta_w|i)$:

$$\langle \dot{q}(\beta_w|i) \rangle_{i,j} = \gamma \phi \sigma_a \langle f_p(\beta_w|i) \rangle \qquad (6.68a)$$

AVERAGE SOURCE RATE, ZONE (i,j), PASS w:

$$E\left[\langle \dot{q}(\beta_w|i) \rangle_{i,j}\right] = \gamma \phi \sigma_a \langle \bar{f}_p(\beta_w|i) \rangle \qquad (6.68b)$$

AVERAGE SOURCE RATE, ZONE (i,j):

$$E_\xi\left[\langle \dot{q}(\beta_w|i) \rangle_{i,j}\right] = \gamma \phi \sigma_a \sum_{w=1}^{W_{max}} \Pi_w \langle \bar{f}_p(\beta_w|i) \rangle \qquad (6.68c)$$

The homogeneous source rate $\dot{q}$ is identical to "q_h" defined in section 6. . Using Eqs. (6.67) and (6.68), these homogeneous sources are converted into $\mathbf{q}(i,j)$ for every pass. Recoil effects are taken into account as described in Section 6.4.

Diffusion transition matrices are computed for each core zone. PDIF assumes that the transition matrices are independent of fuel state. This is an approximation, since the fuel temperature is actually dependent on its local power density, hence its associated branch variable. However, the temperature differences between different pass pebbles in the same zone are small compared to the temperature range experienced by fuel in a single traversal of the core, so the approximation is felt to be reasonable. The result of these calculations is a set of transition matrices $\mathbf{R}(i,j)$ and $\mathbf{S}(i,j)$ for each zone (i,j) in the core model ("i" represents the axial index; "j" the radial).

Following the transition matrix calculation, PDIF determines the fission product profile and release distribution in the stationary core as a function of pass number and core zone. The algorithm is similar to that used in the FUPAR calculation of number densities, and a rough outline of the procedure is shown in Fig. 6.21. In general terms, the profile and release calculations prceed as follows: Let $\bar{\mathbf{c}}$ represent the L-expectation of the profile vector at the *beginning* of pass iw. Let $\mathbf{c}_{pass}$ be a temporary variable which computes the L-expectation of the profile at the *exit* of the current pass; $\mathbf{c}_{old}$ and $\mathbf{c}_{new}$ represent the expected profiles at the entrance and exit of the current zone. The code begins with fresh fuel, in which $\bar{\mathbf{c}}$ is known to be zero for pass 1. $\mathbf{c}_{old}$, the profile at the top of the core, set equal to the expected value at the core inlet for that pass:

$$\mathbf{c}_{old} = \bar{\mathbf{c}}$$

. Then, for each radial zone $irad$ in the core, the successive axial transformations are computed:

$$\mathbf{c}_{new} = \mathbf{R}(iax,irad)\ \mathbf{c}_{old} + \mathbf{S}(iax,irad)\ \mathbf{q}(iax,irad,iw)$$

where iw is the index of the pass under consideration. The volume average of the profile for zone $(iax,irad)$ at pass iw is computed using Eq. (6.50):

$$\langle \mathbf{c} \rangle_{iax,irad,iw} = \mathbf{S}(iax,irad) \left[\frac{1}{\Delta t_{iax}} \mathbf{c}_{old} + \frac{1}{2}\, \mathbf{q}(iax,irad,iw) \right]$$

The pass-dependent volume average profiles are used to update the overall Eulerian expectations for each zone:

$$\mathbf{c}_{Eul}(iax,irad) = \mathbf{c}_{Eul}(iax,irad) + \Pi_{iw} \langle \mathbf{c} \rangle_{iax,irad,iw}$$

$\bar{\mathbf{c}} = \mathbf{0}, \quad \alpha(1) = 1$

PASS LOOP: $iw = 1, \ WMAX$

$\mathbf{c}_{pass} = 0 \ ; \quad p(iw+1|iw) = 0 \ ; \ \Pi_{iw} = \alpha_{iw}/W^{*}$

RADIAL DROP ZONE LOOP: $irad = 1, \ NRAD$

$\mathbf{c}_{old} = \mathbf{c}_{pass}$

AXIAL LOOP: $iax = 1, \ NAX$

$$\mathbf{c}_{new} = \mathbf{R}(iax,irad)\ \mathbf{c}_{old} + \mathbf{S}(iax,irad)\ \mathbf{q}(iax,irad,iw)$$

$$\langle \mathbf{c} \rangle_{iax,irad.iw} = \mathbf{S}(iax,irad) * \left[\frac{1}{\Delta t_{iax}}\, \mathbf{c}_{old} + \frac{1}{2}\, \mathbf{q}(iax,irad,iw) \right]$$

$$\langle \dot{\rho} \rangle_{iax,irad.iw} \sim \langle \mathbf{c} \rangle_{iax,irad,iw}$$

$$\mathbf{c}_{Eul}(iax,irad) = \mathbf{c}_{Eul}(iax,irad) + \Pi_{iw} \langle \mathbf{c} \rangle_{iax,irad,iw}$$

$\mathbf{c}_{old} = \mathbf{c}_{new}$

IF $B_{new} < B_{dis}$ THEN:

$p(iw+1|iw) = p(iw+1|iw) + p_{irad}$

$\mathbf{c}_{pass} = \mathbf{c}_{pass} + p_{irad}\ \mathbf{c}_{new}$

$\alpha(iw+1) = \alpha(iw)\ p(iw+1|iw)$

$\bar{\mathbf{c}} = \mathbf{c}_{pass}/p(iw+1|iw)$

FIG. 6.21: Algorithm for calculating steady state concentration profile distribution.

At the bottom of the core, the fuel element burnup is compared with the fuel discharge value. If the fuel leaving the core at this axial position is to be recycled, its profile contributes to the L-expectation profile for the next pass:

$$\mathbf{c}_{pass} = \mathbf{c}_{pass} + p_{irad}\, \mathbf{c}_{new}$$

where p_{irad} is the drop probability associated with radial zone *irad*. Also, if the fuel is to be recycled, the conditional recycle probability $p(iw|iw-1)$ is incremented:

$$p(iw+1|iw) = p(iw+1|iw) + p_{irad}$$

Once all radial zones have been treated in this manner, the alpha parameter for the next pass may be updated:

$$\alpha_{iw+1} = \alpha_{iw}\, p(iw+1|iw)$$

and the L-expected profile for the next pass is normalized to account for any fuel discharge:

$$\mathbf{c}_{pass} = \mathbf{c}_{pass} \,/\, p(iw+1|iw)$$

The procedure then begins again for the next pass, and repeated until burnup indicates that all fuel is discharged. Pass-dependent release is calculated by applying Eq. (6.48) to the $\langle \mathbf{c} \rangle_{iax,irad,iw}$ vector calculated above.

The primary results of this calculation are:

(1) An array CEUL(*il*,*iax*,*irad*) which contains the fission product profile (atoms/barn-cm) as a function of particle shell *il* in each core zone (*iax*,*irad*). In terms of the previous discussion, CEUL is the overall Eulerian fission product profile in zone (*iax*,*irad*);

(2) An array RPEUL($iax, irad, iw$) which contains the fission product diffusion release rates (atoms/sec) as a function of pass iw in each core zone ($iax, irad$);

(3) An array REUL($iax, irad$) which contains the fission product diffusion release rates (atoms/sec) in each core zone ($iax, irad$);

(4) An array RECEUL($iax, irad$) which contains the fission product release rates due to recoil (atoms/sec) in each core zone ($iax, irad$); and

(5) An array BRATE($iax, irad, iw$) which contains the fission product birth rates (atoms/sec) as a function of pass number iw in each core zone ($iax, irad$).

The recoil release rates are calculated according to Eq. (6.57), the diffusion release rates as a function of pass number are calculated according to Eq. (6.61), and these pass-dependent rates are totalled and weighted according to Eq. (6.64) to become the simple positional quantities. The CEUL array which gives the average fission product profile in each zone will play an important role in the following calculations of transient release.

6.7.2 Diffusion under high-temperature transient conditions

In order to apply the transition matrix theory developed in previous sections to the problem of a reactor undergoing a temperature transient, it is necessary to first divide the transient into small time intervals Δt during which the changes in temperature are negligible. It is also necessary to select some finite number of temperatures, θ_i, for which to evaluate diffusion transition matrices.

The user must direct PDIF to a dataset generated by THERMIX containing core-wide position-dependent temperatures as a function of time following the initiation of the accident. Given a pre-selected Δt, PDIF will step through the THERMIX temperatures and interpolate the temperature which applies at the PDIF internal time. Thus, a PDIF transient is generated from the THERMIX transient, in which temperatures are known at times Δt, $2\Delta t$, and so on.

In addition to a time step, the user must supply PDIF with a maximum and minimum temperature at which diffusion transition matrices are to be calculated. The number of intermediate temperatures at which transition matrices are to be calculated must be provided (up to 198), as well as an activation energy to "release-weight" the temperatures.

The temperatures are release weighted in order to properly emphasize the temperature range in which most of the fission product diffusion and release occurs. If temperatures were simply distributed uniformly between θ_{HI} and θ_{LOW}, a disproportionate number of low temperature matrices would be calculated (all of which imply practically zero diffusion) while the high temperatures would suffer from too little

detail. Thus, a procedure has been developed to provide more detail at high temperatures where most of the diffusion occurs.

The procedure is as follows. Let θ_{HI} and θ_{LOW} represent the maximum and miminum temperatures selected by the user, and let N represent the total number of transition matrices to be calculated (including the ones at θ_{HI} and θ_{LOW}). Also, let Q^* represent the input activation energy for release-weighting, R represent the universal gas constant, and define the "release function" $\rho(\theta) \equiv \exp(-Q^*/R\theta)$. The release limits implied by θ_{HI} and θ_{LOW} are:

$$\rho_{HI} = \rho(\theta_{HI}) = \exp(-Q^*/R\theta_{HI}) \qquad (6.69a)$$

$$\text{and} \quad \rho_{LOW} = \rho(\theta_{LOW}) = \exp(-Q^*/R\theta_{LOW}) \qquad (6.69b)$$

The release-space between ρ_{HI} and ρ_{LOW} is next divided into N-1 equally spaced intervals of width $\Delta\rho$:

$$\Delta\rho = \frac{\rho_{HI} - \rho_{LOW}}{(N-1)}$$

and the i'th release value is given by:

$$\rho_i = \rho_{LOW} + (i-1)\Delta\rho \quad (i = 1, 2 \ldots N) \qquad (6.70)$$

The release values are next converted back to temperature values in order to calculate transition matrices. The i'th temperature for the corresponding transition matrix is the inverse release function of the i'th release value:

$$\theta_i = -\frac{Q^*}{R \ln \rho_i}$$

Finally, the PDIF temperature transient is converted to a "modified PDIF temperature transient" by rounding all temperatures up to the nearest member of the set of release-weighted θ_i. The resulting

transient approximates the original THERMIX transient, except that each time step is of equal length and each temperature is one of the discrete set of θ_i.

Diffusion transition matrices are next calculated for each of the temperatures θ_i. Both and $\mathbf{R}(\theta_i)$ and an $\mathbf{S}(\theta_i)$ are necessary in order to compute profile changes and releases. Though the high temperature transition matrices do not require especially high norms, it is desirable to select a mesh-spacing/time step combination with as high a maximum norm as possible. This will insure that in the bulk of the reactor core (in which temperatures do not approach 1600C) the underestimation of fission product release is minimized.

Each zone in the core has a known distribution of fission product profiles computed by the stationary-reactor mode of PDIF. Let us examine some zone with pass-dependent fission product profiles $\mathbf{c}_0(w)$, where w ranges from 1 to W^*, the maximum number of passes a fuel element may remain in the core. If N_p is the total number of fuel particles in the zone of interest, then the number of pass-w fuel particles in the zone is simply $(\alpha_w/W^*)\ N_p$. Now consider the first time step of the transient, during which the temperature is assumed constant at $\theta(1)$. Let the two transition matrices associated with this temperature be designated $\mathbf{R}_1$ and $\mathbf{S}_1$ in the core zone of interest. The fission product profile at the end of the first time step is given by:

$$\mathbf{c}(\Delta t) = \mathbf{R}_1\ \mathbf{c}_0$$

If $\mathbf{R}_2$ and $\mathbf{S}_2$ denote the transition matrices for the second time step of the transient, the profile following the second step is:

$$\mathbf{c}(2\Delta t) = \mathbf{R}_2\, \mathbf{c}(\Delta t) = \mathbf{R}_2\, \mathbf{R}_1\, \mathbf{c}_o$$

Likewise, the profile after the n'th step of the transient is given by:

$$\mathbf{c}(n\Delta t) = \mathbf{R}_n \cdots \mathbf{R}_2\, \mathbf{R}_1\, \mathbf{c}_o \tag{6.71}$$

The release during a single time step is calculated using Eq. (6.51) with a zero source vector. Thus, if $\rho(i)$ represents the total number of atoms released from a single fuel particle during the i'th step of the transient, we have:

$$\rho(i) = \Delta t_i \langle \dot{\rho} \rangle_i = \left[\frac{8\pi\, r_{out}^2}{\delta r_{out}}\right] D_i\, u_N\, S_i\, c_{i-1} \tag{6.72}$$

where D_i represents the outer particle shell diffusivity evaluated at the temperature associated with the i'th time step, and N is the index of the outer particle shell. Since the total release for the time period $i = 1$ to T is the sum of all the $\rho(i)$, we may write:

$$\rho = \sum_{i=1}^{T} \rho(i) = \left[\frac{8\pi\, r_{out}^2}{\delta r_{out}}\right] \sum_{i=1}^{T} D_i\, u_N\, S_i\, c_{i-1}$$

$$= \left[\frac{8\pi\, r_{out}^2}{\delta r_{out}}\right] \left[\sum_{i=1}^{T} D_i\, u_N\, S_i\, R_{i-1}\, R_{i-2} \cdots R_1\right] c_o \tag{6.73}$$

Now, in reality $\mathbf{c}_o$ is the profile associated with fuel at a particular pass w within the zone of interest, so to be strictly correct we must write:

$$\rho(w) = \left[\frac{8\pi\, r_{out}^2}{\delta r_{out}}\right] \left[\sum_{i=1}^{T} D_i\, u_N\, S_i\, R_{i-1}\, R_{i-2} \cdots R_1\right] \mathbf{c}_o(w) \tag{6.74}$$

Now, the total release from all particles on pass iw is simply:

$$(\alpha_w / W^*)\, N_p\, \rho(w)$$

and the complete release from all particles within the zone of interest is obtained by summing over all values of w:

$$\rho = \sum_{iw=1}^{W^*} (\alpha_w / W^*)\, N_p\, \rho(w)$$

$$= \sum_{w=1}^{W^*} (\alpha_w / W^*)\, N_p \left[\frac{8\pi\, r_{out}^2}{\delta r_{out}}\right] \left[\sum_{i=1}^{T} D_i\, u_N\, S_i\, R_{i-1}\, R_{i-2} \cdots R_1\right] c_0(w)$$

$$= N_p \left[\frac{8\pi\, r_{out}^2}{\delta r_{out}}\right] \left[\sum_{i=1}^{T} D_i\, u_N\, S_i\, R_{i-1}\, R_{i-2} \cdots R_1\right] \left[\sum_{w=1}^{W^*} (\alpha_w / W^*) c_0(w)\right]$$

$$= N_p \left[\frac{8\pi\, r_{out}^2}{\delta r_{out}}\right] \left[\sum_{i=1}^{T} D_i\, u_N\, S_i\, R_{i-1}\, R_{i-2} \cdots R_1\right] E_\ell[c_0] \qquad (6.75)$$

where $E_\ell[c_0]$ is the Eulerian expectation value of the fission product concentration profile in the zone of interest at the start of the transient. This is the same parameter calculated by PDIF in the stationary phase of operation. Thus the transformation:

$$\left[\frac{8\pi\, r_{out}^2}{\delta r_{out}}\right] \left[\sum_{i=1}^{T} D_i\, u_N\, S_i\, R_{i-1}\, R_{i-2} \cdots R_1\right]$$

represents the average release per particle in the zone of interest. When applied to the average profile vector and multiplied by the number of particles in the zone, the result if the expected total release of fission products in that zone.

6.8 EVALUATION OF PDIF RELEASE PREDICTIONS

One way to verify PDIF would be to analyze a reactor design which has already been extensively studied and compare release predictions to those already accepted. Unfortunately, such a direct comparison is impossible due to the high quality fuel model incorporated into PDIF. Published source term estimates usually differ in some fundamental assumption. Therefore, to verify that the PDIF code calculates reasonable estimates of diffusive release under the high quality fuel assumption, a simple physical system has been modeled for which an analytic solution is known.

The "analytic" system chosen for PDIF comparison is a homogeneous sphere of diffusivity D and radius r_o. At time t = 0, the concentration profile of the diffusing species is uniform within the sphere. Under constant conditions, the fractional release as a function of time is given by [C1]:

$$FR(t) = 1 - (6/\pi^2) \sum_{n=1}^{\infty} (1/n^2) \exp[-Dn^2\pi^2 t/r_o^2] \qquad (6.76)$$

where FR(t) represents the fraction of the initial particle inventory which has been released up until time t.

PDIF may be instructed to analyze a homogeneous fuel particle, in which all layer diffusivities are equal and the buffer thickness is zero. If PDIF is predicting accurately, and the initial concentration profile is uniform and "transient" temperatures are held constant, the calculated fractional release should match that given by Eq. (6.76). Figures 6.22 and 6.23 display the results of such a PDIF calculation

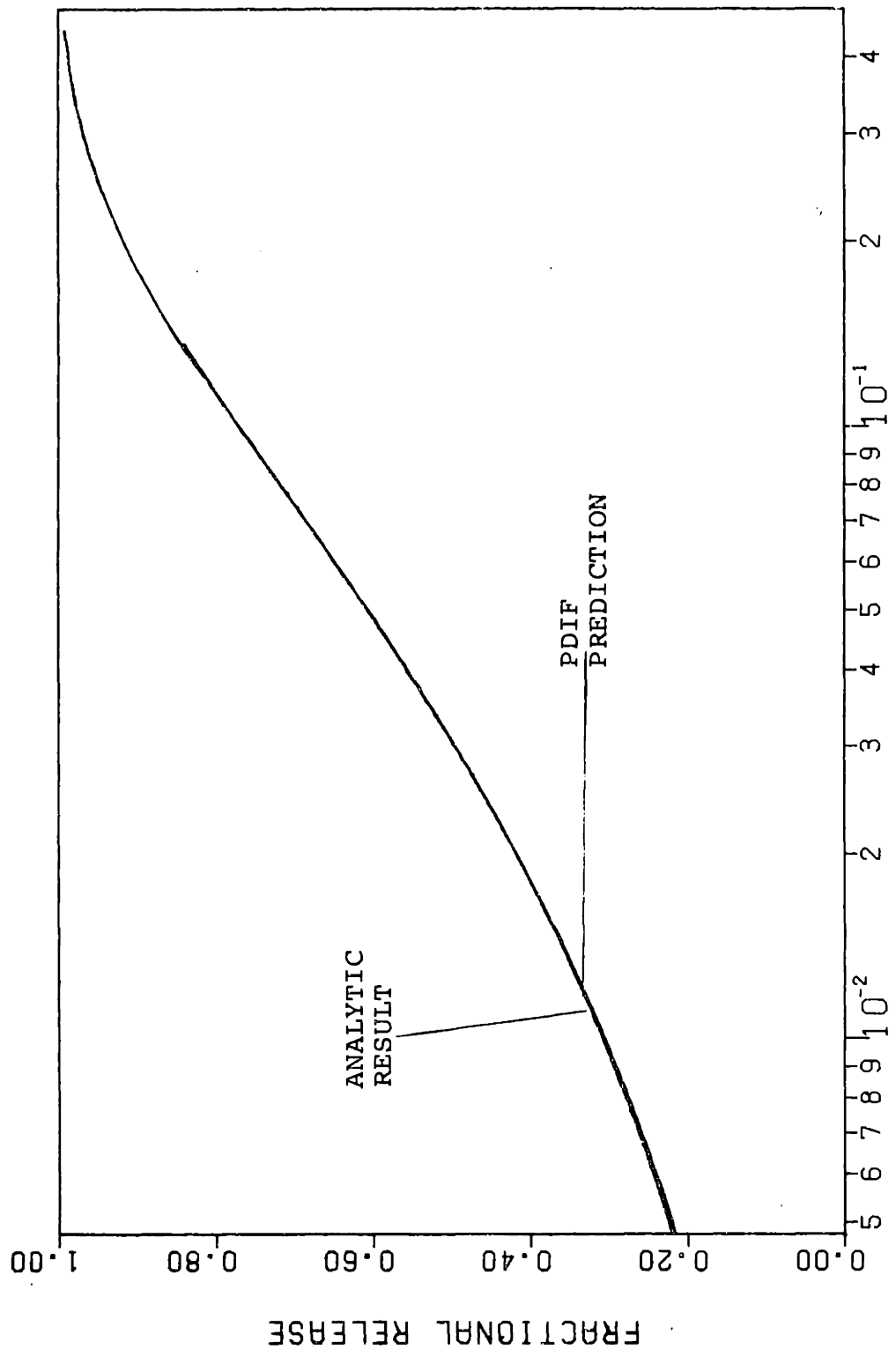

FIG. 6.22 : Comparison of PDIF and analytic fractional release from a uniform sphere at long diffusion times.

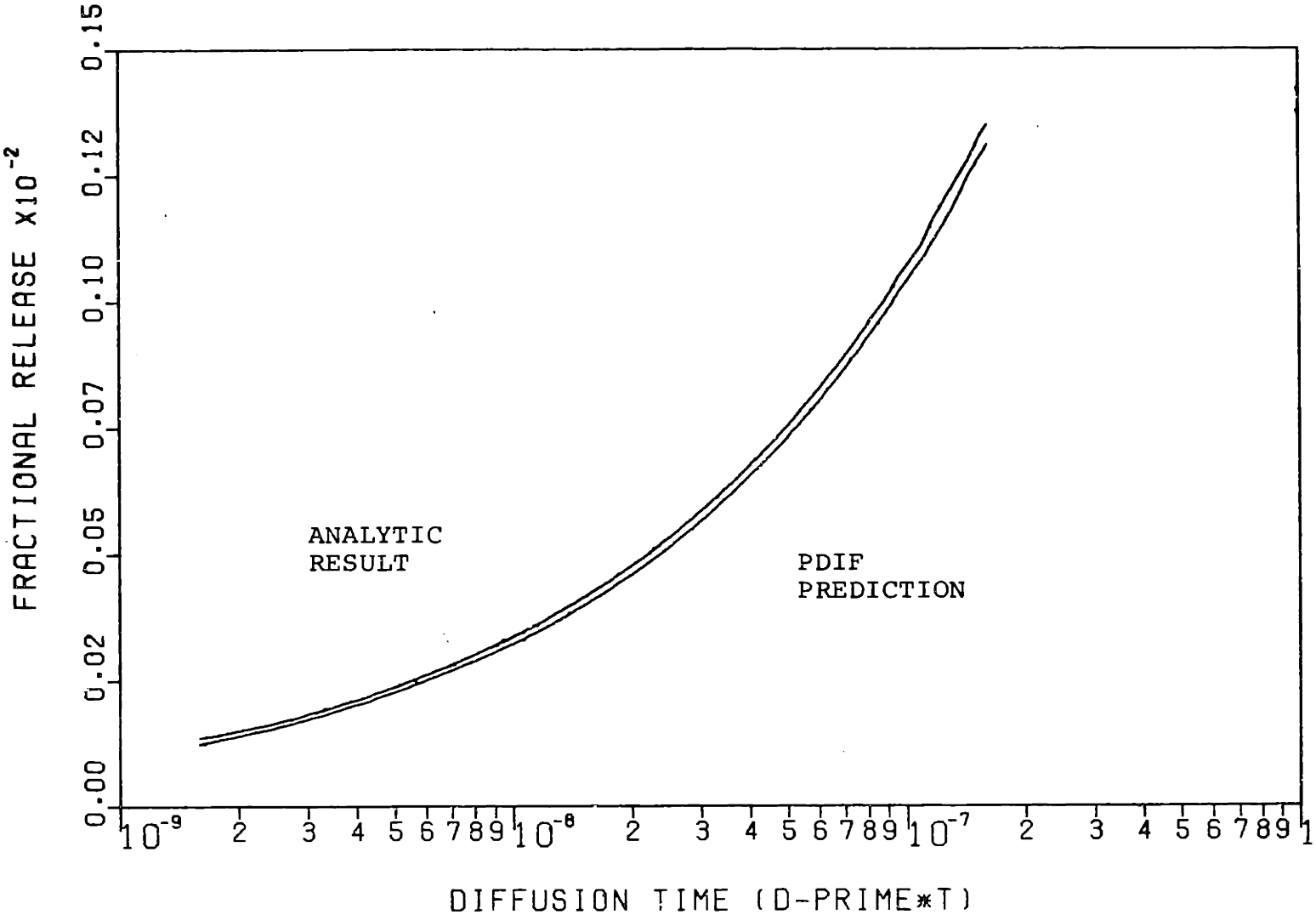

FIG. 6.23 : Comparison of PDIF and analytic fractional release from a uniform sphere at short diffusion times.

alongside the fractional release curves given by the analytic solution. The PDIF calculation was based on a bare fuel kernel of radius 250 μ and constant diffusivity 10^{-16} m^2/sec.

The plots indicate fractional release as a function of "diffusion time," which is a dimensionless time variable. The diffusion time for the spherical system is equal to the diffusivity divided by the squared radius, multiplied by the time since diffusion began:

$$\text{diffusion time} \equiv D\ t\ /\ r_0^2 \qquad (6.77)$$

At long diffusion times, the fission product profile has achieved a semi-linear shape, and PDIF performs quite well. Figure 6.22 indicates the very small difference between PDIF predictions and the analytic fractional release at long diffusion times (0.005-0.5). PDIF slightly underpredicts early fractional releases, due to the early gradient effect. As diffusion begins, the outer concentration profile is very non-linear. The release rate is proportional to the concentration gradient at the surface, which is estimated from the average concentration in the outer shell. Only when the profile in the outer shell approaches linearity does this approximation closely match the actual release. Table 6.6 details the radial mesh spacing used to calculate the displayed curve. Close match was achieved using a relatively coarse mesh spacing.

Shorter diffusion times are more difficult to model. Figure 6.23 compares PDIF calculations for very short diffusion times (0.16×10^{-8} to 0.16×10^{-6}). Though the difference between the two curves is small, the PDIF underestimation is more significant than in the long-diffusion time

TABLE 6.6: PDIF SHELL STRUCTURE FOR ANALYTIC COMPARISON AT LONG DIFFUSION TIMES.

(DIFFUSIVITY = 10^{-16} m^2/sec)

LAYER INDEX	OUTER RADIUS (μ)
1	15
2	30
3	45
4	60
5	75
6	90
7	105
8	120
9	135
10	150
11	160
12	170
13	180
14	190
15	200
16	210
17	220
18	230
19	240
20	250

case. The PDIF mesh spacing used in this calculation is presented in Table 6.7. The thickness of the outer shell is only 0.01μ, a much finer subdivision than was necessary in the long-diffusion time calculation (outer shell thickness in that case was 10μ, four orders of magnitude larger).

Ideal maximum thickness of the outer layer may be estimated based on diffusion theory. The "diffusion front" penetration distance at very short times is equal to the square root of the product Dt [C1]:

$$\delta \simeq \sqrt{Dt} \tag{6.78}$$

We would like an outer mesh spacing such that the diffusion front crosses the entire outer shell in the first time step. In the long-time calculation above, time steps were of length $\Delta t = 3\times10^{6}$ seconds. The ideal maximum outer shell would be of thickness:

$$\delta = \left[(10^{-16}\text{m}^2/\text{sec})(3\times10^{6}\text{sec})\right]^{1/2} \simeq 17\mu$$

Thus, the thickness of 10μ chosen led to very good agreement. For the short-time case, the time step $\Delta t = 1$ sec, and the ideal outer shell thickness should be no greater than:

$$\delta = \left[(10^{-16}\text{m}^2/\text{sec})(1\text{sec})\right]^{1/2} \simeq 0.01\mu$$

which is the selected value. When arbitrary mesh spacing is possible, close agreeement between PDIF and analytical predictions are possible.

TABLE 3.7: PDIF SHELL STRUCTURE FOR ANALYTIC COMPARISON AT SHORT DIFFUSION TIMES.

(DIFFUSIVITY = 10^{-16} m^2/sec)

LAYER INDEX	OUTER RADIUS (μ)
1	245.00
2	248.00
3	249.00
4	249.50
5	249.80
6	249.90
7	249.95
8	249.98
9	249.99
10	250.00

CHAPTER 7: SOURCE TERM ESTIMATION

This chapter presents results from PDIF analyses of the three MHTGR design variants introduced in earlier chapters. The goal is to estimate the fission product release due to postulated accidents which involve core heatup. Cesium-137 is chosen as a characteristic metallic fission product whose release is a measure of fuel performance. There are two release components which must be accounted for: one is due to activity released from fuel due to high temperatures, and the other is that which was released from fuel particles during steady operation and resides somewhere in the reactor primary system. The distribution of fission products between these components depends on key assumptions regarding fission products generated by heavy metal contamination. No assumptions are made regarding further transport of fission products beyond the fuel particles. Therefore, PDIF actually calculates the *potential* magnitude of each release component.

First the major assumptions are carefully reviewed, as these have a large impact on the accounting of fission products. Two types of fuel are defined for analysis: current "nominal" quality (N) and hypothetical "higher quality" (HQ) fuel. Results for both types of fuel are presented for all reactors. In addition to the PDIF analyses, a conservative bounding model is introduced to place an upper limit on the release magnitudes.

7.1: ASSUMPTIONS FOR THE RELEASE ANALYSES

In this section, we review the fundamental assumptions used to predict activity releases from MHTGR fuel. The disposition of fission products generated in heavy metal contamination granules has a large impact on the eventual distribution of fission products between steady state and accident-induced activity release. Additionally, since PDIF has no particle failure model of its own, assumptions are necessary regarding particle breakage during irradiation. Finally, two quality levels of fuel are defined for analysis: nominal quality ("NQ"), which is based upon design values for contamination and breakage, and higher quality ("HQ") based upon laboratory achievements in fuel quality. Table 7.1 lists the properties of cesium-137 used in the following analyses, and Table 7.2 presents the fuel design..

7.1.1. Fission products produced in heavy metal contamination.

There are two assumptions possible regarding the disposition of fission products immediately following generation by fission of a heavy metal contaminant atom. One is realistic, the other is more conservative. The assumptions made in this regard affect both the steady state and transient release calculations.

A realistic model would distribute the fission product source density between fuel particle coating layers and the graphite matrix in a manner consistent with manufacturing data. All contamination resides within the coating layers at the time the particles are removed from the coating bed. During the final heat treatment, however, some fraction of

TABLE 7.1: PROPERTIES OF CESIUM-137 USED IN THE RELEASE ESTIMATES

DECAY CONSTANT	7.37×10^{-10} sec^{-1}
CUMULATIVE FISSION YIELD	6.2%
RECOIL RANGE IN UO_2	7.0 μm

EFFECTIVE DIFFUSIVITIES

MATERIAL	FREQUENCY FACTOR (m^2/s)	ACTIVATION ENERGY (kJ/mole)
UO_2	5.2×10^{-4}	362
LTI-PyC	6.3×10^{-8}	222
SiC	1.8×10^{-11}	176

TABLE 7.2: FUEL DESIGN PARAMETERS FOR RELEASE ESTIMATES

FUEL ELEMENT DIAMETER	6.0 cm
DIAMETER OF FUELED ZONE	5.0 cm
KERNEL MATERIALL	UO_2
KERNEL DIAMETER	500 μm
BUFFER THICKNESS	90 μm
INNER LTI-PYC THICKNESS	40 μm
SIC LAYER THICKNESS	35 μm
OUTER LTI-PYC THICKNESS	35 μm

them migrate out of the coatings into the graphite matrix. Thus, in reality some fission products generated in HMC granules are retained more than others. This phenomenon could be accounted for by proper modification of the source vector in PDIF (for the fission products formed within the coatings) and assuming either immediate release or some form of matrix retention for the remaining fission products.

The more conservative assumption, which is generally used for calculating MHTGR primary system activity, is that all fission products generated by HMC atoms are immediately released into the coolant. For example, the recent evaluation of the KWU/Interatom HTR-MODUL performed at KFA Jülich (M4) assumed immediate release. In order to facilitate comparison with previous estimates, we assume immediate release for these calculations as well. Thus, the **q** vector in PDIF is set equal to zero in the coating layers. This does not affect the calculation of any diffusion from the kernel through the coating layers, since solutions to the diffusion equation with different source distributions are superposable.

The immediate release assumption will greatly affect the distribution between steady state and accident induced activity. In reality, some contamination-bred fission products will be retained in the fuel and matrix and released later due to high temperatures. However, if all HMC fission products are accounted for in the steady state primary system activity, they should not be re-released during the transient. Accident release estimates which follow an immediate-release steady state calculation will be lower than reality, while the primary

system activity will be higher.

In this work, we shall refer to the fission products which escape fuel during operation as "primary system" activity. Primary system activity is composed of fission products in various states. Some of the released fission products are bound to graphite dust particles in the coolant gas, some have adsorbed onto cool graphite, others have plated out on to metal surfaces, particularly the steam generator tubes. Reference M4 gives the following estimate for the distribution of steady state cesium activity:

Total activity: 750 Curies

Plated out in steam generator:	550 Curies;
Bound to dust:	15 Curies;
Bound to reflector graphite:	185 Curies.

Clearly, these populations of fission products will be affected differently by different transients. The fractions of each type that would be released from the primary system are still a subject of debate [M2]. Current investigations of water ingress accidents [W1] indicate that only a small fraction of this activity might actually be released during many accidents.

PDIF only models release from the fuel particles; no assumptions are made concerning accident conditions or further fission product transport. Thus, results reported as a steady state contribution to release must be interpreted as the *maximum potential* release. The actual source due to an accident, as well as the true ratio of steady state to accident components of the source term, depends on a mechanistic transport analysis for the accident considered.

7.1.2. Particle failure

There are three types of particle failure which must be considered for the release estimate: failures which are present from the start of irradiation due to manufacture, failures which occur during normal operation, and failures induced by a high temperature excursion. Accounting for the first failure mode is straightforward; the second and third are somewhat more subtle.

Failures during irradiation may arise due to manufacturing defects in the particles or due to the statistical nature of the coating process. Many published analyses assume that some small fraction of fuel particles have failed in addition to those initially broken before a transient begins. In this work, when it is desired to include the effects of irradiation-induced particle failure, the *entire* fraction of failed particles (i.e., initially broken plus those which fail during operation) will be assumed to behave as bare fuel kernels over the entire course of irradiation. This assumption has minor impact on the steady state activity calculations, which are dominated by release from heavy metal contamination. A small reduction in accident release might be expected, due to the diffusion and recoil of fission products out of the kernels during steady operation. However, the release fractions under these conditions are quite small compared to those under core heatup conditions, and should not be significant.

For all analyses in this work, the high quality assertion made in Chapter 2 is still applies. While core temperatures remain below approximately 1600 C, accident-induced particle failures are assumed to

be zero. Many other reported release estimates make use of temperature dependent failure functions which model particle failure during the transient. Though the number of failed particles due to MHTGR transients are very small, the accident source term is very sensitive to this parameter. For this reason, accident releases reported here may be somewhat smaller than others found in the literature.

7.1.3. Nominal and higher quality fuel particles

Design parameters for nominal quality ("NQ") fuel particles are presented in Table 7.3. Though nominal fuel is the lower quality selection in this work, it should not be overlooked that the absolute quality of this fuel is actually very high. Values for the nominal quality parameters were taken from Reference M4, the KFA analysis of the KWU/Interatom HTR-Modul.

Higher quality ("HQ") fuel is examined to estimate the advantages of increasing the as-manufactured quality of fuel particles to the limits indicated possible by recent experimental results. Heavy metal contamination fractions down to as low as 10^{-6} have been attained [K7] when special care is taken to frequently clean heavy metal granules from the coating furnace walls. Manufacturing defect levels as low as 0.5 particles per pebble have been achieved [N1], which correspond to a failure fraction of 4.5×10^{-5} for the standard HOBEG pebble. It is also assumed that the HQ particles suffer negligible failures during irradiation, due to care in eliminating defective particles during manufacture.

Finally, note that the value of (Φ_{HMC}/Φ_B) is equal to 0.2 for the

TABLE 7.3: FUEL QUALITY PARAMETERS

QUALITY PARAMETER	NOMINAL QUALITY FUEL	HIGHER QUALITY FUEL
Heavy metal contamination fraction	6×10^{-6}	1×10^{-6}
Particle fail-rate due to manufacturing	2×10^{-4}	4.5×10^{-5}
Particle fail-rate due tc irradiation	1×10^{-4}	0

nominal fuel, and 0.022 for the higher quality fuel. For the same core design, we expect the HQ fuel to have a higher accident-induced source term component.

7.2: COMPARISON OF FISSION PRODUCT RELEASE FROM MHTGR DESIGN VARIANTS

The PDIF code has estimated cesium-137 release from the MHTGR core designs analyzed with FUPAR/VSOP and THERMIX. The steady state results from FUPAR/VSOP are the basis for estimating operational release, and the 100-hour temperature transient calculated by THERMIX was used for accident release. In addition, a conservative upper bound for accident release was estimated with the uniform sphere analysis introduced in Chapter 6.

7.2.1. Cesium release from the base core

NOMINAL FUEL

The primary system cesium-137 inventory for the base core during steady operation is presented in Table 7.4. For fuel of nominal quality, the maximum primary system cesium inventory is estimated to be 403 Curies. This is the quantity which builds up over 37 years of operation, with a steady source from the fuel estimated by PDIF to be 2.3×10^{13} atoms per second. For NQ fuel, the majority of this activity is due to fission products generated in heavy metal contamination. A significant fraction (almost 10%) is generated by recoil from kernels in defective particles. Diffusive release from kernels in defective particles contributes very little to the overall activity, and diffusion from intact particles (not shown) is entirely negligible (the steady source is much less than one atom per second).

The maximum temperatures reached in each zone of the core during the THERMIX-calculated depressurization transient are presented in

TABLE 7.4: CESIUM RELEASE ESTIMATES FOR THE BASE CORE

STEADY STATE PRIMARY SYSTEM ACTIVITY (CURIES)

RELEASE MECHANISM	NOMINAL FUEL	HIGHER QUALITY FUEL
HEAVY METAL CONTAMINATION	363	6.06
RECOIL FROM BARE KERNELS	39.5	8.77
DIFFUSION FROM BARE KERNELS	0.42	0.09

ACCIDENT RELEASE (CURIES)

RELEASE MECHANISM	NOMINAL FUEL	HIGHER QUALITY FUEL
DIFFUSION FROM INTACT PARTICLES	0.03	0.01
DIFFUSION FROM DAMAGED PARTICLES	6.08	0.89

ACCIDENT RELEASE, UPPER BOUND (CURIES)

RELEASE MECHANISM	NOMINAL FUEL	HIGHER QUALITY FUEL
DIFFUSION FROM DAMAGED PARTICLES	9.39	1.39

Figure 7.1. PDIF analysis of the transient predicts a total 100 hour release of 6.1 Curies, almost all of which comes from fuel kernels with damaged coating layers. This is much less than the 37-year activity due to steady operation. However, the true fraction of either activity componenet which would actually be released can only be determined by further mechanistic analysis. *Potentially*, the steady state component is dominant for the base core.

There is some uncertainty in these estimates due to the difficulty PDIF has predicting release at low diffusion times. Though we expect the code to be fairly accurate modelling the portions of the core which reach the highest temperatures, most of the core rides out the transient at relatively low temperatures. If the underprediction of release is severe enough over a large enough fraction of the core, very large discrepencies may result. Therefore, a simple, conservative calculation has been performed to place an analytic upper bound on possible fission product release.

The analytic calculation is based on the uniform spherical diffusing system introduced in Section 6.8, which applies only to fuel kernels with failed coatings. This model is useful because fission products generated by heavy metal contamination during operation were assumed to be released immediately. The coating layer concentration levels following steady operation are very low, and diffusive release during the transient is extremely small. In all but the most severe transients, release will be dominated by the cesium escaping from uncoated kernels. For more severe transients, we expect PDIF to perform

z \ r	1	2	3	4	5
1	1357	1266	1167	1014	1014
2	1357	1266	1167	1014	1014
3	1528	1424	1314	1146	1146
4	1598	1492	1381	1218	1218
5	1631	1521	1404	1233	1233
6	1678	1565	1450	1280	1280
7	1693	1580	1465	1296	1296
8	1711	1597	1483	1313	1313
9	1710	1598	1484	1316	1316
0	1704	1594	1480	1313	1312
11	1672	1565	1452	1287	1287
12	1637	1534	1425	1265	1265
13	1594	1493	1385	1223	1223
14	1454	1365	1267	1115	1115
15	1454	1365	1267	1115	1115

FIG. 7.1: Maximum temperatures in each zone of the base core during a depressurized core heatup.

well.

Each zone in the reactor is assumed to spend the entire 100 hours at the maximum temperature achieved by that zone at any time during the interval. Furthermore, the concentration profile within the kernels is assumed to be uniform at the beginning of the transient, and cesium decay is neglected. Release fractions are predicted using Eq. (6.76). All of these assumptions (maximum temperature and uniform concentration) are conservative in the sense that they tend to overpredict release. No numerical diffusion model can predict higher releases than the anlaytic model.

Results from the uniform sphere (US) analysis are summarized in Table 7.4. Figure 7.2 presents the US-fractional release as a function of position in the reactor. For the base case, the US model exceeds PDIF by approximately 50% (9.39 Curies). Considering the conservatism of the US model, PDIF analysis is be judged an adequate predictor of cesium release.

HIGH QUALITY FUEL

The same analysis discussed above was performed for the base core with HQ fuel; results are presented in Table 7.4 as well. The 37-year cesium inventory in this case is approximately 15 Curies. Due to the larger reduction in heavy metal contamination levels relative to the reduction in defective particles, recoil from bare kernels is now the major souce of release during operation, giving rise to about 60% of this activity. Diffusion from bare kernels contributes 0.6% of the operational activity.

z \ r	1	2	3	4	5
1	0.0199	0.0063	0.0014	0.0001	0.0001
2	0.0199	0.0063	0.0014	0.0001	0.0001
3	0.1166	0.0422	0.0117	0.0010	0.0010
4	0.2107	0.0835	0.0261	0.0032	0.0032
5	0.2740	0.1095	0.0340	0.0039	0.0039
6	0.3806	0.1613	0.0550	0.0076	0.0076
7	0.4216	0.1830	0.0642	0.0094	0.0093
8	0.4715	0.2106	0.0763	0.0117	0.0116
9	0.4685	0.2123	0.0772	0.0120	0.0120
0	0.4509	0.2041	0.0740	0.0116	0.0115
11	0.3664	0.1611	0.0564	0.0083	0.0083
12	0.2855	0.1227	0.0424	0.0062	0.0062
13	0.2050	0.0840	0.0274	0.0034	0.0034
14	0.0575	0.0219	0.0064	0.0006	0.0006
15	0.0575	0.0219	0.0064	0.0006	0.0006

FIG. 7.2: Uniform-sphere fractional release during a depressurized core heatup accident in each zone of the base core.

Accident-induced release for the base core/HQ fuel is also summarized in Table 7.4. The total of 0.9 Curies is 6% of the 37-year operational inventory, thus high qualtiy fuel has a relatively higher accident-induced source term component.

The US upper bound estimate for release from the kernels in this case is 1.4 Curies.

7.2.2. Cesium release from the poisoned core

NOMINAL FUEL

PDIF was used to estimate cesium release from the reactor core which utilized gadolinia burnable poisons. Results of the analysis are summarized in Table 7.5. The 37 year circulating activity results are practically identical to those of the base core, as the assumption of immediate release for contamination fission products removes almost all temperature dependence from the operational release calculations. Only diffusion from bare kernels is effected, which is a small fraction of the overall operational release.

The maximum transient temperatures suffered by each zone are displayed in Figure 7.3. As noted in Chapter 5, the higher peak/average power ratio in the poisoned core leads to much higher accident temperatures. The 100-hour release for cesium is estimated to be 21 Curies, two-thirds of which comes from bare kernels and the rest from intact particles. The US upper bound calculation yields a maximum release from bare kernels of 18.9 Curies, higher than the PDIF estimate by about 35%. The core-wide distribution of US-estimated release fractions is presented in Figure 7.4.

TABLE 7.5: CESIUM RELEASE ESTIMATES FOR THE POISONED CORE

STEADY STATE PRIMARY SYSTEM ACTIVITY (CURIES)

RELEASE MECHANISM	NOMINAL FUEL	HIGHER QUALITY FUEL
HEAVY METAL CONTAMINATION	363	6.06
RECOIL FROM BARE KERNELS	39.5	8.77
DIFFUSION FROM BARE KERNELS	0.47	0.10

ACCIDENT RELEASE (CURIES)

RELEASE MECHANISM	NOMINAL FUEL	HIGHER QUALITY FUEL
DIFFUSION FROM INTACT PARTICLES	7.15	3.77
DIFFUSION FROM DAMAGED PARTICLES	14.0	2.07

ACCIDENT RELEASE, UPPER BOUND (CURIES)

RELEASE MECHANISM	NOMINAL FUEL	HIGHER QUALITY FUEL
DIFFUSION FROM DAMAGED PARTICLES	18.9	2.80

z \ r	1	2	3	4	5
1	1070	998	923	811	811
2	1070	998	923	811	811
3	1322	1232	1135	987	987
4	1530	1427	1316	1145	1145
5	1536	1431	1319	1146	1146
6	1681	1568	1447	1267	1267
7	1747	1633	1513	1340	1340
8	1789	1669	1543	1361	1360
9	1844	1722	1596	1415	1414
0	1854	1731	1604	1422	1422
11	1859	1736	1610	1429	1428
12	1825	1706	1582	1404	1403
13	1796	1679	1556	1378	1377
14	1648	1544	1431	1255	1255
15	1648	1544	1431	1255	1255

FIG. 7.3: Maximum temperatures in each zone of the poisoned core during a depressurized core heatup.

z \ r	1	2	3	4	5
1	0.0002	0.0001	0.0001	0.0001	0.0001
2	0.0002	0.0001	0.0001	0.0001	0.0001
3	0.0129	0.0039	0.0008	0.0001	0.0001
4	0.1192	0.0434	0.0121	0.0010	0.0010
5	0.1255	0.0453	0.0125	0.0010	0.0010
6	0.3904	0.1650	0.0535	0.0063	0.0063
7	0.5839	0.2768	0.1015	0.0162	0.0162
8	0.7180	0.3584	0.1335	0.0208	0.0207
9	0.8818	0.5053	0.2077	0.0382	0.0379
0	0.9050	0.5329	0.2218	0.0413	0.0410
11	0.9160	0.5495	0.2317	0.0444	0.0439
12	0.8313	0.4579	0.1854	0.0339	0.0337
13	0.7429	0.3847	0.1498	0.0253	0.0252
14	0.3103	0.1348	0.0451	0.0054	0.0054
15	0.3103	0.1348	0.0451	0.0054	0.0054

FIG. 7.4: Uniform-sphere fractional release during a depressurized core heatup in each zone of the poisoned core.

HIGHER QUALITY FUEL

Analysis of HQ fuel in the poisoned core produces the same trends as in the base core. This is as expected because none of the quality effects considered here depend on core conditions. Thus, the HQ 37-year cesium inventory is 14.9 Curies. Since the poisoned core's operating temperatures are close to those of the base core, the fractions of activity attributable to un-coated kernels are almost equal. Accident release estimated by PDIF amounts to 5.84 Curies. High peak temperatures, combined with the low particle damage fraction, lead to a greater release from the fully-coated than from the damaged particles. The US upper bound on kernel release predicts 2.80 Curies release, compared to PDIF's 2.07.

7.2.3. Cesium release from the DCGT core

Release estimates for nominal and higher quality fuel in the direct cycle, gas turbine core are summarized in Table 7.6. The 37-year inventory of cesium released during operation is almost identical to the other core analyzed. The only difference is the fraction of this activity which is due to diffusion from kernels with damaged coating layers, which is almost 9% in this case. The greater significance of this release mechanism is due to the higher core operating temperatures.

Maximum transient temperatures as a function of position in the core are displayed in Figure 7.5. Even though the maximum temperature is less than that of the poisoned core, inspection reveals that a larger fraction of the DCGT core reaches moderately high temperatures than in the other cases. PDIF's accident release from the DCGT core is about

TABLE 7.6: CESIUM RELEASE ESTIMATES FOR THE DOGT CORE

STEADY STATE PRIMARY SYSTEM ACTIVITY (CURIES)

RELEASE MECHANISM	NOMINAL FUEL	HIGHER QUALITY FUEL
HEAVY METAL CONTAMINATION	363	6.06
RECOIL FROM BARE KERNELS	39.5	8.77
DIFFUSION FROM BARE KERNELS	6.35	1.41

ACCIDENT RELEASE (CURIES)

RELEASE MECHANISM	NOMINAL FUEL	HIGHER QUALITY FUEL
DIFFUSION FROM INTACT PARTICLES	1.23	0.51
DIFFUSION FROM DAMAGED PARTICLES	11.2	1.66

ACCIDENT RELEASE, UPPER BOUND (CURIES)

RELEASE MECHANISM	NOMINAL FUEL	HIGHER QUALITY FUEL
DIFFUSION FROM DAMAGED PARTICLES	19.8	2.92

z \ r	1	2	3	4	5
1	1432	1353	1272	1147	1141
2	1432	1353	1273	1148	1142
3	1603	1509	1415	1272	1263
4	1660	1562	1465	1319	1308
5	1714	1611	1509	1356	1343
6	1761	1655	1551	1397	1380
7	1780	1673	1568	1414	1394
8	1803	1694	1588	1434	1412
9	1809	1700	1594	1443	1419
0	1805	1697	1592	1441	1417
11	1785	1679	1576	1426	1404
12	1746	1643	1543	1395	1376
13	1713	1613	1514	1368	1352
14	1602	1512	1422	1283	1272
15	1598	1509	1418	1279	1266

FIG. 7.5: Maximum temperatures in each zone of the DOGT core during a depressurized core heatup.

2.1 Curies, 1.66 of which are released from kernels with damaged coatings. This is about one-third the PDIF-predicted release from the poisoned core. The US upper bound on kernel release, however, yields 2.92 Curies, which is 40% higher than that predicted for the poisoned core. Figure 7.6 presents the core-wide distribution of US releases.

This discrepency is due to the temperatures at which most of the fission product release originates. In the poisoned core, the majority of release comes from very high temperature zones of the core, in which PDIF is expected to predict well. In the DOGT core, on the other hand, much of the release originates in regions which experience more moderate temperatures. Therefore, the analytic approximation, which is accurate for short as well as long diffusion times, will predict proportionally higher releases from the core with the seemingly more moderate transient.

z \ r	1	2	3	4	5
1	0.0457	0.0190	0.0068	0.0010	0.0009
2	0.0459	0.0190	0.0068	0.0010	0.0009
3	0.2198	0.0980	0.0382	0.0068	0.0060
4	0.3361	0.1574	0.0641	0.0125	0.0109
5	0.4806	0.2346	0.0981	0.0197	0.0168
6	0.6265	0.3256	0.1427	0.0313	0.0258
7	0.6898	0.3692	0.1652	0.0376	0.0304
8	0.7633	0.4254	0.1949	0.0465	0.0371
9	0.7829	0.4423	0.2053	0.0511	0.0397
0	0.7721	0.4336	0.2019	0.0504	0.0390
11	0.7074	0.3845	0.1767	0.0432	0.0337
12	0.5809	0.2993	0.1333	0.0307	0.0248
13	0.4784	0.2377	0.1031	0.0226	0.0187
14	0.2176	0.1009	0.0411	0.0079	0.0068
15	0.2119	0.0979	0.0396	0.0074	0.0062

FIG. 7.6: Uniform-sphere fractional release during a depressurized core heatup in each zone of the DOGT core.

7.3 CONCLUSIONS REGARDING FISSION PRODUCT RELEASE

The cores analyzed in this work have very low releases from the fuel when compared to other cores which are not passively safe. For example, 42.5% of the total cesium inventory in the HTR-500 is estimated to escape the *fuel* in a thermal transient [K8], while the worst release predicted here amounts to only slightly more than the heavy metal contamination fraction, 6×10^{-5}. Thus, modular HTGRs with high quality fuel release significantly less cesium and other metallic fission products than other reactors. Furthermore, since the *accident* induced failure fraction is zero, the fractional release of the gaseous fission product inventory will be on the same order as for the metallic fission products.

Steady state activity has two principal sources: fission products generated by heavy metal contamination, and recoil release from kernels with damaged or defective coatings. If the ratio of the contamination fraction to the particle damage fraction is high, release due to contamination will dominate. For the higher quality fuel, in which the contamination fraction is very low, recoil contributes the greater part to the operating release.

Damaged or defective particles are responsible for the majority of accident-induced release. In part, this is due to the assumption of immediate contamination release during operation. This depletes the coating layers of fission products which could in reality diffuse out from intact particles during the transient.

The potential source term due to operational release is generally much greater than that due to accident releases. Operational releases from all reactors were calculated to be roughly equal. This is also due partially to the immediate release assumption. In reality, the two lower temperature cores (the base and poisoned cores) would be more retentive of fission products in the fuel element graphite. Their operational releases would therefore be less than that of the higher temperature DCGT core.

Tables 7.7 and 7.8 compile the cesium release estimates for the three reactor designs. The differences between designs are apparent primarily through the accident releases. The poisoned core performed most poorly according to PDIF, due to its high peak transient temperatures. However, the uniform sphere calculations indicate that the DCGT core may release as much or more cesium, due to the higher average temperature during the transient. Nevertheless, these releases are all quite small; each core could still be considered passively safe.

Higher quality fuel has the greatest effect on operational fission product release, reducing the 37-year cesium inventory by a factor of almost 30. Additionally, accident releases are reduced as well, due to the smaller number of bare kernels. The reduction is exactly equal to the ratio of broken coatings in nominal fuel to higher quality fuel.

Finally, we conclude that the PDIF computer code is an adequate predictor of fission product release under certain circumstances:

(1) diffusive release from fuel particles during operation contributes only a small fraction to the overall operational release; and

TABLE 7.7: CESIUM RELEASE ESTIMATES FOR NOMINAL QUALITY FUEL

($\Phi_{HMC} = 6\times10^{-5}$, $\Phi_B = 3\times10^{-4}$)

STEADY STATE PRIMARY SYSTEM ACTIVITY (CURIES)

RELEASE MECHANISM	BASE CORE	POISONED CORE	DOGT CORE
HEAVY METAL CONTAMINATION	363	363	363
RECOIL FROM BARE KERNELS	39.5	39.5	39.5
DIFFUSION FROM BARE KERNELS	0.42	0.47	6.35

ACCIDENT RELEASE (CURIES)

RELEASE MECHANISM	BASE CORE	POISONED CORE	DOGT CORE
DIFFUSION FROM INTACT PARTICLES	0.03	7.15	1.23
DIFFUSION FROM DAMAGED PARTICLES	6.08	14.0	11.2

ACCIDENT RELEASE, UPPER BOUND (CURIES)

RELEASE MECHANISM	BASE CORE	POISONED CORE	DOGT CORE
DIFFUSION FROM DAMAGED PARTICLES	9.39	18.9	19.8

TABLE 7.8: CESIUM RELEASE ESTIMATES FROM HIGHER QUALITY FUEL

($\Phi_{HMC}= 10^{-6}$, $\Phi_B = 4.5\times10^{-5}$)

STEADY STATE PRIMARY SYSTEM ACTIVITY (CURIES)

RELEASE MECHANISM	BASE CORE	POISONED CORE	DOGT CORE
HEAVY METAL CONTAMINATION	6.06	6.06	6.06
RECOIL FROM BARE KERNELS	8.77	8.77	8.77
DIFFUSION FROM BARE KERNELS	0.09	0.10	1.41

ACCIDENT RELEASE (CURIES)

RELEASE MECHANISM	BASE CORE	POISONED CORE	DOGT CORE
DIFFUSION FROM INTACT PARTICLES	0.01	3.77	0.51
DIFFUSION FROM DAMAGED PARTICLES	0.89	2.07	1.66

ACCIDENT RELEASE, UPPER BOUND (CURIES)

RELEASE MECHANISM	BASE CORE	POISONED CORE	DOGT CORE
DIFFUSION FROM DAMAGED PARTICLES	1.39	2.80	2.92

(2) transient release is dominated by diffusion in a relativley small high-temperature volume of the core, such as in the poisoned case analyzed here.

Also, the linear nature of PDIF is attractive as it allows explicit modelling of stochastic processes. Nevertheless, additional work is needed before PDIF can be considered an accurate predictor of fission product release. In particular, numerical methods for evaluating transition matrices with very high norms should be investigated, as well as a means of automatically and optimally selecting a mesh spacing for the particle model. Various short-time diffusion approximation may be applicable as well.

8.1: SUMMARY OF RESEARCH

Passively safe nuclear reactors have been proposed as a means of eliminating some of the institutional drawbacks associated with the current generation of light-water cooled reactors. This work focuses on a particular passively safe reactor design: the modular high-temperature gas-cooled reactor (MHTGR). The MHTGR achieves passive safety due to two design features

(1) High-quality coated particle fuel ensures negligible fission product release during both operation and any thermal transient in which the temperature does not exceed some critical value (typically 1600 C); and

(2) Thermal properties of the reactor core (high heat capacity and large surface/volume ratio) enable complete dissipation of reactor decay heat, even with the absence of all coolant, without exceeding the fuel temperature limit.

Fission product retention in the MHTGR does not require that a supply of coolant be maintained to the core. Risk dominance is thereby shifted from loss-of-coolant accidents to an entirely different, much lower frequency class of events.

8.1.1 Fission product retention and fuel quality

Fuel for the high-temperature gas-cooled reactor takes the form of small coated particles embedded in a graphite matrix (see Figure 8.1). In a TRISO fuel particle, a central fuel kernel of fissile material is surrounded by a low-density pyrolitic buffer layer, then by three

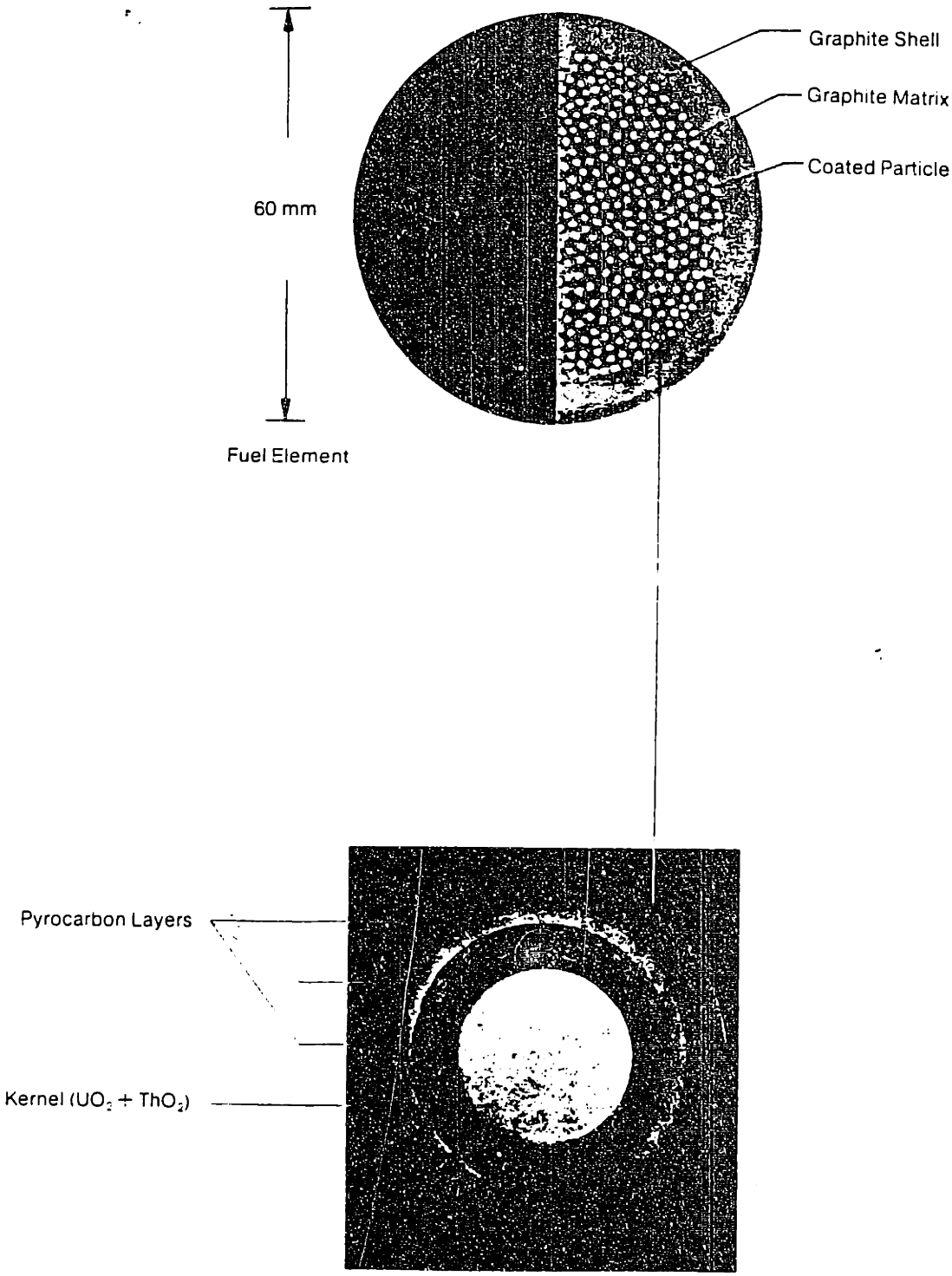

FIG. 8.1: An HTGR coated fuel particle and fuel element.

high-density pyrolitic carbon and silicon carbide coating layers. The roles played by each layer in fission product retention are summarized in Table 8.1. These coating layers provide an effective barrier to the release of fission products generated in the fuel kernel. HTGR fuel performance has been examined, particularly under the conditions anticipated in the MHTGR. High quality fuel in such a reactor can release fission products only by the following mechanisms:

(1) Heavy metal contamination: During the manufacture of the coated particles, a small fraction of fissile material may be deposited outside or within the coating layers. When these atoms are fissioned, the fission products which are generated may easily escape.

(2) Particles damaged during manufacture: When the coated particles and graphite matrix are pressed into final spherical form, some of them may be damaged. Fission products generated in the kernels of these particles are released directly from the kernel surface into the pebble matrix.

(3) High temperature diffusion: Some metallic fission products (such as cesium or silver) have high enough diffusivities through the coating layer materials that, under high-temperature transient conditions, significant quantities can escape even from intact particles. Temperatures in excess of 1600 C are required for significant release.

Recent experimental results from KFA Jülich (see Figure 8.2) indicate that modern particle coatings will not fail even if subjected to temperatures of 1600C for hundreds of hours [H2]. Reactor cores

TABLE 8.1: PARTICLE COATING LAYER FUNCTIONS

LAYER	FUNCTIONS
Kernel	• contains fissile and fertile material • diffusion barrier to metallic FP release • chemical holdup of metallic FPs • C/O ratio controls carbon monoxide generation • enrichment affects fission product yields
Buffer	• attenuate and absorb recoil FPs • accommodate kernel swelling and PyC shrinkage • provide void volume for gaseous FPs • sacrificial layer for amoeba migration
Inner PyC	• protect SiC layer from FP corrosion • reduce tensile stresses in SiC layer • protect buffer and kernel from chlorine intrusion during particle coating process
SiC	• primary diffusion barrier for metallic FPs • primary pressure-retaining layer
Outer PyC	• reduce tensile stresses in the SiC layer • provides better bonding with matrix • gaseous FP barrier should SiC fail

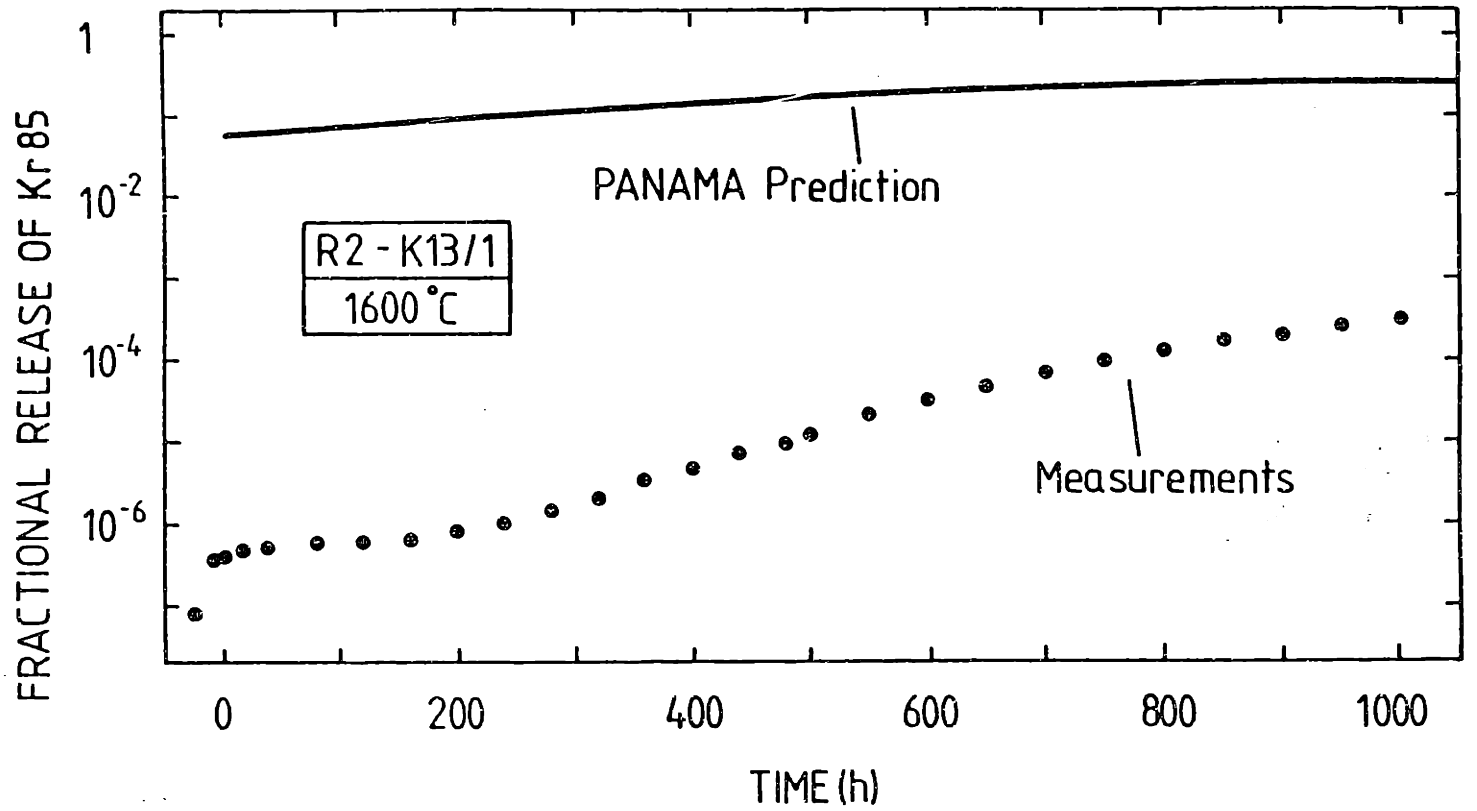

FIG. 8.2: Measured and predicted fractional release of Kr-85 during post-irradiation annealing at 1600 C [H2].

considered to be well designed in this study only achieve these temperatures as an upper limit, and for a much shorter period of time. A model for particle behavior and fission product retention is proposed which does *not* include high temperature particle failure as a significant source of release from a well-designed reactor. The model assumes that an MHTGR will utilize very high quality fuel due to the importance of minimizing fission product release.

The *quality* of fuel is defined in terms of the level of heavy metal contamination (the number of free heavy metal atoms divided by the total number present) and the rate of particle breakage during manufacture. Fuel quality increases as either of these two parameters decrease. The release of fission products during reactor operation is highly dependent on fuel quality. Intact coating layers are a very strong release barrier under normal conditions, so the only sources of fission products are contamination and damaged coatings. Only a small fraction of the core achieves temperatures at which significant diffusion occurs, so it is possible that activity released during normal operation is the primary component of radionuclide release. If this is the case, then that release is said to be *steady state dominated*. If, on the other hand, high-temperature diffusion causes most of the release, than that source term is *accident dominated*. Let Φ_{HMC} represent the heavy metal contamination fraction, and Φ_B the fraction of broken particles at the time of a core heatup accident. It can be shown that the ratio Φ_{HMC}/Φ_B plays an important role in determining whether the release is steady state or accident dominated. If the ratio is much less than one, then

accident-induced fission product release will constitute the majority of released radionuclides. For current quality specifications, the ratio is on the order of 1.0, indicating that MHTGRs have both steady state and accident-induced contributions to their source terms. For extremely high quality particles (manufactured only on a laboratory scale to date), the ratio can be almost an order of magnitude less, indicating increased likelihood of accident domination.

8.1.2 Probabilistic analysis of pebble bed reactors

A mathematical technique for describing processes in continuously, randomly refueled pebble bed reactors has been introduced. The reactor core is divided into a finite number of radial *drop zones*, indexed 1 through N. Each drop zone i is characterized by a *drop probability* p_i, which is the probability that a pebble will travel through that zone on any pass through the core. These concepts are illustrated in Figure 8.3. A fuel element's previous trajectory through the core may be summarized by the *branch variable* β, defined as an ordered list of positive integers. Each member of the list is the index of the radial drop zone which the pebble traversed on the i'th pass through the core, where i is the position in the list of the index. Thus, a pebble which "occupies" branch $\beta = (i,j,k)$ is on its third pass through the core, and the drop zones through which it has passed are i, j, and k, in that order. The w'th order event space, B_w, is the set of all possible w'th order branch variables. The statement $\beta \in B_w$ is equivalent to the statement that the fuel element occupying branch β is on its w'th pass.

Several operations based on the branch variable are defined:

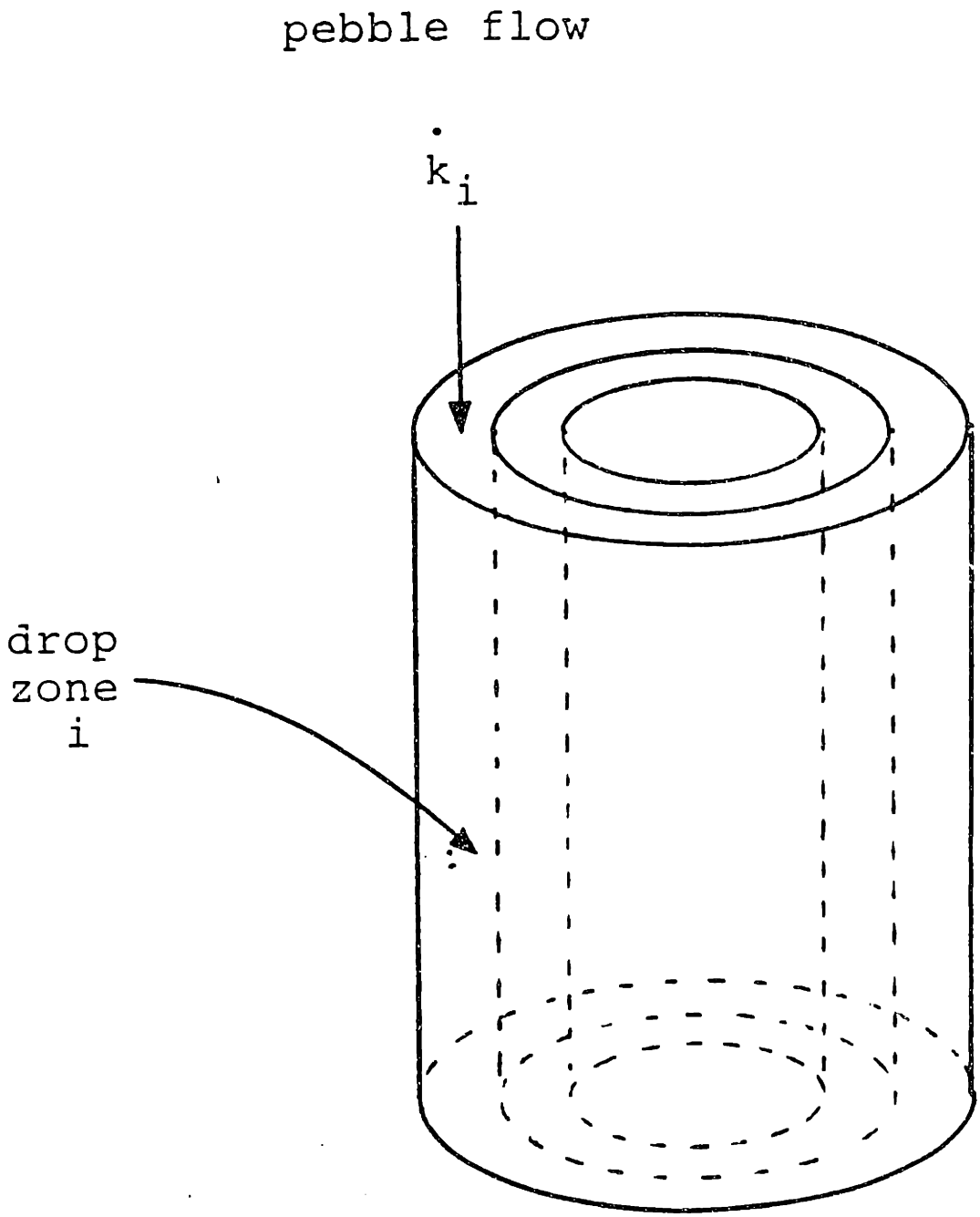

FIG. 8.3: Idealized pebble bed reactor with radial "drop zones."

(1) Parent operation: The parent branch β' of branch β is defined as follows:

$$\text{IF } \beta = (i_1, i_2 \ \ldots \ i_{w-1}, i_w) \ \text{ THEN } \beta' = (i_1, i_2 \ \ldots \ i_{w-1})$$

Equivalently, we may write $\beta = (\beta', i_w)$.

(2) Branch probability operation: The branch probability operator p_β is defined as:

$$p_\beta \equiv p_{(i_1, i_2, \ldots i_w)} \equiv p_{i_1} p_{i_2} \cdots p_{i_w}$$

where p_i is the drop probability associated with the i'th radial drop zone.

(3) Branch Summation Operation: This operation is defined to enumerate all possible values of the branch variable:

$$\sum_\beta \equiv \sum_{i_w=1}^{N} \sum_{i_{w-1}=1}^{N} \cdots \sum_{i_2=1}^{N} \sum_{i_1=1}^{N}$$

(4) Branch expectation operation: The branch- or L-expectation (L for "Lagrangian") is defined as:

$$E[\ ] \equiv \sum_\beta p_\beta$$

A useful identity relates the expectation of pass-w fuel to that of the previous pass:

$$\sum_\beta p_\beta = \sum_{\beta'} \sum_{i_w} p_{\beta'} p_{i_w} = \sum_{i_w} p_{i_w} \sum_{\beta'} p_{\beta'} \tag{8.1}$$

since the index i_w is independent of any of the indices in β'.

These operators have physical significance. The rate of pebble flow through branch β, denoted $\dot{k}_\beta$, is the rate of fresh fuel injection,

$\dot{K}_f$, multiplied by the branch probability::

$$\dot{k}_\beta = p_\beta \dot{K}_f \tag{8.1}$$

It can be shown that p_β, where $\beta \in B_w$, represents the probability density function associated with the flow of pass-w fuel. Furthermore, the branch expectation operator gives the flow or frequency weighted expectation of fuel properties at pass w. If $Z(\beta)$ represents any fuel property which can be expressed as a function of the branch variable,

$$\overline{Z}_w \equiv E[Z] \equiv \sum_\beta p_\beta Z(\beta) \qquad (\beta \in B_w)$$

is the flow-weighted expectation value of Z for pass-w fuel. If an experiment consists of measuring Z values of pass-w pebbles as they exit the core, $\overline{Z}_w$ is the expected value of the data. This is termed the Lagrangian- or L-expectation, as the parameter Z is measured at a *point* in space, over an *interval* in time.

The number of fuel elements in the core which occupy a particular branch β is called the population of that branch, denoted k_β. The population of β is equal to the branch flow multiplied by the residence time in the final drop zone, i_w:

$$k_\beta = \dot{k}_\beta \Delta t_{i_w} \tag{8.3}$$

Any drop zone j contains pass-w pebbles from many different branches $\beta = (\beta', j)$. The Eulerian, or E-probability of drawing a pebble of branch β from zone j is denoted π_β, and is the ratio of the population in (β', j) to the total pass-w population in zone j. This probability is Eulerian as it involves measurements at an instant in

time, over a finite region in the reactor. In most cases, the E-probabilities are identical to the L-probabilities, since all pebbles in zone j have identical last-zone residence times. E-expectations may be taken over the E-probabilities, yielding the volume averaged values of fuel properties. The general definition of an L-expectation does not account for the discharge of pebbles due to high burnup. E-expectations, which must account for this phenomenon, are therefore *not* equal to L-expectations for later passes in which some fuel elements have already been discharged.

When such late passes are considered, approximations for the E-distributions are necessary to avoid enumerating all pebble trajectories out to the last passes. The quasi-two dimensional (Q2D) approximation is a method of approximating the L-expectations in terms of the expected values from the drop zone exits in the previous pass. The assumption is that all fuel elements leaving a drop zone are adequately characterized by the *expected value* of burnup leaving that zone. All or none of these pebbles are discharged, depending on the average burnup. The accuracy of this approximation depends on the ratio of burnup variance of pebbles within the same pass to the burnup variance between passes. Analysis of actual MHTGR cores has shown that between-pass variance is much larger (contributing several hundred times more to the overall variance than the within pass variance), lending credence to the Q2D approximation.

Based on the E-probability distribution, methods have been developed for estimating the likelihood of "random hot spots." Suppose

a certain region of the reactor, containing N pebbles, has an E-expectation $\bar{S}$ of some parameter of interest. A random hot spot of size m and severity δS is defined as a contiguous sub-volume of m pebbles within that zone, with an average value of the parameter greater than or equal to $\bar{S}+\delta S$. The probability of such a zone arising is dependent upon the "ungrouped selection probability" $p(m,\delta S)$, which is the probability of randomly drawing m pebbles from *anywhere* in the region whose average value of the parameter is greater than or equal to $\bar{S}+\delta S$. $p(m,\delta S)$ is determined by the E-distribution of the parameter within the zone. The ungrouped probability must be modified to account for the requirement that a hot spot consist of contiguous pebbles. If it is assumed that there are essentially (N/m) independent sub-volumes, each of which has an *independent* probability $p(m,\delta S)$ of being a hot spot of severity δS, then the probability of *no* such hot spots in the zone, denoted $\mathbb{P}_o$, is approximately given by:

$$\mathbb{P}_o \simeq \exp\left[- \frac{N\, p(m,\delta S)}{m} \right] \qquad (8.4)$$

Application of this equation to a specific reactor will be termed "random hot spot analysis," and specific examples are presented in later sections.

8.1.3 Estimating the characteristics of a stationary pebble bed reactor

Methods have been developed for expressing the isotopic composition of a fuel element as a function of the branch variable β. Given a known neutron flux distribution and neutron cross sections, it is possible to calculate the expected values and variances of heavy metal number densities, fission product number densities, burnup and power density.

This is accomplished by writing the differential equations which describe the generation and decay of heavy metal and fission product isotopes, as well as the accumulation of burnup, in the following form:

$$\dot{\mathbf{n}} = \mathbf{H}\,\mathbf{n} \tag{8.5a}$$

$$\dot{\mathbf{f}} = -\mathbf{A}\,\mathbf{f} + \mathbf{Y}\,\mathbf{n} \tag{8.5b}$$

$$\dot{F} = \phi\,\boldsymbol{\sigma}_f^{+}\,\mathbf{n} \tag{8.5c}$$

where

- $\mathbf{n}$ = a vector of heavy metal number densities;
- $\mathbf{f}$ = a vector of fission product number densities;
- F = local fission density;
- $\mathbf{H}$, $\mathbf{A}$, and $\mathbf{Y}$ = coefficient matrices, with terms wich depend upon cross sections, decay constants, fission yields, branching ratios, and the local neutron flux.
- ϕ = the local neutron flux; and
- $\boldsymbol{\sigma}_f$ = a vector of fission cross sections, whose order corresponds to the order of isotopes in $\mathbf{n}$.

Note that in actuality, there are two heavy metal isotopic chains, one beginning with U-238, the other with Th-232. Even though current HTGRs do not utilize thorium, the Th-232 chain must be included because it contains U-235. For simplicity here, we shall discuss only a single heavy metal chain. All results are easily extrapolated to the two-chain case.

Divide the reactor core axially and radially into small discrete zones. If the neutron flux does not vary with time, then Eq. (8.5) is approximately linear and time invariant. Denote the heavy metal

isotopic concentration vector leaving some zone i by $\mathbf{n}_i$. The analytic solution is:

$$\mathbf{n}_i = \mathbf{T}_i \, \mathbf{n}_{i-1} \tag{8.6}$$

where $\mathbf{n}_{i-1}$ is the concentration vector leaving the zone directly above zone i. $\mathbf{T}_i$ is the isotopic *transition matrix* associated with zone i, defined as:

$$\mathbf{T}_i \equiv \exp[\, \mathbf{H}_i \, \Delta t_i \,] \tag{8.7}$$

where $\mathbf{H}_i$ is the coefficient matrix associated with zone i, and Δt_i is the time required for a fuel element to traverse zone i. Transition matrices may also be derived for ΔF_i, the incremental burnup (fissions/barn-cm) accumulated across zone i, and $\mathbf{f}_i$, the vector of fission product number densities at the exit of zone i.

$$\Delta F_i = \phi_i \, \sigma_{f,i}^{+} \, \mathbf{D}_i \, \mathbf{n}_{i-1} \tag{8.8a}$$

$$\mathbf{f}_i = \mathbf{L}_i \, \mathbf{f}_{i-1} + \mathbf{J}_i \, \mathbf{n}_{i-1} \tag{8.8b}$$

where:

$$\mathbf{D}_i \equiv \mathbf{H}_i \, [\, \exp(\mathbf{H}_i \Delta t_i) - \mathbf{I} \,] \tag{8.9a}$$

$$\mathbf{L}_i \equiv \exp[-\mathbf{A}_i \Delta t_i] \tag{8.9b}$$

$$\mathbf{J}_i \equiv \int_0^{\Delta t_i} \exp[-\mathbf{A}_i(\Delta t_i - \tau)] \, \mathbf{Y}_i \, \exp[\mathbf{H}_i \tau] \, d\tau \tag{8.9c}$$

By successively multiplying by the appropriate transition matrices for axially consecutive zones, it is possible to *collapse* the two-dimensional core into a single dimensional representation. Each radial drop zone in the collapsed core has a single set of transition matrices, which relate the core exit properties of a fuel element to the properties at the exit of the previous pass. Thus, if $\mathbf{n}(\beta)$, $\mathbf{f}(\beta)$, and

$F(\beta)$ represent the isotopic concentrations and cumulative fission density of fuel at the *exit* of pass β, and $\beta = (\beta', n)$, we may write:

$$\mathbf{n}(\beta) = \boldsymbol{\theta}_n \, \mathbf{n}(\beta') \tag{8.10a}$$

$$\mathbf{f}(\beta) = \boldsymbol{\mathcal{L}}_n \, \mathbf{f}(\beta') + \boldsymbol{\mathcal{F}}_n \, \mathbf{n}(\beta') \tag{8.10b}$$

$$F(\beta) = F(\beta') + \boldsymbol{\Delta}_n^{+} \, \mathbf{n}(\beta') \tag{8.10c}$$

where $\boldsymbol{\theta}_n$, $\boldsymbol{\mathcal{L}}_n$, $\boldsymbol{\mathcal{F}}_n$, and $\boldsymbol{\Delta}_n$ are the collapsed transition matrices for drop zone n. If we apply the L-expectation operation to Eq. (8.10a), for example, we obtain:

$$\begin{aligned} \overline{\mathbf{n}(\beta)} = E[\,\mathbf{n}(\beta)\,] &= \sum_{\beta} p_\beta \, \mathbf{n}(\beta) = \sum_{n} \sum_{\beta'} p_n \, p_{\beta'} \, \boldsymbol{\theta}_n \, \mathbf{n}(\beta') \\ &= \sum_{n} p_n \, \boldsymbol{\theta}_n \sum_{\beta'} p_{\beta'} \, \mathbf{n}(\beta') \\ &\equiv \overline{\boldsymbol{\theta}} \, \overline{\mathbf{n}}(\beta') \end{aligned} \tag{8.11}$$

where $\overline{\boldsymbol{\theta}} \equiv \sum_{n} p_n \, \boldsymbol{\theta}_n$. Thus, the entire stationary pebble bed core may be collapsed to a single transition matrix for calculation of the expected values of the heavy metal concentration vectors. In the same manner, core average fission product and burnup transition matrices may be defined which relate the L-expectations from the exit of one pass to that of the previous pass:

$$\overline{\mathbf{f}(\beta)} = \overline{\boldsymbol{\mathcal{L}}} \, \overline{\mathbf{f}(\beta')} + \overline{\boldsymbol{\mathcal{F}}} \, \overline{\mathbf{n}(\beta')} \tag{8.12a}$$

$$F(\beta) = F(\beta') + \overline{\boldsymbol{\Delta}^{+}} \, \overline{\mathbf{n}(\beta')} \tag{8.12b}$$

Any of these quantities may be related to the known initial conditions of fresh fuel through multiplication by the sequence of transition matrices which correspond to the path indicated by the branch variable. Expected values for fuel entering the core for each pass is

calculated with the core average matrices. Multiplication by local (uncollapsed) transition matrices yields expected values for that pass fuel in each core zone. The quasi-2D approximation is necessary once fuel burnup approaches discharge values. Equations similar to (8.12) may be derived for the covariance matrices associated with the concentration vectors and burnup.

The FUPAR computer program performs these calculations, producing a materials density distribution given a known neutron flux distribution and nuclear properties of the materials. A system has been developed to use FUPAR in conjuncition with the VSOP code from KFA Jülich [T2]. VSOP calculates the nuclear properties and neutron flux distribution given a distribution of materials densities in the core. The iterative scheme is illustrated in Figure 8.4. The system differs from previous methods of pebble bed reactor analysis by assuming *a-priori* that the reactor is in steady state operation. Other methods rely on simulating the entire running-in period of operation. Additionally, FUPAR calculates the variances as well as the expected values of core parameters, a capability previous methods do not have.

Results of FUPAR/VSOP analysis of the 200 MWth KWU/Interatom HTR-MODUL are consistent with published values. These results wi l be presented in the following section, along with results from other reactor analyses.

The temperature of a random hot spot is related to the power density difference between the hot spot and its surroundings. Figure 8.5 shows a sub-volume of m pebbles operating with a volume-averaged

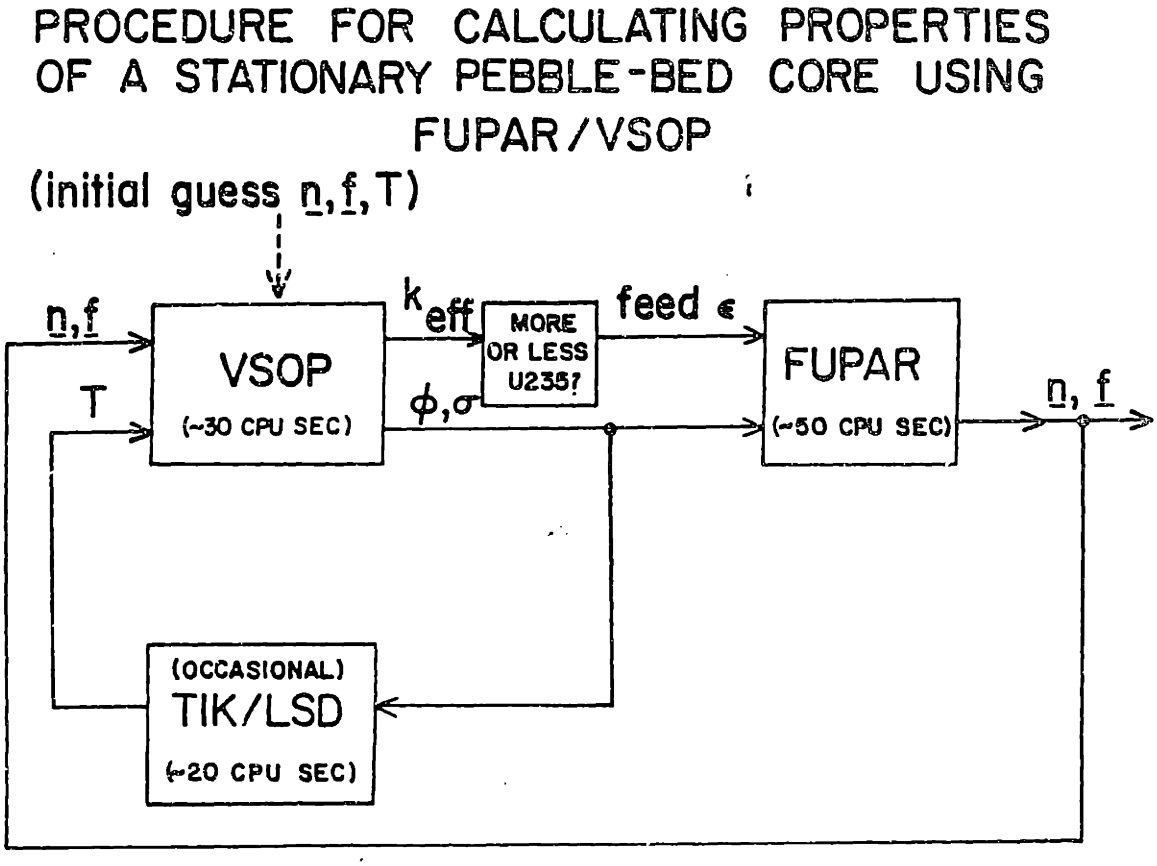

FIG. 8.4: A simple iterative scheme for FUPAR/VSOP.

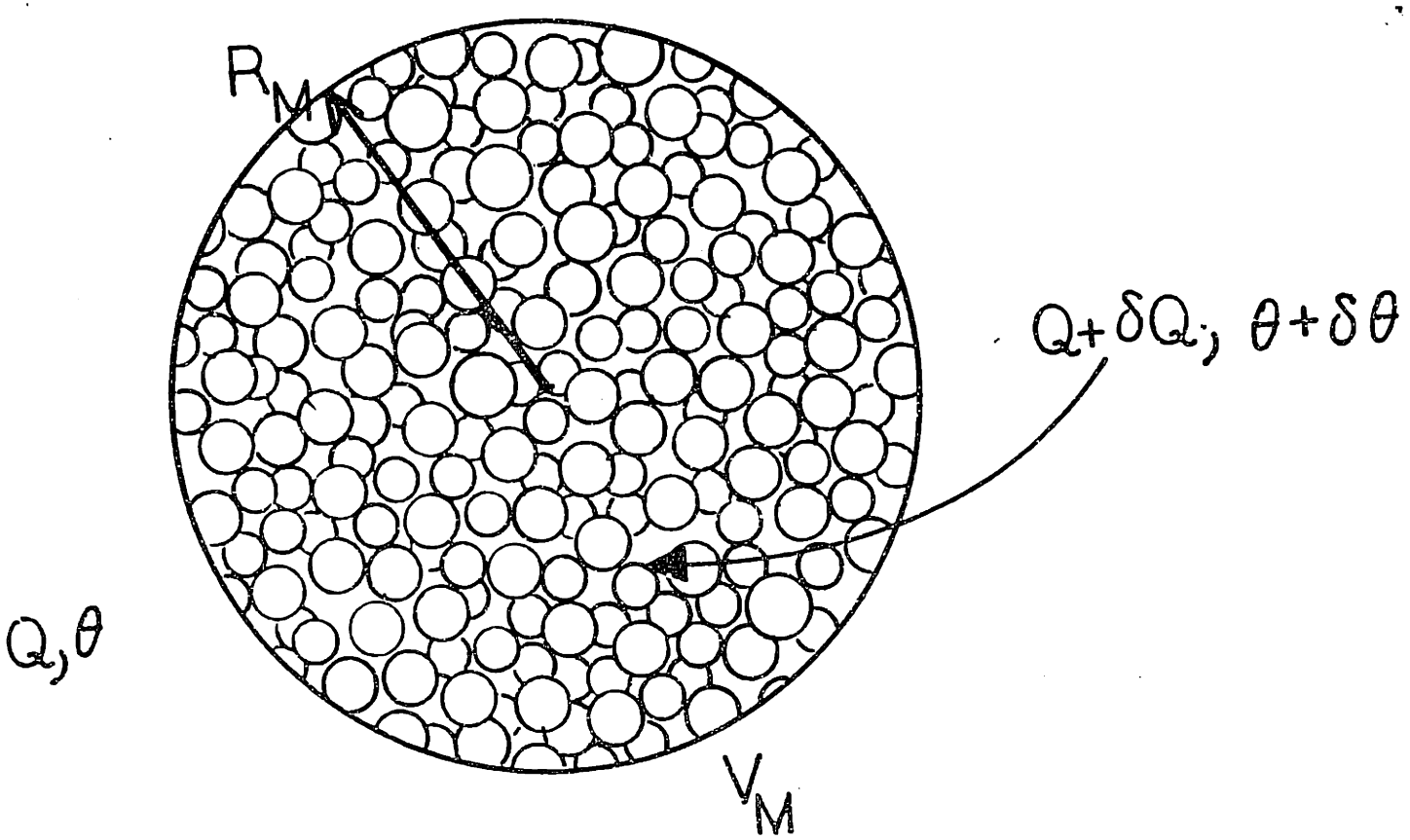

FIG. 8.5: A "hot spot" within a pebble bed reactor.

power density $\overline{Q}+\overline{\delta Q}$ and temperature $\overline{\theta}+\overline{\delta\theta}$. It is surrounded by "zone average" pebbles, at power density $\overline{Q}$ and temperature $\overline{\theta}$. $\overline{\delta Q}$ and $\overline{\delta\theta}$ are the volume-averaged severities of pebbles in the hot spot. The one-dimensional heat transport equation relates temperature severity to the power density severity:

$$\overline{\delta Q} = \left\{ \left[\frac{3(1-\alpha)^{2/3}}{r_p^2} \right] k\, m^{-2/3} + \left[\frac{3(1-\alpha)}{r_p} \right] U \right\} \overline{\delta\theta} \qquad (8.13)$$

where:

r_p = radius of a pebble;

α = void fraction of the pebble bed;

k = thermal conductivity of the pebble bed;

U = overall heat transfer coefficient, relating average pebble temperature to coolant temperature; and

m = number of pebbles in the sub-volume.

The first term in brackets represents conduction through the solid bed, and the second represents convection to the coolant. During operation, the second term is much larger than the first. Pebbles behave as indpendent convective units with temperature severity directly proportional to power density severity. Eq. (8.13) transforms probability statements regarding a region's average power density into statements regarding temperature.

For the case of power density hot spots, the un-grouped selection probablities $p(m,\delta Q)$ are determined using the central limit theorem, applied to the sample mean power density. For the average power density $\overline{Q}$ of m randomly selected pebbles:

$$\bar{Q} \equiv \frac{1}{m}\sum_{i=1}^{m} Q_i \tag{8.14}$$

we can state:

$$\bar{Q} \sim N(\mu_Q, \sigma_Q^2/m) \tag{8.15}$$

for large m. μ_Q and σ_Q^2 are, respectively, the FUPAR-calculated power density mean and variance within the region of interest. The expression " $\sim N(\mu,\sigma^2)$" means "is distributed as a normal random variable with mean μ and variance σ^2." Eq. (8.15) may be rearranged in terms of the hot spot severity δQ:

$$\frac{\bar{Q} - \mu_Q}{\sigma_Q/\sqrt{m}} = \frac{\delta Q \sqrt{m}}{\sigma_Q} \sim N(0,1) \tag{8.16}$$

in which N(0,1) implies distribution as a standard normal random variable. It is possible to find tabulated numbers Z_α such that:

$$\mathbb{P}\left[\delta Q \geq \frac{Z_\alpha \sigma_Q}{\sqrt{m}} \right] = \alpha \tag{8.17}$$

where "$\mathbb{P}$[e]" represents the probability of event e. Z_α is the value of a standard normal random variable above which the probability of occurence is α. Eq. (8.17) states that as the number of pebbles in the subvolume increases, the power density severity at a fixed probability level decreases as $1/\sqrt{m}$. Using Eq. (8.13), similar expressions may be written for the temperature severity $\delta\theta$:

$$\frac{\sqrt{m}}{\sigma_Q}\left\{ \left[\frac{3(1-\alpha)^{2/3}}{r_p^2} \right] k\, m^{-2/3} + \left[\frac{3(1-\alpha)}{r_p} \right] U \right\} \delta\theta \sim N(0,1)$$

and:

$$\mathbb{P}\left[\delta\theta \geq Z_\alpha \sigma_Q \left\{ \left[\frac{3(1-\alpha)^{2/3}}{r_p^2} \right] k\, m^{-2/3} + \left[\frac{3(1-\alpha)}{r_p} \right] U \right\}^{-1} \right] = \alpha \qquad (8.18)$$

The terms on the right-hand side of the inequalities in Eqs. (8.17) and (8.18) are "hot spot severities at probability level α." At a fixed probability level, the temperature or power density may be plotted as a function of sub-volume size m. This is done for power density in Fig. (8.6). The upper bound on severity at very small numbers of pebbles is simply the maximum power density generated by pebbles within the region (i.e., the power density of pass-1 pebbles).

The α probability levels in Eqs. (8.17) and (8.18) are the ungrouped selection probabilties $p(m,\delta Q)$ and $p(m,\delta\theta)$ defined in Eq. (8.4). To calculate the probability of zero hot spots at these severity levels within the zone of interest, they must by modified for pebble grouping effects:

$$\mathbb{P}\left[\begin{matrix}\text{no hot spots of} \\ \text{severity } \delta Q\end{matrix}\right] \equiv \mathbb{P}_o = \exp\left[- \frac{N\, p(m,\delta Q)}{m} \right] = \exp[-N\alpha/m] \qquad (8.19)$$

This "zero-hot spot probability" may be calculated for various values of sub-volume size m and severity levels δQ or $\delta\theta$. Values of $\mathbb{P}_o$ close to 1.0 are desirable, as they give assurance that no such hot spots are likely to be found. $\mathbb{P}_o$ is controlled most strongly by the un-grouped selection probability $p(m,\delta Q)$ (which varies much more quickly with m than the factor 1/m). For large values of m or δQ, $p(m,\delta Q)$ approaches 0, and $\mathbb{P}_o$ gets correspondingly close to 1.0. An plot of $\mathbb{P}_o$ appears in Figure 8.7. Each curve corresponds to a particular severity level δQ. At fixed severity, $\mathbb{P}_o$ appraches 1.0 very rapidly once

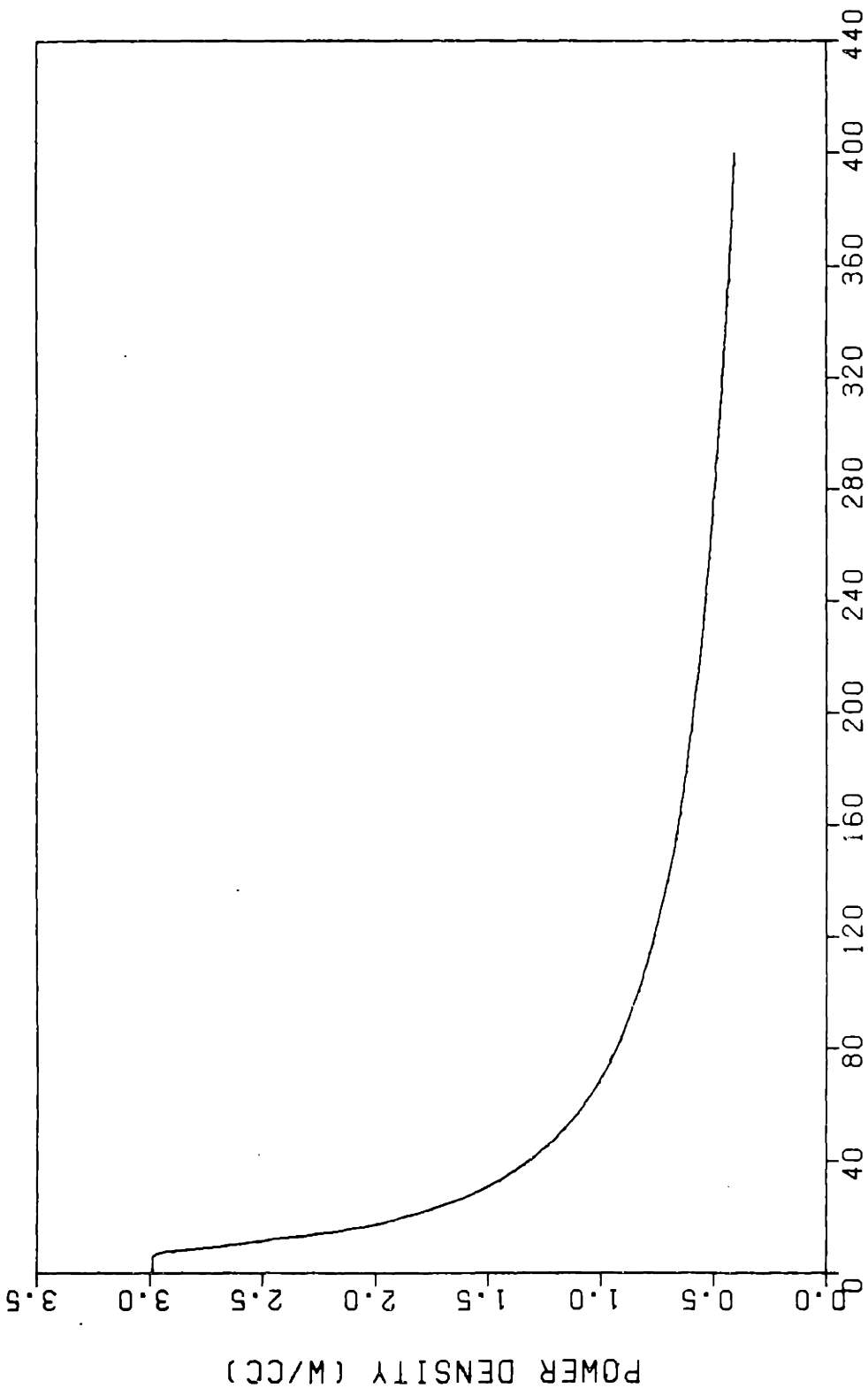

FIG. 8.6: Hot spot severity for power density during operation in the high power density zone of the 200 MWth HTR-MODUL.

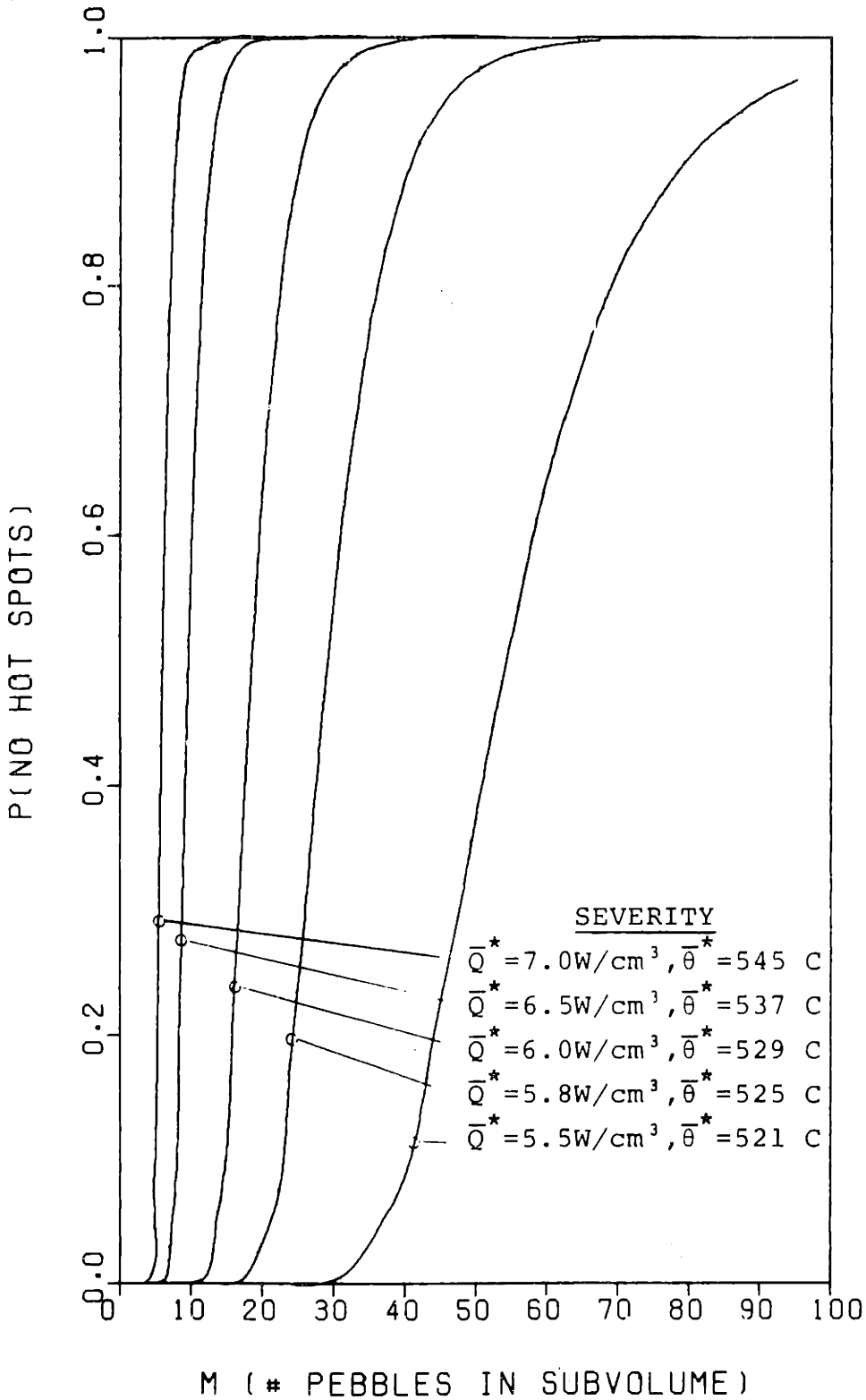

FIG. 8.7: **Zero hot spot probabilities in the base core's high power density zone.**

sub-volume size m passes a critical limit. For high severities, the $\mathbb{P}_o$ plot approximates a step function. In the example shown, it is quite likely that hot spots of severity $\delta Q = 6.0$ W/cm^3 and size 20 pebbles will be present. However, hot spots of the same severity and size 50 pebbles are extremely unlikely. Several more hot spot analyses will be presented in the following section.

8.1.4 Evaluations of several MHTGR cores

Three MHTGR design variants of current interest were analyzed using FUPAR/VSOP to determine steady state operating parameters. The cores analyzed were:

(1) A 200 MWth reactor as similar as possible to the KWU/Interaton HTR-Modul;

(2) A 200 MWth reactor which utilizes a small quantity of gadolinia burnable poison in fresh fuel. All other design parameters are identical to the first reactor; and

(3) A 200 MWth reactor operating at high coolant temperatures for direct cycle applications. Only the temperatures and fresh fuel enrichment differ from the base case.

Random hot spot analyses were performed, and the THERMIX code [V3] was used to analyze temperatures during postulated depressurization accidents. The steady state power distributions generated by FUPAR/VSOP formed the initial conditions for these calculations.

The base core was analyzed to verify that methods developed in this work are consistent with existing methods, as well as to apply new analyses to an existing design. The core generates 200 MWth, fuel is recycled an average of 15 times prior to discharge, and the cutoff burnup for discharge is 80,000 MWD/MTHM. Fuel elements are initially loaded with 7 g of uranium. FUPAR/VSOP analysis yielded the following information:

(1) reactor power density distribution;
(2) power density variance distribution;
(3) reactor temperature distribution;
(4) the total number of pebbles in the core;
(5) reactor effective multiplication factor;
(6) critical feed fuel enrichment; and
(7) the fresh fuel injection rate.

Results of the FUPAR/VSOP analysis agree well with published results for the KWU/Interatom design. FUPAR/VSOP predicts a core containing 360,000 pebbles with a fresh fuel injection rate of 3000 pebbles per day. The converged core has an un-rodded k_{eff} of 1.0090, and a feed fuel enrichment of 7.3 $^{w}/_{o}$. This is somewhat less than published values for feed enrichment (7.4 - 7.8 $^{w}/_{o}$), and is probably due to differences in control margin and slightly lower temperatures in the core analyzed here.

Figure 8.8 presents an axial power density profile for the reactor (z=0 represents the *top* of the core). Also shown in the figure is a three-standard deviation range for pebble power densities within each zone. Note that this variation does *not* apply to the zone as a whole, whose probability of differing significantly from expectation is extremely small. The power density peak near the top of the core arises for two reasons:

(1) Average fuel burnup is less near the top of the core, thus the reactivity is greater there; and

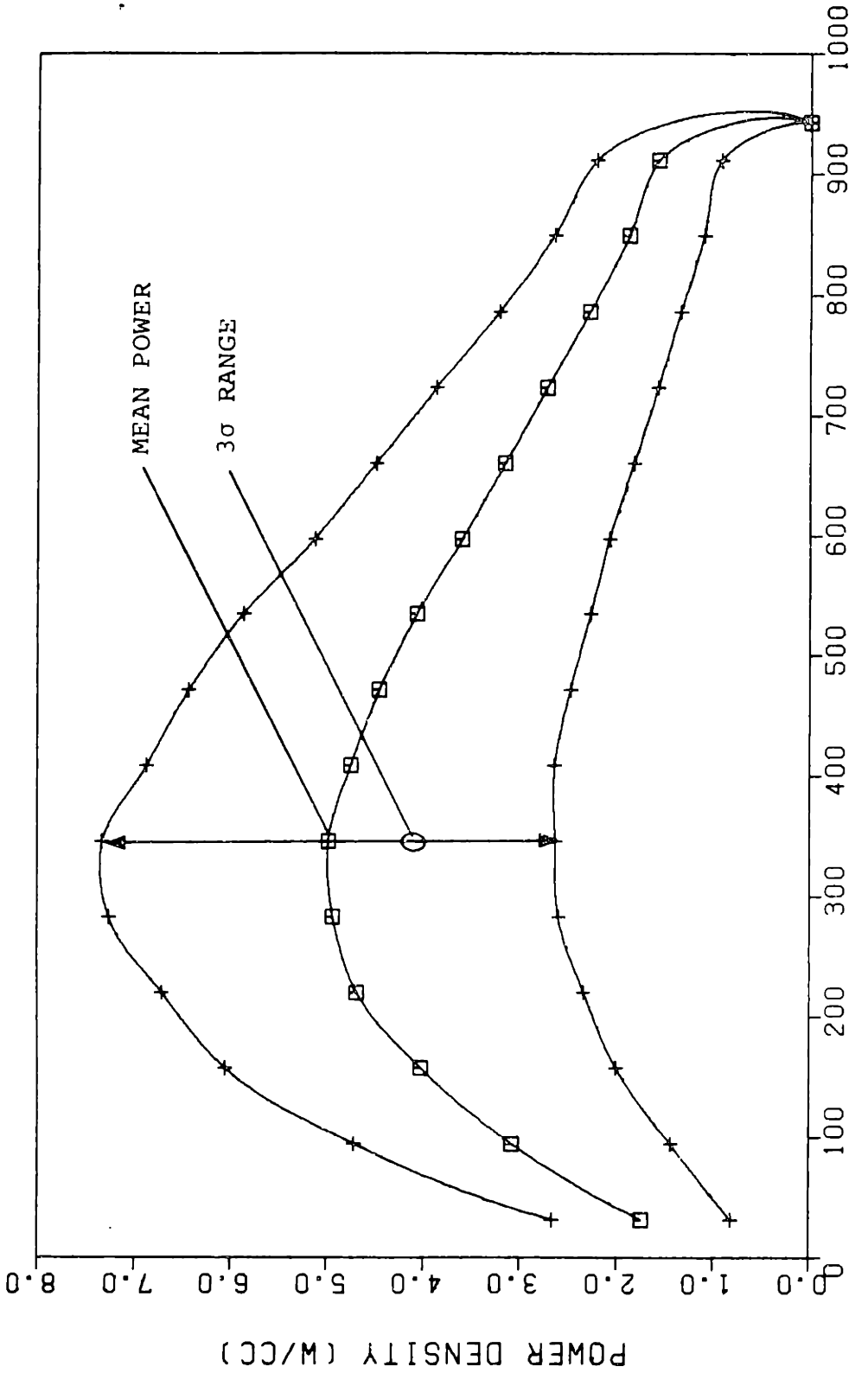

FIG. 8.8: Axial power density and power density standard deviation distribution in the base core.

(2) The burnup effect is enhanced by the direction of coolant flow. The core is cooler and therefore more reactive near the top.

The power density standard deviation is directly proportional to the local mean power density. This has important implications regarding temperature hot spots, since the highest temperature regions of the core are those which also have low power density. As Eq. (8.18) implies, the temperature severity also varies directly with the power density standard deviation. Therefore, hot spot severities which occur in the high temperature zones are small.

The ratio of between-pass to within-pass variances for this core is 435.0. Thus, the quasi-2D approximation is well justified in this case, as pass-mean parameters are clearly representative of the whole distribution. The physical reason lies in the self-compensating property of burnup and power density. Any fuel element which is under exposed on a particular pass will be all the more reactive for the next pass. Its power density, and accumulated burnup, will therefore compensate on the following pass.

A random hot-spot analysis was performed for the base core, and results are summarized in Figure 8.9. The figure presents maximum temperature severity as a function of sub-volume size for three levels of frequency. The three frequencies (10^{-2}, 10^{-4}, and 10^{-6} per reactor year) represent the probability per year of finding one or more hot spots in that zone. The figure includes the effects of the changing populations within the zone. Two features are noteworthy:

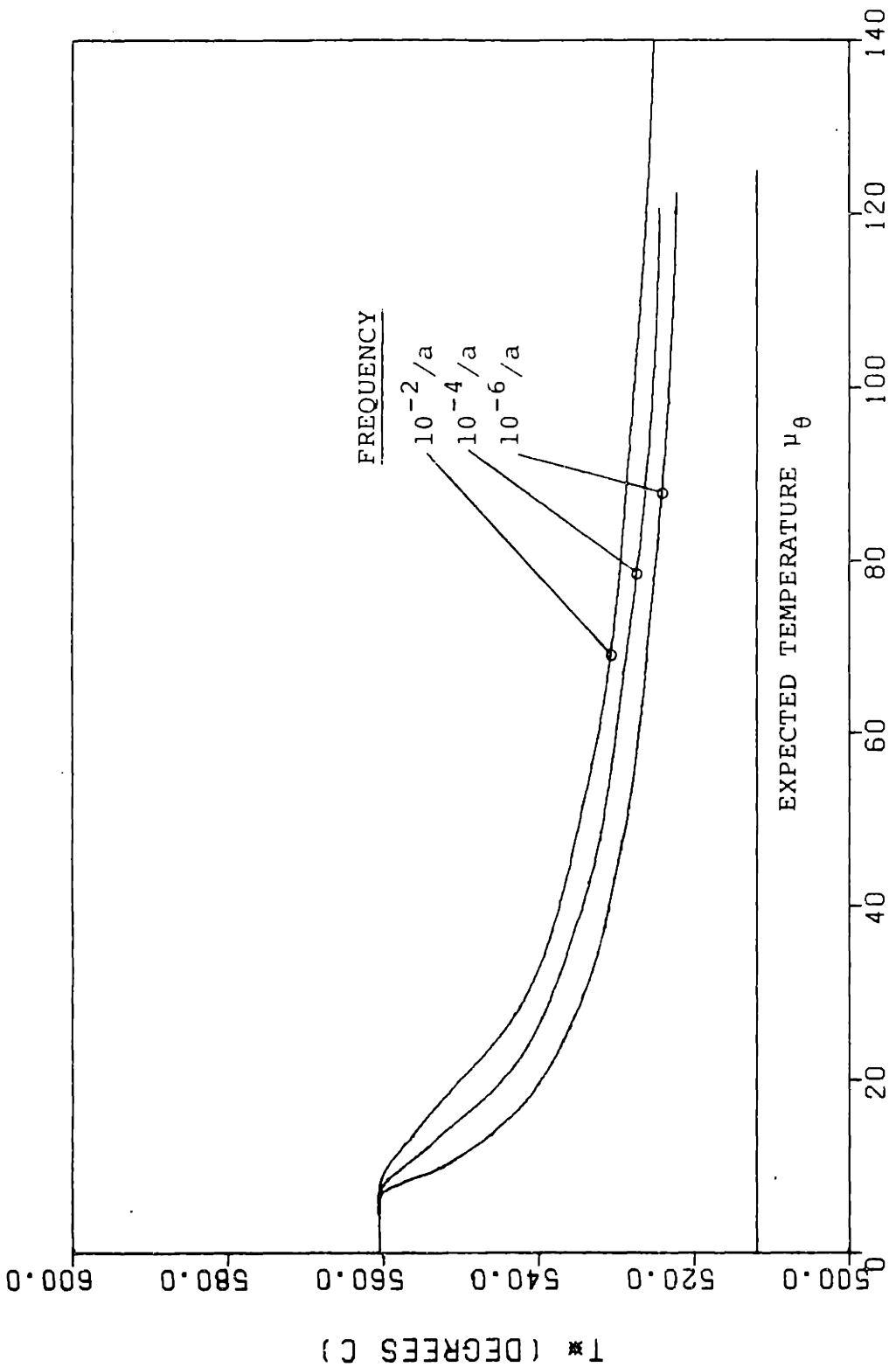

FIG. 8.9: Maximum hot spot severities in the base core's highest power density region

(1) the temperature differences found even at very low frequencies are relatively small. Furthermore, they are always limited by the maximum pebble power within the zone.

(2) Even for a change in frequency of four orders of magnitude, the severity curves remain relatively constant. Extremely low frequencies (much less than 10^{-6} per reactor year) must be assumed before large sub-volumes will approach maximum severity.

Thus, though there are no objective guidelines for judging whether the hot spots indicated in the figure are of safety significance or not, it appears safe to conclude that their impact will be small.

THERMIX analyzed the temperature transient resulting from a postulated depressurization of the base case core. Results are shown in Figure 8.10. The top curve is the fuel temperature in the hottest discrete core zone, and the three lower curves represent temperatures at other points in the reactor. Note that the maximum zone temperature remains below 1600 C at all times.

Use of gadolinia burnable poison was investigated as a means of reducing the reactivity effects of water ingress. However, the specific core analyzed was found to be undesirable in several areas. The concentration of gadolinia used was 0.2 $^{w}/_{o}$, assumed to be evenly dispersed in the fuel kernels. The axial power density profile is presented in Figure 8.11. The peak power region is lower in the core, due to high gadolinium concentrations at the top. Because of this, the core's temperature distribution is shifted significantly from that of

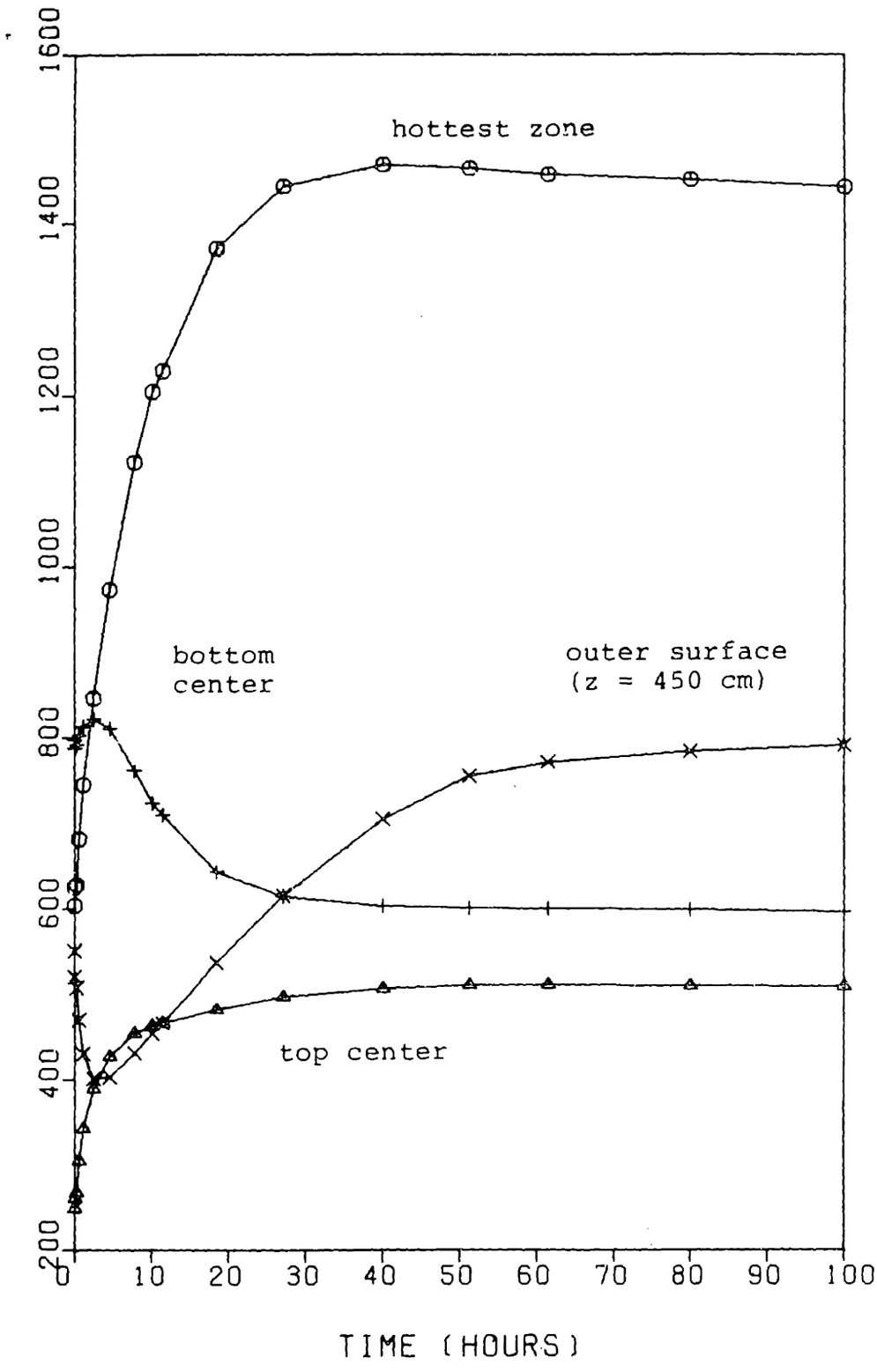

FIG. 8.10: Temperature behavior of the base core following a postulated depressurization accident.

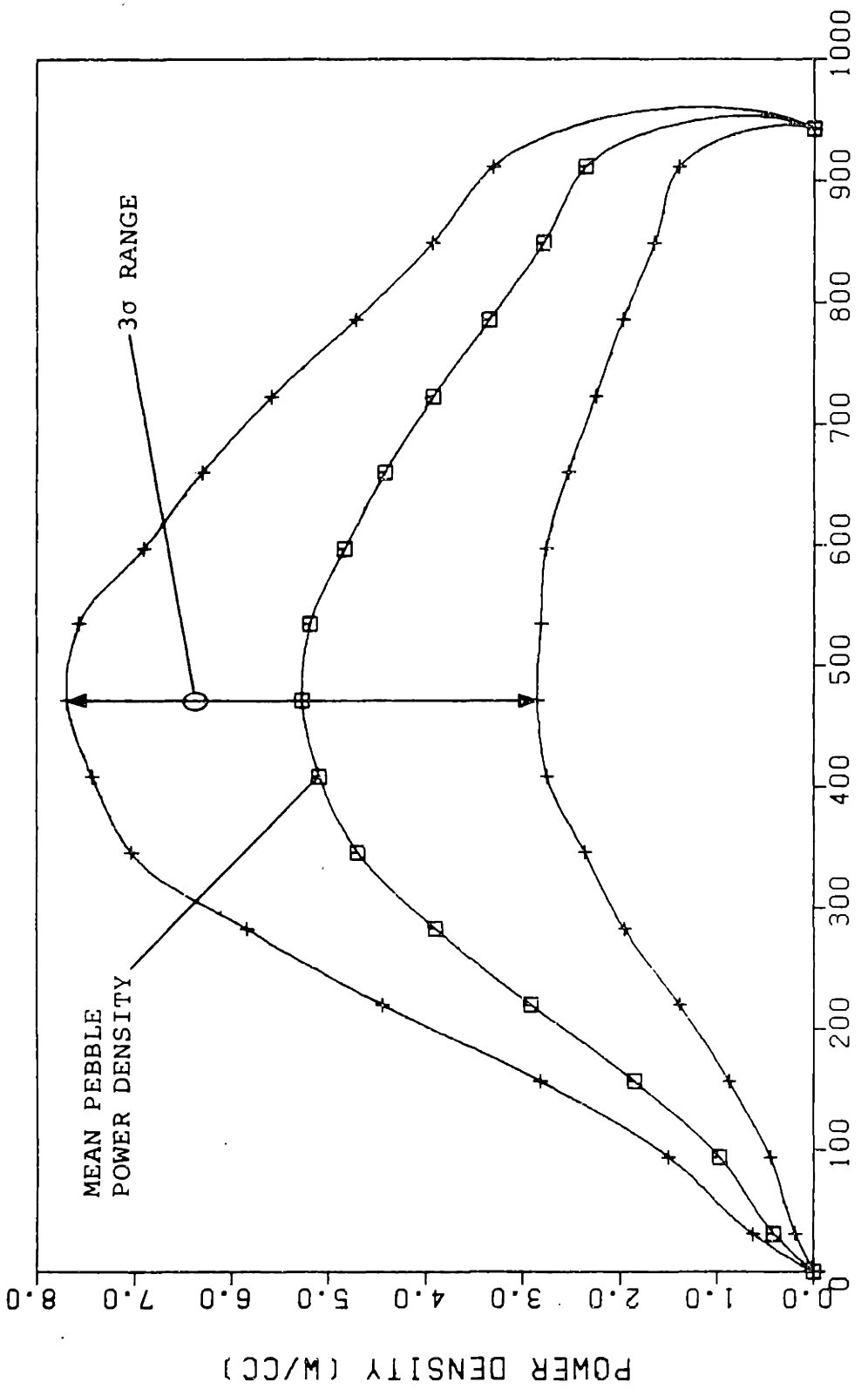

FIG. 8.11: Axial power density and power density standard deviation distribution in the poisoned core.

the base core. Even though poison was added, the feed fuel enrichment was not altered, due to the positive reactivity effects of lower average core temperature.

The effects of water ingress were compared in the poisoned core and the base core. Figure 8.12 presents the reactivity effects (Δk_{eff}) as a function of the amount of water assumed to enter the reactors. As shown, the amount of gadolinium in the poisoned core is not enough to significantly reduce the reactivity increase. Further work is needed to investigate means of increasing the gadolinium concentrations, in particular to accurately model the lumuped poison effects.

The most noticeable effects of the burnable poison are due to the increase in peak power density. Higher peak powers cause random hot spot severity to increase. Even more significant is the effect on post-depressurization temperatures, shown in Figure 8.12. Maximum temperature is well over 1600C for almost 40 hours. Further analysis (see section 8.5) reveals significant effects on accident-induced fission product release.

The direct cycle (DCGT) core has gas inlet/exit temperatures of 600/850 C. Due to increased average core temperature, feed fuel enrichment had to be increased to 7.5 $^{w}/o$. Since the overall core temperature change is relatively low, the reactivity difference between the top and bottom of the core is minimized. The power density profile is more uniform than the other cases. This results in a significant reduction in hot spot severity.

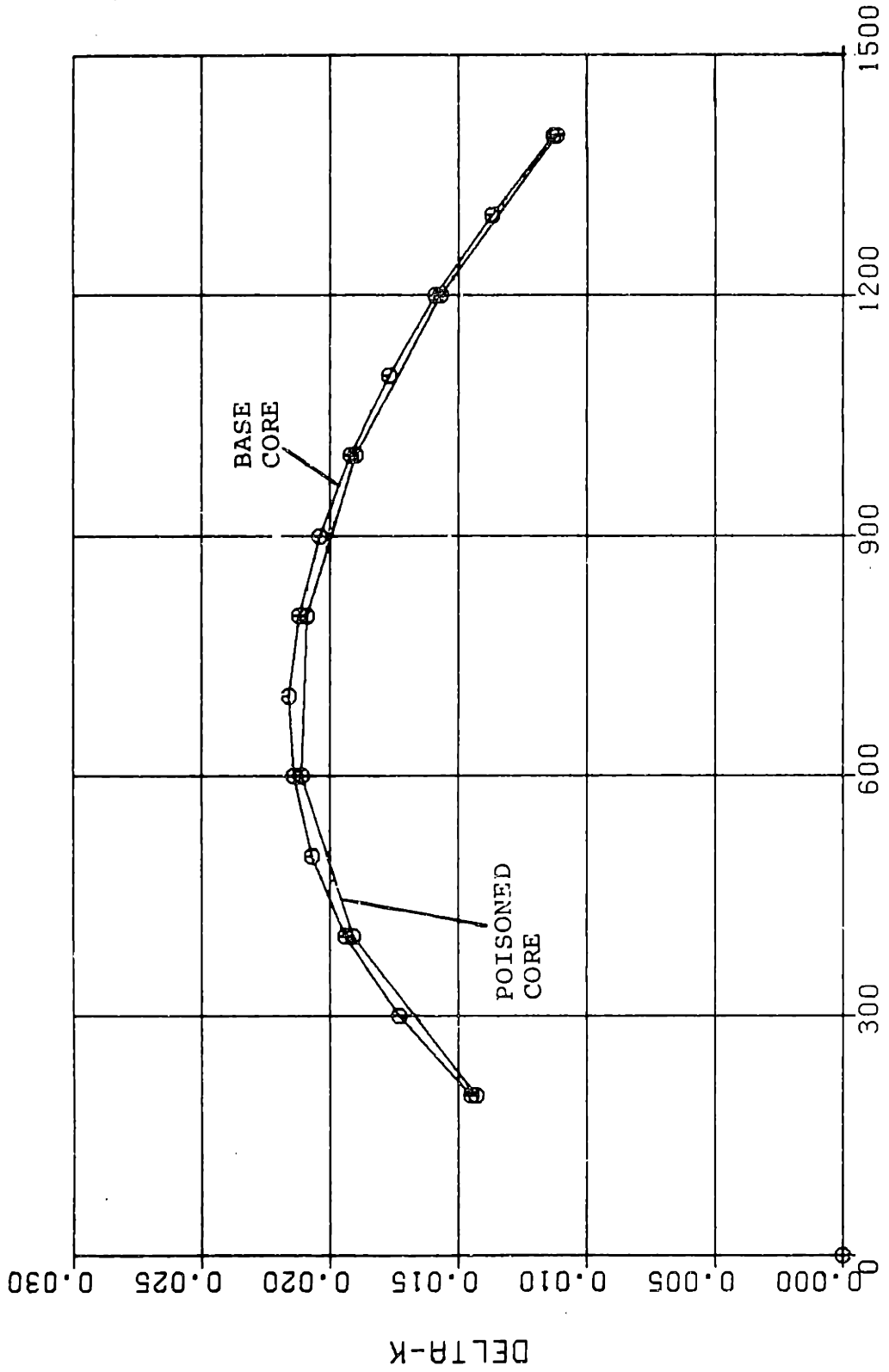

FIG. 8.12: Reactivity effects of water ingress on the base and poisoned cores.

Also of interest are depressurization temperatures compared to the other cores analyzed. THERMIX analysis indicates that peak zone temperatures reach only 1560 C, a decrease from the poisoned core whose initial temperatures were lower. We conclude that the influence of the peak/average power density ratio is more significant than initial temperature distributions.

8.1.5: Fission product transport and release in coated particle fuel

In certain instances, the source term from a modular HTGR can have significant contributions due to diffusive release. A calculational tool has been developed to estimate the fission product release from intact and ruptured fuel particles during steady operation and thermal transients.

The model is based upon *effective diffusivities* for the diffusion of metallic fission products through the fuel particle. These are statistics which enable reproduction of in-pile and post-irradiation release and concentration measurements with a one-phase diffusion model. The model in this work is based on a vector **c**, representing the fission product concentration profile within a single fuel particle. The i'th element of **c** is the volume averaged fission product concentration within the i'th concentric spherical shell of the particle model. The one phase diffusion equation is:

$$\frac{\partial C}{\partial t} = D \nabla^2 C - \lambda C + Q \qquad (8.20)$$

where

$C = C(r,t)$ = concentration of the fission product;

D = effective one-phase diffusivity for the fission product;

λ = the fission product's decay constant; and

Q = the volumetric source rate of new fission products.

The diffusion equation is integrated over one of these shells, yielding an equation for the rate of change of the volume-averaged concentration within that shell. Concentration gradients are approximated by differences in average concentrations divided by the shell spacing. The set of equations for all shells in the particle model may be written as:

$$\dot{\mathbf{c}} = -\mathbf{F}\,\mathbf{c} + \mathbf{q} \qquad (8.21)$$

where:

F = a coefficient matrix, containing geometrical factors, diffusiviities, and the decay constant. Since each shell is coupled only to its inner and outer neighbors, **F** has only three non-zero diagonal stripes; and

q = a vector of volumetric fission product source rates; each element corresponds to a single particle shell.

If the reactor core is subdivided into radial and axial zones as in the FUPAR analysis, Eq. (8.19) may be solved analytically within each zone. Alternately, if a short enough time interval during a transient is examined so that the temperature can be assumed constant, the same form of the solution applies. The situation simplifies during a transient, since the source vector is zero. Let subscript i represent the zone of interest (or the interval of interest), and $\mathbf{c}_i$ represent the fission product concentration profile at the *exit* of zone i. The solution of Eq. (8.19) is:

$$\mathbf{c}_i = \mathbf{R}_i\,\mathbf{c}_{i-1} + \mathbf{S}_i\,\mathbf{q}_i \qquad (8.22)$$

where:

$$\mathbf{R}_i \equiv \exp[\, -\mathbf{F}_i \Delta t_i \,] \tag{8.23a}$$

and

$$\mathbf{S}_i \equiv \mathbf{F}_i^{-1}[\, \mathbf{I} - \mathbf{R}_i \,] \tag{8.23b}$$

The diffusive release rate from the particle, $\dot{\rho}$, is determined using Fick's Law:

$$\dot{\rho} = -4\pi\, r_o^2\, D_o\, \nabla C(r_o) \tag{8.24}$$

in which r_o represents the particle outer radius, and D_o is the diffusivity of the particle's outer shell. The gradient at the particle surface may be approximated in terms of the average concentration in the model's outer shell, divided by a characteristic distance. Thus, the release rate is a linear function of the concentration profile. If $\mathbf{u}_N$ represents a vector whose N'th and last element is equal to 1.0, and all other elements are zero, then it can be shown that the average rate of fission product release due to diffusion in zone i, denoted $\langle \dot{\rho} \rangle_i$, is:

$$\langle \dot{\rho} \rangle_i = \frac{8\pi\, r_o^2\, D_o}{\delta r_o}\, \mathbf{u}_N^{+} \left[\frac{1}{\Delta t_i}\, \mathbf{S}_i\, \mathbf{c}_i + \tfrac{1}{2}\, \mathbf{S}_i\, \mathbf{q}_i \right] \tag{8.25}$$

where δr_o is the thickness of the outer shell in the particle model. Another important release mechanism during operation is direct recoil, especially from kernels with damaged coatings. Recoil is accounted for by altering the source vector and adding the recoil fraction to the diffusive release.

The PDIF computer code performs these diffusion and release calculations. Operating release is calculated based on FUPAR/VSOP core operating data, and accident release uses temperature transients calculated by THERMIX.

PDIF employs a linear model for fission product transport, which causes difficulty at short diffusion times. Since the particle coating layers are quite effective, the fission product profile within them can be quite non-linear during irradiation and the start of a high temperature transient. Estimation of release based on the average outer shell concentration leads to consistent underprediction in this case. stances. In principle, PDIF can model a shell structure with thin enough outer layers to minimize this effect; however, numerical difficulties are encountered for shell structures which are too fine. A simple model, based upon the analytic solution for a uniform sphere under constant conditions, is formulated to provide an upper bound on the actual release from kernels with damaged coatings. The relation for fractional release is:

$$FR = 1 - (6/\pi^2) \sum_{n=1}^{\infty} (-1)^n \exp\left[- \frac{D\, n^2 \pi^2 t^2}{r_o^2} \right] \qquad (8.26)$$

where:

FR = fractional release of the fission product at time t;
D = diffusivity within the sphere; and
r_o = outer radius of the particle

Since diffusive release from kernels with damaged coating layers is generally the major contribution to accident activity (under the assumptions used in this work), this model should provide a conservative upper bound against which to check PDIF releases.

PDIF has analyzed steady state and transient cesium-137 release in the three MHTGR design variants. For "nominal fuel," a contamination

fraction of 6×10^{-5} and a failure fraction of 3×10^{-4} is assumed. These nominal design parameters are historically quite high in quality. Nevertheless, "higher quality" fuel was studied as well, using design parameters corresponding to levels achieved only in the laboratory to date. Table 8.2 presents release estimates for the nominal fuel quality design, and Table 8.3 the results for the higher quality fuel design. All three cores have very low releases and may be considered passively safe. Activity release during operation is nearly identical in all cores, amounting to about 400 curies. The similarity is due to the assumption of immediate release from heavy metal contamination. Differences are apparent only in the accident release estimates, which are much lower than the steady state release for all cores. The poisoned core pays a relatively large penalty for its high peak power density, and is predicted to release three times the activity of the base core under accident conditions. The DOGT core also has increased accident release due to higher temperatures. The performance of PDIF compared to the analytic bounding calculation is adequate, considering the conservatism in the uniform sphere model. In the base case, PDIF's kernel release prediction is 64% of the US release, and in the poisoned core PDIF release is 74% of the US upper bound. As expected, PDIF's predictive ability increases with core temperature. For the DOGT core, however, PDIF predicts only 57% of the kernel release, due to the relatively low core-average temperature.

Releases calculated using the higher quality fuel parameters are much lower than the nominal quality case. Steady state activity release

TABLE 8.2: CESIUM RELEASE ESTIMATES FOR NOMINAL QUALITY FUEL

(Φ_{HMC}= 6×10^{-5}, Φ_B = 3×10^{-4})

STEADY STATE PRIMARY SYSTEM ACTIVITY (CURIES)

RELEASE MECHANISM	BASE CORE	POISONED CORE	DOGT CORE
HEAVY METAL CONTAMINATION	363	363	363
RECOIL FROM BARE KERNELS	39.5	39.5	39.5
DIFFUSION FROM BARE KERNELS	0.42	0.47	6.35

ACCIDENT RELEASE (CURIES)

RELEASE MECHANISM	BASE CORE	POISONED CORE	DOGT CORE
DIFFUSION FROM INTACT PARTICLES	0.03	7.15	1.23
DIFFUSION FROM DAMAGED PARTICLES	6.08	14.0	11.2

ACCIDENT RELEASE, UPPER BOUND (CURIES)

RELEASE MECHANISM	BASE CORE	POISONED CORE	DOGT CORE
DIFFUSION FROM DAMAGED PARTICLES	9.39	18.9	19.8

TABLE 8.3: CESIUM RELEASE ESTIMATES FROM HIGHER QUALITY FUEL

($\Phi_{HMC}= 10^{-6}$, $\Phi_B = 4.5\times10^{-5}$)

STEADY STATE PRIMARY SYSTEM ACTIVITY (CURIES)

RELEASE MECHANISM	BASE CORE	POISONED CORE	DOGT CORE
HEAVY METAL CONTAMINATION	6.06	6.06	6.06
RECOIL FROM BARE KERNELS	8.77	8.77	8.77
DIFFUSION FROM BARE KERNELS	0.09	0.10	1.41

ACCIDENT RELEASE (CURIES)

RELEASE MECHANISM	BASE CORE	POISONED CORE	DOGT CORE
DIFFUSION FROM INTACT PARTICLES	0.01	3.77	0.51
DIFFUSION FROM DAMAGED PARTICLES	0.89	2.07	1.66

ACCIDENT RELEASE, UPPER BOUND (CURIES)

RELEASE MECHANISM	BASE CORE	POISONED CORE	DOGT CORE
DIFFUSION FROM DAMAGED PARTICLES	1.39	2.80	2.92

is proportional to the contamination fraction, and accident release from kernels is proportional to the particle damage fraction. The high quality contamination fraction is a more pronounced improvement over the nominal fuel than the decrease in particle damage fractions. Therefore, the high qualtiy release estimates have much higher fractions due to accident-induced release.

8.2: CONCLUSIONS

Based on the work performed during this study, the following conclusions are made regarding fuel quality, reactor design, and fission product release:

(1) Branch notation provides a means for treating a continuously refueled pebble bed reactor in a probabilistic manner. Any fuel parameter which can be expressed as a function of the branch variable may be analyzed for the moments of its position-dependent probability density function. When the functional relation is linear or independent of the fuel state, then particularly simple relations are possible for the parameter distributions.

(2) The FUPAR/VSOP iterative method for core analysis agrees well with published results for the 200 MWth MHTGR design. Furthermore, an experienced user can converge upon a stationary core solution in significantly less time than possible with previous methods. FUPAR calculates the variances as well as the means for power densities, enabling random hot spot analysis. The quasi-two dimensional approximation has been found to apply particularly well to modular HTGR cores.

(3) Analysis of the reactor designs considered in this study indicates that random hot spots are not likely to present safety problems.

Maximum hot spot severity varies directly with peak power density, thus cores with uniform flux shapes are even less likely to form severe hot spots. The maxiumum severity of a hot spot is a weak function of the frequency level at which it is expected to occur.

(4) Analysis of post-depressurization transients indicates that the ratio of peak/average power density is important in determining maximum temperatures. The poisoned core, though operating with identical inlet/exit coolant temperatures to the base core, reaches higher peak temperatures than the direct-cycle core, even though the latter core's inital temperatures were much higher. The reason is the gadolinia-induced increase in peak power.

(5) Use of gadolinia burnable poisons has drawbacks as well as advantages. In the case studied, the increase in peak power due to the poison led to undesirable effects both for hot spot severity and peak post-depressurization temperatures.

(6) The high quality fuel model indicates that all cores analyzed have very low accident releases (on the order of 20 Curies, maximum). The steady state primary system activity can completely outweigh the accident contribution, depending on the assumption used to model release of this activity from the reactor.

(7) The linear diffusion model in PDIF underpredicts release at short

diffusion times. However, conservative bounding calculations indicate that the discrepancy in release from kernels with damaged coating layers is less than a factor of two, and general conclusions may be drawn from PDIF results.

(8) Source terms arising due to postulated accidents in modular HTGRs are a strong function of fuel quality. Limitation of accident temperatures to less than approximately 1600 C leaves heavy metal contamination and manufacturing defects the primary controlling variables. Source terms will scale directly with either of these parameters. Though current fuel design parameters are quite high, recent experimental results suggest that even higher quality fuel is possible.

8.3: AREAS FOR FUTURE STUDY

Three new analytic techniques have been introduced: branch mathematics and probabilistic core analysis, random hot spot analysis, and linear diffusion analysis. Many avenues for further research are suggested. Regarding branch mathematics and core analysis, some are:

(1) Automatic FUPAR/VSOP iteration: Currently, using FUPAR/VSOP to analyze pebble bed reactors is more art than science. The utility of the code can be much improved if the criticality and equilibrium power density iteration were automated and optimized.

(2) Improved neutron diffusion calculation: Power density distributions calculated by VSOP suffer from the crudity of its flux synthesis technique. Coupling the current FUPAR/VSOP code with a true two-dimensional neutron diffusion code would greatly improve the accuracy of its results.

(3) Monte Carlo studies of fuel trajectories: The quasi-2 dimensional approximation appears well justified for the reactors studied here. Nevertheless, it would be useful to know what the real late-pass distributions of fuel elements are, and now likely it is for pebbles to remain in the core for much longer times than expected. A Monte-Carlo approach is recommended, in which values of the branch variable β are randomly selected. If an approximate stationary flux distribution is known, the burnup analysis for each trajectory only requires heavy metal calculations, which are quite fast. In this manner, empirical estimates of the true late-pass pebble flows may be

obtained.

(4) Further burnable poison studies: Research on the usefulness of gadolinia burnable poison has been inconclusive. Further work is necessary modelling lumped poison effects, which may result in more uniform poison distribution. Techniques for minimizing undesirable side effects of the poison, such as increased power peaking, should also be investigated.

Regarding random hot spot analysis, further research into the following topics is suggested:

(1) Monte-Carlo study of grouping effects: Current methods of random hot spot analysis rely on simple assumptions about the probabilty of pebbles coalescing to the same position in the reactor. Monte-Carlo simulation of the pebble grouping process can estimate these probabilities more accurately.

(2) Reactivity hot spots: Information is available within the FUPAR program to calculate a fuel element's infinite-lattice reactivity as a function of the branch variable. An interesting application of random hot spot analysis would be to estimate the severities and frequencies of high reactivity zones in the core.

(3) Safety implications of random hot spots: Analyses indicate that random hot spots of high severity are a very low frequency event. However, there is no objective way to judge that they are of *negligible* consequence. It would be useful to know a frequency/severity envelope below which random hot spots can be neglected.

Finally, on the topic of fission product diffusion and release,

further work is suggested in these areas:

(1) Improved short-diffusion time model: Approximate ways of treating short-time diffusion should be investigated for inclusion in the PDIF model. Such approximations will complicate analysis by eliminating the time-independence of the transition matrices. Nevertheless, elimination of the release underestimation problem will be well worth the extra effort.

(2) Improved numerical techniques: Another approach to improve the performance of PDIF is improved numerical techniques. If transition matrices for stiffer systems (corresponding to finer mesh spacing) can be successfully calculated, then short time fuel performance is simple to model with the linear model.

(3) Realistic modelling of fission products generated by contaminants: Accident releases would be more realistic if the true distribution of heavy metal contamination particles were accounted for. Immediate release should be assumed only for the fraction of contamination-bred fission products generated outside the coating layers. Fission product concentrations in the coatings would be higher, shifting source term activity from the steady state release to the accident induced category.

(4) Accounting for fission product retention in matrix graphite: For shorter-lived fission products, holdup in the pebble matrix can significantly reduce the activity release during operation. Adsoprtion effects are important during thermal transients. More realistic design comparisons will result if these phenomena are accounted for.

(5) Release of other fission products: Effective diffusivities are available for several metallic fission products besides cesium, and reduced diffusivities for noble-gas fission products are well known. Use of these parameters in PDIF to estimate potential source terms for a range of isotopes will complete the comparison of reactor designs.

REFERENCES

A.1 Altes, J., et.al., compiled by Nabbi, R., "Sicherheitstechnische Untersuchungen zum Störfallverhalten des HTR-500," KFA Jülich, Jül-Spez-240, January 1984.

A.2 Amian, W., "Experimentelle Untersuchungen zum Transportverhalten von Silber in Brennstoffteilchen für Hochtemperaturreaktoren," Institut für Reaktorentwicklung, KFA Jülich, Jül-1731, August 1981.

A.3 Amian, W., "Results of Fission Product and Actinide Studies in Coated Fuel Particles and Matrix Graphite," Gas-Cooled Reactors Today, Vol. 2: Advances in Fuel, Core, and Structural Materials, British Nuclear Energy Society, 1982, p. 145.

B.1 Bedenig, D., Rausch, W., and Schmidt, G., "Parameter Studies Concerning the Flow Behavior of a Pebble with Reference to the Fuel Element Movement in the Core of the THTR 300 MWe Prototype Reactor," Nuclear Engineering and Design 7, (1968), pp. 367-378.

B.2 Bellman, R.E., "An Introduction to Matrix Analysis," New York, McGraw Hill, 1960.

B.3 Breitbach, G., et. al., compiled by Mertens, J., "Sicherheits-technische Untersuchungen zum Störfall verhalten des HTR Modul," Jül-Spez-335, November 1985.

B.4 Bongartz, K., "Status of the Fuel Stress and Failure Rate Calculations at KFA," Jül-1686, November 1980.

B.5 Bastek, H., "Zur Spaltproduktrückhaltung im Hochtemperaturreaktor kleiner Leistung unter Störfallbedingungen," KFA Jülich, Jül-1886, January 1984.

B.6 Brown Boveri Companie, "HKG 300 MWe Nuclear Power Plant Hamm-Uentrop with Thorium High Temperature Reactor," Druckschrift Nr. D HRB 1429 84 E, June 1985.

B.7 Banaschek, J., "Berechnungsmethoden und Analysen zum dynamischen Verhalten von Kraftwerksanlagen mit Hochtemperaturreaktor," Institut für Reaktorentwicklung, KFA Jülich, Jül-1841, April 1983.

B.8 Biedermann, P., "Rechnerische Analyse der Cäsium-Diffusion in Bestrahlungsexperimenten unter Berücksichtigung von Konzentrations- und Freisetzungsmeßergebnissen," Institut für Reaktorentwicklung, KFA Jülich, Jül-1768, February 1982.

B.9 Brookhaven National Laboratory, "Neutron Cross Sections," BNL-325, August 1966.

C.1 Crank, J., "The Mathematics of Diffusion," Oxford University Press, London, 1956.

C.2 Cramer, H., "Mathematical Methods of Statistics," Princeton University Press, 1946.

D.1 Davenport, W.B., "Probability and Random Processes: An Introduction for Applied Scientists and Engineers," New York, McGraw Hill, 1970.

D.2 Drake, A.W., "Fundamentals of Applied Probability Theory," McGraw Hill Book Company, 1967.

E.1 El-Wakil, M.M., "Nuclear Energy Conversion," International Textbook Company, American Nuclear Society, 1982.

G.1 Gulden, et.al., "The Mechanical Design of TRISO-Coated Particle Fuels for the Large HTGR," Nuclear Technology vol. 16, October 1972, pp. 100-109.

G.2 Goodin, D.T., "Accident Condition Performance of High Temperature Gas-Cooled Reactor Fuels," GA-A16508, October 1983.

G.3 Gesellschaft für Hochtemperaturreaktor-Technik, GmbH, "High Temperature Reactor Modular System for Generation of Process Heat," October 1981.

G.4 Greene, D.A., Grewal, S.S., and Wu, T., "Calculational Modules for Modular HTGR Water Ingress Analysis," Prepared for EPRI/CoMO under Project RP 2079-13, General Electric Co., Nuclear Systems Technology Operation, December 1985.

G.5 GA Technologies, "HTGR Fuel Technology Program: Contract Summary Report for Period Ending October 31, 1983," GA-A17369, UC-77, November 1983.

H.1 Heit, W., et.al., "Status of Qualification of High-Temperature Reactor Fuel Elements," Nuclear Technology, vol. 69, April 1985, pp. 44-54.

H.2 Hochtemperatur Reaktor Brennstoff Kreislauf, "Projektbericht 1984," KFA Jülich, KFA-HBK-IB-1/85.

H.3 Honeck, H.C., "THERMOS: A Thermalization Transport Theory Code for Reactor Lattice Calculations," Brookhaven National Laboratory, BNL-5826, 1961.

H.4 Hansen, U., and Teuchert, E., "Influence of Coated Particle Structure in the Thermal Neutron Spectrum Energy Range," Nuclear Science and Engineering 44, 1971.

H.5 Hackstein, K.G., "Entwicklung der Brennelemente," presented at the Seventh International Conference on the High Temperature Gas-Cooled Reactor, Dortmund, Federal Republic of Germany, September 1985.

I.1 Izenson, M.G., "Resolution of FUPAR Numerical Difficulties," Memo from December, 1985.

I.2 IBM Corporation, "VS Fortran Application Programming: Language Reference," Release 3.0, Fourth edition, March 1983.

J.1 Jahn, W., Rehm, W., and Verfondern, K., "Spezielle Analysen zum Temperatur- und Spaltproduktverhalten von HTR-MODUL Anlagen," Jül-Spez-235, December 1983.

J.2 Joanou, G.D., and Dudek, J.S., "GAM-I: A Consistent P_1 Multigroup Code for the Calculation of Fast Neutron Spectra and Multigroup Constants," GA-1850, June 1961.

K.1 Kania, M.J., and Nickel, H., "Performance Assessment of the $(Th,U)O_2$ HTI-BISO Coated Particle Under PNP/HHT Irradiation Conditions," KFA-IRW Report Jül-1685, November 1980.

K.2 Kania, Dr. M.J, personal conversation at Oak Ridge National Laboratory, July 19, 1985.

K.3 Kovacs, W.J., "Characterization of Defective SiC Coatings in TRISO HTGR Fuel Particles," GA-A16215, April 1981.

K.4 Krohn, H., "Freisetzung von Spaltprodukten aus dem Core eines Kugelhaufenreaktors bei Störfällen mit Core Aufheizung," KFA Jülich, Jül-1791, August 1982.

K.5 Kovacs, W.J., Bongartz, K., and Goodin, D., "TRISO-Coated HTGR Fuel Pressure Vessel Performance Models," GA-A16807, October 1983.

K.6 Kuncir, G.F., "A Program for the Calculation of Resonance Integrals," GA-2525, August 1961.

K.7 Conversation with Dr. M.J. Kania at Oak Ridge National Laboratory, July 19, 1985.

K.8 Nabbi, R., et.al., "Nukleare Sicherheitsforschung: Arbeiten des Instituts für Nukleare Sicherheitsforschung in den Jahren 1974-1984," Kernforschungsanlage Jülich, GmbH.

L.1 Lanning, D.D., Lester, R.K., Izenson, M.G., and Lidsky, L.M., "Passively Safe Nuclear Reactors: Issues and Impact on Fuel Management," presented at the ANS/CNS Topical Meeting on Advances in Fuel Management, Pinehurst, NC, March 1986.

L.2 Lefevre, R.L.R., and Price, M.S.T, "Coated Nuclear Fuel Particles: The Coating Process and its Model," Nuclear Technology, vol. 35, pp. 263-278, Sept. 1977.

L.3 Lohnert, G., "The Corrosional and Nuclear Effects of Water Ingress into the Primary Circuit of an HTGR-Module," presented at the IAEA Specialists Meeting on Gas-Cooled Reactor Safety and Accident Analysis, Oak Ridge, TN, May 1985.

L.4 Lane, R.K., Nordheim, L.W., and Sampson, J.B., "Resonance Absorption in Materials with Grain Structure," Nuclear Science and Engineering 14, pp. 390-396, 1962.

M.1 Personal conversation with Dr. R. Moorman at KFA Jülich, September 16, 1985.

M.2 Maneke, J.L., "Radiation Releases from MHTGR Confinement Buildings," Ph.D Thesis, Department of Nuclear Engineering, Massachusetts Institute of Technology, May 1986.

M.3 Myers, B.F., and Morrissey, R.E., "Licensing Topical Report: The Measurement and Modeling of Time-Dependent Fission Product Release from Failed HTGR Fuel Particles under Accident Conditions," GA-A15439, April 1980.

M.4 Mertens, J., et.al., "Sicherheitstechnische Untersuchungen zum Störfallverhalten des HTR-Modul," Institut für Nukleare Sicherheitsforschung, KFA Jülich, Jül-Spez-335, November 1985.

N.1 Nabielek, H., Verfondern, K., and Moorman, R., personal converation at KFA Jülich, Sept. 16, 1985.

N.2 Nabielek, H., and Myers, B.F., "Fission Product Retention in HTR Fuel," Gas-Cooled Reactors Today, Vol. 2: Advances in Fuel, Core, and Structural Materials, British Nuclear Energy Society, 1982, p. 145.

N.3 Nabielek, H., et.al., "Fuel for Pebble Bed HTRs," Nuclear Engineering and Design, vol. 78, 1984, pp. 155-166.

N.4 Nabielek, H., Schenk, W., and Verfondern, K., "Core Heatup Accident Simulation with HTR Fuel Elements," presented at the IAEA Specialists Meeting for Gas-Cooled Reactors, May 13-15, 1985, Oak Ridge National Laboratory.

N.5 Newman, L.W., et.al., "Development of an Advanced Extended-Burnup Fuel Assembly Design Incorporating Urania-Gadolinia," Babcock & Wilcox, DOE/ET/34212-45, October 1984.

O.1 Olander, D.R., "Fundamental Aspects of Nuclear Reactor Fuel Elements," Energy Research and Development Administration, TID-26711-P1, 1976.

R.1 Research and Education Association, "The Linear Algebra Problem Solver," 1980.

R.2 Reutler, H., and Lohnert, G., "Advantages of Going Modular in HTRs," Nuclear Engineering and Design, vol. 78, April 1984, pp. 129-136.

S.1 Silady, F., personal conversation at MIT, October 16, 1985.

S.2 Stansfield, O.M., Simon, W.A., and Baxter, A.M., "Fuel Performance Models for High-Temperature Gas-Cooled Reactor Core Design," GA-A16982, Sept. 1983.

S.3 Shamasunder, B.I., Stansfield, O.M., and Jensen, D.D., "HTGR Fuel Performance Basis," GA-A16982, September 1983.

S.4 Stansfield, O.M., Homan, F.J., and Simon, W.A., "Interaction of Fission Products and SiC in TRISO Fuel Particles: A Limiting HTGR Design Parameter," GA-A17183, 1983.

S.5 Sachs, L., "Applied Statistics: A Handbook of Techniques," Springer Verlag, New York, Heidelberg, Berlin, 1982.

T.1 Todt, F., et.al., "FEVER: A One Dimensional Few-Group Depletion Program for Reactor Analysis," GA-2749, November 1962.

T.2 Teuchert, E., Hansen, U., Haas, K.A., "V.S.O.P.-Computer Code System for Reactor Physics and Fuel Cycle Simulation," KFA-IRE Report Jül-1649, March 1980.

T.3 Tiegs, T.N., "Fission-Product Pd-SiC Interaction in Irradiated Coated Particle Fuels," Oak Ridge National Laboratory, ORNL/TM-7203, 1980.

T.4 Teuchert, E., and Breitbarth, R., "Resonanzintegralberechnung für mehrfach heterogene Anordnung," Institut für Reaktorentwicklung, KFA Jülich, Jül-551-RG, September 1968.

V.1 Von der Decken, C.B., "Mechanical Problems of a Pebble Bed Reactor Core," Nuclear Engineering and Design 18, (1972), pp 323-333.

V.2 Verfondern, K., and Nabielek, H., "PANAMA: Ein Rechenprogramm zur Vorhersage des Partikelbruchanteils von TRISO-Partikeln unter Störfallbedingungen," KFA Jülich, Jül-Spez-298, Feb. 1985.

V.3 Verfondern, K., "Experimentelle Überprüfung des Thermohydraulik Programms THERMIX und rechnerische Analyse der transienten Temperatur- und Strömungsfelder im Corebereich des THTR-Reaktors nach Ausfall der NWA," Institut für Reaktorentwicklung, KFA Jülich, KFA-IRE-IB-13/78, October 1978.

W.1 Wolters, J., Breitbach, G., and Moormann, R., "Air and Water Ingress Accidents in an HTR-MODUL of Side-by-Side Concept," presented at the IAEA Specialists Meeting on Gas-Cooled Reactor Safety and Accident Analysis, Oak Ridge, TN, May 1985.

APPENDIX A: MATHEMATICAL BACKGROUND

A.1. Linear Algebra

The expontial function of a square matrix **A** is defined as follows:

$$\exp[\,\mathbf{A}\,] \equiv \mathbf{I} + \mathbf{A} + (1/2!)\,\mathbf{A}^2 + (1/3!)\,\mathbf{A}^3 + \cdots \qquad (A.1)$$

$$= \sum_{k=0}^{\infty} (1/k!)\,\mathbf{A}^k$$

It can be shown (see ref. B2) that the above series is convergent for any fixed matrix **A**. From the definition, the following properties of the exponential function are clear:

$$\mathbf{A}\exp[\,\mathbf{A}\,] = \exp[\,\mathbf{A}\,]\,\mathbf{A} \qquad (A.2)$$

$$\mathbf{A}^{-1}\exp[\,\mathbf{A}\,] = \exp[\,\mathbf{A}\,]\,\mathbf{A}^{-1} \qquad (A.3)$$

Note that in in general, the product of two exponential functions is *not* the exponential of the sums of the two original arguments:

$$\exp[\,\mathbf{A}\,]\exp[\,\mathbf{B}\,] \neq \exp[\,\mathbf{A}+\mathbf{B}\,] \qquad (A.4)$$

Expansion of the two exponentials on the left-hand side of the above equation reveals that the inequality may be replaced by an equality only in the case where **A** and **B** commute (i.e., if $\mathbf{A}\,\mathbf{B} = \mathbf{B}\,\mathbf{A}$). Note that introduction of a scalar factor, such as t, has the following effect:

$$\exp[\,\mathbf{A}t\,] = \mathbf{I} + \mathbf{A}t + (1/2!)\,\mathbf{A}^2t^2 + (1/3!)\,\mathbf{A}^3t^3 + \cdots \qquad (A.5)$$

If the derivitave of the above expression with respect to t is taken, the result is:

$$\frac{d}{dt}\exp[\,\mathbf{A}t\,] = \mathbf{A} + (1/2!)\,(2)\,\mathbf{A}^2t + (1/3!)\,(3)\,\mathbf{A}^3t^2 + \cdots$$

$$= \mathbf{A}\left\{\mathbf{I} + \mathbf{A} + (1/2!)\,\mathbf{A}^2t^2 + (1/3!)\,\mathbf{A}^3t^3 + \cdots\right\}$$

$$= \mathbf{A}\exp[\,\mathbf{A}t\,] \qquad (A.6)$$

Thus, the matrix exponential is the solution to the following set of linear time-invariant first-order differential equations:

$$\text{If} \quad \dot{\mathbf{x}} = \mathbf{A}\,\mathbf{x}\,, \quad \text{and } \mathbf{x}(0) = \mathbf{x}_o\,.$$

$$\text{Then} \quad \mathbf{x} \quad \exp[\,\mathbf{A}t\,]\,\mathbf{x}_o \tag{A.7}$$

A.1.2 Iterative Calculation of Matrix Exponentials

There are two possible methods for calculating the exponential of a matrix. The first is an analytic technique based on Sylvester's Expansion Theorem, which states that for any function f of an N×N square matrix **A**, the following is true:

$$f(\,\mathbf{A}\,) = \sum_{i=1}^{N} \mathbf{F}_i\, f(\lambda_i) \tag{A.8}$$

where

$$\mathbf{F}_i \equiv \prod_{\substack{j=1 \\ \neq i}}^{N} (\,\mathbf{A} - \lambda_j\,\mathbf{I}\,)/(\,\lambda_i - \lambda_j\,) \tag{A.9}$$

and the λ_i are the eigenvalues of **A**.

In particular, Sylvester's theorem is valid when f(**A**) is the exponential function, exp[**A**t]. However, even though these equations are true in the analytic sense, numerical computation of the $\mathbf{F}_i$ matrices has been found to be extremely diffucult once the dimensions of **A** exceed approximately six [I1]. For this reason, a numerical approach has been adopted for calculation of the exponential matrices in both the FUPAR and PDIF codes.

The alternate approach is to evaluate the matrix exponentials iteratively based on their definition:

$$\exp[\ \mathbf{A}t\ ] \equiv \sum_{k=0}^{\infty} (1/k!)\ (\mathbf{A}t)^k \qquad (A.10)$$

We will evaluate successive terms in the above series until an error criterion is satisfied. Let the true exponential be represented as a partial sum plus a remainder matrix:

$$\exp[\ \mathbf{A}t\ ] = \mathbf{M} + \mathbf{R} \qquad (A.11)$$

where $\mathbf{M}$ is the approximate result we desire:

$$\mathbf{M} \equiv \sum_{k=0}^{K} (1/k!)\ (\mathbf{A}t)^k \qquad (A.12)$$

and $\mathbf{R}$ is the remainder matrix:

$$\mathbf{R} \equiv \sum_{i=K}^{\infty} (1/k!)\ (\mathbf{A}t)^k \qquad (A.13)$$

A value of K can be chosen so that the maximum error in $\mathbf{M}$ (i.e., the maximum absolute value of a member of $\mathbf{R}$) is less than some pre-defined tolerance value. First, define the *norm* of a matrix $\mathbf{A}$ as follows:

$$\| \mathbf{A} \| \equiv \max_i \left\{ \sum_j | a_{ij} | \right\} \qquad (A.14)$$

The norm of $\mathbf{A}$ is the maximum value obtained by summing up the absolute value of the elements of $\mathbf{A}$ across any row. It can be shown [B2] that:

$$\| \mathbf{A}^k \| \leq \| \mathbf{A} \|^k \quad \text{for } k = 1,\ 2,\ 3,\ \cdots \qquad (A.15)$$

Equation (A.15) implies that each element of $\| \mathbf{A}^k \|$ is less than or equal to the single number $\| \mathbf{A} \|^k$. It follows that the maximum absolute value of an element in the remainder matrix $\mathbf{R}$ must be bounded

as follows:

$$| r_{ij} | \leq \sum_{k=k+1}^{\infty} (1/k!) \| \mathbf{A} \|^k t^k \qquad (A.16)$$

Let the ratio of the second term to the first term in the above series be defined as ϵ:

$$\epsilon \equiv \frac{\| \mathbf{A} \|^{k+2} t^{k+2} / (k+2)!}{\| \mathbf{A} \|^{k+1} t^{k+1} / (k+1)!}$$

$$= \| \mathbf{A} \| t / (k+2) \qquad (A.17)$$

Therefore it must be true that:

$$\frac{\| \mathbf{A} \| t}{k} \leq \epsilon \qquad \text{for any } k \geq K + 2 \qquad (A.18)$$

If we substitute Eq. (A.18) into Eq. (A.16), we obtain:

$$| r_{ij} | \leq \sum_{k=K+1}^{\infty} \frac{\| \mathbf{A} \|^k t^k}{k!} \leq \frac{\| \mathbf{A} \|^{K+1} t^{K+1}}{(K+1)!} [1 + \epsilon + \epsilon^2 + \cdots]$$

Or, evaluating the series in the above equation for values of $\epsilon < 1$:

$$| r_{ij} | \leq \frac{\| \mathbf{A} \|^{K+1} t^{K+1}}{(K+1)!} \cdot \frac{1}{1 - \epsilon} \qquad (A.19)$$

Equation (A.19) gives the maximum error in the series evaluation for any finite number of terms, K. In both FUPAR and PDIF, matrix exponentials are evaluated until the K'th term, at which point application of Eq. (A.19) indicates that maximum errors are below some acceptable level.

A.1.3 Choleski Factorization

It is a well known fact from the theory of matrices [R1] that any square matrix may be written as the product of a lower triangular and an upper triangular matrix. Furthermore, this decomposition in not unique,

and it is possible to arbitrarily select the values of all diagonal elements in either of the two factors. Thus, we may write in general that for any N×N matrix **A**:

$$\mathbf{A} = \mathbf{L}\,\mathbf{U} \tag{A.20a}$$

where: $\mathbf{L} = \begin{bmatrix} L_{11} & 0 & 0 & \cdots & 0 \\ L_{21} & L_{22} & 0 & \cdots & 0 \\ \vdots & & & & \vdots \\ L_{N1} & L_{N2} & \cdots & & L_{NN} \end{bmatrix}$ (A.20b)

and $\mathbf{U} = \begin{bmatrix} 1 & U_{21} & U_{31} & \cdots & U_{1N} \\ 0 & 1 & U_{23} & \cdots & U_{2N} \\ \vdots & & & & \vdots \\ 0 & & \cdots & & 1 \end{bmatrix}$ (A.20c)

This factorization is particularly simple for the **F** matrix introduced in Chapter 6. Since the elements of **F** are derived from a one-dimensional finite difference formulation, all elements of **F** are zero except for its main diagonal and the two partial diagonals on either side. The algorithm for factoring **F** into upper and lower diagonal matrices is straightforward.

Choleski factorization is utilized to simplify inversion of the **F** matrix. Since inversion of triangular matrices is particularly simple, and both the **L** and **U** factors are triangular while **F** is not, inversion is simplified by factoring **F** first. Furthermore, only a single algorithm for inverting a lower triangular matrix is necessary. Two identities make this possible:

$$F^{-1} = U^{-1} L^{-1}, \tag{A.21}$$

since $(U^{-1}L^{-1})\ L\ U = F^{-1}F = I$

and also:

$$(U^{-1})^{+} = (U^{+})^{-1}, \tag{A.22}$$

since $(U^{-1})^{+}\ U^{+} = (U\ U^{-1})^{+} = I$

Thus, the following procedure yields the inverse of F:

1) factor F into L and U;
2) transpose U to obtain U^{+};
3) take the inverse of both lower triangular matrices, obtaining L^{-1} and $(U^{+})^{-1}$;
4) transpose again to obtain U^{-1}: $[\ (U^{+})^{-1}]^{+} = (U^{-1})^{++} = U^{-1}$;
5) multiply to obtain F^{-1}: $F^{-1} = U^{-1}L^{-1}$.

This procedure has been found to work well for for F matrices with relatively large norms:

$$\| F \| > 1/\Delta t$$

When this is not the case, the iterative technique discussed in Chapter 6 is preferred.

A.2: RANDOM VARIABLES AND PROBABILISTIC MODELING

A much more thorough exposition of this subject may be found in Ref. D.1. In this work it is assumed that the reader has a fundamental understanding of probabilistic concepts. Here, basic concepts and terminology of multi-dimensional random variables are defined for use in this report.

A.2.1 Random Vectors

A vector-valued function defined on a sample space S:

$$\mathbf{x}(s) = \begin{bmatrix} x_1 \\ x_2 \\ x_3 \\ \vdots \\ x_n \end{bmatrix} = \begin{bmatrix} x_1(s) \\ x_2(s) \\ x_3(s) \\ \vdots \\ x_n(s) \end{bmatrix} \tag{A.23}$$

(where the event s is an element of S) is a random vector if each component x_i is a random variable defined on S.

The joint cumulative distribution function (CDF) for a random vector $\mathbf{x}$ will be denoted by $F_{\mathbf{x}}(\mathbf{x}_o)$, and is defined as the following joint probability:

$$F_{\mathbf{x}}(\mathbf{x}_o) \equiv \mathbb{P}\left[(x_1 \leq x_{1_o}) \cap (x_2 \leq x_{2_o}) \cap \cdots \cap (x_n \leq x_{n_o}) \right]$$

The CDF need not be a continuous function. If any element x_i is a discrete random variable, the CDF consists of a superposition of step functions, each step occuring at one of the discrete x_i's possible values. It can be shown [D.2] that a discrete random variable may be treated formally in the same manner as a continuous one, as long as the proper discontinuity functions are used to represent its CDF. For this reason, no distinction will be made in this work between discrete and continuous random variables and vectors.

The joint probability density function (PDF) for a random vector $\mathbf{x}$ is defined using the joint CDF:

$$f_{\mathbf{x}}(\mathbf{x}_o) \equiv \frac{\partial}{\partial x_1 \, \partial x_2 \cdots \partial x_n} F_{\mathbf{x}}(\mathbf{x}_o) \tag{A.24}$$

The probability that the elements of $\mathbf{x}$ are found within the interval $(\Delta x_1, \Delta x_2, \ldots \Delta x_n)$ is given by the following integral:

$$\mathbb{P}\Big[(x_1 \text{ lies in } \Delta x_1) \cap (x_2 \text{ lies in } \Delta x_2) \cap \cdots \cap (x_n \text{ lies in } \Delta x_n) \Big] = \int_{\Delta x_1} \int_{\Delta x_2} \cdots \int_{\Delta x_n} f_{\mathbf{x}}(\mathbf{x}_o) \, dx_{1_o} \, dx_{2_o} \cdots dx_{n_o} \tag{A.25}$$

A.2.2 The Expectation Operator

For a single-dimensioned random variable x, the expectation value of x is defined by:

$$E[x] \equiv \bar{x} \equiv \int_{-\infty}^{\infty} f_x(x_o) \, x_o \, dx_o \tag{A.26}$$

The expectation operator, $E[\ ]$, is a linear operator, so that if x and y are both random variables:

$$E[ax + by + c] = a \, E[x] + b \, E[y] + c \tag{A.27}$$

If x is a discrete random variable, the integral definition (A.25) reduces to the following summation:

$$E[x] = \sum_{x_o} f_x(x_o) \, x_o \tag{A.28}$$

where the summation is taken over all possible values of x_o.

The expected value of a random vector is simply the vector of expectations of its components:

$$E[\,\mathbf{x}\,] = E\begin{bmatrix} x_1 \\ x_2 \\ x_3 \\ \vdots \\ x_n \end{bmatrix} = \begin{bmatrix} E[x_1] \\ E[x_2] \\ E[x_3] \\ \vdots \\ E[x_n] \end{bmatrix} \tag{A.29}$$

Note that the expected value of a random variable or vector is not itself a random variable. Its value is fixed for any given experiment.

A.2.3 Covariance and Cross-Covariance Matrices

In analogy with the variance of a single-dimensioned random variable, a covariance matrix may be defined for a random vector. Let $\mathbf{x}$ represent a random vector, and $\bar{\mathbf{x}} = E[\mathbf{x}]$ represent its expectation. The covariance matrix $\mathbf{V}_x$ is defined as follows:

$$\mathbf{V}_x \equiv E\left[(\mathbf{x} - \bar{\mathbf{x}})(\mathbf{x} - \bar{\mathbf{x}})^+ \right] \tag{A.30}$$

where the superscript "+" indicates the transposition operation. If $\mathbf{x}$ is an N element vector, then $\mathbf{V}_x$ is an N×N matrix.

Since $\bar{\mathbf{x}}$ is a constant vector, the definition (A.) may be rewritten in a more convenient form:

$$\begin{aligned} \mathbf{V}_x &\equiv E\left[(\mathbf{x} - \bar{\mathbf{x}})(\mathbf{x} - \bar{\mathbf{x}})^+ \right] \\ &= E[\,\mathbf{x}\mathbf{x}^+ - \mathbf{x}\bar{\mathbf{x}}^+ - \bar{\mathbf{x}}\mathbf{x}^+ + \bar{\mathbf{x}}\bar{\mathbf{x}}^+\,] \\ &= E[\,\mathbf{x}\mathbf{x}^+] - E[\,\mathbf{x}\,]\bar{\mathbf{x}}^+ - \bar{\mathbf{x}}E[\,\mathbf{x}^+] + \bar{\mathbf{x}}\bar{\mathbf{x}}^+ \\ \text{or: } \mathbf{V}_x &= E[\,\mathbf{x}\mathbf{x}^+] - \bar{\mathbf{x}}\bar{\mathbf{x}}^+ \end{aligned} \tag{A.31}$$

From the definition, it is evident that $\mathbf{V}_x$ is a symmetric matrix ($\mathbf{V}_x^+ = \mathbf{V}_x$). The i'th diagonal element of $\mathbf{V}$ is the variance of the i'th random variable in $\mathbf{x}$. Any off-diagonal element in position (i,j) is the correlation coefficient between the i'th and j'th random

variables in $\mathbf{x}$.

A function similar to the covariance matrix may be defined for two random vectors. Let $\mathbf{x}$ and $\mathbf{y}$ represent two random vectors with equal numbers of elements, N. The cross-covariance matrix in the "xy sense" is denoted by $\mathbf{V}_{xy}$, and is defined as:

$$\mathbf{V}_{xy} \equiv E\left[(\mathbf{x} - \bar{\mathbf{x}}) (\mathbf{y} - \bar{\mathbf{y}})^{+} \right] \tag{A.32}$$

If we expand $\mathbf{V}_{xy}$ to examine its individual elements:

$$\mathbf{V}_{xy} = E\left[\begin{bmatrix} x_1-\bar{x}_1 \\ x_2-\bar{x}_2 \\ x_3-\bar{x}_3 \\ \vdots \\ x_n-\bar{x}_n \end{bmatrix} \begin{bmatrix} y_1-\bar{y}_1, & y_2-\bar{y}_2, & y_3-\bar{y}_3, & \cdots & y_n-\bar{y}_n \end{bmatrix} \right]$$

$$= \begin{bmatrix} (x_1-\bar{x}_1)(y_1-\bar{y}_1) & (x_2-\bar{x}_2)(y_1-\bar{y}_1) & (x_3-\bar{x}_3)(y_1-\bar{y}_1) & \cdots & (x_n-\bar{x}_n)(y_1-\bar{y}_1) \\ (x_1-\bar{x}_1)(y_2-\bar{y}_2) & (x_2-\bar{x}_2)(y_2-\bar{y}_2) & (x_3-\bar{x}_3)(y_2-\bar{y}_2) & \cdots & (x_n-\bar{x}_n)(y_2-\bar{y}_2) \\ (x_1-\bar{x}_1)(y_3-\bar{y}_3) & (x_2-\bar{x}_2)(y_3-\bar{y}_3) & (x_3-\bar{x}_3)(y_3-\bar{y}_3) & \cdots & (x_n-\bar{x}_n)(y_3-\bar{y}_3) \\ \vdots & \vdots & \vdots & & \vdots \\ (x_1-\bar{x}_1)(y_n-\bar{y}_n) & (x_2-\bar{x}_2)(y_n-\bar{y}_n) & (x_3-\bar{x}_3)(y_n-\bar{y}_n) & \cdots & (x_n-\bar{x}_n)(y_n-\bar{y}_n) \end{bmatrix}$$

Clearly, $\mathbf{V}_{xy}$ is not a symmetric matrix. However, it is apparent from the definition (A.32) that the following relation does exist

between the covariance matrices in complementary senses:

$$\mathbf{V}_{xy}^{+} = E[\,(\mathbf{x}-\bar{\mathbf{x}})(\mathbf{y}-\bar{\mathbf{y}})^{+}]^{+} = E[\,(\mathbf{y}-\bar{\mathbf{y}})(\mathbf{x}-\bar{\mathbf{x}})^{+}\,] = \mathbf{V}_{yx} \quad (A.33)$$

A.2.4 Stationarity

A function of a stochastic variable or process (such as the power or flux distribution in a pebble bed reactor) can never achieve a "steady state" in the deterministic sense, as the variables which determine these parameters are constantly changing with time. The concept of "stationarity" extends the notion of time-independence to functions of random variables.

Definition of a stationary process begins with a general mathematical notation for a time-dependent stochastic process. Let $x(t)$ represent the time-dependent behavior of a stochastic variable. A complete description of the process requires the use of *ensemble* notation, as there are actually an infinite number of possible trajectories, $x(t)$. The complete set of possible time traces of $x(t)$ will be denoted by $\{x(t)\}$, the ensemble of functions $x(t)$. For any fixed value of time t, the function $x(t)$ is a random variable. The randomness of $x(t)$ arises from the different members of the ensemble $\{x(t)\}$.

A CDF may be defined for the ensemble at any time. In particular,

$$F_1(\,x_1,\,t\,) \equiv \mathbb{P}[\,x(t) \le x_1\,] \quad (A.34)$$

This probability applies to the ensemble $\{x(t)\}$ as time varies, thus is itself a function of time. Eq. (A.34) is the basis for defining a PDF for x:

$$f_1(x_1, t) \equiv \frac{\partial}{\partial x_1} F_1(x_1, t) \qquad (A.35)$$

Joint distribution and density functions may be defined using straightforward extensions of the above concepts:

$$F_2[x_1,t_1 ; x_2,t_2] \equiv \mathbb{P}[(x(t_1) \leq x_1) \cap (x(t_2) \leq x_2)]$$

$$f_2[x_1,t_1 ; x_2,t_2] \equiv \frac{\partial^2}{\partial x_1 \, \partial x_2} F_2[x_1,t_1 ; x_2,t_2]$$

Ensemble moments may also be defined:

$$\overline{x(t)} \equiv E[x(t)] \equiv \int_{-\infty}^{+\infty} x \, f(x,t) \, dx$$

$$\overline{x^2(t)} \equiv E[x^2(t)] \equiv \int_{-\infty}^{+\infty} x^2 \, f(x,t) \, dx$$

...and so on. The above integrals are taken across the ensemble $\{x(t)\}$, and remain functions of time.

Now consider the general n'th order CDF:

$$F_n[x_1,t_1 ; x_2,t_2 ; \cdots ; x_n,t_n].$$

The variable x(t) is considered *stationary* if and only if the function F_n is invariant under any shift in time. That is:

$$\left[x(t) \text{ is stationary} \right] \iff \left[F_n[x_1,t_1 ; \cdots ; x_n,t_n] = F_n[x_1,t_1+\Delta t ; \cdots ; x_n,t_n+\Delta t] \right]$$

for any Δt.

Thus, a stationary stochastic variable is *not* constant in time, but its CDF and hence its PDF are (the time derivitive of F_n is identically zero if the above definition applies). In particular, if x(t) is assumed to be stationary, and the definitions of moments are applied, we find that:

$$x(t) \text{ is stationary} \Rightarrow \begin{cases} \overline{x(t)} = \bar{x} \text{ is independent of time} \\ \overline{x(t)^2} = \overline{x^2} \text{ is independent of time} \end{cases}$$

...and so on for any ensemble moment or combination of moments (e.g. the variance) of $x(t)$.

APPENDIX B: REACTOR PHYSICS CALCULATIONS WITH V.S.O.P.

The Very Superior Old Programs (V.S.O.P.) computer code system has been developed by researchers at the KFA, Jülich, primarily for pebble bed graphite-moderated reactor computation. VSOP's direct precursor is the MAFIA-II code by Massimo [T2], whose basic components are well established and proven codes which date back to the early 1960s. All components have been updated to reflect special phenomena associated with HTGRs. VSOP is not intended to be used for highly detailed design calculations; its authors state that it is much more suited to scoping calculations.

This appendix is not intended to discuss all aspects of VSOP. Rather, the intention is to explain only those parts of the VSOP code which are important for understanding the FUPAR/VSOP iterations. The four basic tasks performed by VSOP in this context are:

(1) resonance integral calculation;
(2) thermal neutron spectrum calculation;
(3) epithermal neutron spectrum calculation;
(4) neutron diffusion calculations.

Resonance integrals are calculated by the ZUT/DGL program, a verson of the ZUT code modified to account for double heterogeneity effects (see section B.1 below). Thermal neutron spectra are calculated by THERMOS, also with modifications to reflect double heterogeneity. Fast neutron spectra are calculated by GAM, which employs the resonance integrals produced by ZUT/DGL. Finally, a modified version of the FEVER code is used in an r/z iteration to synthesize a two-dimensional power

distribution. Fig. B.1 illustrates graphically the general flow of data and calculations in VSOP.

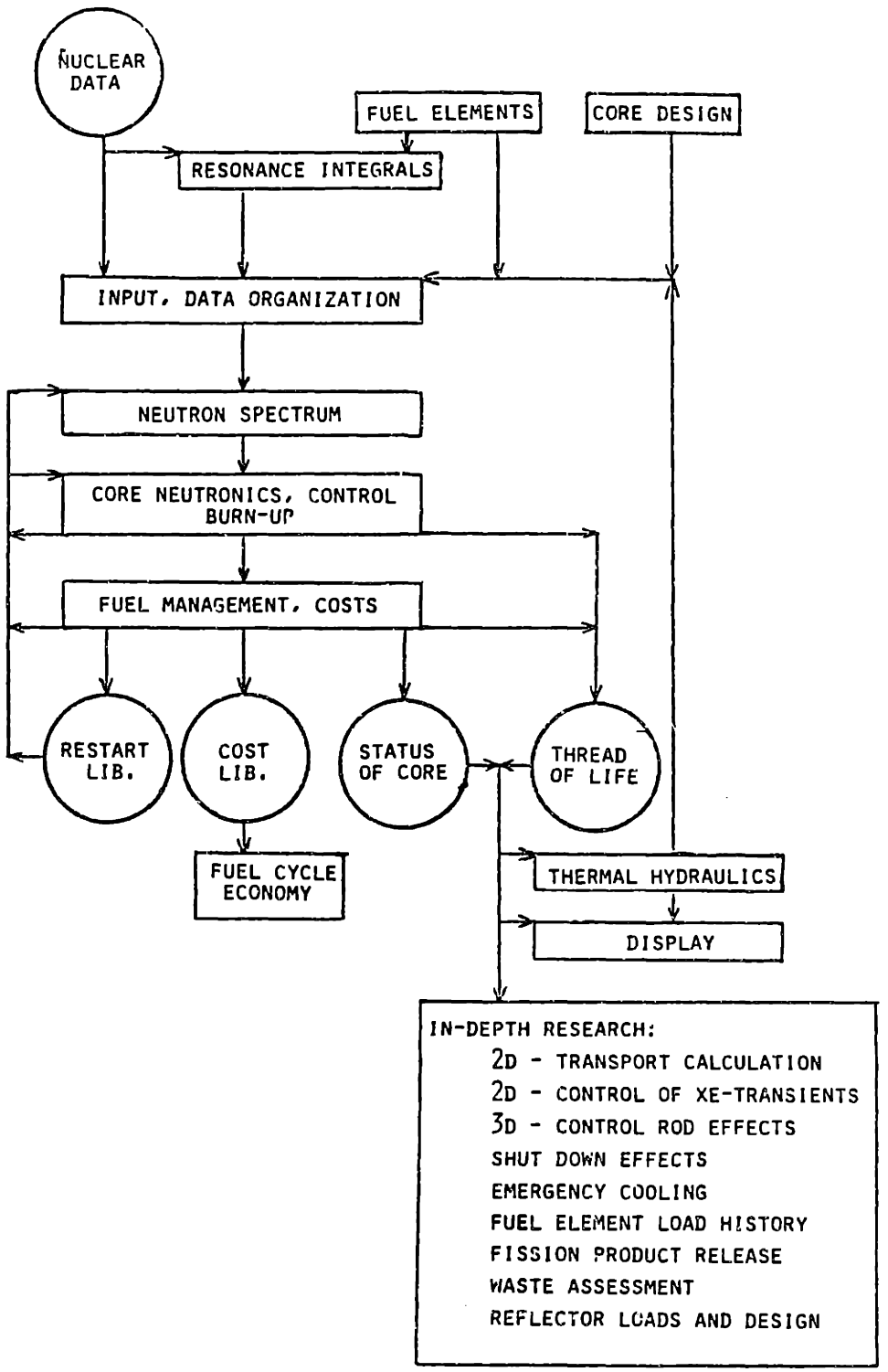

FIG. B.1a: Structure of the VSOP computer code: physics simulation [T2].

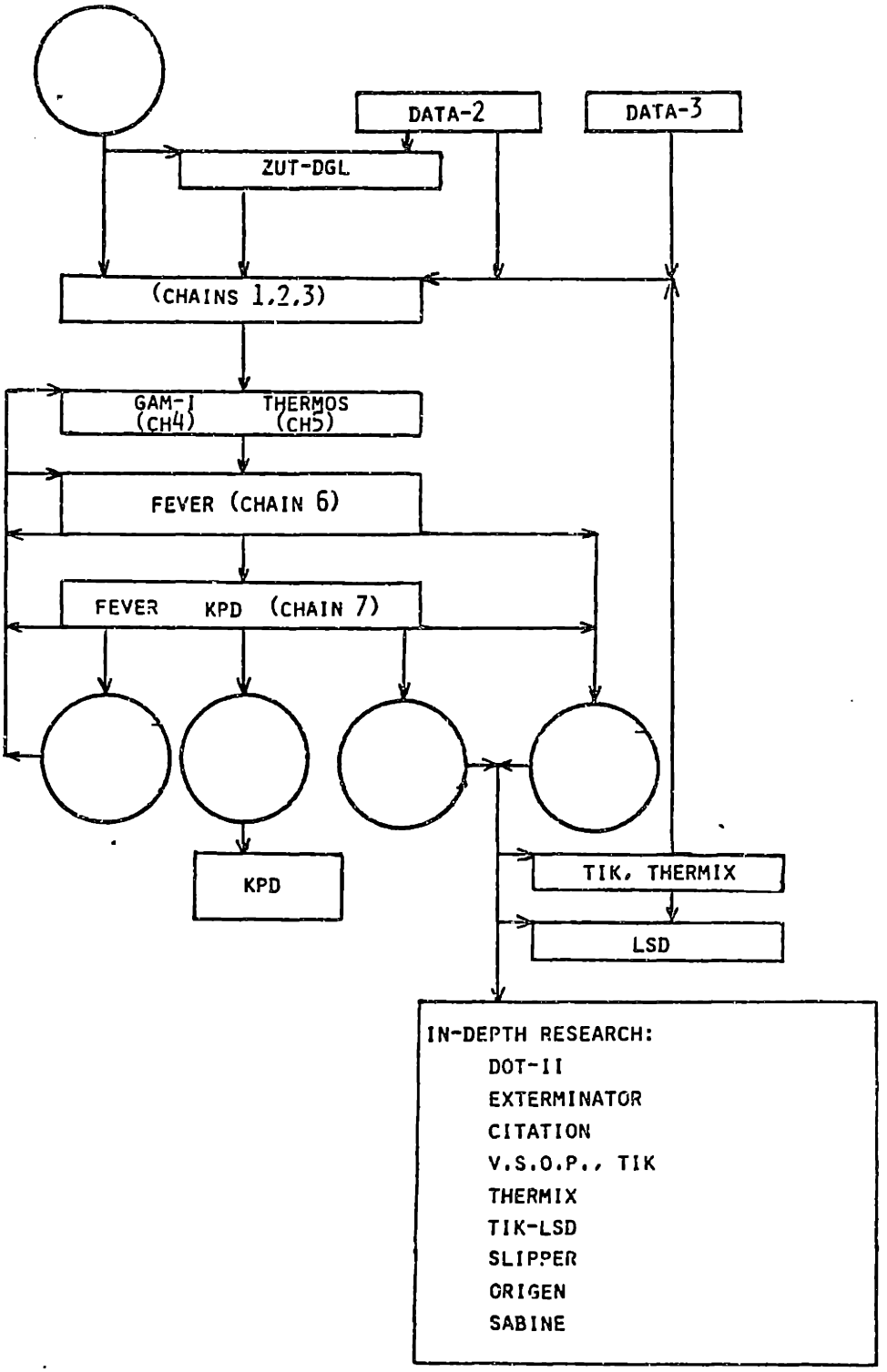

FIG. B.1b: Structure of the VSOP computer code: basic programs [T2].

B.1 Resonance Integral Calculations with ZUT/DGL

The ZUT code [K6] is composed of two major sub-programs: ZUT for calculation of resonance integrals in the resolved resonance region, and TUZ for calculating a single resonance integral for the unresolved resonance region.

ZUT treats resonances as narrow and widely spaced, with the assymptotic neutron flux inversely proportional to energy. Geometry is assumed to be a two-region fuel/moderator cell contained in an infinite lattice. The objective is to calculate an effective resonance integral I, which is the flux-weighted average absorption cross section over the energy interval containing a resonance. Once calculated by ZUT, the resonance integral may be used as a simple cross section in later multi-group spectrum calculations.

Resonance integrals are calculated according to:

$$I \equiv \int \phi \, \sigma_a \, dE = E_1 \int F_z(u) \, \frac{\sigma_a(u)}{\sigma_t(u)} \, e^{-u} \, du \qquad (B.1)$$

where:

ϕ = energy-dependent neutron flux (neutrons/b-sec-eV);

$\sigma_t(u)$, $\sigma_a(u)$ = total and absorption cross sections (barns) *per absorber atom*;

E = neutron energy (eV);

u = neutron lethargy: $u \equiv \ln(E_1/E)$

E_1 = upper reference energy, above which the neutron flux is assumed to vary as 1/E;

$F_z(u)$ = the "ZUT collision density," $\equiv e^u \, \sigma_t(u) \, \phi(u)$.

The collision density $F_z(u)$ represents the loss rate of neutrons from the energy interval du around u. At energies greater than the

reference value E_1, the dependence of the collision density on energy is known to be:

$$F_{ass} = (\sigma_{p_o} + \sigma_{m_1} + \sigma_{m_2}) \frac{e^u}{E_1} \qquad (B.2)$$

where:

σ_{p_o} = absorber potential scattering cross section (barns);

σ_{m_1}, σ_{m_2} = two moderator scattering cross sections, admixed with the absorber atoms.

The collision density in the resonance region is described by the following integral equation:

$$F_z(u) = (1-P_o) \left[T_a + T_{m_1} + T_{m_2} \right] + P_o \sigma_t \frac{e^u}{E_1} \qquad (B.3)$$

where

$P_o = P_o(u)$ = the general escape probability, equal to the probability that a neutron born with equal likelihood anywhere within the fuel region suffers its next interaction in the moderator region.

The T_t terms represent sources of neutrons into du from collision at higher energies. For example, T_a is the source of neutrons into du due to higher energy collisions with absorber atoms, and may be expressed in full integral form as:

$$T_a = \frac{1}{\alpha_o} \int_{u-\ln[1/(1-\alpha_o)]}^{u} F(u') (\sigma_{s_o}/\sigma_t) \, du' \qquad (B.4)$$

where $\alpha_o \equiv 4A_o/(A_o+1)^2$, and A_o = the atomic mass of the absorber nuceus.

ZUT allows the user to select various approximations for the T_a and the T_{m_t} integrals (sources due to collisions with moderator atoms). For

the absorber atoms, the narrow resonance (NR), full integral, or infinite mass (IM) treatments are allowed. Moderator integrals, if present, may be represented in the full integral sense or by the assymptotic (narrow resonance) form.

Calculation of the escape probability P_o is complicated in the HTGR by "double heterogeneity" effects. This refers to the double-scaling present in HTGR fuel which is significant when absorption cross sections reach large resonance values. Heterogeneity must be accounted for both on the macroscopic scale (of an entire fuel element) and on the microscopic scale (of a single fuel particle).

ZUT has been modified to account for double heterogeneity effects. The escape probability from a single fuel particle is based on the component probabilities illustrated in Fig. B.2. The possible paths which a neutron may follow are divided into sub-trajectories. The probabilities of neutrons successfully navigating any one of these trajectories may be rigorously evaluated using a numerical treatment. The details of the numerical procedure are given in Ref. T.4. The eight component probabilities, W_1 through W_8, represent the probabilities that neutrons will pass only through the indicated sub-trajectory before their next collision. For example, W_1 is the probability that a neutron will undergo a collision in the same coated particle in which it was born. The geometric escape probabilty P_o may be calculated using:

$$P_o(E) = W_1 + W_2(W_3 + W_4) + W_2 W_5 \frac{W_6 + W_7}{1 - W_8} \qquad (B.5)$$

ZUT solves the integral equation (B.1) by dividing the integral energy range into a number of discrete steps, the width of each

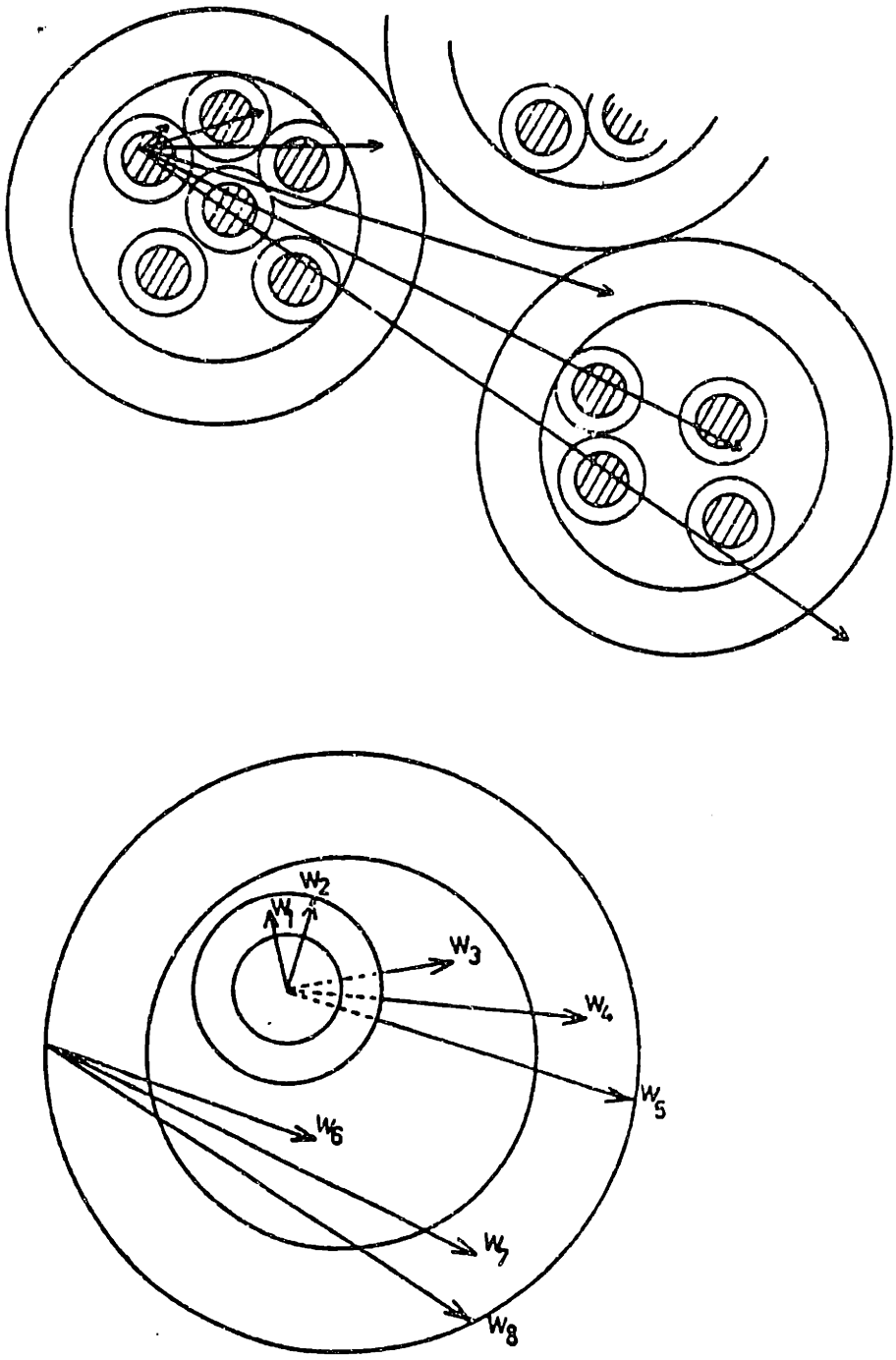

FIG. B.2: Neutron trajectories for doubly-heterogeneous escape probability calculations.

determined by limiting the point-to-point absorber cross section variation due to Doppler broadening. The scattering source into the upper end of the resonance energy range depends only on the assymptotic (known) collision density at higher energies. With this as the "initial condition," the remainder of the integral is solved from high to low energy, each incremental solution contributing to the source term for the next lower energy step.

The actual absorption cross sectons (σ_{a_0} and σ_{s_0}) for the absorber are calculated using a Doppler-broadened Breit-Wigner formula. In this manner, the effects of fuel temperature on resonance absorption are taken into account. Nuclear data requirements are thus the neutron and gamma widths of each resolved resonance, plus the peak resonance energy.

In the region of unresolved resonances, ZUT considers the resonances to be defined by an average over the Porter-Thomas distribution of neutron widths. A single resonance integral, I_{unres}, is calculated in the energy range $E_c \rightarrow \infty$, where E_c is the energy above which the absorber resonances are considered to be unresolved. Ref. K6 describes in detail the numerical procedures used to evaluate I_{unres}.

B.2 Epithermal Neutron Spectrum Calculation: The GAM Code

In order to provide few-group nuclear constants for use in subsequent neutron diffusion calculations, both the thermal and epithermal neutron energy spectra must be evaluated in order to properly average cross sections over the appropriate energy range. The GAM code (see Ref. J2), developed in the early 1960s at General Atomic, performs the neutron spectrum calculation in the fast energy range.

The motivation for GAM begins with the time-independent Boltzmann transport equation for $N(\mathbf{r},E,\Omega)$, the neutron distribution function in $\mathbf{r}$ (position), E (energy), and Ω (solid angle):

$$\Omega\cdot\nabla N(\mathbf{r},E,\Omega) + \Sigma_t N(\mathbf{r},E,\Omega) = \frac{S(\mathbf{r},E)}{4\pi} + \int dE' \int d\Omega' \; \Sigma_s(E'\rightarrow E,\Omega'\rightarrow\Omega) N(\mathbf{r},E',\Omega')$$

where:

Σ_t = the total macroscopic cross section;

S = neutron source (assumed isotropic);

$\Sigma_s(E'\rightarrow E,\Omega'\rightarrow\Omega)$ = the neutron scattering kernel for energy transformation $E'\rightarrow E$, solid angle change $\Omega'\rightarrow\Omega$.

GAM assumes that the neutron distribution function is approximately isotropic, so that $N(\mathbf{r},E,\Omega)$ is adequately represented by:

$$N(\mathbf{r},E,\Omega) \simeq (1/4\pi) \left[\phi(\mathbf{r},E) + 3\Omega\cdot J(\mathbf{r},E) \right] \qquad (B.6)$$

where:

$$\phi(\mathbf{r},E) \equiv \int_{\Omega} d\Omega \; N(\mathbf{r},E,\Omega) = \text{the isotropic component of the flux,}$$

$$J(\mathbf{r},E) \equiv \int_{\Omega} d\Omega \; \Omega \; N(\mathbf{r},E,\Omega) = \text{the net current density.}$$

The consistent P_1 equations are obtained by first substituting the approximation (B.6) into the transport equation, multiplying by 1 and by Ω, and integrating each case over all Ω:

$$\nabla\cdot J(\mathbf{r},E) + \Sigma_t \phi(\mathbf{r},E) = \int \Sigma_s^0(E'\rightarrow E) \; \phi(\mathbf{r},E') \; dE' + S(E) \qquad (B.7a)$$

$$\nabla\phi(\mathbf{r},E) + 3\Sigma_t J(\mathbf{r},E) = \int \Sigma_s^1(E'\rightarrow E) \; J(\mathbf{r},E') \; dE' \qquad (B.7b)$$

where Σ_s^0 and Σ_s^1 are equal to $4\pi s_0$ and $4\pi s_1$, respectively. The quantities s_0 and s_1 are the first two terms in the Legendre expansion of the scattering kernel:

$$\Sigma_s(E'\rightarrow E,\Omega'\rightarrow\Omega) = \sum_i s_i \; P_i(\Omega\cdot\Omega')$$

To solve, Eq. (B.7a) and the divergence of Eq. (B.7b) are integrated over some volume of interest, yielding:

$$\bar{J}(E) + \Sigma(E)\,\bar{\Phi}(E) = \int_E^{E/\alpha} \Sigma_s^o(E' \rightarrow E)\,\phi(E')\,dE' + \bar{S}(E) \qquad (B.8a)$$

$$\mathcal{L}\,\bar{\Phi}(E) + 3\,\Sigma(E)\,\bar{J}(E) = \int_E^{E/\alpha} \Sigma_s^1(E' \rightarrow E)\,J(E')\,dE' \qquad (B.8b)$$

where:

$$\mathcal{L} \equiv \frac{\iiint_V \nabla^2\phi\,dv}{\iiint_V \phi\,dv};$$

$$\bar{J} \equiv \iiint_V \nabla\cdot\mathbf{J}\,dv;$$

$$\bar{\Phi} \equiv \iiint_V \phi\,dv.$$

GAM uses Eqs. (B.8a) and (B.8b) in lethargy form, and converts to a set of coupled algebraic equations by integrating over 68 quarter lethargy intervals from 10 MeV to 0.414 eV. Both $\bar{J}_n$ and $\bar{\Phi}_n$ are solved for.

Geometry effects may enter the calculations in two ways. One option which is not used in VSOP is to define energy-dependent leakage terms $\mathcal{L}_n$, which reflect the geometric bucklings. Geometry effects are most significant for the resonance absorption process. In this case, geometry is accounted for through use of ZUT-DGL-calculated resonance integrals, which account for the fuel's double heterogeneity.

B.3 Thermal Neutron Spectrum Calculation: The THERMOS Code.

The thermal neutron spectrum is calculated in the THERMOS program, which employs integral transport theory to compute the scalar thermal neutron spectrum as a function of position in a one-dimensional lattice. 30 velocity (energy) groups and 20 spatial mesh points are allowed.

The quantity of interest is the scalar neutron density, $N(\mathbf{r},v)$ ($\mathbf{r}$ = position, v = neutron velocity), which will directly yield reaction rates if cross sections are known. The birth rate density H is defined as:

$$H(\mathbf{r},v,\Omega) \equiv \int_0^\infty dv' \int_{\Omega'} d\Omega' \; P(\mathbf{r},v'\rightarrow v,\mu_o)\; N(\mathbf{r},v',\Omega') \qquad (B.9)$$

where

$P(\mathbf{r},v'\rightarrow v,\mu_o)$ = the probability per second per unit solid angle that a neutron of speed v' will scatter to speed v through an angle with cosine μ_o.

The integral equation for the scalar neutron density can then be written:

$$v\; N(\mathbf{r},v) = \int_{\text{all } \mathbf{r}} d\mathbf{r}' \; T_{pt}(\mathbf{r},\mathbf{r}',v)\; H(\mathbf{r}',v) \qquad (B.10)$$

where T_{pt} is the flux at $\mathbf{r}$ due to a unit isotropic point source at $\mathbf{r}'$:

$$T_{pt}(\mathbf{r},\mathbf{r}',v) = \frac{1}{4\pi\,(\mathbf{r}-\mathbf{r}')^2} \exp\left\{ - \left| \int_{\mathbf{r}'}^{\mathbf{r}} ds\; \Sigma_t(s,v) \right| \right\} \qquad (B.11)$$

The neutron speed range is divided into an epithermal range ($v > v^*$) where both the energy and spatial distribution of neutrons is assumed to be known, and a thermal region ($v < v^*$). Let the source of thermal neutrons due to fast neutron scatters be denoted S:

$$S(\mathbf{r}',v) \equiv \int_{v^*}^\infty dv' \; P(\mathbf{r}',v'\rightarrow v)\; N(\mathbf{r}',v')$$

Eq. (B.10) then becomes:

$$N(\mathbf{r},v) = \int_{\text{all } \mathbf{r}'} d\mathbf{r}' \; T(\mathbf{r},\mathbf{r}',v) \left[S'(\mathbf{r}',v) + \int_0^{v^*} dv' \; P'(\mathbf{r},v' \rightarrow v) \; N(\mathbf{r}',v') \right] \quad \text{(B.12)}$$

where the primes on S and P denote division by neutron velocity. The T and P kernels must each satisfy normalization and symmety conditions:

$$\int_0^{\infty} dv' \; P(\mathbf{r},v',v) = v \; \Sigma_s(\mathbf{r},v) \quad \text{(B.13a)}$$

$$\int_{\text{all } \mathbf{r}'} d\mathbf{r}' \; T_{pt}(\mathbf{r}',\mathbf{r},v) \; \Sigma_t(\mathbf{r}',v) = 1 \quad \text{(B.13b)}$$

$$M(v') \; P(\mathbf{r},v,v') = M(v) \; P(\mathbf{r},v',v) \quad \text{(B.13c)}$$

$$T(\mathbf{r},\mathbf{r}',v) = T(\mathbf{r}',\mathbf{r},v) \quad \text{(B.13d)}$$

where M(v) is the Maxwellian distribution.

Replace the upper limit in (B.13a) by v^*, which is a reasonable approximation as long as few neutrons up-scatter out of the thermal range. The THERMOS program solves Eq. (B.12) numerically by dividing the v and r spaces into discrete intervals of width Δv_i and ΔV_j, respectively. Let NX represent the number of subvolumes, and IX the number of velocity intervals. Where practical, the quantities N, T, S, and P are averaged over the discrete elements. In other cases the mid-point of the interval is taken as typical. Define the following discrete terms:

$$N_{n,i} \equiv N(\mathbf{r}_n, v_i) \quad \text{(B.14a)}$$

$$S'_{k,i} \equiv S'(\mathbf{r}_k, v_i) \quad \text{(B.14b)}$$

$$T_{n,k,i} \equiv T(\mathbf{r}_n, \mathbf{r}_k, v_i) \; \Delta V_k \quad \text{(B.14c)}$$

$$P'_{k,i,j} \equiv P'(\mathbf{r}_k, v_i, v_j) \; \Delta v_j \quad \text{(B.14d)}$$

Integrate Eq. (B.12) over volume element n and velocity increment i

to obtain the final numerical form of the integral transport equation:

$$N_{n,i} = \sum_{k=1}^{NX} T_{n,k,i} \left\{ S'_{k,i} + \sum_{j=1}^{IX} P'_{k,i,j} N_{k,j} \right\} \qquad (B.15)$$

The numerical techniques for solving the system of equations (B.15) is detailed in Ref. H.3. The resulting set of $N_{n,i}$, when suitably averaged over portions or all of the cell volume, yields neutron energy spectra suitable for cross section collapsing to produce thermal neutron cross sections.

The double-heterogeneity problem arises in the thermal spectrum calculation due to the presence of low-energy plutonium resonances. A simplified numerical calculation of escape probabilities is used to account for this phenomenon. Let the mean path of a neutron from one coated fuel particle to another be L. L is simply a geometric quantity, which depends upon the diameter of the coated particles and the volumetric filling of the fuel element matrix. Let the probability W(E) denote the probability that a neutron traverses one coated particle plus the associated average amount of matrix material without interaction. This probability is calculated through direct numerical integration, which is detailed in Ref. H.?. W(E) is used to define the *effective* macroscopic total cross section $\Sigma^*(E)$ as follows:

$$W(E) = \exp[-\Sigma^*(E)\, L\,] \qquad (B.16)$$

THERMOS then uses the effective value $\Sigma^*(E)$ in place of the homogenized $\Sigma(E)$.

B.4 Neutron Diffusion Calculation: The FEVER Code.

Once the three neutron spectrum/cross section collapsing codes have

produced few-group cross sections, the FEVER code (Ref. T1) performs neutron diffusion calculations to synthesize a two-dimensional flux profile in the reactor core. FEVER has been written to perform depletion calculations as well, but this capability is not used when VSOP and FUPAR are used in conjunction.

FEVER solves the one-dimensional few group diffusion equations:

$$-D_1\nabla^2\phi_1 + (\Sigma_{a_1} + \Sigma_{s_1} + D_1B_1^2)\,\phi_1 = \frac{1}{\lambda}\sum_{i=1}^{G}\nu\Sigma_{f_i}\phi_i \qquad \text{(B.17a)}$$

and $$-D_i\nabla^2\phi_i + (\Sigma_{a_i} + \Sigma_{s_i} + D_iB_i^2)\,\phi_i = \Sigma_{s_{i-1}}\phi_{i-1} \qquad (i\neq 1) \qquad \text{(B.17b)}$$

The equations are solved with the aid of a finite difference mesh set up over the region of interest. Boundary conditions are albedos specified at each boundary. Continuity of flux and current are set up at each internal lattice point, noting that the coefficients of the diffusion equation may be different on the right- and left-hand sides of the mesh point. FEVER then "steps through" the lattice, using relations for flux ratios at each energy to further refine the estimate of the flux distribution. Fluxes and the resulting multiplication factor are improved through interation until specified convergence criteria are met.

In its present form, FEVER accepts four energy groups. Additionally, the authors of VSOP have devised a system to use the code iteratively to synthesize a two-dimensional flux distribution. This is accomplished by using FEVER to independently calculate a radial power distribution and then one or more axial power distributions. These shapes are multiplied together to create an approximate r-z flux

distribution. Results from the radial calculation are fed back into the axial calculation as transverse bucklings, and vice-versa.

B.5: VSOP DATA REQUIREMENTS

Three general types of data are required to run VSOP in conjunction with FUPAR. These are: standard Fortran input from unit 5, cross section data stored on permament data sets, and Eulerian materials densities as a function of core zone in a direct access data set generated by FUPAR. The cross section data used for FUPAR/VSOP is identical to that used for VSOP alone, and is adequately described in Reference T.2. This section describes input data requirements which are unique to the FUPAR/VSOP system of reactor analysis.

B.5.1. Changes to standard Fortran input.

Standard VSOP input is extensively documented in Reference T.2. A few additions to these instructions are necessary to run VSOP using FUPAR-generated materials concentration distributions. These changes are summarized in Figures B.1a through B.1c. The revised input is to be inserted in the appropriate locations in Reference T2.

B.5.2. VSOP data generated by FUPAR.

VSOP is instructed to read material concentrations from FUPAR datasets by setting NFDEN not equal to zero on VSOP input card V11, as documented in Figure B.1a. When this condition is true, VSOP will expect a direct access data set to be designated as Fortran unit "78" in the execution time Job Control Language. The data control block for this dataset is documented in Appendix C (the FUPAR user's manual), and must be specified in the FUPAR job which creates the dataset.

Card V11		FORMAT(6I4,E12.5,6I4,E12.5)
1	NREAD	>100: Read atom densities of fuel type IJ, variant KL from data set 29 (compare NFUTP on card D6) ≤100: Number of atom densities to be specified on subsequent cards V12
2	NCH1	>0: Number of previously specified composition with the same atom densities (card V12)
3	NCH3	>0: Number of a previously specified radial diffusion region with the same geometric data for control rod materials (card V13)
5	NCH5	>0: Number of a previously specified radial diffusion region with the same control poison data (card V14)
6	NREG	>0: Number of radial diffusion region in which the composition is contained =0: Same NREG as for the preceding composition
7	VPART	>0: Volume of composition/volume of diffusion region NREG =0: Use VPART of the preceding composition
8	NHOT	>0: Number of spectrum calculation for this composition. Reflectors use the no. NXS+1 (card A2) =0: Use NHOT of the preceding composition
9	NFDEN	=0: No effect ≠0: Read materials densites for this composition from data set 78
10	NXTRA	=0: No effect >0: Read NXTRA additional number densities from card V12 as well as densities from data set 78
11	NMULT	=0: No effect >0: Card V12 follows with a *multiplication factor* for the density of the indicated material read from data set 78

FIG. B.3a: New specification for VSOP input card V11.

Card V24	FORMAT(18I4)	
1	IFUPAR(1)	=0: No effect. >0: Save one-group neutron flux and cross section data on data set 77.
2	IFUPAR(2)	=0: No effect. >0: Causes TIK data to be saved on data set 38 even when no burnup calculation is performed (must also set JSER=1 on card V2 and IFUPAR(1)>0)

FIG. B.3b: New VSOP input card V24.

Card V25 is read only if IFUPAR(1) > 0.

Card V25	FORMAT(E12.4)	
1	RXPOW	Reactor power (watts) for flux normalization

FIG. B.3c: New VSOP input card V25.

APPENDIX C: STATIONARY PEBBLE BED REACTOR ANALYSIS WITH FUPAR

FUPAR is written in IBM VS-Fortran [I2], and in its present form requires approximately 4000 Kilbytes of RAM to execute. Presently, FUPAR resides on the IBM 3081 mainframe computer at Stone and Webster Engineering Corporation.

This appendix is intended to serve as a user's manual for the FUPAR computer code. FUPAR's input requirements are covered in detail, as well as the data which is necessary to run the code in conjunction with VSOP. Brief descriptions of several subroutines are included, and the more important variables are defined. Instructions for generating data for use either by VSOP or PDIF are included. This appendix will also be available in a separate document with a complete listing of FUPAR (including complete variable maps generated by IBM's VS-Fortran Compiler) for those who desire more detail or wish to expand on the code.

C.1: PREPARATION OF FUPAR INPUT

Table C.1 is a sequential list of all possible FUPAR input, including a brief description and the units of all variables. If the table is unclear, the listing of subroutine INIT should answer any outstanding questions. Several of the input parameters deserve special attention, particularly the run options, the pebble axial velocities, and the fission product chain definition table.

The run option input (the ten elements of the IOP array on card F2) define the manner in which FUPAR is to be run, and have a great influence on the amount and type of input which must be provided. What follows is a brief explanation of the effects of these variables, a summary version of which appears in Table C.1 as well.

IOP(1): This variable controls transfer of fission product generation data to a permament file (Fortran unit "80") for later use by the PDIF program. IOP(1) = 0 implies no storage, and IOP(1) = 1 causes data to be saved. If data is to be saved, the Job Control Language which submits the FUPAR job must define unit 80 to receive data (see Section C.3). (This data is only necessary when "daughter-type" fission products are to be analyzed by PDIF).

IOP(2): This variable controls calculation of collapsed transition matrices. IOP(2) = 0 implies that no core collapsing is to be performed, while IOP(2) $\geq$ 0 indicates that it will be. For Q2D calculations (i.e., when expected values of materials concentrations are to be calculated), IOP(2) must be set equal to 1. For Lagrangian calculations (i.e., which simply track a particle's course through the

reactor). IOP(2) = 2 implies that collapsed transition matrices will be used instead of the full set.

IOP(3): This variable controls calculation of fission product transition matrices. Since this can be the single most time-consuming segment of FUPAR, it is sometimes desirable to omit these calculations (of course, this is only possible once a converged flux shape has been determined). This is useful, for example, when a probabilistic analysis is desired, for which only the heavy metal transitions are necessary. IOP(3) = 0 turns off the FP transition matrix calculations; IOP(3) > 0 allows them to be performed.

IOP(4): This variable controls the output of the fission product transition matrices (assuming they are calculated). IOP(4) = 0 implies no detailed fission product transition matrix output; IOP(4) > 0 prints the FP transition matrices for each core zone.

IOP(5): This variable controls calculation of core-average transition matrices. IOP(5) = 0 omits this calculation, while IOP(5) > 0 allows it to continue. IOP(5) *must* be set greater than zero for Q2D calculations.

IOP(6): This variable controls the overall mode of calculation:

IOP(6) = 0: This runs FUPAR in a Lagrangian-only mode, tracking individual fuel particles through the reactor.

IOP(6) = 1: This runs FUPAR in the Q2D mode, in order to calculate expected isotopic densities as a function of position in the reactor.

IOP(6) = 2: This is the same as IOP(6) = 1, but the PSTAT subroutine is run as well to calculate core statistical

parameters.

Note that to use FUPAR in conjunction with VSOP, IOP(6) must be greater than or equal to 1.

IOP(7): This is the number fission products with non-zero densities in fresh fuel. This variable is used, for example, to include gadolinium burnable poison in the feed fuel elements. When this variable is non-zero, additional input is required which defines the fission products and their initial densities.

IOP(8): This variable controls data storage for both VSOP and PDIF. VSOP data (E-densities of all materials as a function of core position) is saved on Fortran unit "78," and PDIF data (further core parameters) are saved on Fortran unit "79." If IOP(8) indicates data to be stored in either or both of these data sets, the execution-time Job Control Language must define the appropriate data sets (see section C.3 for the data set attributes).

IOP(8) = 0: Do not save any data.

IOP(8) = 1: Save Eulerian materials densities and burnup on direct access unit 78.

IOP(8) = 2: same as above, and store all FUPAR common blocks on Fortran unit 79 as well.

IOP(9): This varible is a general output control. IOP(9) = 0 produces minimal output, and IOP(9) = 3 yields maximum output. Intermediate values produce intermediate amounts.

IOP(10): This variable controls the location of certain input items:

IOP(10) = 0: All input (including neutron fluxes and

position-dependent cross sections) is read from standard input (unit 5).

IOP(10) = 4: Position-dependent one-group neutron flux, fast neutron flux, heavy metal and fission product one-group cross sections are all read from Fortran unit "77" (generated by VSOP).

These are the only two options available for IOP(10).

Calculation of the pebble axial velocities is based on Eq. (3.70), which gives the fresh fuel injection rate as a function of general core and fuel parameters:

$$\dot{K}_f = \frac{P}{B_d\, m_p}$$

where

$\dot{K}_f$ = the fresh fuel injection rate (pebbles/day);

B_d = pebble discharge burnup (MWD/MTHM);

P = reactor thermal power (MWth); and

m_p = heavy metal loading per pebble (MTHM/pebble).

The user must also estimate N (the number of passes a pebble may be recycled prior to discharge), K (the total number of pebbles in the core), and H (the mean core height (in cm)). The average pebble velocity $\bar{u}$ is simply the total distance traversed by a pebble (NH) divided by the average core residence time (in days) $\overline{\Delta t} = \dot{K}_f/K$. Thus, an estimate of the mean pebble axial velocity is given by the relation:

$$\bar{u} = \frac{N\,H}{\overline{\Delta t}} = \frac{\dot{K}_f N\,H}{K} = \frac{P\,N\,H}{K\,B_d\,m_p} \qquad (C.1)$$

For example, if P = 200 MWth, N = 15 passes, H = 943 cm,

K = 360,000 pebbles, B_d = 80,000 MWD/MTHM, and m_p = 7×10^{-6} MTHM/pebble, then $\bar{u}$ = 14.0 cm/day = 1.62×10^{-4} cm/sec (FUPAR requires the latter units). For modular (i.e., tall and slender) HTGR cores, it is sufficient to use $\bar{u}$ as a uniform radial value. In wider cores, significant changes in axial velocity may occur in the radial direction. A radial distribution of velocities u_i may be specified, as long as the pebble mean velocity (weighted by radial zone cross-sectional area) is still $\bar{u}$:

$$\bar{u}\, A_{tot} = \sum_i u_i\, A \qquad (C.2)$$

where A_{tot} is the core's total cross sectional area, and A_i is the cross sectional area of drop zone i. Eq. C. may be used to determine a normalization constant ξ for an experimental velocity distribution v_i:

$$u_i \equiv \xi\, v_i \quad \Rightarrow \quad \xi = \frac{\bar{u}\, A_{tot}}{\sum_i v_i\, A_i} \qquad (C.3)$$

Finally, though FUPAR is most commonly used with the 43-member fission product chain corresponding to the longest chain in VSOP, it is possible for the user to define an arbitrary fission product chain. This is done using the IXFP array, which is input on cards F34. Each element of IXFP may be designated in the form (*iprod*,*ireac*), in which *iprod* represents the index of a product nucleus, and *ireac* the index of a reactant nucleus. The value of the element IXFP(*iprod*,*ireac*) indicates the type of nuclear reaction relating the product to the reactant nucleus.

For the case when *iprod* ≠ *ireac*, there are seven nuclear reactions

which may be indicated. In the discussion which follows, f_i represents the number density of isotope i, ϕ is the one-group neutron flux, $\sigma_{a,i}$ is the absorption cross section of isotope i, and λ_i is the decay constant for isotope i.

IXFP(*iprod,ireac*) = 0: Fission product *iprod* has no source due to nuclear reactions of isotope *ireac*.

IXFP(*iprod,ireac*) = 1: The product is the result of simple neutron absorption by the reactant. That is, the rate of production of isotope *iprod* due to interactions with isotope *ireac* is $(\phi \sigma_{a,ireac} f_{ireac})$.

IXFP(*iprod,ireac*) = 2: The product is the result of simple radioactive decay of the reactant. That is, the rate of production of isotope *iprod* due to interactions with isotope *ireac* is $(\lambda_{ireac} f_{ireac})$.

IXFP(*iprod,ireac*) = 3: The product is one of two decay products, the fraction of which is equal to a_{ireac}. That is, the rate of production of isotope *iprod* due to interactions with isotope *ireac* is given by $(a_{ireac} \lambda_{ireac} f_{ireac})$. The value of a_{ireac} is the *ireac*'th element of the user-input FPA matrix.

IXFP(*iprod,ireac*) = 4: The product is the *other* radioactive decay product of the reactant. That is, the rate of production of isotope *iprod* due to interactions with isotope *ireac* is given by $((1-a_{ireac}) \lambda_{ireac} f_{ireac})$. The constant

a_{ireac} is identical to that in the IXFP = 3 case.

IXFP(*iprod*,*ireac*) = 5: The product is one of two nuclides produced by neutron absorption of the reactant nucleus. The rate of production of isotope *iprod* due to interactions with isotope *ireac* is given by $(b_{ireac}\phi\,\sigma_{a,ireac}f_{ireac})$. The constant b_{ireac} is the *ireac*'th element of the user-input FPB array.

IXFP(*iprod*,*ireac*) = 6: The product is the *other* nuclide resulting from neutron absorption in the reactant nuclide. The rate of production of isotope *iprod* due to interactions with isotope *ireac* is given by $((1-b_{ireac})\phi\,\sigma_{a,ireac}f_{ireac})$.

Two other values for IXFP are possible, which are allowed only for the case of *iprod* = *ireac*. These values indicate the type of removal processes which the nuclide undergoes:

IXFP(*ireac*,*ireac*) = 7: Isotope *ireac* is removed only by neutron absorption.

IXFP(*ireac*,*ireac*) = 8: Isotope *ireac* is removed by radioactive decay as well as neutron absorption.

Should any questions arise, an examination of subroutine CALCLM should quickly answer any remaining questions regarding fission product chain definition. The IXFP arrays currently existing in FUPAR input data sets all apply to the 43-member VSOP fission product chain.

FUPAR may be instructed via the IOP(10) variable on card F2 to seek various input quantities from Fortran units "67" and "77," which have

been generated by previous VSOP calculations. If this is the case, the Job Control Language submitted to execute the FUPAR load module must contain the following data definition statements which indicate the desired data sets to be read:

```
//FT67F001  DD  DSN=uuuuuuuu.vvvvvvvvv.wwwwwwww,DISP=SHR,
                    DCB=(DSORG=DA,BLKSIZE=400)

//FT77F001  DD  DSN=xxxxxxxx.yyyyyyyy.zzzzzzzz,DISP=SHR,
                    DCB=(DSORG=DA,BLKSIZE=400)
```

where "uuuuuuuu.vvvvvvvv.wwwwwwww" and "xxxxxxxx.yyyyyyyy.zzzzzzzz" are the names of the data sets containing "old" and "new" VSOP-generated cross sections and neutron flux distributions. FUPAR will use a weighted average of the neutron fluxes in these data sets, the weighting factors are the variables W1 and W2 defined on input card F42:

$$\begin{bmatrix}\text{FUPAR effective}\\ \text{neutron flux}\end{bmatrix} = W1\times\begin{bmatrix}\text{flux in data}\\ \text{set 67}\end{bmatrix} + W2\times\begin{bmatrix}\text{flux in data}\\ \text{set 77}\end{bmatrix}$$

If a weighted average of two flux distributions is not desired (which may often be the case), simply refer both units 67 and 77 to the same data set.

TABLE C.1: FUPAR INPUT DESCRIPTION

(NOTE: most input cards are actually preceded by a dummy card which describes the input to follow. Only the VSOP data set descriptors are not. See subroutine INIT or an already prepared input deck for a detailed description)

CARD F1: CASE TITLE				
COLUMNS	FORMAT	VARIABLE	UNITS	DESCRIPTION
1-72	9A8	CSTITL	-	one line description of the case to be analyzed

CARD F2: RUN OPTIONS				
COLUMNS	FORMAT	VARIABLE	UNITS	DESCRIPTION
1- 2	I2	IOP(1)	-	controls FP generation rate data storage for PDIF: =0: do not save generation data >0: save data for PDIF calculations on Fortran unit 80
3- 4	I2	IOP(2)	-	transition matrix collapse flag =0: do not collapse any transition matrices >0: compute collapsed matrices
5- 6	I2	IOP(3)	-	fission product inclusion flag =0: do not calculate FP transition matrices ≠0: perform FP calculations
7- 8	I2	IOP(4)	-	transition matrix output control =0: do not print out FP transition matrices ≠0: print out the FP matrices
9-10	I2	IOP(5)	-	core average transition matrix computation control =0: do not calculate core average transition matrices >0: calculate core avg. matrices

TABLE C.1 (CONT'D): FUPAR INPUT DESCRIPTION

11-12	I2	IOP(6)	-	run-mode control =0: Lagrangian only. Calculate particle trajectories through the core =1: Eulerian only. Calculate expected HM and FP densities =2: same as IOP(6)=1, but calculates core statistical parameters as well.
13-14	I2	IOP(7)	-	number of fission products with non-zero initial densities
15-16	I2	IOP(8)	-	data storage control =0: no effect. =1: save E-densities on unit 78 (for VSOP). =2: same as above, also saves contents of all common blocks on unit 79 (for PDIF)
17-18	I2	IOP(9)	-	overall output level control =0: minimal output =1: more output =2: even more output =3: maximum output
19-20	I2	IOP(10)	-	indicates source of cross section and neutron flux data =0: read all input from unit 5 (standard Fortran input) =4: read one-group flux and cross sections from unit 77.

TABLE C.1 (CONT'D): FUPAR INPUT DESCRIPTION

CARD F3: CORE NORMALIZATION INFORMATION				
COLUMNS	FORMAT	VARIABLE	UNITS	DESCRIPTION
1-12	D12.5	GHM	grams	grams of heavy metal per fuel element
13-24	D12.5	RXPOW	MWth	reactor thermal power

CARD F4: PROBLEM SIZE SPECIFICATION				
COLUMNS	FORMAT	VARIABLE	UNITS	DESCRIPTION
1- 4	I4	MFP	-	number of fission products to be included ($\leq$ 43)
5- 8	I4	NHM	-	number isotopes in each heavy metal chain (ALWAYS USE 6)
9-12	I4	NAX	-	number of axial core divisions ($\leq$ 18)
13-16	I4	NRAD	-	number of radial core divisions ($\leq$ 5)

CARD F5: CORE AXIAL MESH SPACING				
COLUMNS	FORMAT	VARIABLE	UNITS	DESCRIPTION
1-72	6D12.5	ZMESH	cm	ZMESH(i) is the axial thickness of the i'th axial core division (i = 1 → 18 max). Use continuation cards if necessary.

TABLE C.1 (CONT'D): FUPAR INPUT DESCRIPTION

CARD F6: RADIAL MESH SPACING				
COLUMNS	FORMAT	VARIABLE	UNITS	DESCRIPTION
1-72	6D12.5	RMESH	cm	RMESH(i) is the radial width of the i'th radial core division Use continuation cards if necessary.

CARD F7: URANIUM CHAIN ABSORPTION CROSS SECTIONS (WHEN IOP(10) = 0) ONE CARD F7 REQUIRED FOR EVERY CORE ZONE				
COLUMNS	FORMAT	VARIABLE	UNITS	DESCRIPTION
1-72	6D12.5	USIGA	barns	USIGA($iax, irad, ihm$) = the absorption cross section for isotope #ihm in core zone ($iax, irad$). Each line represents a new zone, and the axial index increases most rapidly.

CARD F8: URANIUM CHAIN ABSORPTION CROSS SECTIONS (WHEN IOP(10) ≠ 0)				
COLUMNS	FORMAT	VARIABLE	UNITS	DESCRIPTION
1-72	9A8	-	-	A line describing the VSOP-generated data set from which uranium chain absorption cross sections are read. (This line is reprinted in the program output).

TABLE C.1 (CONT'D): FUPAR INPUT DESCRIPTION

CARD F9: URANIUM CHAIN FISSION CROSS SECTIONS (WHEN IOP(10) = 0) ONE CARD F9 REQUIRED FOR EVERY CORE ZONE				
COLUMNS	FORMAT	VARIABLE	UNITS	DESCRIPTION
1-72	6D12.5	USIGF	barns	USIGF($iax, irad, ihm$) = the fission cross section for isotope #ihm in core zone ($iax, irad$). Each line represents a new zone, and the axial index increases most rapidly.

CARD F10: URANIUM CHAIN FISSION CROSS SECTIONS (WHEN IOP(10) ≠ 0)				
COLUMNS	FORMAT	VARIABLE	UNITS	DESCRIPTION
1-72	9A8	-	-	A line describing the VSOP-generated data set from which uranium chain fission cross sections are read. (This line is reprinted in the program output).

CARD F11: URANIUM CHAIN DECAY CONSTANTS				
COLUMNS	FORMAT	VARIABLE	UNITS	DESCRIPTION
1-72	6D12.5	UDLAM	sec^{-1}	UDLAM(i) is the decay constant of the i'th isotope in the uranium heavy metal chain.

TABLE C.1 (CONT'D): FUPAR INPUT DESCRIPTION

CARD F12: THORIUM CHAIN ABSORPTION CROSS SECTIONS
(WHEN IOP(10) = 0)
ONE CARD F12 REQUIRED FOR EVERY CORE ZONE

COLUMNS	FORMAT	VARIABLE	UNITS	DESCRIPTION
1-72	6D12.5	TSIGA	barns	TSIGA(*iax*,*irad*,*ihm*) = the absorption cross section for isotope #*ihm* in core zone (*iax*,*irad*). Each line represents a new zone, and the axial index increases most rapidly.

CARD F13: THORIUM CHAIN ABSORPTION CROSS SECTIONS
(WHEN IOP(10) ≠ 0)

COLUMNS	FORMAT	VARIABLE	UNITS	DESCRIPTION
1-72	9A8	-	-	A line describing the VSOP-generated data set from which thorium chain absorption cross sections are read. (This line is reprinted in the program output).

CARD F14: THORIUM CHAIN FISSION CROSS SECTIONS
(WHEN IOP(10) = 0)
ONE CARD F14 REQUIRED FOR EVERY CORE ZONE

COLUMNS	FORMAT	VARIABLE	UNITS	DESCRIPTION
1-72	6D12.5	TSIGF	barns	TSIGF(*iax*,*irad*,*ihm*) = the fission cross section for isotope #*ihm* in core zone (*iax*,*irad*). Each line represents a new zone, and the axial index increases most rapidly.

TABLE C.1 (CONT'D): FUPAR INPUT DESCRIPTION

CARD F15: THORIUM CHAIN FISSION CROSS SECTIONS (WHEN IOP(10) ≠ 0)				
COLUMNS	FORMAT	VARIABLE	UNITS	DESCRIPTION
1-72	9A8	-	-	A line describing the VSOP-generated data set from which thorium chain fission cross sections are read. (This line is reprinted in the program output).

CARD F16: THORIUM CHAIN DECAY CONSTANTS				
COLUMNS	FORMAT	VARIABLE	UNITS	DESCRIPTION
1-72	6D12.5	TDLAM	sec^{-1}	UTLAM(i) is the decay constant of the i'th isotope in the thorium heavy metal chain.

CARD F17: URANIUM CHAIN CONCENTRATIONS IN FRESH FUEL				
COLUMNS	FORMAT	VARIABLE	UNITS	DESCRIPTION
1-72	6D12.5	U28C0	#/b-cm	U28C0(i) is the homogenized number density (over non-fuel and void volume) of the i'th isotope in the uranium heavy metal chain in a fresh fuel element.

CARD F18: THORIUM CHAIN CONCENTRATIONS IN FRESH FUEL				
COLUMNS	FORMAT	VARIABLE	UNITS	DESCRIPTION
1-72	6D12.5	T02C0	#/b-cm	T02C0(i) is the homogenized number density (over non-fuel and void volume) of the i'th isotope in the thorium heavy metal chain in a fresh fuel element.

TABLE C.1 (CONT'D): FUPAR INPUT DESCRIPTION

CARD F19: RADIAL CORE VOID FRACTIONS				
COLUMNS	FORMAT	VARIABLE	UNITS	DESCRIPTION
1-72	6D12.5	VDFRAC	-	VDFRAC(i) is the void fraction in the i'th radial core zone.

CARD F20: PEBBLE VELOCITY				
COLUMNS	FORMAT	VARIABLE	UNITS	DESCRIPTION
1-72	6D12.5	VPBL	cm/sec	VPBL(i) is the downward pebble velocity in i'th radial core zone.

CARD F21: ONE GROUP NEUTRON FLUX **(WHEN IOP(10) ≠ 2 AND ≠ 4)** ONE CARD F21 REQUIRED FOR EVERY AXIAL CORE DIVISION				
COLUMNS	FORMAT	VARIABLE	UNITS	DESCRIPTION
1-72	6D12.5	FLUXX	#/b-sec	FLUXX(iax,$irad$) is the one-group neutron flux in core zone (iax, $irad$). Each new card contains NRAD flux values corresponding to the radial zones at that axial position.

CARD F22: ONE GROUP NEUTRON FLUX **(WHEN IOP(10) = 2 OR = 4)**				
COLUMNS	FORMAT	VARIABLE	UNITS	DESCRIPTION
1-72	9A8	-	-	A line describing the VSOP-generated data set from which one-group neutron fluxes are read. (This line is reprinted in the program output).

TABLE C.1 (CONT'D): FUPAR INPUT DESCRIPTION

CARD F23: FAST NEUTRON FLUX (WHEN IOP(10) ≠ 2 AND ≠ 4) ONE CARD F23 REQUIRED FOR EVERY AXIAL CORE ZONE				
COLUMNS	FORMAT	VARIABLE	UNITS	DESCRIPTION
1-72	6D12.5	FFLUXX	#/b-sec	FFLUXX(*iax*,*irad*) is the fast neutron flux in core zone (*iax*, *irad*). Each line contains NRAD flux values corresponding to the radial core zones at that axial position.

CARD F24: FAST NEUTRON FLUX (WHEN IOP(10) = 2 OR = 4)				
COLUMNS	FORMAT	VARIABLE	UNITS	DESCRIPTION
1-72	9A8	-	-	A line describing the VSOP-generated data set from which the fast neutron fluxes are read. (This line is reprinted in the program output).

CARD F25: FUEL TEMPERATURES ONE CARD F25 REQUIRED FOR EVERY AXIAL CORE ZONE				
COLUMNS	FORMAT	VARIABLE	UNITS	DESCRIPTION
1-72	6D12.5	TEMPX	deg. C	TEMPX(*iax*,*irad*) is the fuel temperature in core zone (*iax*, *irad*). Each new line contains NRAD values for the next axial zone which correspond to the radial zones at that level.

TABLE C.1 (CONT'D): FUPAR INPUT DESCRIPTION

CARD F26: LIMITS ON FUEL RESIDENCE IN THE REACTOR CORE				
COLUMNS	FORMAT	VARIABLE	UNITS	DESCRIPTION
1- 4	I4	MXPASS	-	The maximum number of passes a fuel element may remain in the core (use 25).
4- 8	I4	MXSTEP	-	The maximum number of core zones a fuel element may pass through (use 25×NRAD)

CARD F27: FUEL DISCHARGE BURNUP				
COLUMNS	FORMAT	VARIABLE	UNITS	DESCRIPTION
1-12	D12.5	BUMAX	MWD/MTHM	Cutoff burnup for discharging fuel elements at core bottom.

CARD F28: CORE-COLLAPSE CONTROL VARIABLE				
COLUMNS	FORMAT	VARIABLE	UNITS	DESCRIPTION
1- 4	I4	ICLLOP	-	=1: Calculate collapsed core transition matrices

CARDS F29 AND F30 ARE REQUIRED ONLY WHEN ICLLOP = 1

CARD F29: NUMBER OF COLLAPSED AXIAL ZONES PER RADIAL ZONE				
COLUMNS	FORMAT	VARIABLE	UNITS	DESCRIPTION
1-20	5I4	NZNAX	-	NZNAX(i) is the number of collapsed axial zones in radial zone i.

TABLE C.1 (CONT'D): FUPAR INPUT DESCRIPTION

CARD F30: DEFINITION OF COLLAPSED CORE ZONES ONE CARD F30 REQUIRED FOR EVERY UN-COLLAPSED AXIAL ZONE.				
COLUMNS	FORMAT	VARIABLE	UNITS	DESCRIPTION
1-20	5I4	NXCOLL	-	NXCOLL(*ic*,*jc*) is the number of un-collapsed axial zones contained within collapsed zone (*ic*,*jc*). NAX input lines are necessary, each new line corresponding to a new collapsed core zone. Use zeroes for zones which do not exist.

CARDS F31 THROUGH F39 ARE REQUIRED ONLY WHEN IOP(3) $\neq$ 0

CARD F31: FISSION PRODUCT ABSORPTION CROSS SECTIONS **(ONLY WHEN IOP(10) = 0)**				
COLUMNS	FORMAT	VARIABLE	UNITS	DESCRIPTION
1-72	6D12.5	FPSIGA	barns	Enter one-group neutron absorption cross sections in order of FUPAR indexing. Use continuation cards if necessary.

CARD F32: FISSION PRODUCT ABSORPTION CROSS SECTIONS **(ONLY WHEN IOP(10) $\neq$ 0)**				
COLUMNS	FORMAT	VARIABLE	UNITS	DESCRIPTION
1-72	9A8			A line describing the VSOP-generated data set from which fission product neutron absorption cross sections are read.

TABLE C.1 (CONT'D): FUPAR INPUT DESCRIPTION

CARD F33: FISSION PRODUCT DECAY CONSTANTS				
COLUMNS	FORMAT	VARIABLE	UNITS	DESCRIPTION
1-72	6D12.5	FPLAM	sec^{-1}	Enter fission product decay constants in the order of FUPAR indexing. Use continuation cards if necessary.

CARD F34: FISSION PRODUCT CHAIN STRUCTURE INDICATOR MATRIX (ONE CARD F34 REQUIRED FOR EACH FISSION PRODUCT)				
COLUMNS	FORMAT	VARIABLE	UNITS	DESCRIPTION
1-72	72I1	IXFP	-	Each card F34 represents the next FP in FUPAR-index order. Each entry corresponds to a parent FP, and the value is a flag indicating the manner of daughter nuclide production. See section C.1 for a complete explanation.

CARD F35: FISSION PRODUCT BRANCHING RATIOS FOR DECAY				
COLUMNS	FORMAT	VARIABLE	UNITS	DESCRIPTION
1-72	6D12.5	FPA	-	Enter the values of FPA for each fission product in FUPAR index order. FPA(*ireac*) determines the fraction of FP *ireac*'s decays which yield the FP *j* with IXFP(*j*,*ireac*) = 3. Use continuation cards if necessary.

TABLE C.1 (CONT'D): FUPAR INPUT DESCRIPTION

CARD F36: FISSION PRODUCT BRANCHING RATIOS FOR ABSORPTION				
COLUMNS	FORMAT	VARIABLE	UNITS	DESCRIPTION
1-72	6D12.5	FPA	-	Enter the values of FPB for each fission product in FUPAR index order. FPB(*ireac*) determines the fraction of FP *ireac*'s absorptions which yield FP *j* with IXFP(*j*,*ireac*) = 5. Use continuation cards if necessary.

CARD F37: FISSION PRODUCT YIELDS FROM THE THORIUM HM CHAIN (ONE CARD F37 REQUIRED FOR EACH FISSION PRODUCT)				
COLUMNS	FORMAT	VARIABLE	UNITS	DESCRIPTION
1-72	6D12.5	Y02	-	Each card contains the fission yields for the FP from the elements of the Th-02 heavy metal chain.

CARD F38: FISSION PRODUCT YIELDS FROM THE URANIUM HM CHAIN (ONE CARD F38 REQUIRED FOR EACH FISSION PRODUCT)				
COLUMNS	FORMAT	VARIABLE	UNITS	DESCRIPTION
1-72	6D12.5	Y28	-	Each card contains the fission yields for the FP from the elements of the U-28 heavy metal chain.

TABLE C.1 (CONT'D): FUPAR INPUT DESCRIPTION

CARD F39: FISSION PRODUCT NAMES				
COLUMNS	FORMAT	VARIABLE	UNITS	DESCRIPTION
1-72	9A8	FPNAM	-	Enter eight-character names for the fission products in FUPAR index order. Use continuation cards if necessary.

CARDS F40 AND F41 REQUIRED ONLY WHEN IOP(7) > 0
(IOP(7) IS EQUAL TO THE NUMBER OF F40/F41 PAIRS WHICH ARE TO BE READ)

CARD F40: FUPAR INDEX OF A FISSION PRODUCT WITH NON-ZERO INITIAL DENSITY				
COLUMNS	FORMAT	VARIABLE	UNITS	DESCRIPTION
1- 2	I2	JFP	-	JFP is the FUPAR index of a fission product whose non-zero initial density follows immediately on card F41.

CARD F41: FISSION PRODUCT INITIAL DENSITY				
COLUMNS	FORMAT	VARIABLE	UNITS	DESCRIPTION
1-12	D12.5	FPBAR	-	Density of fission product JFP (from card F40) in a fresh fuel element.

TABLE C.i (CONT'D): FUPAR INPUT DESCRIPTION

CARD F42: FLUX DISTRIBUTION INPUT WEIGHTING FACTORS				
COLUMNS	FORMAT	VARIABLE	UNITS	DESCRIPTION
1-12	D12.5	W1	-	Weighting factor for the VSOP-generated neutron flux distribution read from data set 67.
13-24	D12.5	W2	-	Weighting factor for the VSOP-generated neutron flux distribution read from data set 77. (Note W1 + W2 must equal 1.0).

C.2: NOTES ON THE STRUCTURE AND EXECUTION OF FUPAR

This section concerns the internal structure and execution of the FUPAR code. A summary definition of important variables and common blocks is included. The details of the transition matrix calculations are presented, and the two primary subroutines, Q2D and PSTAT, are discussed in some detail. Finally, general information regarding the manner in which FUPAR is coded is presented.

C.2.1 FUPAR Common Blocks

All important variables involved in the FUPAR calculations are included in COMMON blocks, enabling access from any subroutine without the need of lengthy and error-prone argument lists. Common blocks are referenced in the source code through the use of INCLUDE statements [I2]. Each such statment refers to the same dataset containing the actual code listing of the common block. In this manner, errors caused by variations in COMMON listings in different subroutines are avoided.

Table C.2 lists the most important common blocks in the FUPAR code, and gives definitions of the important variables in each block.

C.2.2. Calculation of Transition Matrices

The transition matrices defined in Chapter 4 are the heavy metal and fission product density vector transformations associated with each zone in the reactor core. FUPAR calculates and stores these matrices in the following arrays:

UISTMX(*iax,irad,*,**): The elements indicated by "*,*" are the elements of the T^{28} matrix associated with core zone (*iax,irad*).

TISTMX(*iax,irad,*,**): This array contains elements of the T^{02} array for each core zone (*iax,irad*).

FPL(*iax,irad,*,**): This array contains the elements of the L fission product transition matrix for each core zone.

FPJ02(*iax,irad,*,**): This array contains the elements of the J^{02} matrix for each core zone.

FPJ28(*iax,irad,*,**): This array contains the elements of the J^{28} matrix for each core zone.

Secondary transition matrices (for example the D and G matrices for each heavy metal chain) are calculated as well. Here we address only the primary transformation matrices listed above. The additional calculations for the rest are based on Eqs. 4.20 and 4.54.

The T matrices are calculated in subroutine CALCT. In this routine, two outer loops control the IAX and IRAD variables (indicating position within the core) and cover every core zone. Within each zone, subroutine CALCA is called twice: once to calculate the H^{02} matrix and once to calculate the H^{28} matrix. These calculations require position dependent absorption and fission cross sections (usually provided by VSOP). The fuel transit time across each zone is calucated based on the input axial velocity and the axial thickness of the core zone.

The transition matrices are calculated based on the infinite series definition of the exponential matrix:

$$\mathbf{T} \equiv \exp[\mathbf{H}\,\Delta t] \equiv \sum_{i=0}^{\infty} \frac{(\mathbf{H}\,\Delta t)^i}{i!}$$

The sum is evaluated numerically as outlined in Appendix A. Currently, a maximum of 50 terms in the series may be evaluated, and iterations are halted when the maximum residual error is less than 10^{-10}. Should the norm of $\mathbf{H}\Delta t$ be greater than 5 (which would not be compatible with these restrictions), the time interval Δt is split into n equal subintervals $\Delta t'$ such that the norm of $\mathbf{H}\Delta t'$ is less than or equal to five. The partial transition matrix $\mathbf{T}' \equiv \exp[\mathbf{H}\Delta t']$ is evaluated, and the complete transition matrix $\mathbf{T}$ is then calculated from $\mathbf{T} = (\mathbf{T}')^n$.

All elements of every $\mathbf{T}$ matrix must be greater than or equal to zero. If the numerical procedures used to calculate the matrices are not well conditioned, negative elements will probably result. The iteration conditions discussed in the previous paragraph have proven satisfactory. However, future users are advised to occasionally check the contents of the $\mathbf{T}$ arrays to ascertain that these calculations are running smoothly.

The fission product transition matrices are calculated in subroutine CALCLJ. This routine has the same basic structure as CALCT, but the calculations performed within each zone are more complex. Furthermore, special measures are taken for time and memory economy due to the relatively large number of fission products (43) compared to the number of heavy metals per chain (6).

First, the $\mathbf{A}$, $\mathbf{Y}^{02}$, and $\mathbf{Y}^{28}$ coefficient matrices are computed

according to their definitions in Chapter 4. Position-dependent absorption cross sections are required, and are read from Fortran Unit 77 (generated by VSOP) as needed. The program next computes the L transition matrix, defined as $\exp[-A\Delta t]$. To reduce computing time and memory requirements, this calculation takes advantage of the fact that the A matrix is partitioned into several smaller, independent sub-matrices. Physically, this is because the complete fission product chain is composed of several independent sub-chains. The internal behavior of one of these sub-chains is independent of any other. This partitioning is illlustrated in Figure C.?. The exponential function of a partitioned matrix is a matrix with identical partitions, each of which is the exponential function of the corresponding partition in the original matrix. Figure 4.12 illustrated the chain structure in the standard fission product set. There are actually 20 independent sub-chains, quite a few of which are of length 1 or 2 (for which the exponential matrix is particularly simple to evaluate). The longest sub-chain contains 20 isotopes, which is currently the maximum length allowed for any sub-chain.

Subroutine CALCLJ performs a separate exponentiation calculation for each partition in the A matrix. For subchains of length one or two, analytic expressions for the elements of the exponential matrix are used (see section 4.11). For longer subchains, the same iterative routine (SUMEXP) used in the CALCT subroutine is used, with a tolerance level of 10^{-10} and a maximum of 100 iterations. As before, if the norm of $A\Delta t$ exceeds 5.0, the time interval is split n times, a partial transition

IF:

$$\mathbf{A} = \begin{bmatrix} \mathbf{A}_1 & 0 & 0 \\ 0 & \mathbf{A}_2 & 0 \\ 0 & 0 & \mathbf{A}_3 \end{bmatrix}$$

THEN:

$$\exp \mathbf{A} = \begin{bmatrix} \exp \mathbf{A}_1 & 0 & 0 \\ 0 & \exp \mathbf{A}_2 & 0 \\ 0 & 0 & \exp \mathbf{A}_3 \end{bmatrix}$$

AND:

$$\mathbf{A}^{-1} = \begin{bmatrix} (\mathbf{A}_1)^{-1} & 0 & 0 \\ 0 & (\mathbf{A}_2)^{-1} & 0 \\ 0 & 0 & (\mathbf{A}_3)^{-1} \end{bmatrix}$$

FIG. C.1 : Properties of partitioned matrices.

matrix is calculated, and the complete transition matrix is computed as the product of n partial transition matrices.

The J transition matrices are computed according to the approximate formula derived in section 4.7. Not only is the approximate formula simpler and faster to evaluate than the analytic expression (Eq. 4.39), it is much more stable numerically. The program uses an algorithm based on Eq. 4.43. The only part of this calculation of special note is the inversion of the 43x43 **A** matrix. In order to reduce the time necessary for this computation (which must be performed once for every core zone), the inversion makes use of the partitioned nature of **A**. The inverse of a partitioned matrix is simply the matrix of partition inverses.

As in the case of the heavy metal transition matrices, occasional inspection of the fission product transition matrix elements is recommended. The appearance of negative elements in **L**, $\mathbf{J}^{02}$, or $\mathbf{J}^{28}$ indicate numerical problems which must be addressed by altering the iteration conditions.

C.2.3 The Q2D Subroutine

Once transition matrices have been calculated, what remains is to determine the distribution of materials throughout the stationary reactor core. Subroutine Q2D performs these computations in FUPAR.

The Q2D subroutine has three major duties:

(1) Calculation of the expected values of the following parameters as a function of position in the core:

1. Heavy metal number densities
2. Fission product number densities

3. Burnup
4. Fast neutron dose

(2) Calculation of the following overall core parameters:
1. Total number of pebbles in the reactor
2. L-expectation of pebble residence time
3. L-expectation of pebble discharge burnup
4. The fresh fuel injection rate

(3) Save fission product activation rates for use in later calculations. This data is required by the PDIF program for "daughter type" fission products, such as Ag-110m, which arise due to the activation of parent nuclides calculated by FUPAR.

Q2D uses the quasi-two dimensional approximation (see section 4.11) to relate expected values of fuel properties at the beginning of one pass to those at the exit of the previous pass. For small numbers of passes, in which no fuel is discharged, the approximation is exactly correct. Error is only introduced in later passes if some fuel leaving a drop zone is to be discharged while, in reality, other fuel from the same zone is not. In Q2D, the entire flow from a zone is either discharged or recycled depending on the *average* value of burnup leaving the zone. For modular HTGR cores, this is a particularly good approximation, since the power density variance between pebbles at the same pass is much less than the power density variance between pebbles at different passes (see Figure. 4.10).

The algorithm used by subroutine Q2D to calculate the evolution of fuel burnup and heavy metal concentrations is illustrated in Figure

C.2. The program consists of three major loops, representing (1) the pass a pebble is on, (2) the radial drop zone it occupies on that pass, and (3) the axial zone which it is presently occupies. The burnup $\overline{B}$ or heavy metal concentration vector (HMCV) $\overline{\mathbf{n}}$ at the beginning of each pass loop is equal either to an initial value (for the first pass) or the L-expected value from the end of the previous pass loop. This value is the "old" value at the start of each radial loop. Within each radial drop zone, new burnup and HMCV values are calculated for the exit and interior-average of each axial zone.

$$\mathbf{n}_{new} = \mathbf{T}(iax, irad)\ \mathbf{n}_{old}$$

$$B_{new} = B_{old} + \quad (iax, irad)\sigma_f^+(iax, irad)\mathbf{D}(iax, irad)\mathbf{n}_{old}$$

where $(iax, irad)$ represents the axial and radial coordinates of the current core zone. Within each zone, the average values of heavy metal concentrations $\langle \mathbf{n} \rangle$ and burnup $\langle B \rangle$ are computed, and contribute to the E-expectations at that position (denoted by $\mathbf{n}_{Eul}(iax, irad)$ and $B_{Eul}(iax, irad)$). These contributions are weighted by the current value of α, since the final value for W^* has not yet been computed. At the exit of each drop zone, the fuel's average burnup is examined. If the burnup does not exceed the cutoff value for discharge, the flow of fuel leaving that drop zone contritubes to the expected values for the beginning of the next pass. If the fuel is to be discharged, however, the next-pass values will not include a contribution from the discarded fuel. For every pass iw, a conditional probability $p(iw+1|iw)$ is computed as fuel element burnups at drop zone exits are checked. Once all drop zones have been analyzed for a pass, $p(iw+1|iw)$ is used

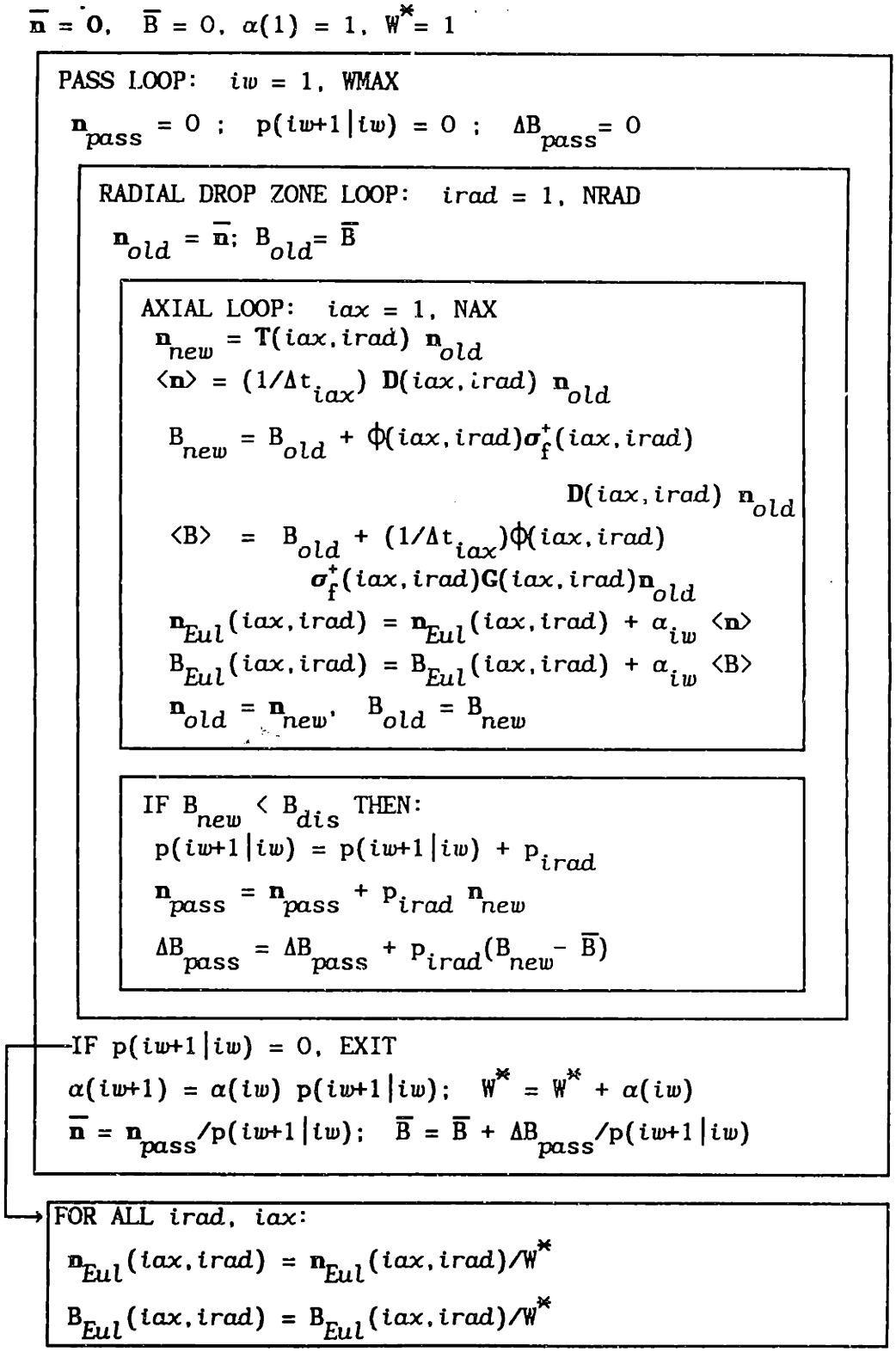

FIG. C.2: Algorithm for calculating steady state burnup and heavy metal concentrations.

to normalize next-pass values. This conditional probability is used to estimate the α parameter for the next pass as well. The L-expected number of passes W^* is equal to the sum of all such α values (see Section 3.5)

Once all fuel has been discharged from the core, the total expected number of passes prior to discharge (W^*) is known. The Eulerian expected values for burnup and HMCVs are divided by W^* (recall that they were initially weighted by α_{iw}, and $\Pi_{iw} \equiv \alpha_{iw}/W^*$). Computation of fission product concentration vectors is analogous to the heavy metal procedure.

C.2.4 The PSTAT Subroutine

Subroutine PSTAT performs the power density variance calculations described in Section 4.10. Its structure is very similar to that of Q2D, with the following exceptions:

(1) No fission product calculations are necessary: The power density and its variance are functions of the heavy metal densities and the neutron flux only. If a converged neutron flux distribution is known, fission product densities do not need to be calculated.

(2) Heavy metal covariance and cross-covariance matrices are computed: These are necessary to calculate the power density variance, as described in Section 4.10.

Output from the PSTAT subroutine includes a core-wide distribution of expected pebble power densities and power density variances, as well as the pass-dependent spectrum of power densities from the highest power density zone.

C.2.5 General Remarks on Coding

Throughout FUPAR, all real numbers are stored as double precision (REAL*8) data. This was found to be necessary for accurate computation of the transition matrices. Throughout the code, the IBM default convention for integer/real variable names has been maintained to avoid confusion.

Finally, much of the computing in FUPAR is done in the form of matrix manipulations. Figure C.3 presents two general algorithms which are frequently used--multiplication of two and three matrices with general dimensions.

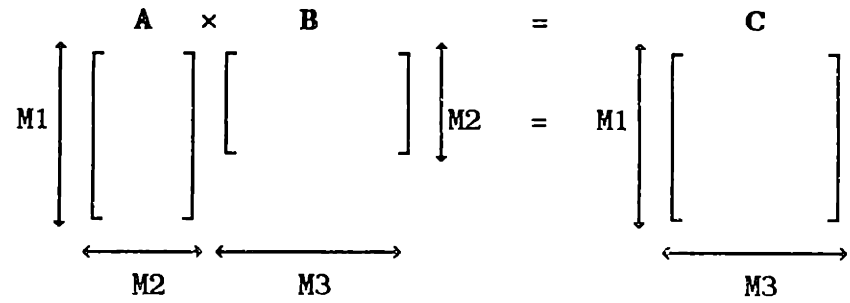


```
      DO 100 jcol = 1, M3
      DO 100 irow = 1, M1
           SUM = 0.0
           DO 50 k = 1, M2
50           SUM = SUM + A(irow,k)*B(k,jcol)
100   C(irow,jcol) = SUM
```

FIG. C.3a: General algorithm for multiplication of two matrices.

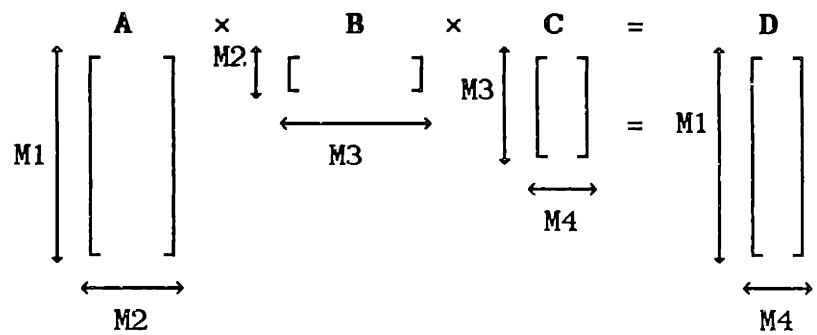


```
      DO 100 jd = 1, M4
      DO 100 id = 1, M1
        SUMABC = 0.0
        DO 75 ja = 1, M2
          SUMBC = 0.0
          DO 50 jb = 1, M3
50          SUMBC = SUMBC + B(ja,jb)*C(jb,jd)
75      SUMABC = SUMABC + A(id,ja)*SUMBC
100   D(id,jd) = SUMABC
```

FIG. C.3b: General algorithm for multiplication of three matrices.

TABLE C.2: FUPAR COMMON BLOCKS AND VARIABLES

COMMON BLOCK NAME: AVTM	
VARIABLE (DIMENSIONS)	DESCRIPTION
AVTU(6,6)	Core average transition matrix for the U-235 heavy metal chain.
AVTT(6,6)	Core average transition matrix for the Th-232 heavy metal chain.
AVL(43,43)	Core average transition matrix for fission product densities.
AVJ28(43,6)	Core average source transition matrix giving U-238 chain contribution to FP density vector.
AVJ02(43,6)	Core average source transition matrix giving Th-232 chain contribution to FP density vector.
AVUDEL(6)	Core average burnup transition matrix for the U-238 chain.
AVTDEL(6)	Core average burnup transition matrix for the Th-232 chain.

COMMON BLOCK NAME: COLCOR	
VARIABLE (DIMENSIONS)	DESCRIPTION
UTHTA (6,5,6,6)	UTHTA(*ic*,*jc*,*,*) is the collapsed U-238 transition matrix in collapsed core zone (*ic*,*jc*).
TTHTA (6,5,6,6)	TTHTA(*ic*,*jc*,*,*) is the collapsed Th-232 transition matrix in collapsed core zone (*ic*,*jc*).
UDLTA(6,5,6)	UDLTA(*ic*,*jc*,*) is the collapsed burnup transition matrix for the U-238 chain in collapsed core zone (*ic*,*jc*).
TDLTA(6,5,6)	TDLTA(*ic*,*jc*,*) is the collapsed burnup transition matrix for the Th-232 chain in collapsed core zone (*ic*,*jc*).

TABLE C.2 (CONT'D): FUPAR COMMON BLOCKS AND VARIABLES

FPLC (6,5,43,43)	FPLC(*ic*,*jc*,*,*) is the collapsed fission product transition matrix in collapsed core zone (*ic*,*jc*).
FPJ02C (6,5,43,6)	FPJ02C(*ic*,*jc*,*,*) is the collapsed source transition matrix from the U-238 chain in collapsed core zone (*ic*,*jc*).
FPJ28C (6,5,43,6)	FPJ28C(*ic*,*jc*,*,*) is the collapsed source transition matrix from the Th-232 chain in collapsed core zone (*ic*,*jc*).
TTRCOL(6,5)	TTRCOL(*ix*,*jc*) is the transit time (sec) through collapsed core zone (*ic*,*jc*).
NZNAX(5)	NZNAX(*irad*) is the number of collapsed axial core zones at radial location *irad*.
NXCOLL(6,5)	NXCOLL(*ic*,*jc*) is the number of *original* core zones contained in collapsed core zone (*ic*,*jc*).
ICLLOP	Overall core collapsing indicator: ICLLOP=0 implies that no collapsing calculations are desired.

COMMON BLOCK NAME: EULER	
VARIABLE (DIMENSIONS)	DESCRIPTION
U28EUL (18,5,6)	U28EUL(*iax*,*irad*,*) is the E-expectation of the U-238 density vector in zone (*iax*,*irad*).
T02EUL (18,5,6)	T02EUL(*iax*,*irad*,*) is the E-expectation of the Th-232 density vector in zone (*iax*,*irad*).
FPEUL (18,5,43)	FPEUL(*iax*,*irad*,*) is the E-expectation of the fission product density vector in (*iax*,*irad*).
BEUL(18,5)	BEUL(*iax*,*irad*) is the E-expectation of fuel burnup (FIMA) in zone (*iax*,*irad*).

TABLE C.2 (CONT'D): FUPAR COMMON BLOCKS AND VARIABLES

BSPEUL (18,5,25)	BSPEUL(*iax*,*irad*,*iw*) is the E-expected burnup (FIMA) of pass-*iw* fuel in zone (*iax*,*irad*).
FDOSE(18,5)	FDOSE(*iax*,*irad*) is the E-expectation of fast neutron fluence (neuts/cm^2) in zone (*iax*,*irad*).
ALPHA(40)	ALPHA(*iw*) is the rate of fuel flow through pass *iw* divided by the fresh fuel injection rate.
RNSTAR	The L-expectation of the number of passes prior to discharge.
NMAX	The maximum number of passes a fuel element can remain in the core prior to discharge.

COMMON BLOCK NAME: FPCNCX	
VARIABLE (DIMENSIONS)	DESCRIPTION
FPL (18,5,43,43)	FPL(*iax*,*irad*,*,*) is the fission product transition matrix in zone (*iax*,*irad*).
FPJ02 (18,5,43,6)	FPJ02(*iax*,*irad*,*,*) is the fission product Th-232 source transition matrix in (*iax*,*irad*).
FPJ28 (18,5,43,6)	FPJ28(*iax*,*irad*,*,*) is the fission product U-238 source transition matrix in (*iax*,*irad*).

COMMON BLOCK NAME: GEOM	
VARIABLE (DIMENSIONS)	DESCRIPTION
NAX	number of axial core subdivisions.
NRAD	number of radial core subdivisions.

TABLE C.2 (CONT'D): FUPAR COMMON BLOCKS AND VARIABLES

RMESH(5)	RMESH(*irad*) is the radial thickness of the *irad*'th radial zone.
ZMESH(18)	ZMESH(*iax*) is the axial thickness of the *iax*'th axial zone.

COMMON BLOCK NAME: HMCNCX	
VARIABLE (DIMENSIONS)	DESCRIPTION
U28AX (18,5,6,6)	U28AX(*iax*,*irad*,*,*) is the **A** matrix for the U-238 chain in zone (*iax*,*irad*).
T02AX (18,5,6,6)	T02AX(*iax*,*irad*,*,*) is the **A** matrix for the Th-232 chain in zone (*iax*,*irad*).
UISTMX (18,5,6,6)	UISTMX(*iax*,*irad*,*,*) is the **T** transition matrix for the U-238 chain in zone (*iax*,*irad*).
TISTMX (18,5,6,6)	TISTMX(*iax*,*irad*,*,*) is the **T** transition matrix for the Th-232 chain in zone (*iax*,*irad*).
U28C0(6)	initial values of the U-238 density vector in fresh fuel elements.
T02C0(6)	initial values of the Th-232 density vector in fresh fuel elements.
U28DX (18,5,6)	U28DX(*iax*,*irad*,*) is the **D** transition matrix for the U-238 chain in zone (*iax*,*irad*).
T02DX (18,5,6)	T02DX(*iax*,*irad*,*) is the **D** transition matrix for the Th-232 chain in zone (*iax*,*irad*).
G02(18,5,6)	G02(*iax*,*irad*,*) is the **G** transition matrix for the Th-232 chain in zone (*iax*,*irad*).
G28(18,5,6)	G28(*iax*,*irad*,*) is the **G** transition matrix for the U-238 chain in zone (*iax*,*irad*).

TABLE C.2 (CONT'D): FUPAR COMMON BLOCKS AND VARIABLES

COMMON BLOCK NAME: KUGELS	
VARIABLE (DIMENSIONS)	DESCRIPTION
GHM	heavy metal loading of a fresh fuel element (grams)
RXPOW	reactor thermal power (MW)
XBD	L-expectation of pebble discharge burnup (MWD/MTHM)
XTRES	L-expectation of pebble core residence time (days)
XKTOT	Total number of pebbles in the reactor core

COMMON BLOCK NAME: NMATLS	
VARIABLE (DIMENSIONS)	DESCRIPTION
NHM	Number of isotopes in each heavy metal chain
MFP	Number of fission products

COMMON BLOCK NAME: NUCDTA	
VARIABLE (DIMENSIONS)	DESCRIPTION
USIGA(18,5,6)	USIGA(*iax,irad,ihm*) is the absorption cross section (b) for isotope *ihm* in the U-235 chain in core zone (*iax,irad*).
USIGF(18,5,6)	USIGF(*iax,irad,ihm*) is the fission cross section (b) for isotope *ihm* in the U-235 chain in core zone (*iax,irad*).

TABLE C.2 (CONT'D): FUPAR COMMON BLOCKS AND VARIABLES

UDLAM(6)	UDLAM(*ihm*) is the decay constant (sec^{-1}) of isotope *ihm* in the U-235 chain.
TSIGA(18,5,6)	TSIGA(*iax,irad,ihm*) is the absorption cross section (b) for isotope *ihm* in the Th-232 chain in core zone (*iax,irad*).
TSIGF(18,5,6)	TSIGF(*iax,irad,ihm*) is the fission cross section (b) for isotope *ihm* in the Th-235 chain in core zone (*iax,irad*).
TDLAM(6)	TDLAM(*ihm*) is the decay constant (sec^{-1}) of isotope *ihm* in the Th-232 chain.
FPSIGA(43)	FPSIGA(*ifp*) is the absorption cross section (b) of the *ifp*'th fission product.
FPLAM(43)	FPLAM(*ifp*) is the decay constant (sec^{-1}) of the *ifp*'th fission product.
FPA(43)	FPA(*ifp*) is the branching ratio for decay of the *ifp*'th fission product (see section C.1).
FPB(43)	FPB(*ifp*) is the branching ratio for neutron absorption for the *ifp*'th FP (see section C.1).
Y02(43,6)	Y02(*ifp,ihm*) is the fission yield of the *ifp*'th fission product from the *ihm*'th heavy metal from the Th-232 chain.
Y28(43,6)	Y28(*ifp,ihm*) is the fission yield of the *ifp*'th fission product from the *ihm*'th heavy metal from the U-232 chain.
IXFP(43,43)	IXFP(*iprod,ireac*) is an integer flag which indicates the manner in which fission product *iprod* is related to fission product *ireac* (see section C.1 for a complete explanation).

TABLE C.2 (CONT'D): FUPAR COMMON BLOCKS AND VARIABLES

COMMON BLOCK NAME: SAVFPS	
VARIABLE (DIMENSIONS)	DESCRIPTION
JFP	The number of fission product activation rates to be saved for PDIF calculations (≤ 5)
ISAVX(5)	ISAVX(*ifp*) is the FUPAR index of the *ifp*'th fission product whose activation rate is to be save for PDIF calculations
FPED (18,5,25,5)	FPED(*iax*,*irad*,*ipass*,*ifp*) is the volumetric activation rate (reactions/b-cm-sec) of fission product *ifp* during a fuel element's *ipass*'th pass through the core in zone (*iax*,*irad*)

COMMON BLOCK NAME: SUBMX	
VARIABLE (DIMENSIONS)	DESCRIPTION
NPART	The number of independent fission product sub-chains, equal to the number of partitions in the **A** and **L** matrices
MXDIV(20)	MXDIV(*ipart*) is the length of the *ipart*'th fission product chain, equal to the dimension of the *ipart*'th partition of the **A** matrix
NCHAIN	Maximum dimension of a fission product partition (20)

COMMON BLOCK NAME: TDCORE	
VARIABLE (DIMENSIONS)	DESCRIPTION
FLUXX(18,5)	FLUXX(*iax*,*irad*) is the one-group neutron flux (neuts/b-cm-sec) in core zone (*iax*,*irad*)

TABLE C.2 (CONT'D): FUPAR COMMON BLOCKS AND VARIABLES

FFLUXX(18,5)	FFLUXX(*iax,irad*) is the fast neutron flux (neuts/b-cm-sec) in core zone (*iax,irad*)
TEMPX(18,5)	TEMPX(*iax,irad*) is the average fuel temperature (C) in core zone (*iax,irad*)
VPBL(5)	VPBL(*irad*) is the axial pebble velocity (cm/s) in radial zone *irad*
TTRANS(18,5)	TTRANS(*iax,irad*) is the transit time (s) for a pebble through core zone (*iax,irad*)
VDFRAC(5)	VDFRAC(*irad*) is the void fraction in radial zone *irad*
RPROB(5)	RPROB(*irad*) is the probability that on any pass a pebble will travel through a drop zone with index equal to or less than *irad*
RIPROB(5)	RIPROB(*irad*) is the *incremental* drop probability, that on any pass a pebble will travel through drop zone *irad*

COMMON BLOCK NAME: TRAJEC	
VARIABLE (DIMENSIONS)	DESCRIPTION
FIMAMX	Cutoff burnup for discharge in units of FIMA
BUMAX	Cutoff burnup for discharge in MWD/MTHM
CONCO	Heavy metal density (atoms/b-cm) in fresh fuel

C.3: STORING DATA FOR USE WITH VSOP AND PDIF

FUPAR can be instructed to save data in three different Fortran data sets for use in other programs. Two actions are necessary to store a particular set of data:

(1) The FUPAR input deck for the job which is to save data must indicate which (if any) type of data storage operation is to take place; and

(2) The Job Control Language (JCL) submitted at the time of FUPAR execution must contain Data Definition statements which define data sets to receive the data.

FUPAR can save Eulerian number densities of heavy metal and fission product isotopes for use by VSOP. The Fortran unit number to which this data is written is "78." To instruct FUPAR to save this data, IOP(8) must be set equal to "1" on input card F2. In addition, the JCL submitted to run FUPAR must contain the following Data Definition statement:

```
//F178F001  DD  UNIT=DISK,SPACE=(240,(100,10),RLSE),DISP=(NEW,CATLG),
                DCB=(DSORG=DA,BLKSIZE=400,RECFM=F),
                DSN=xxxxxxxx.yyyyyyyy.zzzzzzzz
```

where "xxxxxxxx.yyyyyyyy.zzzzzzzz" is the name of the data set to receive the materials densities.

The second type of data which may be saved is intended for use in the PDIF program. The contents of all major FUPAR common blocks at the end of execution may be saved on Fortran Unit 79. FUPAR is instructed

to save this data by setting IOP(8) equal to 2 on input card F2. In addition, the JCL submitted to run FUPAR must contain the following data definition statement:

```
//FT79F001  DD  DSN=xxxxxxxx.yyyyyyyy.zzzzzzzz,DISP=OLD
```

where "xxxxxxxx.yyyyyyyy.zzzzzzzz" is the name of the data set which is to receive the data. Note that this data set must be previously allocated by the user before FUPAR will write to it.

Finally, FUPAR may be instructed to save the burnup accumulation and activation rates of various fission products as a function of position and pass number for use in PDIF. Even if PDIF does not require any activation rates (which is possible if no "daughter-type" fission products are to be analyzed), this data is still required. PDIF uses the burnup information to compute the birth rate of all types of fission products. To save this data, IOP(1) must be set equal to "1" on card F2, and the following data definition card is necessary:

```
//FT80F001  DD  DSN=xxxxxxxx.yyyyyyyy.zzzzzzzz,DISP=OLD
```

where, once again, "xxxxxxxx.yyyyyyyy.zzzzzzzz" is the name of the data set to receive the FUPAR-generated data. As in the case with Fortran unit 79, this data set must be allocated prior to FUPAR execution.

APPENDIX D: THERMIX AND KONVEK

THERMIX and KONVEK are computer programs developed at KFA Jülich for pebble bed reactor thermal analysis. THERMIX performs solid phase transient heat conduction/radiation calculations, while KONVEK calculates quasi-steady gas flows and temperatures. Both codes are two dimensional in (x,y) or (r,z) geometry. Used iteratively together, the position dependent temperature histories of a pebble bed reactor may be estimated under a wide variety of conditions. The Institut für Reaktorbauelemente (IRB) of KFA has performed extensive experimental validation for the THERMIX/KONVEK system. Details of the experimental program may be found in Ref. V3.

What follows is an abridged translation of sections from Banaschek's report on computational methods for HTGR dynamic behavior [ref. B6]. The basic assumptions and mathematical models of THERMIX/KONVEK are reviewed, as well as the solution techniques employed by the codes. Various possible boundary and initial conditions are discussed, so that the reader can understand the variety of situations to which the programs are applicable.

D.1: The THERMIX Program

D.1.1 General characteristics

THERMIX is designed to model two dimensional non-steady heat conduction processes. The code can operate in (x,y), (r,φ), or (r,z) coordinates, though here we are concerned exclusively with the (r,z) case. The user defines a finite difference grid, into which are

assigned a number of *compositions*. Compositions are treated as homogeneous solid bodies, with properties which reflect their detailed internal structure. Local properties (such as thermal conductivity λ or heat capacity c_p) may be both temperature and fluence dependent. Thermal conductivity may be anisotropic. The code itself contains many such constitutive relations as library functions.

THERMIX employs two types of boundary conditions:

(1) Adiabatic boundary condition: No heat transport is permitted across such a boundary; and

(2) Temperature boundary condition: In this case, a region is coupled (via a heat transfer coefficient α) to another area or fluid zone with preset temperatures (which may be functions of time and position). Use of appropriate α's will approximate other conditions: very small values of α correspond to an adiabatic condition, while very large values imply a fixed temperature condition.

As the solution requires an initial temperature distribution, and many different transient calculations may start from the same initial conditions, THERMIX can also perform a steady state calculation on the same finite difference grid. This simplifies obtaining consistent initial conditions for separate cases.

D.1.2. Basic Model Equations

The term for the homogeneous reactor structure has no direct translation, hence it will be called "Feststoff," the term used by the code's developers. Unsteady thermal diffusion is described by differential equations derived from an energy balance on an

infinitesimal control volume. Heat transport out of the volume is related to the temperature gradient through Fourier's Law of heat conduction:

$$(\rho c)\,\frac{\partial\theta}{\partial t} = -\nabla\cdot\vec{q} + q_N + q_K$$

$$\text{and} \qquad \vec{q} = -\lambda\,\nabla\theta$$

$$\text{imply} \quad (\rho c)\,\frac{\partial\theta}{\partial t} = \nabla\,(\lambda\,\nabla\theta) + q_N + q_K \qquad \text{(D.1)}$$

where

θ = Feststoff temperature;

(ρc) = volumetric heat capacity;

λ = *effective* thermal conductivity;

q_N = nuclear heat source density; and

q_K = *convective* heat source density.

There are two important points concerning Eq. D.1. First, radiation heat transfer is accounted for by the effective thermal conductivity λ. This is accomplished by imposing the proper temperature dependence, and is detailed in Ref. V3. λ is made to increase at high temperatures in such a way as to simulate radiative pebble-to-pebble heat transfer. Second, note the presence of a convective heat source density. This is the term which couples the THERMIX conduction solution to the KONVEK convection solution. q_K is a virtual heat source (or sink) whose magnitude and distribution depends on the results of the convection solution.

In cylindrical coordinates, multiply and divide Eq. (D.1) by $dV = (2\pi r\,dr\,dz)$, and recall that $r\,\frac{\partial\theta}{\partial r} = \frac{\partial\theta}{\partial(lnr)}$:

$$(\rho c)\,\frac{\partial\theta}{\partial t}\,dV = d\left[\lambda\,\frac{\partial\theta}{\partial(lnr)}\right] 2\pi\,dz + d\left[\lambda\,\frac{\partial\theta}{\partial z}\right] 2\pi r\,dr + [q_N + q_K]\,dV \qquad \text{(D.2)}$$

This is the basic equation used to model conductive/radiative heat

transport in the homogenous Feststoff regions.

D.1.3. Model Equations for Heterogeneous Regions

The Feststoff concept is most applicable to the reactor structure. The core region, on the other hand, has a distinctly heterogeneous arrangement (surface temperatures of pebbles are not equal to their central temperatures). Only in special cases, such as slow transients with decay heat removal, are the temperature gradients in the pebbles negligible. For power transients, a heterogeneous model is employed.

A fuel element is modeled as one-dimensional and spherically symmetric. The nuclear heat source within the pebble is homogenized over the entire fueled region. At the pebble surface, heat is removed via "macroscopic" heat conduction in the pebble bed ($Q_{\lambda s}$) and transfer to the gas (Q_K) (the "s" in $Q_{\lambda s}$ denotes "schüttung," German for "bed"). Within the fuel element (or "BE" for Brennelement), the heat conduction equation is:

$$(\rho c)_B \frac{\partial \theta}{\partial t} dV_B = 4\pi \lambda_B d\left[R^2 \frac{\partial \theta}{\partial R}\right] + q_{nB} dV_B \qquad (D.3)$$

where:

R = local radial coordinate within a fuel element;

θ = fuel element temperature (function of r, z, and R);

$(\rho c)_B$ = volumetric heat capacity within the fuel element;

λ_B = thermal conductivity of a fuel element;

q_{nB} = nuclear heat source per unit of fuel element volume.

The fuel element temperature calculation uses the following boundary conditions at R=0 (pebble center) and $R=R_a$ (pebble outer surface):

$$@\ R = 0: \qquad \left.\frac{\partial\theta}{\partial R}\right|_{R=0} = 0; \tag{D.4a}$$

$$\text{and } @\ R = R_a: \qquad 4\pi R_a^2 \lambda_B \left.\frac{\partial\theta}{\partial R}\right|_{R=R_a} = \dot{Q}_{\lambda s} + \dot{Q}_K \tag{D.4b}$$

Eq. (D.4b) couples the fuel element calculation with the macroscopic problem through the heat source terms.

D.1.4 Macroscopic Heat Conduction in the Pebble Bed

Heat conduction in the pebble bed is governed by the following equation:

$$q_{\lambda s}\, dV = \nabla\cdot(\lambda\nabla\theta)\,.$$

$$= d\left[\lambda \frac{\partial\theta}{\partial(\ln r)}\right] 2\pi\, dz + d\left[\lambda \frac{\partial\theta}{\partial z}\right] 2\pi r\, dr + [q_N + q_K]\, dV \tag{D.5}$$

Eq. (D.5) is coupled to the boundary condition $\dot{Q}_{\lambda s}$ in the fuel element model:

$$\dot{Q}_{\lambda s} = q_{\lambda s}\,[V_B/(1-\epsilon)] \tag{D.6}$$

where:

V_B = pebble volume = $(4\pi/3)\ R_a^3$; and

ϵ = void fraction.

Note that both the homogeneous and heterogeneous materials are coupled to the gas phase only by means of the convective source/sink density. THERMIX does not determine the convective source/sink distribution; this calculation is performed by KONVEK. THERMIX accepts the convective source distribution as a known input parameter which may vary with time.

D.1.5. Space/Time Discretization

In the discussion which follows, let all points be labelled by the

variables (I,N,K), where (I,N) is the spatial (r,z) coordinate, and K is the local radial coordinate within a pebble. Let time dependence be denoted by the superscripts A for "alte" (old) and N for "neue" (new). Suppose we wish to discretize Eqn. (D.5) above and combine it with Eq. (D.6) for a fuel element in location (I,N). We know that the nuclear heat source from a pebble surface is related to macroscopic pebble bed properties in the following manner:

$$\dot{Q}_{\lambda s} = [V_B/(1-\epsilon)] \left[d\left[\lambda \frac{\partial\theta}{\partial(\ell n r)}\right](2\pi\, dz) + d\left[\lambda \frac{\partial\theta}{\partial z}\right](2\pi r\, dr) \right] (1/dV)$$

Refer now to finite difference mesh in Fig. D.1. Suppose we are interested in evaluating the right-hand side of the above equation at some point (r,z) between the bounds (r_1,z_1) and (r_2,z_2). The derivative of θ with respect to $\ell n r$, for example, is:

$$\frac{\partial\theta}{\partial(\ell n r)} = \frac{\theta(r_2) - \theta}{\ell n r_2 - \ell n r} = \frac{\theta(r_2) - \theta}{\ell n(r_2/r)}$$

Thus, the radial differential becomes:

$$d\left[\lambda \frac{\partial\theta}{\partial(\ell n r)}\right] = \lambda(r_2) \frac{\theta(r_2) - \theta}{\ell n(r_2/r)} + \lambda(r_1) \frac{\theta - \theta(r_1)}{\ell n(r/r_1)}.$$

Similarly, the axial differential may be written as:

$$d\left[\lambda \frac{\partial\theta}{\partial z} \right] = \sum_{i=1}^{2} \lambda(z_i) \left[\frac{\theta(z_i) - \theta}{|z_i - z|} \right]$$

Thus,

$$\dot{Q}_{\lambda s} = (1/\Delta V)\, [V_B/(1-\epsilon)] \left\{ \left[\lambda_{r_2} \frac{\theta(r_2) - \theta}{\ell n(r_2/r)} + \lambda_{r_1} \frac{\theta - \theta(r_1)}{\ell n(r/r_1)}\right](2\pi z\, dz) + \sum_{i=1}^{2} \lambda(z_i) \left[\frac{\theta(z_i) - \theta}{|z_i - z|} \right] A_z \right\} \qquad (D.7)$$

where $\Delta V = A_z \Delta z$, and $A_z = 2\pi r\, dr$. Time dependence will be taken

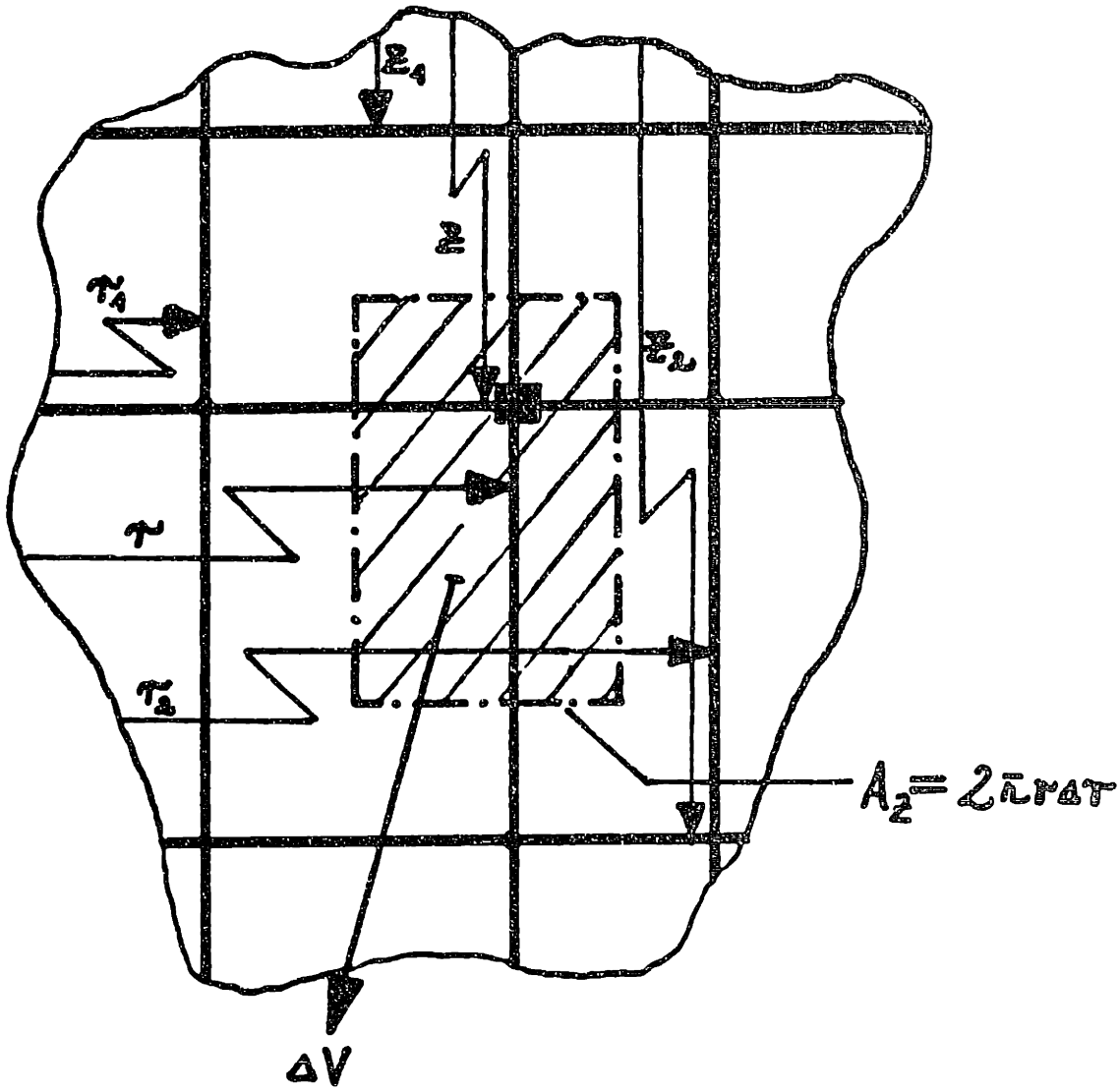

FIG. D.1: Finite difference mesh for heat conduction within the pebble bed [B6].

into account by proper superscripting of the temperatures in Eq. (D.7). Refer now to Fig. D.2, illustrating the spatial discretization of a pebble. The energy balance on the K'th shell is obtained by combining Eqs. (D.3) and (D.4a and b):

$$(\rho c)_B \, \Delta V_{BK} \frac{d\theta_K}{dt} = W_K(T_{K+1} - T) + W_{K-1}(T_{K-1} - T) + q_{NB}\Delta V_{BK} + \dot{Q}_{\lambda s} + \dot{Q}_K$$

where W_K represents the thermal resistance ("Wiederstand") between the K'th and (K+1)'th shell. Note that the last two terms on the right-hand side ($\dot{Q}_{\lambda s}$ and $\dot{Q}_K$) are only present in the equation for the pebble's outermost shell.

Time discretization is accomplished as follows: for any time derivitive on the left-hand side of an equation, use this approximation:

$$\frac{d\theta}{dt} = \frac{\theta^N - \theta^A}{\Delta t}. \qquad (D.9)$$

For temperatures on the right-hand sides of equations, use an implicit approximation:

$$\theta(I,N,K) = (½)[\theta^A(I,N,K) + \theta^N(I,N,K)] \qquad (D.10)$$

When Eqs. (D.7), (D.9), and (D.10) are substituted into Eq. (D.8), a system of equations for $\theta(I,N,K)$ is obtained for each time step. An implicit iterative procedure is used to obtain a solution. For typical mesh sizes, each time step may have on the order of 10^3 to 10^4 unknowns.

Since the time/temperature dependent parameters (such as thermal conductivities) may be non-linear, it is undesirable for large temperature differences to occur in any single time step. Thus, time steps are limited in duration to minimize non-linearities in parameters.

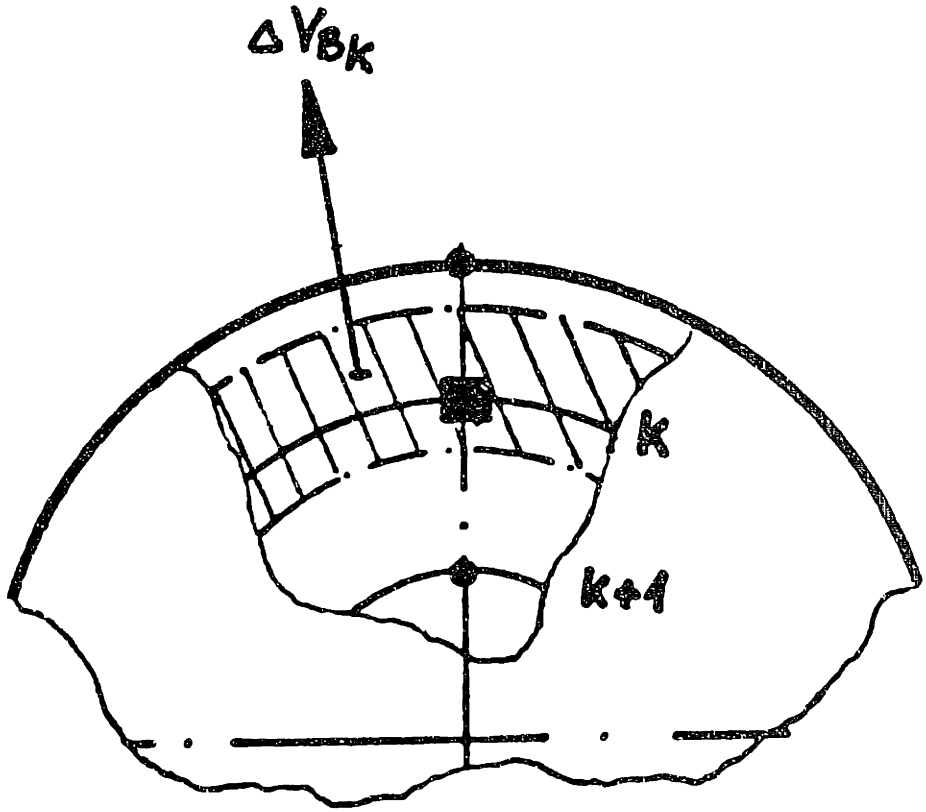

FIG. D.2: Finite difference mesh for heat conduction within a pebble fuel element [B6].

Coefficients at the beginning of a new time step are recalculated after a pre-determined number of steps. More details on the iterative solution method may be found in Ref. B.6

D.2: The KONVEK Program

KONVEK solves for the quasi-stationary two-dimensional gas phase flow and temperature distributions within the pebble bed core. The solution area is a finite difference mesh congruent to that for the THERMIX calculation. Modelling equations are solved partially by means of finite differences, and partially through use of "coarse mesh" techniques.

As in THERMIX, the mesh is covered with compositions, within which uniform hydraulic properties (porosity, hydraulic diameter, etc.) and interior geometry are assumed. KONVEK treats the compositions as porous bodies. Constitutive relations for the regions (pressure drop correlations, for example) may be anisotropic.

In addition to the homogeneous regions described above, KONVEK has three types of special compositions:

(1) Non-flow regions: This designation allows particular regions to be taken out of the calculation (internal or external boundaries, for example).

(2) One-dimensional flow regions: Within such a zone the gas flow may only be parallel or perpindicular to the z axis. The bottom reflector, for example, is treated in this way.

(3) Zones with no pressure loss: These zones couple all adjacent grid points with a homogenous plenum pressure. Flow within the cavity is determined by means of mass conservation alone.

Boundary conditions are partially input by the user and partially generated by KONVEK with the aid of input data. In general, there are

four types of boundary conditions:

(1) Kinematic flow conditions: No mass flow component is allowed normal to these boundaries.

(2) Pressure or net mass flow conditions: These conditions exist at sources or sinks into the system. KONVEK operates internally with pressure boundary conditions. In the course of the flow calculation, these are adjusted to fit those demanded by the input.

(3) System pressure: KONVEK operates internally with a relative pressure field only, so the program must be informed by the user of the local absolute pressure. For KONVEK this is the smallest, time-dependent absolute pressure in the system. An equivalent boundary condition would be the system's gas inventory.

(4) Gas temperatures at mass sources/sinks. The user must provide the gas conditions at all such locations.

Solution is accomplished with two independent subprograms: STROEM calculates the flow field given the gas temperature distribution, and GASTEM determines gas temperatures for a known gas flow distribution. STROEM and GASTEM are brought to convergence through outer iterations.

D.2.1 Model for Determining Pressure Field and Flow

Subprogram STROEM determines the relative pressure field and mass flow vectors for a known gas temperature state. Application of the mass and momentum conservation equations yields the flow field; the energy equation is solved separately in GASTEM. Conservation of mass gives:

$$\frac{1}{r}\frac{\partial}{\partial r}[r\,G_r] + \frac{\partial}{\partial z}[G_z] = 0 \qquad (D.11)$$

Conservation of momentum in the r and z directions, respectively, yields:

$$\frac{\partial p}{\partial r} + \xi \frac{|G|}{2\rho} G_r = 0 \qquad \text{(D.12a)}$$

$$\frac{\partial p}{\partial z} + \xi \frac{|G|}{2\rho} G_z - \rho g = 0 \qquad \text{(D.12b)}$$

where:

p_a = absolute pressure = $p + p_{sys}$; (D.13)

ρ = gas density = $\rho(p_a, T_{gas})$; (D.14)

$\vec{G}_r$ = r component of mass flux = $\rho \vec{V}_r$; and

ξ = the friction factor = f(Reynold's number).

Note that the momentum equations (D.12a and b) neglect inertial forces, a reasonable approximation because frictional forces dominate in the pebble bed. The only forces considered are friction, gravity, and pressure.

Since detailed information about the "fine structure" of the flow is not available in the homogenized model, the friction force cannot be determined through shear stress or boundary layer considerations. Instead, empirical correlations are used which relate the friction factor to the Reynolds number of the homogenized flow. These pressure drop laws are strongly non-linear, so an appropriate numerical procedure is necessary. A detailed description may be found in Ref. V3.

D.2.2 Equations for Determination of Gas Temperatures

Subprogram GASTEM calculates the gas temperature field given a mass flow and solid temperature distribution. Solution is accomplished using the energy equation for the gas. The following formulation assumes that the coolant is an ideal gas with constant heat capacity c_p, and neglects

changes in potential and kinetic energy. In (r,z) geometry, the energy equation is:

$$\frac{1}{r}\frac{\partial}{\partial r}\left[r\,\lambda^{r}_{eff}\frac{\partial}{\partial r}T_{fl}\right] + \frac{\partial}{\partial z}\left[\lambda^{z}_{eff}\frac{\partial}{\partial z}T_{fl}\right] + (c_p/r)\,\frac{\partial}{\partial r}\left[r\,T_{fl}G_r\right] + c_p\,\frac{\partial}{\partial z}\left[T_{fl}\,G_z\right] - q_K = 0 \qquad (D.15)$$

where:

T_{fl} = gas temperature;

G_r, G_z = r and z components of mass flow density;

λ^{r}_{eff}, λ^{z}_{eff} = effective thermal conductivities in the gas in the radial and axial directions, respectively;

q_K = heat exchanged (per unit volume) with solid material.

The boundary phenomena which govern heat transfer between gas and solid material are treated in the same way as the friction pressure loss. Local macroscopic heat transfer coefficients (α) are calculated using empirical relations, which are functions of the Nusselt number.

A special feature of flow through pebble beds arises due to the fine structure of the flow. "Flechtströmung," or "braided flow," introduces an additional heat transport mechanism. This effect is included in the model through modification of the semi-empirical correlations for the gas thermal conductivity, and by allowing the conductivity to be anisotropic. The axes of anisotropy are, in reality, not fixed in relation to the coordinate axes but are determined by the direction of the gas flow.

However, this "dispersive" heat transport either *in* or *against* the primary flow direction must, because of its physical origin, be small compared to the convectively transported heat flow. *Crosswise* to the

direction of gas flow, the dispersive heat transfer is due primarily to heat conduction in the gas, and therefore amounts to very little. Therefore, the relation for determination of the effective thermal conductivity perpindicular to the flow direction is used isotropically in GASTEM.

The equations used by GASTEM to solve for temperatures cannot be derived directly from Eq. (D.15) through finite difference methods. Instead, a coarse mesh procedure was developed utilizing analytic solutions which improves numerical stability due to the coarser discretization. The basis for the coarse mesh procedure is illustrated in Fig. D.3.

Gas temperatures at grid point (node) (I,N) of the KONVEK grid are to be determined. The associated balance volume is comprised of the four bordering 1/4-volumes from the four adjacent grid volumes. Each quarter-volume associated with point (I,N) will, in general, have different properties. The model assumes that point (I,N) is coupled with each of the four neighboring grid points by two channels. The state change of the partial mass flows through these channels can be calculated. Combination of the partial mass flows with the corresponding outlet temperatures, taking into account as well the dispersive heat transfer with the neighboring nodes, yields the gas temperature at node (I,N). The partial mass flows are derived from knowledge of the mass flow vectors in the grid (calculated in STROEM), and in each case is exactly half the radial (or axial) component of the appropriate mass flow vector.

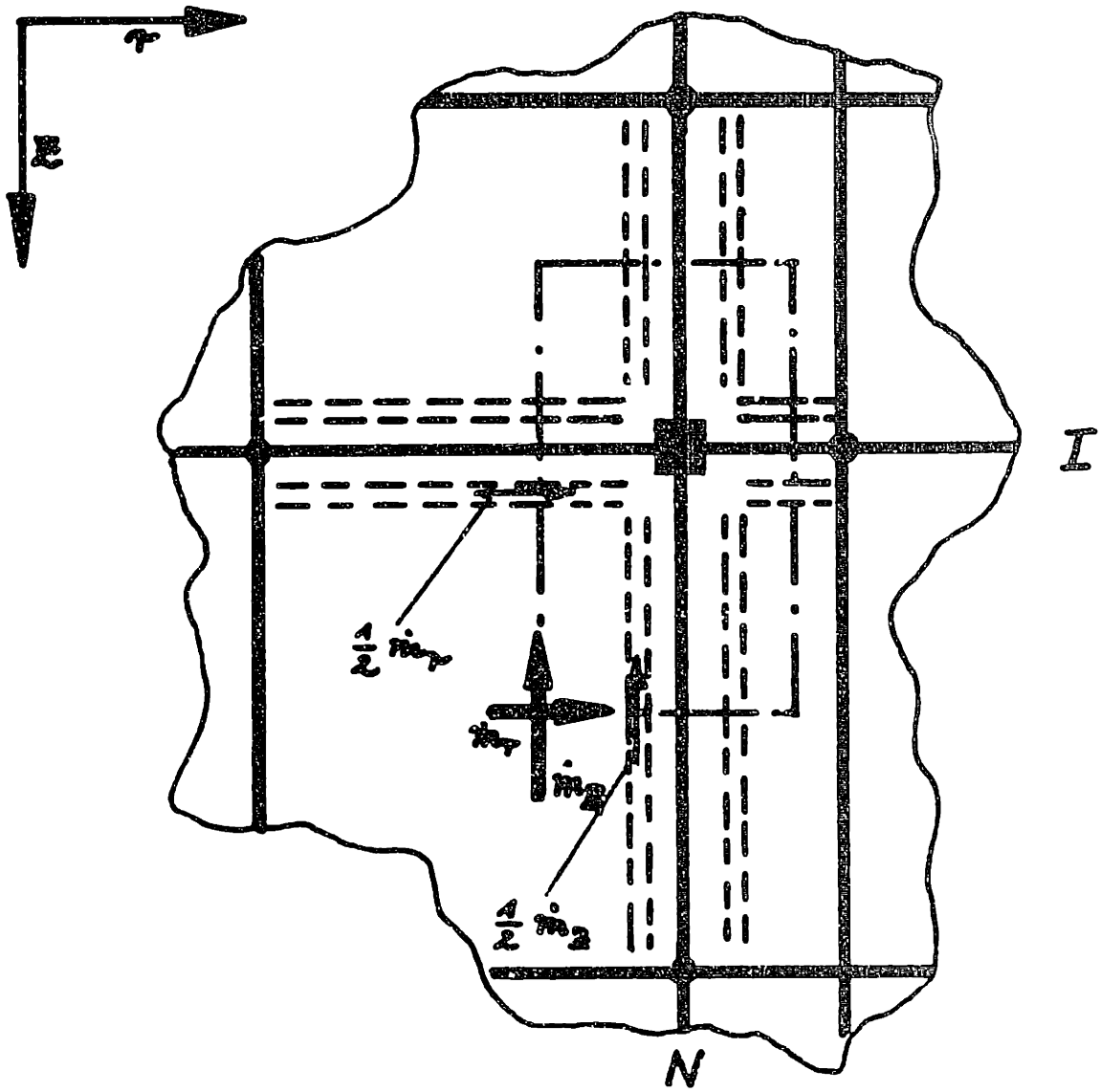

FIG. D.3: Coarse mesh for calculating gas temperatures in KONVEK [B6].

Heat transfer coefficients in the channels are derived from properties of the flow and the material mesh. The product of the mesh's heat transfer coefficient (α) and heat transfer area (F) is alloted to the appropriate direction and mass flow in every axial and radial channel. Axial and radial heat transfer coefficients may differ.

Calculating the state change of the gas is analytic, given the above approximations. The solution shall be derived for a single "partial channel," as illustrated in Fig. D.4.

The state change at grid node "A" of the partial mass flow stream $\dot{m}_t$ between neighboring nodes "N" and "A" is to be calculated (subscript "t" stands for "teil" ≈ "partial"). Let the feststoff temperatures (i.e., the channel wall temperatures) at the nodes be T_A and T_N, and denote the gas entrance temperature by T_N ($T_{fl,e} = T_{fl,N}$). We wish to calculate the gas exit temperature $T_{fl,A}$, as well as the temperature at the control volume boundary, $T_{fl,h}$.

The state change of a gas in a "tube" with variable wall temperature T (taking into account the assujmptions underlying Eq. D.15 and then neglecting dispersive heat transport) is described by:

$$[\ T(x) - T_{fl}(x)\ ]\ \frac{(\alpha F)_t}{\ell_{kan}}\ dx \ = \ \dot{m}_t\ c_p\ dT_{fl} \qquad (D.16)$$

where

x = local coordinate denoting distance in the partial channel;

$T_{fl}(x)$ = fluid temperature at position x in the channel;

$T(x)$ = wall or solid temperature at position x;

ℓ_{kan} = length of the partial channel;

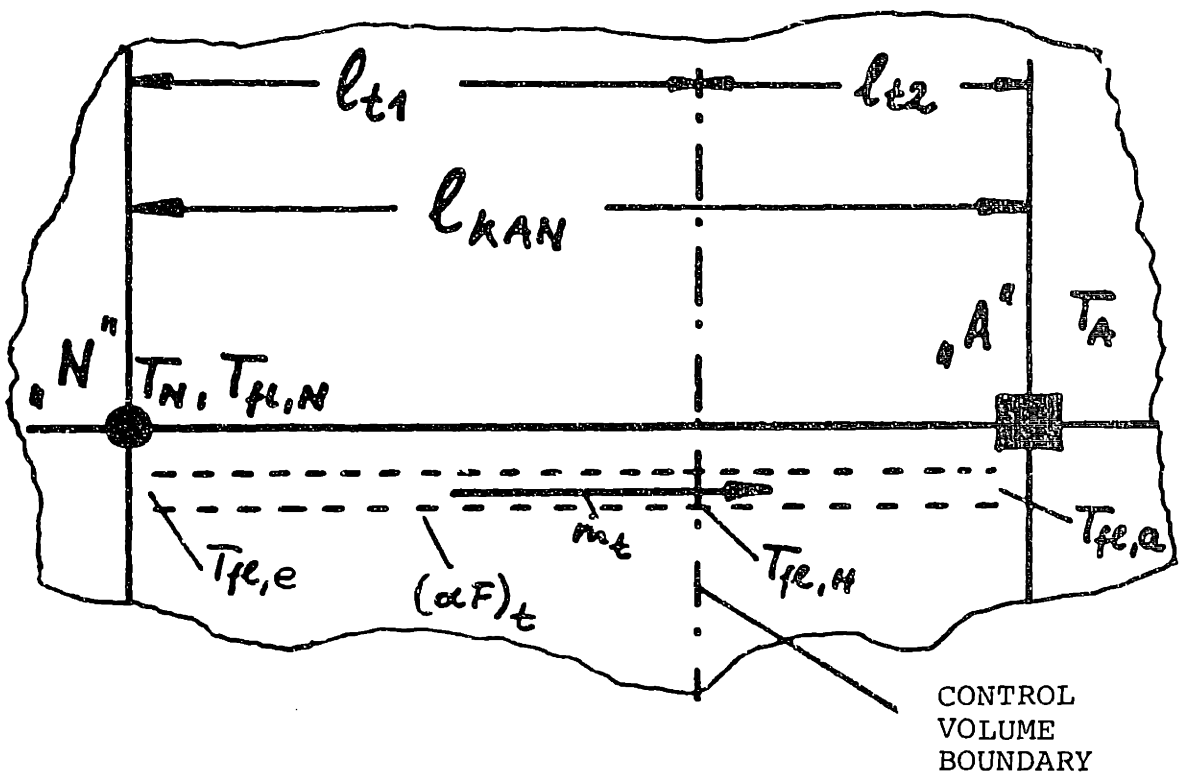

FIG. D.4: Partial channel for calculating gas temperatures [B6].

$(\alpha F)_t$ = heat transfer coefficient associated with the partial mass flow;

c_p = heat capacity of the fluid.

Introduce the "übertemperatur," $T_{ü}$, defined as the difference between fluid and wall temperature:

$$T_{ü}(x) \equiv T_{fl}(x) - T(x) \tag{D.17}$$

and assume linear variation of the wall temperature:

$$T(x) = T_N + \left[\frac{T_A - T_N}{\ell_{kan}}\right] x \tag{D.18}$$

Substitute Eqs (D.17) and (D.18) into Eq. (D.16):

$$\frac{d}{dx} T_{ü} - \frac{(\alpha F)_t}{\dot{m}_t c_p} \cdot \frac{1}{\ell_{kan}} \cdot T_{ü} = - \frac{T_A - T_N}{\ell_{kan}} \tag{D.19}$$

Equation (D.19) may be integrated through determination of homogeneous and particular solutions. The appropriate boundary condition is $T_{ü} = T_{ü,e}$ at $x = 0$. The solution to Eq. (D.19) is thus:

$$T_{ü}(x) = \left\{T_{ü,e} + (T_A - T_N)\frac{\dot{m}_t c_p}{(\alpha F)_t}\right\} \exp\left[\frac{(\alpha F)_t}{\dot{m}_t c_p} \cdot \frac{x}{\ell_{kan}}\right] - (T_A - T_N)\frac{\dot{m}_t c_p}{(\alpha F)_t} \tag{D.20}$$

Eq. (D.20) yields the desired gas temperatures at the channel exit and control volume boundary. The gas temperature at node A is then calculated using all entering mass flows ($\dot{m}_{t,i}$) and channel exit temperatures (T_{fl,a_i}), and also taking heat exchange with neighboring nodes through (effective) heat conduction in the gas phase into account. The balance equation is:

$$\sum_i \dot{m}_{t,i}\, c_{p,i}\, T_{fl,a_i} + \sum \dot{Q}_{\lambda,eff} + \sum \dot{m}_{Q,i}\, c_{p,i} T_{Q,i} = \left\{ \sum \dot{m}_{t,i} + \sum \dot{m}_{Q,i} \right\} c_p\, T_{fl,A} \qquad (D.21)$$

Thus we may solve for the fluid temperature at node A:

$$T_{fl,A} = \frac{\sum_i \dot{m}_{t,i} c_{p,i} T_{fl,a_i} + \sum_i \dot{m}_{Q,} c_{p,i} T_{Q,i} + \sum \dot{Q}_{\lambda,eff}}{\left[\sum_i \dot{m}_{t,i} + \sum_i m_{Q.i} \right] c_{p,A}} \qquad (D.22)$$

Combining Eqs. (D.22) with Eqs. (D.20) and (D.17), we obtain a system of equations to determine the gas temperature field $T_{fl}(I,N)$. KONVEK solves the system using a point relaxation technique with a controlled relaxation factor.

Following the iterative solution for the gas temperature field, the convective heat sources and sinks associated with each grid node is determined. The heat source is simply the algebraic sum of the enthalpy changes in the eight channels within the associated control volume. The partial mass flow presented in Fig. (D.4), for example, gives rise to the following contributions to the convective source at points N and A:

$$\dot{Q}_{N,i} = -\dot{m}_t\, c_p\, (T_{fl,h} - T_{fl,e}) = -m_t\, c_p\, (T_{fl,h} - T_{fl,N})$$

$$\dot{Q}_{A.i} = -\dot{m}_t\, c_p\, (T_{fl,a} - T_{fl,h})$$

Summation of all appropriate contributions yields the entire field of convective heat sources, which is required in THERMIX for calculation of the solid temperatures in the next time step.

D.2.3 Determination of system pressure

Overall system pressure (p_a) was defined in Eq. (D.13) as the smallest absolute pressure in the entire system. p_{sys} is input to the program, and is held constant in the course of the calculations, or changed according to an input time table. This procedure is fine for investigating normal operations, as p_{sys} undergoes only very small fluctuations.

For calculation of accident situations (e.g., decay-heat related operational transients) more exact calculations of transient system pressure may be necessary. For this reason, KONVEK contains an algorithm for determination of system pressure, taking into account not only the core volume but the entire connected primary system as well. The appropriate data is fed to KONVEK by the network program KISMET (not currently available at MIT). The location which is exactly at system pressure does not necessarily lie inside the reactor core. Thus, the calculation begins from a "universal" relative pressure field over all gas-filled portions of the system.

The state equation for every partial volume of the system may be written as an ideal gas equation:

$$p_{sys}V_i + p_iV_i = m_iR_iT_i$$

For HTGR simulation, usually $p_i << p_{sys}$. It is therefore reasonable to neglect the p_iV_i term. However, due to the negligible expense, the universal statement is used in order not to limit the program's applicability. By summing over all partial volumes, we can determine the total inventory of gas in the primary system:

$$M_{gas} = \sum_i m_i$$

Thus, the total system pressure is:

$$p_{sys} = \frac{M_{gas} - \sum_i \frac{p_i V_i}{R_i T_i}}{\sum_i \frac{V_i}{R_i T_i}}$$

APPENDIX E: THE PDIF COMPUTER CODE

This appendix is intended to serve as a brief user's manual for the PDIF code. PDIF currently resides on the IBM-3081 computers at Stone and Webster Engineering Corporation. A description of the input necessary to perform release calculations with PDIF is followed by a table defining the important variables within the code.

Input Preparation

Table E.1 details the input requirements for PDIF. In addition to this card format input, the Job Control Language used to execute the PDIF load module may need to define two permanent data sets. If PDIF is to read THERMIX-generated temperature transient data, Fortran unit "01" must be defined (DISP=OLD) as the THERMIX unit-01 data set containing the desired data. Fortran Units 79 and 80 must also be defined, which are the unit-79 and -80 data sets generated by the FUPAR core analysis job upon which the PDIF job is based.

The user must define a number of run-options, which determine the calculations to be performed by PDIF. The options are chosen by selecting appropriate values of the KOP array on card P2. The choices are:

(1) KOP(1): The first element of the KOP array controls redefinition of the particle mesh for the transient calculation. Set KOP(1) = 1 if redefinition is desired, 0 if not.

(2) KOP(2): This variable is used internally by the program; the user input value is ignored.

TABLE E.1: PDIF INPUT DESCRIPTION

NOTE: "LAYER INDICES" ARE INTEGER FLAGS WHICH INDICATE A PARTICLE COATING LAYER. THEY ARE DEFINED AS FOLLOWS:

1 ⇒ FUEL KERNEL;
2 ⇒ IPyC LAYER;
3 ⇒ SiC LAYER;
4 ⇒ OPyC LAYER
5 ⇒ MATRIX GRAPHITE.

CARD P1: FISSION PRODUCT NAME AND CASE TITLE				
COLUMNS	FORMAT	VARIABLE	UNITS	DESCRIPTION
1-12	A12	$FPNAM	-	Name of the fission product to be analyzed
13-72	5A12	$CASE	-	Description of the case to be analyzed

CARD P2: RUN OPTIONS				
COLUMNS	FORMAT	VARIABLE	UNITS	DESCRIPTION
1- 6	I6	KOP(1)	-	=0: do not redefine the particle mesh for the transient calculation. =1: redefine the particle mesh for the transient calculation
7-12	I6	KOP(2)	-	indicates phase of calculationn (set by program) use 0
13-18	I6	KOP(3)	-	=0: no temperature transient is to be analyzed; =1: temperature transient input to be read from following card input; =2: temperature transient input from Fortran unit 01 (THERMIX generated input).

TABLE E.1 (CONT'D): PDIF INPUT DESCRIPTION

19-24	I6	KOP(4)	-	index of the particle layer whose activation energy is used to release-weight temperatures.
25-30	I6	KOP(5)	-	controls level of output from the steady state transition matrix calculation: =0: no output =1: print **R** matrices only =2: print **R** and **S** matrices =3: print **R**, **S**, and **F** matrices
31-36	I6	KOP(6)	-	fission product source definition: =0: fission product source in kernel and coating layers =1: source in kernel only =2: source from contamination only
37-42	I6	KOP(7)	-	control which calculations are to be performed: =0: steady state and transient calculations; =1: steady state only; =2: transient only; =3: neither steady state nor transient. Use this option to develop particle mesh spacing.
43-48	I6	KOP(8)	-	fission product type: =1: type-1 fission product (has a cumulative yield); =-x: type-2 fission product (parent is the x'th isotope saved by FUPAR)
49-54	I6	KOP(9)	-	fission product type for release rate calculation: =0: metallic fission product =1: gaseous fission product
55-60	I6	KOP(10)	-	not used

TABLE E.I (CONT'D): PDIF INPUT DESCRIPTION

CARD P3: PEBBLE DIMENSIONS				
COLUMNS	FORMAT	VARIABLE	UNITS	DESCRIPTION
1-12	D12.5	RKUGF	m	radius of the fueled region of a pebble
13-24	D12.5	RKUGU	m	radius of the unfueled region

CARD P4: PARTICLES PER PEBBLE AND RECOIL RANGE				
COLUMNS	FORMAT	VARIABLE	UNITS	DESCRIPTION
1-12	D12.5	PPK	-	number of the particles to be analyzed per fuel element.
13-24	D12.5	RANGE	-	fission product recoil range in UO_2.

CARD P5: NUMBER OF SHELLS PER COATING LAYER				
COLUMNS	FORMAT	VARIABLE	UNITS	DESCRIPTION
				NOTE THAT NK+NI+NS+NO MUST BE LESS THAN OR EQUAL TO 39.
1- 6	I6	NK	-	number of shells in the kernel.
7- 12	I6	NI	-	number of shells in the IPyC layer.
13-18	I6	NS	-	number of shells in the SiC layer.
19-24	I6	NO	-	number of shells in the OPyC layer.

TABLE E.I (CONT'D): PDIF INPUT DESCRIPTION

CARD P6: ACTIVATION ENERGIES FOR EFFECTIVE DIFFUSIVITIES				
COLUMNS	FORMAT	VARIABLE	UNITS	DESCRIPTION
1-12	D12.5	ACTEGY (1)	kJ/mole	activation energy for the fission product in the kernel.
13-24	D12.5	ACTEGY (2)	kJ/mole	activation energy for the fission product in the IPyC layer.
25-36	D12.5	ACTEGY (3)	kJ/mole	activation energy for the fission product in the SiC layer.
37-48	D12.5	ACTEGY (4)	kJ/mole	activation energy for the fission product in the OPyC layer.
49-60	D12.5	ACTEGY (5)	kJ/mole	activation energy for the fission product in matrix graphite.

CARD P7: FREQUENCY FACTORS FOR EFFECTIVE DIFFUSIVITIES				
COLUMNS	FORMAT	VARIABLE	UNITS	DESCRIPTION
1-12	D12.5	FRQF(1)	m^2/sec	frequency factor for the fission product in the kernel.
13-24	D12.5	FRQR(2)	m^2/sec	frequency factor for the fission product in the IPyC layer.
25-36	D12.5	FRQF(3)	m^2/sec	frequency factor for the fission product in the SiC layer.
37-48	D12.5	FRQF(4)	m^2/sec	frequency factor for the fission product in the OPyC layer.
49-60	D12.5	FRQF(5)	m^2/sec	frequency factor for the fission product in the IPyC layer.

TABLE E.1 (CONT'D): PDIF INPUT DESCRIPTION

CARD P8: SHELL 1 INNER RADIUS				
COLUMNS	FORMAT	VARIABLE	UNITS	DESCRIPTION
1-12	D12.5	RZERO	m	Inner radius of the particle model's innermost shell.

CARD P9: PARTICLE SHELL DEFINITION EACH CARD P9 DEFINES FOUR SHELLS IN THE PARTICLE MODEL USE AS MANY CARDS AS NECESSARY TO DEFINE ALL SHELLS				
COLUMNS	FORMAT	VARIABLE	UNITS	DESCRIPTION
2	I1	LYRNDX (i)	-	The layer index of the i'th shell in the particle model. Begin with i=1 on the first card.
4-15	D12.5	PRAD(i)	m	Outer radius of the i'th shell in the particle model.
17	I1	LYRNDX (i+1)	-	The layer index of the i+1'th shell in the particle model.
19-30	D12.5	PRAD (i+1)	m	Outer radius of the i+1'th shell in the particle model.
32	I1	LYRNDX (i+2)	-	The layer index of the i+2'th shell in the particle model.
34-45	D12.5	PRAD (i+2)	m	Outer radius of the i+2'th shell in the particle model.
47	I1	LYRNDX (i+3)	-	The layer index of the i+3'th shell in the particle model.
49-60	D12.5	PRAD (i+3)	m	Outer radius of the i+3'th shell in the particle model.

TABLE E.1 (CONT'D): PDIF INPUT DESCRIPTION

CARD P10: DECAY CONSTANT AND CUMULATIVE YIELD				
COLUMNS	FORMAT	VARIABLE	UNITS	DESCRIPTION
1-12	D12.5	DECAY	sec^{-1}	Decay constant of the fission product to be analyzed.
13-24	D12.5	YIELD	-	When KOP(8)=1, this is the cumulative yield of the fission product. When KOP(8)=-x, this is the fraction of parent activations which yield the fission product of interest.

CARD P11: PEBBLE THERMAL CONDUCTIVITY, UO_2 DENSITY, CONTAMINATION FRACTION				
COLUMNS	FORMAT	VARIABLE	UNITS	DESCRIPTION
1-12	D12.5	THCON	W/m-K	Pebble thermal conductivity
13=24	D12.5	RHOUO2	kg/m^3	Density of UO_2 in the kernel
24-36	D12.5	PHIHM	-	Heavy metal contamination fraction.

THE REMAINING CARDS ARE NECESSARY ONLY IF A TRANSIENT CALCULATION IS TO BE PERFORMED (KOP(7) = 0 OR 2)

CARDS P12-P14 ONLY IF KOP(1) = 1

CARD P12: NUMBER OF SHELLS PER COATING LAYER IN THE TRANSIENT MODEL				
COLUMNS	FORMAT	VARIABLE	UNITS	DESCRIPTION
				NOTE THAT NK+NI+NS+NO MUST BE LESS THAN OR EQUAL TO 39.
1- 6	I6	NK	-	number of shells in the kernel.

TABLE E.1 (CONT'D): FDIF INPUT DESCRIPTION

7- 12	I6	NI	-	number of shells in the IPyC layer.
13-18	I6	NS	-	number of shells in the SiC layer.
19-24	I6	NO	-	number of shells in the OPyC layer.

CARD P13: SHELL 1 INNER RADUIS IN THE TRANSIENT PARTICLE MODEL				
COLUMNS	FORMAT	VARIABLE	UNITS	DESCRIPTION
1-12	D12.5	RZERO	m	Inner radius of the first shell in the transient particle model.

ONE CARD P14 IS REQUIRED FOR EACH SHELL IN THE TRANSIENT PARTICLE MODEL

CARD P14: SHELL DEFINITION IN THE TRANSIENT PARTICLE MODEL				
COLUMNS	FORMAT	VARIABLE	UNITS	DESCRIPTION
1- 3	I3	-	-	Dummy space to indicate the index i of the shell being defined.
5-16	D12.5	PRAD(i)	m	Outer radius of the i'th shell in the transient particle model.
18-19	I2	LYRNDX (i)	-	Layer index of the i'th shell in the transient particle model.
21-22	I2	LYRIN	-	Index of the innermost shell from the steady state particle model which is found in the transient particle model.
24-25	I2	LYROUT	-	Index of the outermost shell from the steady state particle model which is found in the transient particle model.

TABLE E.1 (CONT'D): PDIF INPUT DESCRIPTION

CARD P15: DUMMY CARD INDICATING THE START OF TRANSIENT PHASE INPUT

CARD P16: PDIF AND THERMIX CORE MESH DIMENSIONS				
COLUMNS	FORMAT	VARIABLE	UNITS	DESCRIPTION
1- 6	I6	NAX	-	Number of axial zones in the FUPAR or PDIF core mesh (≤18).
7-12	I6	NRAD	-	Number of radial zones in the FUPAR or PDIF core mesh (≤5).
13-18	I6	NZ	-	Number of axial intervals in the THERMIX core mesh.
19-24	I6	NR	-	Number of radial intervals in the THERMIX core mesh.

CARD P17: RADIAL MESH INTERVALS IN THE PDIF CORE MODEL (ENTER ZEROS FOR LAYERS WHICH ARE NOT MODELED)				
COLUMNS	FORMAT	VARIABLE	UNITS	DESCRIPTION
1-12	D12.5	RMESH(1)	m	Radius of the inner PDIF core zone.
13-24	D12.5	RMESH(2)	m	Thickness of the second PDIF core zone.
25-36	D12.5	RMESH(3)	m	Thickness of the third PDIF core zone.
37-48	D12.5	RMESH(4)	m	Thickness of the fourth PDIF core zone.
49-60	D12.5	RMESH(5)	m	Thickness of the fifth PDIF core zone.

TABLE E.i (CONT'D): PDIF INPUT DESCRIPTION

CARD P18: AXIAL MESH INTERVALS IN THE PDIF CORE MODEL (EACH CARD HAS WIDTHS OF 6 AXIAL ZONES--USE CONTINUATION CARDS AS NECESSARY)				
COLUMNS	FORMAT	VARIABLE	UNITS	DESCRIPTION
1-12	D12.5	RMESH(i)	m	Axial thickness of the i'th PDIF core zone. Begin with i=1 on the first card.
13-24	D12.5	RMESH (i+1)	m	Axial thickness of PDIF layer i+1.
25-36	D12.5	RMESH (i+2)	m	Axial thickness of PDIF layer i+2.
37-48	D12.5	RMESH (i+3)	m	Axial thickness of PDIF layer i+3.
49-60	D12.5	RMESH (i+4)	m	Axial thickness of PDIF layer i+4.
61-72	D12.5	RMESH (i+5)	m	Axial thickness of PDIF layer i+5.

CARD P19: TRANSIENT TIME STEP AND TRANSITION MATRIX BOUNDS				
COLUMNS	FORMAT	VARIABLE	UNITS	DESCRIPTION
1-12	D12.5	DELT	sec	Lenth of the discrete transient time step.
13-24	D12.5	TLOW	^{o}C	Lowest temperature for transient transition matrices.
25-36	D12.5	THI	^{o}C	Highest temperature for transient transition matrices.

TABLE E.1 (CONT'D): PDIF INPUT DESCRIPTION

CARD P20: TRANSIENT PROBLEM SIZE SPECIFICATION				
COLUMNS	FORMAT	VARIABLE	UNITS	DESCRIPTION
1- 6	I6	NSTEP	-	Number of time steps in the transient.
7-12	I6	NTMX	-	Number of temperatures between TLOW and THI (inclusive) for which transition matrices are to be evaluated.

CARD P21: NUMBER OF ZONES FOR TRANSIENT EVALUATION				
COLUMNS	FORMAT	VARIABLE	UNITS	DESCRIPTION
1- 6	I6	NZONE	-	Number of PDIF zones in which the transient fission product release is to be calculated. If the entire core is to be modeled, use NZONE = NAX×NRAD
7-12	I6	ICORE	-	=0: Each zone to be analyzed will be input on cards P22 which follow; =1: Analyze the entire core.
13-24	I6	IOUT	-	Controls output level for the whole core calculation. Future users are *strongly* advised to select option 0: =0: minimal output =1: some more output =2: maximum output

TABLE E.1 (CONT'D): PDIF INPUT DESCRIPTION

CARDS P22 AND P23 ARE REQUIRED ONLY FOR ICORE = 0

ONE CARD P22 IS NECESSARY FOR EACH PDIF CORE ZONE TO BE ANALYZED

CARD P22: PDIF CORE ZONE IN WHICH RELEASE IS TO BE ANALYZED				
COLUMNS	FORMAT	VARIABLE	UNITS	DESCRIPTION
1- 6	I6	IAX	-	Axial coordinate of a PDIF core zone in which to calculate transient FP release.
7-12	I6	IRAD	-	Radial coordinate of a PDIF core zone in which to calculate transient FP release.
13-24	I6	IOUT	-	Controls level of output from the (IAX,IRAD) calculation: =0: minimum output =1: intermediate output =2: maximum output

ONE CARD P23 IS REQUIRED AFTER EACH CARD P22 IF KOP(3) = 1

CARD P23: USER INPUT TEMPERATURE TRANSIENT (EACH CARD P23 CONTAINS SIX TEMPERATURES FOR SIX STEPS OF THE TRANSIENT. USE CONTINUATION CARDS AS NECESSARY).				
COLUMNS	FORMAT	VARIABLE	UNITS	DESCRIPTION
1-12	D12.5	TEMPX(i)	°C	Zone temperature during the i'th step of the transient. Begin with i=1 on the first line.
13-24	D12.5	TEMPX (i+1)	°C	Zone temperature during the i+1'st step of the transient.
25-36	D12.5	TEMPX (i+2)	°C	Zone temperature during the i+2'd step of the transient.
37-48	D12.5	TEMPX (i+3)	°C	Zone temperature during the i+3'rd step of the transient.

TABLE E.1 (CONT'D): PDIF INPUT DESCRIPTION

49-60	D12.5	TEMPX (i+4)	°C	Zone temperature during the i+4'th step of the transient.
61-72	D12.5	TEMPX (i+5)	°C	Zone temperature during the i+5'th step of the transient.

(3) KOP(3): This variable determines the location of temperature transient input (i.e., temperatures as a function of time during the transient phase of the calculation). KOP(3) = 0 implies that no temperature transient is to be modeled; KOP(3) = 1 causes PDIF to expect manual temperature transient input on card P23; and when KOP(3) = 2 PDIF expects THERMIX-generated transient input from Fortran unit 01.

(4) KOP(4): This variable is the index of the particle component material which is used to "release weight" temperatures in the calculation (see Chapter 6). The index may be 1 through 5, with the following correspondence:

index = 1 ⇒ kernel;
index = 2 ⇒ IPyC layer;
index = 3 ⇒ SiC layer;
index = 4 ⇒ OPyC layer; and
index = 5 ⇒ matrix graphite.

The activation energy of the indicated material is used to weight temperatures when average values are calculated.

(5) KOP(5): KOP(5) controls the level of output from the steady state transition matrix calculation. The user may select a value from 0 to 3; 0 implies minimal output and 3 produces the maximum output. Use of level 3 is advised during the stage of particle mesh definition; this allows the user to see which particle layers need to be altered to reduce or increase the norm of $F\Delta t$ (see Section 6.3).

(6) KOP(6): This variable defines the location of fission product sources in the particle model. KOP(6) = 0 is the "standard" case, with a source in the kernel and a contamination-induced source in the coating layers. KOP(6) = 1 implies a source in the kernel only, and KOP(6) =2 produces a source in the coating layers only.

(7) KOP(7): KOP(7) controls overall type of calculations:

KOP(7) = 0: perform both steady state and transient analyses;

KOP(7) = 1: perform only the steady state analysis;

KOP(7) = 2: perform only the transient analysis; and

KOP(7) = 3: perform no release calculations.

When option 3 is selected, the code calculates all transition matrices but performs no release calculations. This option is recommended for determining an adequate particle mesh spacing.

8. KOP(8): This variable defines the "birth type" of the fission product. Setting KOP(8) = 1 implies a "yield type" or type-1 fission product (see section 6.7). Setting KOP(8) = $-x$ implies that the fission product to be studied is a "daughter type." The activation rate of its parent is the x'th activation rate stored in FUPAR data set 80.

9. KOP(9): This variable allows the user to model either gaseous or metallic FP release. Note that gaseous release during a transient will be zero. KOP(9) = 0 implies that the fission product is to be treated as metallic; KOP(9) = 1 causes PDIF to treat the fission product as a noble gas. If so, the kernel activation energy and frequency factor should

be set equal to the gaseous fission product's *reduced* diffusivity in UO_2. R/B ratios for gaseous FPs during operation are calculated using Booth's formula (see section 6.1)

The user should strive to select as fine a mesh spacing as possible near the particle boundary in order to minimize the amount by which PDIF underestimates fission product release. PDIF is unable to evaluate transition matrices when $\|FAt\| \geq 20$, and will automatically terminate execution should this occur. The user is advised to run the code several times with KOP(5) = 3 (to examine the contents of the F matrix) and KOP(7) = 3 (to avoid release calculations at this stage) to determine the optimal shell structure for the particle.

Finally, Table E.2 lists the common blocks and variables in PDIF.

TABLE E.2: PDIF COMMON BLOCKS AND VARIABLES

COMMON BLOCK NAME: CX	
VARIABLE (DIMENSIONS)	DESCRIPTION
CEUL(18,5,40)	CEUL(*iax*,*irad*,*) is the E-expectation value of the fission product profile in zone (*iax*,*irad*)
REUL(18,5)	REUL(*iax*,*irad*) is the E-expectation of fission product release in zone (*iax*,*irad*).
RPEUL(18,5,25)	RPEUL(*iax*,*irad*,*kpass*) is the E-expected FP release for fuel on its *kpass*'th pass in zone (*iax*,*irad*).
BRATE(18,5,25)	BRATE(*iax*,*irad*,*kpass*) is the E-expected birth rate for the fission product in a *kpass*''th pass fuel element in core zone (*iax*,*irad*).
RECEUL(18,5)	RECEUL(*iax*,*irad*) is the E-expected FP release due to recoil in zone (*iax*,*irad*).

COMMON BLOCK NAME: EULER
PDIF common block EULER is identical to FUPAR common block EULER. See Appendix C for a description.

COMMON BLOCK NAME: FPPARM	
VARIABLE (DIMENSIONS)	DESCRIPTION
DECAY	Fission product decay constant (sec^{-1})
YIELD	For Type-1 nuclides: YIELD is the fission yield of the FP of interest; For Type-2 nuclides: YIELD is the fraction of parent activations yielding the FP of interest

TABLE E.2 (CONT'D): PDIF COMMON BLOCKS AND VARIABLES

RANGE	Recoil range (microns) for the fission product
RECFRC	Fraction of fission products generated which are released due to direct recoil.
$FPNAM	12-character description of the fission product under investigation

COMMON BLOCK NAME: FPARM$	
VARIABLE (DIMENSIONS)	DESCRIPTION
PRAD(40)	PRAD(il) is the outer radius of the il'th shell in the particle diffusion model.
PVOLS(40)	PVOLS(il) is the volume of the il'th shell in the particle diffusion model.
FRQF(5)	FRQF(il) is the frequency factor of the effective one-phase diffusivity of the fission product within particle constituent material il. Index il has the following meaning: il = 1: kernel il = 2: buffer or A3 matrix graphite il = 3: IPyC layer il = 4: SiC layer il = 5: OPyC layer
ACTEGY(5)	ACTEGY(il) is the activation energy of the effective one-phase diffusivity of the fission product within particle constituent material il
RKUGU	Outer radius of the pebble's unfueled region (m)
RKUGF	Outer radius of the pebble's fueled region (m)
RZERO	Inner radius of the innermost shell in the particle diffusion model (m)
NK	Number of kernel shells in the particle model

TABLE E.2 (CONT'D): PDIF COMMON BLOCKS AND VARIABLES

NI	Number of IPyC shells in the particle model
NS	Number of SiC shells in the particle model
NO	Number of OPyC shells in the particle model
NTOT	Total number of shells in the particle model, equal to NK + NI + NS + NO + 1. Must be $\leq$ 40.
LYRNDX(40)	LYRNDX(il) is the material index (see above) of the il'th shell in the particle diffusion model
RHOUO2	Density of uranium dioxide in the fuel kernel (kg/m^3)
PHIHM	Heavy metal contamination fraction
PPK	Number of particles per fuel element

COMMON BLOCK NAME: GEOM
PDIF common block GEOM is identical to FUPAR's common block GEOM. See Appendix C for a description.

COMMON BLOCK NAME: KUGELS
PDIF common block KUGELS is identical to FUPAR's common block KUGELS. See Appendix C for a description.

COMMON BLOCK NAME: SAVFPS
PDIF common block SAVFPS is identical to FUPAR's common block SAVFPS. See Appendix C for a description.

TABLE E.2 (CONT'D): PDIF COMMON BLOCKS AND VARIABLES

COMMON BLOCK NAME: TRMATX	
VARIABLE (DIMENSIONS)	DESCRIPTION
RX(40,40,18,5)	RX(*,*,*iax*,*irad*) is the **R** transition matrix associated with core zone (*iax*,*irad*).
SX(40,40,18,5)	SX(*,*,*iax*,*irad*) is the **S** transition matrix associated with core zone (*iax*,*irad*).
SXUN(40,18,5)	SXUN(*,*iax*,*irad*) is the last row of the **S** transition matrix for core zone (*iax*,*irad*).

COMMON BLOCK NAME: TRMAT$	
VARIABLE (DIMENSIONS)	DESCRIPTION
R$(40,40)	Temporary storage for an **R** transition matrix.
F$(40,40)	Temporary storage for an **F** coefficient matrix.
S$(40,40)	Temporary storage for an **S** transition matrix.
Q$(40)	Temporary storage for a **Q** fission product source vector.

COMMON BLOCK NAME: TTR	
VARIABLE (DIMENSIONS)	DESCRIPTION
TTRAN(500)	TTRAN(*it*) is the fuel temperature at step *it* of the simulated transient (C).
ITRAN(500)	ITRAN(*it*) is the index of the PDIF fuel temperature during step *it* of the transient.

TABLE E.2 (CONT'D): PDIF COMMON BLOCKS AND VARIABLES

TNDX(90)	TNDX(ix) is the PDIF temperature corresponding to temperature index ix (C).
RTRAN(500)	RTRAN(it) is the "release function" (see section 6.7) associated with the fuel temperature during time step it of the transient.
RNDX(90)	RNDX(ix) is the release function of TNDX(ix).

COMMON BLOCK NAME: TRAJEC
PDIF common block TRAJEC is identical to FUPAR common block TRAJEC. See Appendix C for a description.

COMMON BLOCK NAME: TDCORE
PDIF common block TDCORE is identical to FUPAR common block TDCORE. See Appendix C for a description.

COMMON BLOCK NAME: XMESH	
VARIABLE (DIMENSIONS)	DESCRIPTION
RMESH(5)	RMESH($irad$) is the radial width (cm) of the $irad$'th radial drop zone (FUPAR/PDIF coords.)
ZMESH(18)	ZMESH(iax) is the axial thickness (cm) of the iax'th axial core zone in FUPAR/PDIF coords.
AXFRAC(20)	AXFRAC(iax) is the fraction of the axial dimensions of the PDIF zone in question which lies within the axial boundaries of THERMIX zone iax

TABLE E.2 (CONT'D): PDIF COMMON BLOCKS AND VARIABLES

RFRAC(20)	RFRAC(*irad*) is the volume fraction of the radial dimensions of the PDIF zone in question which lies within the radial boundaries of the THERMIX zone *irad*.
IMH	Number of radial subdivisions in the THERMIX core model.
NMH	Number of axial subdivisions in the THERMIX core model.